The Physical Metallurgy of Microalloyed Steels

Also from The Institute of Materials

Titanium Technology in Microalloyed Steels
Edited by T. N. Baker

The Physical Metallurgy of Microalloyed Steels

T. GLADMAN

School of Materials
The University of Leeds, UK



MANEY
FOR THE INSTITUTE OF MATERIALS

BOOK 0792
First published in 1997 by
The Institute of Materials
This paperback edition first published
for the Institute of Materials
in 2002 by
Maney Publishing
1 Carlton House Terrace
London SW1Y 5DB

© The Institute of Materials 1997
All rights reserved

Typeset in the UK by
Tradespools Ltd, Frome, Somerset
Printed and bound in the UK by
Antony Rowe Ltd, Eastbourne

Contents

		Page No.
	Preface	*ix*
	Acknowledgements	*x*
Chapter 1	The Development of Microalloyed Steels	1
	1.1 Development	1
	1.2 Changes in Steel Production	11
	1.2.1 Continuous Casting	11
	1.2.2 Steelmaking Developments	12
	1.2.3 Continuous Annealing	13
	1.3 Scope	14
	References	16
Chapter 2	Microstructure–Property Relationships	19
	2.1 Tensile and Yield Strength	19
	2.2 Dislocations in Metals	23
	2.3 Strengthening Mechanisms	28
	2.3.1 Solid Solution Strengthening	28
	2.3.2 Experimental Observations of Solid Solution Strengthening	32
	2.3.3 Grain Refinement as a Strengthening Mechanism	39
	2.3.4 Values of the Strengthening Coefficient, k_y	42
	2.3.5 Friction Stress	46
	2.3.6 Combined Strengthening Effects	47
	2.3.7 Dispersion Strengthening – the Orowan and Ashby–Orowan Relationships	47
	2.3.8 Other Strengthening Mechanisms	56
	2.4 Toughness of Microalloyed Steels	57
	2.4.1 Theoretical Aspects of the Ductile–Brittle Transition	59
	2.4.2 Effects of Microstructural and Compositional Variables on the Impact Transition Temperature	62
	2.5 Ductile Fracture	69
	2.5.1 Mechanism of Ductile Fracture	69
	References	78
Chapter 3	Solubility of Microalloy Carbides and Nitrides	81
	3.1 Introduction	81
	3.2 Solubility of Individual Compounds	81

		Page No.
	3.2.1 The Solubility Product	82
	3.2.2 Using the Solubility Product Information	83
	3.2.3 Solubility Data	87
	3.2.4 Comparison of the Solubilities of Microalloy Carbides and Nitrides	100
	3.3 Mutually Exclusive Compounds	103
	3.3.1 The Solubility Products	104
	3.3.2 Phase Boundaries	106
	3.4 Carbo-Nitrides with Extended Mutual Solubility	108
	3.5 Complex Carbo-Nitrides	123
	3.6 More Complex Alloy Systems	131
	3.7 Non-Equilibrium Cooling	131
	3.8 Summary	133
	References	135
Chapter 4	Grain Size Control	137
	4.1 Introduction	137
	4.2 Topological Aspects of Granular Arrays	137
	4.2.1 Two-Dimensional Arrays	138
	4.2.2 The Polyhedron	143
	4.2.3 An Array of Polyhedra	144
	4.2.4 Experimental Observations	146
	4.3 Grain Size Measurement	148
	4.3.1 The Comparator Chart Method	149
	4.3.2 The Hayn Intercept Method	150
	4.3.3 Jeffries Planimetric Method	151
	4.3.4 Relationships Between Grain Size Measurements	152
	4.4 Intersections of Polyhedral Grains	154
	4.4.1 Mean Areal Intercept	155
	4.4.2 Mean Linear Intercept	159
	4.5 Grain Growth	164
	4.5.1 Topological or Angle Driven Growth	167
	4.5.2 Curvature Driven	167
	4.5.3 Energy Change Models	170
	4.5.4 Stochastic Models	175
	4.5.5 General Considerations of the Driving Force for Grain Growth	176
	4.6 Inhibition of Grain Growth	176
	4.6.1 Randomly Distributed Second Phase Particles	178
	4.6.2 Grain Boundary Precipitates	180
	4.6.3 Summary of Grain Size Control by Pinning Particles	182
	References	183
Chapter 5	Precipitation Behaviour and Particle Coarsening	185
	5.1 Introduction	185

Page No.

5.2 Precipitation in Austenite 186
5.3 Precipitation During Decomposition of the Austenite 189
5.4 Precipitation in Ferrite 197
5.5 Ostwald Ripening 201
5.5.1 Ostwald Ripening with Bulk Diffusion Control 203
5.5.2 Ostwald Ripening without Bulk Diffusion Control 209
5.6 Summary 210
References 211

Chapter 6 Thermal and Thermomechanical Cycles 213
6.1 Introduction 213
6.2 Normalising Treatments 213
6.2.1 Reaustenitisation and Grain Size 215
6.2.2 Austenite Grain Growth Inhibition During Normalising 218
6.2.3 Cooling from the Normalising Temperature 225
6.2.4 The Role of Microalloys in Normalising 229
6.3 As-Rolled Products 230
6.3.1 Heating and Soaking for Hot Deformation 231
6.3.2 The Hot Deformation Process 231
6.3.3 Static Recrystallisation 235
6.3.4 The Effects of Microalloying Additions on the Evolution of Microstructure During Hot Rolling 240
6.3.5 Controlled Rolling in the Austenite–Ferrite Range 251
6.3.6 Transformation of Austenite to Ferrite in Hot-Rolled and Controlled-Rolled Products 252
6.4 Summary 259
References 260

Chapter 7 Properties and Applications 263
7.1 Introduction 263
7.2 Characteristics of Microalloying Elements 264
7.3 Low Carbon Structural Steels 266
7.3.1 Hot-Rolled Plate Products 266
7.3.2 Normalised Plate 280
7.3.3 Acicular Structures and Sub-Grain Structures 289
7.4 Low Carbon Steel Hot-Rolled Strip 298
7.5 Inclusions and Ductile Fracture 303
7.5.1 Sulphide Shape Control 305
7.5.2 Desulphurisation 310
7.5.3 Deoxidation 313
7.5.4 The Role of Carbides 315
7.6 Low Carbon Cold Rolled and Annealed Strip 317
7.6.1 Formability 318
7.6.2 Interstitial Free Steels 319

		Page No.
	7.6.3 Dual Phase Steels	325
7.7	Medium and High Carbon Steels	336
	7.7.1 Microstructure–Property Relationships in Higher Carbon Steels	337
	7.7.2 Microalloying of Medium and High Carbon Steels	341
	7.7.3 Titanium Nitride Technology	345
7.8	Weldability of Microalloyed Steels	349
	7.8.1 The Welding Process	349
	7.8.2 Practical Welding	351
	7.8.3 Metallurgical Developments in Welds	352
	References	356
	Index	*361*

Preface

The author is not quite old enough to remember the search for the 'philosopher's stone' that would turn base metal into gold, but there has long been a desire for a special kind of 'moon dust', the lightest sprinkling of which would confer magical impovements in properties. Microalloying additions to steels go some way towards reaching this desire, for the addition of less than one part in a thousand can double or even treble the strength of mild steel. Microalloyed steels have found extensive applications, and it has been estimated that they now constitute some 10% of world steel production. The literature on the subject of microalloyed steels is extensive, being spread over a period of forty years, and appearing in conference proceedings, magazines, and journals in all of the major steel producing countries of the world. The sheer volume of the literature suggested to me that a book, covering the basic physical metallurgy principles, would serve as an introduction for newcomers to the subject, and a guide to some of the key developments.

Following my postgraduate studies, I started work at the Swinden Laboratories of the (then) United Steel Companies and was immediately involved with the study of carbon steels and their development. This coincided with the introduction of microalloyed steels. In the ensuing years, I have been associated with their continued development, and the expansion of their production and use, together with the major changes in steel manufacturing methods that occurred in this period.

The subject of microalloyed steels interacts significantly with many aspects of metallurgy such as strengthening mechanisms, toughness, ductility, hot working, cold working and recrystallisation, non-metallic inclusions, transformation characteristics, grain refinement, and weldability, all of which are included in the book, together with basic solubility relationships of the microalloy carbides and nitrides. With such a diversity of metallurgical interest, the subject of microalloyed steels constituted about one half of my final year lectures on the physical metallurgy of ferrous materials. The book is based on an expansion of these lectures, but follows the same basic pattern.

The book attempts to draw together the fundamental physical metallurgy of strengthening mechanisms, ductile fracture, toughness, microalloy carbide and nitride solubilities, precipitation characteristics, hot working, and grain size control, to provide a basis for the control of microstructure, and hence the properties, in microalloyed steels subjected to industrial heat treatments and hot working practices. Examples are given of the application of microalloying in low-carbon high-strength structural steel strip and plate, medium and high carbon steel

forgings, dual phase steels, bainitic steels and interstitial free steels of high formability. These examples require a not inconsiderable data base, much of which I have tried to include in the book, so that the reader can experiment with his/her own ideas of alloy design and the prediction of microstructure and properties. In some areas, the theories and data base are as yet incomplete, and attention is drawn to the need for further work.

The book is intended not only to serve as a text for undergraduate students of metallurgy, materials science and engineering, but also as a comprehensive introduction to the subject of microalloyed steels for post graduate students and for practising metallurgists in the steel manufacturing and user industries.

ACKNOWLEDGEMENTS

The author would like to thank his many friends and colleagues both at Swinden Laboratories, British Steel plc, and in the School of Materials, University of Leeds, for their help and advice. In particular, I would like to acknowledge the guidance and collaboration of Professor Brian Pickering, over the period 1960Å72, at Swinden Laboratories, Mr Mike George who took the first electron micrograph I had seen of what is now known as interphase precipitation (Fig. 2.21), and Dr Andrew Rose for his agreement to include the work on complex carbo nitrides (Section 3.5). I would also like to thank Dr Georgios Fourlaris, University of Leeds, for supplying the original photomicrographs for Fig. 5.5 and 5.6, Dr David Senogles, now at Swinden Laboratories, for Fig. 7.55, and Mrs Mei Zhang and Professor David Edmonds, University of Leeds, for Fig. 7.56.

Copyright permission is gladly acknowledged from Professor M. F. Ashby (Cambridge University), for Fig. 2.4, 2.5 and 2.15, British Steel Technical plc for Fig. 6.9, Professor H. Fischmeister (Chalmers University of Technology) and the Plenum Publishing Corporation for Fig. 5.9, Professor J. J. Jonas (McGill University) for Fig. 6.10, Dr P. Mitchell (Vanitec) for Fig. 7.51, Professor F. B. Pickering and VCH (Weinheim) for Figs. 2.22 and 7.13, Dr Paul Repas (United States Steel Corp.) for Fig. 7.36, and Professor R. A. Smallman (University of Birmingham) for Fig. 2.12. Fig. 3.21 is reprinted with permission from E. K. Storms and N. H. Krikorian, the Journal of Physical Chemistry, 1960, 64, p.1747 - copyright (1960) American Chemical Society. Fig. 4.5 is reprinted with permission from C. S. Smith, Metal Interfaces (1952), ASM International (formerly American Society for Metals) Materials Park, OH, p.65. Other information used is duly acknowledged in the text, captions, and references.

Finally I would like to thank my wife, Dorothy, for her support and patience during the preparation of this book, and her word processing abilities with my almost illegible script.

CHAPTER 1

The Development of Microalloyed Steels

The name 'microalloyed steels' was first applied to a class of higher strength low carbon steels containing small additions of niobium and/or vanadium. Any attempt at a rational definition of microalloying based on the increases in strength produced by small additions would now include aluminium, vanadium, titanium and of course niobium-treated steels. Such steels contain essentially less than 0.1% of the alloying additions used singly or in combination, and yield strength increments of two or three times that of a plain carbon-manganese steel can be attained. The use of boron as a hardenability enhancing agent had been known for many years prior to the development of niobium steels, but the term microalloying had never been applied to the hardenable engineering type steels. Similarly, aluminium treated steels had been employed to produce good combinations of strength and toughness, but had never been referred to as microalloyed steels. It would appear that 'microalloyed steels' as a name was reserved for the steels containing small additions of an alloying element that will produce grain refinement and/or precipitation strengthening by the formation of relatively stable carbides or nitrides. Thus, microalloyed steels will typically contain niobium, titanium or vanadium, either singly or in combination, and their specific effects may be influenced by other alloying additions such as aluminium, boron, or indeed any of the other more conventional alloying elements used in steel manufacture. The effects of the microalloying elements are also strongly influenced by thermal and thermo-mechanical treatments.

1.1 DEVELOPMENT

Niobium had been considered as an additive to steel prior to 1940[1] but the absence of a sophisticated market and the lack of understanding of the use of niobium discouraged any serious developments.[2] Also, as pointed out by Stuart,[3] the known resources of niobium (also known as columbium) were limited at that time, and the niobium produced was in demand for use in tool steels as a substitute for tungsten, and in stainless steels as a stabilising agent against intergranular corrosion because of its high affinity for carbon and nitrogen. The price of niobium was therefore high, but in 1954 the discovery of an extensive ore body in Canada, followed by another discovery in Brazil in 1958 resulted in a dramatic reduction in the price of niobium from $14 US per pound down to $3 US per pound following

these discoveries. Trials to study the effects of additions of niobium were pioneered in the mid-1950s, and the first publications of these effects were by Binder[4] in 1957, and by the Great Lakes Steel Corporation in 1959.[5] There was intense interest in this development, and the subject became the focus of research and development activity in every major steel producing country in the world.

One of the important factors contributing to the interest in these steels was the fact that niobium (and, incidentally, vanadium) showed a low affinity for oxygen, so that additions of these elements could be made to semi-killed steels. For the benefit of the younger reader, it should be pointed out that commercial continuous casting had not yet been developed in the late 1950s and early 1960s, and all steels were ingot cast. In fully deoxidised (i.e. fully-killed) wrought steels, shrinkage during solidification was accommodated by having a feeder-head (a refractory lined metal box on top of the ingot), which kept the top molten and allowed it to fill the shrinkage cavity (pipe) as it formed. After complete solidification and primary rolling, the remnants of the feeder-head and any heavily segregated material at the head/body junction were discarded, and the yield of prime product from a fully killed ingot was typically of the order of 75%. In semi-killed steels, the oxygen level was controlled by small additions of deoxidant, so that carbon monoxide bubbles, resulting from the reaction between dissolved carbon and oxygen in the steel as it cooled, were created and trapped in the solidifying dendrites, and counterbalanced the solidification shrinkage. Thus semi-killed steels, without a feeder-head, formed a solid shell on the sides and top and bottom faces, and the solidification shrinkage was counterbalanced by well distributed carbon monoxide bubbles, rather than having a pronounced central cavity. During primary hot rolling, the pores caused by the carbon monoxide evolution were welded up and the yield of prime product from these ingots was typically in the range of 95–98%. These differences in prime product yield between fully-killed (75% yield) and semi-killed (95–98% yield) steels, were reflected in steel prices, so that additions such as niobium (or vanadium) that could be made using a semi-killed practice would produce cheaper high strength steels. This is an important feature, as normalised steels, grain refined by aluminium additions, were already in existence, but had to be produced as fully-killed steels due to the high affinity of aluminium for oxygen.

It is interesting to note that both research and development were taking place simultaneously. In the United Kingdom, a provisional specification for niobium steel was issued in 1962 as BS1501-59, covering steels for elevated temperature pressure vessels, and as BS968 covering plates and sections, and several thousand tons of these niobium grade steels were produced in the following year. On the research front, by 1963, it had already been established that the as-rolled niobium steels were significantly strengthened by fine precipitates of niobium carbide[6,7,8] and that normalised niobium steels showed a strength commensurate with the grain refining effect of somewhat larger particles, but the nature of the precipitation reaction in the as-rolled condition had not then been fully appreciated. The linear arrays of fine niobium carbide particles had been seen and reported, but the connection with transformation had not been made.

By 1966, the mechanism of 'interphase' precipitation had been discovered,

together with the important role of transformation temperature in controlling the size and spacing of the 'interphase' precipitated particles[9,10] and data was published on the solubility of niobium, vanadium, titanium and aluminium carbides, nitrides, or carbo-nitrides.[11] The basic foundation for an understanding of the dissolution and reprecipitation kinetics of these compounds was now available. The solubility data for these compounds in austenite, also provided the base for a quantitative understanding of the mechanism of austenite grain refinement which plays such an important role in the development of strength and toughness in normalised steels. In 1967, Irvine[12] reviewed the strong tough structural steels that were being produced worldwide. The full data was tabulated and appendicised (becoming known as Irvine's Appendix) and showed that niobium steels featured highly in Canada, Japan, Sweden, Great Britain, and of course the United States of America. In many of these countries, as well as in France and Germany, vanadium was used as either an alternative to niobium, or in conjunction with niobium to enhance the precipitation contribution to yield strength, whilst in Germany, there also were steels containing titanium or titanium with vanadium.

It was already clear that microalloyed steels were an established feature of available steel grades, and that their full potential had not been realised. There was a growing market for these steels, and the factors which encouraged this expansion are numerous and complex. In these early days of the development, however, the driving forces were strictly economics based.

In the construction industry, the materials cost of building projects could be reduced by using higher strength steels with smaller cross sectional areas for a given force resistance. Although the higher strength materials were more highly priced, the cost per unit of strength decreased as the strength level increased. Thus the application of high strength steels in buildings, bridges, and containers could provide direct savings in material costs. In the automotive industry, mainly in connection with heavy goods vehicles, the vehicle weight could be reduced significantly to give increased payloads, thus giving both a cost saving in initial materials and an 'in service' economy from the increased payloads. In the petroleum industry, the use of oil and gas was increasing rapidly at this time, resulting in a need to transport larger volumes over greater distances. Considerable savings were to be had by using larger diameter pipelines and higher pressure transmission. Both of these factors could be achieved economically by the use of higher yield strength steels.

Traditional methods of increasing the *tensile* strength of mild steels had been to increase the carbon and/or manganese content, but such steels obviously had reduced weldability and were prone to weld cracking. The design codes had been related to tensile strengths, with, of course, an appropriate design stress correction factor. A gradual transition to design stresses based on yield strength was occurring, and this enabled the microalloyed steels with their characteristically higher yield strength to be employed without increasing carbon or manganese contents. In fact, the higher strength levels could be attained with much lower carbon and manganese levels, thus improving the weldability. Fabrication methods had moved from riveting and bolting to fusion welding processes in

the 1940s and 1950s, and weldability of the structural steel grades was becoming a very important consideration.

A further factor contributing to the ability of the steel manufacturing companies to offer these microalloyed steels was the technical and scientific expansion that had occurred in virtually all of the major steel producers during the 1950s. Many of the companies had their own well equipped research and development laboratories, featuring electron microscopical equipment in addition to the more conventional microstructural assessment methods, or at least belonged to national reasearch organisations with these facilities. The technical and scientific back-up to the manufacturing divisions developed strongly, and was further extended to the steel fabricators and steel users.

Thus the factors that led to initial development of these microalloyed steels at least up to the late 1960s were:

(i) Materials cost savings could be obtained directly by the application of microalloyed steels.
(ii) In-service benefits could be obtained in the development of lighter goods vehicles with higher payloads.
(iii) The need for higher strength linepipe that was easily weldable provided an expanding market for higher yield strength steels.
(iv) The extensive use of welding as the principal fabrication method meant that conventional ways of increasing strength, (increased carbon and alloy contents) would result in more expensive and much less practicable welding proceedures, whilst the new microalloyed steels with their generally lower carbon and alloy levels (for a given strength) could often be welded using existing procedures.
(v) The strength increase could be obtained relatively cheaply, as both niobium and vanadium, not being readily oxidised, could be added to semi-killed steels, thereby avoiding the cost increases associated with the yield losses of prime material attached to fully-killed ingot cast steels.
(vi) The technical and scientific back-up available to virtually all steel manufacturing companies could be employed directly on both manufacturing and utilisation problems.

These factors contributed to the exciting and challenging development of microalloyed steels in the early 1960s. Some indication of the success of these developments is given by the UK production figures for the niobium grades of BS 968 in the early 1960s.[13]

Year	Plates (tons)	Sections (tons)
1962	10590	25430
1963	47880	89310
1964	70780	172310
1965	82440	142060
1966	72510	139530

The development of microalloyed steels at this time was not restricted to plates and sections; development work was already being reported for hot-rolled strip and for bar material for reinforcement. Another significant development that

occurred in the period between 1963 and 1967 concerned the hot rolling practices, and a process now known as 'controlled rolling' was developed. This enabled fine-grained microstructures to be obtained in the 'as -rolled' condition, with benefits to both strength and toughness. By allowing the hot rolling process to occur at lower temperatures, finer austenite grain structures were produced which in turn resulted in finer ferrite grain sizes in the transformed product. By 1967, the outlines of this process had been developed[14] and were being exploited all over the world. It was appreciated at this time that niobium had another significant effect in steel, in that small additions of niobium could dramatically reduce the rate of recrystallisation of austenite during hot rolling, and so the scene was set for different regimes of controlled rolling, which could make use of either the fine recrystallised austenite grain size at modestly low finishing temperatures, or the extremely thin deformed austenite grains found with very low finish rolling temperatures. Other microalloys such as vanadium or titanium were also found to be capable of producing some retardation of austenite recrystallisation but the effect was considerably smaller than that observed in association with niobium additions.

The control of grain size by manipulation of the hot rolling process variables of microalloyed steels opened the way for further reductions in carbon and alloy contents, which were so important to weldability. Failures involving niobium grade steels had occurred,[15,16] and the need for lower carbon steels had been indicated as a means of avoiding cold cracking in these high strength steels. The controlled rolling of low carbon microalloyed steel therefore provided the necessary strength and toughness levels whilst at the same time producing steels of improved weldability.

During the latter half of the 1960s, there were many reports of lamellar tearing in weldments in pressure vessels, marine fabrications, and structural applications.[17–21] This phenomenon is a result of delamination along arrays of non-metallic inclusions aligned parallel to plate surfaces when subjected to through thickness stresses associated with certain constrained weldments as in T-joints.[22] During this period and into the early 1970s, considerable interest was shown in the factors controlling ductility and the anisotropy of ductility. Early studies of the ductile fracture process,[23–25] had suggested that the fracture strain of low carbon steels is controlled by the sulphide and oxide inclusions and the shape of the inclusions. Considerable effort was expended in examining methods of controlling both of these factors. Inclusion shape control additives such as rare earths, cerium, titanium, zirconium, and calcium were tried with varying degrees of success. For example, rare earths react to form very stable sulphides or oxysulphides which resist plastic deformation during the hot rolling process. Thus the hot rolled product contains spherical sulphides, rather than elongated manganese sulphides,[26] with consequent benefit to the long and short transverse ductilities.[27] Steels with inclusion shape control were not only successful in overcoming the problems of lamellar tearing, but also were used for longitudinal axis bending products such as heavy goods vehicle chassis members, which were manufactured from narrow strip. Significant cracking and rejection occurred at the bending stage when significant fractions of elongated inclusions were present, particularly when

using small radius bends. Inclusion shape control eliminated this source of rejection even with the tightest of bends.

However, other pressures were building at this time. There was considerable activity in the gas and oil industries in tapping into remote sources in hostile environments such as those in Alaska and Siberia, and in the North Sea.[28] Pipeline diameters were being increased, resulting in the need for higher strength steels to avoid the use of thicker walled pipes and the attendant punitive increases in welding costs. One of the dangers at this time was the risk of a longitudinal burst in the pipeline, as the stored energy in the pipe was sufficient to maintain the fracture process over many kilometres. Such fractures had occurred, and the fracture mechanism was not necessarily of the cleavage type. Low energy ductile fractures had occurred in steels with poor inclusion control. Thus steels with improved long transverse ductility and with sufficient resistance to cleavage failure were required. Also, development work on desulphurisation practices, particularly in Japan,[29–31] were proving successful. Various desulphurising practices have been adopted, including hot metal desulphurisation in the transfer ladle from the blast furnace, and changes in steelmaking practices involving alkali metal injection, lime injection, or slag control; these ultimately were to replace simple inclusion shape control methods.

During the late 1960s and early 1970s, attention had been given to enhancing the strength of microalloyed steels. Combinations of alloying elements such as niobium–vanadium, titanium–vanadium, as well as the use of higher levels of micro-alloying additions, had produced steels with yield strength levels of up to 450 MPa, and development work had already been carried out on low carbon low-alloy steels containing microalloying additions, in order to combine the benefits of microalloying with those of fine grained bainitic or acicular structures,[32] giving yield strengths in excess of 550 MPa. Throughout the 1970s attention was given to compositional and processing refinements that would produce given strength levels at lower cost, or would extend the strength ranges that were attainable. Typical of these efforts was the use of controlled residual levels to reduce the transformation temperature of plate and linepipe steels, yet maintain a ferrite-pearlite transformation product, thereby refining the interphase particle distribution and increasing the strength level, whilst maintaining adequate levels of toughness. Yet another example was the development of titanium precipation strengthened steels, where somewhat higher additions levels (0.15–0.20%Ti) could be used to develop hot strip product yield strengths of 350–700 MPa. An important feature here was that the same steel could yield virtually the full range of yield strengths depending upon the processing conditions during hot rolling. Continous hot strip mills had been developed with various cooling facilities between the finishing train exit and the coilers, e.g. water cooling sprays, laminar flow cooling, etc., as a means of shortening the length of buildings required to give a suitably low coiling temperature. Such cooling systems proved to be excellent metallurgical tools, as the coiling temperature (and hence the austenite–ferrite transformation temperature) could be selected and closely controlled over a wide range. The high titanium level used in these steels also gave sulphide shape control and a non-ageing (due to titanium nitride formation) steel.

The late 1970s also saw the introduction of a fundamentally different type of steel, known as 'dual phase steel'.[33,34] These steels first discovered in 1963, had a microstructure of ferrite and martensite, and exhibited high work hardening rates. A consequence of the high work hardening characteristics was that moderately cold worked components showed higher strengths and higher residual ductility at any given strength level, than were shown by conventional ferrite–pearlite steels. The connection with microalloying additives was that the work hardening characteristics were improved by refinement of the martensite island size , and the microalloyed dual phase steels showed distinct advantages over coarser structures. These steels have found a niche in cold formed components for the automobile industry, but the tonnages are small in comparison with the more conventional microalloyed steels.

The optimisation of alloy and microalloy contents, referred to earlier, to control the transformation temperature, either after hot rolling or normalising, and thus to control the microstructure, was well used, but further developments were envisaged in the early 1970s to include accelerated cooling procedures. The importance of cooling rate and coiling temperature was well appreciated in hot strip mills, and the substitution of cooling sprays during cooling for expensive alloying additions to give the same transformation temperature in other product forms such as plates, bars and sections became an obvious area for development. Although many studies had been carried out on accelerated cooling, the first on-line accelerated cooling systems in a Japanese plate mill was installed in 1980.[35] The process has since been incorporated in heavy section mills, where the selective water spray cooling of large effective cross-sectional areas such as the web/flange joints of H-beams not only can be used to minimise differential cooling throughout the section, thereby reducing any thermal distortion, but also can refine the microstructure and improve the mechanical properties in these areas.

In the mid-1980s, microalloying technology was being extended into the higher carbon steels where vanadium was being used in medium/high carbon steel forgings with the aim of attaining the same strength levels in air cooled forgings as were obtained in quenched and tempered products, thereby providing considerable cost savings in component manufacture of crankshafts, connecting rods, etc.[36] The basic metallurgical features of high carbon microalloyed steel had been investigated previously,[37] and had shown that significant additional strength could be attained by microalloying with vanadium. In many forgings, the deformation is inhomogeneous with some parts only slightly deformed or perhaps not deformed at all. In such regions of the forging, the structure will be typical of the soaking temperature, which for conventional forging is in the region of 1200–1250°C, and will be coarse grained with an attendant loss in toughness. The solution to this problem was found in the use of titanium nitride as a grain refining agent, now known as 'titanium nitride technology'. The effect of titanium on grain growth inhibition in low carbon steels had been known from work in the late 1960s,[38] but difficulties in control of the titanium effect were experienced as the steel making procedures involved ingot casting. Very low titanium levels are essential, requiring to be sub-stoichiometric with respect to the nitrogen content of the steel. The very high stability of titanium nitride (relative to other microalloy

carbides and nitrides) can give rise to very fine stable nitrides when the titanium content is restricted, and grain coarsening temperatures above the forging soak temperature can be obtained. Thus, even parts of the forging that suffer no deformation will have a reasonably fine grained structure, with consequently improved properties.

Such technology can be applied to weldments, but even the titanium nitrides are not effective in inhibiting grain growth at temperatures up to the solidus temperature. They do however restrict the size of the coarse grained heat affected zone. More recent developments, started in the late 1980s, include the use of titanium oxide particles, and although there is little doubt that such steels can develop superior toughness levels in the heat-affected zones, the exact mechanism for this effect is unclear. It may be associated with seeding of acicular ferrite by the titanium oxide particles during the cooling of the weld, rather than by grain growth inhibition at the welding temperature.

An exciting new application of microalloying additions developed in the early/mid-1980s, and concerned the development of higher strength steels and steels with improved cold formability in the form of thin (cold rolled and annealed) sheet and strip. Niobium has been used as a scavenger for interstitial carbon and nitrogen in stainless steels,[3] to avoid chromium carbide precipitation and the attendant weld decay, since 1933. Titanium was also used for this purpose. The development of steelmaking processes that would produce relatively low interstitial carbon and nitrogen contents (less than 0.005wt%) meant that relatively small additions of the microalloying element would allow carbo-nitride precipitation to give an 'interstitial free steel'. The use of microalloying additions in this role is fundamentally different from their conventional functions, and depends on the stability of their carbides and nitrides in ferrite, and effects of these carbide, nitrides and excess solute on the development of crystallographic texture.[39,40] It should be pointed out that interstitial free steels had been developed much earlier, but for steels with much higher carbon levels, using titanium.[41,42] Titanium additions were well known to stabilise nitrogen as titanium nitride, in hardenable boron steels and also in non-ageing steels. The properties of interstitial free steels, and particularly the high values of plastic anisotropy, are very sensitive to processing variables as well as compositional variations.

The advent of continuous annealing practices and the flexibility in thermal cycling has also provided additional opportunities for the control of properties through the practice of 'carbon management', i.e. the control of interstitial carbon levels and the formation of carbides. The carbon management processes led to the development in the mid-1980s of bake hardening steels.[43] In these steels, the carbon and/or nitrogen level in interstitial solid solution is controlled at about 0.001wt%. Cold formed components which are subjected to paint baking treatments, typically at 170°C for automobile components, will undergo strain ageing, and the yield strength of the component will typically increase by some 50 MPa, thereby producing an increase in dent resistance.

The developments in microalloyed steels described above are summarised in Fig. 1.1, where the various developments are shown on a time base, and compared with external influences such as the adoption of modern bulk welding methods,

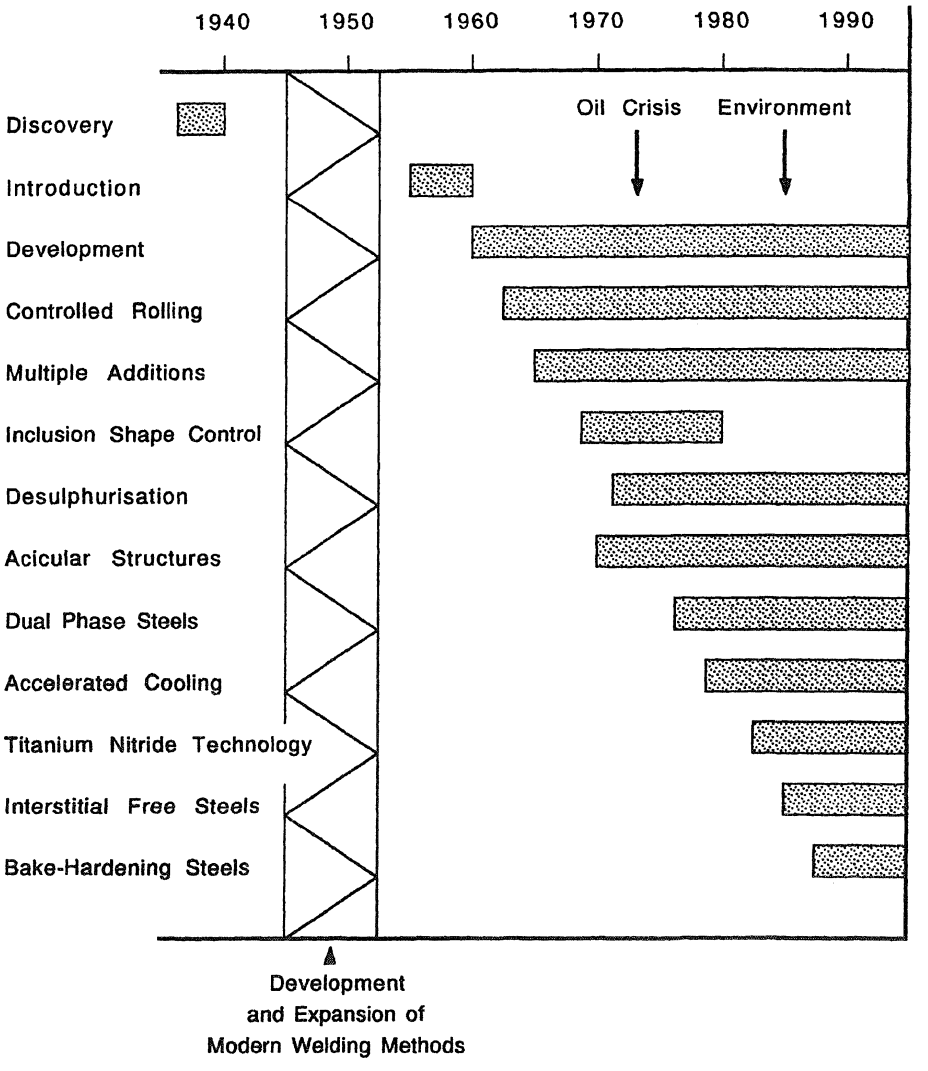


Fig. 1.1 Discovery and development of microalloyed steels in relation to the development of modern welding processes, the first major oil crisis, and the growth of environmental and safety pressures.

the first oil crisis, and the development of environmental pressures. The influence of the demands of modern welding techniques has already been described, together with the lower carbon requirements of microalloyed steels. The oil crisis in 1973 led to detailed examination of fuel consumption across a wide range of industries. The development of lightweight transport vehicles was an obvious area for fuel savings, and microalloyed steels have contributed to vehicle weight reduction together with substitution of lighter weight components by using

alternative materials such as aluminium engine blocks, and polymeric materials for interior panels. A less obvious but equally important saving in this respect derives from the fact that when higher strength steels were substituted for other lower strength steels, the reduced material mass resulted in a substantially reduced materials requirement, with an attendant saving in the energy required for iron extraction and steel refining. The reduced tonnages required also contribute to the requirements of reduced environmental contamination and material conservation.

A further factor, not shown in Fig. 1.1, is that of safety. Automobiles in particular are now subjected to increasing levels of safety legislation, a pressure which has been increasing continually throughout the period under review. Many of the legislative requirements, e.g. impact resistance, could well have resulted in increased vehicle weight had it not been for the introduction of microalloyed steels with their increased strengths.

However, the developments outlined in Fig. 1.1, cannot be regarded as definitive, and some points of explanation are required concerning the time scales shown.

The advent of high-strength, low-alloy steels is substantially correct in terms of their discovery, introduction and development. Their history is closely associated with the development of niobium as a microalloying agent but, as pointed out earlier, all of the conventional microalloying elements, i.e. niobium, titanium and vanadium, had been used in various steels for other purposes. The development of steels containing alloying elements in combination occurred over a time period, the precise times varying from one country to another, and indeed from one steelmaker to another, depending upon their association with particular product requirements, their processing capability, and the product mixes in the company portfolio.

The use of inclusion shape control is shown as a transient over the period 1967–1980. The sulphide shape control process as an isolated procedure is now obsolete, but has become incorporated in the more general aims of desulphurisation. The most commonly used methods of desulphurisation, involving the use of calcium treatment, automatically confer sulphide shape modification when the sulphur contents become extremely low, say below 0.005wt%. In the conventional shape control methods the level of additive required, e.g. rare earth or calcium, increases as the sulphur content increased, and could prove expensive unless the sulphur content is reduced. Cheap and efficient desulphurisation practices have therefore become the predominant method of controlling the adverse effects of sulphides, and have incorporated the effects of sulphide shape control. Because sulphide removal is more easily carried out under reducing conditions, the most common methods of producing low sulphur steels is to give a desulphurisation treatment at the hot metal stage during transfer from blast furnace to steel plant to remove the bulk of the sulphur from the charge, and to attain the lowest final sulphur content by a synthetic slag practice, or by lime or calcium injection. At these low levels of sulphur, specific additional shape control additives are not needed.

The development of acicular low carbon microalloyed steels was in fact preceded by the development of low carbon bainitic steels in the early 1950s.

However, these latter steels contained typically 0.15wt%C and were more conventionally alloyed, having 0.5wt% molybdenum and boron to confer adequate suppression of polygonal ferrite. The development of the microalloyed steels occurred much later, when carbon levels of 0.08wt% and below were easily attained, and the microalloying technology for grain control was established.

Attention has already been drawn to the development of interstitial free steels by substantial microalloying additions in the older 'low carbon' steels. These preceded the modern ultra-low carbon steels currently produced, that form the datum point shown in Fig. 1.1. Similarly, the basis of the 'bake hardening' phenomenon was well established in studies of strain ageing and strain age hardening in the 1950s and 1960s, and these greatly pre-dated the modern bake hardening steels indicated in the diagram. The differences in the older bake-hardening steels and the newer ones is reflected not only in the different carbon levels, but also in the thermal cycles required to control the solution and precipitation of carbides.

In describing the development of microalloyed steel, several references have been made to changes in steel-making practices. These occurred for a variety of reasons, the two main ones being cost reduction in steel making and steel quality improvement. The changes in steel manufacture and processing need to be understood, as they have had important effects on both the quality and the economics of microalloyed steel production.

1.2 CHANGES IN STEEL PRODUCTION

1.2.1 Continuous Casting

In 1960, there were no major production facilities for continuous casting, although some development work was being carried out by the then United Steel Companies in the UK. Today, the Western industrial steelmaking countries produce some 85% of their gross steelmaking tonnage by the continuous casting route. This proportion varies from country to country depending on the production of, for example, steel castings as part of the national product mix. In other countries, particularly the Eastern European nations, the lack of financial resources for massive capital investment in continuous casting plant has retarded its application, but even here the change from ingot route to continuous casting is inevitable. The economics of continuous casting go far beyond the increase in yield of prime product. By casting a smaller section size, e.g. bloom and billet sections, then the amount of hot working required to produce semi-finished billets or finished sections is considerably reduced, with a consequent saving of energy in the hot working process. Development work is in hand to produce continuously cast thin strip that would eliminate certainly the primary hot working stage altogether.

The use of continuous casting has also imposed other constraints on the steel chemistry. For example, aluminium-treated steels will contain alumina inclusions due to the high affinity of aluminium for oxygen. The alumina inclusions form

skeletal dendrites, and during casting will cause a build-up of alumina in the nozzle through which the steel is poured into the continuous casting mould. This alumina build-up gradually constricts the nozzle bore, choking off the stream of molten steel, and can cause complete blockage. In order to overcome this problem, steels containing aluminium may be treated with calcium to produce a low melting point calcium aluminate, which does not cause nozzle blockage. Many hard refractory oxidation products can give this effect and such particles must be avoided.

The best economic advantage is gained from continuous casting when heats of steel are teemed in sequence. Changes in steel cleanliness may occur during the ladle change over, because the liquid pool in the tundish is disturbed and slag protection may be broken when the new ladle is opened up. The whole of the continuous casting process has undergone many changes, including the use of tundishes, inert gas shrouding of the pouring stream, submerged nozzles, together with the development of compatible refractory materials, to the benefit of both economic operation and steel quality.

The effective cooling rate of the liquid steel in continuous casting is generally much higher than that of corresponding ingot cast material, and, by careful attention to the casting variables, the homogeneity of concast steels is better than that of the cast ingot, and the size of precipitated phases is generally smaller if precipitation occurs during the cooling cycle.

1.2.2 Steelmaking Developments

Modern steelmaking methods are well described elsewhere,[44] but it is important to record that many of the sophisticated steels produced today, including the high-strength, low-alloy steels, rely heavily on the development of these steelmaking methods.

In the early 1950s, there were three principal steelmaking processes, the Bessemer Converter, Electric Arc Steelmaking, and the Open Hearth Process. Each of these processes were operated independently and each involved charging, melting and refining stages. The introduction of oxygen lancing in the Bessemer process led to the development of the Basic Oxygen Steelmaking (BOS) process, and eventually this displaced the Open Hearth Process almost completely in most Western countries. Electric arc steelmaking was also improved by the use of oxygen lancing, in the mid-1960s, and by many other productivity enhancing innovations, such as water-cooled walls, the water-cooled roof, eccentric bottom tapping, scrap pre-heating, that have led to a reduction in tap to tap times by a factor of three, with corresponding reductions in electricity consumption.

The demand for cleaner steels also led to the development of desulphurisation processes, as described earlier, involving iron desulphurisation to reduce the sulphur burden during steelmaking, and the slag mixing and calcium injection processes. These latter processes were carried out in the ladle rather than in the steelmaking process, and initially raised some question about the economics of clean steels. Deoxidation practices to produce clean steels were essentially dependent upon the addition of a deoxidant, usually aluminium, which resulted

in the formation of alumina; the steel became 'clean' as a result of the lower density alumina floating to the surface of the steel and being absorbed by steelmaking slags. The physical separation of the steel and the deoxidation product in this way is an important feature of procedure, but is often complicated by other convective flow mechanisms in the steel. The development of vacuum processes, together with inert gas bubbling, has been developed and applied, again as a separate process from the main steelmaking operation. The deoxidation product in this case is gaseous, and easily separates from the liquid steel. The important feature of both the desulphurisation and the new deoxidation practices is that they are conducted in the ladle, rather than the steelmaking vessel. Ladle metallurgy has become increasingly sophisticated and is taking over most of the refining operations, thus shortening the time of residence in the arc furnace or BOS converter dramatically. The capital investment in this secondary steelmaking process is therefore offset by significant productivity gains, and the role of the arc furnace and the BOS plant is to provide a molten metal commodity which can be refined in a separate vessel, and the steel composition can be adjusted by ladle additions under very closely controlled conditions where alloy efficiency is maximised.

The use of vacuum steel treatment was at one time reserved for special high value steels, but the developments described above have enabled tonnage treatment of much lower value steels to be carried out economically with consequent benefit to steel cleanliness in carbon and high-strength low-alloy steels, as well as in the more highly alloyed special steels.

The development of these processes is extremely diffuse, in that processes such as vacuum melting and vacuum treatment had been developed but were not used for tonnage grades of relatively low value steels. The treatment of the latter was adopted through the 1980s. Other practices involving ladle treatments, e.g. argon bubbling, injection and ladle heating, were developed gradually from the mid-1960s to the present day.

1.2.3 Continuous Annealing

Prior to 1970, virtually all of the thinner gauge strip or sheet was produced by cold rolling and batch annealing. In batch annealing, coils are heated to the annealing temperature in bell type or tunnel furnaces. The characteristic heating and cooling rates were dictated by the coil size, each typically weighing several tonnes. Annealing cycles were in the range of one to several days. Property variations could be found between the outside and inside laps of the coiled strip due to the much slower heating and cooling rates experienced at the coil centre.

The production rate and the uniformity of quality could both be improved by changing to a continuous annealing process where the coil is unwound and the strip is fed through the furnace hot zone(s) before being re-coiled. The heating and cooling rates are thus dictated by the furnace temperature and strip thickness rather than by the coil dimension, and are faster by several orders of magnitude. The production rate is obtained from the mass per unit length of strip multipled by the strip velocity. For economic operation, the annealing furnace should be in continuous use to offset the huge capital investment associated with a continuous

annealing line. Although continuous annealing had been in use for some considerable time for special high value products, e.g. electrical steels, its expanded use to cover wide strip in tonnage qualities commenced in the early 1970s, following extensive development work, mainly in Japan.

The huge changes in heating rate involved in converting from batch annealing to continuous annealing, and the much shorter dwell times, have necessitated the use of higher annealing temperatures and changes in steel chemistry in order to attain the high levels of formability previously attained in aluminium-killed batch annealed steels, for example. An excellent account of these changes is given by Hudd.[45] The successful exploitation of dual phase steels is reliant upon an economic method of production of the dual phase structure, and the structure is easily developed in the continuous annealing process, either by tailoring compositions to the prevailing cooling rate, or by increasing the cooling rate through the use of water sprays built into the cooling stage of the continuous annealing line.

Further economies in continuous annealing can be made by combining the annealing process with other processes, e.g. tinning, galvanising and overageing cycles. In the 1990s, examples of cold rolling and annealing processes can be found where hot-band pickling, cold rolling, ultrasonic cleaning, and continuous annealing are carried out in-line as a single process.[46]

1.3 SCOPE

Attention has been drawn to the factors involved in the development of microalloyed steels. The factors include the discovery, the development of the scientific and technological principles upon which these steels are based, and the need for these steels in terms of their ability to satisfy increasingly stringent demands for a variety of applications. These and the capability of the steel manufacturing industry to respond to these factors are summarised in Fig. 1.2.

The benefits of weight savings are essentially cost related, as pointed out earlier. The pressures of safely legislation, energy conservation and material conservation, have all had their impact on the need for weight reduction, whether this arose from increased collapse resistant automobiles, lighter automobiles and structures, or simple conservation of steel and energy. A significant feature of the higher strength levels and materials savings is that the cost per unit of strength is reduced when using microalloying additions due to the small amounts of alloying element required, particularly when processing features such as hot rolling and accelerated cooling are optimised.

The need for the maintenance or improvement of ancillary properties such as weldability, toughness and formability when developing these higher strength steels has also been emphasised, as the conventional strengthening methods used prior to the discovery of microalloying would inevitably have led to deterioration of some or all of these properties.

The development of microalloyed steels also required the necessary alloy resources, and also a steel manufacturing industry that was capable of developing

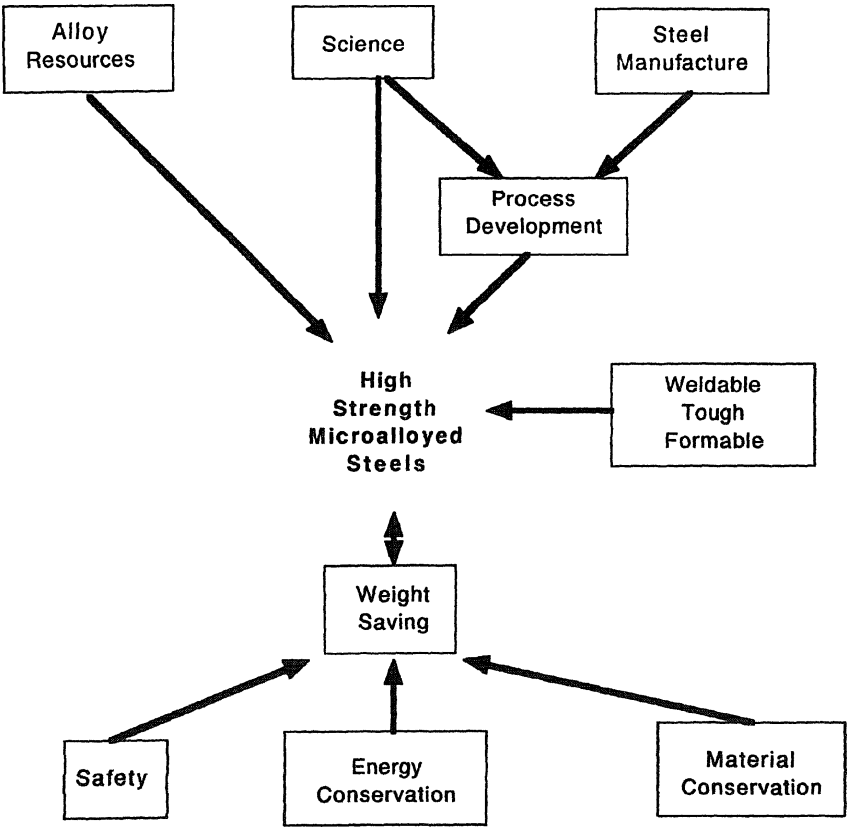


Fig. 1.2 Factors contributing to the development of microalloyed steel.

manufacturing methods to produce lower carbon, cleaner, tougher steels, together with a technological base from which to give customer advice on the utilisation of these new steels. Coupled with the development of microalloyed steels was the need to accommodate changes in the manufacturing process routes for cost reduction purposes such as continuous casting, as referred to earlier.

Also featured in Fig. 1.2 is the science-based input to both the steelmaking process developments, the metallurgical processing aspects, the behaviour of microalloying elements in steel, and the functions that they perform in controlling the mechanical properties of steels. The thermodynamic basis for many of the steelmaking developments were already in existence long before the development of microalloyed steels, but even here the necessary plant and operational procedures required considerable development. From a metallurgical processing and general physical metallurgy standpoint, the introduction of microalloyed steels coincided more or less with the development of a basic understanding of the relationship between the microstructure and properties of steels, and between the metallurgical processing and the evolution of the microstructure in steels. Most of

the mechanical properties of steel are directly related to the microstructure, and any change in the microstructure will cause a corresponding change in the mechanical properties. The exception to this general statement is the elastic modulus. The Young modulus is essentially controlled by interatomic forces rather than by any form of dislocation movement, and substantial variations in elastic modulus are only attained by substantial changes in the chemical composition of steel – generally far greater than are encountered in the class of alloys known as low alloy steels. However, the yield strength is integrally related to the microstructure, depending as it does on the movement of dislocations (plastic deformation) which is highly sensitive to microstructure. The structure in this sense can range from atomic perturbations such as solute atoms, to microstructural features such as grain size, and the distribution of second phase particles.

Not all of the mechanical properties depend on the same microstructural features. For example, cleavage fracture is highly dependent upon grain size, but ductile fracture is highly dependent upon certain second phase particles and is virtually independent of grain size. Yield strength depends on many microstructural features, but not on widely spaced second phase particles, such as nonmetallic inclusions.

The purpose of this book is to draw together the scientific base of the structure–property relationships in steel, and the relationships between metallurgical processing and the evolution of microstructure, that are relevant to microalloyed steels. Such relationships are probably better established for microalloyed steels (and their antecedents, the plain carbon and carbon–manganese steels with ferrite–pearlite structures) than for many other classes of steel, and have been sufficiently well defined as to provide a systematic understanding upon which properties can be predicted almost as well as they can be measured. The studies that have led to this understanding have also generated a considerable scientific data base, most of which is well dispersed in scientific journals and conference proceedings. An attempt is made to draw these data together and to show how they are used in microstructural design. Theoretical developments in physical metallurgy that have taken place during the period of development of microalloyed steels are also reviewed. One of the aspects of these developments is that the effects of processing variables on microstructure and of microstructure on properties have been established in a substantially quantitative manner and, therefore, can be used predictively rather than phenomenologically, although it should be pointed out that there are still several gaps in the quantitative relationships as will become evident.

REFERENCES

1. F. M. Becket and R. Franks: U.S. Patent No. 2158651, 1939 (May) and U.S. Patent No. 2264355; 1941 (Dec.)
2. I. M. McKenzie: Special Report No. 81: *Metallurgical Developments in Carbon Steels*, Iron and Steel Institute, London, 1963, p.30.
3. H. Stuart, *Niobium Proceedings*, Ed. H. Stuart, Met. Soc. AIME, Pennsylvania, 1984, p.1237.

4. R. A. GRANGE *et al.*: *B, Ca, Cb, and Zr in Iron and Steel*, Ed. F. T. Sisco, John Wiley and Sons, New York, 1957.
5. Great Lakes Steel Corporation: *Mechanical Engineer*, 1959, **81**, p.53.
6. W. B. MORRISON: *J. Iron and Steel Inst.*, 1963, **201**, p.317.
7. W. C. LESLIE: *The Relation Between Structure and Mechanical Properties of Metals*, NPL Conference, HMSO, 1963, p.333.
8. F. B. PICKERING and T. GLADMAN: Special Report No. 81: *Metallurgical Developments in Carbon Steels*, Iron and Steel Institute, London, 1953, p.10.
9. J. M. GRAY *et al.*: *J. Iron and Steel Inst.*, 1965, **203**, p.812.
10. J. M. GRAY and R. G. B. YEO: *Trans. A.S.M.*, 1968, **64**, p.255.
11. K. J. IRVINE, F. B. PICKERING and T. GLADMAN: *J. Iron and Steel Inst.*, 1967, **205**, p.161
12. K. J. IRVINE: ISI Publication No. 104, *Iron and Steel Institute.*, 1967, p.1.
13. M. J. MAY: *loc. cit.*, p.11.
14. J. J. IRANI, D. BURTON, J. D. JONES and A. B. ROTHWELL: *loc. cit.*, p.110.
15. *Report of the Royal Commission into the Failure of King's Bridge, Melbourne:* 6351/63, 1963.
16. Failure of a Welded Beam, Fenchurch Street (*Sunday Times*, 15 July 1965).
17. A. H. GOODYEAR: *BSI News*, September 1966, p.10.
18. H. WORMINGTON: *Weld. Met. Fabrication*, 1967, **35**, p.370.
19. M. WATANABE: *Symposium on Welding in Shipbuilding*, The Welding Institute, London, 1961, p.219.
20. A. D. E. THOMSON *et al.*: *Trans ASME, J. Engineering Industry*, 1968, **90**, (series B), p.627.
21. J. PRATT: *Design in High Strength Structural Steels*, Iron and Steel Institute, London, 1969, p.103.
22. J. C. M. FARRAR, J. A. CHARLES AND R. E. DOLBY: *Effect of Second Phase Particles on the Mechanical Properties of Steel.* Iron and Steel Institute, London, 1971. p.171.
23. J. GURLAND and J. PLATEAU: *Trans-ASM*, 1963, **56**, p.441.
24. G. HENRY and J. PLATEAU: *La Microfratographie*, Editions Metaux, IRSID, Paris (St. Germaine), 1966.
25. B. EDELSON and W. BALDWIN: *Trans-ASM*, 1962, **55**, p.230.
26. L. LUYCKX: *Sulphide Inclusions in Steel*, Eds. J. J. deBarbadillo and E. Snape, ASM Publication, Ohio, 1974, p.44.
27. T. GLADMAN, B. HOLMES and F. B. PICKERING: *J. Iron and Steel Inst.*, 1970, **208**, p.172.
28. W. L. MERCER: *Rosenhain Centenary Conference – The Contribution of Physical Metallurgy to Engineering Practice*, The Royal Society, London, 1976, p.41.
29. H. USHIYAMA, G. YUASA and T. YAJINA: *Iron Making and Steel Making*, 1978, **3**, p.121.
30. T. OHYA, F. KODAMA, H. MATSUNAGA, M. MOTOYOSHI and M. HIGASHIGUCHI: *Steelmaking Proceedings*, 1977, **60**, p.345.
31. H. PIRSCHER and W. KLAPDAR: *Proceedings Microalloying 1975*, Union Carbide, New York, 1977, p.232.
32. Y. E. SMITH, A. P. COLDREN and R. L. CRYDERMAN: *Conference Proceedings – Towards Improved Ductility and Toughness*, Climax Molybdenum Company, Ann Arbor, 1971, p.119.
33. M. S. RASHID: *GM980X – A Unique High Strength Sheet Steel with Superior Formability*, SAE Paper No. 760206, February, 1976
34. E. W. WILLIAMS and L. K. DAVIES: *Recent Developments in Annealing*, Iron and Steel Institute Special Report, 1963.
35. K. TSUKADA, K. MATSUMOTO, K. HIRABE and K. TAKESHIGA: *Ironmaking and Steelmaking*, 1982, **9**, p.21.
36. D. J. NAYLOR: *Ironmaking and Steelmaking*, 1989, **16**, p.246.
37. T. GLADMAN, I. D. MCIVOR and F. B. PICKERING: *J. Iron and Steel Inst.*, 1972, **210**, p.916.
38. T. GEORGE and J. J. IRANI: *J. Australia Inst. Metals*, 1968, **13**, p.94.
39. N. OHASHI, T. IRIE, S. SATOH, O, HASHIMOTO and I. TAKAHASHI: SAE Paper No. 810027, 1981.
40. N. YAMADA and Y. TOKUNAGA: *Trans. Iron Steel Inst. Japan*, 1985, **25**, p.640.

41. G. F. Comstock, S. F. Urban and M. Cohen: *Titanium in Steel*, Pitman, New York, 1941.
42. W. C. Leslie and R. J. Sober: *Trans. ASM. Quarterly*, 1967, **60**, p.99.
43. N. Hanai, N. Takemoto, Y. Takunaga and Y. Misuyama: *Trans. Iron and Steel Inst. Japan*, 1984, **24**, p.17.
44. A. Nicholson and D. S. Thornton: *Materials Science and Technology*, Eds. R. W. Cahn, P. Haasen, and E. J. Kramer, VCH, Weinheim, 1992, Volume 7, p.95.
45. R. C. Hudd: *Metals and Materials*, 1987, February, p.71.
46. K. Fudaba, O. Akisue and Y. Tokunaga: *Ladle Steelmaking and Furnaces* (Symp.) Canadian Inst. Min. Metall., Montreal, 1988, p.290.

CHAPTER 2

Microstructure–Property Relationships

Considerable attention has been given to the relationship between microstructure and properties of microalloyed steels. In part, this can be attributed to the development of the designer steel philosophy from 1960, and the introduction of microalloyed steels. Many of the fundamental concepts of alloy strengthening had already been developed by 1960, but their application to commercial steels was only just beginning. Although the concepts were established, there was a not inconsiderable lack of quantitative data, and also a lack of understanding of the role of microalloying elements as pointed out in Chapter 1. The development of the main structure–property relationships has occurred since 1960, and whilst there is an element of empiricism connected with some of these, most are soundly based on fundamental theories of the effects of microstructure on properties. An attempt is made, in this chapter, to draw together the fundamental theories and to show how these relate to microalloyed steel properties, not only in a qualitative way, but also in a quantitative manner. The properties considered here are strength, which is fundamental to the concept of microalloyed steel, and the ancillary, but nonetheless highly important, properties of toughness, ductility and formability. These properties depend upon microstructural features in different ways and in some cases depend upon different microstructural features. Weldability is generally accepted as being composition dependent when considered from the standpoint of cold cracking, but other problems, such as lamellar tearing, are directly related to ductility and toughness, which in turn are dependent upon microstructural features.

The microstructural features also require definition, in quantitative terms, and considerable confusion has arisen in studies of structure–property relationships due to definitions of, for example, grain size. It is important, therefore, in making an evaluation of microstructure–property relationships, that the measures of the microstructural features are clearly defined, and methods for their assessment are also described.

2.1 TENSILE AND YIELD STRENGTH

Attention has already been drawn to the early use of tensile strength as a design criterion, and the subsequent change to a design criterion based on yield strength. The design stress was based on the strength characteristic multiplied by an appropriate safety factor, the safety factor being different of course for the two

strength characteristics. This is important because the strengthening mechanisms, although having the same qualitative effects on each characteristic, do not have the same quantitative effects. Most strengthening mechanisms have greater effects on the yield strength in terms of both absolute and relative magnitudes. The weight saving achieved through the use of microalloyed steels would certainly have been reduced considerably had design stresses remained linked to the tensile strength. The difference between these strength characteristics requires some understanding of both.

The discontinuous nature of the yield point in ferritic steels is well known. Dislocations within the structure are effectively immobilised by interstitial atoms which form Cottrell atmospheres on the dislocation core. Plastic deformation, therefore, requires the creation of new dislocations, and these are created at the upper yield point. This is a local event, and the plastically deformed region grows by propagation of the Luders front over the whole of the stressed region. The propagation of the Luders band occurs at the *lower* yield point. The upper yield point is highly sensitive to surface finish, specimen alignment and localised defects, and shows considerable variability. The lower yield point is far less sensitive and is therefore used as a measure of resistance to plastic deformation. The virtual elimination of interstitial atoms from the b.c.c. base will result in a change from discontinuous yielding to continuous yielding, where the proof stress is used as a guarantee against the introduction of excessive plastic strain, e.g. 0.2%, when it would be known as the 0.2% proof stress.

The tensile strength is very simply defined in engineering terms as the maximum force per unit of the original cross-sectional area that can be withstood without causing fracture. The tensile strength therefore includes not only those factors affecting the yield strength but also the factors that control work hardening and the onset of gross plastic instability. This can be understood by reference to Fig. 2.1. From a metallurgical point of view, the stress required to cause plastic flow is defined by the *instantaneous* stress at any point on the flow curve; this is known as the true stress, σ, defined by

$$\sigma = F/A \tag{2.1}$$

where F is the force at any instant, and A is the instantaneous cross-sectional area.

The engineering stress, s, as indicated above, is defined by

$$s = F/A_0 \tag{2.2}$$

where A_0 is the initial-cross sectional area at the start of straining.

The measure of strain used in Fig. 2.1 is the summation of all small elements of strain, known as the true strain, ε, which is defined by

$$\varepsilon = \Sigma(\Delta l/l) = \ln(l_f/l_0) \tag{2.3}$$

Where Δl is a small increment in length, l is the instantaneous length, l_f is the final length and l_0 is the initial length.

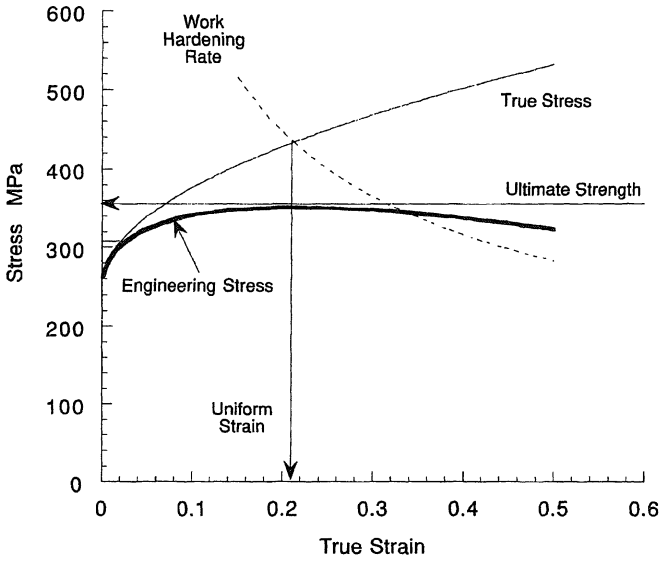


Fig. 2.1 Stress–strain curves, showing the true stress and the engineering stress as a function of true strain. Necking commences when the work hardening rate is reduced to a level below the true stress, and coincides with the maximum in the engineering stress, i.e. the tensile strength.

Because of the constancy of volume during plastic deformation, $l_f/l_0 = A_0/A_f$, and Equation (2.3) may be re-written as

$$\varepsilon = \ln(A_0/A_f) \tag{2.4}$$

The true stress–true strain curve is often approximated by the Ludwik equation

$$\sigma = \sigma_i + k\varepsilon^{n'} \tag{2.5}$$

where σ is the true stress, σ_i is the stress at the onset of plastic strain, k is the work hardening coefficient and n' is the work hardening index.

This is shown in Fig. 2.1. The relationship between true stress and engineering stress is derived from Equations (2.1), (2.2) and (2.4) as

$$s = \sigma/\exp(\varepsilon) \tag{2.6}$$

It is clear that the engineering stress (and the applied tensile force) passes through a maximum and is considerably lower than the true stress at any significant plastic strain. The peak engineering stress is caused by the onset of

plastic instability which in turn is dependent on the flow stress and work hardening rate. From Equation 2.6,

$$\begin{aligned} s &= (\sigma_i + k\varepsilon^{n'})/\exp(\varepsilon) \\ ds/d\varepsilon &= \{n'k\varepsilon^{n'} \cdot \exp(\varepsilon) - (\sigma_i + k\varepsilon^{n'}) \cdot \exp(\varepsilon)\}/\exp(2\varepsilon) \\ &= \{n'k\varepsilon^{n'-1} - (\sigma_i + k\varepsilon^{n'})\}/\exp(\varepsilon) \end{aligned} \tag{2.7}$$

At maximum force, or maximum engineering stress $ds/d\varepsilon = 0$, or

$$\begin{aligned} n'k\varepsilon_u^{n'-1} &= \sigma_i + k\varepsilon_u^{n'} \\ (d\sigma/d\varepsilon)_u &= (\sigma)_u \end{aligned} \tag{2.8}$$

i.e. the work hardening rate is numerically equal to the true stress. This is true irrespective of the precise relationship between true stress and true strain. The strain at which the ultimate tensile strength occurs, ε_u may be derived from Equation 2.7 as

$$\begin{aligned} n'(\sigma_u - \sigma_i)/\varepsilon_u &= \sigma_u \\ \varepsilon_u &= n'(\sigma_u - \sigma_i)/\sigma_u \end{aligned} \tag{2.9}$$

The maximum uniform strain, ε_u, is less than the work hardening index, n', of the Ludwik equation by an amount which is dependent upon the contribution of σ_i to the flow stress, σ. As the contribution of σ_i to the flow stress increases, the maximum uniform strain decreases for a given work hardening characteristic (constant n' and k).

It should be noted that σ_i is *not* the yield strength but represents the intersection of the flow curve with the elastic stress–strain relationship, and is different from the yield strength by virtue of the Luders' extension (yield elongation). If there was no Luders' extension, then σ_i would be equal to the yield strength. Also, the work hardening index n' of the Ludwik equation is not the same as the work hardening index, n, of the Ludwik–Hollomon equation where the approximation

$$\sigma = k\varepsilon^n \tag{2.9a}$$

is made, i.e. $\sigma_i = 0$. Under these circumstances, $\varepsilon_u = n$ [see Equation (2.9)]. The Ludwik–Hollomon equation is most commonly used as an assessment of the work hardening index, and the n value is then used as a measure of the uniform extension.

The distinction between the Ludwik equation and Ludwik–Hollomon equation is important in relation to microalloyed steels where the addition of niobium for example affects the flow stress, but with little or no change in the work hardening rate ($d\sigma/d\varepsilon$), i.e. the addition of niobium increases σ_i.[1]

The tensile strength, T (or ultimate tensile stress), is thus given by

$$T = s_{max} = (\sigma_i + k\varepsilon_u^{n'})/\exp \varepsilon_u \tag{2.10}$$

The complexity of the tensile strength in metallurgical terms is thus demonstrated. The tensile strength is not simply related to the strengthening

mechanisms involved in resisting the onset of plastic flow, but also depends on the work hardening response of the material, and also on the features controlling plastic instability. The situation is further complicated by the fact that although the flow curve is affected in qualitative terms in the same way as the yield strength, the quantitative effects are different, and moreover these differences vary from one strengthening mechanism to another.

The use of yield strength as a design criterion has resulted in a major body of information being generated on the effects of the various strengthening mechanisms, which in turn has led to a good understanding of these strengthening mechanisms and how they can be controlled. The complexity of the tensile strength is considered further in Chapter 7 when dealing with formability and uniform strain.

2.2 DISLOCATIONS IN METALS

The theoretical strength[2] of a metal such as iron can be estimated in terms of the stress required to move one block of atoms *simultaneously* over an adjacent block, Fig. 2.2(a). The *shear* stress required for this movement is quite clearly periodic as the lattice will resist the stress at displacements up to $b/2$ and will assist the stress at displacements between $b/2$ and b. The stress fluctuation can be approximated by

$$\tau = \tau_{max} \cdot \sin(2\pi x/b) \tag{2.11}$$

The value of τ_{max} occurs when the displacement is $b/4$, Fig. 2.2(b). It should be noted that when the displacement is $b/2$, the stress returns to zero as the displacement passes from the 'resist' stage to the 'assist' stage. Given that the shear strain γ is defined by x/a, then

$$\tau = \tau_{max} \cdot \sin(2\pi\gamma a/b) \tag{2.12}$$

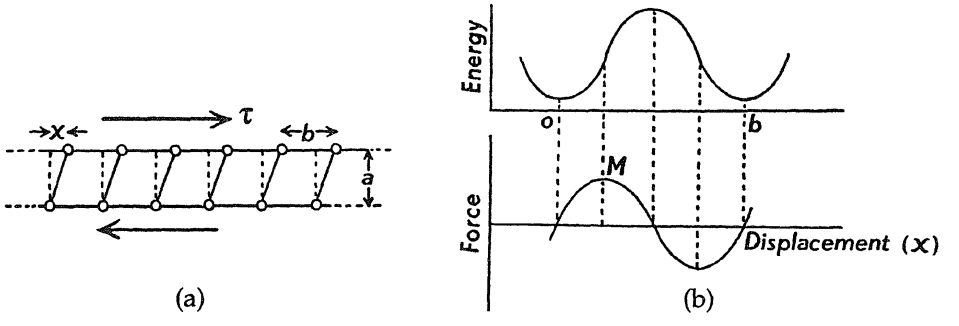


Fig. 2.2 Energy changes accompanying simultaneous displacement of one block of metal over an adjacent block. (a) the atomic displacements, (b) the forces required to cause the displacement.

and by differentiation of Equation 2.12,

$$d\tau/d\gamma = \tau_{max} \cdot (2\pi a/b) \cdot \sin(2\pi\gamma a/b + \pi/2) \tag{2.13}$$

From Equation (2.13), the elastic shear modulus G, measured at very small strains ($\gamma \rightarrow 0$) is given by

$$G = (d\tau/d\gamma)_0 = \tau_{max} \cdot 2\pi a/b \tag{2.14}$$

The maximum shear stress can then be expressed as

$$\tau_{max} = Gb/2\pi a \tag{2.15}$$

As b/a is approximately unity in most operative slip systems, then

$$\tau_{max} \approx G/10 \tag{2.16}$$

More sophisticated treatments of this problem have given values of τ_{max} in the region of $G/15$ to $G/30$. These are very high stresses, equivalent to tensile stresses of the order of $E/10$ to $E/15$, where E is the Young Modulus. For a Young modulus of 210 GPa (for steel) the theoretical strength for block slippage is of the order of 14,000–21,000 MPa, which is considerably in excess of the strongest of steels by a factor of about 10, and is even more excessive for mild steel, where the theoretical strength calculation is equally valid, and exceeds the observed yield strengths by a factor of 100. The reason for this discrepancy is to be found in the mechanism of the deformation process itself, i.e. dislocations. The theory of dislocations was developed extensively through the 1940s, mainly in the field of metal physics, and today it is almost impossible to imagine that there ever was a discipline of metallurgy without dislocations. Dislocations, with their row-by-row atom shifts, allow plastic deformation to occur at these much lower stresses.

In order to strengthen any metallic material, it is, therefore, necessary to consider mechanisms that will impede dislocation movement, i.e. will require higher stresses to cause the movement of dislocations.

In order to understand strengthening mechanisms it is first necessary to establish certain properties of dislocations before considering the detailed interaction between dislocations and microstructural (or atomic) features.[3] The concept of a strain energy term (or line energy) for dislocations is fundamental to their interaction with structural defects. The edge dislocation portrayed in Fig. 2.3 shows a significant local displacement of atoms relative to the stable lattice array. The elastic energy associated with the distortion of the lattice near the dislocation core can be approximated by assuming a shear strain of 0.5 for atoms within a radius b of the core. The strain energy per unit volume is given by

$$\text{Strain energy (per unit volume)} = \int_0^{0.5} \tau \cdot d\gamma$$

$$= \int_0^{0.5} G\gamma \cdot d\gamma$$

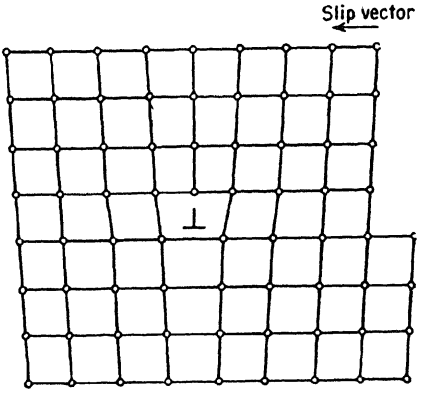


Fig. 2.3 An edge dislocation, viewed along its length, shows an expanded inter-atomic spacing below the extra half plane of atoms the expansion being a maximum at the dislocation core. Similarly, the interatomic spacing is compressed above the dislocation core.

where G is the shear modulus, τ is the shear stress and γ is the shear strain,

$$= [G\gamma^2/2]_0^{0.5}$$
$$= G/8 \tag{2.17}$$

The volume per unit length of dislocation is given as πb^2 and therefore the energy per unit length of dislocations, T, is given by

$$T = \pi b^2 G/8 \quad \text{or} \quad \text{approximately } Gb^2/2 \tag{2.18}$$

The energy per unit length of dislocation, T, may be regarded as a 'line tension', and is analogous to the surface tension and surface energy equivalence in surfaces and interfaces. A dislocation has its lowest energy when it assumes its shortest length. External forces that cause an increase in length of the dislocation require that the attendant increase in energy is supplied by that force

A second feature of the dislocation is its inherent resistance to movement through the pure metal lattice. If a shear stress is applied to a small block of metal containing a dislocation, (see Fig. 2.4), the dislocation displacement is a consequence of the applied stress and the inherent resistance of the material to dislocation movement, which may be regarded as a force per unit length of the dislocation, f. If the applied shear stress is greater than the inherent resistance to motion, then the dislocation will move and the material will be plastically deformed (albeit by a small amount). From Fig. 2.4, the work done by the applied shear stress w_a in moving the upper part of the crystal is given by

$$w = \tau A \cdot b = \tau b l_1 l_2 \tag{2.19}$$

The dislocation moves a distance l_2 against a resistance f per unit length being applied over a length l_1. This work done, w_b, is given by

$$w_b = f l_1 l_2 \tag{2.20}$$

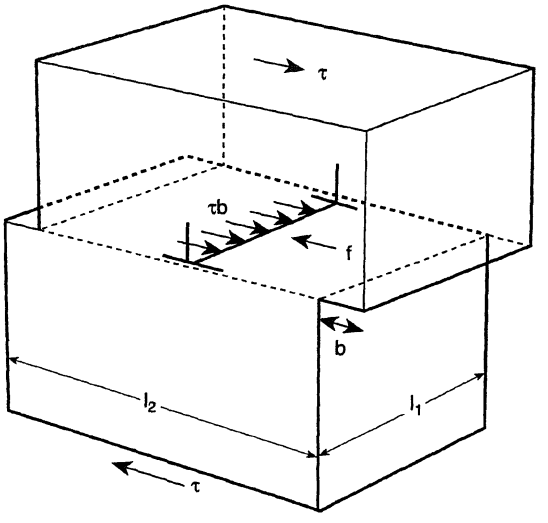


Fig. 2.4 Forces involved in dislocation movement, showing the relationship between the applied shear stress and the forces opposing dislocation motion. After Ashby and Jones.[35]

Equating w_a and w_b gives

$$\tau b = f \tag{2.21}$$

where τ is the shear stress required to effect dislocation movement and b is the Burgers vector.

The resistance to movement is dependent on the nature of the metal atoms and their bonding, and the nature of the dislocation. Slip in crystals is crystallographically oriented and occurs on planes that are typically widely spaced, and that result in a small Burgers vector, i.e. in a direction where the reproducibility of the lattice is achieved by a short slip distance. All dislocations are motivated by shear forces, and tensile stresses depend for their actions on the resolved shear stresses in the active slip plane. Thus, there will be a minimum tensile stress that is required to cause dislocation movement, due to the attainment of the critical resolved shear stress on the slip plane required to overcome the Peierls–Nabarro force. This force is a friction force caused by the need to move a dislocation from one metastable position in the periodic lattice (Fig. 2.3) to the next metastable position. The situation is further complicated in polycrystalline metals where the slip planes may deviate from the applied maximum resolved shear stress and differ from one grain to the next. In the body centred cubic structure of iron, known as ferrite, there are a number of slip planes that show only marginally different Peierls–Nabarro forces, giving rise to 'wavy' slip lines having components of the (110), (112) and (123) slip dislocations. A generalised treatment of these complications involves the resolution of shear stress from a tensile stress, and use of the Taylor factor ($=1.5$) to allow for the misorientation between slip planes and the plane of maximum resolved shear stress.

The resolved shear stress is derived as indicated in Fig. 2.5. The tensile stress, σ, is defined as $\sigma = F/A$. The resolved shear force is thus $F \cdot \sin\theta$ and the area on the shear plane is $A/\cos\theta$. Thus the shear stress, τ, is $F \cdot \sin\theta \cdot \cos\theta/A$ and the resolved shear stress is a maximum at $\theta = 45°$, or

$$\tau_{max} = \sigma/2 \tag{2.22}$$

Applying the Taylor factor increases the tensile stress that needs to be applied, as outlined above, by a factor of 1.5 (τ on the randomly oriented slip planes for polycrystalline metals will be somewhat less than τ_{max}) and therefore

$$\sigma = 3\tau \tag{2.23}$$

where σ is the tensile stress required to cause dislocation movement and τ is the shear stress on the active slip plane.

Despite these complications, and notwithstanding possible differences between the friction stress in the b.c.c. lattice and the stress required to propagate a Luders' band, the relationship between the lower yield stress (tensile) and the stress required to cause dislocation movement has provided the basis for subsequent studies of strengthening mechanisms. These mechanisms are understandably aimed at increasing the resistance to dislocation motion, and therefore the yield strength of the steel. The friction stress assessed from the tensile yield strength of

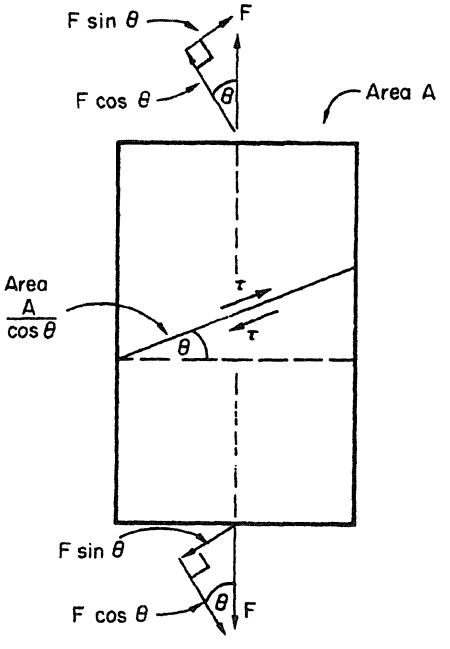


Fig. 2.5 The relationship between the applied tensile stress and the resolved shear stress. After Ashby and Jones.[35]

steel is commonly referred to as the Peierls stress, and typically has a value in the region of 70–100 MPa, so that even a mild steel with a yield strength of about 200 MPa obviously incorporates other strengthening mechanisms.

2.3 STRENGTHENING MECHANISMS

The yield strength of steel can be increased by one or more of several strengthening mechanisms. These include

(i) Solid solution strengthening
(ii) Grain refinement
(iii) Dispersion (or precipitation) strengthening
(iv) Work hardening

These mechanisms all share one common feature, which is the ability to increase the applied stress required for the onset of plastic deformation. In the following sections, consideration is given to these strengthening mechanisms and the way in which the strength is affected, and to the magnitude of these effects when applied in the strengthening of steel, with particular reference to microalloyed steels.

2.3.1 Solid Solution Strengthening

The nature of solid solution strengthening is to increase the lattice resistance to deformation. There are several ways in which solute atoms in the b.c.c. iron lattice can interact with dislocations, some of which involve elastic interactions between the strain fields of solute atoms with those of dislocations, and some of which depend on chemical, electrical, or geometrical interactions. The theories of solid solution hardening are complex, involving temperature dependent and temperature independent components, with attendant implications for solution hardening at different temperatures. The solute concentration dependency of the yield strength can also vary, with a root concentration dependency being observed in many f.c.c. metals. However, Suzuki[3] has presented data for b.c.c. metals showing extensive linear hardening, and has suggested that this type of hardening is caused by clusters of solute (hard spots) which affect the temperature dependent component of the yield strength. However, Arsenault[4] expressed reservations concerning this theory due to the significant effect of solutes on strengthening at elevated temperatures in b.c.c. metals. From the standpoint of microalloyed steels and their room temperature properties, however, the composition dependency can be assumed to be linear; the solute contents of these steels generally do not exceed 1–2% and are often considerably lower, depending upon the solute, so that even with a square root dependency, a linear approximation at low solute contents introduces very little error.

The elastic distortion of an edge dislocation varies with position around the dislocation, and with distance from the dislocation core. Atoms above the slip plane are compressed locally, whilst atoms below the slip plane are extended. The degree of compression or extension decreases as the distance from the core of the

edge dislocation increases. It should be pointed out that the edge dislocation has both shear and hydrostatic components, unlike the screw dislocation which only has a shear component. Substitutional solute atoms give rise to a hydrostatic distortion and only interact therefore with edge dislocations. A large solute atom will give rise to a hydrostatic compression that will be relieved if the solute occupies a position below the slip plane. There would be a significant increase in energy if a large solute atom were inserted in the compressed lattice above the slip plane. Similarly, small solute atoms would relieve the total elastic energy of the system by occupying the hydrostatically compressed region above the slip plane, but would increase the energy at hydrostatically extended regions below the slip plane.

Interstitial atoms, such as carbon and nitrogen in iron, give rise to assymetrical distortions which have both hydrostatic and shear components and can thus interact with both edge and screw dislocations. The low energy position for these interstitial solutes is in the extended lattice below the slip plane, for although these atoms are small enough to form interstitial solid solutions, they are sufficiently large to cause a local assymetric dilation in an otherwise perfect b.c.c. lattice. There is ample experimental evidence for the interaction of solute atoms with elastic distortions of the solvent lattice. If the elastic distortion is introduced by stress cycling, the ordering of carbon atoms to align their own distortions with those provided by the applied stress, give rise to relaxation phenomena, and cause internal friction or damping effects in a cyclic stress situation. The origin of this phenomenon was described by Snoek in 1941[5] for carbon atoms in α-iron. The interstitial carbon atoms would normally be uniformly distributed between x- y- and z-sites of the cubic lattice (see Fig. 2.6) in the unstressed condition, but a tensile stress acting to separate the iron atoms in the z-direction would cause the interstices between them to become favoured sites and carbon atoms would jump from x- and y-sites to the more energetically favourable z-sites; the degree of partitioning increases as the stress is increased. Because the carbon jump process is essentially a diffusion process, it is time dependent and the overall strain is composed of an instantaneous elastic strain and a time dependent 'anelastic' strain due to ordering of the carbon atoms, Fig. 2.6(b). Reversal of the stress causes the z-sites to become energetically unfavourable and carbon atoms partition to the x- and y-sites, thus giving a hysteresis loop with an associated energy absorption for each cycle. Stress cycling at high frequencies or low temperatures give insufficient time for the carbon atoms to diffuse, and there is no energy absorption. At high temperatures or low cyclic frequencies, the carbon atoms maintain an equilibrium partition between sites at all stresses, and again do not cause any energy absorption, but give a lower apparent Young's modulus, known as the relaxed modulus. The critical cyclic frequency at which energy is absorbed thus increases as the temperature increases due to the faster migration of the carbon atoms. At room temperature, this critical frequency is of the order of 1 Hz, indicating that a considerable proportion of the carbon atoms can jump in a period of about 1 second. Substitution atoms give a hydrostatic distortion and are not therefore subject to this particular form of stress ordering.

The importance of these elastic interactions is also shown in the behaviour of

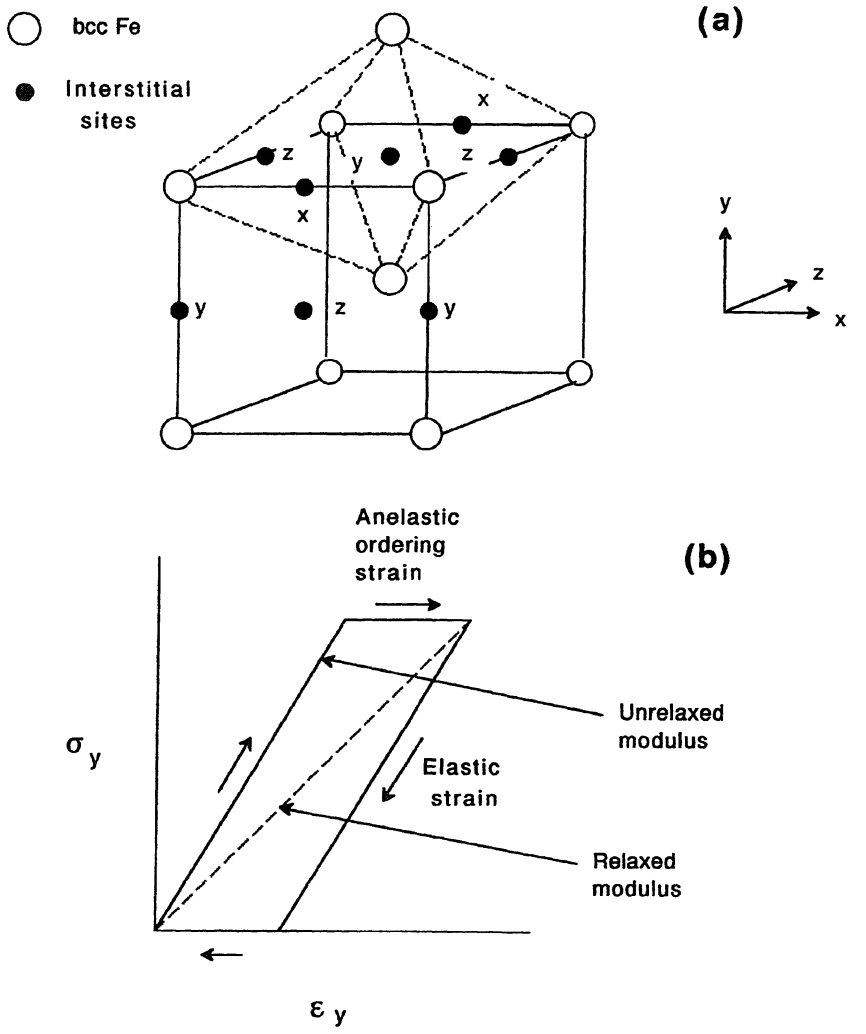


Fig. 2.6 (a) Octahedral interstitial sites for carbon and nitrogen atoms in the body centred cubic lattice; (b) the elastic and anelastic strains are indicated, giving rise to the concept of relaxed and un-relaxed moduli.

interstitial carbon and nitrogen atoms in iron. Tensile testing of ferrite–pearlite structures gives the characteristic discontinuous yield behaviour. If the interstitial atoms, carbon and nitrogen, are removed by hydrogen annealing, the material will show continuous yielding and the yield point phenomenon will disappear, i.e. there is no upper yield point, no yield plateau, and no yield extension. Continuous yielding can also be produced by introducing a small plastic strain, for example, by cold rolling This plastic strain can be less than the Luders' extension. Thus the process of continuous yielding can be produced either by removing interstitial

atoms from the pre-existing dislocations, or by introducing fresh dislocation. However, on ageing at near ambient temperatures, the lightly deformed material will show a reversion to the discontinuous yield behaviour, i.e. a return of the yield point. This phenomenon is known as strain ageing. In steels without interstitials, strain ageing does not occur. The yield point in steel is associated with an absence of mobile or free dislocations. Any pre-existing dislocations appear to be tightly bound by the formation of 'atmospheres' of carbon or nitrogen atoms at or near the dislocation core. Cottrell and Bilby[6] have given an elegant treatment of the formation of these atmospheres. If a solute atom, causing a volume change Δv, is introduced at some point in a lattice where the local hydrostatic pressure of the stress field is p, there will be an interaction energy V, where

$$V = p\Delta v = K\phi \cdot \Delta v \tag{2.24}$$

where K is the bulk modulus and ϕ is the local dilatation strain.

The local dilatation strain ϕ, around a positive edge dislocation, is given by

$$\phi = b(1 - 2v)\sin\theta/2\pi R(1 - v) \tag{2.25}$$

where (R, θ) are the polar co-ordinates of the point with respect to the dislocation core and v is Poisson's ratio.

The bulk modulus K can be expressed in terms of the shear modulus, G, and Poisson's ratio, as

$$K = 2G(1 + v)/3(1 - 2v)$$

Substituting these in Equation (2.24) gives

$$\begin{aligned} V_{(R\theta)} &= b(1 + v)G\Delta v \sin\theta/3\pi R(1 - v) \\ &= AGb\Delta v \cdot \theta/R \end{aligned} \tag{2.26}$$

The minimum in $V_{(R,\theta)}$, corresponding with a maximum binding energy, V_{max}, occurs at $\theta = 3\pi/2$, $R = r_0 \approx b$ when Δv is positive, and at $\theta = \pi/2$, $R = r_0 \approx b$ when Δv is negative. Thus there is a strong binding energy for large solute atoms on the expanded side of the slip plane, and a strong binding energy for small solute atoms on the compressed side of the slip plane.

The partitioning of solute atoms between the sites around the dislocation is given by

$$c_{(R,\theta)} = c_0 \exp(V_{(R,\theta)}/kT) \tag{2.27}$$

where $c_{(R,\theta)}$ is the solute concentration at co-ordinates (R, θ), c_0 is the solute concentration remote from the dislocation, k is Boltzmann's constant and T is the absolute temperature.

Considering the maximum binding energy site

$$c_{V\max} = c_0 \exp(V_{\max}/kT) \tag{2.28}$$

the concentration of solute near the dislocation core is dependent on the solute content of the alloy, the magnitude of the binding energy and the absolute temperature. The partitioning to the core will decrease as the temperature is

increased, provided that the value of c_0 is less than unity. This is described as a dilute or Maxwellian atmosphere. Obviously, for certain solute concentrations and binding energies, Equation (2.28) would indicate a particular temperature at which c_0 becomes unity. This is known as the condensation temperature and at lower temperatures a condensed (or saturated) atmosphere will exist with a solute atom at the core of each atom plane intersecting the dislocation. It is interesting to note that for the case of carbon in iron, with a dislocation density of 10^8 per square centimetre (as is typical of well annealed iron) the carbon content required to saturate the dislocations is of the order of 10^{-6}wt%.

The formation of atmospheres, whether of the Maxwell or Cottrell (saturated) types, may have some importance for the onset of plastic flow in materials showing continuous yielding, or where the binding energy is low and the dislocation can be induced to separate from its atmosphere. However, in mild steel, the formation of Cottrell atmospheres at near ambient temperatures results in a very stable configuration and the onset of plastic straining at the yield point is observed to occur by the creation of new dislocations, rather than by the unpinning of locked dislocations.

It is important to remember, however, that yielding in low carbon steels represents the stress required to propagate a Luders band into undeformed material. The stress required for this propagation obviously involves the applied stress directly, but may also involve local stress itensification by the cascade of dislocations produced in the deformed grain just behind the Luders front. This process is repeated throughout the yield point plateau as the Luders band extends to include the whole of the material under stress, and may involve engineering deformations up to several percent. The concept of a Luders front advancing across the whole of the specimen width in a polycrystalline material is indeed complex. Nevertheless, the low energy positions provided by dislocation–solute elastic interactions will provide stable positions for dislocations from which extra energy will be required to separate the dislocation and solute, and the theoretical treatment at least provides a basis on which to assess the strengthening effects of a number of solutes in the b.c.c. ferrite.

Little can be said of the other solid solution strengthening mechanisms, i.e. the chemical, electrical, and geometrical effects, as little is known of them, and there is no coherent theory that would provide even a qualitative prediction of the effects of various solutes in ferrite. The main source of information derives from experimental observation of the effects of solutes on yield strength, some of which have been obtained by careful control of solute contents and testing procedures (e.g. carbon), and some of which are provided from statistical treatments of the factors controlling yield strength in large numbers of steels of different solute contents.

2.3.2 Experimental Observations of Solid Solution Strengthening

The addition of solute elements to steel may have many effects on the microstructure. Traditionally, alloying elements are added to steel to change their microstructure. A common example is the addition of manganese, nickel,

chromium and molybdenum to enhance hardenability and promote the development of a hard martensitic structure. Other less extreme effects can be produced by such solutes because of their effects on the continuous cooling transformation temperature, even when a ferrite–pearlite structure is formed. By depressing the transformation temperature, the nucleation rate of ferrite can be enhanced, coupled with a reduction in the ferrite growth rate, thereby developing a finer grained structure. The addition of these solutes also change the proportions of ferrite and pearlite, either by constitutional effects, or by kinetic effects, and may also cause the formation of dilute pearlites at low transformation temperatures. The effects of any given solute, therefore, are complex, and include changes in ferrite grain size, the pearlite content in ferrite–pearlite structures, and of course the solute content of the ferrite matrix itself. All of these factors can change the strength of the steel, and in making an assessment of the solid solution strengthening effect, due allowance must be made for these other changes.

Another factor that is pertinent to the assessment of solid solution strengthening is the extent of solid solubility of the various solutes. This is perfectly obvious for carbon, for example, where any carbon in the form of cementite is clearly not in solid solution in the ferrite. In order to assess the interstitial solute content, a method has to be used that is specific to interstitial carbon atoms. The internal friction technique referred to earlier is just such a method and has been used to determine the interstitial contents of carbon (and nitrogen). Further, variations in the bulk carbon content found in the classical low carbon steels is merely reflected in a variation in the cementite content, the interstitial level being substantially independent of the bulk alloy level. The interstitial level can be changed substantially at a constant bulk alloy content by thermal treatments designed to give supersaturated solid solutions. This method has been used to assess the solid solution strengthening effect of carbon. The substitutional solutes, such as manganese, nickel and chromium, show extensive solid solubility and their addition increases the dissolved content directly, even at relatively high levels (several percent), the limitation being set by their effects on hardenability and transformation characteristics.

The solid solution hardening effects of various substitutional solutes in the b.c.c. ferrite structure are shown in Fig. 2.7, where the change in yield strength is shown as a function of the wt% of solute. As pointed out earlier, it has been assumed that the solid solution strengthening is approximately linear at the low concentrations that are relevant to microalloyed steels,

$$\Delta y_i = k_i \cdot c_i \tag{2.29}$$

where Δy_i is the strength increase due to the ith solute, c_i is the concentration of the ith solute (wt%) and k_i is the strengthening coefficient for the ith solute.

It is clear that the different solutes give very different strengthening factors. The coefficient for phosphorous is much higher than those of tin and silicon, which in turn are significantly higher than those of copper, manganese and molybdenum. Nickel showed no solid solution strengthening at all, and chromium apparently showed a negative strengthening effect. The solid solution strengthening effect of

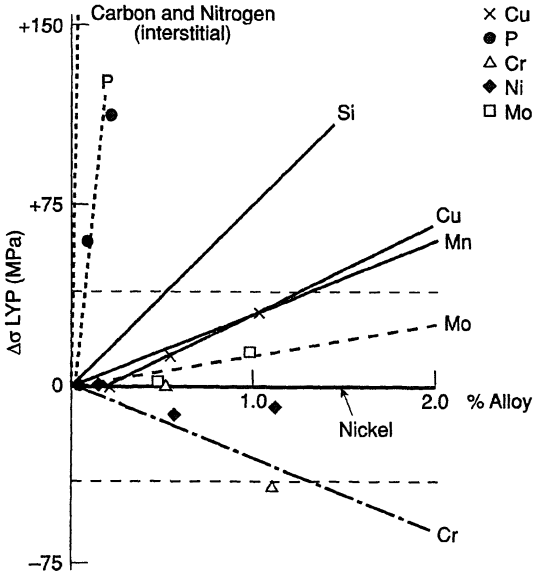


Fig. 2.7 Solid solution strengthening of b.c.c. iron. The effects of differing substitutional solute contents (wt%) on the yield strength are shown.

carbon was evaluated separately using three differing steels. The interstitial carbon content was varied in each by soaking at various subcritical temperatures and brine quenching. In this way the interstitial content was maintained at a level characteristic of the solubility limit of carbon in equilibrium with cementite at the soaking temperature. Internal friction curves obtained after quenching from the various sub-critical temperatures are shown in Fig. 2.8. The Snoek peaks in steels are complicated in that both carbon and nitrogen are present, and these give rise to individual but closely overlapping Snoek peaks. Further, interactions between nitrogen and manganese atoms give rise to yet other overlapping Snoek peaks, as shown by Ritchie and Rawling[7] and by Gladman and Barker.[8] Nevertheless, the solute contents can be obtained by mathematical methods of peak resolution and can be converted to interstitial contents from a knowledge of the relaxation strength. This may be approximated by

$$\text{wt\%C (interstitial)} = 0.4\delta_{max} \tag{2.30}$$

where δ_{max} is the Snoek peak maximum and the factor 0.4 represents the relaxation strength.

The yield strengths are shown as a function of the interstitial carbon and nitrogen content in Fig. 2.9. Each steel shows a consistent effect of interstitial carbon/nitrogen on the yield strength, indicating a strengthening coefficient of about 5,544MPa/lwt% of interstitial.[9] Over the limited range of solute examined, the linear approximation for the relationship between strength and solute content is well justified. The displacement of the lines for the three different steels is

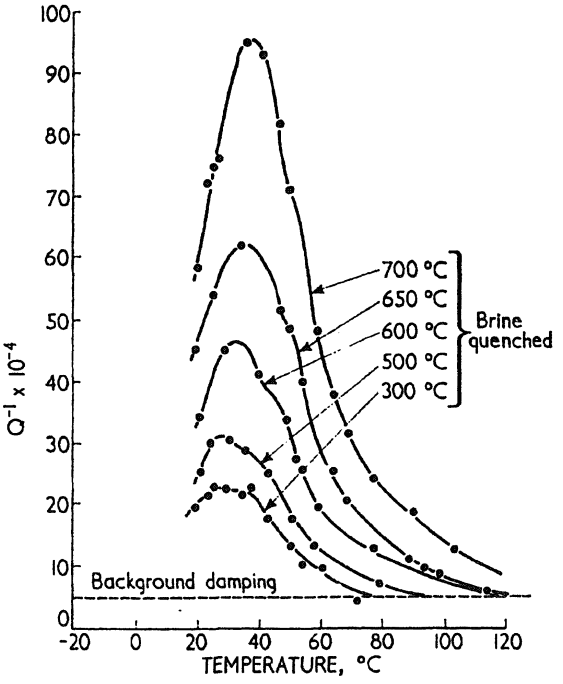


Fig. 2.8 Internal friction curves of a low carbon steel quenched from various sub-critical temperatures. The peak heights indicate the interstitial solute contents and increase with increasing temperature.

associated with differences in other solutes, such as manganese and silicon, and with different grain sizes. Additional experimentation was carried out for one of these steels and showed that the solid solution strengthening effect was independent of the grain size.

In order to compare the hardening effects of these solutes, it should be noted that the strengthening coefficients derived from Figs. 2.7 and 2.9 are based on the weight (mass) percentage of the solutes, so that solutes with a lower atomic weight will be present in larger numbers than would solutes with a higher atomic weight for a given weight percentage. The strengthening coefficients from these figures are collected in Table 2.1, and the corresponding values based on the atomic percentage are also shown.[9] It can now be seen that on an atomic basis, silicon and manganese have approximately the same solid solution strengthening coefficients. The apparently larger effect of silicon on a weight basis arises from the fact that there are twice as many silicon atoms as there are manganese atoms per 1wt%.

The elastic distortion caused by each solute atom would ideally be described by their atomic diameters in the b.c.c. iron lattice. However, due to the lack of data, this distortion has been derived from X-ray measurements of the effects of these solutes on the average lattice parameter of the b.c.c. iron unit cell. Collected data

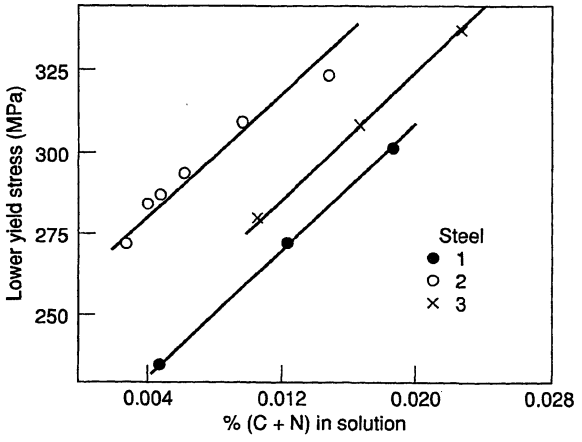


Fig. 2.9 Yield strength as a function of the interstitial contents. The interstitial contents were derived from the internal friction peaks in Fig. 2.8.

for the solutes of interest are given in Pearson,[10] and the elastic distortion can be defined by

$$\% \text{ dilation} = 100\Delta a/a \tag{2.31}$$

where Δa is the increase in lattice parameter for a 1% solute addition and a is the lattice parameter of the pure iron lattice.

The average lattice dilation expressed in terms of both wt% and at% is included in Table 2.1. The lattice dilation expressed on the basis of at% should be linearly related to the term Δv in Equation (2.24) and thus to the interaction energy, V. The solid solution strengthening coefficients (on an at% basis) for the various solutes

Table 2.1 Solid solution strengthening of α-iron. The strengthening coefficients and ferrite lattice distortion effects are shown for a number of solutes based on both at% and wt%

Solute	Relative atomic mass	ΔY/lwt% (MPa)	$(\Delta a/a)$/lwt% (%) (4)	ΔY/lat% (MPa)	$(\Delta a/a)$/lat% (%)
Fe	56	–	–	–	–
C(and N) (1)	12	5,544	4.000	1,188	0.869
C(and N) (2)	12	4,620	4.000	990	0.869
P (1)	31	678	0.000	384	0.000
Sn (1)	119	123	0.110	262	0.224
Si (1)	28	83	−0.042	42	0.021
Cu (1)	64	39	0.046	44	0.052
Mn (1)	55	32	0.020	32	0.020
Mn (3)	55	31	0.020	31	0.020
Mo (1)	96	11	0.041	18	0.070
Ni (1)	59	0	0.018	0	0.019
Cr (1)	52	−31	0.020	−29	0.019

(1) F. B. Pickering and T. Gladman (see reference 9).
(2) A. Cracknell and N. J. Petch (see reference 12).
(3) J. Heslop and N. J. Petch (see reference 11).
(4) W. B. Pearson (see reference 10).

are shown as a function of the lattice dilation (again on an at% basis) in Fig. 2.10. In general, the strengthening coefficient appears to increase with increasing lattice dilation, but the general trend is dominated by the interstitial carbon, which gives a dilation that is not only larger than that of the largest substitutional solute (Sn), but is also assymetric. Tin gives a substantial lattice dilation and also a substantial strengthening coefficient, whereas many of the other solutes, such as manganese, copper and silicon, cause a relatively small lattice dilation, of the order of 0.02%, and consequently have relatively small strengthening cofficients, of the order of 30–40 MPa per 1at%.

There are two features in Fig. 2.10 which are worthy of further comment. Firstly, phosphorus has a substantial strengthening coefficient, of the order of 400 MPa per 1at%, but gives no lattice dilation. The reasons for this are not at all clear. One possible explanation is that the effect of phosphorus is based on a mechanism other than elastic interaction with dislocations, such as chemical, electrical or geometrical interactions. Given the metalloid nature of phosphorus, it would be surprising if all such effects were absent. Secondly, the negative strengthening effect of chromium requires some explanation. One possible explanation is that chromium, being a strong nitride former, acts as a scavenger for nitrogen. Thus the addition of chromium, particularly when the steel is cooled at a sufficiently slow rate to avoid the formation of martensite or intermediate transformation products, results in the removal of nitrogen from solid solution. As the interstitials have been shown to have such a large strengthening coefficient, the effect of removing nitrogen could dominate the strength change. The removal of 0.008wt% N would

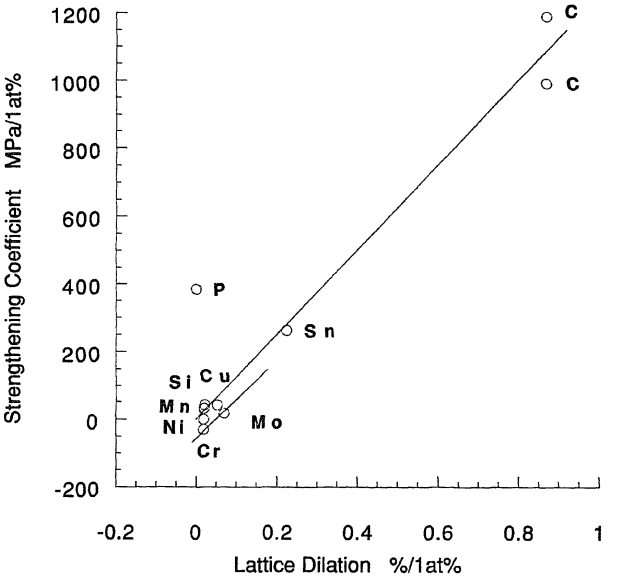


Fig. 2.10 Solid solution strengthening coefficients shown as a function of the lattice dilation due to the solute additions. Both strengthening and lattice dilation are expressed in terms of the *atomic* percentage of solute.

be expected to result in a reduction of yield strength of the order of 30–40 MPa. The effect of chromium on the change in yield strength shown in Fig. 2.8, however, suggests a linear decrease in strength up to 1wt% Cr, and as the nitrogen content could be completely scavenged by much lower contents, the solid solution softening may be a real effect. Similar observations have been made by Jaffe and Hahn,[11] for chromium in other b.c.c. metals. It has also been shown that metals belonging to group VI(a), such as chromium and molybdenum, are susceptible to electron bond weakening at certain critical electron/atom ratios which might offset the elastic interaction effect. A separate line, such as is shown in Fig. 2.10, may thus fairly reflect the electron bond weakening of these elements. Irrespective of the validity of these explanations, however, the solid solution strengthening coefficients of the various solutes are substantially as shown in Table 2.1.

The use that is made of these solutes in commercial steels does not depend on the absolute magnitude of the strengthening coefficient. There are many other factors that need to be taken into account, as follows.

Carbon

The interstitial carbon content in normalised or hot-rolled and air-cooled steels is usually very low and reflects the extremely low solubility of carbon in ferrite at near ambient temperature. Quenching from elevated sub-critical temperatures will enchance the carbon in solution but the supersaturated solid solution is unstable at ambient temperatures and will decompose. This phenonemon is known as quench ageing and can result in precipitation/dispersion hardening.

Phosphorus

Phosphorus finds limited use as a solid solution strengthener, mainly in thin strip, but is avoided in other steels because of its particularly adverse effects on toughness, as will be shown later.

Silicon and manganese

These elements are used extensively in steels – not because of their solid solution strengthening – but for other reasons. Silicon is a commonly used deoxidising element and silicon levels generally reflect the amount needed to give satisfactory deoxidisation. Again, like phosphorus, some use is made of enhanced silicon additions in thin strip products to give solid solution strengthening, but it is not generally used at such levels in structural steels. Manganese, initially introduced to form manganese sulphide and obviate hot shortness, is now used to give controlled transformation characteristics during cooling from the austenite temperature range. Although not used specifically as solid solution strengtheners, the levels of silicon and manganese added for other purposes do in fact contribute appreciably to the yield strength of many structural steels as will be shown in a later section.

Tin

Although tin gives a relatively high strengthening coefficient that is commensurate with the iron lattice dilation, it is not used as a solid solution strengthener in steel

because of its adverse effect on hot workability. Tin, like copper, is less easily oxidised than iron, and on heating in an oxidising atmosphere prior to hot rolling, iron is preferentially oxidised. Elements such as copper and tin which are not oxidised give rise to the phenomenon of sub-scale enrichment, where very high levels of copper and tin are found (5–10%), resulting in the formation of a liquid copper–tin phase. Tin is particularly harmful in this respect as it has a relatively low solubility in austenite. The presence of this liquid phase gives rise to surface hot-shortness.

Copper

Copper is sometimes used in structural steels because it improves the atmospheric corrosion resistance, and features in the weathering grades of structural steel. Care has to be taken to control the phenomenon of sub-scale embrittlement and the ensuing hot-shortness.

Nickel, chromium and molybdenum

These alloying elements have powerful effects on hardenability, i.e. the tendency to form martensite, and are therefore of limited applicability in weldable structural steels. Although they are used in limited amounts to control the transformation characteristics of certain structural steels, they are expensive additions and give, at best, very little as solid solution strengtheners, as shown in Fig. 2.10.

In summary, therefore, the solid solution strengthening effect of solutes is broadly commensurate with the lattice dilation, the notable exception being phosphorous which has a high strengthening coefficient, yet produces no significant lattice distortion. The use of solid solution strengthening in steels is generally limited by other considerations such as solubility limits, weldability, toughness, hot workability, and cost. The notable exception is the use of silicon and phosphorus as solid solution strengthening agents in cold rolled and annealed thin strip. The use of these particular solutes is not obvious from Fig. 2.10, but when judged on a weight percentage basis, Fig. 2.11 (and more importantly, on a cost basis), their selection is better appreciated.

2.3.3 Grain Refinement as a Strengthening Mechanism

The awareness of the effect of adding small amounts of aluminium to plain carbon steels is reflected in many old specifications for plain carbon and aluminium treated steels. It was well known that aluminium treated steels have higher yield strengths and superior toughness, and would have a much finer ferrite grain size, and these steels were produced as bulk tonnage steels. The quantitative relationship between yield strength and grain size in metals was first described by Hall,[14] based on experimental observations, and by Petch,[15] based on both experimental and theoretical approaches. These workers had collaborated and the experimental evidence was based on observations in steel. The relationship

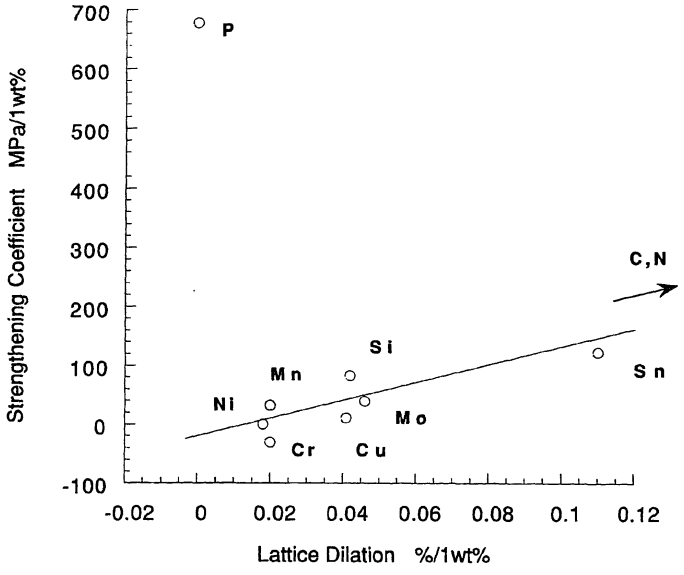


Fig. 2.11 Solid solution strengthening coefficients shown as a function of the lattice dilation due to the solute additions. Both strengthening and lattice dilation are expressed in terms of the *weight* percentage of solute.

between yield strength and grain size is now commonly known as the Hall–Petch equation.

$$\sigma_y = \sigma_i + k_y d^{-1/2} \tag{2.32}$$

where σ_y is the lower yield stress, σ_i is the friction stress, k_y is the strengthening coefficient and d is the 'grain size'.

The theoretical basis for this equation relies on the stress intensification at the head of a pile-up of dislocations, as shown in Fig. 2.12. The grain boundary offers a resistance to the first dislocation due to the discontinuity of both slip plane and slip direction, and the dislocation is arrested. Further dislocations of like sign arrive, and the elastic interaction between successive dislocations, induced by the (increasing) applied stress, force the first dislocation closer to the boundary and enhances the elastic strain (and stress) in the neighbouring grain. The stress at the head of the pile-up is dependent upon the number of dislocations in the pile-up, and the number increases as the grain size is increased. If τ_i is the friction (shear) stress, and τ an increased (shear) stress applied to a polycrystal, then the resistance offered by the grain boundary is $(\tau - \tau_i)$. There is a limiting or critical value of $(\tau - \tau_i)$ above which slip will be induced in the neighbouring grain. The stress concentration at some short distance, r, into the next grain, from the head of the slip band is proportional to $(d/4r)^{1/2}$. The maximum shear stress at a distance, r, from the head of the slip band, τ_{max}, is given by

$$\tau_{max} = (\tau - \tau_i)(d/4r)^{1/2} \tag{2.33}$$

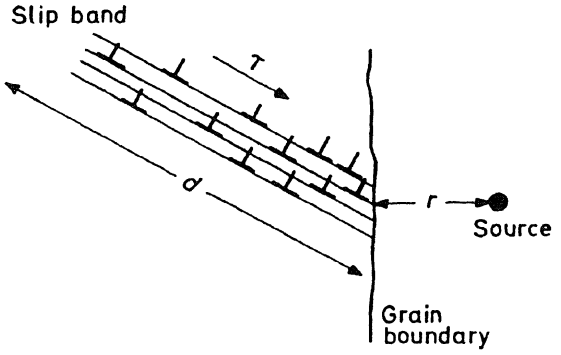


Fig. 2.12 Stress intensification arising at the head of a dislocation pile up at a grain boundary. After Smallman.[2]

When the value of τ_{max} reaches some critical value, dislocation sources at r are activated in the next grain and the applied shear stress, τ, becomes the yield shear stress, τ_y. Equation (2.33) can then be written as

$$\tau_y = \tau_i + (\tau_{max} \cdot 2r^{1/2})d^{-1/2} \tag{2.34}$$

It should be noted that the shear stresses given in Equation (2.34) all relate to shear stresses in the slip band, and as the dislocation source in the next grain will have a slip plane of a different orientation, then τ_{max} will be sensitive to the orientation of the slip plane and slip direction of the new source, and indeed the strength of the new source. Thus the value of τ_{max} in the pile up will be higher than the shear stress required to activate the new source, when referred to the slip orientation of the new source. For simplicity, it is commonly assumed that the combined Taylor factor can be applied to the local misorientation as well as the macroscopic misorientation, and thus

$$\tau_{max} = 3\tau_c/2 \tag{2.35}$$

Substituting in Equation (2.34) gives

$$\begin{aligned}\tau_y &= \tau_i + (3\tau_c \cdot 2r^{1/2}/2)d^{-1/2} \\ &= \tau_i + (3\tau_c \cdot r^{1/2})d^{-1/2}\end{aligned} \tag{2.36}$$

Conversion to tensile stress using Equation (2.12) then gives

$$\sigma_y = \sigma_i + (9\tau_c \cdot r^{1/2})d^{-1/2} \tag{2.37}$$

Comparison of this equation with the Hall–Petch equation (2.32) shows that k_y is represented by the term $(9\tau_c \cdot r^{1/2})$, and depends on the shear stress required to activate the new source, τ_c, and the distance of that source from the grain boundary. Initially, the concept identified k_y with the strength of the dislocation–

atmosphere interaction, and this factor is not irrelevant, as will be shown later when considering the effects of pinch passing and strain ageing. However, for commercial HSLA steels in the normalised or hot rolled conditions, experimental observations have suggested that the bound dislocations, with their atmospheres of carbon and nitrogen atoms, and perhaps carbide particles in addition, play no part in yielding, and remain locked. The plastic yielding is observed to occur by the creation of new dislocations, apparently providing constant levels of τ_c and r and a virtually constant value for k_y. Significantly lower k_y values are only observed when fresh dislocations are introduced into the system as for example by very light rolling deformations (pinch passing), or by severe reductions in the interstitial content, thereby reducing the locking strength.

2.3.4 Values of the Strengthening Coefficient k_y

So far, the term d in the Hall–Petch equation has been referred to as the 'grain size'. It is vitally important that the measure of grain size is defined. From the above theoretical treatment, the 'grain size' is introduced as a measure of the length of the slip band, and as such may be interpreted as the grain 'diameter', although this is by no means definite, as the active slip band may or may not coincide with the maximum possible length of slip band in a polyhedral grain. However, if it is reasonably assumed that the maximum stress concentration will occur at the maximum slip line length, then this would define the grain 'diameter' as the definitive variable. Even here there is a problem, as the grain diameter in (opaque) metals cannot be measured directly, firstly because the grains are polyhedral and do not have a unique 'diameter', and secondly because the practical measurement of grain size is made on a planar intersection of the three-dimensional array of polyhedral grains. The most common method used in the quantitative assessment of 'grain size' is the Heyn intercept method, which defines the mean intercept length of the grains with a linear intersecting line made on the planar metallographic section of the three-dimensional array of grains. This is often referred to as the mean linear intercept. Although the standard method for intercept measurement involves a circular intersecting line in the metallographic plane, in order to overcome problems of elongated grain structures, this is not recommended for quantitative relationships between grain size parameters and mechanical properties, as a single measure from an anisotropic structure may not give the same contribution to yield strength as, for example, the same numerical value derived from a completely isotropic structure. The mean linear intercept method is strongly recommended, and is discussed in more detail in Chapter 4.

Having determined a mean linear intercept grain size, a further problem may arise in converting the mean linear intercept to some measure that is pertinent to grain 'diameter' (or to the mean slip line length of the array). The conversion is frequently based on the assumption of a spherical grain, i.e. the diameter of a spherical grain having the same mean linear intercept as that observed for the polycrystalline array, as shown in Fig. 2.13(a). The mean linear intercept of a

sphere is defined by the volume of the sphere divided by the area available for intersection

$$\begin{aligned} \text{m.l.i.} &= 4\pi r^3/3 \cdot \pi r^2 = 4r/3 \\ d &= 2r \qquad\qquad = 3(\text{m.l.i.})/2 \end{aligned} \tag{2.38}$$

It can be seen that the 'diameter' of the grain is larger than the mean linear intercept by some 50%. Thus in equations derived directly from mean linear intercept measurements, i.e.

$$\begin{aligned} \sigma_y &= \sigma_i + k_y' i^{-1/2} \\ &= \sigma_i + k_y'(2d/3)^{-1/2} \\ &= \sigma_i + k_y'(2/3)^{-1/2} \cdot d^{-1/2} \end{aligned} \tag{2.39}$$

$$\text{then} \quad k_y = k_y' \cdot (3/2)^{1/2} \tag{2.40}$$

i.e. k_y' will be smaller than k_y by about 20%. This will obviously be important when comparing equations where d is defined differently. For example, in the work of Cottrell and Fisher,[16] Cracknell and Petch,[12] and Armstrong *et al.*[17] their grain size measurements were obtained from the number of grains per unit area in a plane section, n_a. If the grain diameter is obtained from the mean area of intersection of the array of grains ($1/n_a$), then given the assumption of spherical grains, the mean area of intersection, a, will, as indicated in Fig. 2.13(b), be given by

$$a = 4\pi r^3/3 \cdot 2r = 2\pi r^2/3 = \pi d^2/6$$

$$a = \pi(d')^2/4$$

where d' is the diameter of a circle of area a.

$$\pi(d')^2/4 = \pi d^2/6$$

$$d = (3/2)^{1/2} d'$$

It can be seen that the diameter of the grain is larger than the diameter of a circle equal in area to the mean planar area of intersection by a factor of $(3/2)^{1/2}$ or some 23%. Thus in equations derived directly from d', i.e.

$$\begin{aligned} \sigma_y &= \sigma_i + k_y''(\mathrm{d}')^{-1/2} \\ &= \sigma_i + k_y''((3/2)^{-1/2} d)^{-1/2} \\ &= \sigma_i + k_y''(3/2)^{1/4} \cdot d^{-1/2} \end{aligned}$$

$$\text{then,} \quad k_y = k_y''(3/2)^{1/4} \tag{2.42}$$

i.e. k_y'' will be smaller than k_y by some 10%.

It should be pointed out that there is a clear option for researchers to use the measures of grain size directly, e.g. i in Equation (2.39), and derive the modified proportionality constant k_y', or d' in Equation (2.41), to obtain k_y''. These are related

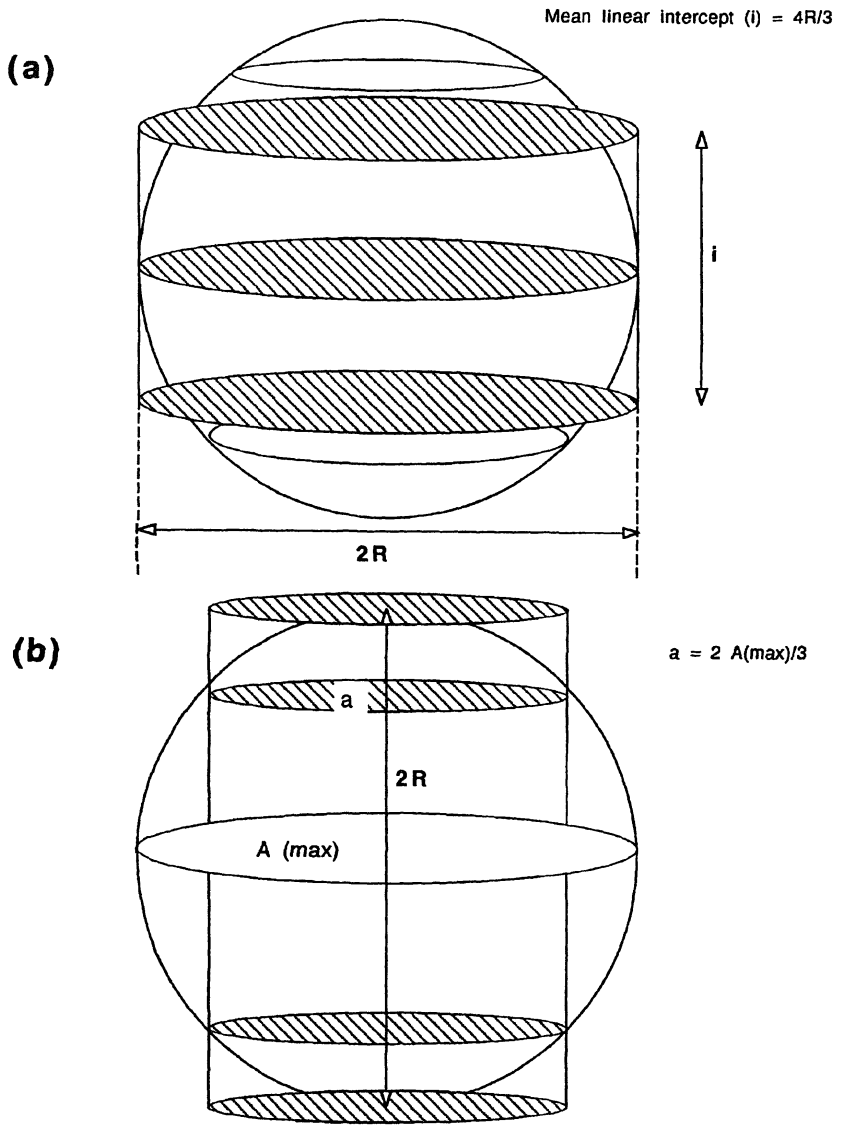


Fig. 2.13 (a) A spherical grain can be intersected by random linear intercepts. The intercepts have a mean length which, when multiplied by the maximum cross sectional area, is equal to the volume of the sphere. (b) A spherical grain can be intersected by random planar intercepts. The intercepts have a mean area, which, when multiplied by the diameter of the sphere, is equal to the volume of the sphere.

to k_y as indicated in Equations (2.40) and (2.42). Alternatively, researchers may make the appropriate corrections to evaluate d from their measurements and obtain k_y directly. Comparisons between k_y and k'_y (or k''_y) would obviously be expected to show differences as illustrated in Table 2.2. Evaluation of the apparent k_y based on raw mean linear intercepts gives lower values than are obtained for the real k_y based on converted measures derived from the number of grains per unit area. Correction of all measures to grain diameter d, gives a surprising consistency of the observed values of k_y ranging from 21.4 to 23.5 MPa mm$^{1/2}$. The importance of specifying both the methods of grain size measurement and the derivative used in the Hall–Petch relationship is clear. All methods would indicate the same contribution of grain size to the yield strength, i.e. $k_y d^{-1/2}$ or $k'_y i^{-1/2}$, or $k''_y (d')^{-1/2}$, but $k_y > k''_y > k'_y$.

It is interesting to note the theoretical value of k_y given by Dingley and McLean.[18] This is based on a value of d equated to the active slip band length, the dislocations being newly created at the grain boundary. Following the work of Cottrell,[20] these require a critical shear stress of 4.7 GPa for their creation at a distance some 2.7 Burgers vectors from the boundary. The equation given by Eshelby *et al.*[21] for the stress distribution ahead of the slip band, including the orientation factor, is

$$\tau_c \approx (\sigma/5.66)(d/2x)^{1/2} \tag{2.43}$$

where τ_c is the critical shear stress (4.7 GPa), σ is the effective tensile stress, d is the slip band length and x is the distance ahead of the slip band ($=2.7b$)

Given that the Burgers vector on the active slip system in body centred cubic iron is ~ 0.25 nm (or 0.25×10^{-6} mm),

$$\sigma = 21.9 \text{ MPa mm}^{1/2} \cdot d^{-1/2}$$

$$\text{or} \quad k_y = 21.9 \text{ MPa mm}^{1/2}$$

Table 2.2 Comparison of experimental values for k_y corrected for grain size assessment method. The theoretical value obtained by Dingley and McLean[18] is also shown

Reference	Measure of d	σ_i	Apparent k_y MPa mm$^{1/2}$	k_y MPa mm$^{1/2}$
Morrison[19]	m.l.i.[a]	70	18.1	22.3
Cracknell and Petch[12]	d[b]	47	23.5	23.5
Armstrong *et al.*[17]	d[b]	71	22.4	22.4
Pickering and Gladman[9]	m.l.i.[a]	54	17.4	21.4
Dingley and McLean[18] – Experimental	Not known	15	21.4	21.4?
Dingley and McLean[18] – Theoretical	c	–	–	21.9

[a] Observed m.l.i. ($= 2d/3$).
[b] Calculated from $d = (3/2)^{1/2} d' = (6/\pi N_A)^{1/2}$ where N_A is the number of grains per unit area of plane section.
[c] Assumed d.

The agreement between this theoretical estimate of k_y and the observed values is excellent, and gives some confidence in postulating that the mechanism of yielding in most normalised, annealed or as-rolled steels is by the generation of new dislocations, and that the effective slip band length can be equated with the grain diameter, as calculated from either the mean intercept length or the number of grains per unit area.

A word of caution is required here, however, in that the value of k_y observed is relevant to structures in which the pre-existing dislocations are tightly bound. If free dislocations or less tightly bound dislocations are present, then the k_y values will undoubtedly be lower than those reported here, as was shown by Cottrell. Also, k_y values begin to decrease at temperatures near to, or slightly above, room temperature, so that adiabatic heating with even moderate strain rate deformation processes may reduce the value of k_y. The effect of temperature in the range 20–350°C is quite pronounced, the k_y values decreasing from about 22 MPa $mm^{1/2}$ down to about 4 MPa $mm^{1/2}$. More will be said about the changes in k_y in Chapter 7, when dealing with bake hardening steels.

2.3.5 Friction Stress

The values quoted as friction stress in Table 2.2 show considerable variation. This is perhaps not too suprising, however, when the steel compositions are taken into consideration. Dingley and McLean[18] used virtually pure iron with less than 0.03wt% of substitutiontal solutes, and their carbon and nitrogen levels were extremely low. The results of other workers shown in Table 2.2 reflect the effects of substantial solute additions, and the intercepts quoted from the Hall–Petch relationship can more properly be regarded as the friction stress of iron *plus* the hardening effect of these solutes. This has been amply demonstrated by Cracknell and Petch,[12] where the Hall–Petch intercept increased with increasing solute content of steels 1–6, but for each steel the k_y value was sensibly constant, Fig. 2.14. Thus the generalised form of the Hall-Petch relationship can be written as

$$\sigma_y = \sigma_0 + k_y \cdot d^{-1/2} \tag{2.44}$$

where

$$\sigma_0 = \sigma_i + \Sigma k_i \cdot c_i \tag{2.45}$$

The second term summates the effects of various solutes with concentrations, c_i, having strengthening coefficients, k_i.

It was also noted that the values of σ_0 in Equation (2.44), were sensitive to cooling rate, in normalised steels, and the σ_0 value was some 25 MPa lower for annealed materials than for material air cooled as 20 mm dia. bar. This may well reflect an effect of dislocation densities or of interstitial solute precipitation during cooling; the effects of carbide/nitride distribution will be shown later in this chapter.

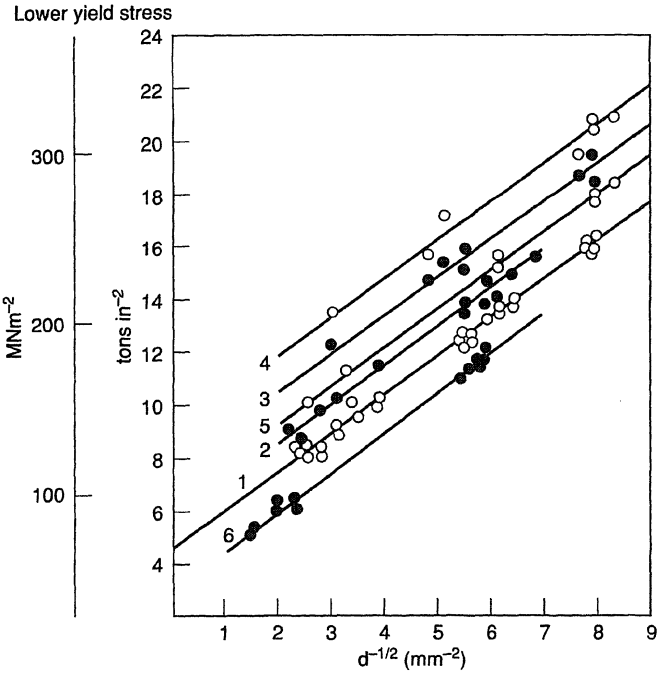


Fig. 2.14 Effect of solutes on yield strength. The solutes affect the σ_0 in the Hall–Petch equation and not the k_y term (provided that the pre-existing dislocations are fully locked). After Cracknell and Petch.[12]

2.3.6 Combined Strengthening Effects

The important feature of combined solute strengthening and grain size strengthening is that the solute affects σ_0 in the Hall–Petch equation and *not* k_y. Thus Equation (2.44) can be written in expanded form to give

$$\sigma_y = \sigma_i + \Sigma k_i \cdot c_i + k_y d^{-1/2} \tag{2.46}$$

where σ_y is the (tensile) yield stress, σ_i is the friction stress of iron, c_i is the concentration of the ith solute, k_i is the strengthening coefficient of the ith solute, k_y is the strengthening coefficient for grain size and d is the grain diameter (spatial)

The term $k_y \cdot d^{-1/2}$ can be substituted by $k'_y i^-$ or $k''_y(d')^{-1/2}$ as explained earlier in this section, where i is the mean linear intercept grain size, and d' is the diameter of a circle having the same area as the mean area of planar intersections.

2.3.7 Dispersion Strengthening – The Orowan and Ashby–Orowan Relationships

In systems which show precipitation from a single phase solid solution, a considerable body of evidence has been accumulated to show that there are a

number of mechanisms that can contribute to the observed increases in strength. These include coherency strengthening, which relates to the coherency strains developed in the matrix around a coherent precipitate, chemical hardening, which arises from the development of antiphase boundaries when a dislocation cuts through a particle, and dispersion hardening, which arises from looping of the dislocation between hard undeformable particles as described by Orowan,[22] (Fig. 2.15). In addition to the above mentioned effects, there are other considerations which arise when dislocations intersect second phase particles. The dislocation compatability in terms of both the Burgers vector and the slip plane orientation will have significant effects, as will the deformation of the particle, involving creation of additional matrix/particle interfacial areas, as shown in Fig. 2.16.

In microalloyed steels, the fine strengthening precipitates are usually formed during the austenite–ferrite transformation – the interphase precipitation process – and results in the formation of small discrete microalloy carbides/nitrides. These carbide/nitrides are very hard and extensive dislocation bowing is commonly

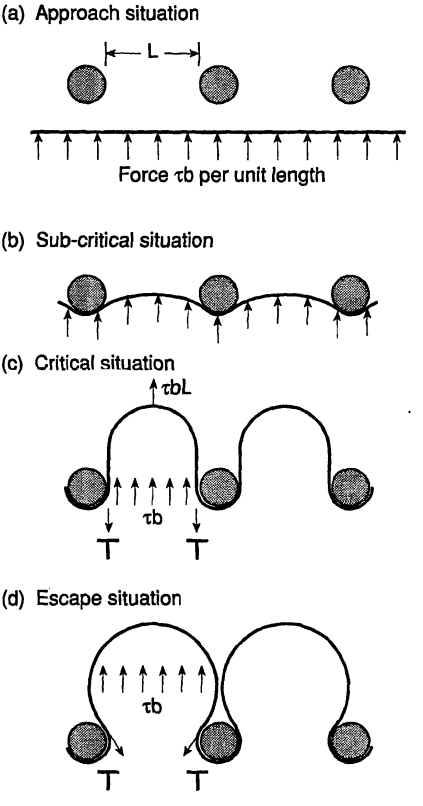


Fig. 2.15 A dislocation meets hard undeformable second phase particles and loops between then. Dislocation release at higher stresses may occur by Orowan looping or by cross slip. After Ashby and Jones.[35]

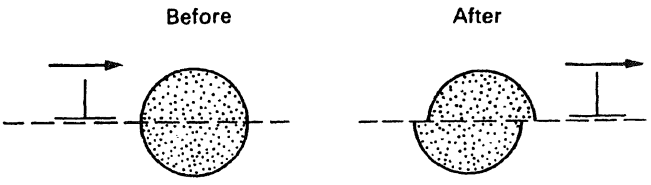


Fig. 2.16 Dislocations may continue through the second phase particles (particle cutting). The second phase particle becomes deformed and the interfacial area of the particle/matrix is increased.

seen. As pointed out by Nicholson,[23] it cannot be argued that particle cutting never takes place in a particular system, but the transition from a cutting mechanism to the Orowan type looping will occur at a very small particle size, due to the characteristics of the microalloy carbides and nitrides. Direct evidence of the mechanism by which dislocations bypass the interphase precipitated particles is lacking, mainly due to difficulties in observing such small particles, usually a few nanometres in diameter, in a deformed structure. Nicholson has drawn an important distinction between the mechanisms of particle shearing and particle bypass in their response to particle size. The particle shearing mechanisms generally show a positive dependence on particle size, whereas the looping mechanism shows an inverse dependence with particle size. As will be shown later in this section, the strengthening contribution of the hard carbides or nitrides appears to decrease with increasing particle size, and shows remarkably good agreement with theories based on dislocation bypassing.

The basic model of dislocation looping between particles was developed by Orowan.[22] The line tension of a dislocation, T, has already been derived in Equation (2.18) as

$$T \approx Gb^2/2$$

This line tension represents an energy per unit length, and consequently each dislocation behaves like a piece of elastic and tries to maintain its shortest length in order to minimise the energy of the system. If the dislocation is caused to move under an applied shear stress, then, in a dispersion hardened system such as b.c.c. ferrite with a fine dispersion of, say, niobium carbide, the dislocation movement will cease when it meets one or several hard undeformable particles along its length. A balance of forces can be established as the dislocation begins to bow out between the particles (Fig. 2.17).

The repelling force of the particle, F, is balanced by the resolved line tension of the bowing dislocation

$$F = 2T \sin\theta \tag{2.47}$$

The bowing force, B, is given by

$$B = \Delta\tau \cdot b \cdot L \tag{2.48}$$

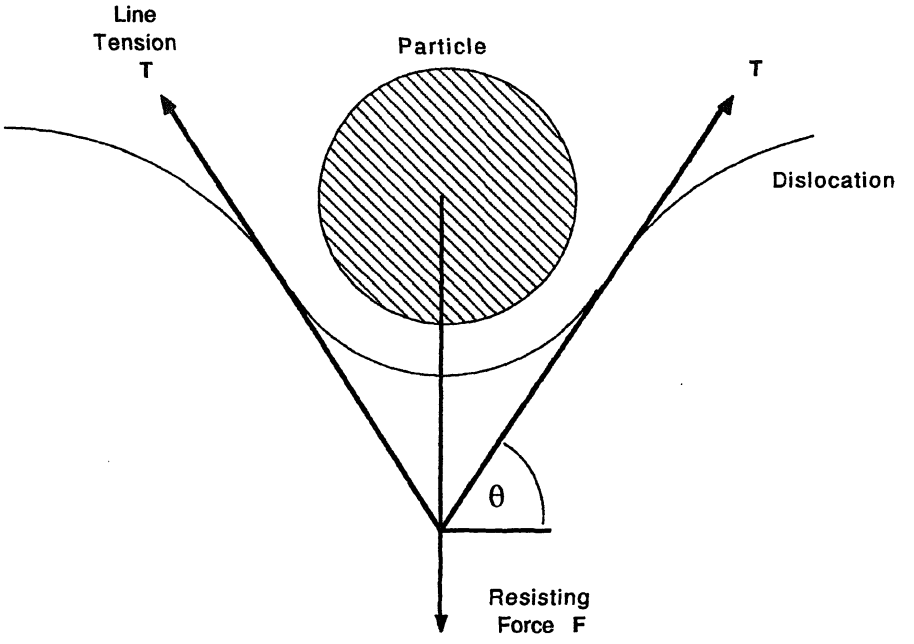


Fig. 2.17 The balance of forces between the particle resistance to dislocation movement and the line tension of the dislocation.

where L is the spacing between particle centres and $\Delta\tau$ is the increased stress required, due to the particles, defined by

$$\Delta\tau = \tau_a - \tau_m \tag{2.49}$$

where τ_a is the applied shear stress and τ_m is the shear yield stress in the absence of particles. Equations (2.47) and (2.48) give

$$\Delta\tau b \cdot L = 2T \sin\theta \tag{2.50}$$

and the resistance force is maximised when $\sin\theta = 1$, and thus

$$\Delta\tau_{\max} b \cdot L = 2T \tag{2.51}$$

Substituting from Equation (2.18) gives

$$\Delta\tau_y = 2Gb^2/2bL$$

$$\text{or} \quad \Delta\tau_y = Gb/L \tag{2.52}$$

This is the Orowan equation, where the particle spacing can be converted to the volume fraction and size of particles based on some assumption of the distribution of particles. The simplest model is of a (two-dimensional) square array of particles in the slip plane, resulting from a three-dimensional distribution of particles of diameter, X, and volume fraction, f. From stereological considerations, the area

fraction of particles in the slip plane will also be given by f (because the area fraction is equal to the volume fraction), but the average diameter of the particles in the plane of intersection, x, will not be equal to the true particle diameter, X. The relationship between the true three dimensional diameter, X, and the diameter x, of particles of mean area in the plane of intersection (in this case, the slip plane), has already been considered in an earlier section of this chapter, see Fig. 2.13(b), and is given by

$$X = (3/2)^{1/2}x \tag{2.53}$$

Note that x is the diameter of a circle having the same area as the mean area of all circles of intersection, and is *not* the mean diameter of intersected grains. The volume (or area) fraction of particles is thus given by

$$f = n_A \cdot \pi x^2/4 \tag{2.54}$$

where n_A is the number of particles intersected per unit area of the slip plane.

The particle spacing was estimated by assuming that the particles lie on a square grid in the slip plane, so that the edge length of the square represents the effective particle spacing, L.

$$L = (1/n_A)^{1/2} \tag{2.55}$$

Substitution of Equations (2.53), (2.54) and (2.55) together with Equation (2.49) into Equation (2.52) gives

$$\begin{aligned}\tau_y &= \tau_m + Gb/L \\ &= \tau_m + GbnA^{1/2} \\ &= \tau_m + 2Gb \cdot f^{1/2} \cdot /\pi^{1/2}x \\ &= \tau_m + 2Gb(3f/2\pi)^{1/2}/X\end{aligned} \tag{2.56}$$

Converting this to the corresponding tensile yield strength and using the Taylor factor gives

$$\sigma_y = \sigma_m + 6Gb(3f/2\pi)^{1/2}/X \tag{2.57}$$

where σ_m is the tensile yield strength in the absence of a dispersion of particles.

Equation (2.57) represents an overestimate of the stress required to cause dislocation bypassing of the particles. For example, Equation (2.55) implies that the dislocation is parallel with one edge of the assumed square array of particles in the slip plane. The effective particle spacing would be increased by a factor of $2^{1/2}$ if the dislocation was parallel with the diagonal of the square. Further, when the particles are present in a random array, rather than a regular array, some of the wider spacings offer no resistance at all to the passage of dislocations when the stresss has reached a level that would allow bypassing on the basis of the regular array. Thus, Equation (2.57) represents an upper bound to the strengthening effect of a dispersion of fine particles. Kocks[24] and Foreman and Makin[25] have used computer-based simulation processes with random arrays of small obstacles in the

slip plane. The near neighbours of a reference obstacle are defined as those which can be placed at opposite ends of the diameter of a circle without occluding any other particle in the circle as shown in Fig. 2.18. In this way the effective obstacle spacing can be evaluated and compared with the square grid spacing. These workers found that

$$\sigma_y = 0.81Gb/L \qquad \text{(Foreman and Makin)}$$
$$\sigma_y = 0.84Gb/L \qquad \text{(Kocks)}$$

Ashby[26] has considered these effects, together with the use of the interparticle distance (surface to surface) rather than the centre to centre spacing implied by Equation (2.55). This latter feature, however, is more important in steels with high volume fractions of large particles, but has little significance for microalloyed steels where the particle size is negligible with respect to the particle spacing due to the low volume fractions of particles used.

The Ashby–Orowan equation is given as

$$\Delta\tau_y = 0.84(1.2Gb/2\pi L) \cdot \ln(x/2b) \tag{2.58}$$

where $L = (n_s^{-1/2} - x) \approx n_s^{-1/2}$, x is the diameter of the mean area of intersection of spherical particles of diameter X and n_s is the number of particles intersected by unit area of slip plane.

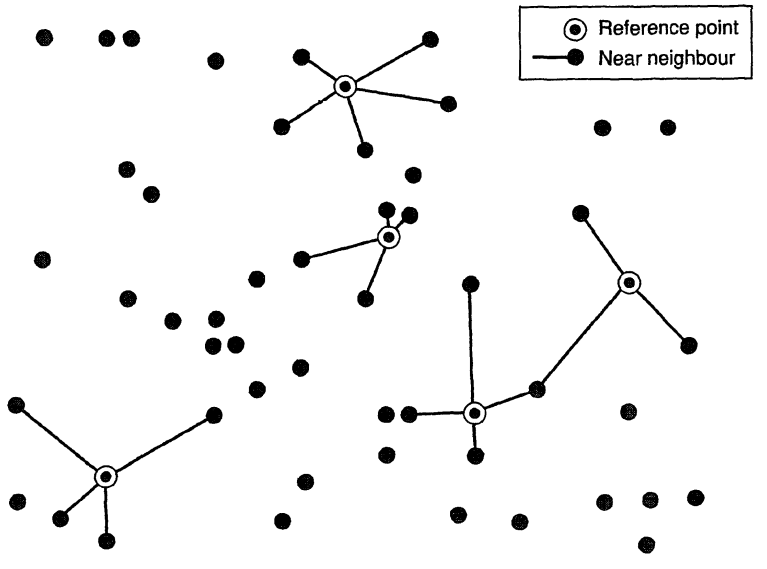


Fig. 2.18 The near neighbours of a particle lie at opposite ends of the diameter of a circle which does not occlude other particles.

Making the appropriate substitutions from Equations (2.53) to (2.55) in Equation (2.58) and substituting values of $G = 80{,}300$ MPa, $b = 2.5 \times 10^{-4}$ μm gives

$$\Delta\sigma_y(\text{MPa}) = (10.8f^{1/2}/X)(\ln(X/6.125 \times 10^{-4})) \tag{2.59}$$

when X is expressed in μm.

This equation differs marginally from that given by Gladman *et al.*,[27] in the use of a Taylor factor of 3 rather than 2 and the correct use of $2b$ in the last term of Equation (2.58) rather than b in the earlier work. Also, Equation (2.59) expresses the particle size as a real particle diameter, X, rather than that obtained from the mean area in the plane of section. The values of $\Delta\sigma_y$ calculated for various particle sizes are shown as a function of the volume fraction in Fig. 2.19. The values of the yield stress increase, $\Delta\sigma_y$, shown in this figure must obviously reflect the $f^{1/2}$ dependency of Equation (2.59), and, being plotted on logarithmic co-ordinates, the slope of the line is 1/2. The effect of particle size on the increase in yield stress clearly shows the dominance of the $1/X$ term over the $\ln(X/6.125 \times 10^{-4})$ term in Equation (2.59), so that the refinement in particle size produces significant increases in yield strength, as would be expected from the Orowan equation. The direct comparison of the Orowan equation (2.57) and the Ashby–Orowan equation (2.59) is also shown in Fig. 2.19 for a particle size of 5 nm. The Orowan equation indicates a significantly larger increase in yield strength than is forecast by the Ashby–Orowan equation, and this is due to the use of a minimum spacing of a

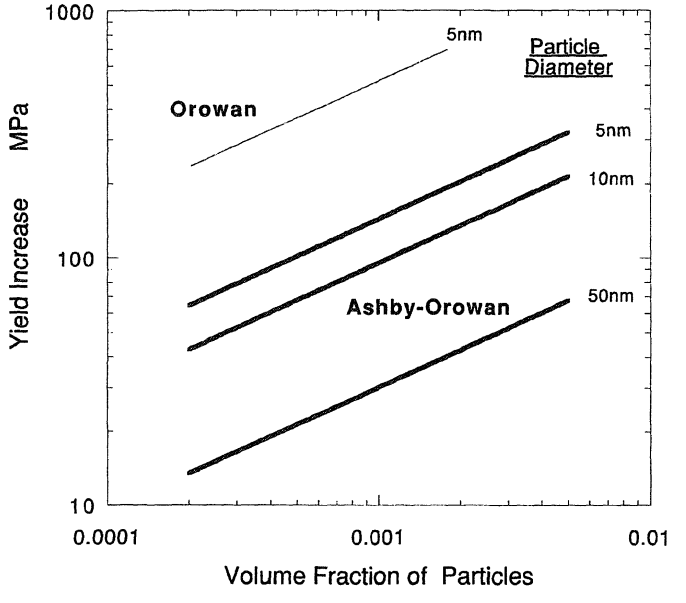


Fig. 2.19 The Ashby–Orowan relationship, Equation (2.59), showing the added strength to be expected from small volume fractions of particles of different sizes. The Orowan relationship is also shown for 5 nm particles.

regular array of particles in the Orowan equation as compared with the effective spacing of the random array of particles in the Ashby–Orowan equation.

Typical values of $\Delta\sigma_y$ (MPa) obtained from a considerable body of published data on niobium and vanadium microalloyed steels are shown in Fig. 2.20. Niobium steels with a volume fraction of 0.0003 to 0.0004 (equivalent to volume percentages of 0.03 to 0.04 vol%) often give increments in yield strength of about 100 MPa over and above that predicted from a knowledge of solid solution strengthening and grain size, Equation (2.46), when the precipitated particle size has a diameter of 3–5 nm. This shows very reasonable agreement with the predictions of the Ashby–Orowan equation. Vanadium steels with volume fractions of vanadium carbide/nitride of 0.0010–0.0015 can show a wide range of values of $\Delta\sigma_y$ (MPa) up to about 150 MPa depending on the particle size developed. The maximum strengthening occurs with particles of about 3–5 nm, but the added strengthening contribution can vary considerably depending on the cooling rate after hot-rolling or during normalising, which causes significant changes in the particle size. The finer particles are associated with faster cooling rates, given that a ferrite structure is maintained. This effect is also present in niobium steels but to a lesser degree.

The electron micrograph shown in Fig. 2.21 is of a niobium microalloyed steel. The fine particles of niobium carbo-nitride are of the order of 4 nm in diameter, and from the steel composition and treatment, the volume fraction of fine carbo-nitride is about 0.0004 (or 0.04%). Using Equations (2.53) to (2.55), the effective

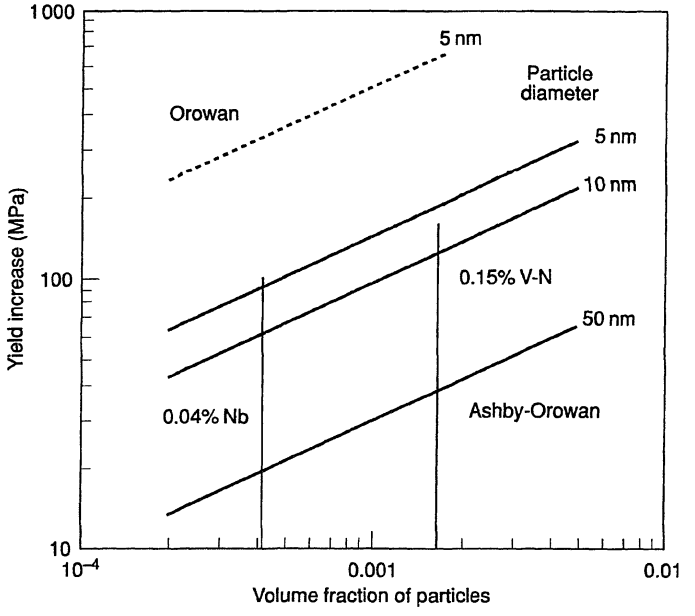


Fig. 2.20 Observed increments of yield strength in microalloyed steels compared with the predictions of the Ashby–Orowan equation.

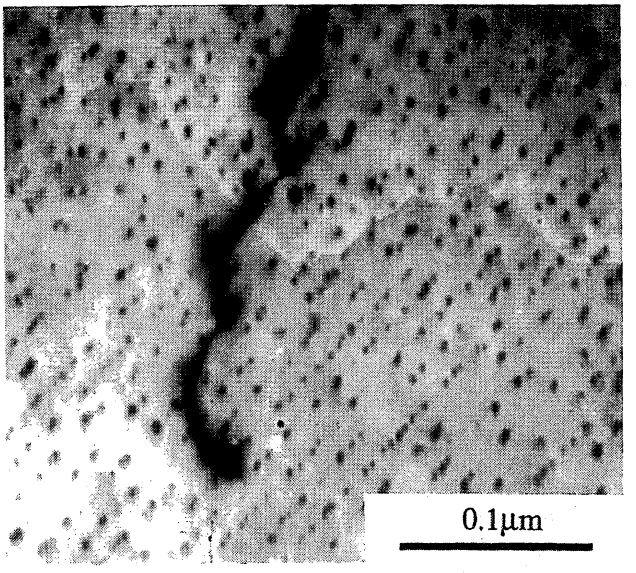


Fig. 2.21 An old transmission electron micrograph (1963) of the interphase precipitation in a 0.1wt%C – 0.04wt%Nb steel, showing the interaction of a dislocation with the particulate array of Nb (CN).

particle spacing on the slip plane should be of the order of 0.07 μm. An examination of the spacings between particles attached to the bowed dislocation shown in Fig. 2.21 should correspond with the effective spacing on the slip plane and is roughly of the correct dimension, i.e. about 8 mm at the magnification of $\times$ 120,000 diameters. The question of the control of volume fraction of fine dispersoids is dealt with in Chapter 3, and that of the precipitate sizes is described in Chapter 5.

The development of a satisfactory constitutive equation to describe the quantitative effects of dispersed second phase particles on the additional increment in yield strength, i.e. the Ashby–Orowan equation, now allows a more complete description of the yield strength of a microalloyed steel in terms of the microstructural features. By adding the Ashby–Orowan equation (2.59), to the expanded Hall–Petch relationship [Equation (2.46)], we get

$$\sigma_y = \sigma_i + \Sigma_1^i k_i c_i + k_y d^{-1/2} + (10.8 f^{1/2}/X)(\ln(X/6.125 \times 10^{-4})) \qquad (2.60)$$

Thus the yield strength of a microalloyed steel is defined in terms of the solute contents, the values of k_i having been given in Section 2.3.2, the grain size contribution with the value of k_y having been defined in Section 2.3.4, and the dispersion stengthening defined here in terms of the real particle diameter, and the volume fraction of particles.

There is still some question concerning the additivity of each of these strengthening terms. Their contributions in microalloyed steels are generally

found to give excellent agreement with the yield strengths observed when the contributions are added. This is not the case in ultra-high strength steels, where excessive use of one mechanism appears to diminish other contributions, and the observed strengths are generally lower than the summed contributions according to Equation (2.60). There are other areas of uncertainty in the contributions that relate to the state of dissolution or precipitation of the alloying elements in the steel. For example, although the carbon contents of various microalloyed, low-carbon steels, may range from 0.002wt% up to 0.2wt% (in round terms), there is very little carbon in solid solution in air-cooled materials. It is clear that most of the carbon will be precipitated as cementite in the pearlite eutectoid reaction (when the carbon content is substantially greater than 0.02wt%). The carbon which is dissolved in the ferrite at the eutectoid reaction temperature will precipitate, usually on existing carbides during air-cooling, leaving very little or no carbon in solid solution at ambient temperatures. The pearlitic carbides are far too widely spaced (one pearlite colony to another) to effect any significant strengthening. In very low carbon steels (less than 0.02wt%C), precipitation during cooling is expected at temperatures much lower than the eutectoid temperature, and the carbides may then assume a finer distribution with individual carbides being much more closely spaced than the pearlite colonies. The spacings under these conditions depend upon the temperature at which they precipitate, as this will control both the nucleation and growth rates, making some degree of precipitation (dispersion) strengthening possible. The situation is less clear with nitrogen, but in the absence of specific nitride-forming alloying elements, it is expected that most of the nitrogen will remain in solid solution. However, when specific nitride formers are present in the steel, some account has to be taken of the nitrogen removal by the nitride former. This is in the main dealt with by a consideration of the nitride solubility product and the specific thermal cycles that are applied. This aspect will be dealt with in Chapter 3.

2.3.8 Other Strengthening Mechanisms

The metallographic features described quantitatively in Equation (2.60) are not the only factors that can control strength levels. In high carbon steels for example, the yield strength is greatly influenced by the interlamellar spacing of the pearlite structure, and grain size has little significance.

The effects of cold deformation on the yield strength is another factor which affects all metals and both low- and high-carbon steels. This mechanism is dependent upon the dislocation density, and the dislocation arrangements, e.g. forest dislocations, cell structures, or sub-grain development. Cold deformation is not commonly used in microalloyed steels although instances can be cited, as, for example, in cold twisted reinforcing bars or drawn wire for suspension ropes. Aspects of dislocation strengthening will be dealt with under the appropriate section in Chapter 7, when dual phase steels are considered. Variations in dislocation density may also cause variations in yield strength in controlled rolled steels, particularly when low finishing temperatures are used.

The effects of texture hardening have also been omitted so far. There are two

basic reasons for this. Firstly, texture hardening does not seem to be as potent as other hardening mechanisms. Secondly, the development of texture is difficult in steels having a dispersed second phase, particularly when this is further compounded by the allotropic transformation of iron. Use is made of textures in relation to through thickness strength and plastic anisotropy, but specific reference to this important aspect of texture effects will be made in Chapter 7, when considering formable sheet steels.

2.4 TOUGHNESS OF MICROALLOYED STEELS

There are many ways of defining toughness. Current methods of assessing toughness are closely linked to the engineering applications, in which components are exposed to certain stresses, constraints and environments. In the engineering approach, the toughness of the steel is quantified in relation to the externally applied stress and the presence of an assumed defect – usually the largest defect that cannot be detected by currently available inspection techniques. There are few data available to relate such measures of toughness to microstructural features in a quantitative manner. Such data as do exist suggests that the fracture toughness responds to microstructural features in the same way as conventional quality tests of toughness, i.e. Charpy V-Notch impact test, as applied to steel.

There are two different assessments of toughness that can be made from the common quality test when applied to steels. These are

(i) The ductile shelf energy. This energy is controlled by the metallurgical features that control the extent of energy absorption when an impact test specimen fails in a ductile mode.

(ii) The impact transition temperature. Body centred cubic metals, such as iron, show a transition from ductile fracture behaviour at high temperatures to a brittle failure mechanism at low temperatures. The transition may occur over a range of only a few Celsius degrees, or it may extend over a wide range of temperature (up to a hundred or so Celsius degrees), and the fractures within the transition range show mixtures of ductile and brittle regions which are geometrically disposed with respect to the specimen shape, depending on the distribution of triaxial stresses in the notched specimen.

It should be pointed out that the fracture mechanics tests also show these two features, i.e. an energy-absorbent ductile mode, and a transition from ductile to brittle failure which can give variations in defect tolerance. The important feature of fracture toughness is that it is quantified in terms of a stress, and as such can be used in design in much the same way that yield strength is used. Basically the relationship between toughness, stress and defect size is given by the Griffiths equation

$$\sigma_f \approx (2\gamma E/\pi c)^{1/2} \tag{2.61}$$

where σ_f is the fracture stress, γ is the fracture surface energy, E is the Young Modulus and 2c is the crack length.

This equation, developed by Griffiths in 1920, was based on glass, which is extremely brittle and where the fracture surface energy was basically the new surface energy of the expanded crack. There are several points of difference when this equation is applied to metals, not least of these being the crystalline nature of metals with the attendant plasticity accompanying dislocation motion. When applied to metals, the cleavage plane is crystallographically oriented, and cracking may occur by mechanisms other than purely brittle transgranular or intergranular cleavage. In many cases, particularly those relating to microalloyed low carbon steel, the fracture process may involve considerable plastic deformation, and the fracture energy then includes not only the surface energy, but also the localised high degree of plastic work required. This is expressed in the Orowan–Irwin relationship.

$$\sigma_f \approx (EGc/\pi c)^{1/2} \tag{2.62}$$

G_c represents the combined energy requirement per unit area of crack extension and is known as the plane strain fracture toughness. Extensive and detailed consideration of this subject is given elsewhere[28] and there is a considerable body of information relevant to the engineering applications of steels and other materials. However, there are still two aspects of the toughness problem, when considering steels (or almost any of the body centred cubic metals), and these are (i) the energy absorption when fracture occurs by the ductile failure mode and (ii) the ductile–brittle transition behaviour.

The most important distinction between these two aspects of toughness from a metallurgical standpoint is that they depend on different metallurgical variables, or when both ductile fracture energy and the ductile–brittle transition temperature depend on the same feature of the microstructure – for example, carbide particles – then they do so in very different ways and for very different mechanistic reasons.

The ductile–brittle transition temperature has obvious importance in relation to the avoidance of almost completely brittle fracture, i.e. very low energy fractures. Mild steel with a transition temperature in the region of 0–40°C would be far more prone to brittle failure than a steel having a transition temperature of −120°C. However, it should be pointed out that the transition temperature is very sensitive to test conditions and specimen geometry. For example, mild steel with a Charpy V-notch impact transition temperature above room temperature could persist in showing completely ductile fractures if tested in simple tension at temperatures down to −50°C. The test factors that are important to the definition of the ductile–brittle transition temperature are the strain rate and the stress state. Higher strain rates give higher transition temperatures, and triaxial stress states that effectively constrain plastic deformation also increase the transition temperature. The routine Charpy impact test gives a measure of the resistance to brittle fracture by defining the energy absorbed during facture and the transition temperature when repeated at various temperatures. The results cannot be compared directly with tensile test results or any stress-related measure of toughness, although information from

automated Charpy tests with dynamic stress and strain measurements have been obtained successfully. However, direct quantitative interpretation of the fracture toughness from the notched impact test is not possible. Thus the impact transition curve is characterised by relatively high energy absorption at temperatures above the transition temperature and extremely low values (as low as 1 or 2 Joules) at lower temperatures, as indicated in Fig. 2.22. The possibilities of improving toughness, either by increasing the *strain* to cause ductile fracture or by reducing the impact transition temperature, are indicated in the diagram.

Specifications of toughness may require a guaranteed minimum energy absorption at some specified low temperature, and attention will need to be given to both the shelf energy, to guarantee the energy requirement under conditions of ductile failure, and the impact transition temperature to guarantee freedom from low energy brittle fractures.

2.4.1 Theoretical Aspects of the Ductile–Brittle Transition

In the earlier section on yield strength, attention was given to the metallurgical features that control the room temperature yield strength. The strength however shows a marked dependency on temperature. In the case of α–iron, there is a considerable body of evidence to show that σ_i in the Hall–Petch Equation (2.32) is strongly temperature dependent, whilst the k_y value, for materials with strongly locked pre-existing dislocations, shows little variation at temperatures below 300 K. At temperatures above 300 K, the σ_0 value is maintained at a roughly

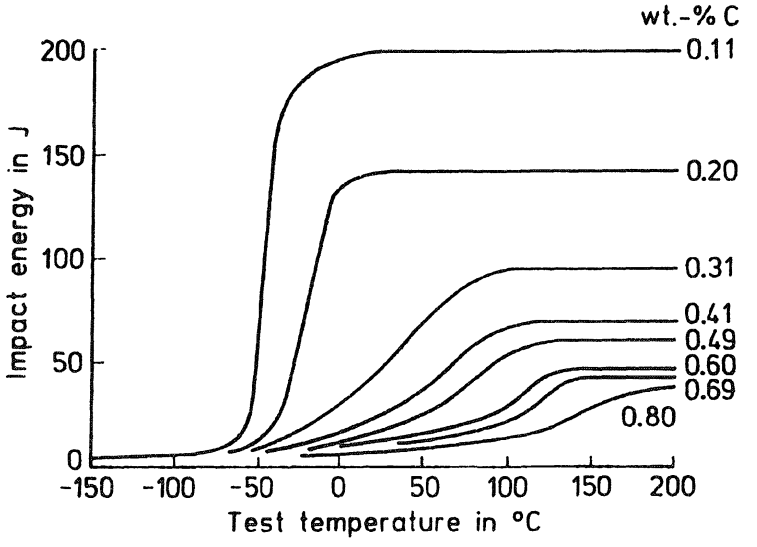


Fig. 2.22 Charpy impact transition curves for steels with differing carbon contents. The variation in the impact transition temperature and in the levels of ductile shelf energy are readily appreciated. After Burns and Pickering.[36]

constant low value, not dissimilar to that given in Table 2.2, but the k_y value decreases substantially, as shown by Dingley and McLean,[18] Fig. 2.23. The overall effects of temperature changes on the yield strength of α-iron are complex. There is a minimum temperature at which measurements can be obtained due to the transition to brittle fracture without general yielding. There is an upper temperature above which the lower yield point cannot be measured due to the disappearance of the discontinuous yield phenonemon (at about 570 K). In the temperature interval 370 K to 550 K, the stress–strain behaviour is influenced by dynamic strain ageing behaviour. The elevated temperature characteristics are obviously affected by the breakdown of the solute atmospheres associated with the dislocations, when continuous yielding is observed, whereas in the dynamic strain ageing range the atmospheres are being continually discarded and then re-formed as new dislocations become pinned by free interstitials that can diffuse at a rate sufficient to effect dislocation pinning.

Despite these complications, the yield strength of polycrystalline α-iron at room temperature and below, combined with the response of the cleavage (or other brittle fracture) mechanism to microstructural features, can be used to construct a schematic diagram of the transition behaviour. The friction stress increases markedly as the temperature is reduced. Decreasing the grain size gives an added contribution which is virtually the same at all temperatures shown due to the constancy of k_y over this temperature range. The transition from ductile to brittle fracture occurs when the yield stress equals or exceeds the brittle fracture stress. The brittle fracture stress, however, in the absence of any substantial discontinuous yielding, is also sensitive to grain size, and, according to Petch, the brittle fracture stress shows a higher grain size dependency than does the lower yield point by a factor of about 4. The effects of grain size on brittle fracture stress and on yielding

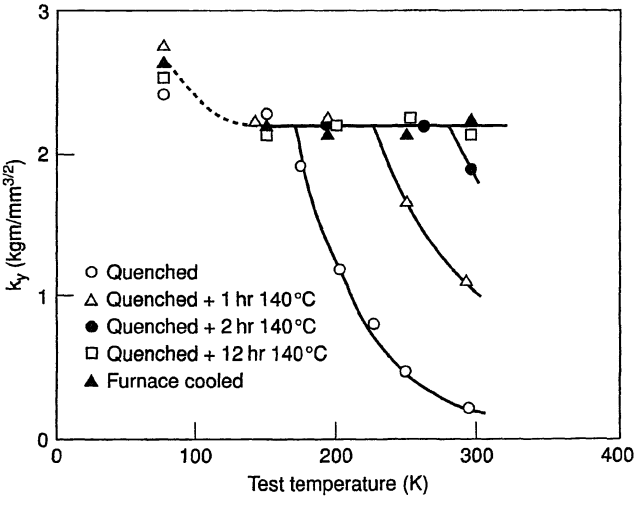


Fig. 2.23 The effect of test temperature and ageing treatments on the grain strengthening coefficient, k_y, in the Hall–Petch equation. After Dingley and McLean.[18]

depicted in Fig. 2.24 therefore indicate a beneficial effect of grain refinement on the impact transition temperature, so that despite an increase in yield strength, the material becomes tougher (i.e. less likely to fail by the brittle cleavage mechanism).

This phenomenon raises two important questions. Firstly, changes in metallurgical variables can obviously cause changes in the impact transition temperature, and a considerable amount of work has been carried out to define the effects of a wide variety of metallurgical variables on the ductile–brittle transition, in order to define the requirements of a higher toughness steel. Secondly, the observed interaction between yield strength and brittle fracture strength which gives rise to the transition behaviour, raises the question of the preferred strengthening mechanisms to be employed in the development of high-strength notch-ductile steels. The beneficial effect of grain refinement on both strength and impact transition temperature has been shown to derive from a strong effect of grain refinement on the brittle fracture stress. It cannot be assumed that other strengthening mechanisms will also have the same relative effects on the brittle fracture stress. Such differences between strengthening mechanisms lead directly to the conclusion that steels of the same yield strength level may exhibit different toughness characteristics, depending on the effects of the strengthening mechanisms on the cleavage stress. The argument can be further extended to a consideration of metallurgical features that may reduce the fracture stress without enhancing the strength in any way.

The process of cleavage fracture has been described in terms of a nucleation and

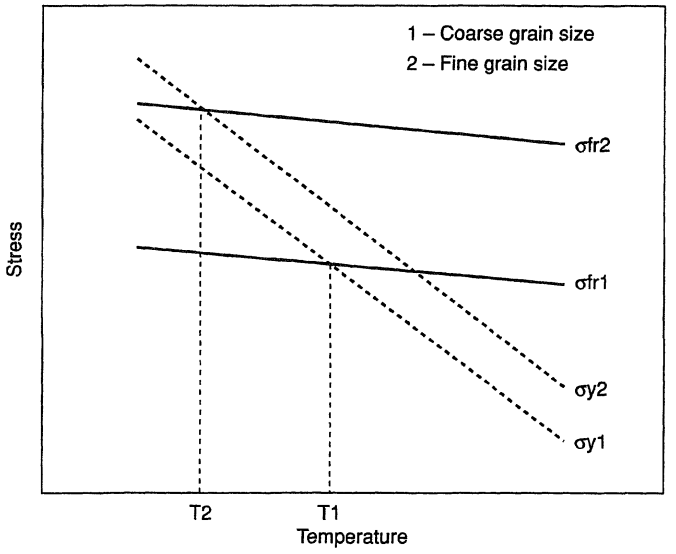


Fig. 2.24 Schematic diagram of the effect of grain refinement on the ductile–cleavage transition temperature. Decreasing the grain size increases the yield strength but has a more pronounced effect on the cleavage fracture strength, thus lowering the transition temperature.

growth process. The first cleavage fracture may be formed by any one of several mechanisms such as by dislocation pile-up stresses, stress intensification by carbide cracking, or stress intensification at the incoherent head of a mechanical twin. Such processes are important in forming a cleavage crack within a grain, but may not necessarily result in a rapidly expanding cleavage crack. There are many instances of the observation of isolated cleavage cracks, usually confined to a single grain, that have not propagated to cause brittle failure. Cleavage failures are highly dependent upon the maximum principal stress acting together with the lateral constraints produced by either artificial notches or induced cracks, unlike plastic deformation, which is dependent upon resolved shear stresses. Whichever of these mechanisms is operative, lowering the temperature, which increases the yield strength, will result not only in the formation of isolated cleavage cracks, but eventually will result in a completely brittle fracture. The temperature at which these events occur, however, may be closely related to the specific nucleation mechanism which is operating.

2.4.2 Effects of Microstructural and Compositional Variables on the Impact Transition Temperature

The evaluation of microstructural variables on the impact transition temperature is complex, in that many solute additions will have effects on the microstructure in addition to causing solid solution strengthening. For example, manganese additions will affect the transformation characteristics during cooling from the austenite temperature range by depressing the transformation temperature. The depression of the transformation temperature will in general decrease the growth rate of the newly formed ferrite grains and will result in a significant refinement of the ferrite grain size of the transformed product. The depression of the transformation temperature also results in the formation of a larger volume fraction of pearlite, the pearlite formed under these conditions having a lower carbon content than is observed in lower manganese steels cooled at the same rate, or steels of similar manganese content cooled at a slower rate (giving a higher transformation temperature). In order to produce information on the solid solution effects of manganese, it is important that variations in grain size and pearlite content are produced by independent means. This applies to all variables used in regression work, and it is necessary to relate all variables to ensure that no statistically inter-related variables exist. Results obtained in this way have been published by Pickering and Gladman,[9] giving a relationship for the Charpy V-Notch impact transition temperature (50% fracture appearance transition temperature) as

$$\text{ITT}(^\circ\text{C}) = 19 + 44(\%\text{Si}) + 700(N_f)^{1/2} + 2.2(\%\text{Pearlite}) - 11.5d^{-1/2} \qquad (2.63)$$

where N_f is the 'free' nitrogen content (wt%) and d is the mean linear intercept ferrite grain size (mm).

There are a number of features in this equation which require some explanation. The equation was based on low carbon structural steels containing up to about

0.20%C, corresponding to a maximum pearlite content of about 25–30%. The grain size was again expressed as the mean linear intercept, and again raises the question of the appropriate descriptor of the grain size with the attendant uncertainties when comparing the grain size coefficient in Equation (2.63) with others, as was the case for the yield strength described earlier (see Table 2.2).

The nitrogen content is expressed in terms of a square root function. The statistics of multiple regression work are such that it is not possible to distinguish between linear and root functions when dealing with relatively low solute contents (about 0.013wt%N maximum). Attention is drawn to the concept of 'free' nitrogen. If one considers an aluminium treated steel in the normalised condition (see Chapter 3), the nitrogen is bound in the form of aluminium nitride particles. This can be regarded as chemically combined nitrogen, and is not present in solid solution in the body-centred cubic iron lattice, thus precluding any solid solution strengthening effect. The term free nitrogen is used rather than soluble nitrogen to avoid confusion with the terminology used by the analytical chemist, who will report soluble and insoluble nitrogen contents in terms of whether the nitride is dissolved or not in chemical solvents used during analysis. The 'free' nitrogen will always be represented in the soluble fraction, but the soluble fraction may also contain some nitrides that have been dissolved by the chemical solvent.

The effects of silicon were assessed by comparing the transition temperature of high silicon steels with those of a silicon-deoxidised steel. The lowest silicon levels were therefore of the order of 0.2wt%. The effect shown in Equation (2.63), therefore, fairly reflects the solid solution effect of silicon, but takes no account of the beneficial effect of silicon as a deoxidiser at levels up to 0.2wt% which has been observed and reported by many workers.

The major features of Equation (2.63) however show that

(i) Grain refinement improves the toughness and causes a significant lowering of the impact transition temperature, as would be expected from the theoretical considerations given in the previous section.

(ii) The effects of silicon and 'free' nitrogen contents are to increase the impact transition temperature, free nitrogen being by far the most detrimental on a weight percentage basis. For example, a 1% addition of silicon would

Table 2.3 Embrittlement vectors for strengthening by solutes and by microstructural variables

Feature	ΔY, MPa	ΔITT, °C	ΔITT/ΔY, °C MPa^{-1}
Mn	32	0	0
Cu	39	20	0.5
Si	83	45	0.51
Sn	123	136	1.11
P	678	450	0.66
$N_f^{1/2}$	354	700	1.99
$d^{-1/2}$	17	−11.5	−0.66
$P'p't'n$ Strengthening	–	–	0.26
Cold deformation	–	–	0.35
Pearlite	0	2.2	∞

increase the transition temperature by some 44°C, whereas the addition of only 0.01wt% of free nitrogen raises the impact transition temperature by about 70°C.

(iii) Increasing the pearlite content in the microstructure increases the impact transition temperature significantly despite the minimal strengthening caused by the presence of pearlite in these structures.

Using Equation (2.63) as a basis, other solute additions, such as phosphorus and tin, have also been examined, and show changes in transition temperature of 459°C per 1wt%P, and 136°C per 1wt%Sn.

When assessing the effects of other microstructural features, problems arise in relating the changes in transition temperature to the microstructural feature. For example, it is well established that dispersion strengthening, using microalloy carbides and nitrides, adversely affects the impact transition temperature. Petch has suggested that the change in transition temperature should be related to changes in yield strength, other than that deriving from grain refinement, to the extent of some +0.3°C per 1 MPa increase in yield stress. On this basis, strengthening by fine dispersed phases or by work hardening, should give this order of shift in the transition temperature. This has been confirmed by many studies of microalloyed steels, and values of +0.26°C/1 MPa for dispersion strengthening and +0.39°C/1 MPa for work hardening have been quoted.

The concept of a vector approach for any strengthening mechanisms is useful for the design of high strength notch-ductile steels. If a steel is designed purely for toughness, then it is clear that a fine-grained steel with a minimal solute content is required (given that the optimum toughness will be attained at an optimum silicon content of about 0.2–0.3% Si). The design of a high strength steel with optimum toughness however, may be judged on slightly different premises. Grain refinement as a strengthening mechanism is an obvious first choice, as, in this case, the increased strength is accompanied by a marked improvement in toughness. Grain refinement is unique in this respect, being the only strengthening mechanism that improves toughness, and results from the effect of grain refinement in raising the brittle fracture stress. If, however, higher strength levels are required than can be attained by grain refinements alone, then additional strengthening should be sought from those mechanisms that give least embrittlement per unit increase in strength (see Table 2.3).

This basis of selection for strengthening mechanisms is illustrated in Fig. 2.25, where the embrittlement vectors for the microstructural variables are shown together with those of the solid solution strengthening effects. Grain refinement has the obvious advantage stated above, whilst manganese in solid solution will increase the yield strength without causing any significant embrittlement. The next strengthening mechanism to be used should be dispersion strengthening which only raises the impact transition temperature by 0.26°C/1 MPa. Although cold deformation may give similar impact transition temperatures, the impracticality of implementing cold work on large plates and sections, and the possibility of strain age embrittlement, precludes its widespread use. Solute elements that are capable of substantial solid solution strengthening, such as silicon, phosphorus and tin,

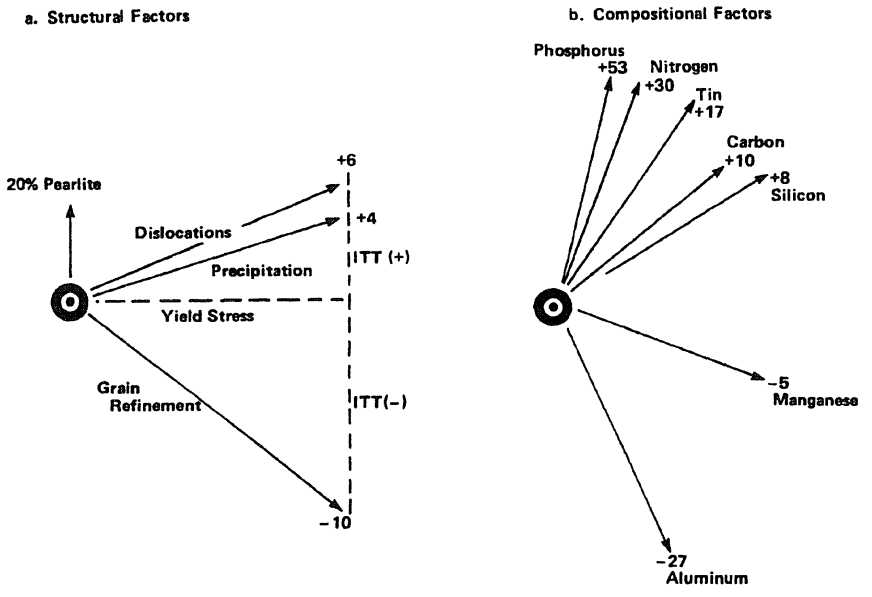


Fig. 2.25 The embrittlement vectors, defined by the change in the impact transition temperature per unit increase in yield strength, are shown for various microstructural and solid solution strengthening effects in (a) and (b) respectively. Grain refinement has obvious advantages for high strength steels with good toughness.

show very high levels of embrittlement per unit increase in yield strength and should therefore be excluded from high strength notch ductile steels. However, some of these solutes find favour in certain high strength steels where toughness poses no problem, e.g. in thin strip.

It is interesting to note the much higher vectors of the solute atoms compared with those obtained for precipitation strengthening. The implication here is that either the solid solution strengthening is more temperature dependent than is dispersion strengthening, or the solutes give rise to a lower fracture stress than does precipitation strengthening. Alternatively, it has been suggested that solutes may change the stacking fault energy of ferrite, leading to the formation of Neumann bands (mechanical twins) and that the stress intensification at the end of the Neumann band is sufficient to initiate cleavage fractures.

The vectors shown in Fig. 2.25 relate to ferrite–pearlite structures such as are found in the bulk of low carbon structural steels, and represent the individual effects of the solutes and/or microstructural features. The use of alloying additions in steels may however be more complex than is suggested by the individual vectors. This can be illustrated by considering a few examples. Consider the addition of carbon to a steel. The primary effect of carbon is to increase the pearlite content of a normalised microstructure, but an additional effect arises from the effect of carbon on the transformation temperature during cooling. The depression of the transformation temperature causes a refinement of the ferrite grain size. The

net effect of adding carbon arises from both the change of grain size and the change in pearlite content. If the appropriate vectors are used to reflect these changes, there will be a resultant vector as indicated in Fig. 2.26. This type of resultant should be present in the case of all solutes, depending upon their effect on the austenite–ferrite transformation during the cooling part of the normalising heat treatment cycle, and the magnitude of the effect will not be unique as the

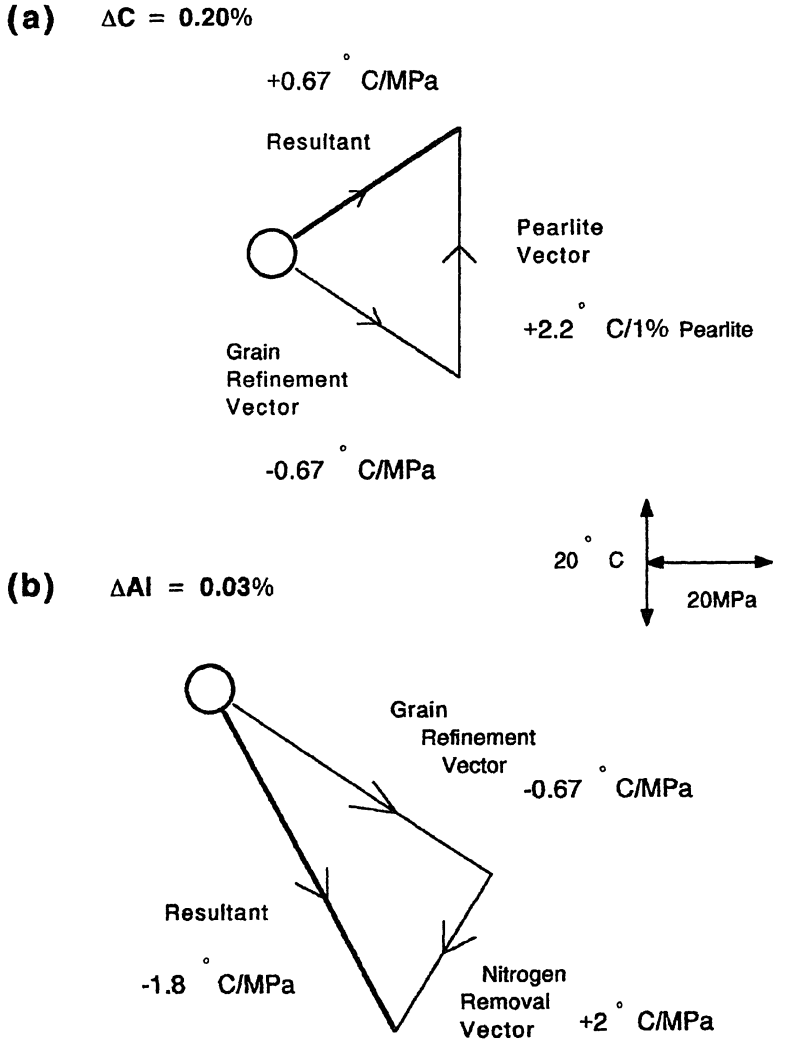


Fig. 2.26 The embrittlement vectors obtained for changes in steel chemistry may reflect direct effects of the solute and indirect effects produced by induced changes in microstructure. (a) Carbon additions increase the pearlite content but also refine the grain size. (b) Aluminium additions reduce the grain size due to aluminium nitride formation, and also reduce the interstitial nitrogen contents, thereby, giving enhanced toughness.

effect of the solute on the transformation behaviour is synergistic with those of other solutes and with the effect of cooling rate. Nevertheless, such resultants can often be traced in amassed data over a relatively wide composition range in carbon–manganese and microalloyed steels having ferrite–pearlite structures.

The effect of small aluminium additions can be assessed in a similar manner. Aluminium treatments, giving a residual aluminium content of 0.02wt% or higher, in normalised steels, will cause considerable grain refinement, and will also result in a considerable reduction in the free nitrogen content, due to the formation of aluminium nitride at the normalising temperature. The appropriate vectors reflecting the changes in grain size and free nitrogen content are shown in Fig. 2.26, and give a resultant of about −1.75°C/MPa. This resultant reflects the removal of some 0.007wt% of free nitrogen and an increase in the root reciprocal mean linear intercept grain size of 3.3 $mm^{-1/2}$, and is obtained by adding the aluminium to a silicon-killed carbon-manganese steel in the absence of other grain refiners, and having a total nitrogen content of the order of 0.008wt%. The resultant for aluminium would obviously be very different if the aluminium addition was made to a steel with a much lower nitrogen content or to a steel containing some other grain refining addition. However, the principle of establishing mechanistic vectors (those associated with grain refinement, pearlite content, precipitation strengthening, and solid solution strengthening), and using these to predict the resultant effects on strength and toughness, alloying and/or thermal treatments, and to select the most appropriate strengthening mechanisms that will optimise toughness, has been demonstrated.

There are certain limitations on the use of the resultants that are associated with an inability, at the present time, to predict the microstructure in quantitative terms, mainly deriving from the various synergisms of solutes and other factors on the austenite transformation characteristics. A further difficulty concerns the limits of alloy addition that are imposed by the need to maintain a ferrite pearlite structure. Excessive solute additions will of course bring hardenability concepts into play, and this will be reflected in the appearance of acicular transformation products in the microstructure, usually in the form of bainite in low carbon structural steels. The appearance of relatively small proportions of bainite can have disproportionate effects on the mechanical properties, such as the development of continuous yielding at a lower stress than is seen in the absence of bainite. Toughness properties can also be adversely affected by the presence of relatively coarse bainitic regions, and increases in the impact transition temperature of up to 100°C have been observed when hardenability limits were exceeded.

One other microstructural feature that is known to affect the impact transition temperature is the presence of coarse brittle second phase particles. Most of the information available on this effect derives from observations made for isolated grain boundary cementite in low carbon steels. Dislocation pile-ups will occur at these coarse carbide particles, and the stress intensification at the head of the pile-up, coupled with the tensile stresses applied to induce the pile-ups, eventually cause carbide cracking. The carbide crack itself, however, may be sub-critical with regard to propagation of cleavage fracture into the ferrite matrix. The cracked carbide may then remain in the structure, with the crack being blunted by

subsequent plastic deformation of the ferrite. However, if the crack in the carbide is sufficiently large, then the crack may propagate through the ferrite matrix. The cracking of larger carbides is reflected in a shift in the impact transition temperature. The effect is illustrated in Fig. 2.27. In low carbon steels cooled at modest rates, and having relatively high transformation temperatures, isolated carbides are formed at the ferrite grain boundaries. The impact transition temperature is little affected until the carbide attains a thickness of about 2 μm, but with larger carbide sizes, the impact transition temperature is increased significantly, until at carbide thicknesses of 5–10 μm the impact transition is increased by 70–90°C. The effects of other alloying additions, by changing the austenite transformation characteristics, may give significant changes in the impact transition temperature by virtue of their effects on the carbide size in these low-carbon steels. For example, additions of manganese, in addition to causing solid solution strengthening, will also induce some grain refinement of the ferrite, and, importantly, will also reduce the carbide thickness or even eliminate the isolated grain boundary carbide. This latter effect of manganese would of course be absent in steels that already possessed the attributes necessary to avoid grain boundary carbide formation.

Certainly, the structure/property relationships presented here are capable of predicting the toughness and strength from the microstructure, and clearly indicate the preferred strengthening mechanisms to be used in the design of high-strength notch-ductile steels. The various sections in this chapter have shown how the industrial development of microalloyed steels have been closely associated with the theoretical understanding that is currently available, and that the development work was not undertaken on a purely empirical basis, even though some of the equations produced may involve certain approximations.

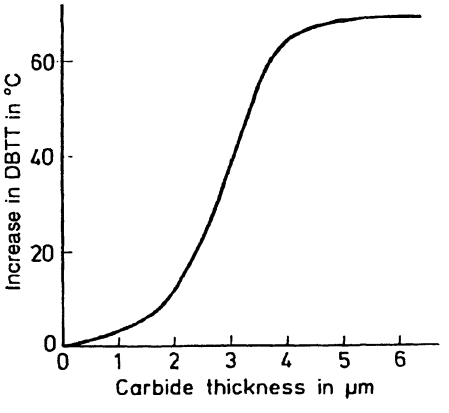


Fig. 2.27 Coarse filamentary carbides in low carbon steels may crack during stress applications and these cracks then initiate cleavage in the adjacent ferrite grains. The presence of these isolated carbides can raise the impact transition temperature to an extent that is dependent upon the carbide thickness. After Gladman *et al.*[27]

2.5 DUCTILE FRACTURE

The ductile–cleavage transition temperature, presented in the previous section, describes one aspect of toughness. Many 'brittle' fractures have been seen in service conditions where the failure mechanism involved is in fact the ductile fracture mechanism. Such fractures, for example in linepipe steels, can cause extensive running cracks where the ductile fracture energy is less than that available from the stored energy in the (pressurised) pipe. The brittle fracture concepts of Griffith expressed in Equation (2.62) indicate that both the surface energy, and the deformation accompanying the propagation of the fracture, are subsumed into G_c, which, in the ductile fracture process, is associated mainly with the plastic deformation energy. The value of G_c as a material property is obviously related to the notched impact test ductile shelf energy, the reduction of area in the tensile test, and bendability, all of which can be heavily dependent on the ductile fracture process.

2.5.1 Mechanisms of Ductile Fracture

The ductile fracture process involves three distinct stages. These are:

(i) Void nucleation
(ii) Void growth
(iii) Void coalescence.

These processes are directly associated with the presence of second phase particles, particularly their abundance, shape and distribution.

Void nucleation occurs either by second phase particle cracking, or by decohesion of the interfaces of the second phase particles. Detailed experimental observation of the various stages of the fracture process have indicated that non-metallic inclusions such as sulphides and oxides have extremely weak interfaces with the iron matrix, and that decohesion between particle and matrix occurs immediately when the matrix undergoes any plastic deformation. The initial void shape and size is thus defined by the shape and size of the inclusions themselves. The situation with regard to the cementite particles in lamellar pearlite or elongated grain boundary cementite appears to be quite different. A ferrite–pearlite structure can undergo a considerable plastic strain without any obvious particle cracking or decohesion. At some high strain level, cracks appear in the cementite lamellae, the individual cracks in successive lamellae in a pearlite colony forming in linear arrays (as seen on metallographically sectioned surfaces) coinciding with shear bands traversing the pearlite colony. Once the pearlitic carbides have cracked, shear deformation of the ferritic component of the pearlite results in a shear crack across the complete pearlite colony which then acts as a void. Studies of structures with spheroidal carbides in a ferrite matrix have shown that both interface decohesion and particle cracking may occur, but both of these processes only occur after a significant matrix strain. Even in the case of decohesion of the cementite–ferrite interface, only one end of the spheroidal

carbide is detached, and the void formed in this case is a relatively sharp crack rather than a spheroid of the same size and shape as the spheroidal cementite.

An early theory of the ductile fracture process for material strained in tension was developed initially by Henry and Plateau,[29] who suggested that the strain concentration at a discontinuity could be treated in the same way as is done for stress concentration. The stress concentration (and hence the strain concentration) is dependent upon the frontal radius of curvature. The concept of the frontal radius of curvature is illustrated in Fig. 2.28. For particles suffering complete decohesion, as is usually the case for non-metallic inclusions in steel, the void starts with a size equal to that of the inclusion. Void growth occurs in the direction of the tensile stress. The presence of the hard non-deformable inclusion maintains the void at its original dimension normal to the stress axis. As the void grows in the tensile direction, the radius of curvature decreases, and the strain concentration at the edge of the void decreases throughout void growth. For particles that suffer cracking during straining, the crack in the particle acts as a void (provided that it does not propagate by a brittle mechanism into the surrounding matrix) and grows from an initially sharp crack into a more extended void. The growth of such sharp

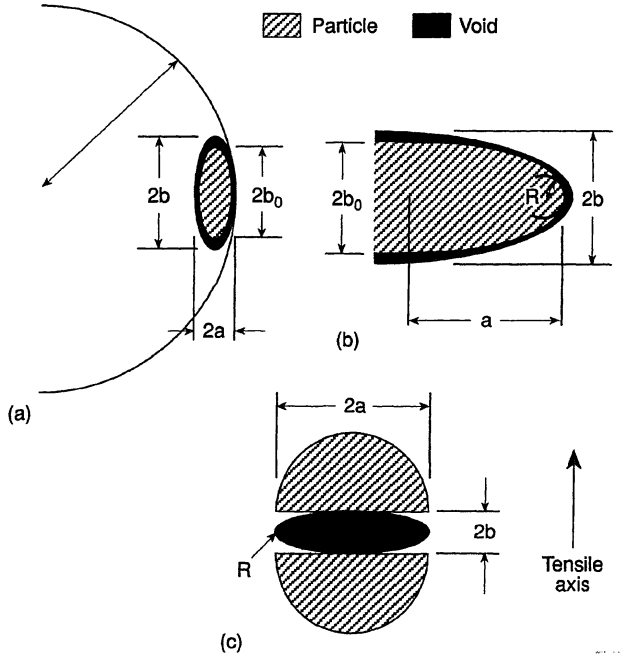


Fig. 2.28 Illustration of the concept of the frontal radius of curvature for voids formed at second phase particles during plastic straining. The void growth during straining is universely proportional to the frontal radius of curvature. (a) Prolate spheroid–large frontal radius of curvature; (b) oblate spheroid–small frontal radius of curvature; (c) particle cracking. After Gladman *et al.*[27]

cracks can be treated by the same mathematical model that is used for the decohesion type voids by representing the crack as a very thin oblate spheroid.

Gurland and Plateau[30] postulated that the strain concentration factor, c, is defined by

$$c = \mathrm{d}\varepsilon_b/\mathrm{d}\varepsilon \tag{2.64}$$

where $\mathrm{d}\varepsilon_b$ is the increment of true strain for the void dimension b and $\mathrm{d}\varepsilon$ is the increment of strain for the specimen as a whole.

The strain concentration factor should decrease towards unity as the frontal radius of curvature, R (mathematically defined by $R = b^2/a$) tends towards infinity, and will increase towards infinity as the frontal radius of curvature approaches zero. In a homogeneous matrix, the strain concentration near the crack front should be distributed over a region whose dimensions were dependent primarily on a/R. The strain concentration factor can therefore be expressed as

$$c = 1 + ka/R = 1 + ka^2/b^2 \tag{2.65}$$

where k can be regarded as a strain concentration constant. As $\mathrm{d}\varepsilon_b = \mathrm{d}b/b$, by the definition of true strain, then Equations (2.64) and (2.65) can be combined to give

$$\mathrm{d}b/b = (1 + ka^2/b^2)\mathrm{d}\varepsilon \tag{2.66}$$

Note that in the current model, b is the half dimension of the void parallel to the tensile axis, and a is the radius of the void measured normal to the tensile axis and remaining substantially constant. Under these conditions, Equation (2.66) can be integrated to give

$$\varepsilon - \varepsilon_0 = \ln[(b^2 + ka^2)/ka^2]^{1/2} - \ln[(L^2 + ka^2)/ka^2]^{1/2} \tag{2.67}$$

where $\varepsilon - \varepsilon_0$ is the interval of strain over which the void grows, ε_0 is the void initiation strain, ε is the true strain and L is the initial half dimension of the void when it is formed.

If the particles crack, then $L = 0$ at ε_0, and the equation reduces to that given by Gurland and Plateau. If, however, complete particle decohesion occurs at ε_0, then b_0 is the initial half dimension of the inclusion parallel with the tensile axis before straining.

Thus for particle decohesion, as is the case for non-metallic inclusions in steel,

$$\varepsilon - \varepsilon_0 = \ln[(b^2 + ka^2)/ka^2]^{1/2} - \ln[(b_0^2 + ka^2)/ka^2]^{1/2} \tag{2.68}$$

whereas for particle cracking, the initial void is defined by $b_0 = 0$, and

$$\varepsilon - \varepsilon_0 = \ln[(b^2 + ka^2)/ka^2]^{1/2} \tag{2.69}$$

The void growth under the specified conditions of tensile straining are thus given by Equations (2.68) and (2.69), for particle decohesion and particle cracking

respectively. These equations may be rewritten to express the void half length, b, in terms of the true strain to give

$$b^2 = (b_0^2 + ka^2)e^{2(\varepsilon-\varepsilon_0)} - ka^2 \tag{2.70}$$

for particle decohesion, and

$$b^2 = ka^2(e^{2(\varepsilon-\varepsilon_0)} - 1) \tag{2.71}$$

for particle cracking.

The effects of non-metallic inclusions in steel have been observed to result from decohesion, usually with negligible void initiation strains. Dividing Equation (2.70) by b_0^2 and obtaining the root to find an expression for b, gives

$$b = b_0[(1 + ka^2/b_0^2)e^{2(\varepsilon-\varepsilon_0)} - ka^2/b_0^2]^{1/2} \tag{2.72}$$

Expressing the aspect ratio of the original inclusion, b_0/a, as r, gives

$$b/b_0 = [(1 + k/r^2)e^{2(\varepsilon-\varepsilon_0)} - k/r^2]^{1/2} \tag{2.73}$$

If the voids are ellipsoidal as shown in Fig. 2.28, then the void volume, v, is given by

$$v = 4\pi a^2 b/3 \tag{2.74}$$

and the volume fraction of voids, f, given that they all have the same size and shape, and suffer immediate decohesion, is

$$f = n_v 4\pi a^2 b/3 \tag{2.75}$$

where n_v is the number of voids per unit volume.

Prior to straining,

$$f_0 = n_v 4\pi a^2 b_0/3 \tag{2.76}$$

where f_0 is the volume fraction of inclusions immediately before decohesion.

Combining Equations (2.75) and (2.76) yields

$$f/f_0 = b/b_0 \tag{2.77}$$

and substituting this in Equation (2.73) results in

$$f = f_0[(1 + k/r^2)e^{2(\varepsilon-\varepsilon_0)} - k/r^2]^{1/2} \tag{2.78}$$

Thus the volume fraction of voids present at any given strain is dependent upon the initial volume fraction of voids and also upon the aspect ratio of the inclusions. The rate of increase in void fraction with strain increases directly with increasing volume fraction. The rate of increase in void fraction with strain also increases as the aspect ratio of the inclusion decreases, i.e. inclusions present as prolate spheroids with their long axis parallel with the tensile force result in lower volume fractions of void than do oblate spheroids with their short axis parallel with the tensile force, at any given strain.

At some stage in the void growth process, the intervoid matrix becomes

mechanically unstable, leading to the final stage in ductile fracture, i.e. void coalescence. There is considerable uncertainty concerning this stage of the fracture process. Experimentally it is clear that the material between voids thins to develop the cusp so characteristic of the ductile fracture surface, and that the coalescence generally occurs at the centre of the tensile specimen spreading radially as a circular ductile crack, until the material near the specimen surface fails by shear, giving the classic cup and cone fracture. The conditions for the development of the central ductile crack have been variously assumed. Gladman *et al.*[27] assumed that void coalescence would occur at some critical volume fraction of voids, based on a critical ratio of void width to void spacing (in the direction normal to the tensile axis). A similar criterion was adopted by Gurland and Plateau.[30] However, the Gurland and Plateau model was derived for the cracking of spherical particles and was based on a critical ratio of the void length (in the tensile direction) to the void spacing (in the direction normal to the tensile axis).

Following the Gladman *et al.*[27] decohesion model of void growth, Equation (2.78), it is necessary to define the change in void spacing normal to the tensile axis. The number of voids per unit area, intersecting a plane normal to the tensile axis, is depicted in Fig. 2.29. In order that a void should intersect the specified plane, the void centre should lie within a distance $+b$ or $-b$ from the plane. Thus, the number of voids per unit area, n_A, in the plane is the same as the number of void centres in a volume of thickness $2b$ and having unit area, i.e.

$$n_A = n_V \cdot 2b \tag{2.79}$$

where n_V is the number of voids per unit volume, and will be directly equal to the number of inclusions per unit volume prior to straining.

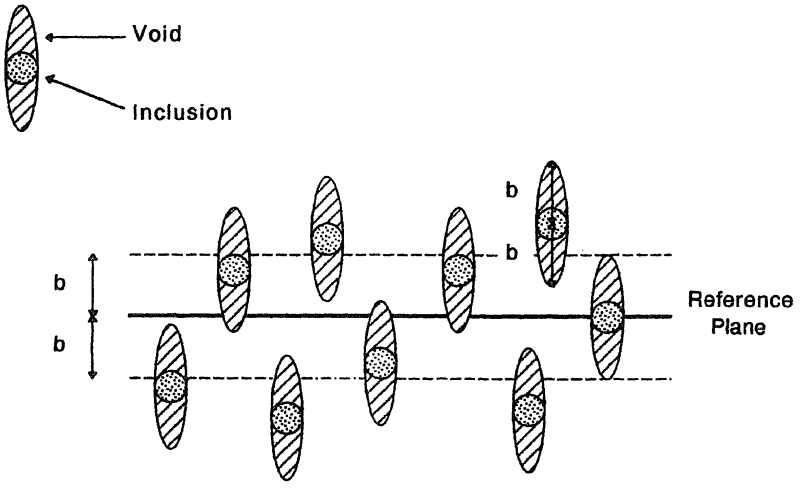


Fig. 2.29 Number of voids per unit area in a planar intercept normal to the tensile axis. The void centre must lie within a distance of one half of the void dimension, measured parallel with the tensile axis.

The number of voids per unit area increases directly as the void length increases. The average area A occupied by a single void is defined by

$$A = n_A^{-1} \tag{2.80}$$

It is assumed that this area can be represented by a circle centred on the void, then the radius, P, of such a circle (of mean area A) is given as

$$P = (A/\pi)^{1/2} \tag{2.81}$$

Substituting from Equations (2.79) and (2.80) gives

$$P = (\pi \cdot n_V \cdot 2b)^{-1/2} \tag{2.82}$$

Now the number of voids per unit volume can be specified as the original number of inclusions per unit volume, and given that the volume fraction of inclusions, f_0, is equal to the number of inclusions per unit volume, n_V, multiplied by the mean volume of the inclusions, i.e.

$$\begin{aligned} f_0 &= n_V \cdot 4\pi a^2 b_0/3 \\ \text{then} \quad n_V &= 3f_0/4\pi a^2 b_0 \end{aligned} \tag{2.83}$$

Substituting this in Equation (2.82) gives

$$\begin{aligned} P &= (\pi \cdot 3f_0 \cdot 2b/4\pi a^2 b_0)^{-1/2} \\ &= (2a^2 b_0/3f_0 b)^{1/2} \end{aligned} \tag{2.84}$$

If the critical condition for void coalescence is that the ratio of the void width to the void spacing attains some critical value, ϕ, i.e.

$$\begin{aligned} (a/P)c &= \phi \\ \text{then} \quad \phi &= (a/P)c = (3f_0 b_c/2b_0)^{1/2} \end{aligned} \tag{2.85}$$

and from Equation 2.77

$$\phi = (3f_c/2)^{1/2} \tag{2.86}$$

Note that the suffix c denotes the critical value for void coalescence and fracture, and f_c is the critical volume fraction of voids that corresponds with the critical ratio of void width to void spacing. Note also that Equation (2.86) is stereologically correct in that the area fraction of void (which is equal to the volume fraction) is given by

$$f_c = 2a^2/3P^2 \tag{2.87}$$

and expresses the mean size of the void in the plane of section as $(2/3)^{1/2}$ times the

initial inclusion width. Substituting the critical volume fraction in Equation (2.78), and noting that the strain at which the void fraction is equal to f_c becomes the fracture strain, ε_T, yields

$$f_c = f_0[(1 + k/r^2)e^{2(\varepsilon_T - \varepsilon_0)} - k/r^2]^{1/2}$$

which can be transposed to give

$$\varepsilon_T = \varepsilon_0 + (1/2)\ln[(f_c^2/f_0^2 + k/r^2)/(1 + k/r^2)] \tag{2.88}$$

Equation (2.88) therefore describes a limiting strain for voids formed by decohesion of the inclusion /matrix interface, where the strain concentration factor is related to the void (inclusion) width, and depends on the inverse of the frontal radius of curvature. It is assumed that the lateral void dimension, a, does not change with strain until the critical intervoid spacing is attained, when rapid lateral expansion of the voids occurs during the unstable shearing of inter-void material involved in the final ductile fracture process, leading to the cusps observed on the final fracture surface.

Experimental assessments of the above equation were attempted by Gladman *et al.*,[27] who followed the evolution of the void fraction with strain, by quantitative assessment of the void area on cleavage fractures of pre-strained specimens having known inclusions contents (mainly sulphides), and controlled inclusion shapes. At small strains, the strain concentration constant was observed to have a value of $k = 2$, giving strain concentration factors ($c = k/r^2$) of $c = 0.08$ for $r = 5$, $c = 3$ for $r = 1$, and $c = 8$ for $r = 0.5$, at the start of straining. As straining progresses, then the strain concentration factor, c, decreases as the voids lengthen and increase the frontal radius of curvature.

The experimental assessment also provided an estimate of the critical volume fraction of voids, giving $f_c^2 = 0.0018$, or $f_c = 0.042$ (i.e. 4.2% of voids). In this evaluation, it was assumed that $\varepsilon_o = 0$, as void growth appeared to have occurred at the smallest strains used.

There is considerable uncertainty attaching to the above assessment of ductile fracture. Firstly, the steels contained other second phase particles, e.g. about 0.3% of cementite, and 0.1% of oxides, both of which would give rise to voids at some stage of the straining process. Another feature of both experimental and commercial steels is that the distribution of second phase particles is not regular, as is implied in the above model, but can exhibit clustering. In fact, some local void coalescence was observed at strains considerably below the fracture strain, in regions of the specimens which contained inclusion clusters. These prematurely coalesced clusters of inclusions were described as supervoids, as their formation provides an increased void width with attendant adverse effects on the strain concentration. Finally, the criterion for the onset of the ductile crack and final ductile separation is purely arbitrary. Considerable attention has been given to devising a mechanically valid criterion for the onset of ductile crack formation. These have been reviewed by Thomason,[31] and the instability of the inter-void material has been related to the stress/strain state and the volume fraction of voids. This aspect raises important features concerning the failure criterion when

considering plastic deformation processes other than simple tension, for example by wire drawing, or by triaxial tension at the root of a notch. There is no doubt that such changes in stress state can influence the final macroscopic strain at failure, as well as influencing the rate of void growth and changes in the lateral dimensions of the void. Wire drawing, for example, can be used to impart strains of up to $\varepsilon = 11$, without failure, even though the material at the die exit is subjected to a uniaxial tension. It is clear that the void growth rate is reduced, probably by the lateral compressive stress of the die which reduces the width of the voids as straining proceeds.

The implications of the stress state are discussed extensively by Thomason, and in this respect it is also necessary to draw attention to the macroscopic neck formed as a result of plastic instability during tensile testing [see Equation (2.8)]. The onset of necking results in a change from the unaxial tension condition to a state of triaxial tension as described by Bridgman.[32] In a state of triaxial tension, some lateral growth of voids might be expected which would obviously influence the strain to rupture as described above.

Despite the above shortcomings, which mainly relate to the mechanical environment and its effects on void nucleation, growth, and coalescence, the metallurgical factors concerning the relationship between ductility and non-metallic inclusions are clearly shown by Equation 2.88, and may be summarised as follows

(i) The strain to fracture decreases as the initial volume fraction of inclusions increases. This effect is reflected in the reduction of area in the tensile test, the ductile shelf energy during notched impact testing, and on bendability.
(ii) The strain to fracture decreases as the shape of the inclusions changes from being elongated in the direction of tensile straining to being elongated in a direction normal to the tensile straining axis. This affects the same properties as given above, i.e. those which are controlled by the ductile fracture process.
(iii) The void initiation strain is very small for non-metallic inclusions in steel, and can be ignored for all practical purposes. These effects are illustrated in Fig. 2.30.

Before completing this section on the theoretical aspects of ductile fracture, it is necessary to consider the case of particle cracking, particularly in relation to the presence of carbides in steel. All steels contain particles other than non-metallic inclusions, i.e. carbides and nitrides, which are present by design. The complete eradication of non-metallic inclusions in steel will not give infinite strains to fracture, but will give values that are controlled by other void forming processes such as the cracking of carbide or nitride particles. The void development connected with these particles differs from that observed for non-metallic inclusions in several important ways.

As indicated by Equation (2.69), the initial size of the void is described by a flat sharp crack, of radius a and thickness $b_0 = 0$ within the particle, and is indicative of a high degree of interfacial cohesive strength between particle and matrix. Particle cracking gives an initially infinite rate of growth as the radius of curvature is

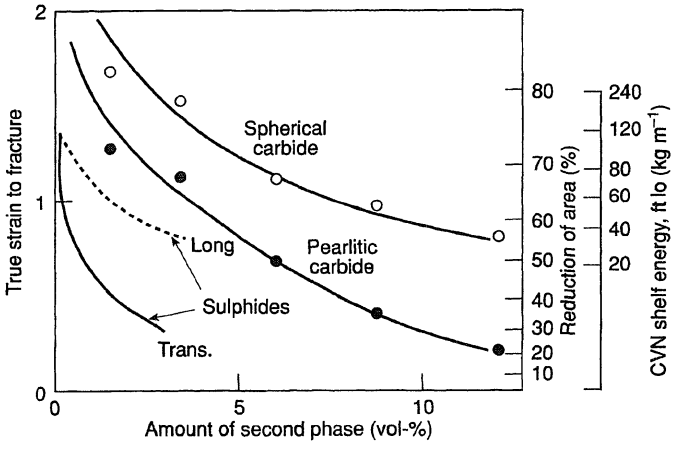


Fig. 2.30 The effects of sulphide inclusions on ductility (true strain to fracture in the tensile test) and the effect of inclusion shape. The effect of carbides on ductility are also shown for comparison. After Gladman *et al.*[27]

virtually zero. A second important difference is that the void initiation strain can represent a considerable proportion, sometimes the major proportion, of the total strain to fracture. The third important feature is that the void initiation process is observed to occur in selected second phase particles, and that the proportion of cracked particles increases as the strain (and associated flow stress) increases. A full treatment of the effects of highly cohesive particles should, therefore, take account of the distribution of void initiation strains, as well as the growth and coalescence criteria. Treatment of a model system where all particles undergo simultaneous cracking at a void initiation strain ε_0, starting from Equation (2.71) gives

$$\varepsilon_T - \varepsilon_0 = (1/2)\ln(1 + 4r^2 f_c^2/9kf_0^2) \tag{2.89}$$

the definitions of the terms being the same as those for Equation (2.88). A comparison of the void growth strains (from ε_0 to ε_T) has shown (Fig. 2.29) that these are very small in relation to the total ductility, ε_T, of ferrite with spheroidal carbides, and illustrates the effects of having a large initiation strain coupled with the cracking of only a fraction of the total number of carbide particles present. The stress dependence of particle cracking, when the interface bond strength is significant, is considered in detail elsewhere.[33]

Attention should be drawn to the special case of pearlitic structures where the carbides are present in a lamellar eutectoid form. Cracking of the pearlite lamellae within a pearlite colony is a co-operative process leading to the formation of shear cracks in the pearlitic structure. The process occurs by cracking of the cementite particles along an intense slip band, followed by shearing of the inter-carbide ferrite lamellae to give a shear crack having a length equal to that of the pearlite colony dimension. Such shear cracks grow in much the same manner as for

cracked carbides until void coalescence occurs. The cracked pearlite lamellae can still be seen in the dimples of the fracture surface, and are usually contained in larger than average dimples.[27] However, the effects of pearlite on ductility and toughness are not dissimilar to those of isolated carbides in exhibiting significant void initiation strains, with the voids starting as sharp cracks. A comparison of the effects of carbides on ductility with those of sulphides is included in Fig. 2.30.

Although the general principles of designing ductile steels are well established, the quantitative prediction of strain to fracture is not precise, and experimental verification of void growth and coalescence mechanisms, particularly in relation to the effects of carbides in steel, are still required. The application of advanced methods of void measurement, e.g. by high precision densitometry or by X-ray microvoid imaging techniques (tomography), offers considerable scope for improvement of the quantitative relationships.[34]

REFERENCES

1. T. Gladman, B. Holmes and F. B. Pickering: *J. Iron and Steel Inst*, 1970, **208**, p.172.
2. R. A. Smallman. *Modern Physical Metallurgy*, 4th Edn., Butterworths, London, 1985.
3. H. Suzuki: *Nippon Kinzoku Gakkai Kaiho*, 1969, **8**, p.90.
4. R. J. Arsenault: Proc. 3rd International Conference on 'The Strength of Metals and Alloys. The Institute of Materials/Iron and Steel Institute, London, 1973, p.520.
5. J. Snoek: *Physica*, 1941, **8**, p.711.
6. A. H. Cottrell and B. A. Bilby: *Proc. Phys. Soc.*, 1949, **62A**, p.49.
7. I. G. Ritchie and R. Rawlings: *Acta Met.*, 1967, **15**, p.491.
8. T. Gladman and R. L. Barker: *J. de Physique*, 1971, **32**, supplement C2, p.57.
9. F. B. Pickering and T. Gladman: *Metallurgical Developments in Carbon Steels*, Iron and Steel Institute, Special Report No. 81, 1963, p.10.
10. W. B. Pearson: *Handbook of Lattice Spacings of Structures of Metals and Alloys*. Pergamon Press, London, 1958.
11. J. Heslop and N. J. Petch: *Phil. Mag.*, 1957, **2**, p.649.
12. A. Cracknell and N. J. Petch: *Acta Met.*, 1955, **3**, p.186.
13. R. I. Jaffe and G. J. Hahn: NPL Conference, *Structure and Strength in Metals and Alloys*, HMSO, London, 1963, p.707.
14. E. O. Hall: *Proc. Phys. Soc.*, 1951, **64B**, p.747.
15. N. J. Petch: Journ. Iron Steel Inst., 1953, **174**, p.25.
16. A. H. Cottrell and R. M. Fisher: see A. H. Cottrell, NPL Conference *Structure and Strength in Metals and Alloys*, HMSO, London, 1963, p.456.
17. R. Armstrong, I. Codd, R. M. Douthwaite and N. J. Petch: *Phil. Mag.* 1962, **7**, p.45.
18. D. J. Dingley and D. McLean: *Acta Met.*, 1967, **15**, p.885.
19. W. B. Morrison: *Trans. A.S.M.*, 1966, **59**, p.824.
20. A. H. Cottrell: *Dislocations and Plastic Flow in Crystals*, Clarendon Press, 1964.
21. J. D. Eshelby, F. C. Frank and F. R. N. Nabarro: *Phil Mag.*, 1951, **42**, p.351.
22. E. Orowan: *Internal Stress in Metals and Alloys*, The Institute of Metals, London, 1948, p.451.
23. R. B. Nicholson: *Effect of Second Phase Particles on the Mechanical Properties of Steel*, Iron and Steel Institute, London, 1971, p.1.
24. U. F. Kocks: *Phil. Mag.*, 1966, **13**, p.541.
25. A. J. E. Foreman and M. J. Makin: *Phil Mag.*, 1966, **14**, p.911.

26. M. F. ASHBY: *Oxide Dispersion Strengthening*, Eds. G. S. Ansell, T. D. Cooper and F. V. Lenel, Gordon and Breach, New York, 1958, p.143.
27. T. GLADMAN, B. HOLMES and I. D. McIVOR: *Effect of Second Phase Particles on the Mechanical Properties of Steels*, The Iron and Steel Institute, London, 1971, p.68.
28. J. F. KNOTT: *Fundamentals of Fracture Mechanics*, Butterworths, Oxford, 1973.
29. G. HENRY and J. PLATEAU: *La Microfractographie*, Editions Metaux, IRSID, Paris - St. Germaine, 1967.
30. J. GURLAND and J. PLATEAU: *Trans. A.S.M.*, 1963, **56**, p.442.
31. P. F. THOMASON: *Ductile Fracture of Metals*. Pergamon Press, Oxford, 1990.
32. P. W. BRIDGMAN: *Trans. A.S.M.*, 1944, **32**, p.553.
33. T. C. LINDLEY, T. OATES and C. E. RICHARDS: *Acta Met.*, 1970, **18**, p.1127.
34. P. MUMMERY, B. DERBY, P. ANDERSON, G. R. DAVIS and J. C. ELLIOTT: *J. Microscopy*, 1995, **177**, p.399.
35. M. F. ASHBY and D. R. H. JONES: Engineering Materials, Vol 1, Pergamon Press, Oxford, U.K., 1980.
36. K. W. BURNS and F. B. PICKERING: *J. Iron Steel Inst.*, 1964, **202**, p.899

CHAPTER 3

Solubility of Microalloy Carbides and Nitrides

3.1 INTRODUCTION

The strengthening effect of microalloying additions may be produced by the dispersion strengthening effect of very fine precipitated particles, or by grain refining, i.e. inhibition of grain growth by second phase particles, or by a combination of these two effects. In order to understand these effects, it is necessary to understand the factors controlling the dissolution of the various microalloy carbides and nitrides. Fine ferrite grain sizes in the final product are generally attained from fine austenite grains prior to transformation, although the inhibition of ferrite grain growth after transformation may play some part in deciding the final grain size. In order to maintain a fine austenite grain size, particles that remain undissolved, in the austenite, or particles that will precipitate at sub-solvus temperatures, are required. In order to produce the very fine particles that are responsible for dispersion strengthening (see Chapter 2), i.e. particles that are some 3–5 nm in diameter, it is necessary that these should be freshly precipitated, either as interphase precipitated particles, or precipitated after transformation. In order to produce such particles, it is implicit that these carbides/nitrides should be in a dissolved state in the austenite, as any undissolved carbides or nitrides will suffer relatively rapid coarsening at the elevated temperatures where austenite is the stable phase. In order to achieve the desired metallurgical states, a detailed knowledge of the solubilities of the microalloy carbides and nitrides is required, together with a knowledge of their precipitation behaviour. The present chapter considers the solubility aspects of the various microalloy compounds in steel. Although the solubilities of these compounds in austenite are of prime importance, attention is also given to their solubilities in the liquid and ferritic phases where such information has relevance to the final metallurgical state and to the mechanical properties of the product.

3.2 SOLUBILITY OF INDIVIDUAL COMPOUNDS

The component parts of the microalloy constituent phases may be present either in solution, in a simple single constituent, or in one or more simple or complex constituents. For example, aluminium will react with nitrogen (aluminium and nitrogen being the components)to form aluminium nitride (the constituent phase). Aluminium nitride shows little or no solubility for microalloying elements such as

niobium, titanium or vanadium, and will only be influenced by the available aluminium and nitrogen. If a more stable nitride former is added, this may limit the nitrogen available to the aluminium and may restrict or inhibit aluminium nitride formation. Under these conditions there may be two separate nitride phases. When considering other nitride-forming microalloying elements, such as titanium, vanadium and niobium, considerable mutual solubility exists, and complex carbo-nitrides of these elements may exist as a single constituent phase. However, in all of these cases, the thermodynamic stabilities of the simple components, e.g. aluminium nitride, niobium carbide, etc., are used to obtain that of the complex compounds, and a consideration of their individual solubilities is necessary.

3.2.1 The Solubility Product

Consider a reaction between a microalloying element, M, with an interstitial, X, both being dissolved in the austenite, to give a compound, MX, at a temperature T.

$$[M] + [X] \leftrightarrow (MX) \tag{3.1}$$

where $[M]$ represents the concentration of M dissolved in austenite, $[X]$ represents the concentration of X dissolved in austenite, and (MX) represents the constituent.

The equilibrium constant may be written as

$$k_s = a_{[M]} \cdot a_{[X]} / a_{(MX)} \tag{3.2}$$

where $a_{[M]}$ is the activity of the dissolved microalloy, $a_{[X]}$ is the activity of the dissolved interstitial and $a_{(MX)}$ is the activity of the constituent phase.

It should be noted that the convention for the equilibrium constant used by chemists is the inverse of that given in Equation (3.2), but the equation given is widely used by the metallurgist, the equilibrium constant, k_s, being referred to as the solubility product.

The activities in Equation (3.2), can be expressed in terms of the elemental concentrations and activity coefficients, γ, through

$$a_{[M]} = \gamma_{[M]}[M] \tag{3.3}$$

$$\text{to give} \qquad k_s = \gamma_{[M]}[M] \cdot \gamma_{[X]}[X] / a_{(MX)} \tag{3.4}$$

In a very empirical manner, it is assumed that the activity coefficients, $\gamma_{[M]}$ and $\gamma_{[X]}$, are equal to unity. The activity of the pure product MX is of course unity, so that Equation (3.4) would be written as

$$k_s = [M][X] \tag{3.5}$$

Strictly speaking, $[M]$ and $[X]$ should be the molar fractions, but, particularly at low concentrations, the use of these elements expressed in terms of percentage by weight merely alters the value of k_s; this is of little significance provided that it is understood that the k_s value has been defined in this way. There would be little point in converting the k_s value to a molar fraction basis only to reconvert the

molar fractions obtained from a true k_s back to the weight percentages of the elements dissolved. Similarly, the assumption of activity coefficients of unity is not serious provided that the activities are directly proportional to the weight percentages, as they usually are at the very low concentrations encountered in microalloyed steels. The introduction of low activity coefficients due to significant deviations from Raoult's Law is unnecessary provided that the activity is linearly related to the percentage by weight of the components.

For compounds with different atomic ratios, for example V_4C_3, the solubility product may be defined as

$$4[V] + 3[C] \leftrightarrow (V_4C_3)$$

$$k_s = [V]^4[C]^3/a_{(V_4C_3)} \tag{3.6a}$$

$$4[V]/3 + [C] \leftrightarrow (V_4C_3)/3$$

$$k_s = [V]^{4/3}[C]/a_{(V_4C_3)}{}^{1/3} \tag{3.6b}$$

Equation (3.6a) is based on the production of 1 mole of V_4C_3 whereas Equation (3.6b) is based on the consumption of 1 mole of carbon.

The temperature dependence of the solubility product is expressed by an Arrhenius relationship

$$\ln k_s = -(Q/RT) + c \tag{3.7}$$

$$\text{or} \quad \log_{10} k_s = -(Q/2.303RT) + c/2.303 \tag{3.8}$$

where Q is the heat of dissolution and R is the gas constant.

Historically, equations of the form shown by Equation (3.8), have been used, but in a condensed form such as

$$\log k_s = A - B/T \tag{3.9}$$

where A and B are constants for a given system, $\log k_s$ is the logarithm to the base 10, k_s is defined by Equations (3.5) or (3.6), the terms $[M]$ and $[X]$ being expressed as weight percentages and T is the thermodynamic temperature (K).

This definition of the solubility product and the temperature dependence is used throughout this chapter, unless otherwise specified.

3.2.2 Using the Solubility Product Information

Given the constants A and B to express the solubility of a particular compound in austenite, for example, it is possible to construct the boundary between the austenite single phase region and the austenite + MX two-phase region in the ternary system $Fe - M - X$ over a range of temperatures, as shown in Fig. 3.1. For each isotherm, the product of $[M]$ and $[X]$ is equal to the solubility product k_s for the specified temperature, and the change of the boundary with temperature reflects the Arrhenius type relationship depicted by Equation (3.9). Any alloy composition lying below or to the left of the curve at a given temperature will exist (at equilibrium) as the single phase austenite. Any alloy lying above or to the right

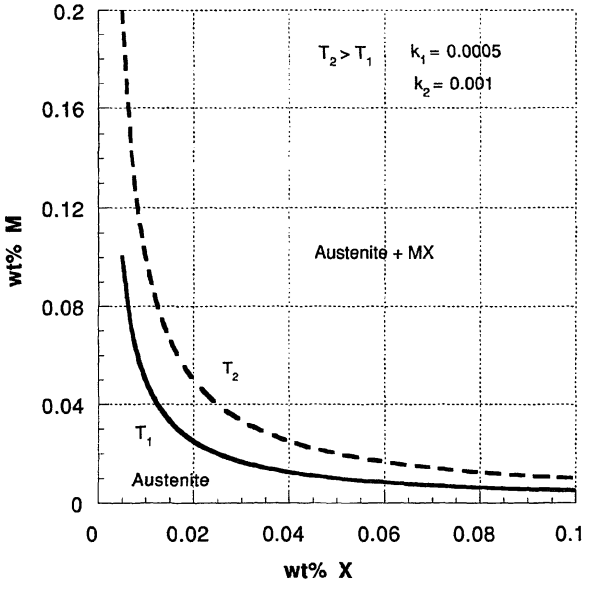


Fig. 3.1 Solubility diagram showing the single phase field for austenite and the two phase fields for austenite and microalloy carbide or nitride, MX. The boundary between the phase fields is given by an equation such as Equation (3.5) or (3.6) and the temperature dependence is obtained from an equation such as Equation (3.9).

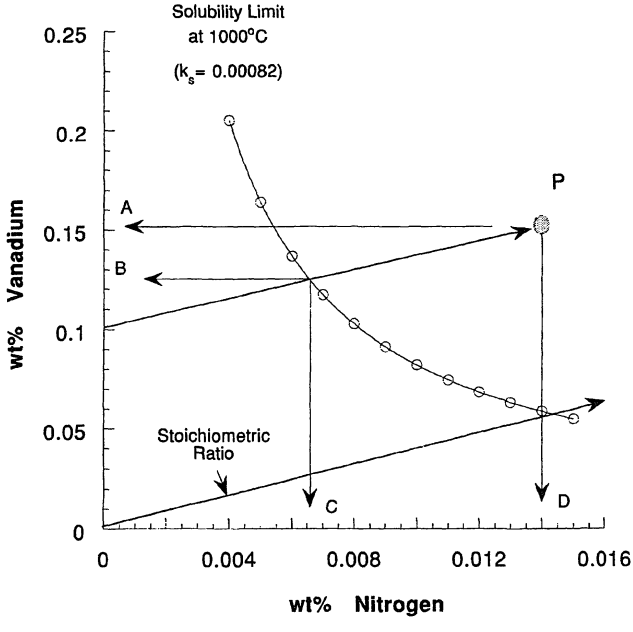


Fig. 3.2 Solubility diagram showing the stoichiometric ratio between M and X. using vanadium nitride (VN) as an example.

of the curve at a given temperature will exist as a two phase alloy of austenite $+MX$.

Consider now a specific alloy composition, e.g. alloy P, at a specified temperature, Fig. 3.2. This clearly lies in the two phase domain. In order to assess the amount of the second phase MX, and the magnitude of the solute concentrations, it is necessary to consider the nature of the second phase. The components of the compound react together in the ratio of their atomic masses. For example

$$[V] + [N] \leftrightarrow (VN)$$
$$1\,\text{g atom} + 1\,\text{g atom} \leftrightarrow 1\,\text{g mole}$$
$$51\,\text{g}\,V + 14\,\text{g}\,N \leftrightarrow 65\,\text{g}\,VN$$

The relative atomic masses of vanadium and nitrogen are 51 and 14 respectively, and these elements will always react in these proportions (by weight) to form vanadium nitride. In the two-phase alloy P, therefore, the ratio of the relative atomic masses that react, known as the stoichiometric ratio, can be shown passing through the composition given for alloy P. It can be seen that this line does not pass through the origin of the graph, because the original composition of the alloy does not have the elements present in the stoichiometric ratio. Stoichiometric alloys may be defined as those in which the ratio of vanadium to nitrogen (on a weight percentage bases) is in the ratio 51:14, as indicated in Fig. 3.2. The composition of alloy P is indicated by the points A and D, i.e. 0.15wt%V and 0.014wt%N. As VN is stable in this alloy at the temperature shown (1000°C or 1273K), then the composition of the austenite matrix must lie along the stoichiometric line passing through the alloy P, and if equilibrium is attained, then the matrix composition will lie at the intersection between the stoichiometric line and the solubility limit. The composition of the austenite matrix is thus indicated by the points B and C i.e. 0.125wt%V and 0.0066wt%N. From the concept of stoichiometry, it follows that, for VN,

$$(\text{A} - \text{B})/(\text{D} - \text{C}) = 51 : 14$$

If we designate the following

V_T = the wt%V in the alloy
$[V]$ = the wt%V dissolved in the matrix
V_{VN} = the wt%V present as VN
N_T = the wt%N in the alloy
$[N]$ = the wt%N dissolved in the matrix
N_{VN} = the wt%N present as VN
A_V = the relative atomic mass of vanadium
A_N = the relative atomic mass of nitrogen
(VN) = the wt%VN separated from the matrix

then there are a number of simple relationships that can be noted

$$[V] + V_{VN} = V_T \tag{3.10}$$

$$[N] + N_{VN} = N_T \tag{3.11}$$

$$[V][N] = k_s \tag{3.12}$$

$$V_{VN} \cdot A_N/A_V = N_{VN} \tag{3.13}$$

$$(VN) = V_{VN} \cdot (A_V + A_N)/A_V \tag{3.14}$$

$$(VN) = N_{VN} \cdot (A_V + A_N)/A_N \tag{3.15}$$

From Equations (3.10) to (3.13)

$$\begin{aligned} k_s &= [N][V] \\ &= (V_T - V_{VN})(N_T - N_{VN}) \\ &= (V_T - V_{VN})(N_T - V_{VN} \cdot A_N/A_V) \end{aligned} \tag{3.16}$$

or $$A_N(V_{VN})^2/A_V - (N_T + V_T \cdot A_N/A_V)(V_{VN}) + (V_T \cdot N_T - k_s) = 0 \tag{3.17}$$

This is a simple quadratic equation for V_{VN}, for which the solution is given by:

$$\begin{aligned} V_{VN} = A_V[(N_T + V_T \cdot A_N/A_V) - ((N_T + V_T \cdot A_N/A_V)^2 \\ - 4A_N(V_T \cdot N_T - k_s)/A_V)^{1/2}]/2A_N \end{aligned} \tag{3.18}$$

The amount of vanadium as *VN* can be obtained from the steel composition and k_s, and, from Equation (3.18), the weight percentage of *VN* can be obtained simply by substitution of V_{VN} in Equation (3.14). The significance of Equations (3.10) to (3.18) is that given any two of the variables C, D, E, or F, in Fig. 3.2, and the solubility data *A* and *B* in Equation (3.9), then the metallurgical state can be defined in terms of the amount of precipitated *VN* and the composition of the matrix, given that $V_T \cdot N_T > k_s$, i.e. that the steel composition lies in the two-phase region. Thus the amount of *VN* which is undissolved at a given temperature and is available for grain growth inhibition, and the dissolved vanadium and nitrogen contents that are available for the formation of fine interphase precipitation during cooling, can be calculated. It should be pointed out that the amount of fine interphase precipitation that can be formed on cooling will be limited by one or other of the two solutes in all steels other than those having the absolute stoichiometric ratio. For example, in Fig. 3.2, the alloy *P* has a substantial excess of vanadium, so that the extent of vanadium nitride precipitation during cooling will be limited by the dissolved nitrogen content. In this particular case the nitrogen is sub-stoichiometric with respect to the vanadium. If, however, the vanadium content of alloy *P* were to be changed so that the vanadium became sub-stoichiometric with respect to the nitrogen, then the vanadium content would limit the extent of fine interphase precipitation.

The above arguments relate, strictly, only to *Fe–V–N* ternary alloys. Due to the fact that all structural steels contain carbon, then the fine interphase precipitation would be augmented by vanadium carbo-nitride precipitation in alloys where the vanadium content exceeds that required for stoichiometric combination with the

nitrogen. The undissolved precipitate would also be a carbo-nitride but in low carbon steels the carbo-nitride would contain very little carbon and the example used, i.e. undissolved *VN* is a reasonable approximation.

3.2.3 Solubility Data

(a) Aluminium Nitride

The solubility data for aluminium nitride in austenite has been evaluated by many workers using either classical thermodynamic methods involving equilibration with gaseous atmospheres of known nitrogen activity, or chemical methods designed to evaluate nitrogen in the form of nitride, such as the Beeghly ester-halogen technique. This involves the dissolution of the steel matrix, usually in a bromine–methanol solution, filtration of the residue, and distillation of the residue in an alkaline solution, where the nitrogen is converted to ammonia, and this is determined either volumetrically of photometrically. The advantages and shortcomings of this technique have been discussed extensively[1] but can be summarised as follows:

(i) The Beeghley ester-halogen technique successfully discriminates between nitrogen as aluminium nitride and nitrogen dissolved in the steel matrix.
(ii) The Beeghly technique is not specific in indentifying nitrogen as aluminium nitrides, but is also known to include nitrogen as silicon nitride, and nitrogen as titanium nitride. It is possible that the Beeghley nitrogen will include other nitrides, and suitable chemical treatment of the extracted residues can be carried out to give a 'total nitride' nitrogen.

Thus, care is required in interpreting the Beeghly nitrogen value in steels where it is suspected that other nitrides may be present.

Data for the solubility of aluminium nitride[2–9] in austenite are given in Table 3.1 and are shown in graphical form in Fig. 3.3, covering the temperature range of 900–1350°C. k_s values range from 1.2×10^{-5} to 4.9×10^{-5} at 900°C and from 0.71 to 2.5×10^{-3} at 1350°C. The early results of Darken *et al.*[2] based on an equilibration technique, together with the results of Shimose and Narita[3] appear to be significantly higher than the majority of the results obtained by the Beeghley method for steels reheated into the austenite temperature range for periods of 1–4

Table 3.1 Solubility relationships for aluminium nitride in austenite

Logarithm of solubility product (log k_s)	Method	Temperature range (°C)	Reference
$-7400/T + 1.95$	Seiverts	1050–1350	(2)
$-7184/T + 1.79$	Beeghley	800–1300	(3)
$-6770/T + 1.03$	Beeghley	810–1260	(4)(9)
$-7750/T + 1.80$	Beeghley	900–1350	(5)
$-6180/T + 0.73$	Beeghley	900–1200	(6)
$-7500/T + 1.48$	Beeghley	950–1300	(7)
$-9200/T + 2.92$	Beeghley	850–1300	(8)

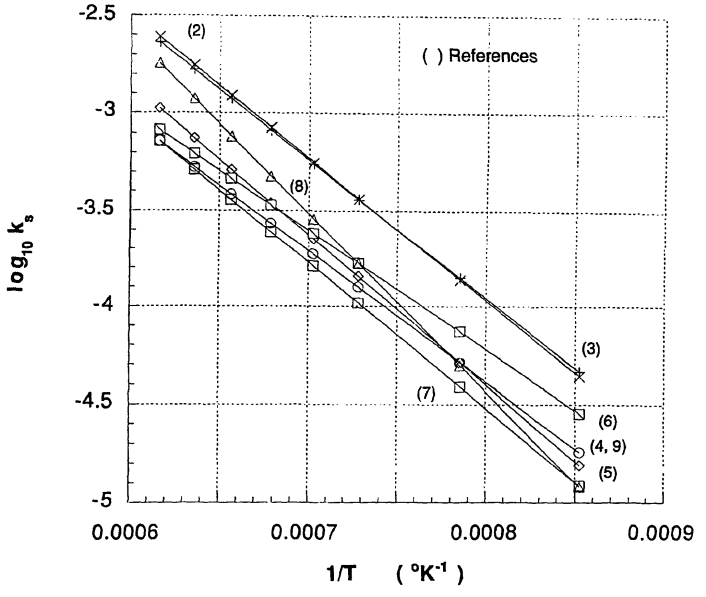


Fig. 3.3 Experimental evaluation of the temperature dependence of the solubility product of aluminium nitride in austenite.

hours. The latter results may be regarded as more representative of commercially reheated steels and are recommended on this basis. It should be noted that the scatter of individual results obtained within a given study can span the whole of the relationships given by references 4–9, and a mid-range value for these results is obtained from the equation given by Leslie *et al.*[4] and supported by Irvine *et al.*,[9] i.e.

$$\log k_s = -6770/T + 1.03 \tag{3.19}$$

Using this equation, the solubility products can be evaluated for a range of temperatures, Table 3.2, and the solubility limits at these temperatures can be depicted as shown in Fig. 3.4. It is worth emphasising that the isotherms shown in Fig. 3.4 can be regarded as a contour map showing the interface between the single

Table 3.2 Solubility products for aluminium nitride at various temperatures in the austenite range

Temperature (°C)	Temperature (°K)	Log k_s	k_s
900	1173	−4.74	1.82×10^{-5}
1000	1273	−4.29	5.15×10^{-5}
1100	1373	−3.90	1.26×10^{-4}
1150	1423	−3.73	1.87×10^{-4}
1200	1473	−3.57	2.72×10^{-4}
1250	1523	−3.42	3.84×10^{-4}
1300	1573	−3.27	5.32×10^{-4}
1350	1623	−3.14	7.22×10^{-4}

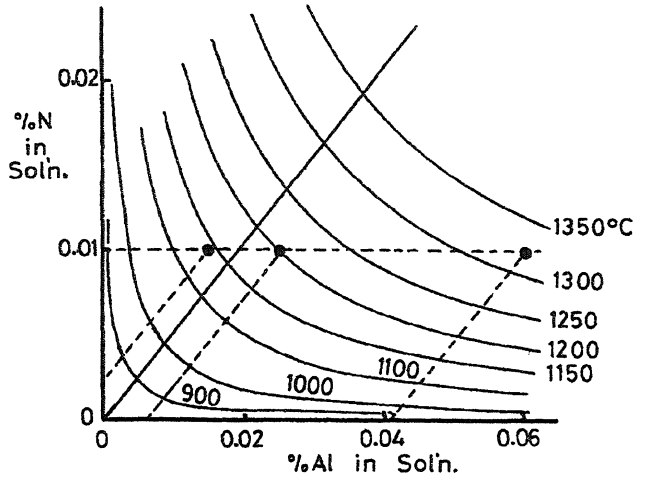


Fig. 3.4 Limits of the mutual solubility of aluminium and nitrogen at various temperatures in the austenite range.

phase field for austenite and the two-phase field for austenite and aluminium nitride. For a steel of any given aluminium and nitrogen content, therefore, the constitution at any given temperature can be checked using Fig. 3.4, or Equation (3.19),[4,9] and the matrix compositions and amount of precipitated aluminium nitride can be determined by the procedures given in Section 3.2.2.

(b) Vanadium Nitride

The solubility of vanadium nitride has been assessed from thermodynamic data for the reaction between vanadium and nitrogen together with the thermodynamics of nitrogen and vanadium dissolution in iron. Experimental results have also been obtained using matrix dissolution techniques involving dilute sulphuric acid followed by separation and analysis of the extracted residues. Considerable care is required with the type of acid, the acid concentration, dissolution temperature and dissolution time, as lack of attention to these details can lead to considerable variations in the results. This has resulted in considerable confusion between chemists and metallurgists, and the terms 'acid soluble' and 'acid insoluble' nitride may or may not equate with the metallurgical concept of soluble nitrogen (and vanadium) and undissolved vanadium nitride. However, with careful control of the dissolution process in 10% sulphuric acid, the acid insoluble vanadium nitride can be equated to the metallurgically undissolved vanadium nitride.

Data for the solubility of vanadium nitride in austenite[9–12] are given in Table 3.3, and the various solubility relationships are shown graphically in Fig. 3.5. The data

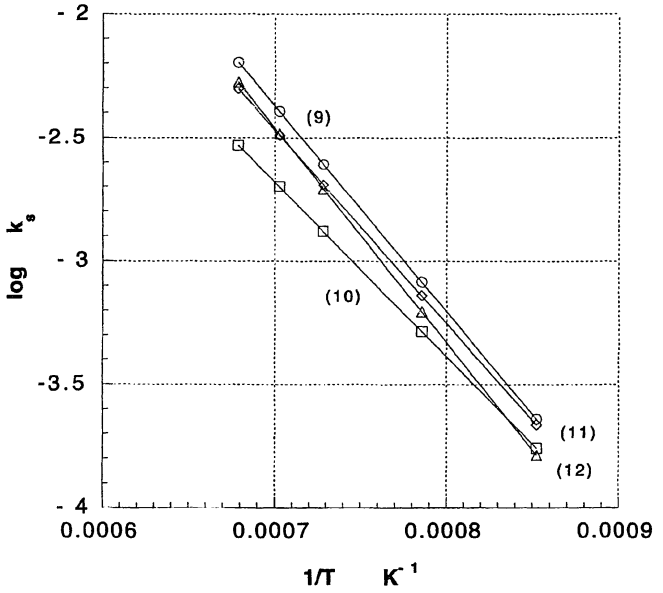


Fig. 3.5 Evaluation of the temperature dependence of the solubility product of vanadium nitride in austenite.

from different sources, obtained by various methods, show reasonably close agreement apart from the Frohberg and Graf data[10] at the higher temperatures which appear to indicate a lower solubility than is shown by other workers.[9,11,12] Irvine *et al.*[9] noted that the solubility product for VN in austenite increased slightly with increasing manganese content in the steel according to the equation

$$\log k_s = -8,330/T + 3.40 + 0.12[\%\text{Mn}] \tag{3.20}$$

Their equation presented in Table 3.3 and illustrated in Fig. 3.5, was for a steel containing 0.5wt%Mn.[9] Reducing the manganese content to zero would reduce the solubility product at any given temperature by 0.06 and would give even better agreement with the results of Roberts *et al.*[11] and Narita.[12] A second interesting feature of the results of Irvine *et al.*[9] was the absence of any effect of carbon content on the solubility product. The same solubility product was obtained in both 0.05wt%C and 0.15wt%C steels, suggesting that the precipitate is a simple

Table 3.3 Solubility relationships for vanadium nitride in austenite

Logarithm of solubility product (log k_s)	Method	Reference
−8330/T + 3.46	Precipitate extraction	(9)
−7070/T + 2.27	Thermodynamic calculation	(10)
−7840/T + 3.02	Precipitate extraction	(11)
−8700/T + 3.63	Gaseous equilibrium	(12)

Table 3.4 Solubility products for vanadium nitride at various temperatures in the austenite range and at differing manganese contents

Temperature (°C)	Temperature (°K)	0.5% Mn		1.0% Mn		1.5% Mn	
		log k_s	k_s	log k_s	k_s	log k_s	k_s
900	1173	−3.64	2.3×10^{-4}	−3.58	2.6×10^{-4}	−3.52	3.0×10^{-4}
1000	1273	− 3.08	8.2×10^{-4}	−3.02	9.5×10^{-4}	−2.96	1.1×10^{-3}
1100	1373	−2.61	2.5×10^{-3}	−2.55	2.8×10^{-3}	−2.49	3.3×10^{-3}
1150	1423	−2.39	4.0×10^{-3}	−2.33	4.6×10^{-3}	−2.27	5.3×10^{-3}
1200	1473	−2.20	6.4×10^{-3}	−2.14	7.3×10^{-3}	−2.08	8.4×10^{-3}
1250	1523	−2.01	9.8×10^{-3}	−1.95	1.1×10^{-2}	−1.89	1.3×10^{-2}
1300	1573	−1.84	1.5×10^{-2}	−1.78	1.7×10^{-2}	−1.72	1.9×10^{-2}
1350	1623	−1.67	2.1×10^{-2}	−1.61	2.4×10^{-2}	−1.55	2.8×10^{-2}

vanadium nitride, rather than the complex V(C,N). This aspect is considered in more detail in a later section.

The solubility of VN in austenite can be described by any of the equations given in references 9, 11 and 12, but for microalloyed steels with significant manganese contents, Equation (3.20) is recommended. The values of k_s for vanadium nitride in austenite for different levels of manganese are given in Table 3.4, whilst the solubility limits of vanadium and nitrogen are shown in Fig. 3.6

(c) Niobium Nitride

The solubility of niobium nitride is largely based on thermodynamic data for the heat of formation of niobium nitride and the heat of dissolution of the elements in

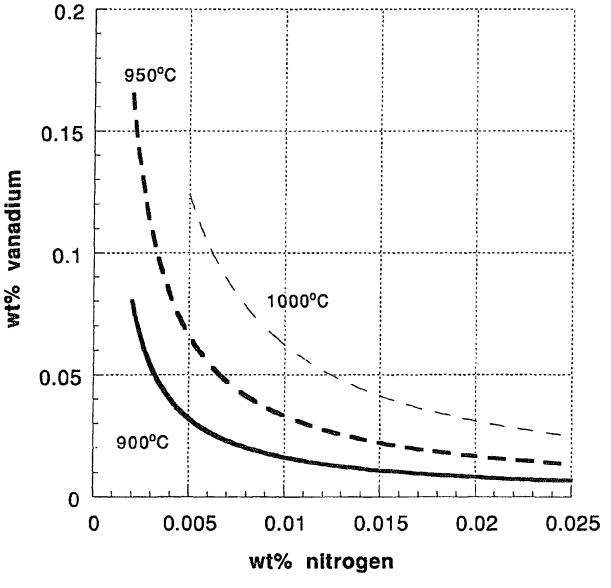


Fig. 3.6 Limits of the mutual solubility of vanadium and nitrogen at various temperatures in the austenite range (Equation (3.20) for a 1.0wt% Mn steel).

Table 3.5 Solubility relationships for niobium nitride in austenite and ferrite phases

Logarithm of solubility product (log k_s)	Method	Reference
Austenite	–	–
$-8500/T + 2.80$	Gaseous equilibrium	(12)
$-10230/T + 4.04$	Gaseous equilibrium	(13)
$-7000/T + 1.71$	Solvent extraction	(15)
Ferrite	–	–
$-12230/T + 4.96$	Thermodynamic Calculation	(14)

an iron matrix. The solubility data are given in Table 3.5 and illustrated in Fig. 3.7. The data for the solubility product in austenite[12,13] show reasonable agreement, and the calculated data for the solubility product of niobium nitride in ferrite[14] suggest that niobium nitride will be less soluble in ferrite than in austenite at a given temperature. The data of Narita are recommended for the austenite range and solubility products are shown in Table 3.6. The solubility limits of niobium and nitrogen in austenite are depicted in Fig. 3.8, and those for niobium and nitrogen in ferrite are shown in Fig. 3.9.

(d) Titanium Nitride

Studies of the solubility of titanium nitride have indicated that of all the microalloy carbides and nitrides, titanium nitride is by far the most stable, and equations for the solubility product of titanium nitride have been obtained in both the liquid

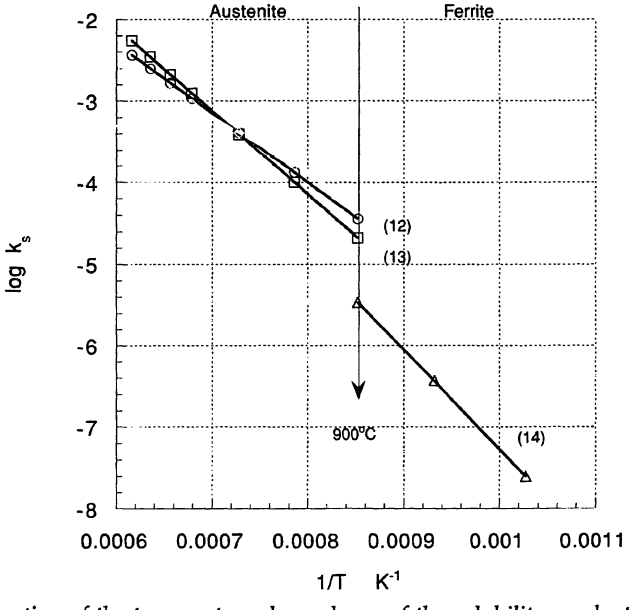


Fig. 3.7 Evaluation of the temperature dependence of the solubility products for niobium nitride in the austenite and in ferrite. The solubility of niobium nitride in ferrite is shown to be lower than that in austenite at temperatures in the ferrite range.

Table 3.6 Solubility products for niobium nitride at various temperatures in austenite and in ferrite

Temperature (°C)		
Austenite	**log k_s**	**k_s**
900	−4.45	3.6×10^{-5}
1000	−3.88	1.3×10^{-4}
1100	−3.39	4.1×10^{-4}
1200	−2.97	1.1×10^{-3}
1250	−2.78	1.7×10^{-3}
1300	−2.60	2.5×10^{-3}
1350	−2.44	3.7×10^{-3}
Ferrite		
600	−9.05	8.9×10^{-10}
700	−7.61	2.5×10^{-8}
800	−6.44	3.6×10^{-7}

steel and in austenite. The data are presented in Table 3.7, and illustrated in Fig. 3.10. The solubility of titanium nitride is considerably higher in liquid steel than in austenite, but the solubility product in austenite as given by Matsuda and Okamura[16] shows considerable divergence from that given by Narita.[12] Bearing in mind the very low solubility of titanium nitride in austenite, this is perhaps not too surprising. For example, taking the most optimistic level of solubility indicated by the Matsuda data (see Table 3.8), only 0.01wt% Ti would be in equilibrium with 0.004wt% N, in solution in the austenite at 1400°C. At 900°C, the solubility product is decreased by a factor of 100, equivalent to, say, 0.001wt% Ti and 0.004wt% N. The data given by Narita[12] show an even more restricted solubility in austenite, by

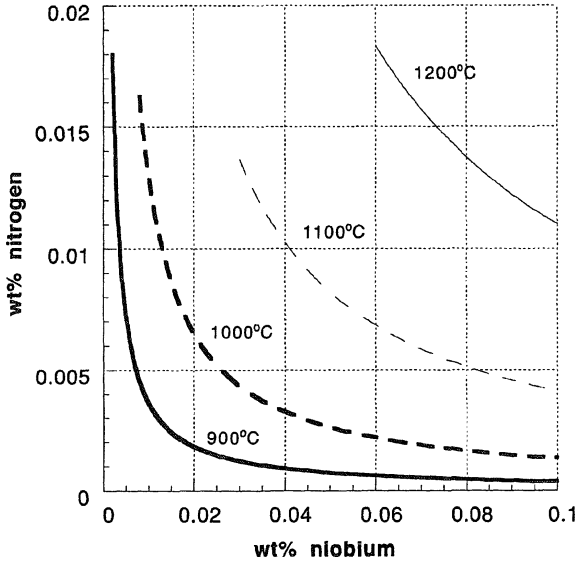


Fig. 3.8 Limits of the mutual solubility of niobium and nitrogen in austenite.

Table 3.7 Solubility relationships for titanium nitride in the liquid and austenite phases

Logarithm of solubility product	Method	Reference
Liquid	–	–
$-16586/T + 5.90$	Gaseous equilibrium	(12)
Austenite	–	–
$-15020/T + 3.82$	Gaseous equilibrium	(12)
$-8000/T + 0.32$	Precipitate Extraction	(16)

a factor varying from 6 at 1400°C to 400 at 900°C. Metallographic evidence confirms the limited solubility of titanium nitride in steel. At conventional levels of microalloying (say, 0.03wt% to 0.10wt%), large orange cuboids can be seen by optical microscopy being several microns in size, these having precipitated in the liquid steel. Electron microscopy indicates other cubic particles of about 1 μm in edge length, typical of particles precipitated during solidification due to the discontinuous solubility change with consequently fewer finer nitrides precipitated in the solid state.

The gap between data for the liquid state and that for the solid state shown in Fig. 3.10, represents the δ-ferrite temperature range of low carbon steels for which there is no available data.

The limits of mutual solubility of titanium and nitrogen in austenite at various temperatures are shown in Fig. 3.11. If it is assumed that the liquid solidifies directly as austenite, the proportions of TiN precipitated in the liquid state, A–B, during solidification, B–C, and in the solid austenite, C–D, can be derived directly from this figure. The data of Narita[12] have been used for both liquid and solid (austenitic) states.

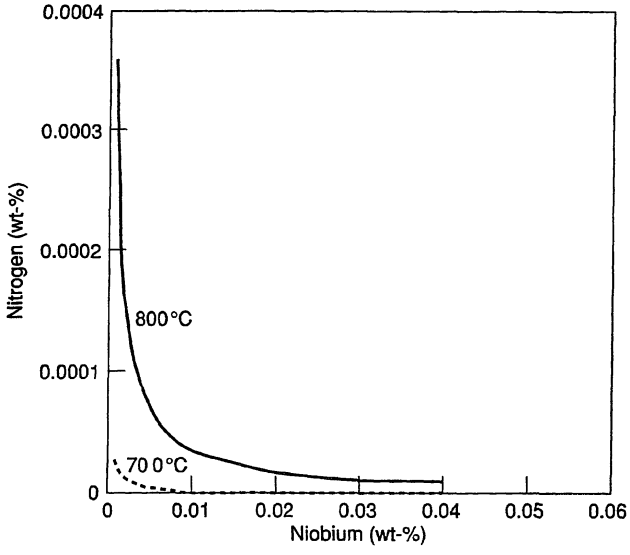


Fig. 3.9 Limits of the mutual solubility of niobium and nitrogen in ferrite.

Table 3.8 Solubility products for titanium nitride at various temperatures in liquid steel and in austenite

	Matsuda and Okumura[16]		Narita[12]	
Temperature (°C)	**log k_s**	**k_s**	**log k_s**	**k_s**
900	−6.50	3.2×10^{-7}	−8.98	1.0×10^{-9}
1000	−5.96	1.1×10^{-6}	−7.98	1.0×10^{-8}
1100	−5.51	3.1×10^{-6}	−7.12	7.6×10^{-8}
1200	−5.11	7.7×10^{-6}	−6.38	4.2×10^{-7}
1250	−4.93	1.2×10^{-5}	−6.04	9.1×10^{-7}
1300	−4.77	1.7×10^{-5}	−5.73	1.9×10^{-6}
1350	−4.61	2.5×10^{-5}	−5.43	3.7×10^{-6}

(e) Vanadium Carbide

The description of the solubility product for vanadium carbide in steel is made a little more complicated by evidence of differences in stoichiometry. There is considerable evidence that the chemical formula for vanadium carbide is V_4C_3, as indicated in section 3.2.1, and that the solubility product can be defined as in Equation (3.6b). However, not all workers have accepted this definition, and solubility products exist which conform with Equation (3.5), i.e. assume that the compound is VC. The data presented in Table 3.9 reflect these approaches, in that the solubility product used by Narita[12] is based on VC and defined by Equation (3.5), whilst those of Bungardt *et al.*[17] and Sekine *et al.*[19] are based on V_4C_3 and defined by Equation (3.6b). The solubility products are shown in Fig. 3.12. The

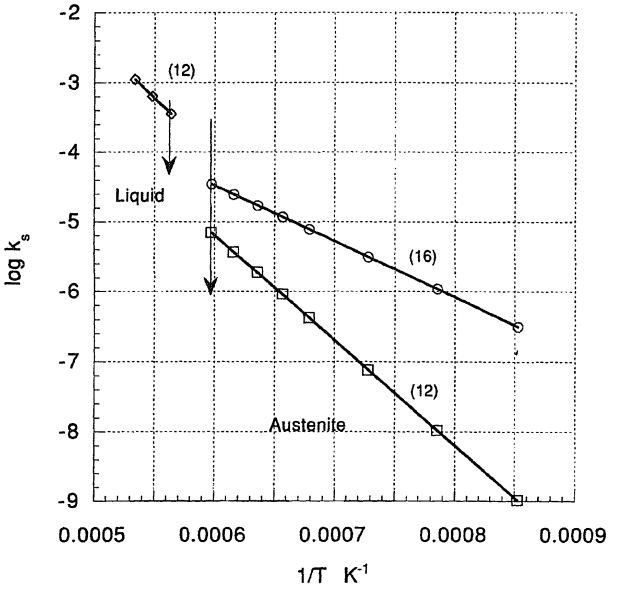


Fig. 3.10 Evaluation of the temperature dependence of the solubility products of titanium nitride in the liquid and austenite phases.

Table 3.9 Solubility relationships for vanadium carbide in austenite and in ferrite

Logarithm of solubility product, log k_s	Method	Reference
Austenite	–	–
$-9500/T + 6.72$ (VC)	Gaseous equilibrium	(12)
$-10800/T + 7.06$ (V_4C_3)	Gaseous equilibrium	(17)
$-9407/T + 5.65$ (V_4C_3)	Precipitate extraction	(19)
Ferrite	–	–
$-12265/T + 8.05$ (VC)	Thermodynamic calculation	(20)

solubility products for vanadium carbide in austenite differ significantly and this cannot be attributed solely to the different bases. Evaluation of the solubility products at 900, 1000. and 1100°C were carried out for both data sets (see Table 3.10), and were appropriately treated according to their defined bases to obtain the mutual solubility limits of vanadium and carbon in austenite. These are shown in Fig. 3.13, and it is clear that the data of Narita show significantly higher solubility limits at each temperature than are given by Bungardt *et al.* Studies of the solubility of vanadium carbide in austenite by Savost'yanova and Shvartsman,[18] however, support the results of Narita, in providing a solubility product (for V_4C_3) of about 0.1 and Narita's data are therefore recommended.

A significant feature of the solubility of vanadium carbide in austenite is that it is considerably higher than those of the other microalloy carbides and nitrides, suggesting that vanadium carbide will be completely dissolved even at low austenitising temperatures (900°C) given that the vanadium level is typical of that

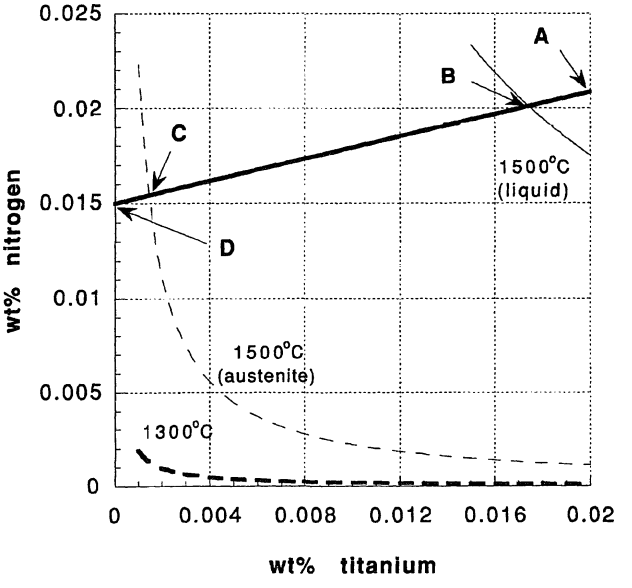


Fig. 3.11 Limits of mutual solubility of titanium and nitrogen in liquid steel and in austenite.

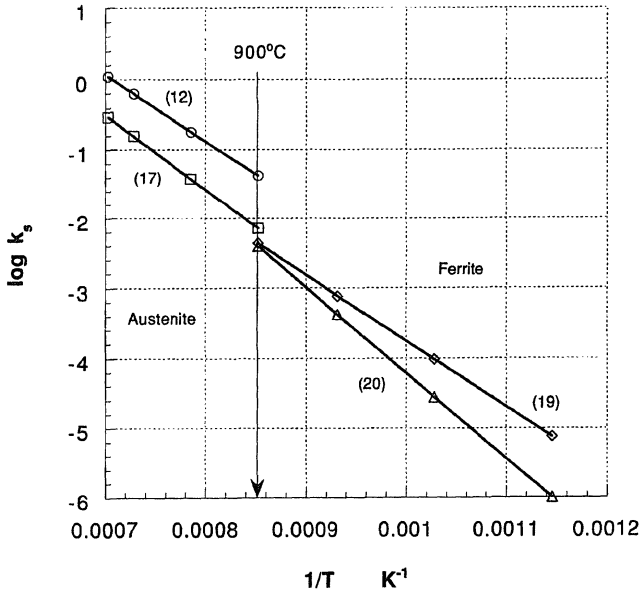


Fig. 3.12 Evaluation of the temperature dependence of the solubility products for vanadium carbide (VC and V_4C_3) in austenite and ferrite.

used in microalloyed steels (up to 0.15wt% in the case of vanadium). The solubility of vanadium carbide in ferrite is lower than that in austenite, but still shows an appreciable level, with $k_s \approx 10^{-4}$ at 700°C when k_s is based on V_4C_3 and somewhat lower when based on VC.

(f) Solubility of Niobium Carbide

The solubility product equations for niobium carbide in both austenite and ferrite are presented in Table 3.11, and shown graphically in Fig. 3.14. The data from different sources relating to the austenite phase are reasonably close and all suggest that niobium carbide is more soluble in austenite than in ferrite. It should be emphasised, however, that the data for the ferrite phase is based on calculations from thermodynamic data and may be subject to considerable error. The relationship presented suggests that niobium carbide is less soluble in ferrite than is vanadium carbide, the solubility product being $k_s \approx 10^{-6}$ at 700°C.

Table 3.10 Solubility products for vanadium carbide (VC and V_4C_3) in the austenite and ferrite phases

	Sekine[19]-Ferrite		Narita[12]-Austenite	
Temperature (°C)	**log k_s**	**k_s**	**log k_s**	**k_s**
900	−2.37	4.3×10^{-3}	−1.38	4.2×10^{-2}
1000			−0.74	1.8×10^{-1}
1100			−0.20	6.3×10^{-1}

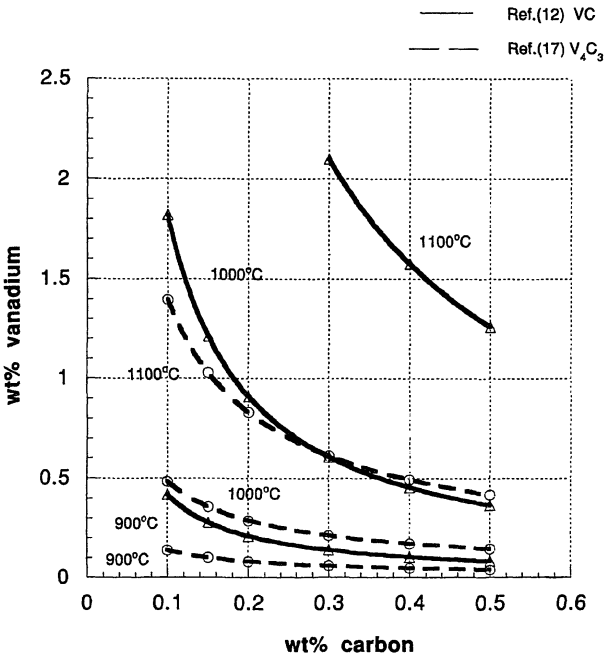


Fig. 3.13 Limits of the mutual solubility of vanadium and carbon in austenite. The solubility products have been based on either VC or V_4C_3 as indicated.

The direct comparison of the solubility products for niobium carbides in austenite shown in Fig. 3.14 could be misleading. It is well established that niobium carbide shows extensive mutual solubility with niobium nitride. The solubility of niobium nitride is considerably less than that of niobium carbide, and the complex carbo-nitride, as will be shown later, may exhibit intermediate solubility. Nordberg and Aronsson's[21] results relate specifically to the carbide, as do those of Narita[12] and Johansen *et al.*,[22] whereas those of Irvine *et al.* reflect a complex carbo-nitride. Further differences exist in that Nordberg and Aronsson consider a niobium carbide given by the formula $NbC_{0.8}$, whereas both other

Table 3.11 Solubility relationships for niobium carbide in austenite and in ferrite

Logarithm of the solubility product, log k_s	Method	Reference
Austenite		
$-6770/T+2.26$	Precipitate extraction	(9)
$-7900/T+3.42$	Gaseous equilibrium	(12)
$-7510/T+2.96$	Thermodynamic calculation	(21)
Ferrite		
$-10960/T+5.43$	Thermodynamic calculation	(14)
$-9930/T+3.90$	Thermodynamic calculation	(20)

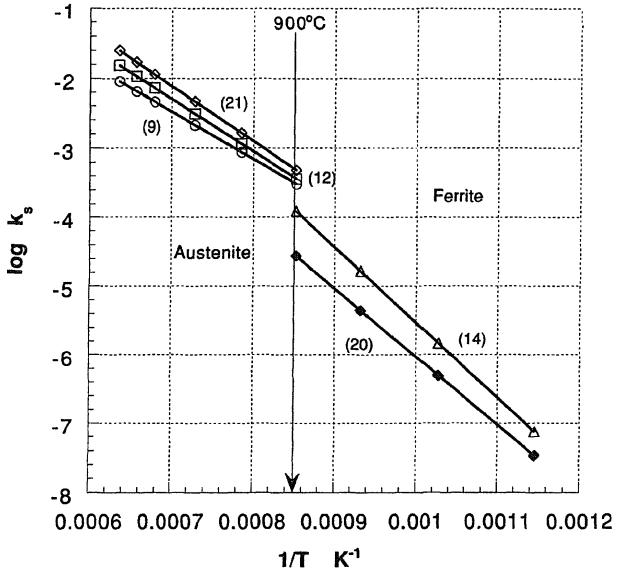


Fig. 3.14 Evaluation of the temperature dependence of the solubility products for niobium carbide in austenite and in ferrite.

references[9,12] assume NbC or Nb(C, N). The variations in stoichiometry have been discussed by Hudd *et al.*,[14] who considered that the lower carbon/niobium ratio may be a real effect arising as a consequence of the high activity of carbon in niobium carbide, or may be an artefact arising from the occlusion of nitrogen and/or oxygen atoms in the niobium carbide. Whilst the literature often gives a solubility product relating to NbC, in those studies where the soluble and insoluble carbon have been evaluated in addition to the soluble and insoluble niobium, the experimental results indicate a formula NbC_x and the solubility product is then defined as $k_s = [Nb][C]^x$ where x is approximately 0.87. It is interesting to note that the atomic ratio of niobium to interstitial in the complex carbo-nitride approaches unity. More will be said of the complex precipitates in Section 3.4 of this chapter. The mutual solubility limits of niobium and carbon in austenite[(9)] are shown in Fig. 3.15.

(g) Titanium Carbide

The solubility product equations for titanium carbide in austenite and ferrite are shown in Table 3.12 and are shown graphically in Fig. 3.16. The data show some divergence, particularly at the lowest and highest temperatures in the austenite range, although the data of Mori *et al.*[15] were only studied over the temperature range of 1,000°C–1350°C. One of the difficulties associated with titanium carbide solubility data is related to the presence of nitrogen in the steels used. Titanium nitride is extremely stable and needs to be considered when interpreting experimental results. As all of the data for the solubility in austenite was

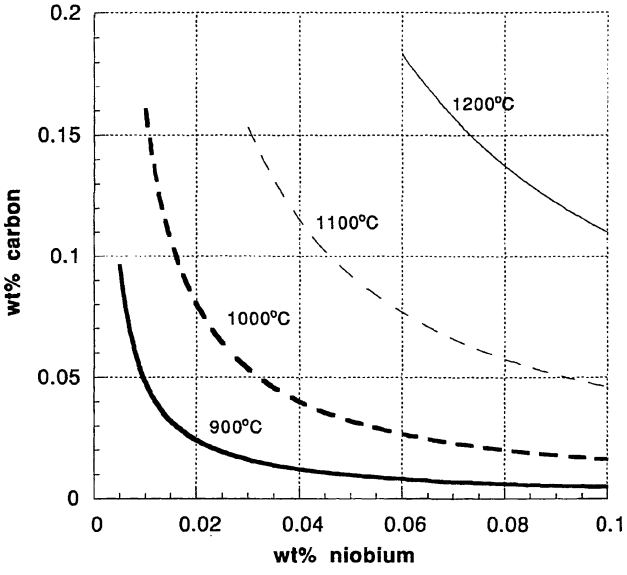


Fig. 3.15 Limits of the mutual solubility of niobium and carbon in austenite. The solubility in the ferrite is not shown due to the very low levels of solubility in the ferrite range ($\approx 10^{-6}$ at 700°C).

generated by acid dissolution techniques, there is no *a priori* reason to select a particular solubility equation, but the close similarity of the Mori and the Narita data may suggest that these are to be preferred. The mutual solubility limits of titanium and carbon in austenite are shown in Fig. 3.17.

3.2.4 Comparison of the Solubilities of Microalloy Carbides and Nitrides

The solubility products of the microalloy carbides and nitrides are compared in Fig. 3.18. Despite the variations in cited solubility product equations presented above, there are several important conclusions that can be drawn from the assembled data.

Table 3.12 Solubility relationships for titanium carbide in the austenite and ferrite phases

Logarithm of the solubility product log k_s	Method	Reference
Austenite	–	–
$-7000/T + 1.71$	Precipitate extraction	(9)
$-10475/T + 5.33$	Gaseous equilibrium	(12)
$-10300/T + 5.12$	Precipitate extraction	(15)
Ferrite		
$-9575/T + 4.40$	Thermodynamic calculation	(20)

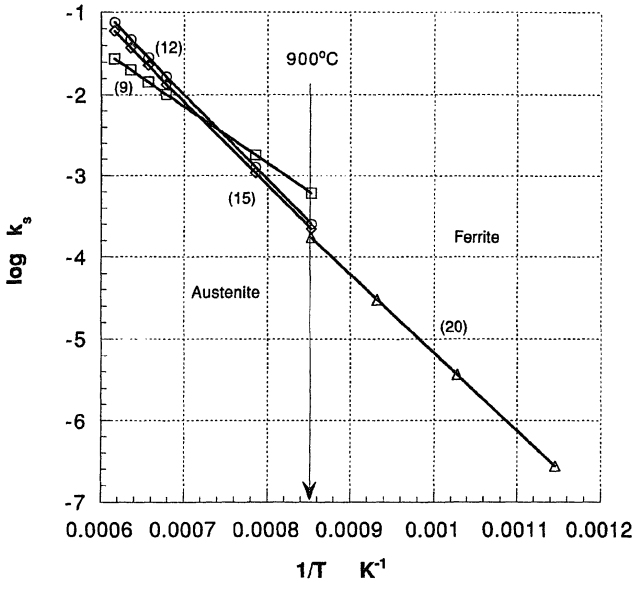


Fig. 3.16 Evaluation of the temperature dependence of the solubility products for titanium carbide in austenite and in ferrite.

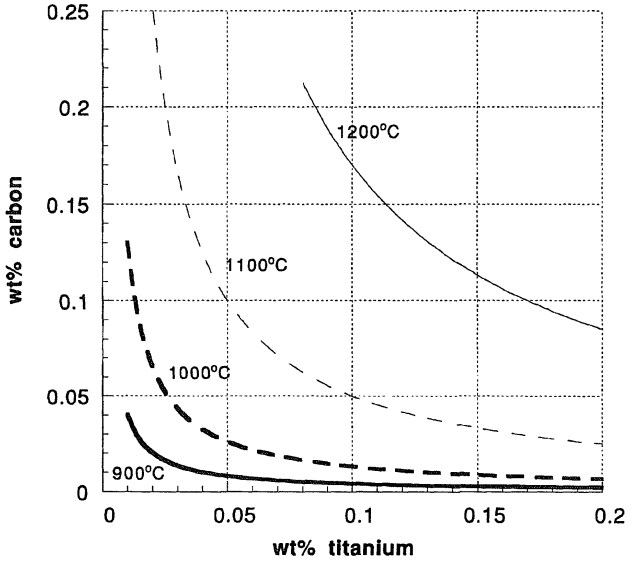


Fig. 3.17 Limits of the mutual solubility of titanium and carbon in austenite. Solubility limits for ferrite are not shown due to the low levels of solubility in the ferrite range $k_s < 10^{-5}$ at 700°C.

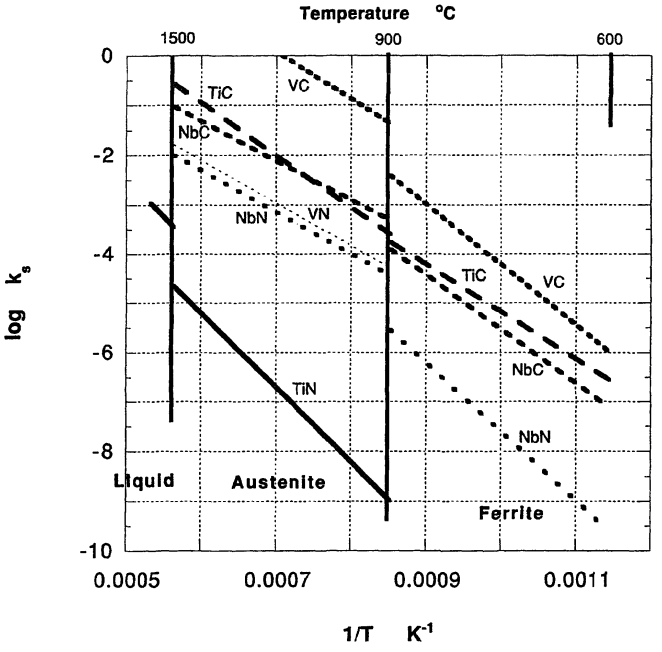


Fig. 3.18 A comparison of the solubility products of the microalloy carbides and nitrides, showing the greater stabilities of the nitrides relative to those of the carbides. Of particular note is the very low solubility of TiN in austenite and the very high solubility of VC in austenite. The solubilities for carbides and nitrides in ferrite are lower than in the austenite at temperatures in the ferrite range.

(i) For each of the microalloys the nitride is more stable than the carbide in austenite. The absolute differences in solubility between the microalloy carbides and the microalloy nitrides differ significantly, depending upon the microalloying element. Large differences are observed between vanadium carbide and vanadium nitride and between titanium carbide and titanium nitride, whilst the difference between the solubilities of niobium carbide and niobium nitride is much less, although still significant in showing a lower solubility for the nitride. Although aluminium nitride shows a similar solubility to niobium nitride, aluminium carbide has never been reported to occur in steels, even in steel with substantial aluminium and carbon contents, indicating that aluminium carbide is even more soluble in steel than the most soluble of microalloy carbides (vanadium carbide)

(ii) Many of the microalloy carbides and nitrides show broadly similar levels of solubility in austenite, with two notable exceptions. Titanium nitride is markedly more stable than other microalloy carbides and nitrides by a factor of about 1000. On the other hand, vanadium carbide is far more soluble than other microalloy carbides and nitrides, again by a factor of about 1000.

(iii) Whilst the solubility in the liquid phase of steel is not known for the majority of microalloy carbides and nitrides, the data for titanium nitride show that the solubility of titanium nitride in liquid steel is of the order of about 10–100 times larger than that in austenite at the same temperature. Thus, the solubility of titanium nitride in liquid at temperatures up to 1600°C is very similar to those of most other microalloy carbides and nitrides in austenite at temperatures of around 1200°C.

(iv) The solubilities of niobium carbide, and niobium nitride in ferrite, calculated from thermodynamic data, suggest that the solubilities of these compounds are about an order of magnitude less in ferrite than the corresponding solubilities in austenite at the same temperature. The solubility of vanadium carbide in ferrite, as determined experimentally, is approximately one order of magnitude less than that in austenite, in agreement with the thermodynamic calculations.

The individual solubilities of the microalloyed carbides and nitrides offer clear directions for the selection of specific microalloying additions for specific purposes. For example, the use of vanadium in normalised steels, or in high carbon steels, is a direct consequence of the high solubility of vanadium carbide. The use of titanium as the preferred grain refining agent at high temperatures in the austenite range is a direct consequence of the high stability of titanium nitride in austenite. The practical applications of selected microalloying elements will be considered in a later chapter, but because more than one element may be required to fulfil different requirements of the steel, and because all steels contain both carbon and nitrogen, it is necessary to consider the effects of the mutual presence of both interstitials and the reactions that occur when more than one microalloying elements is added to the steel.

3.3 MUTUALLY EXCLUSIVE COMPOUNDS

Aluminium treated steels have been in use for a considerable period of time, but it is within the time span of microalloyed steels, i.e. since 1957, that the mechanism by which the aluminium produced the grain refinement has been elucidated. Aluminium additions are commonly used to produce clean steels. Aluminium is a very strong oxide former, resulting in the formation of skeletal alumina crystals, which, when lost from the steel by flotation or by reaction with slag or refractory containment material, results in extremely clean steels. More recently, vacuum methods have been adopted as a part of the secondary steel-making process for many bulk steels, but aluminium is still used in the lower carbon steels to ensure complete deoxidation.

The addition of vanadium to low-carbon steels, to produce enhanced strength levels in the normalised condition, is practised for both aluminium-treated and non-aluminium-treated steels. Nitrogen will react with both aluminium and vanadium to produce nitrides, and it is of interest to consider the extent of nitride formation and also the nature of the nitride.

So far, little has been said of the structure of the nitrides. Most of the microalloy carbides and nitrides have a face-centred cubic structure, and could be expected to show extensive mutual solubility with each other. However, aluminium nitride has a hexagonal structure, and all experimental observations show that, in steels containing alumimium and a microalloying additive, there are two distinct types of precipitate, i.e. the hexagonal aluminium nitride, and a face centred cubic carbide or nitride. These are the mutually exclusive compounds. The quantitative aspects of such systems will be described using aluminium–vanadium steels by way of example.

3.3.1 The Solubility Products

As described in Section 3.2, the solubility products for aluminium nitride and vanadium nitride are defined as

$$[Al] + [N] \leftrightarrow (AlN) \quad \text{hexagonal}$$
$$k_A = [Al][N] \tag{3.21}$$
$$[V] + [N] \leftrightarrow (VN) \quad \text{f.c.c.}$$
$$k_V = [V][N] \tag{3.22}$$

Aluminium nitride will be formed when the product of the dissolved aluminium and nitrogen contents exceed k_A at any given temperature, and vanadium nitride will be formed when the product of the dissolved vanadium and nitrogen contents exceed k_V, at any given temperature. From the data given in Section 3.2, and illustrated in Fig. 3.18, it is clear that the solubility product for aluminium nitride, k_A, is much lower than that for vanadium nitride, k_V, and that for any steel having sufficient vanadium and nitrogen in solution, there would be sufficient nitrogen to form aluminium nitride, provided that the alumimium dissolved in the steel gave a product in excess of k_A. The converse argument would also apply. The formation of a second nitride phase, however, might change the dissolved nitrogen to preclude the formation of any other nitride. For example, given that the product of the total nitrogen and vanadium contents just exceeded k_V, the addition of sufficient aluminium to cause substantial precipitation of alumimium nitride could so reduce the dissolved nitrogen level that its product with the total vanadium would no longer exceed k_V, and vanadium nitride would not be stable. It is also clear, however, that the co-existence of two mutually exclusive nitrides could be arranged by selection of vanadium, aluminium, and nitrogen contents. The co-existence of the two nitrides would obviously have to satisfy both Equations (3.21) and (3.22). It should be noted that the activities of aluminium nitride and vanadium nitride both remain at unity because they are present as quite separate nitrides with no mutual solubility.

The solution for this simultaneity can be obtained as follows. The total nitrogen content, N_T, in the steel is the sum of the dissolved nitrogen, [N], the nitrogen

present as aluminium nitride, N_{AlN}, and the nitrogen present as vanadium nitride, N_{VN}, i.e.

$$N_T = [N] + N_{AlN} + N_{VN} \tag{3.23}$$

The wt% nitrogen as aluminium nitride is equal to the wt% aluminium as aluminium nitride, Al_{AlN}, multiplied by the ratio of their relative atomic masses, so that

$$N_{AlN} = 14 \cdot Al_{AlN}/27 \tag{3.24}$$

and

$$N_{VN} = 14 \cdot V_{VN}/51 \tag{3.25}$$

Substitution of these values in Equation (3.23) gives

$$N_T = [N] + 14 \cdot Al_{AlN}/27 + 14V_{VN}/51 \tag{3.26}$$

The aluminium present as aluminium nitride can be substituted by the difference between the total aluminium content Al_T, and the dissolved aluminium content $[Al]$. Similarly, the vanadium present as vanadium nitride, V_{VN}, can be substituted by the difference between the total vanadium content V_T and the dissolved vanadium, $[V]$, to give

$$N_T = [N] + 14(Al_T - [Al])/27 + 14(V_T - [V])/51 \tag{3.27}$$

Given that there are two nitrides present each complying with their individual solubility products as indicated by Equations (3.21) and (3.22), then the simultaneous compliance enables substitution for $[Al]$ and $[V]$ in Equation (3.27) to give

$$N_T = [N] + 14(Al_T - k_A/[N])/27 + 14(V_T - k_V/[N])/51 \tag{3.28}$$

Multiplying both sides of Equation (3.28) by $[N]$ and collecting like terms in $[N]$ gives

$$[N]^2 + (14Al_T/27 + 14V_T/51 - N_T)[N] - (14k_A/27 + 14k_V/51) = 0 \tag{3.29}$$

This equation is a quadratic in $[N]$ and can readily be solved; all other terms involved represent the steel composition, N_T, V_T and Al_T, and the solubility products, k_A and k_V, the latter incorporate the effects of temperature. The equation is valid for all situations where there are both types of nitride present. There are no realistic solutions to be found from Equation (3.29) under conditions where there is only one precipitate. The absence of a realistic solution is indicated by using Equations (3.21) and (3.22) to calculate the dissolved aluminium and vanadium contents. If either the dissolved aluminium content or the dissolved vanadium content exceed their respective total contents in the steel, the solution must be discarded, as there will be an apparent negative quantity of that particular nitride. If, for example, the dissolved vanadium exceeds the total vanadium content, the amount of aluminium nitride can be evaluated from the single nitride method described in Section 3.2.2.

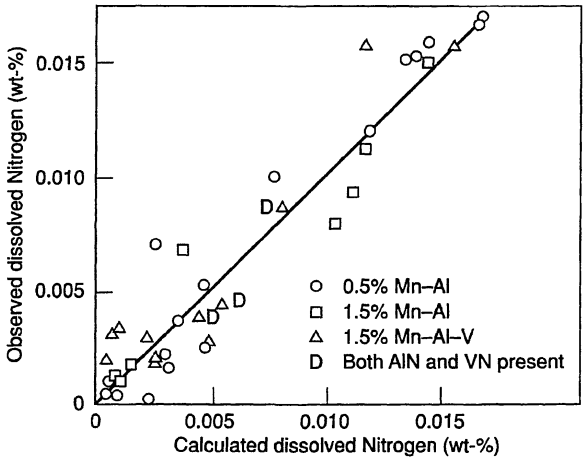


Fig. 3.19 Calculated and experimental levels of free nitrogen in Al–V–N steels. The calculations were carried out using Equation (3.29).

The use of Equation (3.29), coupled with Equations (3.21) and (3.22), is obviously simplistic, in that the activity coefficients are assumed to be unity, and the various solutes are assumed to have negligible interaction coefficients. However, reasonable results have been obtained from Equation (3.29), and the correspondence between the calculated soluble nitrogen contents and experimental values for a 0.02% Al–0.15% V–0.015% N steel were at least as good as those obtained for a simple aluminium–nitrogen steel[23] (Fig. 3.19).

3.3.2 Phase Boundaries

Using the solubility equations and mass balance equations, the amounts of aluminium and vanadium nitrides can be calculated from the dissolved contents indicated above, but it is also possible to calculate the phase boundaries of the γ, $\gamma + VN$, $\gamma + AlN$, and $\gamma + AlN + VN$ regions of the quaternary Fe–Al–V–N system and to establish *a priori*, the range of compositions over which the two nitrides will co-exist. From Equations (3.21) and (3.22), and given that the nitrogen in solution is mutually in equilibrium with both nitrides, then

$$[Al]/[V] = k_A/k_V \tag{3.30}$$

Substituting for $[V]$ from Equation (3.30), and for $[N]$ from Equation (3.21) into Equation (3.27) gives

$$N_T = k_A/[Al] + 14(Al_T - [Al]/27 + 14(V_T - k_V[Al]/k_A)/51 \tag{3.31}$$

Expanding and collecting like terms in $[Al]$, gives

$$(14/27 + 14k_V/51k_A)[Al]^2 - 14Al_T/27 + 14V_T/51 - N_T)[Al] - k_A = 0 \tag{3.32}$$

This is clearly a quadratic equation and can be solved for the dissolved aluminium content, but, by considering the case where the dissolved aluminium

content becomes equal to the total aluminium content, under the conditions of simultaneity implied by Equation (3.27), then putting $[Al] = Al_T = Al_x$, gives

$$(14k_V/51k_A)Al^2 - (14V_T/51 - N_T)Al_x - k_A = 0 \qquad (3.33)$$

where Al_x is the limiting aluminium content that can be added to a steel in which vanadium nitride is present without forming aluminium nitride, i.e. Al_x describes the locus of the boundary between the (γ + VN) and the (γ + VN + AlN) regions of the quaternary system for given values of vanadium and nitrogen contents, and, through the solubility products, for any given temperature. A similar procedure can be followed from Equation (3.27), by substituting Equations (3.22) and (3.30), to give the locus of V_x. V_x is the limiting vanadium content that can be added to a steel in which aluminium nitride is present without forming *VN* and thus describes the phase boundary between the (γ + AlN) and the γ + (VN + AlN) region.

The phase boundaries calculated from solubility data[4,9] at 900°C are shown in Fig. 3.20. The phase boundaries between the γ and (γ + AlN), and the γ and (γ + VN) regions, are also shown, as defined by the solubility products for aluminium nitride and vanadium nitride respectively. The effects of vanadium content on the aluminium required to enter the three phase region and of aluminium content on the vanadium required, are clearly shown, and are not linear as can be appreciated from the forms of Equations (3.31) and (3.32). Also shown in Fig. 3.20 is the effect of the nitrogen content. Reducing the nitrogen content of the steel clearly expands the γ range with respect to the aluminium and vanadium contents that can be

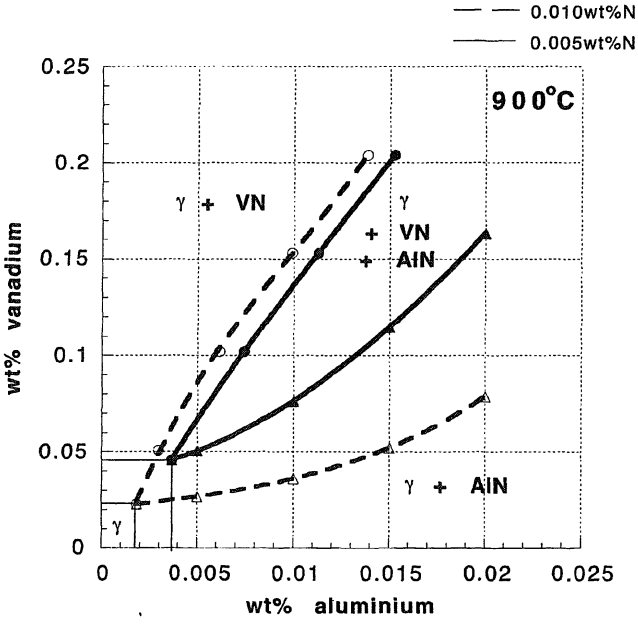


Fig. 3.20 Calculated limit of the γ + AlN + VN phase field at 900°C. The limits are shown for two different levels of nitrogen.

dissolved without precipitation, and the boundaries of the three phase region move to higher solute contents relative to their respective nitrides. An increase in the austenitising temperature would give a qualitatively similar effect to that of reducing the nitrogen content but the relative movements of the boundaries would depend on the temperature dependencies of the solubility products.

The method illustrated for the hexagonal aluminium nitride and the cubic vanadium nitride should also work for other systems with immiscible nitrides (or carbides), such as might be found in Al–Ti steels or Al–Nb steels. However, there are other factors which may influence the presence or absence of these nitrides. Both niobium and titanium carbides are much more stable than is vanadium carbide. Under these circumstances, complex carbo-nitrides may be formed which would perturb the model of two immiscible nitrides. Also, the model of two immiscible nitrides provides information on the equilibrium or near equilibrium state. As will be shown in a later chapter, the kinetics of precipitation may influence the nitrides present within commercial heat treatment times. Reference to Fig. 3.20 shows that the solubility of vanadium can be far more extensive in a steel where aluminium nitride is the equilibrium precipitate. Consider a 0.02%Al–0.15%V steel treated at a high temperature to dissolve all nitride. Precipitation at 900°C should give only aluminium nitride, but, because of the high level of vanadium and the attendant shorter diffusion path, vanadium nitride is favoured from a kinetic standpoint, and has been observed to form extensively as a metastable phase, only to be replaced by aluminium nitride with protracted exposure at 900°C.

3.4 CARBO-NITRIDES WITH EXTENDED MUTUAL SOLUBILITY

The microalloying elements Ti, V and Nb all react with both carbon and nitrogen to give carbides and nitrides respectively, the individual solubilities having been described in Section 3.2 of this chapter. However, the carbides and nitrides show extensive mutual solubilities, and the resulting solid solution is described as a carbo-nitride. The extensive mutual solubilities undoubtedly arise from the fact that they have the same cubic crystal structure and have very similar lattice parameters. There is some uncertainty in the case of niobium nitride for which Narita[12] has suggested a hexagonal type lattice with lattice parameters of $a_0 = 0.2960$–0.2968nm and $c_0 = 1.125$–1.128 nm, but Pearson[24] has indicated a cubic lattice for niobium nitride with complete miscibility between the carbide and nitride. There is ample experimental evidence that niobium carbo-nitride has a cubic crystal structure, with lattice parameters ranging from that of the carbide to that of the nitride, depending upon the carbon/nitrogen ratio.

The lattice parameters in nm of the f.c.c. carbides and nitrides[12] are as follows:

	Nitride	Carbide
Titanium	0.4230/0.4236	0.4312/0.4315
Vanadium	0.4106/0.4130	0.4149/0.4158
Niobium	0.4382/0.4392	0.4455/0.4468

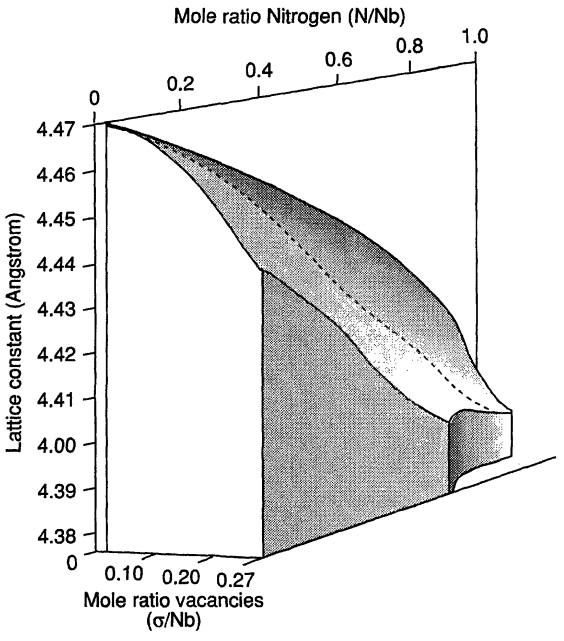


Fig. 3.21 Variations in the lattice parameter of niobium carbo-nitride showing the effects of the carbon, nitrogen, and vacancy concentrations. After Storms and Krikorian.[25]

The parameters for each carbo-nitride are claimed to vary systematically with the carbo/nitrogen ratio, and the miscibility between the different carbo-nitrides also leads to lattice parameters intermediate between those of the individual carbo-nitrides. Storms and Krikorian[25] have presented a comprehensive view of the variation in lattice parameter for niobium carbo-nitrides with variations in the carbon/nitrogen ratio and with variations in the vacancy concentration in the interstitial sites, Fig. 3.21, which suggests that a linear interpretation may be too simplistic.

Nordberg and Aronsson[21] considered the solubility of mixed carbo-nitrides of composition $NbC_x\ N_{(1-x)}$, and assumed that the standard free energy varied linearly from that of NbC to that of NbN. The configurational entropy of mixing was also taken in consideration, and the solubility of the carbo-nitride was then expressed as

$$\log k_{NbCN} = x \log k_{NbC} + (1-x) \log k_{NbN} + (x \ln x + (1-x) \ln(1-x))/R \qquad (3.34)$$

where R is the Gas Constant.

Although this equation shows broad agreement with the published solubility data given in Section 3.2.2 for steels containing both carbon and nitrogen, the solubility of the carbo-nitride is expressed as having a constant carbon/nitrogen ratio at different temperatures.

In a more detailed examination, Hudd *et al.*[14] considered the separate solubility products as defined in Equation (3.2)

$$k_1 = a_{[Nb]} \cdot a_{[C]}/a_{(NbC)} \tag{3.35}$$

$$k_2 = a_{[Nb]} \cdot a_{[N]}/a_{(NbN)} \tag{3.36}$$

where k_1 and k_2 are the equilibrium constants for the carbide and the nitride respectively.

The difference between the treatment of mutually exclusive precipitates (see Section 3.3) and that relating to extended mutual solubility, is that the activity of the NbC, $a_{(NbC)}$, in the carbo-nitride is not unity, and neither is the activity of the NbN, $a_{(NbN)}$, in the carbo-nitride. If the solid solution of NbN in NbC is considered to be ideal, then the activities of carbide and nitride can be represented by their respective fractions in the carbo-nitride, i.e. x and $(1 - x)$. Assuming, as before, that the activity coefficients of niobium, carbon, and nitrogen dissolved in the austenite are unity, the solubility products for NbC and NbN can be written as -

$$k_1 = [Nb][C]/x \tag{3.37}$$

$$k_2 = [Nb][N]/(1-x) \tag{3.38}$$

Raising Equation (3.37) to the power x and Equation (3.38) to the power $(1-x)$, and multiplying the resultant equations gives

$$k_1^x k_2^{(1-x)} = [Nb]^x[C]^x[Nb]^{(1-x)}[N]^{(1-x)}/x^x(1-x)^{(1-x)} \tag{3.39}$$

$$\text{or} \quad k = [Nb][C]^x[N]^{(1-x)} = k_1^x k_2^{(1-x)} x^x (1-x)^{(1-x)}$$

where k is the solubility product of the carbo-nitride.

In logarithmic form, this gives

$$\log k = \log([Nb][C]^x[N])^{(1-x)} = x\log k_1 + (1-x)\log k_2 + x\log x + (1-x)\log(1-x) \tag{3.40}$$

Note that this is the correct form of Equation (3.34) given by Nordberg and Aronsson.[21]

Using the mass balance equations and stoichiometric ratios,

$$Nb_T = [Nb] + Nb_{NbCN}$$

$$Nb_{NbC} = xNb_{NbCN}$$

$$Nb_{NbN} = (l-x) \cdot Nb_{NbCN}$$

$$C_T = [C] + C_{NbCN}$$

$$N_T = [N] + N_{NbCN}$$

$$C_{NbC} = 12 \cdot Nb_{NbC}/93$$

$$N_{NbN} = 14 \cdot Nb_{NbN}/93$$

where 12, 14, and 93 are the relative atomic masses of carbon, nitrogen and niobium respectively, equations (3.37) and (3.38) can be expressed in the form

$$xk_1 = [Nb](C_T - x(Nb_T - [Nb])12/93) \tag{3.37a}$$

and $$(1-x)k_2 = [Nb](N_T - (l-x)(Nb_T - [Nb])14/93) \tag{3.38a}$$

Expanding these equations, and collecting like terms in x, allows Equation (3.38a) to be divided by Equation (3.37a) to eliminate x. Collecting the terms in powers of $[Nb]$ gives[14]

$$\begin{aligned}
&-(12\times 14)[Nb]^4\\
&+(2Nb_T\times 12x14 - C_T\times 14\times 93 - N_T\times 12\times 93)[Nb]^3\\
&+(12\times 93\times k_2 + N_TNb_T\times 12\times 93 - Nb_T^2\times 12\times 14 + 93\times 14xk\\
&+C_TNb_T\times 14\times 93)[Nb]^2\\
&+(N_Tk_1\times 93\times 93 - Nb_T\cdot k_2\times 93\times 12 - Nb_Tk_1\times 93\times 14 + C_Tk_2\times 93\times 93)[Nb]\\
&-(k_1k_2\times 93\times 93) = 0
\end{aligned} \tag{3.41}$$

Equation (3.41) is a fourth power equation in $[Nb]$ which can be solved numerically by inserting possible meaningful values for $[Nb]$ lying between 0 and Nb_T, and selecting the appropriate $[Nb]$ level showing conformity with this equation. Consider a steel containing 0.1%C–0.005wt%N–0.03wt%Nb at 950°C. The values for the solubility products of niobium carbide and niobium nitride, at this temperature, are 0.000913 and 0.000071 respectively. Inserting these in Equation (3.41) and substituting values of $[Nb]$ in the range 0.001 to 0.029 gives a solution y, to the L.H.S. of Equation (3.41). The correct solution for $[Nb]$ is obviously that for which $y = 0$ as shown in Fig. 3.22. It should be noted that the computational stability is improved by scaling the variables in the equation. In the example shown, the carbon, nitrogen, and niobium contents were multiplied by 10^2 and, accordingly, the solubility products ($k_1 = [Nb][C]$) have to be scaled by 10^4. The solution then attained from Fig. 3.22 is divided by 100 to give a dissolved niobium content of 0.006wt% at 950°C. At a higher temperature, and substituting the appropriate values of k_1 and k_2, the dissolved niobium increases.

Hudd *et al.*,[14] compared the results calculated from Equation (3.41) with published experimental values[15,26–29] and showed that

(i) The calculated wt%Nb present as niobium carbo-nitride was in excellent agreement with the experimental values at temperatures in the austenite range.

(ii) There was general agreement between the dependency of the carbon and nitrogen contents of the carbo-nitride upon the carbon and nitrogen contents of the alloys, but the temperature dependency of the carbo-nitride composition predicted by Equation (3.41) was less consistent in some alloys than in others, whereas the experimental work suggested a systematic decrease in the carbon fraction (x) with increasing temperature in the austenite range.

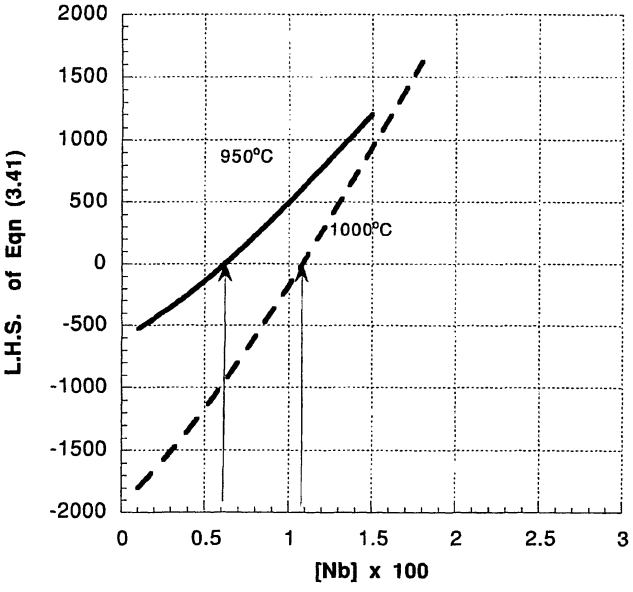


Fig. 3.22 Solving Equation (3.41). A steel containing 0.1wt%C – 0.005wt%N – 0.03wt%Nb is equilibrated at 950°C. The equilibrium dissolved niobium content is found when the left-hand side of Equation (3.41) (y) is equal to the right hand side (=0). The variables are scaled to ease calculation. The appropriate dissolved niobium content is 0.006wt%.

Hudd *et al.*[14] suggested that discrepancies in the temperature dependence of the carbide fraction in the carbo-nitride, x, may well derive from errors in the solubility products. Bearing in mind the variations in estimates of the solubility products by different workers, (Figs. 3.7 and 3.14), which also exhibit significantly different temperature dependencies of the solubility product, the comparison of calculated and experimental results for x has been repeated using the solubility equations of Narita[12] for both niobium carbide and niobium nitride. These equations have the advantage of not being based on materials having both carbon and nitrogen present, and of having NbC and NbN as the basic compounds upon which the solubility products were based, rather than for example NbCN. These equations are

$$\log k_1 \text{ (for niobium carbide)} = -7900/T + 3.42 \quad (3.42)$$

$$\log k_2 \text{ (for niobium nitride)} = -8500/T + 2.80 \quad (3.43)$$

The calculated values of niobium in solution, and as carbo-nitride, are shown in

Table 3.13 Effects of steel chemistry and temperature on the dissolution of niobium carbide and on the carbide fraction of the carbo-nitride

Steel composition (Wt%)			Tempera-			
C	N	Nb	ture (°C)	[Nb] (wt%)	Nb_{NbCN} (wt%)	x
0.10	0.005	0.03	950	0.0062	0.0238	0.665
0.10	0.010	0.03	950	0.0046	0.0154	0.496
0.10	0.005	0.08	950	0.0074	0.726	0.753
0.10	0.010	0.08	950	0.0056	0.0744	0.579
0.80	0.005	0.03	950	0.0011	0.0289	0.960
0.80	0.010	0.03	950	0.0010	0.0290	0.916
0.10	0.005	0.03	1100	0.030	0	–
0.10	0.010	0.03	1100	0.0225	0.0075	0.483
0.10	0.005	0.08	1100	0.080	0	–
0.10	0.010	0.08	1100	0.0272	0.0528	0.564
0.80	0.005	0.03	1100	0.0055	0.0245	0.945
0.80	0.010	0.03	1100	0.0052	0.0248	0.893
0.80	0.005	0.03	1200	0.0134	0.0166	0.938
0.80	0.010	0.03	1200	0.0126	0.0174	0.882

Table 3.13, together with the selected steel chemistries. The fraction of carbide in the carbo-nitride, x, can be derived from the mass balance for carbon, i.e.

$$C_T = [C] + C_{NbCN} \tag{3.44}$$

where
$$[C] = xk_1/[Nb] \tag{3.37}$$

and
$$C_{NbCN} = xNb_{NbCN} \cdot 12/93 \quad \text{(stoichiometry)}$$

Thus
$$C_T = xk_1/[Nb] + xNb_{NbCN}(12/93)$$

hence
$$x = C_T/(k_1/[Nb] + 12Nb_{NbCN}/93) \tag{3.45}$$

The values of x are also shown in Table 3.13.

The fraction of carbide in the carbo-nitride, x, clearly changes with changes in the niobium, carbon and nitrogen contents, and also with the austenitising temperature. The decrease in x values with increasing austenitising temperature is, however, fairly modest, as was predicted by Hudd *et al.*,[14] whereas the changes observed experimentally are generally larger, although it should be pointed out that in both the predictions of Hudd, and the experimental work of Mori *et al.*,[28] the effect of austenitising temperature varied in magnitude depending upon the compositional variation in the steel. It is clear that an increase in the carbon to nitrogen ratio in the steel will increase the carbon fraction of the carbo-nitride, but the changes with austenitising temperature are less certain in both magnitude and direction.[14] Nevertheless, Equations (3.41) and (3.45) can be regarded as substantively correct for the prediction of the dissolved niobium (and hence the niobium present as NbCN) and the carbide fraction of the carbo-nitride (and hence the dissolved carbon and nitrogen contents).

The main measures of interest in microalloyed steels are the volume fraction of undissolved carbo-nitride, which is pertinent to the control of austenite grain size, and the amount of niobium that is in solution, which is pertinent to the development of fine interphase or other precipitation process on cooling to lower

temperatures. These measures are shown in Table 3.13 and the following observations can be made.

(i) Increasing the austenitising temperature from 950°C to 1100°C dramatically increases the dissolved niobium content as is observed even in simple systems. There is an attendant decrease in the undissolved niobium content.
(ii) Increasing the nitrogen content of 0.1%C steels from 0.005wt% to 0.01wt%, decreases the dissolved nitrogen content, and increases the minimum temperature at which complete dissolution takes place.
(iii) Increasing the niobium content of these 0.1%C steels from 0.03wt% to 0.08wt% increases not only the amount of niobium present as carbo-nitride at temperatures below total dissolution, but also slightly increases the amount of dissolved niobium.
(iv) The large increase in carbon content portrayed in Table 3.13, causes a substantial decrease in the dissolved niobium content and an increase in the amount of undissolved carbo-nitride. The carbide fraction of the carbo-nitride is greatly increased into the range 0.88 to 0.96.

All of these changes are exactly those that would be predicted from a knowledge of the individual solubility products for the simple precipitate types. What is far less clear from Table 3.13 is the extent of precipitation as compared with that of the individual carbides and nitrides. The separate solubilities of niobium carbide and of niobium nitride in a 0.1%C – 0.03%Nb and a 0.01%N – 0.03%Nb steel are shown as a function of temperature in Fig. 3.23. At a low temperature in the austenite range, e.g. 950°C, approximately 0.02wt%Nb would be present as NbC in the C–Nb alloy and a similar amount of niobium would be present as NbN in the N–Nb alloy. Such amounts could not be present in a 0.10%C – 0.01%N – 0.03%Nb steel as there is insufficient niobium to satisfy both, and also, as pointed out in Section 3.3, the formation of any niobium nitride would deplete the matrix in niobium and would reduce the extent of niobium carbide formation. Similarly, any niobium carbide precipitation would reduce the extent of niobium nitride precipitation for the same reason. If the simultaneous formation of niobium carbide and niobium nitride is considered, using the appropriate form of Equation (3.29), i.e.

$$[Nb]^2 + (93C_T/12 + 93N_T/14 - Nb_T)[Nb] - (93k_1/12 + 93k_2/14) = 0$$

then the individual values of niobium as niobium carbide and niobium as niobium nitride *when both are present* can be obtained from the dissolved niobium content through the use of the solubility products as described in Section 3.3, and can be compared with the values for the carbo-nitride given in Table 3.13. These values are compared in Table 3.14. The origins of the differences are clearly seen. For the mutually exclusive precipitates, the product of $[C]$ and $[Nb]$ is k_1, the solubility product for niobium carbide, and the product of $[N]$ and $[Nb]$ is k_2, the solubility product for niobium nitride. For the mutually soluble carbo-nitride, the product of $[C]$ and $[Nb]$ is xk_1 (x being the fraction of carbide in the carbo-nitride, which is assumed to be the carbide activity) and the product of $[N]$ and $[Nb]$ is $(1-x)k_2$. The

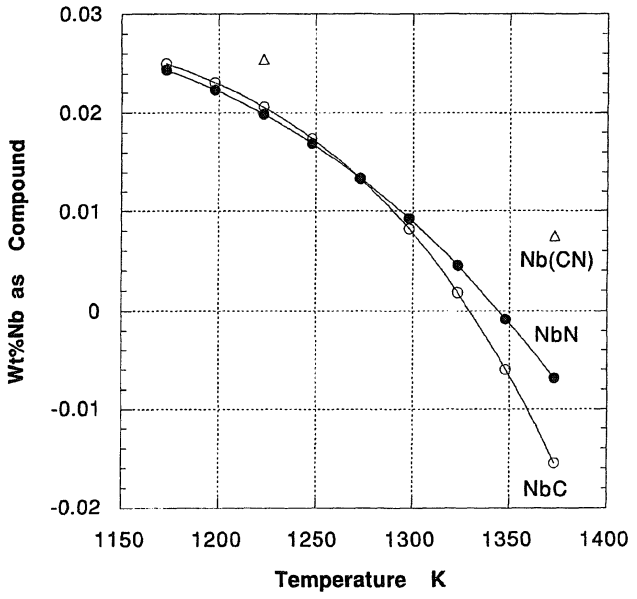


Fig. 3.23 Dissolution of niobium carbo-nitride in a 0.1wt%C–0.01wt%N–0.03wt%Nb steel. The values are compared with those obtained for formation of the carbide in a 0.1wt%C–0.03wt%Nb steel and nitride in a 0.01wt%N–0.03wt%Nb steel. The increased stability of the carbo- nitride is clear. The carbo-nitride can exist at temperatures where either the carbide in the Fe–C–Nb alloy or the nitride in the Fe–N–Nb alloy, are completely dissolved.

significance of this comparison, is that the dissolved carbon, nitrogen and niobium values, when the carbides and nitrides are mutually soluble, are those that might be expected from a reduction in the solubility product, i.e. $k_1 \rightarrow xk_1$, and $k_2 \rightarrow (1-x)k_2$. This leads to the corresponding observation at higher temperatures (1100°C) in Fig. 3.23, where it can be seen that there is a significant fraction of niobium carbo-nitride at a temperature where both the niobium carbide and the niobium nitride, if precipitated separately, would be completely dissolved. This is a natural

Table 3.14 Comparison of the dissolution of niobium carbo-nitride with the dissolution that would be expected if the carbide and nitride were mutually exclusive, in a 0.1wt%C–0.01wt%N–0.03wt%Nb steel

	Mutually exclusive, NbC + NbN	**Mutually soluble, Nb(C_x N_{1-x})**
Nb as NbC (wt%)	0.0059	0.0126*
Nb as NbN (wt%)	0.0151	0.0128*
[*Nb*] (wt%)	0.0090	0.0046
[*C*] (wt%)	0.0078	0.0081
[*N*] (wt%)	0.0078	0.0081

* Obtained from Nb as Nb(C_xN_{1-x}) in Table 3.13.

consequence of the dependence of the solubility product of Nb (C_xN_{1-x}) on the carbide fraction, x. As pointed out by Hudd *et al.*[14] the solubility product of the carbo-nitride k is given by Equation (3.40) as

$$\log k = x \log k_1 + (1-x) \log k_2 + x \log x + (1-x) \log(1-x)$$

The effect of variations in x on the solubility product of niobium carbo-nitride is shown in Fig. 3.24. The solubility product shows a minimum at a value of x in the range 0.05 – 0.1. In steels which have a total carbon and niobium product less than the solubility product of pure niobium carbide, the carbo-nitride will form when sufficient nitrogen is added, even though the nitrogen addition may be less than that required to form niobium nitride in an Fe–Nb–N alloy.

The main conclusions from the thermodynamics, therefore, is that the formation of the carbo-nitride increases the volume fraction of precipitate at a given temperature (compared with the mutually exclusive model) and increases the temperature required for total dissolution of the precipitate.

The 0.1wt%C–0.01wt%N–0.03wt%Nb steel so far considered is very much a sub-stoichiometric alloy, and the niobium level is sub-stoichiometric even with respect to the nitrogen level. A similar steel with 0.08wt%Nb, which is still sub-stoichiometric overall with respect to the carbon and nitrogen level, but is super-stoichiometric with respect to the nitrogen level, confirms the increased carbo-nitride precipitate stability, Fig. 3.25. A comparison between the mutually exclusive and mutually soluble precipitates for the 0.08% Nb steel is shown in Table 3.15. In addition to showing the enhanced stability of the precipitate

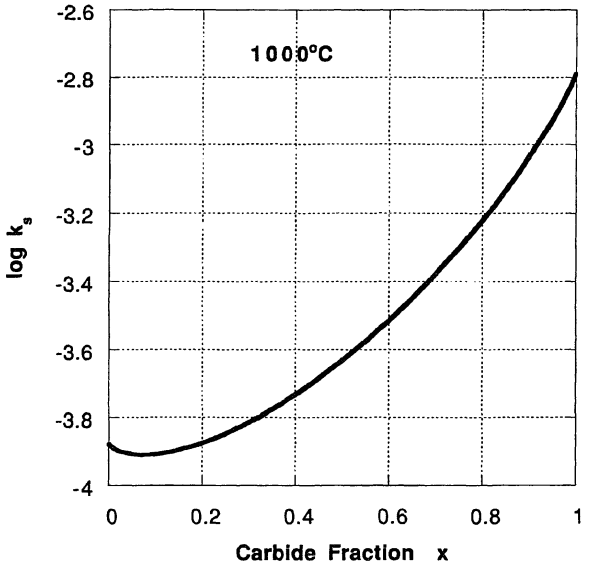


Fig. 3.24 The effect of the carbide fraction in niobium carbo-nitride on the effective solubility product at 1000°C. The effective solubility product for the carbo-nitride passes through a minimum at a carbide fraction of about $x = 0.07$.

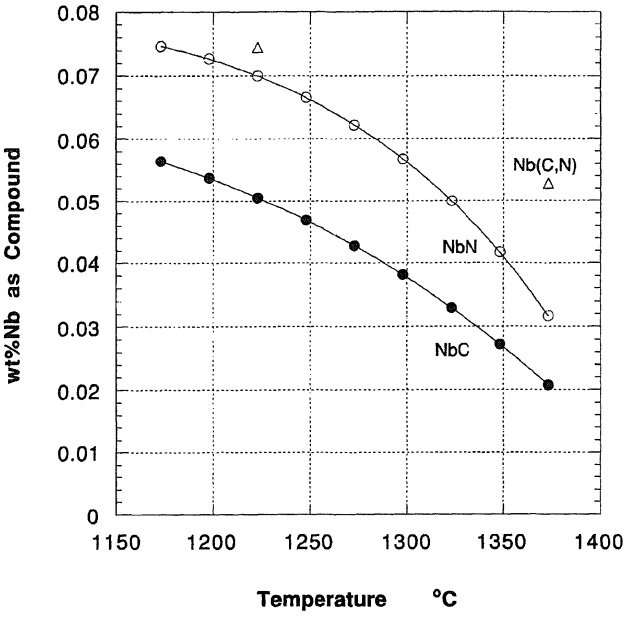


Fig. 3.25 Dissolution of niobium carbo-nitride in a 0.1wt%C–0.01wt%N–0.08wt%Nb steel. The values are compared with those expected for NbC in an Fe–C–Nb alloy and for NbN in an Fe–N–Nb alloy.

compared with the mutually exclusive model, the 0.08% Nb steel shows a different balance in the carbo-nitride constituent, compared with the 0.03% Nb steel, resulting in a significant lowering of the dissolved nitrogen content. This effect undoubtedly results from the increased carbide fraction which, by lowering the activity of the nitride, $(1-x)$ to give an apparent solubility product of $(1-x)\ k_2$, gives a much lower soluble nitrogen content than would be expected from the slight increase in dissolved niobium.

The greater thermodynamic stability of the niobium nitride in austenite, relative to that of niobium carbide, is reflected by an increased nitrogen-carbon ratio in the carbo-nitride compared with the bulk carbon to nitrogen ratio in the alloy. This is a

Table 3.15 Comparison of the dissolution of niobium carbo-nitride with that to be expected for mutually exclusive carbide and nitride phases in a 0.1wt%C–0.01wt%N–0.08wt%Nb steel

	Mutually exclusive, NbC + NbN	**Mutually soluble, $Nb(C_xN_{1-x})$**
Nb as NbC	0.0520	0.0431*
Nb as NbN	0.0182	0.0313*
[*Nb*]	0.0098	0.0056
[*C*]	0.0933	0.0944
[*N*]	0.0073	0.0047

* Obtained from Nb as $Nb(C_xN_{1-x})$ in Table 3.13.

feature of both the experimental results and the predictions of the Hudd *et al.*[14] thermodynamic model.

As an example of the usefulness of Equations (3.41) and (3.45), the predictions of the wt% Nb as $NbC_xN_{(1-x)}$ and the carbide fractions, are compared with the experimental values given by Meyer,[26] Mandry and Dornelas[27] and Mori *et al.*[28] in Table 3.16. The wt% Nb in the form of carbo-nitride and the range of steel chemistries, i.e. different carbon, nitrogen and niobium contents, and equilibrium temperatures are indicated. The comparison of the theoretical predictions and the experimental values is shown in Fig. 3.26. The agreement between the two is excellent, particularly when bearing in mind the wide range of compositional variables and different temperatures. As pointed out earlier, the undissolved niobium carbo-nitride in the austenite temperature range is important in controlling the austenite grain size, and a theoretical equation capable of giving such precision in predicting the extent of niobium carbo-nitride precipitation is of inestimable value. The predicted carbide fractions of carbo-nitrides show reasonable agreement with the experimentally determined fractions (Fig. 3.27), as was demonstrated by Hudd *et al.*[14] Given the greater thermodynamic stability of the nitrides, the enhanced nitrogen contents of the carbo-nitride relative to the matrix are entirely reasonable. The prediction of the dissolved niobium content in the matrix will naturally be predicted from differences between the total niobium content and the niobium present as carbo-nitride, and will be predicted with a precision defined by Fig. 3.26, provided that the dissolved niobium is substantial, thus providing information relevant to the development of dispersion strength-

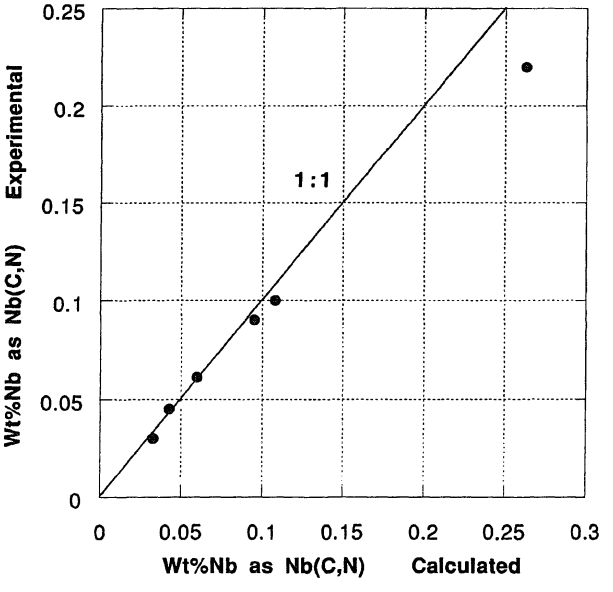


Fig. 3.26 Comparison of experimental determinations of undissolved niobium carbo-nitride with those predicted from the Hudd model for mutually soluble carbide and nitride phases. After Hudd *et al.*[14]

Table 3.16 Comparison of theoretical and experimental values of Wt%Nb as $Nb(C_xN_{1-x})$ and of the carbide fraction, x, of the carbo-nitride

Steel Composition			Temperature	[*Nb*]	wt%Nb as NbCN		x	
Wt%C	Wt%N	Wt%Nb	(°C)	(wt%)	Calc.	Exp.	Calc.	Exp.
0.22*	0.0050	0.035	900	0.0018	0.033	0.030	0.81	0.90
0.20*	0.0039	0.110	900	0.0021	0.108	0.100	0.82	–
0.036*	0.0073	0.038	900	0.0052	0.033	0.030	0.37	–
0.025*	0.0065	0.105	900	0.0100	0.095	0.090	0.41	0.65
0.025*	0.0065	0.105	1000	0.0270	0.078	–	0.35	0.61
0.180†	0.0036	0.0065	950	0.0046	0.060	0.061	0.87	0.83
0.180†	0.0036	0.065	1100	0.0225	0.043	0.045	0.85	0.83
0.074‡	0.0360	0.329	1200	0.0060	0.263	0.220	0.36	0.44
0.004‡	0.0170	0.094	1000	0.0200	0.074	–	0.04	0.05

* See reference 26. † See reference 27. ‡ See reference 28.

ened steels where interphase or other low temperature precipitation takes place. The importance of nitrogen partitioning, in addition to controlling the stability of the carbo-nitride, also controls the level of dissolved nitrogen content under conditions where the equilibrium or near-equilibrium carbo-nitrides are formed, as for example in normalising treatments. Changes in the stability and composition of the carbo-nitride naturally influence the nitrogen in solution in the austenite, and in the absence of subsequent precipitation treatments, result in effects on the nitrogen in solution in the ferrite, and the attendant effects on the mechanical

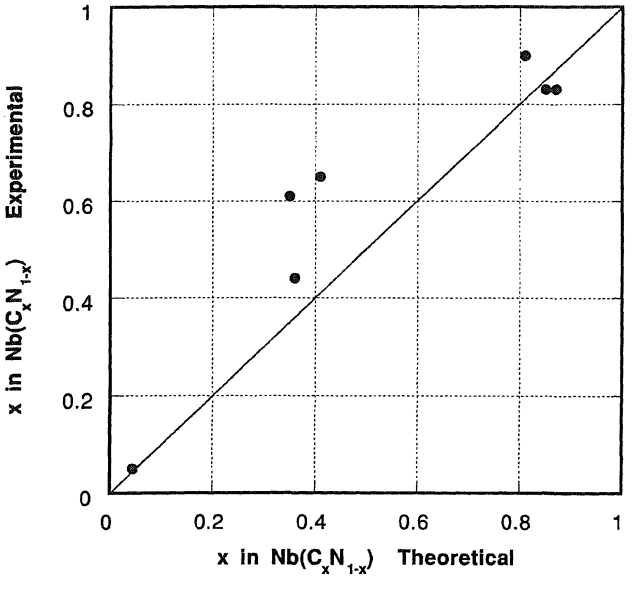


Fig. 3.27 Comparison of the experimental and theoretical carbide fractions in the niobium carbo-nitride of a range of niobium steels. After Hudd *et al.*[14]

properties, such as strength and toughness, and also on the response to strain ageing treatments.

An earlier approach by Irvine *et al.*[9] assumed that the carbon and nitrogen fractions were substantially the same in the carbo-nitride as in the bulk steel compositions, using only an atomic mass correction to balance the carbon and nitrogen contents, i.e.

$$K_s = [Nb][C + 12N/14]$$

where the term $12N/14$ represents the carbon equivalent of the nitrogen (wt%). This approximation, provided that it is used with the appropriate solubility relationship obtained by Irvine *et al.*,[9] gives reasonable results provided that the carbon content of the steel greatly exceeds the nitrogen content by a factor of some 10–20 times. In many of the older microalloyed steels with carbon contents of about 0.15wt%, and nitrogen contents of 0.005–0.010wt%, this approach would be reasonable, as pointed out by Nordberg and Aronsson,[21] but in many modern day microalloyed steels, where carbon contents may be much reduced, this approximation would undoubtedly lead to significant errors. With the advent of modern personal computers, such approximations are not necessary and the use of Equation (3.41) is recommended.

Attention has so far been given to the Fe–Nb–C–N system and the formation of niobium carbo-nitride. The carbides and nitrides of both vanadium and titanium also show stable cubic forms which are mutually soluble. The principal reason for concentrating on niobium is that the solubility products of niobium carbide and niobium nitride differ by only one order of magnitude, and, with the concentration of carbon in steel usually (though not invariably) exceeding the nitrogen content by about one order of magnitude ($\times 10^1$), the formation of carbo-nitrides with wide variations in the carbide and nitride fractions can be expected. The carbo-nitrides of titanium and of vanadium, however, may be expected to behave in a different manner from that of niobium as the solubility products for their respective carbide and nitride compounds differ significantly by about five orders of magnitude ($\times 10^5$) in the case of titanium carbide and titanium nitride. The solubility products of the carbides and nitrides of vanadium, niobium and titanium at selected temperatures are shown in Table. 3.17. The ratio of the solubility products of the carbides and nitrides of each of the microalloying elements show the nitride to be less soluble, but the magnitude of the differences vary significantly from element to element.

As indicated above, the niobium carbide has a solubility product which is consistently about one order of magnitude higher than that of niobium nitride over the whole of the practically important austenite temperature range. Vanadium carbide shows a solubility product which is some 200–300 times that of vanadium nitride at low temperatures in the austenite range increasing to 300–400 times at the higher temperatures. This difference in solubility products is even greater for titanium carbide and nitride, where the solubility product of the carbide is some 2.5×10^5 times that of the nitride at low temperatures in the austenite range, but reduces to about 2×10^4 times that of the nitride at the higher temperature.

Table 3.17 Values of the solubility products of vanadium, niobium and titanium, carbides and nitrides in austenite (after Narita[12])

Temperature (°C)	Vanadium		Niobium		Titanium	
	Carbide	Nitride	Carbide	Nitride	Carbide	Nitride
900	4.2×10^{-2}	1.6×10^{-4}	4.8×10^{-4}	3.6×10^{-5}	2.5×10^{-4}	1.0×10^{-9}
950	9.0×10^{-2}	3.3×10^{-4}	9.1×10^{-4}	7.1×10^{-5}	5.8×10^{-4}	3.5×10^{-9}
1000	1.8×10^{-1}	6.2×10^{-4}	1.6×10^{-3}	1.3×10^{-4}	1.3×10^{-3}	1.0×10^{-8}
1050	3.5×10^{-1}	1.1×10^{-3}	2.8×10^{-3}	2.4×10^{-4}	2.6×10^{-3}	2.9×10^{-8}
1100	6.3×10^{-1}	2.0×10^{-3}	4.6×10^{-3}	4.1×10^{-4}	5.0×10^{-3}	7.6×10^{-8}
1150	1.1	3.3×10^{-3}	7.4×10^{-3}	6.7×10^{-4}	9.3×10^{-3}	1.8×10^{-7}
1200	1.9	5.3×10^{-3}	1.1×10^{-2}	1.1×10^{-3}	1.7×10^{-2}	4.2×10^{-7}
1250	3.0	8.3×10^{-3}	1.7×10^{-2}	1.7×10^{-3}	2.8×10^{-2}	9.1×10^{-7}
1300	4.8	1.3×10^{-2}	2.5×10^{-2}	2.5×10^{-3}	4.7×10^{-2}	1.9×10^{-6}
1350	7.4	1.9×10^{-2}	3.6×10^{-2}	3.7×10^{-3}	7.5×10^{-2}	3.7×10^{-6}

Calculations of the vanadium as vanadium carbo-nitride at low temperatures in the austenite range, typical of the normalising temperatures used for vanadium microalloyed steels, and the carbide fraction of the carbo-nitride, are generally much lower for these steels than those observed in niobium steels for similar carbon and nitrogen levels (Table 3.18). Also shown in this table are calculations for the carbide fractions in the carbo-nitride of 0.015% titanium steels. In this case, with such huge differences in the solubility products, it is not surprising that the carbide fraction is negligibly small, and is of the order of 10^{-3}. The precipitate formed in these steels is thus substantially TiN, and the dissolution of TiN with increasing temperature would conform with a solubility product in excess of 0.999 k_s, i.e. it would behave as the pure nitride.

The stability of titanium nitride is well illustrated by the steel compositions chosen. Specifically, with a 0.005wt%N level, the selection of the titanium level is important. At 0.015wt%Ti, the titanium is sub-stoichiometric with respect to the

Table 3.18 Calculated titanium carbo-nitride and vanadium carbo-nitride contents at different temperatures and for the steel chemistries shown. The carbide fractions of the carbo-nitrides are also shown

(*a*) *Vanadium Carbo-nitride at 900°C*

C_T (wt%)	N_T (wt%)	V_T (wt%)	[*V*] (wt%)	V_N (wt%)	*x*	(1 − *x*)
0.05	0.010	0.15	0.113	0.037	0.13	0.87
0.15	0.010	0.15	0.100	0.050	0.35	0.65
0.15	0.015	0.15	0.081	0.069	0.28	0.72

(*b*) *Titanium carbo-nitride in 0.05(wt%)C – 0.005(wt%)N Steels*

Temperature (°C)	Ti_T (wt%)	[*Ti*] (wt%)	$Ti_{Ti(C,N)}$ (wt%)	*x*
1000	0.015	0.16×10^{-4}	0.014984	7×10^{-4}
1200	0.015	5.35×10^{-4}	0.014465	16×10^{-4}
950	0.030	0.0041	0.0259	0.34
1000	0.030	0.0064	0.0236	0.24
1200	0.030	0.0123	0.0177	0.04

nitrogen. Thus, the extremely low solubility of titanium nitride results in a minute level of titanium in solution because of the effect of the residual dissolved nitrogen content. This has the effect of reducing the extent of carbide precipitation to extremely low levels, as shown by the carbide fractions of the carbo-nitride of about 10^{-3}, i.e. only about one thousandth part of the carbo-nitride is carbide. However, if the titanium level is increased to, say, 0.03wt%, where it is super-stoichiometric with respect to the nitrogen content, then the formation of the extremely stable titanium nitride severely depletes the nitrogen in solution, thereby leaving a significant residual level of dissolved titanium that can effectively react with the carbon to give a significantly higher carbide fraction, as shown in Table 3.18, where values up to 0.34 are found at low temperatures in the austenite temperature range. It can also be seen from Table 3.18 that the carbide fraction of the carbo-nitride is low at higher temperatures in the austenite range even when the titanium content is super-stoichiometric. It can be appreciated, however, that the carbide fraction of the carbo-nitride at high temperatures in the austenite temperature range, when the titanium content exceeds the stoichiometric ratio with respect to the nitrogen content, will be very dependent upon the total carbon content and the 'excess' titanium level, and an increase in either of these variables will increase the carbide fraction of the precipitated carbo-nitride.

The main consequences of the formation of carbo-nitrides having complete mutual solubility of the carbide and nitride constituents can be stated as follows

(i) Differences between the solubility products of the carbide and nitride phases produce relative enrichment of the least soluble compound (nitrides) in the carbo-nitride.
(ii) The difference in solubility products of the carbide and the nitride increases, for the common microalloying additions, in the order niobium; vanadium; titanium.
(iii) The relative enrichment of the *nitride* fraction in the carbo-nitride increases in the reverse order, i.e. titanium; vanadium; niobium.
(iv) The carbide and nitride fractions are dependent upon the total carbon and nitrogen contents of the steel, and as the carbon content of most steels greatly exceeds the nitrogen content, the generally higher carbon levels tend to offset the differences in solubility product to a greater or lesser extent depending upon the difference in carbide and nitride solubilities.
(v) The fractions of carbide and nitride in the carbo-nitride are dependent upon the microalloy content. Higher microalloy levels tend to reduce the fraction of the most stable compound (nitride), and this is most noticeable when the microalloy content becomes super-stoichiometric with respect to the nitrogen level in the steel.
(vi) Increasing the temperature will generally increase the proportion of the more stable compound.
(vii) The amount of undissolved carbo-nitride is higher than would be expected from a mutually exclusive precipitation model, and, importantly, the carbo-nitride phase can exist at temperatures above the solvus temperatures of the individual carbides and nitrides.

3.5 COMPLEX CARBO-NITRIDES

The basic concepts developed in the preceding section depend on the mutual solubility of the carbide and nitride compounds of a particular microalloying element, which in turn depends on the fact that these compounds have the same crystallographic structure and have similar lattice parameters,as pointed out in Section 3.4. Because of the similarity in crystal structure and lattice parameter of all the carbides, nitrides and carbo-nitrides of each of the microalloying elements, vanadium, niobium and titanium, these compounds all appear to exhibit mutual solubility. The thermodynamic and mathematical treatments developed in Section 3.4 relate to steels with both carbon and nitrogen, but with a single microalloying addition. These treatments would be equally relevant to a steel containing a single interstitial element and two microalloying additions, e.g. an Fe–Ti–Nb–N alloy. However, when there are two interstitials and two microalloying additions, a complex carbo-nitride can be formed which is a solid solution of the carbide and nitride compounds of each of the microalloying elements present.

Such complex carbo-nitrides are defined in the following manner.

Consider a steel having Awt%Ti, Bwt%Nb, Cwt%C and Dwt%N. The two microalloying elements from carbides and nitrides according to the equations

$$[Ti] + [C] = (TiC); k_1 = [Ti][C]/a_{TiC}$$
$$[Nb] + [C] = (NbC); k_2 = [Nb][C]/a_{NbC}$$
$$[Ti] + [N] = (TiN); k_3 = [Ti][N]/a_{TiN}$$
$$[Nb] + [N] = (NbN); k_4 = [Nb][N]/a_{NbN}$$

where a_i represents the activity of the ith component. As before, the element in square brackets denotes the solute concentration in the matrix, and the components in round brackets denotes solutions in the complex carbo-nitride phase. Consider the formation of a complex carbide of titanium and niobium.

$$x[Ti] + (1 - x)[Nb] + C = Ti_xNb_{(1-x)}C$$

and for a complex nitride of titanium and niobium

$$y[Ti] + (1 - y)[Nb] + N = Ti_yNb_{(1-y)}N$$

where x and y are the titanium atom fractions of the microalloying elements in the carbide and nitride respectively. If the carbide and nitride then form the carbo-nitride

$$xz[Ti] + (1 - x)z[Nb] + z[C] + y(1 - z)[Ti] + (1 - y)(1 - z)[Nb] + (1 - z)[N] = (Ti_{xz+y(1-z)}Nb_{(1-x)z+(1-y)(1-z)}C_zN_{(1-z)})$$

where z is the carbon atom fraction of the interstitials in the carbo-nitride.

Based on the assumption of ideal solutions in the complex carbide and the complex nitride, and that the mixing of these gives an ideal solution which does

not perturb the balance in the carbide and nitride, the activities of the various components can be written as

$$a_{TiC} = xz \tag{3.46a}$$
$$a_{NbC} = (1-x)z \tag{3.46b}$$
$$a_{TiN} = y(1-z) \tag{3.46c}$$
$$a_{NbN} = (1-y)(1-z) \tag{3.46d}$$

Again, substituting the above information into the mass balances and the solubility product equations will provide a series of equations capable of yielding a complete description of the matrix and the complex carbo-nitride, as follows.

Let the wt% nitrogen in the matrix be $[N]$.
Thus, the wt% nitrogen in the carbo-nitride is $D-[N]$
and the wt% carbon in the carbo-nitride is $(D-\ [N]\ 12z/14(1-z)$

The titanium in the carbo-nitride is defined by the sum of that which is in the form of titanium carbide and that which is in the form of titanium nitride, i.e.

wt%Ti in the carbo-nitride $= (D-[N])\ 48(xz+y(1-z))/14(1-z)$
wt%Nb in the carbo-nitride $= (D-[N])\ 93((1-x)z+(1-y)(1-z)/14(1-z)$

From these, the matrix compositions (wt%) can be identified as

$$[C] = C-(D-[N])12z/14(1-z) \tag{3.47a}$$
$$[Ti] = A-(D-[N])48(xz+y(1-z))/14(1-z) \tag{3.47b}$$
$$[Nb] = B-(D-[N])93((1-x)z+(1-y)(1-z))/14(1-z) \tag{3.47c}$$

Thus substitution from Equations (3.46) and (3.47) into the solubility product equations gives

$$\begin{aligned} k_1 &= [Ti][C]/a_{TiC} \\ &= [A-(D-[N]48(xz+y(1-z))/14(1-z)] \\ &\quad \times [C-(D-[N])12z/14(1-z)]/xz \end{aligned} \tag{3.48a}$$
$$\begin{aligned} k_2 &= [Nb][C]/a_{NbC} \\ &= [B-(D-[N])93((1-x)z+(1-y)(1-z))/14(1-z)] \\ &\quad \times [C-(D-[N])12z/14(1-z)]/z(1-x) \end{aligned} \tag{3.48b}$$
$$\begin{aligned} k_3 &= [Ti][N]/a_{TiN} \\ &= [A-(D-[N])(xz+y(1-z))48/14(1-z)][N]/y(1-z) \end{aligned} \tag{3.48c}$$
$$\begin{aligned} k_4 &= [Nb][N]/a_{NbN} \\ &= [B-(D-[N])93((1-x)z+(1-y)(1-z))/14(1-z)] \\ &\quad \times [N]/(1-y)(1-z) \end{aligned} \tag{3.48d}$$

If Equation (3.48c) is rearranged to express y in terms of the other variables and

this expression is substituted for y in Equations (3.48a, b and d), then three further equations are obtained, each being linear in x.

$$x = f_1([N], z)/f_2([N], z) \tag{3.49a}$$
$$x = f_3([N], z)/f_4([N], z) \tag{3.49b}$$
$$x = f_5([N], z)/f_6([N], z) \tag{3.49c}$$

where the six functions are given by

$$\begin{aligned}
f_1([N], z) &= A(1-z)k_3[C(1-z) - z(D-[N])12/14] \\
f_2([N], z) &= z[(1-z)k_1((1-z)k_3 + [N](D-[N])48/14) \\
&\quad + (D-[N])k_3 48(C(1-z) - z(D-[N])12/14)/14] \\
f_3([N], z) &= [(((1-z)k_3 + [N](D-[N])48/14)((D-[N])93/14 - B(1-z)) \\
&\quad - A[N](1-z)(D-[N])93/14)(C(1-z) - z(D-[N])12/14]) \\
&\quad + z(1-z)^2 k_2((1-z)k_3 + [N](D-[N])93/14)] \\
f_4([N], z) &= z(1-z)[(1-z)k_2((1-z)k_3 + [N](D-[N])48/14) \\
&\quad + (D-[N])k_3\, 93(C(1-z) - z(D-[N])12/14)/14] \\
f_5([N], z) &= B[N](1-z)[(1-z)k_3 + [N](D-[N])48/14] \\
&\quad - [(1-z)k_4 + [N](D-[N])93/14][(1-z)^2 k_3 + [N](D-[N])48/14 \\
&\quad - A[N](1-z)] + z[N](1-z)(D-[N])[k_4 48/14 - k_3 93/14] \\
f_6([N], z) &= z[N](1-z)(D-[N])[k_4 48/14 - k_3 93/14]
\end{aligned}$$

Equating any two of Equations (3.49) gives three further equations, only two of which are independent. These two independent equations are written as

$$f_1([N], z)/f_2([N], z) = f_3([N], z)/f_4([N], z)$$
$$f_1([N], z)/f_2([N], z) = f_5([N], z)/f_6([N], z)$$

or alternatively:

$$f_1([N], z) \cdot f_4([N], z) = f_2([N], z) \cdot f_3([N], z)$$
$$f_1([N], z) \cdot f_6([N], z) = f_2([N], z) \cdot f_5([N], z)$$

Defining two further functions of ([N], z) as

$$F_1([N], z) = f_1([N], z) \cdot f_4([N] \cdot z) - f_2([N], z) \cdot f_3([N], z)$$
$$F_2([N], z) = f_1([N], z) \cdot f_6([N], z) - f_2([N], z) \cdot f_5([N], z)$$

then we have a basis for the numerical (iterative) solution of [N] and z. Any valid solution must give

$$0 < [N] < D$$
$$0 < z < 1$$

and must also comply with

$$F_1([N], z) = F_2([N], z) = 0$$

Values of z between 0 and 1 are assumed, and for each value of z, the quantity $[N]$ can be determined by iterative procedures which result in $F_1([N], Z) = 0$ at each level of z. A similar procedure is followed giving pairs of z and $[N]$ values at which $F_2([N], z) = 0$. The solution for a given steel composition and temperature is given by the $[N]$ and z value satisfying both $F_1([N], z) = 0$ and $F_2([N], z) = 0$. This is shown schematically in Fig. 3.28. The relationship between $[N]$ and z for which $F_1([N], z) = 0$ is shown by curve A, and the relationship between $[N]$ and z for which $F_2([N], z) = 0$, is shown by curve B. The intersection of the two curves yields the solution for z and $[N]$ which complies with all of the above criteria.

The above treatment of complex carbo-nitrides due to Rose and Gladman[29] was used to evaluate the solute contents and complex carbo-nitride content and chemistry. Results for a steel containing 0.1wt%C and 0.01wt%Ti are shown in Fig. 3.29 for one level of nitrogen, i.e. 0.009wt%. In this steel, despite the great disparity between the carbon and nitrogen levels, the interstitial fraction of the carbo-nitride is predominantly nitrogen, particularly at the higher austenitising temperatures where the nitrogen constitutes virtually the whole of the interstitial content. Similarly, the titanium content dominates the metal fraction of the carbo-nitride, and again, at the higher temperatures, the precipitate chemistry is almost wholly titanium nitride. These results reflect the extremely low solubility of titanium

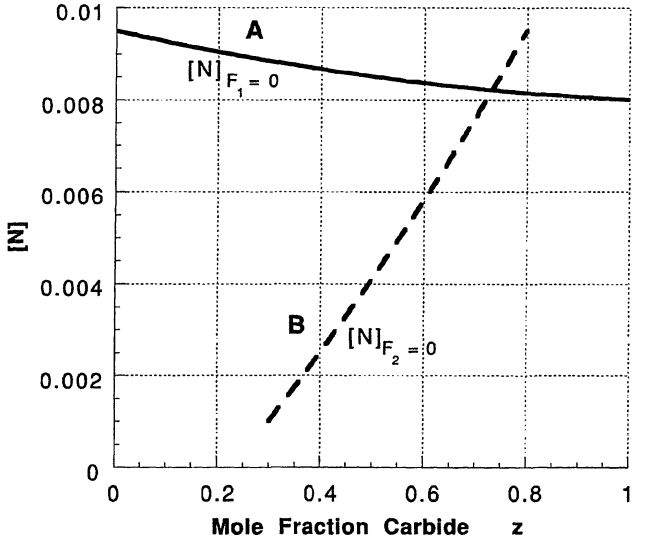


Fig. 3.28 Schematic solution for the determination of soluble and insoluble Ti, Nb, C, and N in complex microalloyed steels. Line A shows the combinations of $[N]$ and z for which $F_1([N], z) = 0$ and line B shows the combinations of $[N]$ and z for which $F_2([N], z) = 0$. The real values of $[N]$ and z are shown by the intersection of lines A and B.

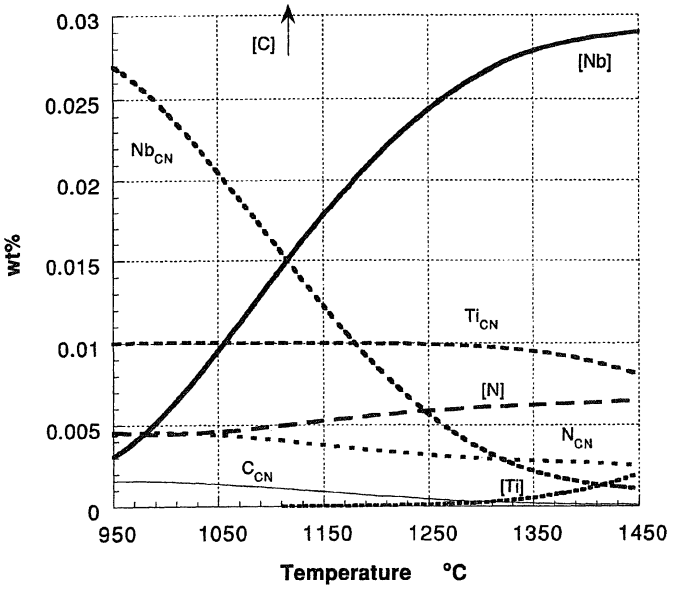


Fig. 3.29 Solutions for the complex carbo-nitride and austenite chemistries in a 0.1wt%C–0.009wt%N–0.01wt%Ti–0.03wt%Nb steel in the austenite temperature range.

nitride relative to those of the niobium carbide, niobium nitride, and titanium carbide, as indicated in Table 3.17. A direct consequence of the stability of the titanium nitride is the low level of titanium dissolved in the austenite (less than 10^{-3}wt%), at temperatures up to 1200°C and only 35% of the titanium is dissolved at 1400°C. Increasing the nitrogen content would result in only a slight increase in the wt% equilibrium precipitate present at low temperatures in the austenite range, but the relative increase (and indeed the absolute increase) becomes larger at the higher temperatures. Increasing the nitrogen content of the steel also has significant effects on the austenite chemistry, not only by increasing the dissolved nitrogen content of the austenite, but also by decreasing both the titanium and niobium dissolved in the austenite at a given temperature.

It should be emphasised that these changes, and particularly the quantitative aspects of these changes, are peculiar to the steel chemistry chosen. The particular steel chemistry chosen may be described as having a nitrogen content in excess of that required for the stoichiometric formation of titanium nitride with the total titanium content of the steel. 0.01wt%Ti would require only 0.0015wt%N (i.e. $0.01 \times 14/93$). Thus the dissolved nitrogen can be expected to vary significantly with the total nitrogen content at any given temperature in the austenite range. On the other hand, the increased nitrogen content has little effect on the amount of undissolved carbo-nitride at low temperatures in the austenite range, where the extent of precipitation is largely controlled by the sub-stoichimetric titanium and the niobium contents. The effect of nitrogen on the extent of precipitation is more

pronounced at higher temperatures, where, because of the increased solubility products, the dissolved niobium and titanium is more influenced by the nitrogen in solution. Increasing the niobium content (because of the sub-stoichiometric titanium and niobium levels), however, causes a marked increase in the extent of precipitated carbo-nitride at low temperatures, but, this effect decreases with increasing temperature as the relatively more soluble niobium carbo-nitride is substantially dissolved. One feature of all these changes is that they are calculated for a steel in which the carbon content is greatly in excess of that required for stoichiometric combination with the niobium and titanium, and the significance of the changes in nitrogen content are exerted at this level of carbon mainly by the decreased solubilities of the nitride-rich compounds compared with the carbon-rich compounds

It is very difficult to predict *a priori*, the expected changes in austenite chemistry for the generality of steels from the individual solubility products, as there are a number of conflicting factors. Mutual solubility of niobium and titanium carbo-nitrides would decrease the interstitial solute content due to the reduced activity of the component parts of the precipitated phase, but the effect of niobium on the dissolved titanium content, although subject to the same argument about reduced activity, is counterbalanced by the reduced interstitial level (due to the formation of niobium compounds) and the consequent effect on the dissolved titanium level. This counterbalance is sensitive to the overall chemistry of the steel with respect to each of these elements, the stoichiometry considerations and the temperature at which such deductions are to be made.

Speer, *et al.*[30] and Adrian[31] have also considered the thermodynamic consequences of the formation of mutually soluble microalloy carbo-nitrides using a slightly different approach, due to Hillert and Staffanson.[32] In the Hillert–Staffanson model, the complex carbo-nitride would be depicted as $Ti_xNb_{(1-x)}C_yN_{(1-y)}$ in Ti–Nb steels, and the activities of the compounds in the complex carbo-nitride are given by

$$a_{TiC} = xy$$
$$a_{NbC} = (1-x)y$$
$$a_{TiN} = x(1-y)$$
$$a_{NbN} = (1-x)(1-y)$$

This gives one less variable than the Rose and Gladman model, but imposes the condition that the Ti:Nb ratio associated with the carbon is equal to the Ti:Nb ratio associated with nitrogen.

Suzuki *et al.*[33] examined the response of carbo-nitride particles in Ti–Nb steels to weld thermal cycles and showed that higher heat input weld cycles resulted in considerable enrichment of the titanium fraction of the carbo-nitride, which is consistent with the approach to a titanium-rich equilibrium after increased high temperature exposure. Adrian[35] further made corrections for the effects of interactions between solutes on the activities of the solutes. Despite these differences, some of the major findings were the same. Notably, the titanium and nitrogen fractions of the complex carbo-nitride increased markedly with

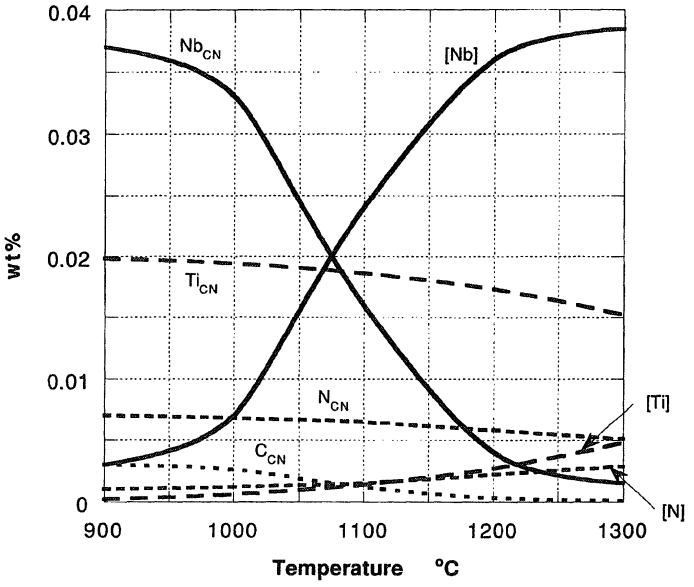


Fig. 3.30 Solutions for the complex carbo-nitride and austenite chemistries in a 0.1wt%C–0.008wt%N–0.02wt%Ti–0.04wt%Nb steel given by Adrian[31] using the Hillert–Staffanson model of carbide and nitride activities in the carbo-nitride.

increasing temperature. These effects are illustrated in Fig. 3.30, where the similarities are clearly shown. Any further attempt at rationalising the differences becomes increasingly tenuous due to the fact that

(i) The models differ in their ascribed activity of the components of the complex carbo-nitride.

(ii) The assumed chemical compositions of the steels differ slightly in the illustrated examples as shown below:

Rose and Gladman: 0.1%C–0.009%N–0.03%Nb–0.01%Ti
Adrian: 0.1%C–0.008%N–0.04%Nb–0.02%Ti

(iii) The solubility equations for TiC, TiN, NbC, and NbN used by Rose and Gladman were those of Narita (Table 3.17). Adrian used Narita's expression for the solubility product of TiC, but all other solubility products used by Adrian were from different sources.

Adrian also examined the complexes formed in Ti–V steels, as did Wang and Chen[34] and both showed the dominance of titanium nitride at high temperatures in the austenite temperature range, reflecting the low solubility of titanium nitride compared with other components of the complex carbo-nitride. The expected higher titanium fraction in the carbo-nitrides of Ti–V steels, compared with Ti–Nb steels (due to the lower solubilities of the niobium compounds), was not demonstrated because the example calculations were based on 0.04wt%Nb in

the Ti–Nb steels and on 0.15wt%V in the Ti–V steels. The solubility effect expected to giver higher Ti ratios in the carbo-nitrides of Ti–V steels is counterbalanced by the mass effect of 0.15wt%V in the Ti–V steel compared with only 0.04wt%Nb in the Ti–Nb steel.

Speer *et al.*[30] examined the carbo-nitride and austenite chemistries of Nb–V steel after holding at various temperatures in the austenite range. Experimental results on the niobium fraction in the carbo-nitride showed reasonable agreement with values calculated by the Hillert–Staffanson method (Fig. 3.31). The calculations yielded similar results to those obtained by Adrian, who also used the Hillert–Staffanson method, and also used the same solubility data, although direct equivalence was not attained due to minor differences in the steel compositions examined. Nevertheless, experimental and theoretical values of the niobium fraction of the carbo-nitride increased with increasing temperature in steels containing 0.1wt%C–0.03/0.04wt%Nb–0.05/0.20wt%V and 0.008/0.016wt%N.

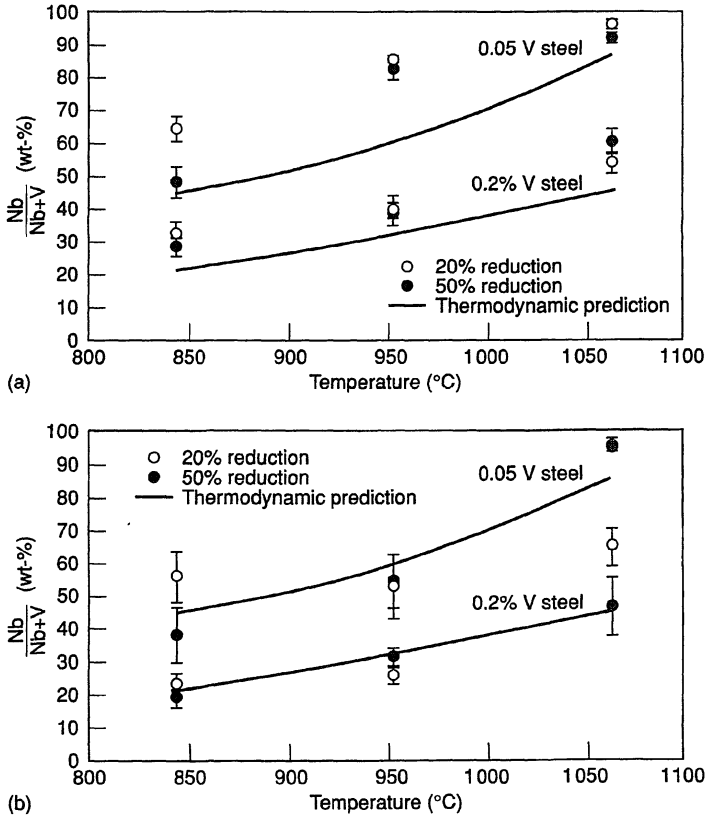


Fig. 3.31 Solution for the complex carbo-nitride and austenite chemistries in Nb–V steels. After Speer *et al.*[30] (a) Matrix precipitate, (b) Grain Boundary precipitate.

3.6 MORE COMPLEX ALLOY SYSTEMS

In Sections 3.4 and 3.5, the formation of simple carbo-nitrides and of carbo-nitrides formed from two microalloying elements showing complete mutual solubility, have been examined. In Section 3.3 the formation of mutually exclusive compounds was examined. Adding a third microalloying element to a given steel, whether this forms a mutually soluble carbo-nitride, as in a Ti–Nb–V steel, or a mutually exclusive compound, such as aluminium nitride in a Nb–V–Al steel, can be dealt with, conceptually, by the principles outlined in Sections 3.3–3.5. Only the mathematical difficulty increases. These cases have been considered by Adrian[35] together with that of the system Fe–Al–Nb–V–Ti–C–N. The details of the mathematical solution will not be considered here, and the reader is directed to the paper by Adrian.

3.7 NON-EQUILIBRIUM COOLING

Previous sections in this chapter have considered equilibrium compositions developed between the precipitated phases and the matrix. In many commercially important process routes, it is doubtful whether equilibrium conditions will be established, but such considerations are probably more important for the complex carbo-nitrides.

In a simple carbo-nitride, such as $NbC_xN_{(1-x)}$, reheating for hot-rolling or applying thermal cycles such as are used in normalising, appears to follow the equilibrium conditions insofar as the extent of precipitation or dissolution is concerned. In steels where two mutually exclusive precipitates are formed, such as in the Al–V steels discussed in Section 3.3, there is ample evidence that a metastable vanadium nitride can form in preference to the more stable aluminium nitride if short heat treatment times are involved, but, on extended holding, the metastable vanadium nitride is replaced by the more stable aluminium nitride. The extent to which the metastable phase will develop is conditioned by the steel chemistry. In steels where the vanadium content greatly exceeds the aluminium content, but where the equilibrium nitride is still aluminium nitride (see Fig. 3.20), the abundance of vanadium and/or the ease of nucleation of vanadium nitride allows kinetic considerations to dominate at short holding times, and vanadium nitride can be formed (provided that the vanadium–nitrogen product in the steel exceeds the solubility product for vanadium nitride). Prolonged holding will allow the equilibrium precipitate, aluminium nitride, to form, and as the nitrogen content of the matrix is reduced, so the vanadium nitride will dissolve. Konig *et al.*[36] studied the precipitation reactions in aluminium–vanadium steels and an example of their findings is shown in Fig. 3.32. The steel, containing 0.2wt%C–0.052wt%Al–0.14wt%V–0.023wt%N was solution treated at 1350°C to give substantial dissolution of the nitrides, and was then cooled and held at 950°C for the times shown. Aluminium nitride precipitation is sluggish in austenite, and substantial aluminium nitride precipitation is only seen after about 20 h. Up to 20 h

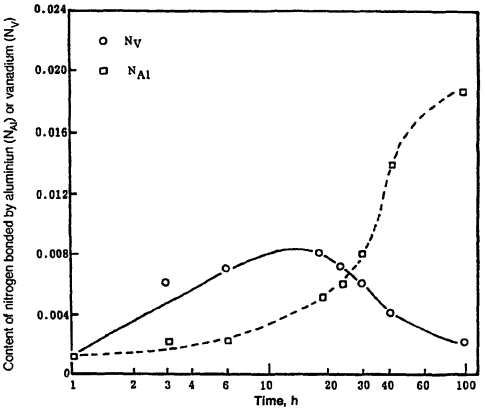


Fig. 3.32 Kinetics of the precipitation of aluminium and vanadium nitrides in an Al–V steel at 950°C. The steel contained 0.052wt%Al–0.14wt%V–0.023wt%N. After Konig *et al.*[36]

the dominant nitride is VN, but as the equilibrium nitride AlN is formed at longer times, so the VN is progressively dissolved.

The complex mutually soluble carbo-nitrides may suffer kinetic competition from the relative abundance standpoint, but the ease of nucleation should be similar for all of these carbo-nitrides. The high diffusion rates of carbon and nitrogen in austenite should allow equilibrium carbon and nitrogen partitioning in a relatively short time, although there is little information on the diffusivity of carbon and nitrogen in the carbo-nitride phases. A more difficult problem could be the homogenisation of the metal atoms in a mixed carbo-nitride. It has already been shown that the equilibrium carbo-nitride at high temperatures in an Fe–Ti–Nb–C–N steel is substantially titanium nitride. At low temperatures in the austenite range, the equilibrium precipitate contains a substantial if not major proportion of niobium carbide (these proportions being of course dependent upon the alloy composition). During continuous cooling the development of the equilibrium compound is virtually dependent upon the intra-particle diffusion of the components. There is considerable evidence that such homogenisation does not take place and that a heavily cored particle is formed, with a substantially titanium nitride core, and substantially a niobium carbide shell. This situation has been modelled by Rose and Gladman, where the composition of the precipitate deposited at any given moment was solely a function of the austenite composition and solubility products, and on the assumption that there was no diffusion in the carbo-nitride. The austenite chemistries obtaining at temperatures in the austenite range under coring conditions, for comparison with those obtaining under equilibrium conditions are shown in Fig. 3.33 for a 0.1wt%C–0.03wt%Nb–0.01wt%Ti–0.009wt%N steel. Such differences are generally slight, being mainly confined to the temperature range over which niobium carbide is the dominant precipitating species. These relatively small changes in austenite composition hardly reflect the vast changes in particle chemistry from core to surface shown in Fig. 3.34, compared with the expected equilibrium values of Ti: (Ti + Nb) = 0.42

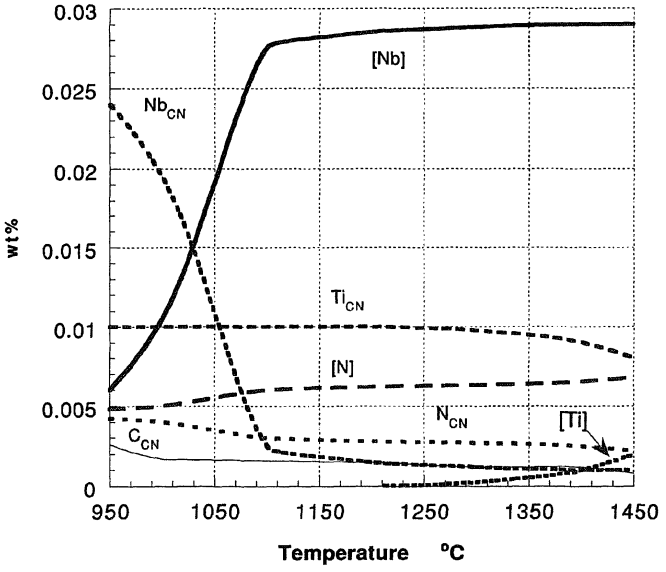


Fig. 3.33 Austenite composition at various temperatures in the austenite range under non-equilibrium cooling conditions in a titanium–niobium steel of the same composition as shown in Fig. 3.29. It is assumed that there is no diffusion of elements within the precipitated complex carbo-nitride.

and C: (C + N) = 0.36. Figure 3.34 illustrates the concept of core and shell, based on the assumption that all particles are identical. In reality, the precipitation process at low temperatures in the austenite range, where nucleation may become relatively easy and diffusion may become relatively difficult, may result in some of the niobium carbide shell component forming as separate particles of almost pure niobium carbo-nitride, thus giving particles of different chemistries in different size ranges, a feature which has often been observed.

Despite the difficulties posed by non-equilibrium effects, a knowledge of the particle and matrix equilibrium chemistries developed (or approached) during commercial reheating cycles is advantageous as will be shown in later chapters.

3.8 SUMMARY

The basic concepts of the solubility of microalloy carbides and nitrides have been described. The solubility products of the individual carbides and nitrides, which have provided some direction for alloy design, have been reviewed, and show varying degrees of accord between different sources depending upon the system considered. Nevertheless, the published data confirm that

(i) Nitrides of the various microalloys are less soluble than their respective carbides.

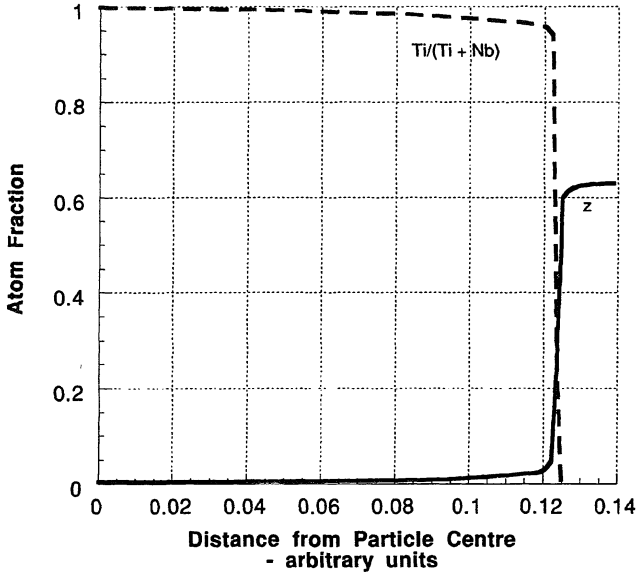


Fig. 3.34 Compositional changes within precipitated particles calculated from the assumption of a complete lack of diffusion within the complex titanium–niobium carbo-nitride.

(ii) Titanium nitride in particular is far less soluble than the other microalloy carbides and nitrides.
(iii) Vanadium carbide is far more soluble than the other microalloy carbides and nitrides.

The formation of simple carbo-nitrides can be defined by a single equation incorporating the solubility products of the particular carbide and nitride, although the equation has be to solved by a numerical method.

The case of mutually exclusive nitrides was also considered and an analytical solution is provided.

More complex mutually soluble carbo-nitrides arising from the simultaneous additions of two or more of the microalloy elements are considered, and models of these systems are described. The equations derived are complex and have to be solved by numerical procedures. Predictions obtained by these methods have been compared with the relatively few experimental results available. Reasonable agreement is obtained between predictions and experimental values, although it is clear that the models are capable of further development especially in the selection of suitable solubility data for the individual microalloy carbides and nitrides.

Finally, some consideration is given to possible non-equilibrium effects which can result in the presence of metastable phases, or phases of different chemistries within the same sample when equilibrium would predict a single phase of the miscible carbo-nitrides.

REFERENCES

1. F. G. WILSON and T. GLADMAN: *Int. Materials Reviews*. 1988, **33**, p.221.
2. L. S. DARKEN, R. P. SMITH and E. W. FILER: *Trans A.I.M.E.* 1951, **191**, p.1174.
3. T. SHIMOSE and K. NARITA: *J. Iron Steel Inst. Japan*, 1954, **40**, p.242.
4. W. C. LESLIE, R. L. RICKETT, C. L. DOTSON and C. S. WALTON: *Trans. A.S.M.*, 1954, **46**, p.1470.
5. P. KONIG, W. SCHOLZ and W. ULMER: *Archive f.d. Eisenhuttenwes*, 1961, **32**, p.5541.
6. L. A. ERASMUS: *J. Iron and Steel Inst.*, 1964, **292**, pp.32–41.
7. T. GLADMAN and F. B. PICKERING: *J. Iron and Steel Inst.*, 1967, **205**, p.563.
8. K. E. HONER and S. BALIKTAY: *Proc. 44th Int. Foundry Conf. Florence*, 1977, Paper 11 (B.I.S.I.16033).
9. K. J. IRVINE, F. B. PICKERING and T. GLADMAN: *J. Iron and Steel Inst.*, 1967, **205**, p.161.
10. M. G. FROHBERG and H. GRAF: *Stahl und Eisen*, 1960, **80**, p.539.
11. W. ROBERTS and A. SANDBERG: *Report I.M. 1489*, 1985, Swedish Inst. for Metals Research.
12. K. NARITA: *Trans. Iron and Steel Inst. of Japan*, 1975, **15**, p.145.
13. R. P. SMITH: *Trans. A.I.M.E*, 1962, **224**, p.190.
14. R. C. HUDD, A. JONES and M. N. KALE: *J. Iron and Steel Inst.*, 1971, **209**, p.121.
15. T. MORI, K. FUZITA, M. TOKIZANE and K. YAMAGUCHI: *Tetsu-to-Hagane*, 1964, **50**, p.911.
16. S. MATSUDA and N. OKUMURA: *Trans. Iron Steel Inst. Japan*, 1978, **18**, p.198.
17. K. BUNGARDT, K. KIND and W. OELSEN: *Archiv. f.d. Eisenbuttenwes*. 1956, **27**, p.6.
18. N. A. SAVOST'YANOVA and L. A. SHVARTSMAN: *Fiz. Met. Metallov*, 1960, **9**, p.515.
19. H. SEKINE, T. INOUE and M. OGASAWARA: *Trans. Iron Steel Inst. Japan*, 1968, **8**, p.101.
20. K. A. TAYLOR: *Scripa Met. et Mat.*, 1995, **32**, p.7.
21. W. NORDBERG and B. ARONSSON: *J. Iron and Steel Inst.*, 1968, **206**, p.1263.
22. T. H. JOHANSEN, N. CHRISTENSEN and B. ANGLAND: *Trans. Met. Soc. AIME*, 1967, **239**, p.1651.
23. T. GLADMAN and I. D. McIVOR: *Scandinavian Journal of Metallurgy*, 1972, **1**, p.247.
24. W. B. PEARSON: *Handbook of Lattice Spacings and Structures of Metals and Alloys*, vol. 2, Pergamon Press, 1967.
25. E. K. STORMS and N. H. KRIKORIAN: *J. Phys. Chem.*, 1960, **64**, 1747.
26. L. MEYER: *Z. Metalkunde*, 1967, **58**, p.334.
27. P. MANDRY and W. DORNELAS: *Comptes Rendue*, 1966, **263**, p.1118.
28. T. MORI *et al.*: *Tetsu-to-Hagane*, 1965, **51**, p.2031.
29. A. J. ROSE and T. GLADMAN (unpublished work).
30. J. G. SPEER, J. R. MICHAEL and S. S. HANSEN: *Met. Trans. A.* 1987, **18A**, p.211.
31. H. ADRIAN: *Microalloyed Vanadium Steels*, Eds. M. Korchynsky, S. Gorczca and M. Blicharski, Akad. Gom.-Hutz., Krakow, Poland, 1990, p.105.
32. M. HILLERT and L. I. STAFFANSON: *Acta. Chem., Scand.*, 1970, **24**, p.3618.
33. S. SUZUKI, G. C. WEATHERLY and D. C. HOUGHTON: *Acta. Met.*, 1987, **35**, p.341.
34. G. WANG and J. CHEN: *HSLA Steels, Processing, Properties and Applications*. Eds. G. Tither and Z. Shouhua. Trans. Min. Met. Mat. Soc., Warrendale, 1992, p.197.
35. H. ADRIAN: *Microalloying 95*, I.S.S., Pittsburgh, June, 1995, p.285.
36. P. KONIG, W. SCHOLZ and H. ULMER: *Archiv. f.d. Eisenhutte.*, 1961, **32**, p.541.

CHAPTER 4

Grain Size Control

4.1 INTRODUCTION

Whilst dislocation theory was developed in the 1930s and 1940s, the study of grains and grain shapes is much older. C. S. Smith[1] cites the early considerations of Archimedes, Reamur in 1724, Grignon in 1776[2] and Lord Kelvin in 1887.[3] The studies of grains (or cells) also covers a wide range of disciplines, and was of particular interest to botanists in connection with plant cells, biologists in connection with animal tissue, physicists in connection with froths and metallurgists in connection with metallic grains. Studies of the general topological aspects of aggregates of grains have been augmented by studies of grain growth and the inhibition of grain growth particularly with the introduction of the metallurgical microscope, and the development of microstructure/property relationships. The important effects of grain size on the strength and toughness of metals, and of steels in particular, have already been described in Chapter 2, and considerable attention has been given to maintaining a fine grained structure to secure the benefits of increased strength and improved resistance to brittle (cleavage) fractures. Considerable developments have taken place in studies of normal and abnormal grain growth aimed at producing the coarsest grain sizes in order to improve the magnetic properties associated with hysteresis losses. The development of crystallographic texture also has important consequences, not only for magnetic properties, but also for sheet metal formability because of its dependence on the plastic anisotropy induced in suitably textured metals.

The purpose of the present chapter is to outline the nature of the granular structure of metals and the factors that give rise to the phenomenon of grain growth. Methods of inhibiting grain growth are also considered, and the current understanding of the quantitative aspects of grain growth inhibition are also considered, particularly as they relate to microalloyed steels.

4.2 TOPOLOGICAL ASPECTS OF GRANULAR ARRAYS

Many of the early concepts associated with grains and grain growth were developed from two-dimensional (2-D) models, and these concepts have subsequently been applied to the three-dimensional (3-D) granular array, with suitable adaptations for the increased geometrical constraints. Consequently, the

topological aspects for the 2-D array will be considered before developing those of the 3-D arrays.

4.2.1 Two Dimensional Arrays

In any array of (2-D) space filling polygons, there is a simple relationship between the number of corners, where three or more polygons meet, the number of edges (where two polygons meet) and the number of polygons in the array, which can be stated as

$$P - E + C = 1 \tag{4.1}$$

where P, E and C are the number of polygons, edges and corners respectively. This equation is true, irrespective of whether three, or more than three, polygons meet at a corner, or whether the array is composed of straight or curved lines. It should be noted that the number of polygons meeting at a corner at the boundary of the array is only two, and that the edges at the boundary of the array are associated with a single polygon. Nevertheless, Equation (4.1) gives the relationship between any limited array of space filling polygons as shown in Fig. 4.1.

It is interesting to note that the relationship given by Equation (4.1) will be identical with Euler's Law, which describes the relationship between the edges, corners and polygons on the *surface* of a polyhedron, i.e.

$$P - E + C = 2 \tag{4.2}$$

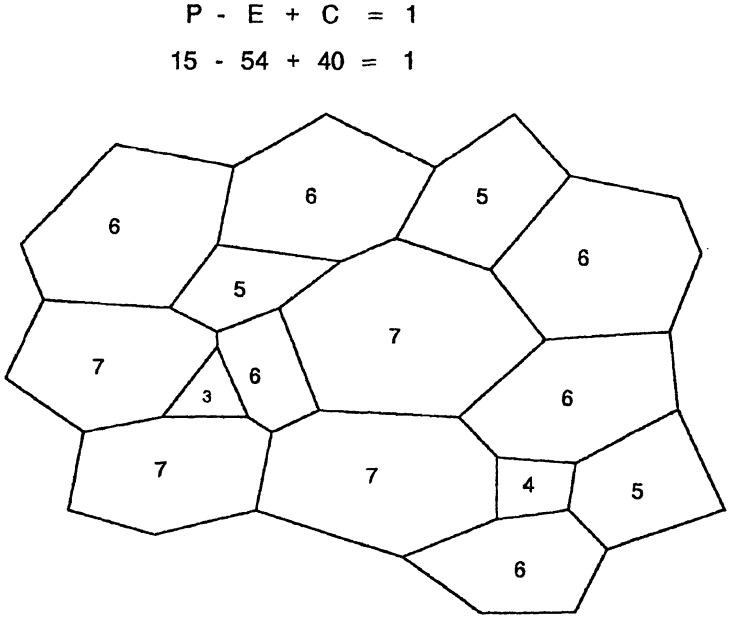


Fig. 4.1 The relationship between the number of edges, corners and polygons in a 2-D array.

if the area outside the 2-D array is counted as a single polygon. The number of edges and corners asociated with this exterior polygon will be equal to those associated with the boundary of the original array, and the number of boundary edges will be equal to the number of boundary corners, thus resulting in the addition of the single external polygon to Equation (4.1), resulting in Euler's Law, Equation (4.2). This procedure is closely represented by the Schlegel[4] diagram which gives a 2-D representation of the topological features of the surface of a polyhedron. The Schlegel diagram is constructed by drawing a frame having the same number of edges (and corners) as one of the polygons forming a single face of the polyhedron. Looking into the polyhedron through this particular face will reveal all of the connected surfaces of the polyhedron, and a portrayal of these will give the topologically correct Schlegel diagram, the 'frame' of the Schlegel diagram corresponding with the boundary of the 2-D array and constituting one surface of the polyhedron. One example of a polyhedron is shown in Fig. 4.2(a). This is Kelvin's 14 plane-faced solid, otherwise known as the tetrakaidecahedron or the cubo-octahedron. This has eight hexagonal faces and six square faces. Two Schlegel diagrams can be drawn, one obtained by using one of the square faces as the frame, and the other by using one of the hexagonal faces as the frame. The Schlegel diagram seen through a hexagonal face is shown in Fig. 4.2(b). If Fig. 4.2(b) is treated as a truly 2-D array of polygons, then the number of polygons, 13, plus the number of corners, 24, minus the number of edges, 36, is equal to unity, thus conforming with Equation (4.1). If however, Fig. 4.2(b) is treated as a Schlegel

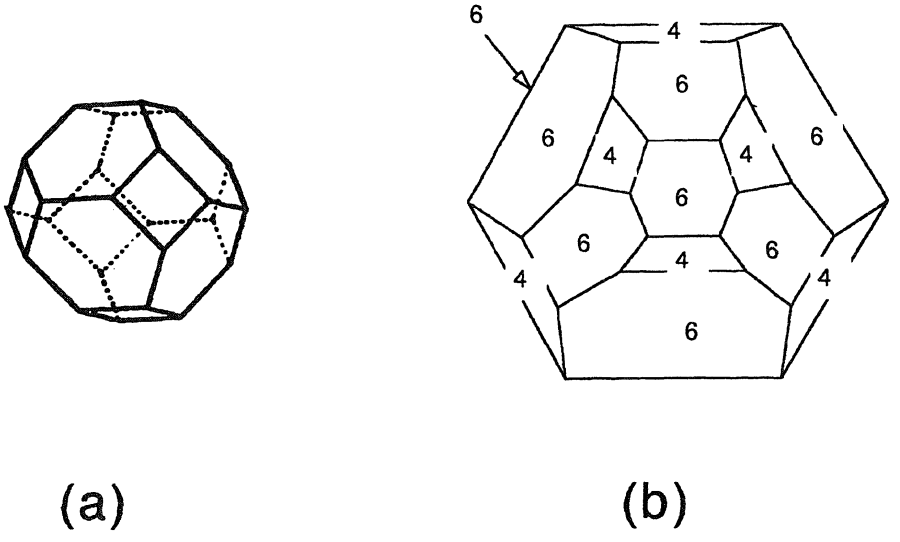


Fig. 4.2 The Schlegel diagram for a tetrakaidecahedron. (a) The 3-D tetrakaidecahedron seen in perspective. (b) The Schlegel diagram constructed by viewing through a hexagonal face of the polyhedron.

diagram (a 2-D representation of the tetrakaidecahedron) the hexagonal frame adds a further polygon ($P = 14$) without adding further edges or corners, thus giving $P - E + C = 2$ in accordance with Euler's Law.

Whilst these topological rules are universally correct, they do not give any direct measure of shape or size, and further considerations have to be invoked to provide a more meaningful interpretation of the shapes of metal grains. As pointed out by Smith,[1] the edges between (2-D) grains are influenced by the boundary energies associated with the atomic lattice mis-fits between grains. Geometric adjustments of the boundary will occur to minimise the boundary area and hence the total boundary energy, given that there is adequate boundary mobility to effect such short range boundary movements.

There are two relatively simple calculations that serve to introduce the effects of boundary energy. The first of these concerns the number of grains (polygons) meeting at a corner within the (2-D) array. Consider the 4-rayed corner depicted in Fig. 4.3 as solid lines. Coalescence of adjacent grain boundaries to give an edge between grains A and B (depicted as dashed lines) rather than the two grains meeting at a point, will result in a change in the total grain boundary length. Because of the symmetry of Fig. 4.3, only one half of the boundary system needs to be considered having dimensions as shown in Fig. 4.3. The length of boundary, L, in the half system, when the 4-rayed corner divides to give two 3-rayed corners is given by

$$L = 2(b^2 + (a - x)^2)^{1/2} + x \tag{4.3}$$

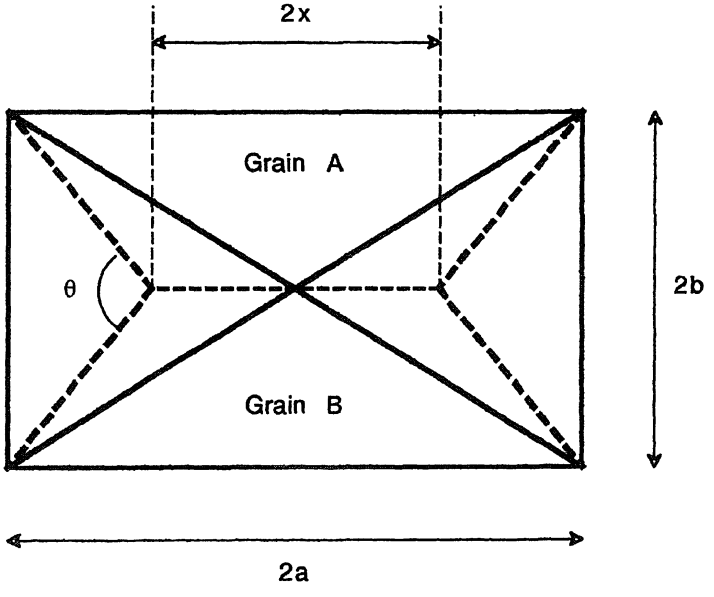


Fig. 4.3 Changes in grain boundary length (or energy) when a 4-rayed corner (solid lines) decomposes into two 3-rayed corners (dashed lines).

and the rate of change of L with the merged half length, x, is given by

$$dL/dx = 1 + 2(x-a)/(b^2 + (a-x)^2)^{1/2} \tag{4.4}$$

Any minimum position will be described when

$$dL/dx = 0, \text{i.e.}$$
$$2(a-x) = (b^2 + (a-x)^2)^{1/2} \tag{4.5}$$

or $b/(a-x) = \sqrt{3}$

It can easily be seen that $b/(a-x)$ is equivalent to tan θ, and at tan $\theta = \sqrt{3}$, $\theta = 60°C$, thus leading to a situation where the three boundaries meet at a corner with the minimum energy occurring when the three angles between the boundaries are at 120°C. It should be noted that if $b > a$, then merging of the 4-rayed boundaries would occur to give a vertical merged boundary in Fig. 4.3, as the rate of change of length of boundaries for a given value of x would be greater than for the horizontal boundary shown.

This simple calculation shows that the boundary energy of the system will be decreased if a 4-rayed corner splits into two 3-rayed corners. There are, however, simplifying assumptions that are implicit in this calculation, namely:

(i) The boundary energy is independent of the nature of the boundary, i.e. the misorientation of atomic lattices across the boundary. If the element of new boundary, x, had a much higher boundary energy than those of the original boundaries, the changes could be inhibited.
(ii) The boundary energy remains unchanged by rotation of the original boundaries. Again, if such rotations increased the boundary energies, the changes could be inhibited.

The calculation of the equilibrium position of the 3-rayed corners, i.e. with angles of 120°, confirms the more general finding of Shuttleworth[5] who developed the expression

$$\lambda_1/\sin\alpha_1 = \lambda_2/\sin\alpha_2 = \lambda_3/\sin\alpha_3 \tag{4.6}$$

where λ_1, λ_2 and λ_3 are the boundary energies of three boundaries meeting at a corner and α_1, α_2 and α_3 are the opposite angles as shown in Fig. 4.4. If $\lambda_1 = \lambda_2 = \lambda_3$, then α_1, $= \alpha_2 = \alpha_3 = 120°$. In these 2-D arrays, the boundary energy is a line energy and two grains are separated by the line (boundary). Three grains meet at a corner, and a minimum energy situation exists when the three angles subtended at the corner are equal (= 120°), given that the boundary energies are equal. The angles will not be equal if the boundary energies differ.

If these features are incorporated into the topological equation for an array of polygons [Equation (4.1)], then the relationships between the number of polygons, the number of edges and the number of corners become more clearly defined. Each polygon with n edges contributes $n/2$ edges to the array, since each edge belongs to two polygons. The exception to this general statement occurs at the boundary of

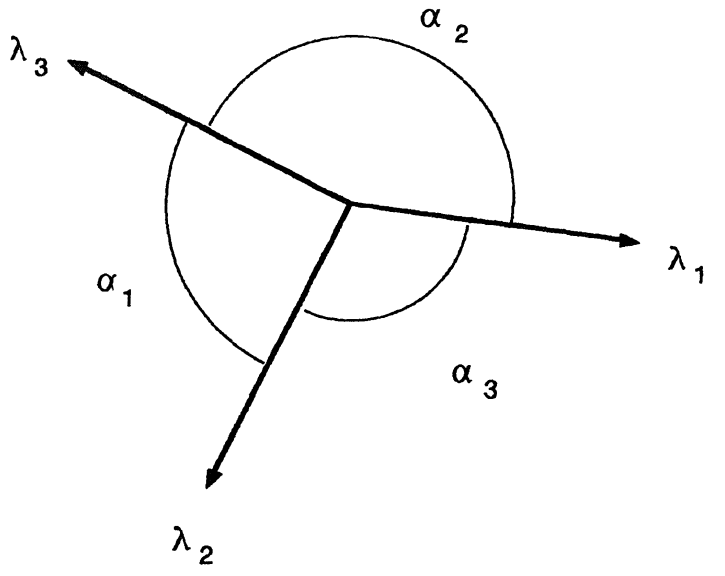


Fig. 4.4 The equilibrium angles at a 3-rayed corner in a 2-D system of polygonal grains.

the array, where each edge belongs to only one polygon. Thus in the array, the number of edges, E, is given by:

$$E = \Sigma P_n n/2 + E_b/2 \tag{4.7}$$

where P_n is the number of polygons having n sides and E_b is the number of edges forming the boundary of the array.

Also, the number of corners, C, in the array is defined by the relationship between edges and corners. Each corner is associated with 3 edges (when interfacial energy controls the array), and each edge is bounded by 2 corners. Thus each corner is associated with 3 half-edges, and the number of edges is equal to 3/2 times the number of corners, C, i.e.

$$3C = 2E \tag{4.8}$$

If the values from Equations (4.7) and (4.8) are substituted into Equation (4.1), then

$$\Sigma P_n - (\Sigma P_n n + E_b)/2 + (\Sigma P_n n + E_b)/3 = 1 \tag{4.9}$$

which can be simplified to give

$$\Sigma(6 - n)P_n - E_b = 6 \tag{4.9a}$$

It should be noted that Equation (4.9a) relates to a special type of 2-D array in which all of the corners on the boundary of the array are shared by two of the polygons (i.e. all of the corners are three-rayed). The situation that arises when drawing a sample array of grains from a micrograph where some grain corners at

the edge of the array may not be shared by any other grain within the array obviously violates the condition $3C = 2E$, and a correction has to be made for the unshared corners. This has been considered in detail by Smith[1] and will not be considered further here.

4.2.2 The Polyhedron

As pointed out in Section 4.2.1, Euler's Law expresses the relationships between the number of polygons, number of edges and the number of corners of a single polyhedron, and eliminates the need for the considerations of boundary effects of the flat 2-D array of polygons, as the polyhedron gives a closed system of polygons. Thus

$$P - E + C = 2$$

We can now apply the same surface energy considerations to the polyhedron that were applied to the flat 2-D array of polygons, i.e. that 2 polygonal faces meet at an edge, and that 3 edges (and 3 polygons) meet at a corner.

Let the polyhedron have P polygonal faces, and let P_n be the number of polygons having n edges, so that $P = \Sigma P_n$. Because of the surface energy constraints, then the number of edges on the polyhedron, E, is given by

$$E = \Sigma P_n n/2 \tag{4.10}$$

and the number of corners on the polyhedron, C, is given by

$$C = \Sigma P_n n/3 \tag{4.11}$$

Substitution from Equations (4.10) and (4.11) into Euler's Law [Equation (4.2)] gives

$$P - \Sigma P_n n/2 + \Sigma P_n n/3 = 2$$

which reduces to

$$P = 2 + \Sigma P_n n/6 \tag{4.12}$$

Using the expressions for the number of edges and corners from Equations (4.10) and (4.11) in Equation (4.12) gives

$$P = 2 + C/2$$

$$\text{and} \quad P = 2 + E/3$$

$$\text{or} \quad C = 2(P - 2) \tag{4.13}$$

$$\text{and} \quad E = 3(P - 2) \tag{4.14}$$

Equations (4.13) and (4.14) show that for any polyhedron where 3 polygons meet at a corner and 2 polygons meet at an edge, the number of edges and the number of corners are uniquely related to the number of faces (polygons) of the polyhedron.

The average number of edges per polygonal face, n_a, can be obtained from

$$n_a = 2E/P = 6(P-2)/P$$
$$\text{or} \quad n_a = 6 - 12/P \tag{4.15}$$

For a tetrahedron, which has the smallest number of faces that will comply with the 3 edges per corner criterion then $n_a = 3$. For polyhedra with 12 faces, the average number of edges per face is 5 (cf. the pentagonal do-decahedron) and as the number of faces increases further, the average number of edges per polygonal face approaches 6. Equation (4.15) is true for both regular and irregular polyhedra.

It can be seen from the Schlegel diagram in Fig. 4.2 that the average number of edges per polygonal face of the tetrakaidecahedron is given by $(8 \times 6) + (6 \times 4)$ edged divided by $(8+6)$ faces or $5\frac{1}{7}$ edges per polygonal face.

4.2.3 An Array of Polyhedra

The granular structure of metals is generally considered as an array of polyhedra. Due to space-filling considerations and the surface energy considerations outlined previously, there are a number of restrictions which are applied to the array of polyhedral grains. These are

(i) each polygonal face of a polyhedron is shared by a matching face on a contiguous polyhedron.
(ii) each edge of a polyhedron is shared between three polyhedra
(iii) each corner of a polyhedron is shared between four polyhedra

The basic topological relationship relating to a finite array of polyhedral grains is[1]

$$P' - E' + C' - G' = 1 \tag{4.16}$$

where G' is the number of polyhedral grains in an array, P' is the number of polygonal interfaces, E' is the number of grain edges in the array and C' is the number of grain corners in the array.

In an infinite array of grains, Equation (4.16) has to be modified to give

$$P' - E' + C' = G' \tag{4.16a}$$

The primes are used to differentiate the polygons, edges and corners in the array, from those associated with the single polyhedron, as there are different associations between them. For example, in an infinite array, each edge is associated with two corners and each corner is associated with four edges. Thus

$$E' = 2C'$$

as opposed to $2E = 3C$ for the isolated polyhedron. Bearing in mind the surface

tension constraints and the space-filling requirements, the number of edges and corners in the array can be substituted into Equation (4.16a) in a similar manner to that used for the single polyhedron, but now

$$E' = \Sigma P'_n n/3 \tag{4.17}$$

$$C' = \Sigma P'_n n/6 \tag{4.18}$$

$$\text{and} \quad P' - \Sigma P'_n n/3 + \Sigma P'_n n/6 = G'$$

or in simplified form

$$\Sigma(6 - n)P'_n = 6G' \tag{4.19}$$

It can be shown from Equations (4.16a) to (4.19) that the average number of polygonal faces per grain (P'/G') is related to the mean number of edges (or corners) per face, a, by

$$P'/G' = 6/(6 - a) \tag{4.20}$$

The average number of edges per grain, E'/G', is given by

$$E'/G' = 2P'/G' - 2 \tag{4.21}$$

and the average number of corners per grain, C'/G' is given by

$$C'/G' = P'/G' - 1 \tag{4.22}$$

From Equations (4.20) to (4.22) it is immediately clear that the topological relationships are uniquely expressed, in that the selection of the average number of corners, or edges, or polygonal faces, per grain, immediately defines the other topological parameters. However, the topological specification given above does not allow any deduction of the grain shape, which is dependent upon space filling requirements, and surface energy requirements, as indicated earlier. The angular relationships implied by three polygonal faces meeting at an edge, and four polyhedral grains meeting at a corner, should imply angles between adjacent polygonal faces of 120° at the grain edge, and angles between edges of 109°28′ at the grain corner. Unfortunately, there is no regular polyhedron that will comply with these requirements. Whilst the hexagon complies with surface tension requirements and the filling of 2-D space, there is no equivalent shape for the 3-D case. The pentagonal do-decahedron with 12 equal pentagonal faces has corner angles of 108° but will not stack together to fill space. The tetrakaidecahedron (Kelvin's 14 plane faced solid) complies with the space filling requirement, as has been depicted by Barrett,[6] and the array conforms with the requirements of three grains meeting at an edge and four grains meeting at a corner. However, at each edge, there are two hexagonal faces and one square face. The two angles between the hexagonal faces and the square face are about 125°16′ and the angle between the two hexagonal faces is about 109°28′ and thus deviate only slightly from the equiangular 120°. The corner angles are obviously 120° between edges associated with the hexagonal faces and 90° between edges associated with the square faces,

there being four hexagonal faces and two square faces associated with each corner, and again show some deviation from the 'ideal' corner with its 109°28′ angles.

Smith[1] has discussed the concept of curved rather than flat surfaces, following the experiments of Kelvin,[3] and the doubly curved hexagonal surfaces clearly allow the angles at the edges and corners to adopt their equilibrium values. These doubly curved surfaces have zero mean curvature and the displacements of the curved surfaces from the corresponding hexagonal plane surfaces are relatively small.

Nevertheless the tetrakaidecahedron with its 14 faces meets the surface energy criteria of three grains meeting at an edge and four grains meeting at a corner, and will fill space when equally sized tetrakaidecahedra are arrayed on a body centred cubic lattice. From Equation (4.15) for the isolated polyhedron, a 14-faced solid ($P = 14$) will have an average of $5\frac{1}{7}$ edges per face. The tetrakaidecahedral array will have seven faces per grain ($P' = 7$) because each polygonal face in the array is shared by two polyhedral grains, and Equation (4.20) then conforms with the average of $5\frac{1}{7}$ edges per interface.

4.2.4 Experimental Observations

The topological principles discussed above do not in themselves allow a direct prediction of grain shapes. However, Smith[1] drew attention to the work of Matzke[7] and Matzke and Nestler[8] and Desch[9] who made observations on soap froth,[7] vegetable cells,[8] and beta-brass grains.[9] The distributions of the number of edges (or corners) per face were evaluated and are shown in Fig. 4.5. The modal value of the number of edges per face was 5, i.e. there were more pentagonal faces than any other particular polygonal faces. The number of edges per face, n, varied from three to eight, clearly indicating that the grains were not tetrakaidecahedral (such polyhedra would have only 6-sided and 4-sided faces in the ratio 8 : 6 respectively). In fact the grains were not regular in shape. The main topological features of these arrays are summarised in Table 4.1. The average number of edges per polygonal face (averaged over all grains), varies between $5\frac{1}{9}$ to $5\frac{1}{7}$. The average number of polygonal faces per grain varies between 13.7 and 14.50. Thus the average number of faces per grain is approximately 14, but the non-integer values of these averages clearly indicates that the array contains a mixture of grains having different numbers of faces. It should be noted that the values of edges per polygonal face given in Table 4.1 express the average number of edges per polygonal face in the array of G' grains and *not* the average number of edges per polygonal face in a grain. It is not possible to deduce the average number of polygonal faces per grain from the edges per face values shown in Table 4.1 using either Equations (4.15) or (4.20).

The high incidence of grains with about 14 faces must reflect the included angles at the junction edges between two grains which will allow the insertion of a mutually contiguous grain which will approximately conform with the surface energy requirements for edges, and also for corners when a fourth grain is added to the array. As described previously, there is no single regular polyhedral shape that will fill space and comply with the angular requirements. The development of

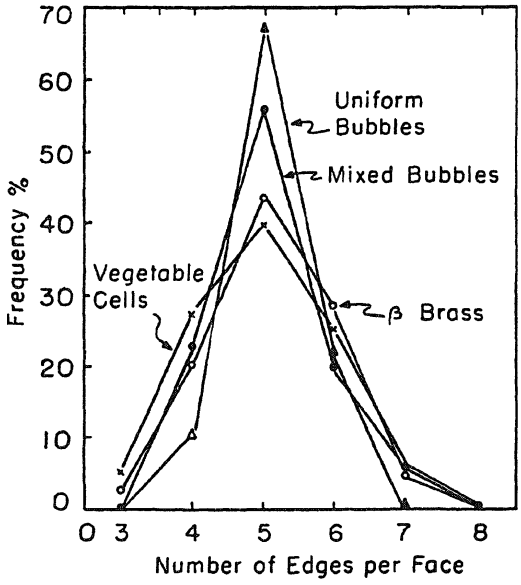


Fig. 4.5 The distribution of the number of edges per face in soap froths, vegetable cells, and the beta-brass grains. After Smith.[1]

an array of uniform regular tetrakaidecahedra is highly unlikely, given the mechanisms by which granular structures are developed in metals. The granular structures derive from nucleation and growth processes, and a regular tetrakaidecahedral array of grains would require geometrically disposed nuclei. If the nuclei were randomly distributed, a variety of grain shapes would develop when growth from the nuclei allowed collision between neighbouring grains to form a grain boundary. Such irregular granular structures might rapidly adjust to

Table 4.1 Grain shapes in froths, vegetable cells, and beta-brass grains. The average number of faces per grain is approximately 14

	Matzke[7] (froth)	Matzke[8] (vegetable cells)	Desch[9] (brass)
Number of bubbles cells or grains (G')	600	450	30
No. of polygonal faces with n sides			
$n=3$	–	32	11
$n=4$	866	1694	88
$n=5$	5503	2465	190
$n=6$	1817	1575	123
$n=7$	35	390	20
$n=8$	–	50	3
$n=9$	–	5	–
Total no. of faces	8221	6211	435
Average no. of edges	5.111	5.123	5.142
P'/G'	6.85	6.90	7.25
Faces per grain	13.70	13.80	14.50

allow conformity with surface energy considerations. Grain growth in fact reflects the processes by which surface energy reductions are achieved, and are discussed in a later section of this chapter.

The development of an array of irregular polyhedra of various sizes, but having on average about 14 faces, is a reasonable generalisation of the granular structure of metals, and will not be dissimilar to the bubble structure in a soap froth (or indeed an array of vegetable cells). A photograph of a soap froth is shown in Fig. 4.6. Even in a translucent soap froth it is difficult to illustrate clearly all of the individual bubble shapes, but it can be seen that there is a variety of shapes, with an occasional tetrahedral bubble, having four triangular faces. It is interesting to note that Matzke[7] did not observe a single triangular face amongst the 8200 faces in his 600-bubble array. This may reflect the method by which the array was formed; the array was described by Matzke as comprising 'uniform bubbles'.

4.3 GRAIN SIZE MEASUREMENT

The preceding section dealing with the topological, surface energy and space filling requirements of a granular structure allowed some insight into grain shape. However, the size of the grains is vitally important to the properties of steels as

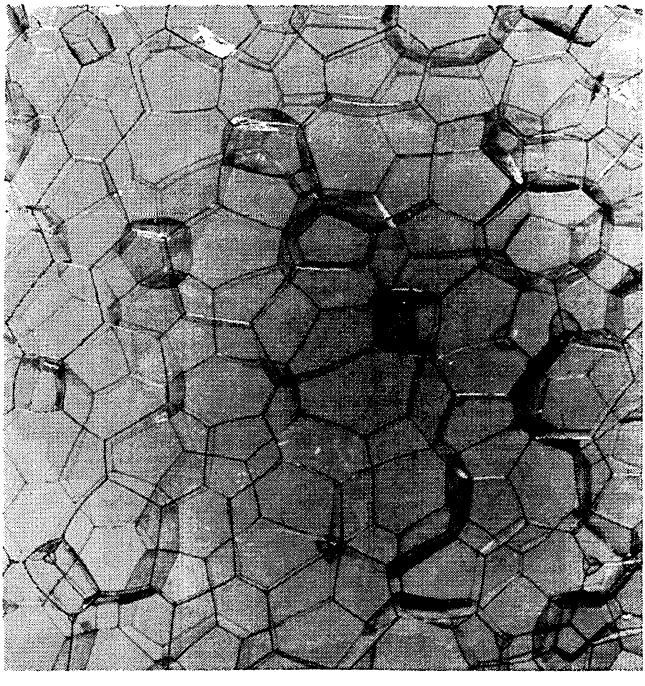


Fig. 4.6 Photograph of a soap froth, a close analogy of the 3-D granular structure of a polycrystalline metal.

indicated in Chapter 2. Measurement of the grain size is therefore important and will be considered here.

There are three principal methods of grain size measurement that are commonly used either for quality control purposes or for research studies. These are:

(i) Comparator chart method
(ii) Heyn intercept method
(iii) Jeffries' planimetric method

Exact details of these methods are given in ASTM Standard E112, and only a brief summary of the methods is presented here.

4.3.1 The Comparator Chart Method

As the name implies, this method involves the preparation of a metallographic specimen in a manner which reveals the relevant grain structure of the metal, examination of the structure at a known magnification, usually $\times 100$ diameters, and a comparison of the observed grain size with a series of standard charts showing a range of different grain sizes. Each of the grain sizes depicted in the charts has an associated ASTM grain size number, G, and the grain size number most closely describing the grain size of the test specimen is quoted. The ASTM grain size number, G, has a rational basis defined by

$$n = 2^{G-1} \tag{4.23}$$

where n is the number of grains per square inch as seen at a magnification of $\times 100$ diameters. Thus, for an ASTM grain size of $G = 1$, there will be one grain per square inch as seen at a magnification of $\times 100$ diameters, or 100×100 grains per square inch at $\times 1$. For an ASTM grain size of $G = 8$, there are 128 grains per square inch at $\times 100$ diameters or 128×10^4 grains per square inch at $\times 1$ (real size). It is clear from Equation (4.23) that, for each unit increase in G, the number of grains per square inch doubles, the area of the grain is halved, and the grain diameter decreases by $\sqrt{2}$.

The comparative method gives a relatively coarse measurement of grain size, each unit of the scale representing a change of some 40% in grain diameter. The accuracy of the method is claimed to give estimates within $\pm 1/2$ for G, thus giving an estimate of grain diameter within 20% of the real value. It is a useful method for the determination of austenite grain size in transformable ferritic steels when the precise location of the grain boundary may be difficult to asssess. Methods of revealing the prior austenite grain boundaries are discussed in the ASTM standard.

It should be noted that this description relates to the micro grain size. There is an alternative scale for very coarse grained specimens which is termed the macro grain size number and the number is usually prefixed by the letter M. The macro grain size number, MG, is defined by

$$n' = 2^{MG-1} \tag{4.23a}$$

where n' is the number of grains per square inch without magnification. It is easy to show that

$$MG = G + 13.3$$

With wrought steels and with microalloyed steels in particular, only the micro grain size system is used.

4.3.2 The Heyn Intercept Method

The Heyn intercept method is probably the most commonly used method of assessing the grain size when quantitative results are required for correlation with mechanical or other properties. It is a relatively simple procedure in which the number of grain boundaries intersected by a straight line of a given length, imposed on a metallographic image, is counted. The length of the intercept recommended in the ASTM Standard E112 should be such as to include at least 50 grains, and is attained by using a 500 mm length of intercept, and adjusting the magnification of the micrograph to allow between 50 and 200 grains to be counted. The true length of the intercept of course varies with the magnification. The intercept can be constructed by drawing a line, (or lines) on a micrograph, using a transparency on the ground glass screen of a projection micrograph, or by traversing a specimen over a given distance under a reference point in the eye-piece of the microscope. In each case, the number of grains intersected by the line (or reference point), n, and the real length of intersecting line (or distance traversed), l, is recorded, and the mean linear intercept, i, is calculated from

$$i = \ell/n \tag{4.24}$$

This procedure is relatively simple for a single phase alloy, but for a two-phase alloy, such as ferrite–pearlite structures typical of low carbon microalloyed steels, then

$$i_\alpha = \ell(1 - f_p)/n_\alpha$$
$$\text{and} \quad i_p = \ell f_p/n_p \tag{4.24a}$$

where i_α is the mean linear intercept grain size of the ferrite, i_p is the mean linear intercept grain size of the pearlite, f_p is the volume fraction of pearlite, n_α is the number of ferrite grains intersected, n_p is the number of pearlite grains intersected and ℓ is the real length of the intercepting line.

The statistical errors associated with measurement of the mean linear intercept have been considered by Woodhead (see ref. 10). Based on the intercept distributions of Hull and Houk,[11] Woodhead suggested that the relative error of individual intercepts (σ_i/i) is almost constant for a variety of regular and space filling polyhedra, and has a value of 0.7. The relative error, ϕ, of the mean linear intercept based on the measurement of n grains (SE_i/i) is given by

$$\phi = SE_i/i = (\sigma_i/i)/n^{1/2} = 0.7/n^{1/2}$$

For a selected value of the relative error the number of grains that are required for the mean linear intercept determination [Equation (4.24)] is given by

$$n = 0.7^2/(SE_i/i)^2 \tag{4.25}$$

The relationship between the selected relative error, the number of grains to be counted, and the approximate 95% confidence limits, are shown in Table 4.2. The important feature of this table is that 95% confidence limits of ± 10% of the mean linear intercept value (i.e. a lower limit of $0.9i$ and an upper limit of $1.1i$) can be attained with a count of some 200 grains. Obviously narrower limits can be attained by measuring a larger number of grains as indicated in Table 4.2.

In the ASTM Standard E112, this method is recommended for non-equiaxed structures, or for measurements requiring high precision. For non-equiaxed structures, intercept directions are important and it is recommended that separate measures be made along the three principal axes of the specimen (longitudinal, transverse and normal) or that circular intercepts be used to produce an average intercept length that could be useful for the prediction of grain boundary area per unit volume. Any average intercept of a non-equiaxed structure should be accompanied by annotations of the ratios of the mean intercept length in different directions.

4.3.3 Jeffries' Planimetric Method

The principle of this measurement is closely related to the comparator method in that it uses the areal intercept of the grains. However, the expression of grain size is based directly on the measure, i.e. number of grains per mm^2, rather than a derivative number. The method, as described in the standard, involves a circle or rectangle of known area, usually 5000 mm^2, imposed on a micrograph or ground glass screen, and the magnification of the micrographic image is adjusted to give at least 50 grains within the area. Grains intersected by the perimeter of the area are counted as half grains and these are added to the grains contained entirely within the area. The grain size may be expressed as the number of grains per square millimetre, n_A, and is given by

$$n_A = NM^2/5000 \tag{4.26}$$

where N is the number of grains counted and M is the linear magnification.

Repeat measurements on a given specimen plane may be used to obtain the

Table 4.2 Accuracy of mean linear intercept, i

Relative error ϕ (specified)	Number of intercepts required	Lower 95% confidence limit	Upper 95% confidence limit
0.010 (1%)	4900	$0.98i$	$1.02i$
0.020 (2%)	1225	$0.96i$	$1.04i$
0.025 (2.5%)	784	$0.95i$	$1.05i$
0.050 (5%)	196	$0.90i$	$1.10i$

mean and standard deviation of n_A, from which the standard error of the mean value of n_A can be evaluated.

The reciprocal of the number of grains per unit area gives the average area of intersection of the grains,

$$a_a = 1/n_A \tag{4.27}$$

Note that the mean area derived from several estimates of n_A is obtained from the mean reciprocal of n_A and not from the reciprocal of the mean value of n_A.

4.3.4 Relationships Between Grain Size Measurements

The relationships between the various measures of grain size are tabulated in ASTM Standard E112 and an abbreviated version is shown in Table 4.3. The mathematical bases for these relationships are essentially based upon spherical grains and circular areas of intersection by the intersecting (metallographic) plane.

Given the ASTM Grain Size Number, G, as the basis for comparison, the average area of intersection of the grain, a_a, can be obtained directly from the definition of G

$$n = 2^{G-1}$$

where n is the number of grains per square inch at a magnification of $\times 100$ diameters, i.e. the number of grains per 10^{-4} square inches without magnification. Thus there are $n \times 10^4$ grains per square inch and $n_a = n \times 10^4/25.4^2$ grains per square millimetre ($15.5n$ grains per square millimetre). Thus

$$a_a(\text{mm}^2) = (15.5 \times 2^{G-1})^{-1} \tag{4.28}$$

Table 4.3 Conversion table for mean linear intercept, mean areal intercept, and the ASTM grain size number (abbreviated from ASTM E112). The calculated number of grains per unit volume and the Feret diameter are also given

ASTM Grain Size No. G	Nominal Diameter d_n (μm)	Feret Diameter D_f (μm)	Mean Linear Intercept l (μm)	Ave. Area of Plane Section a (μm²)	No. per Unit Volume (mm⁻³)
0	360	403	320	129000	17
1	250	285	226	64500	49
2	180	202	160	32300	138
3	125	143	113	16100	391
4	90	101	80	8070	1105
5	64	71	56.6	4030	3126
6	45	50	40	2020	8842
7	32	36	28.3	1008	25010
8	22	25	20	504	70750
9	16	18	14.1	252	200000
10	11	13	10	126	566000
11	8	8.9	7.1	63	1600000
12	5.6	6.3	5	31.5	4527000
13	4	4.5	3.5	15.8	12800000
14	2.8	3.2	2.5	7.7	36200000

The mean linear intercept is derived from the average grain intercept area by assuming a circular grain of average area, having a diameter d'. The mean linear intercept is defined by the quotient of the area of the circle to the diameter, d', i.e.

$$i = \pi d'^2/4d' = \pi d'/4 \tag{4.29}$$

$$\text{and as} \quad d' = (4a_a/\pi)^{1/2} \tag{4.30}$$

$$\text{then} \quad i = (\pi a_a/4)^{1/2} \tag{4.31}$$

The Feret diameter of the grain section is defined as the distance between two parallel lines, tangential to opposite edges of the grain section, that are parallel to the line of intersection used in measuring the mean linear intercept. This is illustrated in Fig. 4.7. For a polygonal area of intersection, the Feret diameter can vary slightly depending on the orientation of the intersection line with respect to the corners of the polygon, but for an assumed circular grain, the Feret diameter is in fact the diameter of the grain of average area, i.e. $d_f = d'$. The value of d' has already been defined in terms of the area in Equation (4.30).

Table 4.3 also shows a nominal diameter, d_n, defined as the geometric mean of the Feret diameter and the mean linear intercept

$$d_n = (d_f i)^{1/2} \tag{4.32}$$

which from Equations (4.30) and (4.31) give

$$d_n = a_a^{1/2} \tag{4.32a}$$

The significance of the nominal diameter is unclear and is only included here to explain the definition as given in ASTM Standard E112. If the grains were obviously non-equiaxed, the nominal diameter would be the diameter of a spherical grain of the same area as the non-equiaxed grain.

The mean linear intercept derives not only from an intersecting line on the

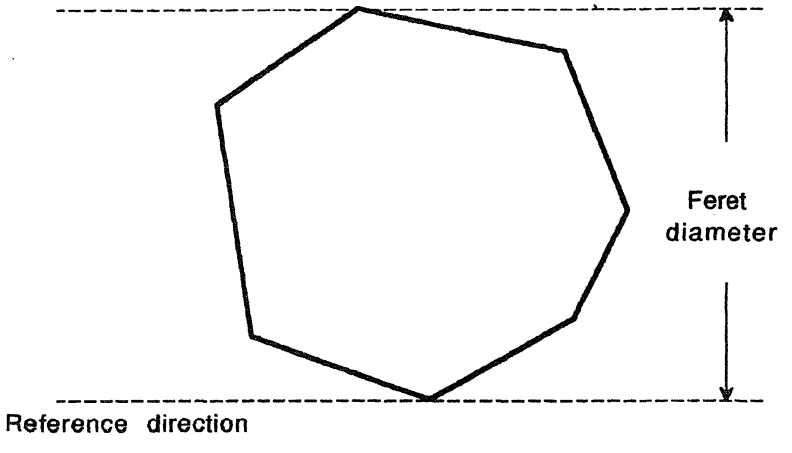


Fig. 4.7 Illustration of the Feret diameter of the polygonal planar intersection of a grain.

prepared surface, but also as a selected intersecting line through the volume of the metallographic sample. The definition of the mean linear intercept for the 3-D assembly of grains is the quotient of the volume of the grain and the projected area of the grain. The projection is made along the axis parallel with the intercepting line onto a surface normal to this direction. If a spherical grain is assumed, the mean linear intercept can be defined as

$$i = (\pi d^3/6)/(\pi d^2/4) = 2d/3 \tag{4.33}$$

Thus d, the 3-D grain diameter, not to be confused with the diameter, d', of the grain of average area in the metallographic intersecting plane, can be obtained from

$$d = 3i/2 \tag{4.34}$$

The volume of a grain having the average diameter, d, can be obtained on the assumption that the grain is spherical and the reciprocal of the volume expresses the number of grains per unit volume shown in Table 4.3.

Finally, the mean linear intercept, i, of a 3-D array of space-filling grains can be used to define the surface area of grain boundaries per unit volume, S_v, of the polycrystalline material from

$$S_v = 2n_i = 2/i \tag{4.35}$$

where i is the mean linear intercept averaged over the three principal directions, or in the case of an equiaxed grain structure, averaged in any one direction, and n_i is the reciprocal of the mean linear intercept, i.e. the corresponding number of grains per unit length.

These methods underpin the estimates of 'grain size' used in the correlation with mechanical properties as outlined in Chapter 2. It is clear from the above discussion that the direct measures of 'grain size', whether this is the mean linear intercept or the mean areal intercept, may require some assumptions in order to relate these measures to the actual grain size, and the common assumption for the conversion to 'grain diameter' is that the grains are, to all intents and purposes, spherical. Such conversions are those shown in Table 4.3. However, it is interesting to examine the corresponding conversions if the grains are assumed to be polyhedral, rather than spherical.

4.4 INTERSECTIONS OF POLYHEDRAL GRAINS

The quantitative methods of measuring grain sizes are based on either the mean areal intercept or the mean linear intercept. Even the comparator method of obtaining ASTM grain size numbers is mathematically related to the mean areal intercept as shown in the previous section. However, work has been carried out, using stereological principles, to relate these measures to the 3-D 'grain size', when the grain shape is polyhedral rather than spherical. The first problem that emerges is the definition of the grain size. Whilst the size of a sphere is uniquely defined by

the diameter, there are several measures that may be used in the case of a polyhedron. For example, diagonally opposite faces or diagonally opposite corners may be used, each of which may have one or more values. The tetrakaidecahedron has a distance between opposite square surfaces that is larger than the distance between opposite hexagonal faces, although these are geometrically related. Thus the definition of 'grain size' needs to be specific. A further possible measure that avoids the specific geometry and enables unlike polyhedra to be compared is the volume of the polyhedron or the diameter of a sphere having the same volume as the polyhedron. In the following consideration of areal and linear intercepts, the relationships between the mean intercept and measures of the spatial size will be illustrated.

4.4.1 Mean Areal Intercept

The distribution of areal intercepts of a given body has been considered by Hull and Houk[11] and by Malinski *et al.*[12] Hull and Houk used wire frame models of various polyhedra that could be tilted, rotated and elevated. Characteristics of the area intersected by a given reference plane included the number of edges and the area of intersection. These measures were made at various heights of the intersecting plane with respect to the position of the polyhedra at each angle of tilt and at each angle of rotation. The selection of angles of tilt and rotation were aimed at giving a uniform coverage of all possible angles of intersection between the plane and the polyhedron. Of particular interest in their work were the results for the cube, the pentagonal do-decahedron and the tetrakaidecahedron. The distribution of areas of intersection for these shapes are shown in Fig. 4.8, the areas being normalised in terms of the maximum possible area of intersection for the given polyhedron. All of these distributions are characterised by a high occupancy of the smaller size classes at $A/A_{max} < 0.2$ and by a significant peak in the region of $0.7 < A/A_{max} < 0.9$, the exact position of the peak depending upon the particular polyhedron being considered. In the case of the cube, the sharp increase in frequency of occurrence at $A/A_{max} = 0.7$ can be related to the area of the square face of the cube and reflects the high spread of intercept orientations which give rise to approximately square intercepts. A similar peak was observed when only 4-sided intercepts were considered.

The position of the peak might be expected to move to higher values of A/A_{max} as the number of faces of the polyhedron is increased. In the limit, a sphere, which can be considered as a polyhedron with an infinite number of faces, gives the highest frequency at A_{max}. However, this is clearly not true of the pentagonal do-decahedron (12 faces) and the tetrakaidecahedron (14 faces), the peaks occurring at 0.85–0.90 and 0.80–0.85 respectively. This may well reflect the greater uniformity of the pentagonal do-decahedron compared with the irregular faces and angles of the tetrakaidecahedron.

The distributions shown in Fig. 4.8 can be used to give the mean area of intersection, A_a, of each of the various polyhedra relative to the maximum area of intersection. These were given by Hull and Houk as follows

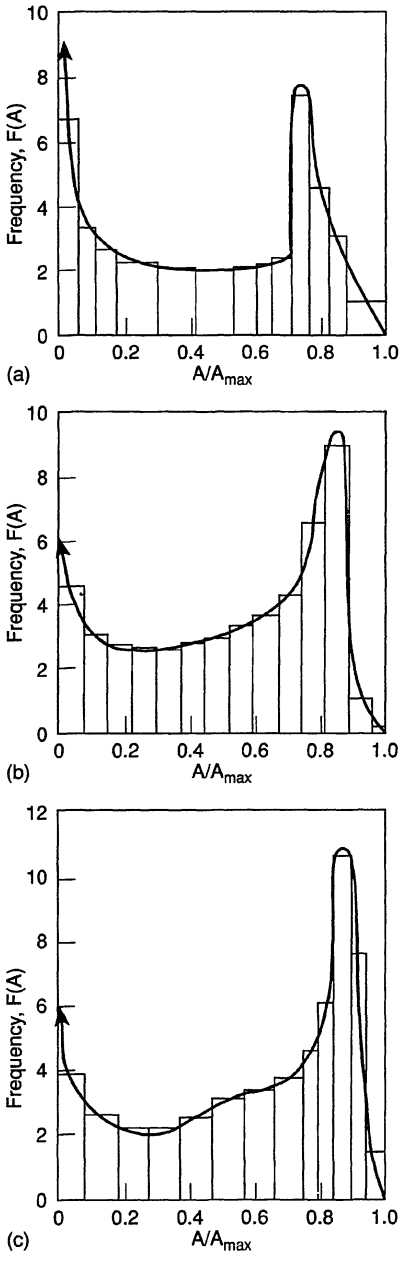


Fig. 4.8 Frequency distribution of the areas of intersection for various polyhedra: (a) cube; (b) tetrakaidecahedron; (c) pentagonal do-decahedron. After Hull and Houk.[11]

	A_{max}/A_a	A_a/A_{max}
Cube	2.14	0.467
Tetrakaidecahedron	1.83	0.546
Pentagonal do-decahedron	1.69	0.592
Sphere	1.50	0.667

These values of A_a/A_{max} enable the maximum area of intersection of a shape to be evaluated from the mean areal intercept, A_a, which is obtained from $1/n$, where n is the number of grains per unit area. It should be noted that this procedure assumes a grain shape and also that variations in areal intercepts derive from random sections of that same shape. If only one size is present in a 3-D array of such shapes, the distribution of areas would conform with the appropriate distribution in Fig. 4.8. If a range of sizes existed, then the maximum intercept area would represent the weighted average of the range.

The conversion of a mean area of intersection to a maximum area of intersection, although giving a measure that is directly related to the 3-D size of the polyhedron, does not give a readily understood measure. For example, the maximum area of intersection of a cube is along the (110) plane, and is given as $A_{max} = \sqrt{2}\, e^2$ where e is the cube edge. Thus the volume of the cube in a uniform array of cubes can be obtained from the mean areal intercept, A_a, from

$$V_{cube} = e^3 = (2.14A_a/\sqrt{2})^{3/2} = 1.861A_a^{3/2} \tag{4.36}$$

whilst the diameter of a sphere having the same volume as the cube, d_{eq}, is given by

$$d_{eq} = (6/\pi)^{1/3}V_{cube}^{1/3} = 1.516A_a^{1/2} \tag{4.37}$$

Similarly for the tetrakaidecahedron, the maximum area of intersection includes the diagonals from opposite edges of opposite square faces, and is given by $A_{max} = 7e^2$ where e is the edge length of the square face (which is equal to all the other edge lengths of the tetrakaidecahedron). The volume of a tetrakaidecahedron, V_{tkdh}, given by Rutherford *et al.*[13] can be expanded to give

$$V_{tkdh} = 8\sqrt{2}e^3 = 8\sqrt{2}(1.83A_a/7)^{3/2} = 1.512A_a^{3/2} \tag{4.38}$$

The diameter of the sphere having this same volume

$$d_{eq} = 1.424A_a^{1/2} \tag{4.39}$$

To complete the consideration of the relationships between mean areas of

intersection, volume and equivalent diameter, the commonly used shape is the sphere. The volume of the sphere, V_{sph}, of diameter, d, is

$$V_{sph} = \pi d^3/6$$

$$A_{max} = \pi d^2/4$$

$$A_{max}/A_a = 1.5$$

$$\text{Thus} \quad V_{sph} = (4A_{max}/\pi)^{3/2}\pi/6 = (6A_a/\pi)^{3/2}\pi/6 = 1.382A_a^{3/2} \tag{4.40}$$

$$\text{and} \quad d_{eq} = d = 1.382A_a^{1/2} \tag{4.41}$$

The main features of these relationships are given in Table 4.4. In general, the shapes with fewer faces show a larger maximum intersection, volume and equivalent diameter for a given average areal intercept, the exceptions to this generality being related to the uniformity of the shape, as pointed out earlier for the pentagonal dodecahedron and the tetrakaidecahedron. The volume of a tetrakaidecahedron for a given mean areal intercept is about 10% larger than that of a sphere having the same mean areal intercept. The equivalent diameter differs by only about 3% with these shapes for a given mean areal intercept. The differences between the cube and the sphere are much greater, being about 35% for volume and 10% for the equivalent diameter.

The selection of a shape for the grain is not necessarily arbitrary. For example, spherical grains do not comply with space-filling requirements, whilst cubes, although space filling, cannot meet with the surface tension requirements of three grains meeting at an edge and four grains meeting at a corner. The pentagonal dodecahedron, although having angles close to those required for surface tension (for example, corner angles of 108° compared with the 109°28′ of the minimum energy configuration), does not comply with the space-filling requirements. The tetrakaidecadedron fills space, and the angles approach those required by the minimum energy configurations for edges and corners.

In real granular arrays or froths, it is not necessary for all grains or bubbles to be of the same size or shape, as shown in Fig. 4.6. As discussed earlier, experimental evidence has shown that grains have *approximately* 14 faces, and most commonly have 5-sided interfaces. Thus the grains would approximate the tetrakaidecahedron or the pentagonal dodecahedron in shape, but could be irregular, and be of different shapes. The cube, with its six faces, would obviously be inappropriate,

Table 4.4 Stereological conversions from mean areal intercept

Shape	No. of faces	Volume	A_{max}	A_{max}/A_a	Volume	d_{eq}
Cube	6	e^3	$\sqrt{2}e^2$	2.14	$1.861A_a^{3/2}$	$1.526A_a^{1/2}$
TKDH	14	$8\sqrt{2}e^3$	$7e^2$	1.83	$1.512A_a^{3/2}$	$1.424A_a^{1/2}$
Pentagonal dodecahedron	12	–	–	1.69	–	–
Sphere	∞	$\pi d^3/6$	$\pi d^2/4$	1.5	$1.382A_a^{3/2}$	$1.382A_a^{1/2}$

e is edge length of the polyhedron. A_a is mean areal intercept.

and the tetrakaidecahedron would equally obviously give a closer approximation. It is clear from Table 4.4 that the assumption of a tetrakaidecahedral grain would give approximately 10% fewer grains per unit volume for a given number per unit area than would be obtained from the assumption that the grains are spherical. The difference in equivalent diameters, however, between the two assumptions is quite small, of the order of 3%. Because of the small difference, and because all of the quantitative microstructural work for structure–property relationships has been derived from the assumption of spherical grains, it is considered that the spherical assumption gives a reasonable approximation and its future use is recommended. For the pedantic, the conversion factor for the equivalent diameter of polyhedral (TKDH) grains is shown in Table 4.4. It is worth remembering, however, that the equivalent diameter is the diameter of a sphere having the same volume as that of a tetrakaidecahedron with a mean linear intercept equal to that observed experimentally. It cannot be regarded as a mean diameter of grains of different shapes and sizes. Given that grains of different shapes and sizes exist in real metals, there is no other completely analytical method of characterising the grain size distribution.

The value of the equivalent diameter of the tetrakaidecahedron obtained from the mean areal intercept is dependent on the distribution of areal intercepts given by Hull and Houk.[11] More recently, Malinski *et al.*[12] have published results for the areal intercept distribution of the tetrakaidecahedron (described as the truncated octahedron). Direct comparison of these frequency distributions is difficult due to the differences in class size, both between and within these works, but the normalised cumulative frequency distribution is easily computed and is independent of the class sizes. A comparison of the results by Hull and Houk with those of Malinski *et al.* is shown in Fig. 4.9. Although the distributions differ slightly, there is sufficiently close agreement, particularly in the occurrence and position of peaks in the frequency distribution (indicated by changes in the slope of the cumulative frequency curve), to give considerable confidence in the value of A_{max}/A_a derived in the Hull and Houk paper for the tetrakaidecahedron.

4.4.2 Mean Lineal Intercept

The mean lineal intercept (often referred to as the mean linear intercept) is the most commonly used quantitative measure of grain size in the ferritic or ferrite–pearlite structures found in plain carbon and microalloyed steels. The errors associated with the measurement of mean linear intercept have been described (see Table 4.2). Again, the calculation of a grain diameter from a linear intercept measurement is usually based on the assumption of spherical grains.

The lineal intercept distribution in polyhedral grains has been considered[14] by the author. The intercept lengths in various polyhedra (tetrahedron, cube and tetrakaidecahedron) were assessed by computer methods. The polyhedron was established in terms of the 3-D co-ordinates of the corners, and equations for the faces, and a square grid array of parallel linear intersecting lines were used to establish the distribution of the length of the intersections between the point of entry to, and the point of exit from, the polyhedron. The polyhedron was tilted by

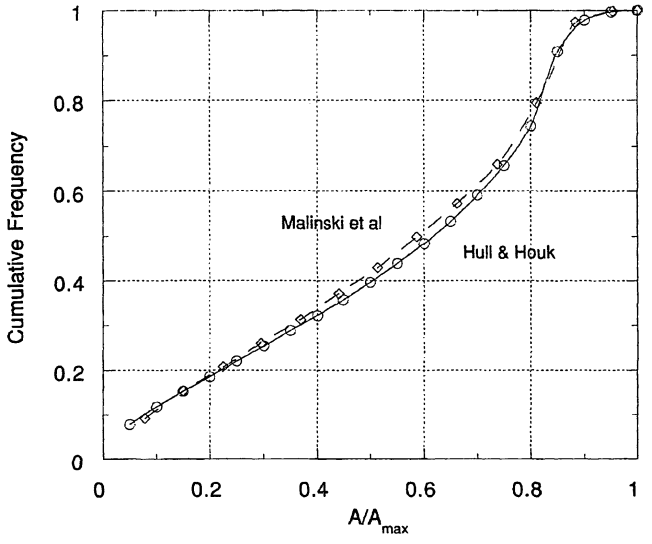


Fig. 4.9 The cumulative frequency distribution of areas of intersection for the tetrakaidecahedron. The results of Hull and Houk[11] and Malinski *et al.*[12] show close agreement.

an angle, ϕ, and rotated by an angle, θ, and the intersection process repeated. The tilt angles were increased uniformly (at about 5° intervals) from the polar position to near equatorial positions, i.e. up to almost 90°. The rotation angle, θ, was increased at about 5° intervals up to almost 90°, when the tilt angle was near 90°. The number of θ values at lower values of ϕ was reduced sinusoidally towards the polar position ($\phi = 0°$) so that a uniform density of intercept orientations was produced on the surface of the polyhedron over the quadrant considered. Due to the symmetry of the chosen shapes, the distribution of intercepts in the quadrant is merely repeated when the range of possible intercept orientations over the whole of the spherical surface is considered. In order to avoid unfortunate geometric coincidences between the dimensions of the polyhedron and the spacing of the rectangular grid of intersecting lines, the geometric centre of the polyhedron was displaced with respect to the origin of the grid of intercepts by a small fraction of the grid size, and the intercept length distribution repeated over all orientations of the polyhedron. Thus, with some 200 orientations, approximately 200 intersecting lines per orientation, and 6 or 7 origin shifts, a total of some 250 000 intercept lengths were generated for each polyhedron. The intercept lengths thus generated were classified into a system of 60 uniform class intervals covering the range of possible intercept lengths. The distribution of intercept lengths are shown as frequency distributions in Fig. 4.10. The corresponding distribution of intercept lengths for a sphere is also shown.

The purpose of obtaining these frequency distributions is to relate the mean intercept length to the maximum intercept length and thence to the volume of the polyhedron and the equivalent diameter of a sphere of equal volume. The main

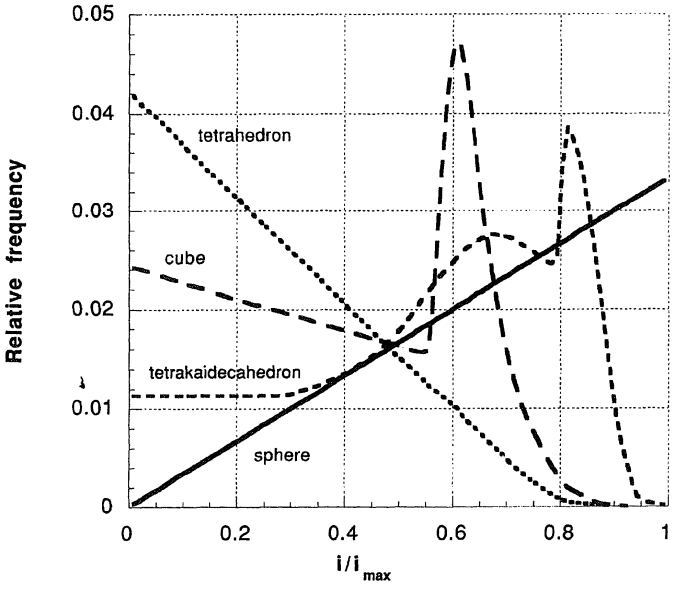


Fig. 4.10 The distribution of intercept lengths for the tetrahedron, the cube and the tetrakaidecahedron. The distribution of intercept length for the sphere is shown for comparison.

stereological conversion factors for the various polyhedra are given in Table 4.5. Information on the sphere is also given for comparison. The first four columns of Table 4.5 give the shapes of the bodies and the geometrical features of these, i.e. the number of faces, the volume defined in terms of the edge length of the polyhedron, and the maximum intercept length of the polyhedron, again expressed in terms of the edge length. For the sphere, with its hypothetically infinite number of faces of infinitely small size, the diameter is used to derive the volume and maximum intercept length, i_{max}. The volume of each of the bodies considered here can be expressed in terms of the maximum intercept length. Taking the cube, for example, i_{max} is given as $\sqrt{3}e$ (column 4) and the volume can therefore be expressed as $(i_{max}/\sqrt{3})^3$. From the frequency distributions of the intercept lengths, the relationship between the mean linear intercept, i, and the maximum intercept length is given by $i = 0.387\ i_{max}$ (column 5), and the volume can therefore be

Table 4.5 Stereological conversions from mean linear intercept

Shape	No. of faces	Volume	i_{max}	i/i_{max}	Volume	d_{eq}
Tetra-hedron	4	$e^3/8$	e	0.265	$6.70i^3$	$2.34i$
Cube	6	e^3	$\sqrt{3}e$	0.387	$3.31i^3$	$1.85i$
Tetrakai-decahedron	14	$8\sqrt{2}e^3$	$\sqrt{10}e$	0.546	$2.19i^3$	$1.61i$
Sphere	∞	$\pi d^3/6$	d	0.667	$1.77i^3$	$1.50i$

e is the edge length of the polyhedron. i is the mean linear intercept.

expressed as $(i/0.387\sqrt{3})^3$ or $3.31i^3$ as indicated in column 7. The equivalent diameter given in column 8 is the diameter of a sphere having the same volume as that of the cube derived from the observed mean linear intercept.

Thus, for given mean intercept length the tetrahedral grain would require a much larger volume ($6.70\ i^3$) than the sphere ($1.77\ i^3$) with the grain volume generally decreasing as the number of polygonal sides on the polyhedron is increased. Alternatively, for a given grain volume, the intercept length of say the tetrahedron, i_t, would be much less than that of the spherical grain, i_s, as defined by $6.70\ i_t^3 = 1.77\ i_s^3$ or $i_t = (1.77/6.70)^{1/3}\ i_s$.

The intercept lengths of the tetrahedron and cube were considered merely to illustrate the effects of the sharpness of the edges and corners. Hull and Houk expressed this in terms of the radii of inscribed and circumscribed spheres. The larger the difference between these two measures, the sharper are the edges and corners. An alternative measure of the protrusion of the corners of the polyhedron can be obtained from the ratio of the distance of the corner of the polyhedron from the centre of the polyhedron to the radius of the sphere of equivalent volume. These ratios are

Tetrahedron	1.974
Cube	1.396
Tetrakaidecahedron	1.135

The corner of the tetrahedron is almost twice the distance from the centre as the radius of a sphere of the same volume. The projection of the corners decreases as the number of faces increases, and the mean intercept lengths reflect the protrusion of the corners, the mean linear intercept increasing (for a given grain volume) as the protrusion of the corners decreases. The evaluation of these factors for the various polyhedra in no way implies that metal grains in a polycrystalline metal actually have a particular shape. As indicated by the experimental evaluation of the average number of edges on polygonal grain faces, the average of $5\frac{1}{9}$–$5\frac{1}{7}$ suggests that the metal grains have about 14 faces. The individual experimental observations however, showed a wide range in the number of edges per face ranging from 3 to 7, clearly indicating less regular arrangements than would be obtained from the tetrakaidecahedron. These observations, coupled with the nucleation and growth origins of most of the granular structures of metals, indicate that grains with different shapes, having irregular arrangements of faces, are to be expected. Differences in real grain sizes within the polycrystal could be accommodated by a procedure similar to that developed by Scheil,[15] to give the 3-D spherical size distribution from the observed diameters of circles of intersection, but using the frequency distribution appropriate to a polyhedral grain such as the tetrakaidecahedron.

The relative frequency factors for a Scheil type of table with up to 10 class intervals for the linear intercepts is shown in Table 4.6. The number of experimentally observed intercepts in the tenth class interval is multiplied by the relative frequency factors for the ninth, eighth, seventh etc. class intervals to assess the numbers of small intercept lengths that have arisen as a result of intersecting the largest grains at positions giving smaller intercept lengths. The

Table 4.6 Relative frequency factors for linear intersections of the tetrakaidecahedron for data with up to 10 class intervals. The conversion from classified intercept lengths to the spatial size distribution is carried out by the same procedure as described by Scheil[15]

Class	0 – 1	1 – 2	2 – 3	3 – 4	4 – 5	5 – 6	6 – 7	7 – 8	8 – 9	9 – 10
9 – 10	5.0	5.0	5.0	5.4	6.8	9.4	11.7	11.3	12.5	1.00
8 – 9	3.3	3.3	3.4	3.9	5.3	7.4	7.8	8.6	1.00	–
7 – 8	2.24	2.24	2.34	2.97	4.4	5.3	5.9	1.00	–	–
6 – 7	1.51	1.60	1.58	2.42	3.48	3.91	1.00	–	–	–
5 – 6	1.03	1.04	1.31	2.13	1.69	1.00	–	–	–	–
4 – 5	0.73	0.77	1.19	1.70	1.00	–	–	–	–	–
3 – 4	0.65	0.77	1.42	1.00	–	–	–	–	–	–
2 – 3	0.58	0.96	1.00	–	–	–	–	–	–	–
1 – 2	0.59	1.00	–	–	–	–	–	–	–	–
0 – 1	1.00	–	–	–	–	–	–	–	–	–

sum of these gives the total number of grains that properly belong to the largest class interval. These individual class values are then subtracted from the experimentally observed distribution of intercept lengths and the whole process is repeated for grains with a maximum intercept length in the ninth class interval, and so on until the spatial distribution of maximum intercept lengths is obtained. One of the major problems with this procedure is that small errors in the largest class interval can be magnified for smaller intersections due to the relatively low frequency of occupation of the largest intercept size. If other ranges of class interval are required, then the appropriate multiplying factors can be obtained from the cumulative frequency distribution of intercept lengths for the tetrakaidecahedron shown in Table 4.7. A comparison of the cumulative frequency curves for the tetrakaidecahedron and the sphere is shown in Fig. 4.11. Division of the abscissa into the required number of class intervals will show the relative frequencies to be expected for these class intervals on the ordinate.

If the polycrystalline metal contains grains of widely differing shapes (e.g. with some mixed tetrahedra), the selection of an appropriate intercept distribution could be problematical. However, if the average number of faces per grain is approximately 14, then the selection of the tetrakaidecahedron and its intercept distribution may provide a reasonable approximation of the polycrystalline metal,

Table 4.7 Data for the cumulative frequency curve of intercept lengths for a tetrakaidecahedron

i/i_{max}	Cumulative frequency	i/i_{max}	Cumulative frequency
0.05	0.034	0.55	0.430
0.10	0.068	0.60	0.500
0.15	0.102	0.65	0.578
0.20	0.136	0.70	0.660
0.25	0.170	0.75	0.740
0.30	0.204	0.80	0.815
0.35	0.240	0.85	0.924
0.40	0.278	0.90	0.986
0.45	0.322	1.95	0.999
0.50	0.371	1.000	1.000

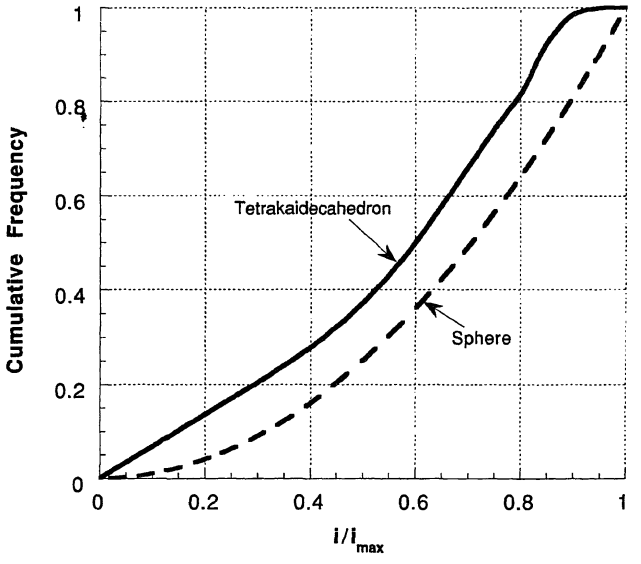


Fig. 4.11 Cumulative frequency distribution of linear intercepts for the tetrakaidecahedron. The cumulative frequency distribution for the sphere is also shown.

and would certainly give a better estimate of the grain size than would be obtained from the spherical intercept distribution.

The difference in equivalent diameter for the sphere and the tetrakaidecahedron is only of the order of 8%, and if such differences are acceptable, the spherical approximation has the advantage of producing results that are comparable with all earlier published works that have almost unequivocally used the spherical approximation. Whichever measure of 'grain size' is used, it is important to *define* the measure and the method of derivation, in order to avoid confusion, as for example in assessing the value of k_y in the Hall–Petch relationship.

4.5 GRAIN GROWTH

Grain growth is a cannibalistic process. In any body of metal, the growth of certain grains must be accommodated by the shrinkage and ultimate disappearance of other grains, due to the conservation of mass. The question of which grains grow and how many grains are growing is generally dependent upon the size of the grains. It is generally accepted that large grains will grow and small grains will shrink and be consumed. The reason for grain growth is the reduction in energy of the polycrystal. Each grain boundary is a region of high distortion as atoms at the grain boundaries take positions that represent compromises between the requirements of two mismatching lattices of the contiguous grains. The high energy states of the grain boundary atoms gives rise to the concept of grain boundary energy. An increase in the average size of the grains in a given body of

metal reduces the grain boundary area and thus reduces the grain boundary energy.

Considering the tetrakaidecahedral grain shape, the surface area A and volume V are given by

$$A = (6 + 12\sqrt{3})e^2$$

$$\text{and} \quad V = 8\sqrt{2}e^3$$

where e is the edge length of the tetrakaidecahedron. As each surface in the stacked array of grains is shared by two grains, the grain boundary area per unit volume (A_v) of the array is one half of the area per unit volume of the single tetrakaidecahedron, i.e.

$$A_v = (6 + 12\sqrt{3})/(16\sqrt{2}e) = 1.184/e \tag{4.42}$$

Thus the area per unit volume changes inversely as the edge length for the tetrakaidecahedron, or indeed, with any other linear dimension of the tetrakaidecahedron.

The driving force for grain growth is thus the reduction in grain boundary energy that accompanies the decrease in grain boundary area. Considerable effort has been devoted to the measurement of grain boundary energies, and to the theoretical prediction of grain boundary energies. The precise nature of a grain boundary is defined by the relative orientations of the atomic lattices of the neighbouring grains, in terms of both tilt and twist, and also the plane of the grain boundary with respect to the lattices.[16] The grain boundary energy per unit area is known to vary depending upon the nature of the grain boundary, and thus a given change in area of grain boundary (see Fig. 4.3) is not necessarily equivalent to the change in energy. However, the grain boundary energies vary only slightly over a wide range of misorientations of contiguous grain lattices, and only near coincident boundaries showed marked decreases in the boundary energy, resulting in relatively sharp cusps in the grain boundary energy versus misorientation relationships. On the basis of random misorientations across grain boundaries, it would be expected that the majority of grain boundaries would have similar energies. It has already been demonstrated that any grain in a 3-D polycrystal will have on average, 14 interfaces with 14 neighbouring grains, and thus the majority of these boundaries would be expected to have similar energies. Some experimental evidence is available to support this view from the work of Watanabe *et al.*[17] who found more than 80% of 'random' boundaries in an annealed Fe–3%Si alloy.

With the above reservation in mind, it is possible to consider that Equation (4.42) could be written as

$$E_v = \gamma A_v = 1.184\gamma/e \tag{4.43}$$

where E_v is the grain boundary energy per unit volume and γ is the grain boundary energy per unit area

Given that the grain boundary energy per unit volume is decreased by having larger grains, there is a question of which grains should grow and which should

disappear, because any grain size changes must of necessity conserve the volume of material. There have been many approaches to the driving force for the growth of a specific grain in a polycrystalline array. These include

(i) Topological considerations (angle driven)
(ii) Grain boundary curvature driven
(iii) Direct boundary energy changes
(iv) Stochastic approaches dealing with grain size distributions

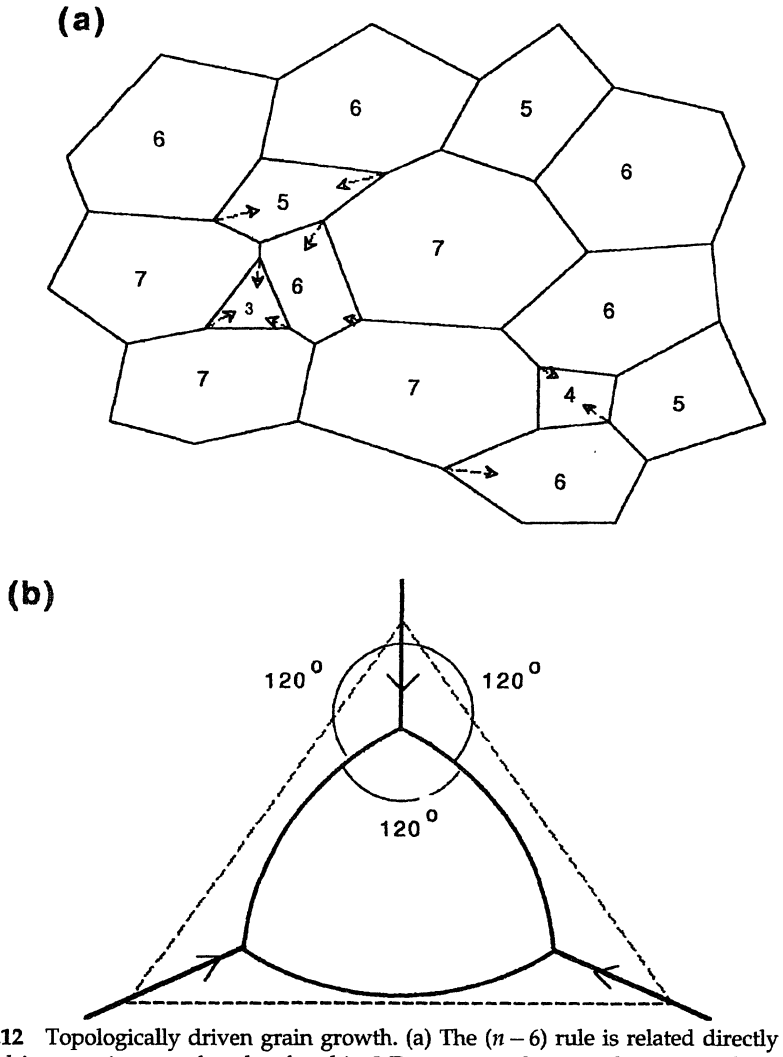


Fig. 4.12 Topologically driven grain growth. (a) The $(n-6)$ rule is related directly to the angle-driven grain growth rules for this 2-D system, where angles approach 120°. (b) Shrinkage of a tetrahedron by migration of corners and edges to maintain 120° angles at grain edges and 108° grain corners in this 3-D system.

4.5.1 Topological or Angle Driven Growth

The topologically based theories have commonly been applied to 2-D models, where the angles and grain shapes are simpler and more easily treated. Grain corners in the 2-D array are assumed to be in equilibrium when they attain 120°. Thus, in 3-, 4- and 5- sided polygons, the corners will move towards their centres, whilst for 7-, 8-, etc. sided polygons, the corners would move away from their grain centres. The driving force for corner movement is thus proportional to $n-6$; when $n > 6$, the 2-D grain will 'grow', and when $n < 6$, the 2-D grain will shrink. Such an argument should of course only be applied to equiaxed grains. These movements are illustrated in Fig. 4.12(a), where the consequential curvature of the 2-D grain edges is readily apparent.

The same kind of argument can be applied to a 3-D array of polyhedral grains, except that, in this case, the angles between the three grain faces meeting at a grain edge should approach 120°, and the angles between the four grain edges meeting at a grain corner should approach 108°. Unlike the 2-D model with its hexagonal equilibrium shape, there is no equilibrium polyhedron for the 3-D model, as discussed earlier. The principle however can be illustrated for the tetrahedral grain. The corner angles are 60°, and the angle between faces meeting at an edge is 70°32′, so that the corners and edges, provided that they comply with the energy requirements of three grains meeting at an edge and four grains meeting at a corner, will move towards the centre of the tetrahedron causing grain shrinkage. Conversely, a convex polyhedron with many more than 14 sides will have very obtuse edge angles, and corner angles approaching 120°. Thus corners and edges would move away from the centre of the convex polyhedron, causing grain growth. Such movements would give rise to curved surfaces on both the tetrahedron, Fig. 4.12(b), and the multifaceted convex polyhedron, the difference being that the surfaces are convex on the tetrahedron but concave on the multifaceted convex polyhedron. Difficulties arise with irregular polyhedra where some edges and corners should move towards the centre whilst others move away from the centre (as would be the case for the tetra-kaidecahedron), giving a double curvature of certain surfaces but with zero mean curvature.[1]

The application of this concept leads to a growth or shrinkage rate given by[1,18,19]

$$da/dt = M_b \sigma_b \pi (n-6)/3 \tag{4.44}$$

where M_b is the boundary mobility, σ_b is the grain boundary energy and da/dt is the rate of change of the area of the 2-D grain in the polycrystal

A shortcoming of this theory is that the rate of growth appears to be simply defined by the growing (or shrinking) grain with a complete neglect of the character of neighbouring grains which are bound to be affected by the growth or shrinkage.

4.5.2 Curvature Driven

A consequence of the local equilibrium established at grain corners or grain edges, as a result of local surface energy considerations, is the development of curved

surfaces, as depicted in Fig. 4.12 for the various 2-D polygons and the tetrahedron. It is clear from Fig. 4.12 that a further reduction in the area of grain boundaries is easily attained if the curved surface flattens, i.e. the centre of the face migrates to a position in the plane of the corners. The boundary migration will occur towards the centre of curvature (Fig. 4.13), but in so doing will obviously upset the local low energy equilibrium at the grain corners and edges. This gives a clear indication that the local minimum energy attained at corners and edges, when the angles are 109°28′ between edges, and 120° between faces respectively, is not a sufficient definition of the minimum energy of the total system. Rather, it is a stage in the progressive development of an inherently unstable system.

A simple illustration of the energy reduction caused by the grain boundary flattening is shown in Fig. 4.14 for the 2-D case. It should be noted that the migration of the boundary towards the centre of curvature as indicated in the diagram is accompanied by a decrease in the boundary length between the triple points. This same motion increases the radius of curvature of the boundary and therefore decreases the driving force for grain boundary movement. In this type of curvature-driven grain growth, the radius of curvature increases as the boundary flattens, and should not be confused with the radius of the disappearing grain, which would decrease as the boundary moved, thus increasing the driving force. Qualitatively, boundary flattening will give rise to boundary area and energy reductions in the 3-D model.

The boundary-flattening process, although reducing the boundary energy of the arrays, by reducing the grain boundary length in 2-D models and grain boundary

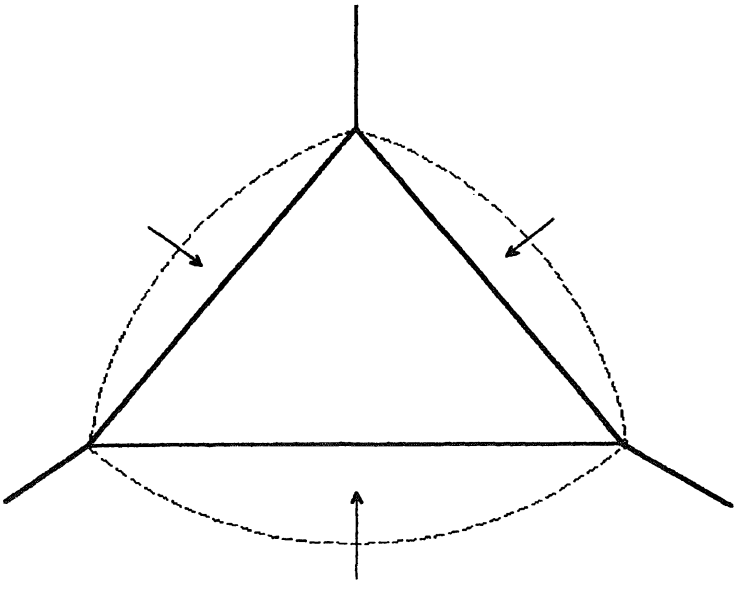


Fig. 4.13 Curvature driven grain boundary movement. Flattening of edges in 2-D and faces in 3-D systems reduces the total grain boundary energy by reducing the length or area of the boundary.

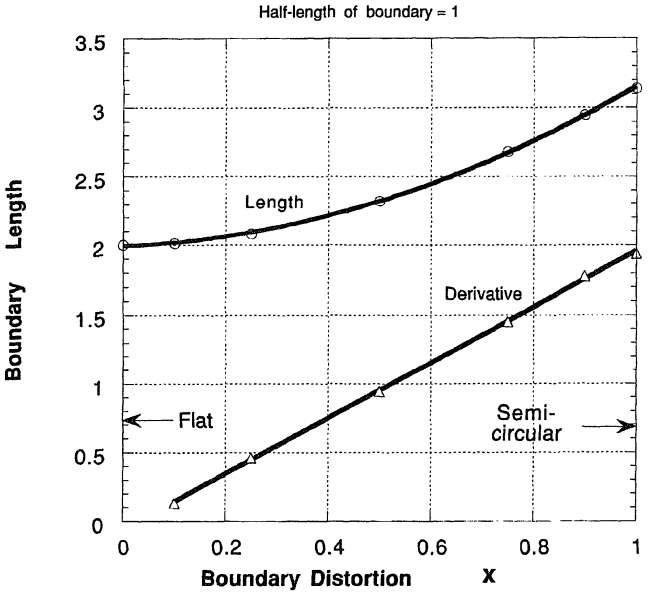


Fig. 4.14 The energy change accompanying grain boundary flattening in a 2-D system.

area in 3-D models, will restore a non-equilibrium condition at grain corners and edges, thereby enabling further changes due to corner and edge movements and the attendant development of curvature.

The combination of corner equilibrium, and curvature-driven flattening of boundaries, both of which are energy driven, give rise to a sustainable growth process, and points to the development of the much broader energy change theories developed by Hillert[20] and Gladman.[21] However, before proceeding, some of the assumptions implicit in the above treatment need to be addressed. The first of these concerns the grain boundary energy. It has been assumed that all grain boundaries have the same energy. The consequences of this assumption are that boundaries will move to give 120° angles at grain edges, and 109°28′ angles between edges at grain corners. Variations in boundary energy would change the equilibrium angles, but would not invalidate the concepts of the angle-driven motion, nor of the curvature driven flattening. The second assumption is that the grain boundary energy between two grains would not change with rotation of the boundary. The migration of a grain edge or grain corner results in a minimisation of the local surface area, as does the flattening of a boundary surface. All of these processes involve the rotation of grain boundaries. If the geometric requirement of the rotation results in an increase in boundary energy per unit area, then the boundary changes could be retarded or even inhibited. However, such retardations would be counterbalanced by other rotations where the geometric requirement leads to a reduction in the grain boundary energy per unit area, which would further assist the changes; the concepts of angle-driven motion and curvature-driven flattening, although modified, are not invalidated. A third

assumption is that the grains are equiaxed and that all internal angles are approximately equal. As grains may be irregular, the particular interfaces being developed by collision between the growing crystals, then the internal angles may not be equal, giving rise to differential rates of change at different edges and corners of the same grain. Such inhomogeneities would again modify the details of the grain growth rates, but would not invalidate the general principle.

4.5.3 Energy Change Models

Hillert[20] developed a model for grain growth in which the driving force for grain growth or shrinkage was dependent on the curvature of the grain boundary, in this case equated to the radius of the grain. It was acknowledged that not all grains could grow and the concept of a critical grain radius was introduced.

$$dE/dR = k(1/R - 1/R_c) \tag{4.45}$$

where R is the radius of curvature of a grain, R_c is some critical radius of curvature, and k is a constant.

If the radius of curvature R of a particular grain exceeded a critical radius, R_c, then the energy change accompanying grain growth is suitably negative. If the radius of curvature was smaller than R_c then the energy change would be positive and the grain would not grow. Equating the radius of curvature with the grain radius clearly shows that only grains with a radius larger than some critical value will grow.

Gladman[21] considered the energy changes accompanying the growth of a large tetrakaidecahedral grain of 'radius', R, in a matrix of smaller tetrakaidecahedral grains of 'radius' R_0, see Figs. 4.15 and 4.16. The 'radius' in this instance was defined as the half distance between opposite hexagonal faces. There are two major contributions to the energy change when the large grain grows.

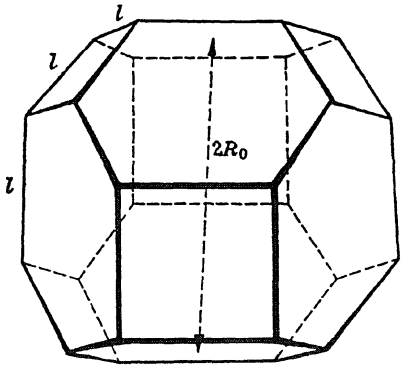


Fig. 4.15 The tetrakaidecahedron (Kelvin's 14 plane faced solid). The radius, R, is defined as the half distance between the opposite hexagonal faces, and can be equated with the radius of an inscribed sphere.

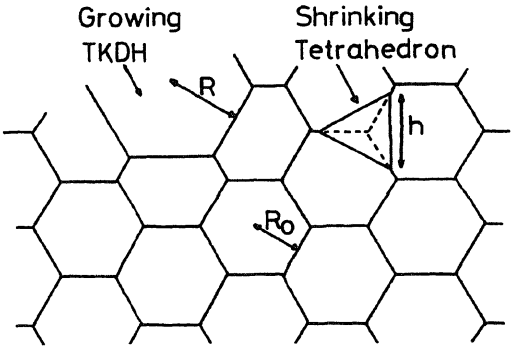


Fig. 4.16 Two-dimensional representation of a large tetrakaidecahedral grain of radius R in a matrix of smaller tetrakaidecahral grains of radius R_0. Also depicted is a small tetrahedral grain present in the structure. In three dimensions, the tetrahedron would be bounded by four tetrakaidecahedra.

(i) The boundary area of the growing grain increases, and on the assumption of a uniform boundary model, UBM, then the boundary energy of this grain increases. As the grain grows from a radius R to $R+\delta R$, so the boundary area increases from kR^2 to $k\ (R+\delta R)^2$ where k is a constant depending upon the shape of the grain (and on the definition of the 'radius' if the grain is not spherical). If the change in area or boundary energy is expressed in terms of unit area of the growing grain boundary, then

$$\delta E = (k(R+\delta R)^2 - kR^2)\gamma/kR^2 = 2\gamma\delta R/R$$

and $\delta E/\delta R=2\gamma/R$

where γ is the grain boundary energy.

In the limit as δR approaches zero, then

$$dE/dR = 2\gamma/R \tag{4.46}$$

(ii) As the grain grows into the polycrystalline matrix, then matrix grain boundaries disappear, as shown in Fig. 4.16. The grain boundary elimination process depends on the product of the volume increase of the growing grain and the density of matrix grain boundaries that existed in this added volume, and if this is again expressed as a driving force per unit area of the growing grain, then the energy change can be added to that given by Equation (4.46).

The grain boundary area (or energy) density, A_V, (or E_V), in a matrix of tetrakaidecahedral grains is given by

$$A_V = \Lambda/2V \tag{4.47}$$

where Λ is the surface area of the polyhedral grain and V is the grain volume

The factor of 2 appears in the denominator of Equation (4.47) as the matching polygonal faces of two grains constitute a single grain boundary. For the

tetrakaidecahedron, the volume, V_0, and surface area, Λ_0, given by Rutherford *et al.*,[13] can be expressed in terms of the radius of the matrix grains, R_o, (see Fig. 4.15), by

$$V_0 = k_1 R_0^3 \tag{4.48}$$

$$\text{and} \quad \Lambda_0 = k_2 R_0^2 \tag{4.49}$$

where k_1 and k_2 are constants depending upon the chosen grain shape.

Thus the area density of grain boundaries per unit volume of matrix A_V is obtained by substitution into Equation (4.47) to give

$$A_V = k_2 R_0^2 / 2k_1 R_0^3 \tag{4.50}$$

If one considers the growing tetrakaidecahedron of 'radius', R, the rate of change of volume, V, with radius, $\mathrm{d}V/\mathrm{d}R$ is

$$\mathrm{d}V/\mathrm{d}R = 3k_1 R^2 \tag{4.51}$$

giving a total area decrease of

$$(\mathrm{d}V/\mathrm{d}R)A_V = 3k_1 R^2 k_2 R_0^2 / 2k_1 R_0^3 \tag{4.52}$$

If this decrease per unit advance of the boundary is expressed as an area loss, $\mathrm{d}A_e$, per unit area of the growing grain surface

$$\mathrm{d}A_e/\mathrm{d}R = 3k_1 R^2 k_2 R_0^2 / 2k_1 R_0^3 \cdot k_2 R^2 \tag{4.53}$$

which simplifies to

$$\mathrm{d}A_e/\mathrm{d}R = 3/2R_0$$

The equivalent energy change per unit advance of the grain boundary per unit area of the advancing boundary is

$$\mathrm{d}E_e/\mathrm{d}R = 3\gamma/2R_0 \tag{4.54}$$

This simple equation holds true irrespective of the grain shape chosen; these could be cubes, spheres or any other shape. However, it should be noted that this simple equation only holds if the growing grain has the same shape as the matrix grains thus allowing cancellation of the proportionality constants k_1 and k_2. If the growing grain shape is different from the matrix grains then the factor 3/2 in Equation (4.54) has to be modified slightly and can only be regarded as an approximation. For example, if a spherical grain of radius R was growing into a matrix of tetrakaidecahedral grains of radius R_0 (as defined in Fig. 4.15), then the factor 1.5 (3/2) in Equation (4.54) would be changed to 1.45. This value is specific to the definition of R_0 and is slightly different for other definitions of R_0, as for example R_{eq} or R_{max}. Nevertheless Equation (4.54) would give a good approximation of the grain boundary area consumed per unit area of the growing grain boundary, and the approximation would still be valid if the growing grain changes shape from being tetrakaidecahedral to a shape with many more faces, in the limit reaching a virtually spherical shape.

The factor of 3 in Equation (4.54) derives from the differentiation of R^3 (giving $3R^2$), and the factor of 2 in the denominator derives from the sharing of 2 grain faces at a boundary in the polycrystal.

Summing the energy changes arising from expansion of the growing grain surface and a decrease in energy due to consumption of the neighbouring grains from Equations (4.46) and (4.54) gives the net rate of energy change, dE_n/dR.

$$dE_n/dR = (2/R - 3/2R_0)\gamma \tag{4.55}$$

This equation has interesting implications. If $R = R_0$, then the energy change will be positive and the growth of a grain of the same size as its neighbour should not occur. In fact, only when $R > (4/3)\ R_0$ would the energy change be negative, and the growth of this larger grain could then proceed. The equation is thus in accord with the general concepts of grain growth, where larger grains grow and smaller grains are consumed, and gives a physical significance to the critical radius used by Hillert.

It is of direct interest to consider the shrinkage of a small grain and the accompanying energy changes. This problem has been considered previously,[22] where consideration was given to a small tetrahedral grain bounded by four larger grains as represented (2-D) in Fig. 4.16. The collapse of a tetrahedron eliminates the four faces of the tetrahedron, but drags in the six grain faces that are connected with the edges of the tetrahedral grain, as illustrated in Fig. 4.17. The surface area of the tetrahedron, S_1, is given by[23]

$$S_1 = \sqrt{3}e_t^2 \tag{4.56}$$

where e_t is the edge length of the tetrahedron.

The total area of the six surfaces between the six edges and the centroid of the tetrahedron, S_2, created when it shrinks, is given by

$$S_2 = 3e_t^2/2\sqrt{2} \tag{4.57}$$

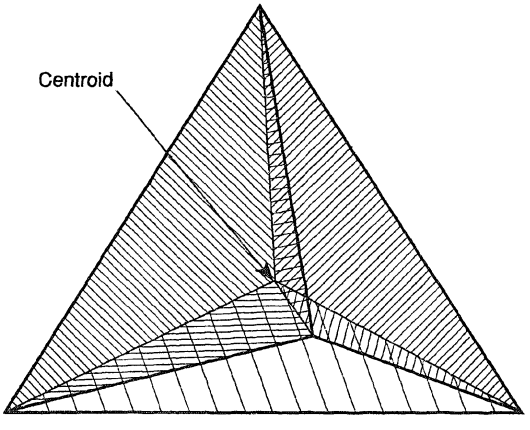


Fig. 4.17 The disappearing tetrahedron, illustrating the reduction in surface area of the tetrahedron and the increase in area of the interconnected grain boundaries.

The change in radius of an inscribed circle, R, represents the distance that each surface of the tetrahedron must move towards the centroid in a direction normal to the surface in order to collapse the tetrahedron.

$$R = e_t\sqrt{6}/12 \tag{4.58}$$

From these equations the change in energy per unit advance of the interfaces per unit area of the grain boundary is given by

$$dE = 6(1 - 2\sqrt{2}/\sqrt{3})\gamma/e_t \tag{4.59}$$

From this equation, it can be seen that the tetrahedral grain is inherently unstable and would lead to a lowering of energy by shrinking, whatever its size. In fact, as the tetrahedron becomes smaller, the driving force per unit area of grain boundary increases. There is, however, a limit to the edge length of a tetrahedron if it is to maintain this shape when placed in a matrix of polyhedra with many more faces. The radius of a circumscribed circle around the tetrahedron represents the length of the edge between three neighbouring polyhedra that is created as the tetrahedron shrinks. Thus the radius of the circumscribed circle has a maximum value equal to the final edge length of these polyhedral neighbours. The radius of the circumscribed circle, R_c, is related to the edge length, e_t, by[23]

$$R_c = e_t\sqrt{6}/4 \tag{4.60}$$

and if this is equated to the edge length of a tetrakaidecahedron, e,

$$R_c = \sqrt{6}e_t/4 = e \tag{4.61}$$

and as the edge length of a tetrakaidecahedron is related to its 'radius', R_0, by[21]

$$R_0 = \sqrt{3}e/\sqrt{2} \tag{4.62}$$

then, from Equations (4.61) and (4.62),

$$e_{t\max} = 4\sqrt{2}R_0/\sqrt{3}\sqrt{6}$$

$$\text{or} \quad e_{t\max} = 4R_0/3 \tag{4.63}$$

Both Equations (4.59) and (4.63) differ slightly from those given in Reference 22, due to the correction of previously incorrect assumptions. Although these equations are now rigorous for a shrinking tetrahedron, there is still an implicit assumption that the grain corner where the four remaining grains meet will have the ideal configuration of grain faces meeting at 120° and grain edges meeting at 109°28′. This implies that the tetrahedral grain may not have been a regular tetrahedron, as real grains only approximate the ideal condition. Nevertheless, the shrinking regular tetrahedron is possible but may only approximate the energy changes for a non-regular tetrahedron.

The case of the unstable shrinking grain is interesting because the process ends with the disappearance of the grain. At the end of this process, the initial volume of the tetrahedron has been added to all or some of its four neighbours. In this sense, the four neighbouring grains have been growing, but with the dis-

appearance of the tetrahedral grain, this growth process stops. This is a prominent feature of grain growth in general, i.e. it is a discontinuous process. The case of the growing grain, described by Equation (4.55) gives no indication of a discontinuity. As the radius of the growing grain, R, increases, so the driving force for grain growth increases, thus indicating a continuous growth process. However, this postulation assumes that the matrix grains which are being consumed remain unchanged. This is the situation for abnormal grain growth (to be discussed in a later section) and continuous growth of the abnormal grain is observed. In normal grain growth, the matrix grain size, R_0, does not remain unchanged. All grains with an adequate size advantage ($Z = R/R_0 > 4/3$) will grow, and any particular grain which is undergoing the growth process will eventually come into contact with other growing grains, thus providing an increase in R_0 and a corresponding decrease in the driving force for continued growth. When several large grains collide, having consumed the intervening small grains, growth of the grain may either continue, stop, or even be reversed depending upon the size of the grain with which it has collided. In this way, grain growth may again be regarded as a discontinuous process.

4.5.4 Stochastic Models

A major disadvantage of the above approaches is that they are confined to the start of the growth process, and describe the status of particular grain configurations, such as larger grains of different size advantage, and small grains down to the vanishing tetrahedral grain. Hillert[20] presented a deterministic model of the change in the grain size distribution. In this model, all grains of size R in an array grow at a given rate. Other models[24,25] introduce a degree of randomness in that the growth rate of a grain of 'radius' R will show some random statistical variation, or 'noise', which, though not specifically stated, may reflect the variation in the (local) grain size of the immediate neighbours. The physical situation is of a grain of radius, R, surrounded by grains of different sizes, so that it would be possible for the grain to have anisotropic growth rates even to the extent of advancing on one side whilst retracting on the other. Nevertheless, these models are becoming increasingly sophisticated, and are capable of describing the evolution of the grain size distribution as well as the change in mean grain size with time, and, through the grain boundary mobility constant, with temperature. These approaches are being still further developed, and are being augmented by computer models of grain growth, as for example by Srolovitz *et al.*[26] However, the computer models are generally limited to 2-D modelling due to the complexity and memory required for a 3-D model of any significant size.

The author has no wish to be dismissive of these efforts, which offer the prospect of significant advances in the development of, for example orientation controlled structures, but from the standpoint of microalloyed steels, the object of grain control is to eliminate grain growth processes, so that fine grained structures can be obtained, with their associated high strengths and high levels of toughness (resistance to cleavage fracture). Recent developments in grain growth have been well covered in a recent conference.[27]

4.5.5 General Considerations of the Driving Force for Grain Growth

The angle-driven, curvature-driven and energy-driven grain growth forces do not pose any significant contradictions for equiaxed convex grains. The larger grains in a structure will be surrounded by smaller grains. The large grains, because of the shared faces, will have more polygonal faces, and the edge angles will exceed 120°, whilst the corner angles will exceed 109°28′, due to the increase in the average number of edges per face that accompanies the increase in the number of faces per polyhedron, as outlined previously. Thus the grain corners will move outwards giving concave grain faces. The curvature of the faces will flatten by moving outwards, and both of these process may be regarded as providing the mechanism by which large grains grow, as described in earlier sections of this chapter. The energy models merely summate these changes, all of which occur as a result of the surface energy minimisation. With smaller grains, as for example the tetrahedral grain, the edge angles are much less than 120° (in fact for a regular tetrahedron the included angle between adjacent faces is only 70°32′) and the corner angles (because of the triangular geometry of the faces) are 60°. Inward movement of the corners and edges will cause the faces to bulge convexly and the curvature so developed will allow the grain faces to flatten and the tetrahedron to shrink. The net energy change described in Section 4.5.3 reflects these energy changes exactly.

The overall effect of these energy changes results in the general phenomenon of grain growth, where large grains grow and small grains shrink, and although regular polyhedra have been used as model grain shapes, the principles are equally applicable to the irregular polyhedra commonly found in real polycrystalline metals. The energy changes per unit advance of the interface (per unit area of the grain boundary) expressed in Equations (4.55) and (4.59) give reasonable estimates of the magnitudes of the maximum and minimum driving forces per unit area that will be encountered in the real polycrystal for reasonable values of the size of the growing or shrinking grains. (Note that if R is not greater than $4R_0$ / 3, then the driving force for grain growth per unit area of boundary is 0, and if the edge length of the tetrahedron approaches zero then the driving force per unit area approaches infinity.)

The control of grain size requires the application of a restraining force that will overcome the driving force for grain growth. This is considered in the following section.

4.6 INHIBITION OF GRAIN GROWTH

There are several ways in which grain growth can be retarded or inhibited, but the only known method of completely inhibiting grain growth in bulk material (as opposed to thin films or filaments) is by the introduction of second phase particles to give the Zener[28] drag effect. This arises from the fact that a small area of grain boundary disappears when the grain boundary intersects a particle, as shown in Fig. 4.18. If the particles are spherical, the lowest energy situation occurs when the

boundary intersects the particle diametrically. Zener gave the pinning force, p, required to separate the boundary from the particle as

$$p = \pi r \gamma \tag{4.64}$$

where r is the radius of the particle and γ is the surface energy of the boundary.

As the boundary, reacting to the driving forces of grain growth, attempts to move away from the particle, the need to create a new area of boundary causes it to distort as shown in Fig. 4.18. The distortion of the boundary, from its planar position, decreases inversely as the distance from the particle. Eventually the distorted boundary attains an increased area (and energy) that can allow the boundary to become unpinned. The new area created by detachment from the particle is supplied by the reduction in distortion. The boundary is assumed to maintain contact with the particle at an angle normal to the surface. Derivations by Gladman,[21] Ashby *et al.*,[28] Hellman and Hillert[29] and Louat[30] have yielded similar results, and the pinning force, which is the maximum rate of change of area (energy), did not differ significantly from that described by Equation (4.64).

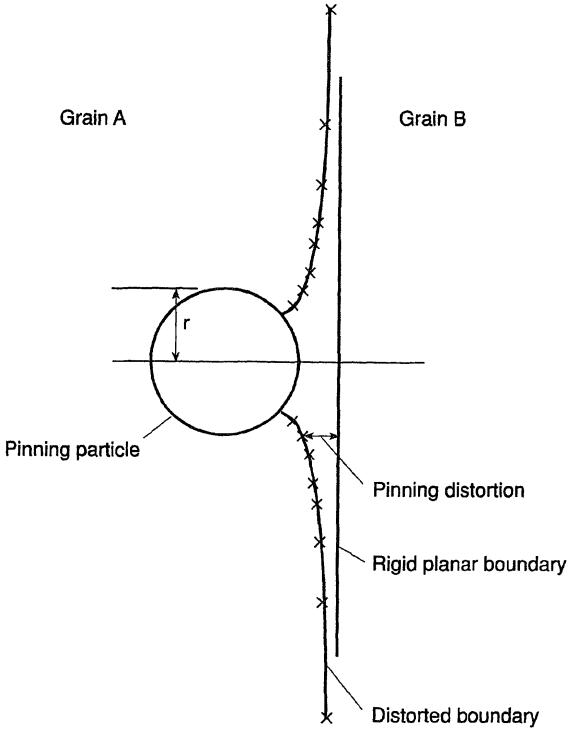


Fig. 4.18 Grain boundary pinning by second phase particles. An elimination of grain boundary area occurs when the boundary intersects the particle. Unpinning requires that additional energy is supplied by the driving force for grain boundary movement.

4.6.1 Randomly Distributed Second Phase Particles

Zener postulated that grain boundary movement would cease when the driving force for grain growth was equal to the pinning force exerted by an array of randomly dispersed particles. By way of example, Zener considered the shrinkage of an isolated spherical grain of radius R. Here, the rate of disappearance of the boundary area (energy) per unit area of the boundary and per unit decrease of the radius is given by

$$dE/dR = -2\gamma/R \tag{4.65}$$

The pinning force per unit area of the grain boundary, P, is expressed as

$$P = p \cdot n_a \tag{4.66}$$

where n_a is the number of pinning particles per unit area of the shrinking boundary.

The number of particles in contact with the boundary, when the particles are randomly distributed throughout the structure, is governed by the need for the particle centre to lie within a distance $+r$ to $-r$ from the boundary, i.e. within a volume of $2r$ per unit area of the boundary. Thus, n_a will be given by

$$n_a = n_v \cdot 2r \tag{4.67}$$

where n_v is the number of particles per unit volume.

Equation (4.67) can be expressed in terms of the volume fraction of particles, f, and particle radius, as

$$n_v = 3f/4\pi r^3 \tag{4.68}$$

Substitution of Equation (4.67) and (4.68) into equation (4.66) gives

$$P = 3f\gamma/2r \tag{4.69}$$

If $P > dE/dR$, then the pinning force is dominant and the grain boundary will not move. If $dE/dR > P$, then the grain boundary force is dominant and the spherical grain can shrink. The limit between these is obviously

$$dE/dR + P = 0 \tag{4.70}$$

Substitution from Equations (4.65) and (4.69) gives

$$-2\gamma/R + 3f\gamma/2r = 0$$

or

$$R = 4r/3f \tag{4.71}$$

which is the Zener equation.

Although there is an implicit assumption in Equation (4.66) that all particles associated with the boundary exert their maximum pinning force at the same time, this may not be unreasonable in microalloyed steels where the particles are present as extremely small particles (relative to the grain size), and the volume fractions are generally less than 0.001. Very little boundary flexing would be required for all particles to be diametrically intersected. The boundary drag effect would in fact increase the number of particles in contact with the boundary, which would to

some extent offset the fact that not all particles were exerting their maximum drag effect at the same time. In fact Gladman[21] suggested that separation would occur when the boundary was displaced a distance of $2r$ from the diametral position.

The Zener equation (4.71) embodies the major features of grain growth inhibition by second phase particles. A finer grain size can be stabilised by an increased volume fraction of particles for a given particle size and finer particles are capable of stabilising a finer grain size for a given volume fraction of particles. Thus the increase in pinning force with increasing size for a single particle [Equation (4.64)], is more than offset by the accompanying reduction in the number of particles per unit area.

The shrinkage of an isolated spherical grain gives a much larger driving force for grain growth than was obtained for the growing tetrakaidecahedral grain or the shrinking tetrahedral grain. These can be treated in the same way to establish the critical grain size at which the pinning forces and the driving forces are equal. In the case of the shrinking tetrahedron

$$6(1 - 2\sqrt{2}\sqrt{3})\gamma/e_t + 3f\gamma/2r = 0$$
$$e_t = 2.53r/f \tag{4.72}$$

Although the numerical proportionality constant in Equation (4.72) is much higher than the value of 4/3 in the Zener equation, it must be remembered that Equation (4.72) gives the edge length of a tetrahedron whereas the Zener equation gives the radius of a sphere, and thus the two numerical values are not directly comparable. If the comparison is made on the basis of the half edge length ($e_t/2$), or on the basis of the radius of a sphere of equivalent volume ($R_{eq} = e_t/3.29$), then the proportionality constant would be less than that of the Zener equation.

In the case of the growing tetrakaidecahedron, and putting $Z = R/R_0$ (Z is the physically real variable representing the size advantage of the growing grain over that of its neighbours),

$$(2/Z - 3/2)\gamma/R_0 + 3f\gamma/2r = 0$$
$$R_0 = (1 - 4/3Z)r/f \tag{4.73}$$

The proportionality constant between R_0 and f quite clearly depends upon the size advantage of the growing grain, ranging from 0 at $Z = 4/3$ to 1 at $Z = \infty$, all of which are smaller than the factor of 4/3 in the Zener equation. A more appropriate value of Z, selected either from experimental work,[21,31] or from limiting grain size distribution functions[20,24,25] would be $Z = 2$. With $Z = 2$, the proportionality constant in Equation (4.73) is 1/3, i.e. one quarter of the Zener constant.

One problem with the grain size heterogeneity factor, Z, is the high sensitivity of the critical grain size (i.e. the grain size at which the driving force and pinning force are equal) to changes in Z. This is particularly true when considering the critical particle radius, for a given grain size and volume fraction of particles, above which grain growth can occur, as shown in Fig. 4.19. Changes in the size advantage between $Z = \sqrt{2}$ and $Z = 2$ cause the critical particle radius to change between 17.5 $R_0 f$ and $3R_0 f$. Although this is seen as a problem, it must be

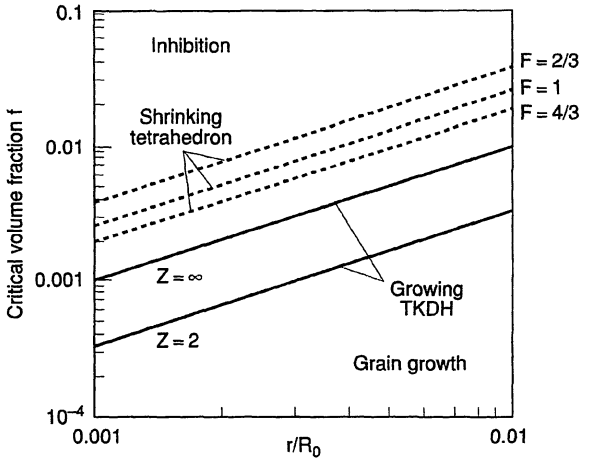


Fig. 4.19 Domains for grain growth and the inhibition of grain growth by second phase particles.

remembered that Z is a physical feature of grain growth and cannot be avoided in any realistic theory.

4.6.2 Grain Boundary Precipitates

During the modelling of grain growth inhibition by second phase particles, Srolovitz *et al.*[26] found that the stable grain size was dependent upon the square root of the inverse of the volume fraction of particles in contrast with the linear dependence on the inverse of the volume fraction shown by Equations (4.72) and (4.73). As explained by Doherty *et al.*,[32] the particles observed in this 2-D simulation were almost exclusively associated with grain boundaries after relatively little 'grain coarsening', and this would change the relationships. This raises some important points in connection with the assumptions about the initial particle distribution. In the Zener treatment and in the derivations given in Section 4.6.1, a random distribution of particles was assumed. This distribution may well be relevant to a microalloyed steel in which a small volume fraction of very small (and therefore numerous) particles are precipitated prior to the development of a new grain structure by transformation. The particle distribution attained by a precipitation process in an existing grain structure may however result in grain boundary precipitation due to the nucleation assistance at grain boundaries. Under these conditions, the random distribution of particles described by Equation (4.67) is entirely inappropriate, and the number of particles per unit area will greatly exceed the value of $2rn_v$, given in Equation (4.67). If all particles are precipitated on grain boundaries, then the number of particles per unit area of grain boundary depends on the number of particles per unit volume, and the grain boundary area

per unit volume. The surface area per unit volume, A_v, can be expressed by Equation (4.47) as

$$A_v = \Lambda/2V$$

The relevant volumes, surface areas, and radii of inscribed spheres, for various shapes, are given in Table 4.8. Calculation of the surface area per unit volume according to Equation (4.47) gives a surface area per unit volume which is obviously dependent upon the reciprocal of a linear dimension of the grain, and the coefficient of proportionality varies from one shape to another if the edge length is used as the measure of grain size. However, if the 'radius' of the grain is defined as the radius of the inscribed sphere, R_0, then for the regular polyhedra such as the tetrahedron, cube, pentagonal dodecahedron and the sphere, the grain boundary area per unit volume is given by

$$A_v = 3/2R_0$$

The tetrakaidecahedron is not a regular polyhedron, and the radius of the inscribed sphere will only touch the eight hexagonal faces, but not the six square faces. Thus R_0, defined earlier as the distance between opposite hexagonal faces, does not give this exact correspondence and gives a proportionality constant of 1.45 rather than 1.5. In view of the irregular grain shapes present in metals, it is perhaps appropriate to write

$$A_v \approx 3/2R_0 \tag{4.74}$$

In subsequent treatments, Equation (4.47) (the equality) will be used, but small errors (less than 5%) will be present due to the approximation explicitly stated in Equation (4.74), when dealing with equiaxed convex polyhdedral shapes.

Thus, for particles confined to grain boundaries, the number per unit area n_a derives from

$$\begin{aligned} n_v &= 3f/4\pi r^3 \\ A_v &= 3/2R_0 \\ \text{and as} \quad n_a &= n_v/A_v \\ \text{then} \quad n_a &= R_0 f/2\pi r^3 \end{aligned} \tag{4.75}$$

With the pinning forces defined by Equation (4.66), substitution of Equation (4.75) gives

$$P_g = n_a \pi r \gamma = R_0 f \gamma / 2r^2 \tag{4.76}$$

The suffix g is added to denote the pinning effect when the particles are exclusively associated with grain boundaries. If the driving forces of the growing tetrakaidecahedron and the shrinking tetrahedron are equated with the pinning force of the grain boundary array of particles, then for the shrinking tetrahedron

$$6(1 - 2\sqrt{2}/\sqrt{3})\gamma/e_t + R_0 f \gamma/2r^2 = 0$$

or

$$e_t = 7.6r^2/R_0 f \tag{4.77}$$

and for the growing tetrakaidecahedron

$$(2/Z - 3/2)\gamma/R_0 + R_0 f\gamma/2r^2 = 0$$

or

$$R_0 = (3 - 4/Z)^{1/2} r/f^{1/2} \tag{4.78}$$

The $1/f^{1/2}$ dependence of the critical grain size obtained by Srolovitz *et al.*[26,32] is clearly seen in Equation (4.78) for the growing tetrakaidecahedron and gives considerable support to the modelling work of Srolovitz. It has been shown[26,33] that the $1/f^{1/2}$ dependency is obtained for grain boundary distributed particles for both 2-D and 3-D models, whilst for the randomly distributed particles there is a $1/f$ dependency for both 2-D and 3-D models.

The root dependency is less obvious for the shrinking tetrahedron, but if the edge length of the tetrahedron is regarded as a fraction F of the size of the tetrakaidecahedron as indicated by Equation (4.63) (i.e. $e_{t\,max} = 4R_0/3$), then Equation (4.77) can be written as

$$R_0 = (7.6/F)^{1/2} r/f^{1/2} \tag{4.79}$$

This gives the $1/f^{1/2}$ dependency when the size of the shrinking tetrahedron is expressed in terms of the size *dis*advantage of the tetrahedron with respect to the matrix of tetrakaidecahedral grain, i.e. is made compatible with Equation (4.78). The definition of F for Equation (4.79) is

$$F = e_t/R_0 \tag{4.80}$$

and has a maximum value of 4/3.

4.6.3 Summary of Grain Size Control by Pinning Particles

The effects of particle pinning forces and the driving forces for grain growth can be defined in several ways. The equality between driving forces and pinning forces constitutes a boundary between grain growth (or shrinkage), when the driving force exceeds the pinning force, and stable grain structures, when the pinning force exceeds the driving force. The boundary can be expressed as a critical matrix grain size, R_c, for any given particle fraction, particle size and size advantage. Similarly, critical particle fractions or critical particle sizes could be defined for given values of the other variables. An obvious problem in defining these critical levels is the value of the size advantage (disadvantage), Z. This cannot be measured directly for bulk metals, as mentioned earlier, but conservative estimates of Z can be made depending on whether it is important to inhibit grain growth, or, in some cases, whether it is important to guarantee grain growth. Selecting a high value of Z, e.g. $Z = 2$ would be appropriate to grain growth inhibition, as any metallic system with $Z < 2$ would not grow if the particles were capable of inhibiting growth at $Z = 2$. Conversely, if grain growth has to be guaranteed (as for example in hardenable steels[34]) a low value of Z would be chosen, e.g. $Z = 3/2$, so that any grain growth that could occur at $Z = 3/2$ would be sure to occur at higher levels of Z. Irrespective of these philosophical approaches, uncertainty in the value of Z

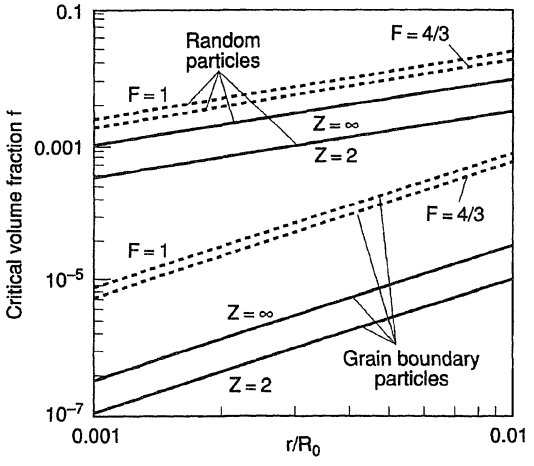


Fig. 4.20 The effects of randomly distributed particles and grain boundary precipitated particles on grain growth inhibition.

effectively produces a diffuse boundary between growth and inhibition, in which growth or inhibition will be dependent on the actual size advantage.

The boundaries obtained in this way are indicated in Fig. 4.20, for growth, shrinkage and stability, and are shown both for a random distribution of particles and for particles wholly confined to grain boundaries. It can be seen that grain shrinkage generally requires more effective inhibition than does the growth of a larger grain. It can also be seen that structures containing only grain boundary particles are far more resistant to growth than structures with randomly distributed particles. The implications of this diagram will be considered in later chapters, when attention is given to the compositional requirements of grain-refined microalloyed steels.

REFERENCES

1. C. S. Smith: *Metal Interfaces, A.S.M., Cleveland*, 1952, p.65.
2. Grignon: *Mem. de Physique*, Paris, 1775.
3. Lord Kelvin: (a) *Phil. Mag.*, 1887, **24**, p.503; (b) *Proc. Roy. Soc.*, 1894, **55**, p.1.
4. D. Aboav: *Materials Science Forum*, 1993, **94–96**, p.275.
5. R. Shuttleworth: *Imperfections in Nearly Perfect Crystals*, Ed. W. Shockley, Wiley, 1952, p.343.
6. C. S. Barrett: *Structure of Metals*, 2nd Edition, McGraw-Hill, 1952.
7. E. B. Matzke: *American J. Botany*, 1946, **33**, p.58.
8. E. B. Matzke and J. Nestler: ibid, p.130.
9. C. H. Desch: *J. Inst. Metals*, 1919, **22**, p.241.
10. T. Gladman and J. R. Blank: *Tools and Techniques in Physical Metallurgy*. Ed. F. Weinberg, Marcel Dekker, New York, 1970, p.265.
11. F. C. Hull and W. J. Houk: *Trans. A.I.M.E. (Metals Div.)*, 1953, **197**, p.565.
12. M. Malinski, J. Cwajna and J. Chapronski: *Mat. Science Forum*, 1992, **94–96**, p.285

13. J. B. RUTHERFORD, R. H. ABORN and E. C. BAIN: *Metals and Alloys*, 1937, **8**, p.345.
14. T. GLADMAN: Unpublished work, 1968.
15. E. SCHEIL: *Z. Anorg. Allgem Chem.*, 1931, **201**, p.259.
16. D. MCLEAN: *Grain Boundaries in Metals*, Clarendon Press, Oxford, 1957, p.62–68.
17. T. WATANABE, Y. KAWAMATA and S. KARASHIMA: *Trans. J.I.M.*, 1986, **27**(supp.), p.601.
18. J. VON NEWMANN: *Metal Interfaces, A.S.M., Cleveland*, 1952, p.108.
19. W. W. MULLINS: *J. App. Phys.*, 1956, **27**, p.900.
20. M. HILLERT: *Acta Met.*, 1965, **13**, p.227.
21. T. GLADMAN: *Proc. Roy. Soc., A.* 1966, **294**, p.298.
22. T. GLADMAN: *Proc. 1st. R.I.S.O. International Symposium*, Eds. N. Hansen, A. R. Jones and T. Leffers, Roskilde, Denmark, 1980, p.183.
23. L. RADE and B. WESTERGREN: *Beta Mathematics Handbook* (2nd Edition), Student literatur Akergranden, Sweden, 1990, p.71.
24. C. S. PANDE: *Acta. Met.*, 1987, **35**, p.2671.
25. N. RYUM and O. HUNDERI: *Acta. Met.*, 1989, **37**, p.1375.
26. D. J. SROLOVITZ, M. P. ANDERSON, G. S. GREST and P. S. SAHNI: *Scripta. Met.*, 1983, **17**, p.241; *Acta. Met.*, 1984, **32**, p.783; ibid., 1984, **32**, p.793; ibid., 1984, **32**, p.1429; *Scripta. Met.*, 1987, **21**, p.675.
27. *Grain Growth in Polycrystalline Metals*, Eds. G. Abbruzzese and P. Brozzo, Metals Science Forum, 1992, vols. 94–96.
28. M. F. ASHBY, J. HARPER and J. LEWIS: *Trans. A.I.M.M.E.*, 1969, **245**, p.413.
29. P. HELLMAN and M. HILLERT: *Scan. J. Met.*, 1975, **4**, p.211.
30. N. LOUAT: *Phil Mag.*, 1983, **47A**, p.903.
31. W. M. WILLIAMS and C. S. SMITH: *Trans A.S.M.*, 1953, **45**, p.533.
32. R. D. DOHERTY, D. J. SROLOVITZ, A. D. ROLLETT and M. P. ANDERSON: *Scripta Met.*, 1987, **21**, p.1569.
33. T. GLADMAN: *Scripta Met. et Mat.*, 1992, **27**, p.1569.
34. T. GLADMAN: *Heat Treatment of Metals*, 1994, **22** (1), p.11.

CHAPTER 5

Precipitation Behaviour and Particle Coarsening

5.1 INTRODUCTION

The solubilities of the microalloy carbides and nitrides, presented in Chapter 3, are useful in defining the dissolved microalloy and interstitial contents that are in equilibrium with the microalloy carbide, nitride or carbo-nitride. A direct consequence of the solubility data is that the amount of undissolved carbo-nitride can be calculated for any given steel composition, together with the temperature at which all of the carbo-nitride can be dissolved.

The undissolved carbo-nitride is present in particulate form, and thus has direct relevance to the evolution of the grain structure at elevated temperatures. If the carbo-nitride particles are present in sufficient numbers of suitably small particles, then inhibition of grain growth will occur by Zener pinning as described in Chapter 4. On the other hand, dissolution of carbo-nitride at high temperatures, followed by subsequent cooling and exposure at lower temperatures, will cause precipitation of the carbo-nitride, the extent of precipitation and the size of the precipitated particles depending upon the time of exposure to lower temperatures.

Such treatments are common in a wide range of alloys, being particularly well documented for the age hardening aluminium alloys. Similar processes occur in carbon steels where dissolution of cementite in the ferrite at elevated temperatures in the sub-eutectoid range, followed by quenching to ambient or near ambient temperatures, gives rise to a supersaturated solid solution of carbon in α-iron. Subsequent ageing results in the precipitation of a carbide (and/or nitride) phase. The particle size and extent of precipitation is controlled by the time and temperature of ageing, and, in carbon steels, the process is known as 'quench ageing'. Significant hardening may be produced by such treatments. However, the situation may be more complex in an allotropic material such as steel, where the solubilities of the microalloy carbo-nitrides in the high temperature austenite are higher than their solubilities in the low temperature ferrite phase (see Chapter 3), but the precipitation may be influenced by the austenite to ferrite transformation.

Dissolution of the microalloy carbide/nitride at high temperatures in the austenite range offers a number of options for the subsequent re-precipitation process at lower temperatures; these are:

(i) Precipitation in the austenite following a reduction in temperature, either during slow cooling, or isothermally during a holding treatment in the austenite temperature range.

(ii) Precipitation during the austenite–ferrite decomposition process where the solubility decreases discontinuously at the austenite–ferrite boundary.
(iii) Precipitation following transformation to ferrite, usually as a result of rapid cooling through the austenite and transformation temperature ranges.

The latter process may occur upon reheating a rapidly cooled microalloy steel during, for example, a sub-critical annealing or normalising treatment. The re-precipitation process is extremely important in that it is responsible for the size of the finer particles of the microalloy carbides/nitrides, that are responsible for dispersion strengthening, as described in Chapter 2. The size and volume fraction of the particles are important to their efficacy in controlling grain size and in enhancing dispersion strengthening, both of which may contribute to higher yield strengths.

One further important phenomenon that can affect the particle size is known as Ostwald ripening. The phenomenon of Ostwald ripening relates to the increase in particle size which occurs at a constant volume fraction of precipitate, and can result in a significant loss of performance of the particles.

These precipitation phenomena form the subject of this chapter.

5.2 PRECIPITATION IN AUSTENITE

The long-standing practice of heating steels to temperatures in the range of 1250°C to 1320°C prior to hot working was aimed at a reduction in strength in order to limit the hot working forces, thereby reducing the loads imposed on forging presses, rolling mills or other hot forming machines. As many of these processes are multi-stage operations designed to effect significant reductions in the cross-sectional area of components, a sufficient reserve of heat was required to ensure that, even after extensive forming operations, the heat loss would not cause excessive forming loads in the later stages of the deformation process.

With the introduction of the carbide/nitride forming microalloying elements, with their restricted solubilities, it is pertinent to relate the dissolution of these carbides/nitrides to soaking or hot working temperatures and to the subsequent evolution of the microstructure. The soaking temperature for the hot working of ingots, slabs, blooms or billets is concerned with the hot deformation process itself, and the ability to accomplish the required shape change is paramount. However, the hot deformation process is instrumental in controlling the evolution of the microstructure, and in particular the final structure of the hot rolled product. Many of these hot-rolled products are used directly as, for example, reinforcing bars, plate, strip for helically welded pipeline, etc., and so some compromise is usually made to balance the properties of the product with manageable hot working forces.

The soaking temperature, together with the steel composition, is important in controlling the extent of dissolution of the microalloy carbide/nitride. The subsequent precipitation behaviour would be expected to depend on the extent of dissolution in two ways:

(i) Increasing the solute content by heating to higher temperatures, thereby dissolving more of the carbide/nitride in accord with the solubility data (Chapter 3), will increase the supersaturation on cooling and would be expected to increase the rate of precipitation at lower temperatures.
(ii) Partial dissolution of the carbide/nitride will leave particles of the microalloy carbide/nitride available as nuclei for subsequent re-precipitation processes on cooling. Lower dissolution temperatures would therefore favour accelerated precipitation of the solutes on the pre-existing particles.

However, within the range of times and temperatures of interest in hot working processes, and in the absence of any hot deformation, the precipitation of the microalloy carbides and nitrides in austenite appears to be extremely slow,[1,2,3] as is the case for aluminium nitride. For aluminium nitride, isothermal precipitation in the austenite temperature range shows a C-curve for precipitation[4,7] following a high temperature solution treatment, with a maximum rate of precipitation at about 1100°C, though even here, complete precipitation of the equilibrium amount of aluminium nitride took some 6 h. In the case of niobium carbo-nitride, Hoogendorn and Spanraft[3] found that there was little precipitation of niobium carbo-nitride even after 67 h at 900°C following a high temperature solution treatment, whilst Begin and Simoneau[2] found progressive precipitation over a period from 10 min to 80 h at 950°C following solution treatment at 1350°C. Thus the solute content of austenite can reasonably be expected to remain unchanged during cooling from the soaking temperature in the absence of hot deformation.

The situation changes dramatically when hot deformation is applied. The introduction of dislocations, dislocation cells and low angle sub-grain boundaries during the hot working process, provides numerous sites for the precipitation of the carbides and nitrides, provided that the deformation is carried out at temperatures below the solvus. Under these conditions, the precipitation in austenite is accelerated considerably. Typical precipitation curves are shown in Figs. 5.1 and 5.2 for niobium carbo-nitride[8] and titanium carbide.[9] In both cases, the precipitation process is rapid and can be completed in about 1 min at temperatures of 900–1000°C. The nose of the C-curve will obviously depend on the level of supersaturation, as little precipitation would be expected with low levels of supersaturation, and no precipitation would ever occur at temperatures above the solvus. At temperatures below the nose of the C-curve, the retardation to be expected from diffusion controlled precipitation processes may be disrupted by the transformation of austenite to ferrite, i.e. at temperatures of 900°C and below, and the exact point of disruption will be dependent upon the carbon and alloy contents of the austenite and their effects upon the Ar_3. The strain induced precipitation of titanium carbide appears to show a slight dependence on the manganese content of the alloy. The effect of manganese has been attributed to the reduction in the activity of nitrogen with increasing manganese content.[9]

In the case of vanadium microalloyed steels, the extremely high solubility of vanadium carbide (See Chapter 2) results in the carbo-nitride being predominantly vanadium nitride. The solvus temperature for vanadium nitride in vanadium microalloyed steel with 0.1–0.15wt%V and nitrogen contents of 0.006–0.009wt%N

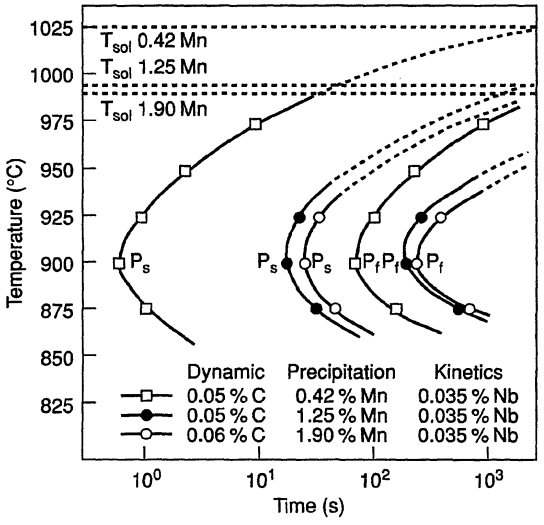


Fig. 5.1 Typical precipitation curves for niobium carbo-nitride in austenite following a 50% reduction in thickness by hot rolling. After Jonas and Weiss.[8]

is relatively low, and even with the maximum vanadium and nitrogen contents in these ranges, a solvus temperature below 1050°C would be expected, thus limiting the temperature range for strain induced precipitation of vanadium nitride in austenite.

Precipitation of microalloy carbide/nitride in austenite in the absence of hot deformation is a very slow process which can take several hours, even at optimum precipitation temperature, whilst hot deformation causes a marked acceleration of

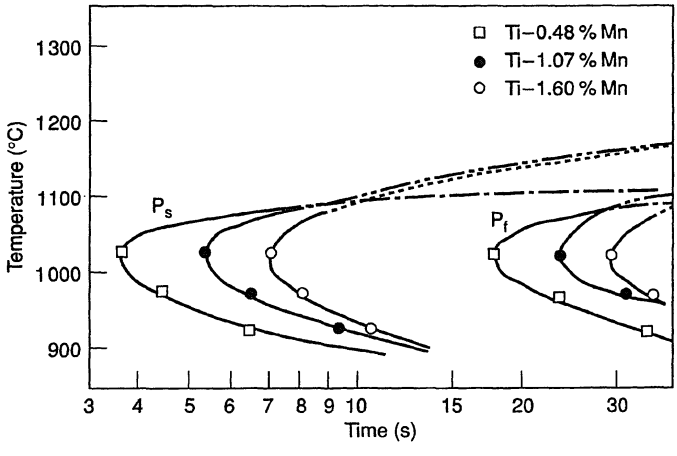


Fig. 5.2 Typical precipitation curves for titanium carbo-nitride in austenite during dynamic straining at a strain rate of $0.028s^{-1}$. P_s represents the start of precipitation and P_f represents the end of precipitation. After Chandra *et al.*[9]

the precipitation, to the extent that it can be substantially completed within a minute at temperatures of 900–1000°C. The strain-induced acceleration of the precipitation process is, of course, dependent upon the level of strain, as shown by Hoogendorn and Spanraft[3] and the figures quoted above relate to a 50% reduction in thickness. With a 20% hot reduction, the times for precipitation increase by a factor of 5–10 times.

Detailed microscopical studies of the precipitation processes for niobium and titanium carbo-nitrides in austenite have been confined to steels with stable austenitic structures at ambient temperatures, such as austenitic stainless steels. Honeycombe[10] has reviewed the precipitation behaviour of these carbides/nitrides in austenite, and has pointed out that the precipitation occurs with a cube-on-cube Widmanstatten relationship. The lattice parameter of the precipitate is 20–25% greater than that of the matrix, and a flux of vacancies to the precipitated particles is required in order to accommodate the internal stresses arising from the growth of these particles. Such vacancy fluxes are provided by hot deformation processes, and the dislocation density is also increased, thereby providing an increased number of nucleation sites. Honeycombe has also pointed out that grain boundaries and dislocations are highly preferred nucleation sites; random precipitation in the matrix, in the absence of dislocations, rarely occurs. In the coarse grained structures associated with the high soaking temperatures used, it is not surprising that nucleation on dislocations plays such an important role, and that hot deformation causes such a dramatic acceleration of the precipitation process.

5.3 PRECIPITATION DURING DECOMPOSITION OF THE AUSTENITE

Although the solubility of the microalloy carbides and nitrides in austenite, and also their precipitation behaviour, follow similar principles in both microalloyed steels and highly alloyed austenitic stainless steels, there are important changes, in both the solubility and precipitation behaviour, when the microalloyed steels undergo austenite decomposition on cooling after hot working.

The arrays of aligned particles, which are so typical of microalloyed steels,[11,12] were shown in Fig. 2.20. Investigations of the mechanism of formation of this type of particle distribution were carried out by Honeycombe and his co-workers.[13] The spatial distribution of the fine carbides is such that when viewed from certain directions by transmission electron microscopy, distinct rows of particles are seen with quite distinctive spacings. If the same region is tilted, the linear arrays are lost and the particles appear to be randomly distributed. The particles are randomly distributed in two dimensions, but in the third dimension, they occur as distinct sheets of particles, with clear matrix between these sheets. When viewed 'edge-on' the particles appear as rows. The sheets or rows of particles were found to form parallel with the interface between the growing ferrite and the austenite matrix. The widely accepted mechanism for their formation is that they are nucleated periodically at the γ/α interface during transformation. Honeycombe[13] has pointed out that different morphologies of the microalloy carbides/nitrides can occur, and

the specific morphology adopted is dependent upon the conditions obtaining during the γ–α transformation. Fibrous or 'grass' carbides may form under certain circumstances whilst the 'sheet' or 'row' morphology can occur in the same alloy under different cooling conditions. However, many of the model alloys studied by Batte and Honeycombe[14] were produced to clarify the mechanisms of carbide formation, and the alloying additions such as vanadium, molybdenum and chromium were present in large quantities of 1% or more. In microalloyed steels with their relatively sparse levels of alloying (0.03–0.15wt%), the precipitate morphology of the carbide/nitride formed during the austenite to ferrite transformation appears to be restricted to the sheet morphology.

The mechanism of formation of this structure is suggested to derive from the ledge growth of ferrite as indicated in Fig. 5.3. The provision of a ferrite surface during transformation provides an excellent nucleation site for the microalloy carbide or nitride. This interface remains stationary and is available for carbide/nitride nucleation and growth until the next ferrite ledge sweeps over this surface and occludes the particles precipitated thereon. The process is repeated for each ledge. The particles formed on each step are not geometrically arranged, but there may be a degree of uniformity imposed by the diffusivity of the microalloy atoms. The association of the particle formation with the ferrite interface is clearly indicated by the orientation relationship found between the carbide/nitride and the ferrite. Davenport and Honeycombe[15] showed that the orientation relationship between the carbides and ferrite in the interphase precipitated condition (sheets of finely distributed carbides) was the same as that for vanadium carbide precipitated in ferrite during tempering, i.e. the Baker–Nutting orientation relationship.[16]

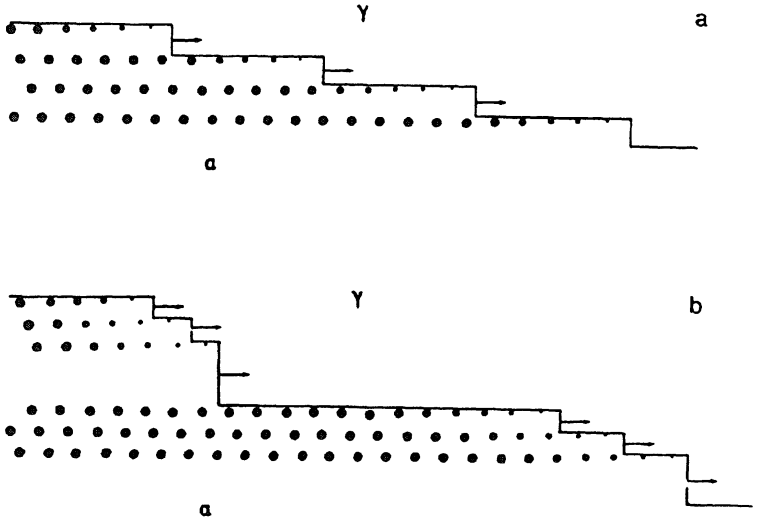


Fig. 5.3 Interphase precipitation as a result of ferrite growth by the 'ledge' mechanism. After Honeycombe.[13]

$$(001)_c \parallel (001)_\alpha$$
$$[010]_c \parallel [110]_\alpha$$

The inter-atomic spacings in the [110] direction in the f.c.c. carbides/nitrides of the common microalloying additives given in Chapter 3 range from 0.290 nm for vanadium nitride to 0.315 nm for niobium carbide. The inter-atomic spacing in the [100] directions of α–iron is 0.286 nm, thus giving lattice misfits in the range of 1.4% for vanadium nitride, to 10% for niobium carbide, in the plane of correspondence. However, in the direction normal to the plane of correspondence, the misfit is high. The atomic spacing of the carbide/nitride is 0.410 nm to 0.446 nm, whilst that of the ferrite remains at 0.286 nm, giving misfits of the order of 50%. The expectation from this orientation relationship is that the particles would form as flat discs or squares, with coherently bonded faces and incoherently bonded edges. Such particle morphologies are indeed observed for vanadium and titanium carbo-nitrides, whereas the shape of niobium carbo-nitride particles is generally less well defined. These differences may well be attributed to the lattice misfits and coherency effects, and the general concept of particles being precipitated incoherently in the austenite may also derive from misfits in excess of 10% for the cube on cube orientation relationship.

Batte and Honeycombe[14] also made interesting observations of the sheet spacing and particle sizes in low carbon Nb–V steels, observed after isothermal transformation of austenite to ferrite at various temperatures in the range 725–820°C. Their results are shown in Fig. 5.4. In general the sheet spacing increases with increasing transformation temperature and with decreasing carbon content. It should be noted that their steels contained high vanadium contents, which may have contributed to the apparent effect of carbon. Similar effects are seen on the particle size, although these effects are less pronounced at low transformation temperatures and higher carbon (and vanadium) contents.

There are interesting implications of the data presented in Fig. 5.4. Since there are specific distances between the sheets of particles, and the 'sheets' contain all particles in the microstructure, it follows that there is a mean spacing of particles within sheets that may or may not resemble the sheet spacing. A crude appraisal of the particle spacing within the sheets can be made by assuming that the sheets have a thickness equal to the 'cube edge' of the particles. The concentration of microalloy carbo-nitride is then enhanced by the ratio of the sheet spacing to sheet thickness. If, for example, the sheet centre-centre spacing, D, is twice the particle size, d, (edge length), then the volume fraction within the sheet is twice that of the bulk material, or

$$f_s = f\,D/d \tag{5.1}$$

where f_s is the volume fraction of particles in the sheet and f is the volume fraction of particles in the steel.

Honeycombe and Davenport[15] have shown that only one variant of the Baker–Nutting orientation relationship occurs within a given sheet of precipitates, and suggested that this is the variant which has the (100) plane most nearly parallel with the austenite–ferrite interface. The implications of this observation is that the

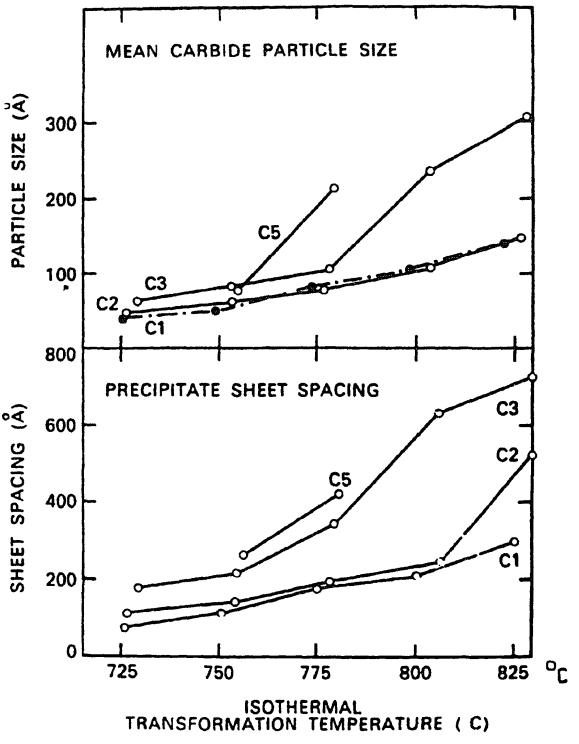


Fig. 5.4 The effects of the isothermal austenite/ferrite transformation temperature on the sheet spacings and particle sizes of the interphase precipitation. After Batte and Honeycombe.[14]

(100) cube face of a cubic precipitate will not be parallel with the austenite–ferrite interface, and if the precipitate has the form of a square disc, then the disc would be tilted with respect to the transformation interface.

The number of particles per unit volume within the sheet, n_v, can be obtained from the enhanced volume fraction within the sheet and the mean particle size.

$$n_v = f_s/d^3 \tag{5.2}$$

(Strictly this should be the mean particle volume, but, in this crude assessment, the cube of the mean edge has been used – this is a reasonable approximation if the particles are fairly uniform in size.) The volume of the sheet is given as the particle edge length multiplied by the area of the sheet, and the number of particles per unit area, n_A, is then given by

$$n_A = n_v \cdot d \tag{5.3}$$

Substituting from Equation (5.2) gives

$$n_A = f_s/d^2$$

and further substitution from Equation (5.1) gives

$$n_A = f\,D/d^3 \tag{5.4}$$

The mean area occupied by a single particle is then given by $1/n_A$ and if it is assumed that the particles in the sheet are arranged in a square grid, then the particle spacing, s, is given by

$$s = (1/n_A)^{1/2} \tag{5.5}$$

or by substitution from Equation (5.4)

$$s = (d^3/f\,D)^{1/2} \tag{5.6}$$

Values of the particle spacing within the sheets for the data shown in Fig. 5.4, according to Equation (5.6), are given in Table 5.1. In all cases, the particle spacing within the sheets exceeds the sheet spacings, and the particle spacing within the sheet increases with increasing transformation temperature. This calculation, though crude, suggests that the particle spacing within sheets is greater than that between the sheets if the particles are assumed be to cubic. If, however, in accordance with the lattice misfit, the particles are present as thin square discs, then the number of particles per unit area within the sheets would increase, which could alter the perceived differences in spacing within and between sheets, to give closer correspondence than is shown in Table 5.1.

The calculated spacings in Table 5.1 are thus subject to significant error, but serve to direct attention to the factors which control the inter-sheet spacing and the intra-sheet spacing of the microalloy carbides. The growth rate of a polygonal ferrite grain, growing by the ledge mechanism, must be directly related to the product of the ledge height and the frequency of the ledge initiation. The ledge

Table 5.1 Particle spacings of the interphase precipitated particles in a vanadium steel

C (wt%)	V or Nb (wt%)	Trans. (°C)	*f*	*D* (nm)	*d* (nm)	*s* (nm)
0.20	1.04 (V)	725	0.0123	8	4	25.5
–	–	750	0.0123	11	5	30.4
–	–	775	0.0123	18	8	48.1
–	–	800	0.0123	21	10	62.2
–	–	825	0.0123	30	14	86.2
0.15	0.75 (V)	725	0.0093	13	5	32.2
–	–	750	0.0093	15	6	39.3
–	–	775	0.0093	20	8	52.5
–	–	800	0.0093	26	11	74.2
–	–	825	0.0093	53	15	82.7
0.09	0.48 (V)	725	0.0055	19	6	45.5
–	–	750	0.0055	22	8	65.0
–	–	775	0.0055	36	11	82.0
0.04	0.55 (V)	750	0.0023	27	8	90.8
–	–	775	0.0023	44	21	302.5
0.10	0.08 (Nb)	*	0.0008	24	4	57.7

* Continuously cooled.

height can, according to the observations of Batte and Honeycombe, be directly equated to the sheet spacing of the interphase precipitation process. The nucleation and growth of the microalloy carbo-nitride takes place on the tread of the stepped interface rather than on the riser. The time available for this process is dependent upon the distance between successive risers of the stepped transformation interface and the velocity of the risers along the interface, the distance between rises reflecting the step initiation frequency.

There are mathematically simple expressions that can be applied to the system of ledge wise growth. For example, the time that the step tread is exposed to the austenite is dependent upon the length of the step tread, δ, and on the velocity, v, of the step riser (edge) across the transformation interface.

$$t = \delta/v \tag{5.7}$$

The time is also a direct measure of the ledge initiation frequency, ϕ,

$$\phi = 1/t \tag{5.8}$$

and the step tread length is given by

$$\delta = vt = v/\phi \tag{5.9}$$

The overall rate of advance of the austenite–ferrite transformation front (the growth rate of the ferrite), G, is given by

$$G = D\phi = D/t \tag{5.10}$$

where D is the step riser height.

It is clear from the results of Honeycombe and Batte that the step height, D, decreases with decreasing temperature (Fig. 5.4), but the temperature range of their studies coincides with that in which the ferrite growth rate, G, would be expected to *increase* with *decreasing* temperature,[17] thus indicating a much shorter time between steps and a reduction in the nucleation or growth of carbo-nitrides, or both. The reduced time available at lower temperatures, coupled with the increased supersaturation of the precipitate may explain the increased number and decreased size of the interphase precipitated particles. The decreased spacing within the sheets and the decreased particle size, with increasing carbon and/or vanadium content at any given transformation temperature would also be expected from a consideration of the effect of supersaturation on the nucleation rate. The situation, is, however, complex, in that changes in ferrite growth rates could be achieved by changes in the step riser height or by changes in the frequency of step initiation, and these systems are obviously worthy of further study. Any extended systematic study should also consider whether the isolation of a carbo-nitride particle from the transformation interface need necessarily cause a cessation of growth, as the diffusion rates of carbon and the microalloying elements (all of the latter are ferrite formers) are faster in ferrite than in austenite at a given temperature.

Edmonds[18] has observed bulging of the ferrite between the interphase particles at various points on the transformation interface, which suggests an alternative

mechanism for ferrite growth. Honeycombe[13] suggested that this occurred predominantly at the higher transformation temperatures, but pointed out that this ferrite growth process would not require the planar array of particles so evident in the interphase precipitation mechanism. Whilst it is tempting to explain the absence of bulges at lower temperatures to a Zener type particle pinning effect, Ashby[19] has pointed out that the chemical driving force for transformation gives an effective pressure on the transformation boundary of 10^7–10^{11} N/m^2, which is some 10^4 times larger than that for grain growth, so that it is unlikely that particles would block the advance of a transformation front, except at low levels of undercooling, where the chemical driving force is small. It is interesting to speculate, however, that once a bulge has formed, its propagation as a ledge would not be impeded by the particle effect, whereas a general advance of the interface would have a Zener drag, however small in relative terms.

The previous discussions of the results of Honeycombe and his co-workers have related to isothermal transformation conditions, and Honeycombe described the effect of other additions of alloying elements such as manganese, nickel and chromium on the interphase precipitation processes. By retarding the transformation, and reducing growth rates, Honeycombe suggested that the increased time would produce coarser carbo-nitrides at a given transformation temperature, in very much the same way that interlamellar spacings in pearlite are increased by alloying additions at a given isothermal transformation temperature. Honeycombe further suggested that alloying elements such as silicon and aluminium, which accelerate the ferrite reaction, should reduce the particle size and increase the number of particles, thereby increasing their contribution to the yield strength of the steel.

The effects of alloys on precipitation in isothermally transformed materials are, however, very different from their effects under the continuous cooling transformation conditions that are generally prevalent in commercial practices. Alloying elements such as manganese, nickel, etc., which retard transformation, will, for a given cooling rate, cause a depression of the transformation to lower temperatures. The transformation temperature is not imposed, as in the case of isothermal transformation, but results from the combined effects of the cooling rate and the effects of alloying elements on the transformation kinetics. More highly alloyed steels will transform at lower temperatures so that the diffusion controlled precipitation of the microalloy carbo-nitrides gives smaller and more closely spaced carbo-nitrides. The essential mechanisms of ferrite growth (i.e. ledge migration) and interphase precipitation are not changed, but the characteristics of the precipitate dispersion derive from the resultant transformation temperature.

The characteristic measures of the dispersed niobium carbo-nitride in a continuously cooled HSLA steel (Fig. 2.20) are included in Table 5.1, and again indicate that the square grid spacing within the sheet is larger than the sheet centre–centre spacing. Increasing the manganese content of such steels generally produces finer microalloy carbo-nitride particles due to the depression of the transformation temperature and will enhance the particle dispersion strengthening. A similar effect can be produced with other alloying elements, including carbon, and with other microalloy carbo-nitrides.

As the transformation temperature is progressively lowered by increasing the alloy content, at a given cooling rate, a limiting temperature is attained, below which the diffusivity of the microalloying element is insufficient to allow precipitation of the carbo-nitride. Under these circumstances the microalloy is retained in supersaturated solid solution and there is no dispersed second phase contribution to the yield strength. A similar effect can be produced by increasing the cooling rate at a given alloy content. Increasing the cooling rate of low carbon steels can so depress the transformation temperature that precipitation of the microalloy carbide is inhibited.

The effects of transformation temperature on the carbo-nitride precipitate are of particular importance in relation to hot-rolled coiled strip product, where the hot strip is rapidly cooled as it leaves the hot rolling mill to give a pre-determined coiling temperature. Control of the coiling temperature in this way gives a pre-determined transformation temperature which can extend to temperatures below the critical temperature required for suppression of the precipitation process. This aspect will be discussed further in Chapter 7.

A particularly fascinating aspect of the interphase precipitation reaction is observed in medium and high carbon steels, having a predominantly or wholly pearlitic microstructure. The pearlite transformation temperature range extends from about 500–550°C up to the A_1 temperature, and therefore shows considerable overlap with the range over which the interphase precipitation mechanism occurs in a predominantly ferritic microstructure in low carbon steel. As the pearlite/austenite interface consists of ferrite–austenite, and cementite–austenite interfaces due to the lamellar nature of the pearlite eutectoid structure, the possibility of an interphase precipitation process occurring in either or both of the ferrite and cementite phases must be considered. In fact, in medium and high carbon vanadium steels, vanadium carbo-nitride has been observed with an interphase morphology in the ferritic lamellae of the eutectoid structure. A typical example of interlamellar interphase precipitation is shown in Fig. 5.5. This is a dark field electron micrograph based on a vanadium carbo-nitride reflection, so that the vanadium carbo-nitride particles appear white, whilst the ferrite and cementite appear dark. A slight difference in shade allows the lamellar structure to be seen, and the wider bands are of ferrite whilst the narrow bands are of cementite, reflecting the 88:12 ratio of the equilibrium pearlitic constitution. It can be seen that the vanadium carbo-nitride interphase precipitate occurs exclusively in the ferrite, and furthermore, all of the carbo-nitrides are illuminated from the same diffraction spot, indicating a common variant of the same orientation relationship. Thus the characteristics of the interlamellar interphase precipitates in pearlitic ferrite are basically the same as those of the interphase precipitates in low carbon-ferritic structures.

In a medium carbon steel exhibiting both ferrite and pearlite, dark field electron micrographs frequently reveal interphase precipitation in the ferrite of both microstructural constituents (Fig. 5.6). It is interesting to note that the same vanadium carbo-nitride reflection will illuminate the interphase precipitates (under dark field conditions) in both the ferrite and pearlite regions, where these are contiguous, suggesting some continuity in the ferrite orientation between

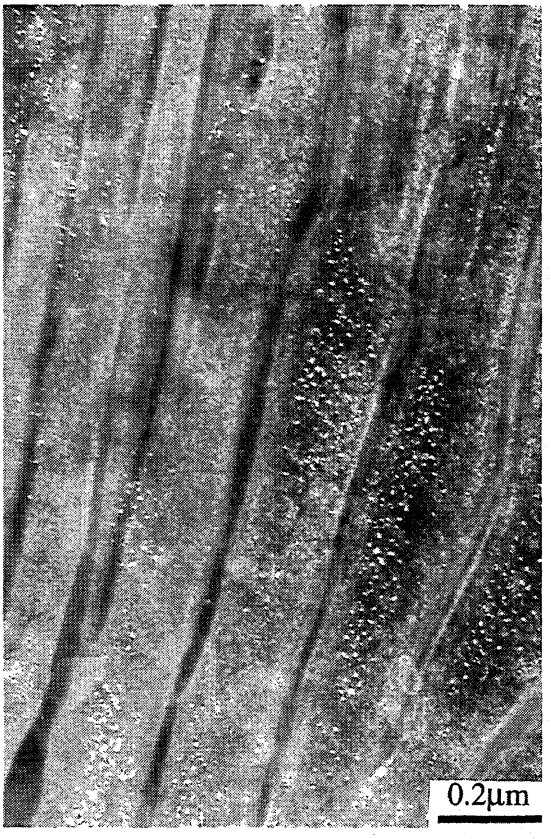


Fig. 5.5 Vanadium carbo-nitride particles having the interphase precipitate morphology and distribution in the interlamellar ferrite of the pearlite eutectoid structure (dark field transmission electron micrograph).

the polygonal ferrite and the interlamellar ferrite. More will be said of these steels in Chapter 7.

5.4 PRECIPITATION IN FERRITE

As pointed out in the previous section, rapid cooling rates applied to low carbon steels can effectively suppress the interphase precipitation reaction, or indeed any precipitation of the microalloy carbo-nitride, whilst still maintaining a substantially ferritic microstructure. Upon reheating in the ferrite temperature range, such steels will generally show a precipitation hardening reaction, with carbo-nitride particles forming either on dislocations, or as matrix precipitates. These precipitation hardening effects are the ferritic equivalent of secondary hardening in tempered martensitic steels and the hardening peaks are observed at similar temperatures and times.



Fig. 5.6 Vanadium carbo-nitride precipitation in a medium carbon steel having a ferrite–pearlite structure. Note that the vanadium carbo-nitride in both the ferrite and the contiguous pearlite are illuminated by the same diffracted beam, indicating a common variant of the same orientation relationship in a common ferrite orientation (dark field transmission electron micrograph).

A typical precipitation hardening curve is shown in Fig. 5.7 for a low carbon steel containing 0.02wt%Nb.[20] The steel was hot rolled and rapidly cooled to avoid interphase precipitation whilst still allowing the formation of a polygonal ferrite–pearlite microstructure. The yield strength of the steel in this condition was 380 MPa as shown in Fig. 5.7. The ageing treatments, originally carried out at 593°C and 621°C, produced significant increases in yield strength, the magnitude of which was dependent upon the tempering treatment. Such a precipitation process in ferritic steels can conveniently be expressed in terms of the Larsen–Miller Parameter, P, describing the combined effects of time and temperature, defined by

$$P = T(20 + \log_{10} t) \tag{5.11}$$

where T is the ageing temperature (K) and t is the ageing time (h).

Any particular value of the parameter, P, expresses a metallurgical state of precipitation, which can be attained through the temperature compensated ageing time by Equation (5.11). Any combination of ageing temperature and time that gives the same parameter value will show the same state of precipitation and therefore the same property response, so that the property changes resulting from ageing at different temperatures can be expressed in terms of a unique relationship with the tempering parameter. Once such a relationship has been illustrated, as for example in Fig. 5.7, then the effects of ageing at any time and temperature can be assessed, provided that that Larsen–Miller (L–M) parameter is within the range over which the property–parameter relationship has been established.

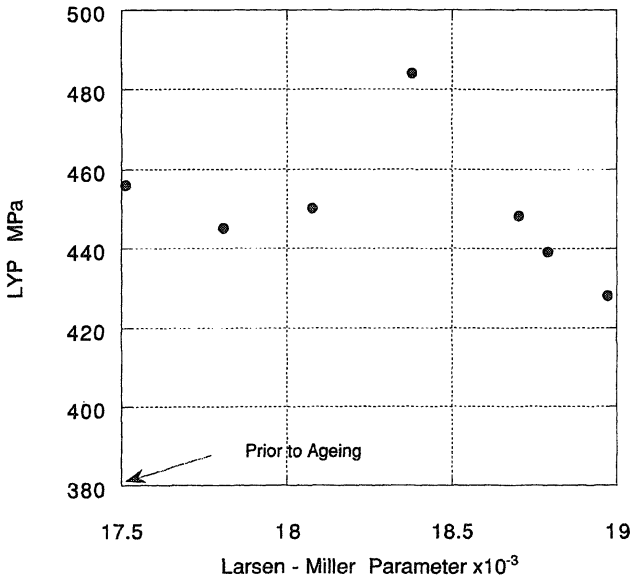


Fig. 5.7 Precipitation strengthening due to niobium carbo-nitride. The 0.02wt%Nb steel was hot-rolled and then cooled rapidly to avoid carbo-nitride precipitation. Sub-critical heat treatments, expressed by the Larsen–Miller parameter, allow precipitation giving rise to a classic precipitation hardening curve. After Bucher and Grozier.[20]

The increase in yield strength caused by the ageing treatment was already of the order of 60 MPa at a parameter value of 17.5×10^3 which is equivalent to 1 h at about 600°C. The precipitation process further increases the dispersion strengthening contribution up to 100 MPa at a tempering parameter of about 18.4×10^3 which corresponds to a 1 h ageing treatment at about 650°C. With higher parameter treatments the yield strength is observed to decline progressively as the precipitated particles become coarser, either by reduced nucleation or by Ostwald ripening of the fully precipitated niobium carbo-nitride particles. The dispersion strengthening contribution to yield strength is seen to decrease to a value of about 40 MPa at a parameter value of 19×10^3 equivalent to 1 h at 677°C.

Thus all the features of a relatively simple age-hardening reaction are seen, and the peak hardening occurs at a L–M parameter corresponding to 1 h at 650°C. Reference to the Ashby–Orowan strengthening relationship [Equation (2.59)], as depicted in Fig. 2.19, shows that a volume fraction of about 0.0002 (approximately that obtained from 0.02wt%Nb) would give 100 MPa contribution to the yield strength when the particle size is about 4 nm which is not untypical of niobium carbide formed at the peak temperature. Underageing might be expected to give smaller particles but only with incomplete precipitation, thereby reducing the volume fraction. Overageing obviously gives rise to coarser particles and, consequently, a reduced strengthening contribution.

Other similar observations have been made on steels containing niobium, vanadium, or titanium.[21] Subcritical ageing (tempering) treatments were applied

to the hot rolled steels. The basic difference between these results and those described above lies in the initial state prior to ageing. In the latter steels there was a considerable amount of interphase precipitation in the as-rolled state. The effects of ageing are shown in Fig. 5.8. The results appear to be very similar to those of Bucher and Grozier,[20] but only because the range of the L–M parameter is restricted to that in which extensive precipitation can occur. In the as-rolled condition, Bucher and Grozier had suppressed precipitation to obtain a yield strength of 380 MPa, which increased to 480 MPa on ageing. In the titanium steel results of Fig. 5.8, the as-rolled material exhibited a yield strength of 480 MPa which only rose to 510 MPa at peak hardening. Nevertheless, it is interesting to see

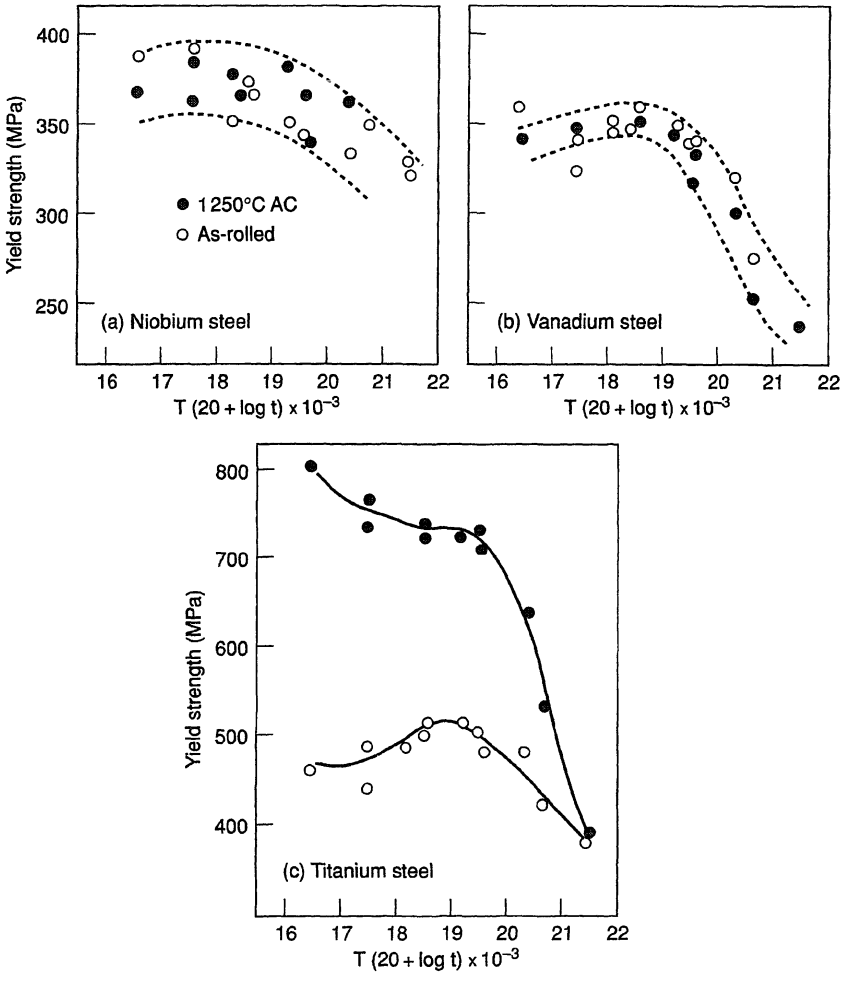


Fig. 5.8 Precipitation hardening curves for (a) niobium, (b) vanadium and (c) titanium microalloyed steels containing some prior interphase precipitated particles. After Irvine *et al.*[21]

that there is no significant softening of the steel until the L–M parameter value exceeds 19×10^3 which is equivalent to 1 h at 677°C.

5.5 OSTWALD RIPENING

As indicated in the previous section, particles of a dispersed second phase can be made to coarsen by holding at elevated temperatures in the ferrite range, and reference was made to the Ostwald ripening process. Ostwald ripening is an extremely important process in microalloyed steels, because it has direct significance not only for subcritical annealing treatments, but also for any elevated temperature treatment in which there is some undissolved second phase. Microalloyed steels heated into the austenite range, but below the solvus temperature, contain particles that will undergo this 'ripening' process, i.e. cannibalistic particle growth, sometimes with disastrous consequences for grain size control. The importance of particle size in inhibiting grain growth has already been described in Chapter 4. A situation in which some particles grow at the expense of others is thus vitally important, and so the subject of 'Ostwald ripening' requires some consideration.

A definition of Ostwald ripening can be given as the selective growth of some second phase particles, usually the larger particles, at the expense of other particles of the same phase, usually the smaller particles, the latter decreasing in size until they disappear completely. The definition must also include the condition that there is no *substantive* change in the solute content of the matrix during the ripening process. This definition distinguishes the Ostwald ripening process from precipitation, dissolution and transformation processes.

The Ostwald ripening process, like the grain growth process, effects a significant reduction in boundary energy. In the case of grain growth, it is the grain boundary energy that is reduced, whereas, in Ostwald ripening, the interfacial energy between matrix and precipitate is reduced by coarsening of the particles, at a constant volume fraction. The difference between the two is that grain growth is a 'tactile' process in that any grain is in direct contact with its neighbour, and becomes aware of the neighbours and their superiority (or otherwise) through its own edge and corner angles, but in the Ostwald ripening process, the second phase particles are separated by an often not inconsiderable thickness of matrix phase. In order that the isolated large particles should grow and the similarly isolated, small particles should shrink and disappear, thereby reducing the interfacial energy, there has to be a means of communication between the particles through the matrix, i.e. a non-tactile communication. (The author hopes that the reader will excuse the personalisation of the particles in this way, but such a simile gives an excellent description of the problem.) Consider any one of the particles, completely surrounded by the matrix phase. How does it know whether there is a larger particle beyond the matrix, in which case it should shed atoms and commence the shrinking and disappearance routine, or whether there is a smaller particle beyond the matrix, in which case it should start to gather atoms and grow larger?

The answer to this problem lies in the Gibbs–Thomson or Thomson–Freundlich[22] equation, relating the local solubility at the particle–matrix interface with the particle size.

$$\ln(S_r/S) = 2\Omega\sigma/RTr \tag{5.12}$$

where S_r is the solute content in equilibrium with a particle of radius r, S is the true equilibrium solubility (with an infinitely large particle), Ω is the molar volume of the precipitate, σ is the interfacial energy between particle and matrix, R is the gas constant and T is the absolute temperature, K.

The derivation of this equation has been described elsewhere,[23] and for present purposes it is only necessary to draw attention to the assumptions that are implicit in the present treatment, i.e. that the precipitate is spherical, and that the interfacial energy is independent of either the orientation relationships between the lattices or the orientation of the interface itself. The interfacial energy is assumed to be constant. These assumptions are not necessary to the validity of the concept but merely simplify the mathematical expressions.

The molar volume of the precipitate appears in the above expression as a conversion factor between the volume of the particle and the molar concentration of the solute.

It can readily be seen from Equation (5.12) that a small particle will give a high level of solute in the matrix near the particle surface; a larger particle will give a lower level of solute near the particle. In the absence of any infinitely large particles, the general level of solute in the matrix will be intermediate between the equilibrium levels for the smallest and largest particles, such that diffusion of the solute will occur from the high concentration regions near the small particles, and towards the low concentration regions near the large particles. Any diffusion of solute from the vicinity of small particles will obviously upset the local equilibrium described by the Gibbs–Thomson equation, and some dissolution of the particle will occur to re-establish the equilibrium solute content, and in so doing will decrease the particle size and further increase the local equilibrium content. This continuing cycle of diffusion and dissolution will ultimately result in the disappearance of the small particles. The diffusion of solute to the low concentration regions near the large particles will result in a local supersaturation followed by precipitation and particle growth to re-establish the Gibbs–Thomson equilibrium level. The further growth of the large particle of course results in a lower local equilibrium solute concentration in the matrix, and again, the cycle of diffusion and precipitation results in the stable growth of larger particles. The continued disappearance of the smaller particles will ultimately place some of the particles which have grown, into the smaller size category of those that remain, and these particles will then begin to dissolve.

The diffusion path is shown schematically in Fig. 5.9, but does not adequately reflect the complexity of a three-dimensional array of particles of different sizes. The concept remains simple, but the mathematical treatment describing the kinetics of the change in the particle size is highly complex. Analytical solutions containing certain simplifying assumptions have been derived by Greenwood,[24] Lifshitz and Slyozov[25] and Wagner.[26] A number of limiting conditions for the

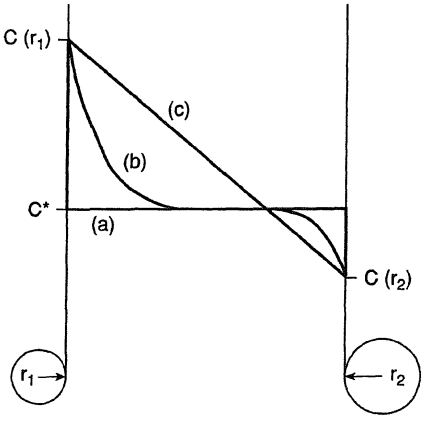


Fig. 5.9 Ostwald ripening. The diffusion path operating when remote particles of different sizes show differing equilibrium solute concentrations. (a) Interface controlled mechanism; (b) Diffusion control with large particle spacings; (c) Diffusion control with small particle spacings. Mechanism (b) appears to be more appropriate to microalloyed steels. After Fischmeister and Grimvall.[27]

ripening process have been identified, each leading to different analytical solutions, depending on the rate limiting step in the growth process. These include interface limited growth, where the slowest step is the transfer of atoms across the phase boundary from the matrix to the particle, and diffusion limited growth, where the slowest step is the transport of solute atoms along the diffusion path, whether this involves bulk diffusion, grain-boundary diffusion, or other preferred diffusion paths. These processes have been surveyed by Fischmeister and Grimvall[27] and the derivations have been given for the various limiting conditions. From the standpoint of microalloyed steels, such studies as have been carried out, have indicated that the process is diffusion controlled (by bulk diffusion), and it is also worth noting that one of the assumptions of the analytical treatments, i.e. that the interparticle spacing is large with respect to the particle size, is reasonably true of microalloyed steels with their small volume fractions f of second phase particles ($f < 0.001$).

5.5.1 Ostwald Ripening With Bulk Diffusion Control

Under conditions of diffusion control, the rate of change of particle radius, dr/dt, is given by[26]

$$dr/dt = D\Omega(dc/dx)_r \tag{5.13}$$

where D is the diffusion coefficient of the solute, Ω is the molar volume and $(dc/dx)_r$ is the concentration gradient at the surface of a particle of radius r.

Using Zener's approximation[28] for the stationary diffusion flux from a supersaturated infinite medium of concentration S^*, to that, Sr, at a particle of radius r, yields

$$dr/dt = D\Omega(S^* - S_r)/r \tag{5.14}$$

Bearing in mind that the volume fraction of particles is substantially constant (as is the amount of solute) as defined by

$$4\pi \sum r_i^2 (\mathrm{d}r_i/\mathrm{d}t) = 0 \tag{5.15}$$

then substitution of Equations (5.12) and (5.15) into Equation (5.14) gives[27]

$$\mathrm{d}r/\mathrm{d}t = \sigma S D \Omega^2 (1/r^* - 1/r)/RTr \tag{5.16}$$

where σ is the interfacial energy between matrix and precipitate, D is the diffusion coefficient for the rate limiting specie, r^* is a critical particle radius that would be in equilibrium with a solute concentration C^* beyond the local perturbation caused by the particle.

The rate of growth of the particle is positive only when r is above the critical size and is negative, i.e. the particle shrinks when r is less than the critical size. In fact, the critical particle radius can be equated to the mean particle radius, r_m, and thus S is the solute concentration in the matrix that is in equilibrium with a particle of average radius.

Integration of Equation (5.16) is quite complex. A relatively simple treatment has been presented by Martin and Doherty,[23] and more rigorous solutions have been presented by Lifshitz and Slyozov[25] and by Wagner.[26] The Wagner equation is given as

$$r^3 - r_0^3 = 8D\sigma\Omega St/9RT \tag{5.17}$$

This equation, in addition to assuming an effectively infinite particle spacing with no overlap of the influence of neighbouring particles, is also only strictly valid for the steady state size distribution. The progressive growth of the larger particles and dissolution of smaller particles, together with the total volume conservation of the particulate array, leads to a steady state frequency distribution when the particle size is expressed in relative terms with respect to the mean particle size in the array. Ardell[29] has considered the effects of finite interparticle spacings such as occur with high volume fractions of second phase particles, as has Asimow.[30] The differences between their treatments relate to the definition of the sphere of influence of a single particle. Asimow used the radius of the average (spherical) volume of matrix per particle, whereas Ardel used the radius of a sphere having the same volume as that of a polyhedron formed by planes normal to bi-particle axes and equidistant between the particles. Both workers showed that the basic form of the Wagner equation was maintained, but included a substantial enhancement factor, ζ. The factor ζ, obtained by Ardell, was unity for infinite spacing (very low volume fractions of particles), 2 for a 1% volume fraction, and 5 for a 10% volume fraction of particles. The values obtained by Ardell were substantially higher than corresponding values obtained by Asimow. However, with the volume percentage of second phase particles present in microalloyed steels being less than 0.1%, Equation (5.17) can be used directly.

The concept of Ostwald ripening was originally developed for the coarsening of solid particles in a liquid matrix, but the mathematical solutions have been applied

successfully to second phase particles in a solid matrix, usually for cases where an elemental solute is precipitated as an elemental second phase, e.g. the Cu–Cr system, or in systems where the elemental solute forms a compound with the matrix phase, e.g. the Ni–Al system forming Ni_3Al. In these cases, the diffusion limited kinetics, having the cubic dependency indicated by Equation (5.17), can be related directly to the diffusion rate of the solute, e.g. Cr in a Cu matrix forming Cr particles, or Al in a Ni matrix forming Ni_3Al particles. In microalloyed steels, however, there are two or more solutes in the matrix which combine to form an interstitial compound of the form $MC_xN_{(1-x)}$ or $M'_yM''_{(1-y)}C_xN_{(1-x)}$. This gives rise to the problem of defining the rate limiting specie in a diffusion controlled ripening situation.

This problem has been discussed by Fischmeister and Grimvall,[27] who pointed out that the Gibbs–Thomson or Thomson–Freundlich equation (5.12) is modified by inserting the solubility products rather than the elemental solubility, i.e.

$$\ln(k_r/k_s) = 2\Omega\sigma/RTr \tag{5.18}$$

where k_s is the solubility product (see Chapter 3) and k_r is the solubility product that is in equilibrium with a particle of radius, r.

It is clear that the rate of coarsening of the carbo-nitride will, under conditions of diffusion limited growth, be controlled by the lowest diffusion flux in relation to its concentration in the precipitated phase. This is dealt with in the survey by Fischmeister and Grimvall who distinguish between situations where a major component of the precipitate is present in small concentrations in the matrix and has a low diffusion flux, and situations where near stoichiometric compositions of elements with similar diffusion coefficients require the use of an effective diffusion coefficient.

The complexity of a diffusion controlled Ostwald ripening process involving two or more solutes, coupled with the complexities of the solubility products in complex microalloyed steels, has so far precluded any rigorous assessment of the quantative application of the Wagner equation, but there are several important qualitative aspects that arise from these concepts, as follows:

(i) The diffusion coefficients of the interstitial solutes, carbon and nitrogen, are large in comparison with those of substitutional solutes, and the diffusion flux of the micro alloying element would normally be the rate controlling factor in the ripening of any diffusion controlled carbo-nitride. Data on the diffusion coefficients of microalloys and the interstitials carbon and nitrogen taken from *Smithell's Metals Reference Book*[31] are shown in Table 5.2. Data for aluminium in ferrite and for the self diffusion of iron are also included. The diffusion coefficient, D, at any given temperature is defined by

$$D = D_0 \exp(-Q/RT) \tag{5.19}$$

where D_0 is a constant, Q is the activation energy for diffusion, R is the gas constant (8.314 J mole^{-1} K^{-1}) and T is the temperature (K).

Table 5.2 Diffusion data for microalloy and interstitial solutes in austenite and in ferrite. The diffusion coefficients of these elements at 1200°C in austenite, and at 700°C in ferrite, are also shown

Element/Phase	D_0 ($m^2 s^{-1}$)	Q (kJ mol^{-1})	D_α 700°C ($m^2 s^{-1}$)	$D\gamma$ 1200 °C ($m^2 s^{-1}$)
C/α	0.62×10^{-6}	80.4	3.00×10^{-11}	–
C/γ	0.10×10^{-4}	135.7	–	1.59×10^{-10}
N/α	0.50×10^{-6}	77.0	3.66×10^{-11}	–
N/γ	0.91×10^{-4}	168.6	–	9.60×10^{-11}
Ti/α	3.15×10^{-4}	248.0	1.56×10^{-17}	–
Ti/γ	0.15×10^{-4}	251.2	–	1.86×10^{-14}
V/α	0.61×10^{-4}	267.1	2.80×10^{-19}	–
V/γ	0.25×10^{-4}	264.2	–	1.07×10^{-14}
Nb/α	–	–	–	–
Nb/γ	5.30×10^{-2}	344.6	–	1.56×10^{-13}
Al/α	0.30×10^{-2}	234.5	7.80×10^{-16}	–
Al/γ	–	–	–	–
Fe/α	1.67×10^{-4}	256.7	2.79×10^{-18}	–
Fe/γ	0.49×10^{-4}	284.1	–	4.13×10^{-15}

Values of D_0 and Q for the various species are presented, together with values of the diffusion coefficients both in the α-phase at 700°C and in the γ-phase at 1200°C. In the ferrite (α-phase), the diffusion coefficients for the interstitials at 700°C are of the order of 3×10^{-11}, whilst for the substitutional microalloys they are in the range 10^{-19} to 10^{-15}. The diffusion fluxes are directly related to these values of D. In the austenite (γ-phase), the diffusion coefficients of the interstitials at 1200°C are of the order 10^{-10} whilst those of the microalloys range from 10^{-17} for niobium to 2×10^{-14} for titanium. The diffusion coefficients for the microalloys are of a similar order to that of the self diffusion of iron.

(ii) The diffusion flux of any particular solute is dependent upon the product of the diffusion coefficient and the matrix concentration, $D \cdot S$, and thus the concentration of solute in the matrix is important to the coarsening rate. Both the diffusion coefficient and the solute concentration in the matrix are strongly temperature dependent, and these factors are dominant in the temperature dependence of the particle coarsening rates.

(iii) The matrix concentration of the rate limiting solute at a given temperature can be changed by composition control of the steel. The solubility of a microalloy carbide or nitride, MX, in steel is defined by the solubility product, $k_s = [M][X]$, and, as shown in Chapter 3, the concentration of $[M]$ at a given temperature is dependent on the ratio of the total microalloy content, M, and total interstitial content, X ($= C$ or N), in the steel. If the microalloy diffusion flux is rate controlling, the particle coarsening rate can be reduced by increasing the carbon or nitrogen content of the steel. This reduces the ratio of $[M]$ to $[X]$ whilst maintaining the defined solubility product, k_s, and reduces the value of $[M]$ at temperatures below the solvus.

(iv) For different microalloys, with similar diffusion coefficients, lower particle coarsening rates are expected for those carbo-nitrides having the lowest solubility products. As indicated in Chapter 3, titanium nitride, showing by

far the lowest solubility product would be expected to give the slowest particle coarsening rate. This subject will be dealt with in greater detail in Chapter 7.

The effects of molar volume, and of the interfacial energy, on particle coarsening rate are largely fixed by the structure of the particle when present in steel. The molar volumes of the various carbides and nitrides, derived from their atomic masses, crystalline structures and lattice parameters, are shown in Table 5.3.

The density, ρ, is obtained from the gram molecular mass, m_{mx}, as follows

$$\rho = m_{mx}n/Aa^3 \tag{5.20}$$

where n is the number of molecules per unit cell, A is Avogadro's Number (6.0222×10^{23}) and a is the lattice parameter (cube edge of the f.c.c. unit cell).

The molar volume, Ω, is obtained from

$$\Omega = m_{mx}/\rho = Aa^3/n \tag{5.21}$$

Although the densities show significant variations, mainly arising from the variations in the atomic masses of the microalloy atoms, the molar volumes are all in the range $10.52\,cm^3$–$13.39\,cm^3$ due to the similarities in the lattice parameters. Data for aluminium nitride are also shown in Table 5.3, and although the density is much lower than those of the microalloy carbides and nitrides, the molar volume is well within the range of those given for these compounds. On this basis, the coarsening rates of the various carbides and nitrides should be virtually unaffected by variations in molar volume. Also, given that the lattice parameters of the

Table 5.3 Molar volumes of microalloy carbides and nitrides (based on room temperature lattice parameters)

Compound (structure)	Molecular mass	Lattice parameter (nm)	Molecules per unit cell	Density (Mgm^{-3})	Molar volume (cm^3)
NbC (f.c.c.)	105	0.4462	4	7.84	13.39
NbN (f.c.c.)	107	0.4387	4	8.41	12.72
VC (f.c.c.)	63	0.4154	4	5.83	10.81
VN (f.c.c.)	65	0.4118	4	6.18	10.52
TiC (f.c.c.)	60	0.4313	4	4.89	12.27
TiN (f.c.c.)	62	0.4233	4	5.42	11.44
AlN (c.p.h.)	41	$c=0.4965$ $a=0.311$	6	3.27	12.54
γ-Fe (f.c.c.)	56	0.357	4	8.15	6.85
α-Fe (b.c.c.)	56	0.286	2	7.85	7.11

(Based on room temperature lattice parameters.)

individual carbo-nitrides lie between those of their repective carbides and nitrides, the molar volumes will also lie within the range shown in Table 5.3.

However, an important feature arises in the case of complex carbo-nitrides. Consider, for example, a complex carbo-nitride of titanium and niobium, having equal atom fractions of the two microalloys in the carbo-nitride. The diffusion fluxes for the two solutes could be very different, arising from differences in their diffusion coefficients (Table 5.2), and their solute concentration in the matrix. The two substitutional solutes do not diffuse as a compound pair, and one or other of these solutes would therefore be rate limiting, as pointed out earlier. However, when a flux of the rate limiting solute arrives at the larger particle and forms the equilibrium precipitate, then, in the case cited, the molar volume would be double that shown in Table 5.3 because the arrival and precipitation of the rate limiting specie will be accompanied by the precipitation of an equal amount of the complementary element. The precipitation of 1 mole of Ti(CN) would in this case be accompanied by the precipitation of 1 mole of Nb(C,N). It follows that the effective molar volume would be further increased if the equilibrium fraction of the rate limiting specie in the complex carbo-nitride was further reduced.

The equilibrium fractions in such complex carbo-nitrides are known to change with temperature, for a given steel composition, and the effective molar volume would also change with temperature. Consider a generalised case for $(Ti_yNb_{1-y})(C_xN_{1-x})$. For each gram atom of titanium, there would be $1/y$ gram moles of carbo-nitride, and the molar volume m_{mx} of the carbo-nitride would be dependent on the specific composition with regard to both y and x, i.e. would have a value $(m_{mx})_{(x,y)}$. Thus the effective molar volume of the rate limiting specie would be

$$\Omega = (m_{mx})_{(x,y)}/y \quad \text{if titanium were rate limiting}$$

$$\text{or} \qquad \Omega = (m_{mx})_{x,y}/(1-y) \quad \text{if niobium were rate limiting}$$

There has been little theoretical development of these aspects of the Ostwald ripening process, due, in part, to the complexities and the non-analytical solutions of the solubility relationships. Also, there are many observations of variations in chemical composition between and within particles that can further complicate the interpretation of particle coarsening, due, presumably, to the difficulties associated with the diffusion of metal ions within the carbo-nitride particles. It is this diffusional difficulty which is believed to give rise to the commonly observed cored particles that are developed during continuous cooling.

Little can be said of the interfacial energy term of the Wagner relationship [Equation (5.17)]. Many of the interfacial energies measured in ferrous and other systems generally lie in the range 0.5–1.0 Jm^{-2} for incoherent particles and in the range 0.1–0.2 Jm^{-2} for coherent particles.[23] There is evidence for coherency in certain of the microalloy carbo-nitrides in the early stages of formation in the ferrite, e.g. V(CN) in ferrite.[21] Vanadium carbo-nitride would be expected to maintain coherency to larger particle sizes than the other carbo-nitrides due to the smaller lattice mis-match with the ferrite. However, in transformable microalloyed steels, the coherency is unlikely to persist through phase transformations, as for

example when particles are precipitated in the austenite and the austenite subsequently transforms to ferrite during cooling. Interphase particles sometimes show coherency strain effects with the ferrite, but this would not survive a normalising treatment. In situations where ripening is likely to be of interest, the microalloy carbo-nitrides are most likely to have incoherent interfaces and would therefore be expected to have interfacial energies in the range 0.5–1.0 Jm^{-2}. Although the interfacial energy normally decreases with increasing temperature, Fischmeister and Grimvall[23] have suggested that these variations are generally small over the temperature ranges of interest in many alloy systems.

5.5.2 Ostwald Ripening Without Bulk Diffusion Control

Although the majority of studies of Ostwald ripening have found the cubic relationship given in Equation (5.17), indicating bulk diffusion of the solute as the rate controlling process, there are other factors that may be rate limiting. Wagner developed equations for a number of other rate limiting situations. When the rate limiting step in the ripening process is the rate of transfer of atoms from the precipitate to the matrix,

$$r^2 - r_0^2 = 64K_T S\sigma\Omega^2 t/81RT$$

where K_T is the temperature dependent rate transfer coefficient.

Under these conditions, the square of the mean particle radius increases linearly with time, compared with the cube of the mean particle radius for the bulk diffusion controlled process.

When particles are predominantly distributed on grain boundaries, due to the ease of nucleation at such sites, then the growth of the particles may be controlled by the diffusion flux along the grain boundaries, rather than by bulk diffusion.[32] Under these circumstances the appropriate diffusion coefficient is that for grain boundary diffusion which results in a much faster coarsening rate. The geometry of the diffusion flux gives rise to an equation of the form

$$r^4 - r_0^4 = kt$$

i.e. the fourth power of the mean radius increases with time. Kreye[33] has considered the coarsening of particles on low angle boundaries where dislocation pipe diffusion is important and suggested an $r^5 \propto t$ relationship.

As mentioned earlier, the bulk diffusion controlled process is by far the more common, but there are two notable exceptions that have been found in connection with steels.

(i) The coarsening of cementite, Fe_3C, in well tempered martensitic structures, α-iron, although complying with a bulk diffusion controlled process, gives an activation energy that relates to the self diffusion of iron rather than the diffusion of carbon in ferrite. It has been suggested[10] that the volume change which accompanies the local precipitation of cementite, giving rise to a volume expansion, requires a flux of vacancies to accommodate the volume change, whilst at dissolving particles the local decrease in volume

provides an excess of vacancies that must diffuse away, i.e. there is an opposite flux of iron atoms. Thus the bulk diffusion of vacancies from small (dissolving) carbide particles to large (growing) particles would appear to be rate controlling. This illustrates an important feature of the ripening process, in that it is not only the solute that may have to diffuse for particle growth to occur, particularly when the precipitation / dissolution processes involve significant volume changes.

(ii) The coarsening of vanadium carbide in ferrite was studied by Schwartz and Ralph,[34] using field ion microscopy. They studied the coarsening of fine interphase precipitated vanadium carbide and found the r^2 v t power law relationship, suggesting an interface controlled process, having an activation energy of 196 KJ mole^{-1}, which is significantly less than the 267 KJ mole^{-1} for the diffusion of vanadium in ferrite, especially as the observed activation energy had not been corrected for the increase in solubility of vanadium carbide in ferrite with increasing ageing temperature. Although suggestions were made concerning the nature of interphase precipitation, this observation remains unexplained but interesting.

5.6 SUMMARY

The precipitation of microalloy carbo-nitrides in steels can occur in the austenite, during the austenite–ferrite transformation (to give interphase precipitation), or in the fully transformed ferrite, depending upon the thermal and thermomechanical treatments applied to the steel, and also upon the composition of the steel, particularly where this affects the transformation characteristics.

Precipitation in the austenite is generally sluggish but can be considerably enhanced by the application of hot deformation cycles. Interphase precipitation is refined by changes in the transformation temperature, low transformation temperatures giving smaller inter-sheet spacings, smaller particle spacings within the sheets of interphase precipitation, and smaller particle sizes. Precipitation from supersaturated ferrite gives rise to a classical age hardening reaction with maximum hardening after a treatment of 1 h at 650°C; thermal treatments for longer times or at higher temperatures produced classical overageing.

The subject of Ostwald ripening has been considered in relation to the behaviour of microalloy carbo-nitrides. Whilst there is considerable evidence that many systems show bulk diffusion limited particle coarsening, the interpretation of the coarsening rates can be difficult when complex multi-solute particles are involved. The effects of solute diffusion coefficients, solute concentrations and molar volumes have been considered. Particles with low solubility, and, decomposing into solutes with low diffusion coefficients, are required.

REFERENCES

1. J. H. Woodhead and W. B. Morrison: *J. Iron and Steel Inst.*, 1963, **201**, p.43.
2. G. Begin and R. Simoneau: *Microalloying 75*, p.85.
3. T. Hoogendorn and M. J. Spanraft: *Microalloying 75*, p.75.
4. K. E. Honer and S. Baliktay: *Proc. 44th Int. Foundry Cong.*, Florence 1977, paper 11.
5. M. Mayrhofer: *Berg. Huttenmann. Monatsh.*, 1975, **120**, p.312.
6. T. Gladman and F. B. Pickering: *J. Iron and Steel Inst.*, 1967, **205**, p.653.
7. P. Konig, W. Scholz and H. Ulmer: *Arch. F.D. Eisenhuttenwes*, 1961, **32**, p.541.
8. J. J. Jonas and I. Weiss: *Metal Science*, 1979, **13**, p.238.
9. T. Chandra, M. G. Akben and J. J. Jonas: *Proc. 6th. Conference on Strength of Metals and Alloys*, Melbourne, Australia, Ed. R. C. Gifkins, 1982, p.499
10. R. W. K. Honeycombe: *Steels–Microstructure and Properties*, Edward Arnold, London, 1981.
11. J. M. Gray and R. B. S. Yeo: *Trans A.S.M.*, 1968, **61**, p.255.
12. F. B. Pickering and T. Gladman: *Iron and Steel Inst. Special Report No. 81*, London, 1963, p.10.
13. R. W. K. Honeycombe: *Trans A.I.M.E.*, 1976, **7A**, p.915.
14. A. D. Batte and R. W. K. Honeycombe: *J. Iron and Steel Inst.*, 1973, **211**, p.184.
15. A. T. Davenport and R. W. K. Honeycombe: *Proc. Roy. Soc.*, 1971, **322**, p.191.
16. A. J. Baker and J. Nutting: *Iron and Steel Inst. Special Report No. 64*, 1959, p.1.
17. D. J. Swinden and J. H. Woodhead: *J. Iron and Steel Inst.*, 1971, **209**, p.883.
18. C. J. Middleton and D. V. Edmonds: *Metallography*, 1976.
19. M. F. Ashby: *1st. RISO Conference, Recrystallisation and Grain Growth*, Eds. N. Hansen, A. R. Jones and T. Leffers, Roskilde, Denmark, 1980, p.325.
20. J. H. Bucher and J. D. Grozier: *J. Iron and Steel Inst.*, 1966, **204**, p.1253.
21. K. J. Irvine, F. B. Pickering and T. Gladman: *J. Iron and Steel Inst.*, 1967, **205**, p.161.
22. H. Freundlich: *Kapillarchemie, Akdd*, Verlagsges, Leipzig, 1922.
23. J. W. Martin and R. D. Doherty: *Stability of Microstructure in Metallic Systems*, Cambridge University Press, Cambridge, 1976.
24. G. W. Greenwood: *Acta Met.*, 1956, **4**, p.243.
25. I. M. Lifshitz and V. V. Slyozov: *J. Phys. Chem. Solids*, 1961, **19**, p.35.
26. C. Wagner: *Z. Electrochemie*, 1961, **65**, p.243.
27. H. Fischmeister and G. Grimvall: *Materials Sci. Res.*, 1973, **6**, p.119.
28. C. Zener: *J. App. Phys.*, 1949, **20**, p.950.
29. A. J. Ardell: *Acta Met.*, 1972, **20**, p.61.
30. R. Asimow: *Acta Met.*, 1963, **11**, p.72.
31. *Smithells Metals Reference Book* (6th Edn.), Ed. E. A. Brandes, Butterworths, London, 1983.
32. H. P. K. Kirchner: *Met. Trans.*, 1971, **2**, p.2861.
33. H. Kreye: *Z. fur. Metallkunde*, 1970, **61**, p.108.
34. D. M. Schwartz and B. Ralph: *Phil. Mag.*, 1969, **19**, p.1069.

CHAPTER 6

Thermal and Thermomechanical Cycles

6.1 INTRODUCTION

The two main effects of microalloying are in providing undissolved second phase particles that will impart grain coarsening resistance to the matrix structure, and to provide a fine distribution of second phase particles, usually by the interphase precipitation mechanism, that will impart strength to the material. The principles of grain size control by Zener pinning, and strengthening by the Ashby–Orowan relationship, have already been described in Chapters 4 and 2 respectively. However, it is important to recognise that these principles are employed within a much broader metallurgical framework of industrial manufacturing processes, and the ultimate control of microstructure (and properties) is highly dependent upon variables within the manufacturing process itself.

For example, the use of Zener pinning to inhibit grain growth gives a good quantitative evaluation of the size of grains that can be prevented from growing for any given volume fraction and size of particle, but it may have little to do with the manner in which such sizes of grains are produced. The creation of the grain structure is dependent on factors other than the particulate distribution that may eventually cause grain growth inhibition, such as the transformation characteristics either of ferrite to austenite, or of austenite to ferrite, in these allotropic steels. Other phenomena, such as are involved in hot working, can also have important effects on the microstructure and properties of microalloyed steels. The effects of industrial hot working variables are important to metallurgical control, as well as to the economic operation and shape control of this important metal shaping process. Cold working and annealing practices can also have important effects on the microstructure and properties of sheet and strip products and on wire products, but these will be considered in connection with specific product developments in Chapter 7.

The principles of microstructural control during normalising treatments and hot working are considered in this chapter, these treatments being applied to a substantial proportion of the microalloyed steels produced.

6.2 NORMALISING TREATMENTS

'Normalising' is the term used to describe heating a transformable steel to a temperature in the austenite temperature range, soaking at this temperature, and

then air cooling the steel after removal from the normalising furnace. The normalising temperature is defined as A_{c3} + 30°C, and is consequently highly dependent upon the carbon content of the steel. The normalising time is sufficient to allow the stock to attain and soak at the normalising temperature, and this is dependent upon the effective section size. The normalising time is customarily based on 1 h per 25 mm diameter of round bar. The bar equivalent of non-circular cross section can be obtained from heat flow tables; for a flat plate, rule of thumb suggests an equivalent diameter of twice the plate thickness, so that a 15 mm plate would require the same length of time as a 30 mm diameter bar. The stock is then removed from the normalising furnace and allowed to air cool.

The normalising treatment was introduced to eliminate the variability in properties that could be found in hot-rolled materials from different sources. In the absence of any deliberate control of the hot-rolling process, considerable variations in microstructure and properties can occur as a result of variations in the extent of hot deformation, the deformation temperature, and differences in cooling rates on the rolling mill run-out table. Normalising these products produces a more uniform austenite structure and a guaranteed cooling cycle during which the austenite to ferrite transformation takes place. The sources of variability in hot-rolled products will be dealt with in greater detail in a later section, but the factors controlling the microstructure and properties of normalised carbon-manganese and microalloyed steels provide a useful introduction to the roles of austenite grain size and transformation characteristics.

A schematic normalising cycle is shown in Fig. 6.1. The initial stock material may have a wide variety of structures, comprising ferrite, pearlite and/or bainite. The metallurgical changes that occur on normalising include the nucleation and

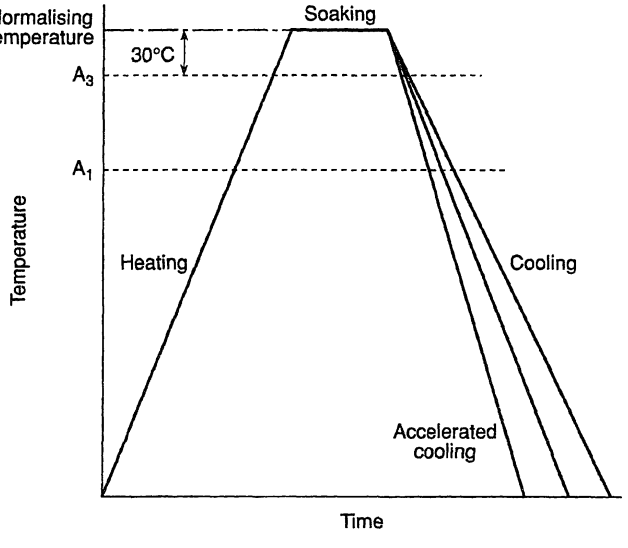


Fig. 6.1 A schematic normalising treatment. The heating and cooling rates are influenced by the effective section size of the stock to be normalised.

growth of the austenite phase during heating through the A_{c1} and A_{c3} change points, austenite grain coarsening during exposure at temperatures above the A_{c3} temperature, i.e. in the austenite temperature range, and transformation during the cooling cycle.

6.2.1 Reaustenisation and Grain Size

Reaustenisation during the heating cycle occurs by a nucleation and growth process. Austenite grains will nucleate primarily at the ferrite–cementite interfaces,[1] and at slow heating rates, i.e. characteristic of thick plates or large sections, these nuclei will grow as the temperature rises, until collision of the austenite grains occurs. Finally a complete austenite structure will be formed when the last ferrite disappears on heating through the A_{c3} temperature. The phase change under conditions of slow heating will be exactly the reverse of those observed according to the Fe–Fe_3C equilibrium diagram (Fig. 6.2), during slow cooling. At a temperature intermediate between the A_{c1} and A_{c3} temperature, the proportions of austenite and ferrite and their compositions would be close to those indicated by the diagram, and pearlitic blocks would be completely reaustenitised and diluted in carbon content to an extent dictated by the temperature attained during the slow heating cycle.

With more rapid heating rates and particularly in low carbon steels, austenite nucleation may occur at ferrite–ferrite grain boundaries, as well as at the carbide interfaces, thus giving an increase in the total number of austenite nuclei. The ferrite transformation to austenite during heating differs from the reverse transformation during cooling in that the driving force for transformation increases with increasing temperature, as does the diffusion coefficient for

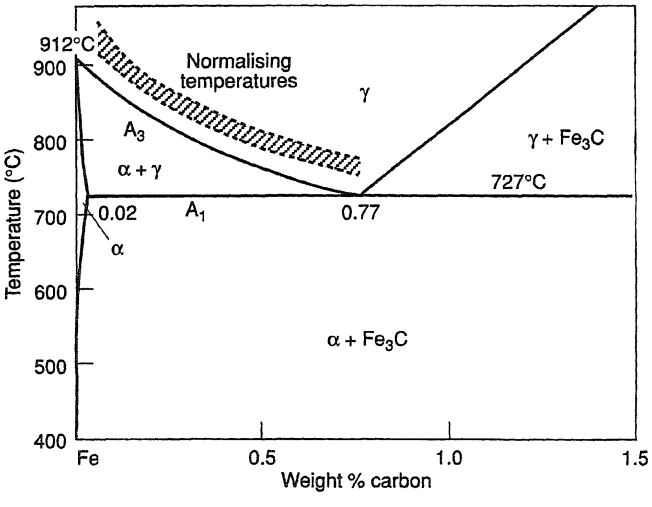


Fig. 6.2 The iron–iron carbide equilibrium diagram showing the A_1 and A_3 temperatures, and the recommended normalising temperature for plain carbon steels.

carbon in austenite, and also, under non-equilibrium heating conditions, the transformation will occur at a higher temperature than that observed for the cooling transformation. For example, hypo-eutectoid steels show a characteristic C-curve for isothermal transformation on down quenching, due to the increase in driving force as the temperature is lowered, and the reduced diffusion of carbon in austenite. The nose of the C-curve typically occurs at 600–650°C. On up-quenching, there is no corresponding C-curve, as both the chemical driving force and the diffusional aspects of the transformation increase simultaneously, thus increasing the rate of transformation progressively as the up-quenching temperature is increased. Such up-quenching treatments would characteristically give a transformation range above the eutetoid temperature, i.e. above 723°C. Although there has been some exploitation of rapid reaustenitisation treatments, using resistance heating or H.F. induction heating, and significant enhancement of the nucleation frequency coupled with a minimal grain growth due to the very short times of holding (a few seconds), the method is generally limited to engineering components of limited size.

The nucleation and growth mechanism for the reaustenitisation process on heating, coupled with the preferred nucleation sites at carbide particles and ferrite–ferrite grain boundaries, gives rise to a degree of sensitivity to the prior structure. A coarser prior structure will tend to give a coarser austenite structure during normalising. Double-normalising treatments have been used to overcome the problems associated with very coarse prior structures.

Following complete reaustenitisation, grain growth will occur unless grain growth inhibitors are employed. The grain growth in carbon steels was initially described by an equation of the form

$$d^2 - d_0^2 = Kt \tag{6.1}$$

where d is the mean grain diameter at time t, d_0 is the initial mean grain diameter and K is the rate constant.

The rate constant, K, is temperature dependent and follows the usual Arrhenius relationship[2]

$$K = K_0 \exp(-Q_G/RT) \tag{6.2}$$

where K_0 is a constant, Q_G is the activation energy for grain growth and T is the temperature (K).

Considerable doubt has been expressed[3,4] concerning the value of the time exponent in Equation (6.1), and Hu and Rath[4] suggested that the value of 2 was the exception rather than the rule. A more general relationship was offered as

$$d^n - d_0^n = Kt \tag{6.3}$$

Nevertheless the important features of austenite grain growth as they affect the austenite grain size of plain carbon steels during normalising treatments are

(i) For a given temperature of normalising, the grain size increases with time.
(ii) For a given time, the grain size increases exponentially with the normalising temperature.

(iii) The initial austenite grain size developed immediately after complete reaustenitisation is reflected after all exposures, though this effect becomes less significant as the austenitising time and temperature are increased due to the particular form of Equation (6.3) when $n > 1$.

The effect of the austenitising temperature on the austenite grain size for 1 h exposure times is shown in Fig. 6.3. In general, the austenite grain size increases from ASTM 4, with a mean linear intercept of 80 μm (see Table 4.3), at 900°C, up to ASTM 0, with a mean linear intercept of 320 μm, at 1250°C. As indicated in Fig. 6.3, there is considerable variation in the grain sizes observed at a given temperature. For example, at 900°C, the grain size can vary from ASTM 5, with a mean linear intercept of 57 μm, to ASTM 3 with a mean linear intercept of 113 μm. This range of variation is commonly seen when collecting data from a variety of sources and investigations, and shows general agreement with that published by Bain.[5] The variations observed at a given temperature can be expected, due to variations in the prior structure, particularly at the lower austenitising temperatures. Variations in the non-metallic inclusion contents of the various steels may affect the austenite grain size at the higher temperatures when the grain size becomes sufficiently large. The grain boundary pinning equation (4.73) allows that small volume fractions of second phase particles, even of the size of inclusions (>1 μm), can inhibit grain growth provided that the grain size is sufficiently large.

Given that the normalising temperature is specified as A_{c3} + 30°C, it is clear that higher carbon steels can be normalised at lower temperatures. Whilst Fig. 6.3 shows an austenite grain size of ASTM 4 at 900°C, which is an appropriate temperature for a low carbon steel, with or without a microalloying addition, near-eutectoid steels can be normalised at much lower temperatures. The data

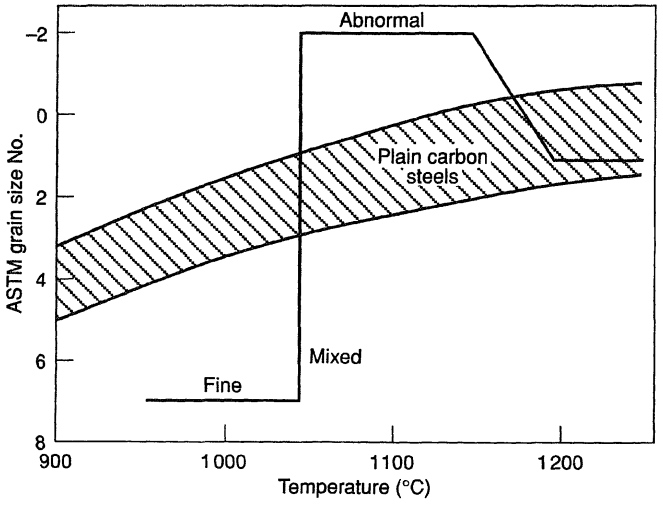


Fig. 6.3 The effect of austenitising temperature on the austenite grain size of plain carbon steels (shaded area) and a grain refined steel for a 1 h treatment time.

published by Bain[5] confirm this, and austenite grain sizes of ASTM 7, with a mean linear intercept of 28 μm, are observed on normalising at 750°C

6.2.2 Austenite Grain Growth Inhibition During Normalising

When a microalloying element is added to the steel, the austenite grain size developed at common normalising temperatures, e.g. up to 920°C for the lower carbon steels, is considerably less than that observed in plain carbon steels due to the austenite grain growth inhibiting effect of microalloy carbo-nitrides. From this standpoint, aluminium nitride behaves in exactly the same way as the microalloy carbo-nitrides and acts as a grain growth inhibitor. The grain size variations with increasing austenitising temperature for steels with these additives are also shown in Fig. 6.3, and the restricted grain growth in the vicinity of the normalising temperature is maintained up to considerably higher temperatures. At some higher temperature, usually in the vicinity of 1050°C for aluminium grain controlled steels, grain coarsening is observed. The grain growth that occurs in this region is of the 'abnormal' type, often referred to as 'secondary recrystallisation' or 'elephant grain growth'. In this mode of grain growth, only a few grains grow, consuming an otherwise stable array of fine grains. Unlike normal grain growth, where many grains grow and collide, thereby reducing the driving force for grain growth and slowing the growth rate, the abnormally large grain is growing into an unchanged fine grained matrix and maintains a rapid growth rate, at least until it collides with other abnormal grains. Under these circumstances, the abnormal grain growth phenomenon gives considerably coarser austenite grain sizes than would be observed in steels without any grain refining additive. At considerably higher austenitising temperatures, the microalloyed or aluminium treated steel will revert to a normal grain growth process and the grain sizes developed may be indistinguishable from those of a plain carbon steel, due to the substantive dissolution of the growth inhibiting particles.

Whilst it would be comforting to regard the temperature at which abnormal grain growth commences as an unambiguous 'grain coarsening temperature', this is unfortunately not the case. An increase in holding time, above the 1 h for which Fig. 6.3 is relevant, will result in grain growth occurring at a somewhat lower temperature than is shown in Fig. 6.3. The concept of a 'grain coarsening temperature' is only valid for a fixed reheat time.

The basic reason for the time dependence of the 'grain coarsening temperature' is found in the Ostwald ripening effect. Increasing the exposure time and/or temperature results in fewer and larger second phase particles, as discussed in Chapter 5 [Equation (5.17)]. The need for an adequate volume fraction of sub-critically sized particles was defined in Equation (4.73) of Chapter 4. Transposing this equation gives

$$r_c = R_0 f(1 - 4/3Z)^{-1} \tag{6.4}$$

where r_c is the critical particle size at which the pinning force is equal to the driving force for grain growth. It will be remembered that a particle size smaller than r_c

provides stable pinned boundaries, whilst a particle size larger than r_c allows grain growth to occur. The significance of Ostwald ripening is now clear. The particle size increases progressively on holding at temperature, and increases more rapidly at high temperatures. This temperature effect is compounded by increased dissolution of the particulate substance, giving a lower volume fraction of particles, which limits the permissible extent of particle coarsening according to Equation (6.4), and also increases the solute content in the matrix, thereby accelerating particle coarsening as shown by the Wagner equation (5.17).

The grain coarsening response of grain controlled steels during reaustenitisation can thus be calculated, first by calculating the critical particle radius from Equation (6.4) and second by calculating the mean particle radius from Equation (5.17), over a range of reaustenitising times and temperatures. If the actual particle sizes are smaller than the critical particle size, the fine grain sizes will be stable, but if the actual particle size is coarser than the critical particle size, then grain coarsening will occur. The temperature at which the two are equal will give an indication of the 'grain coarsening temperature' relevant to the austenitising time used to calculate the particle size from the Wagner equation.

There are two main problems with this procedure.

(i) Calculation of the volume fraction of particulate material is reasonably straightforward, but there is a need to assume some level of grain size heterogeneity, i.e. the factor Z in Equation (6.4). This problem has already been discussed in Chapter 4, and a high level of heterogeneity (e.g. $Z = 2$) is recommended as a conservative method of calculating r_c. If lower levels of Z are operating, this will not prevent grain growth inhibition. (n.b. If a coarse grained structure needs to be guaranteed, as in some hardenable steels, a low level of Z would be chosen, e.g. $Z = 1.5$, to define the maximum tolerable volume fraction of second phase particles that would *not* inibit grain growth.) This is not a scientific procedure, but is a conservative quality assurance philosophy.

(ii) Calculation of r_c from Equation (6.4) relates to a uniform particle size, whereas the Ostwald ripening process gives rise to a distribution of particle sizes of which the defined quantity is the mean particle size, r. The pinning effect of an array of differently sized particles is not necessarily the same as the pinning effect of an array of uniformly sized particles when both arrays have the same average size. Given that the spread of sizes in the distributed particle size is restricted, the approximation

$$r \approx r_c \tag{6.5}$$

can be made, bearing in mind that any inequality may already be compensated by the selection of a conservative Z value. It has already been pointed out that the critical particle size is extremely sensitive to the grain size heterogeneity factor and small differences between r_c and r would hardly change the value of Z. This problem is dealt with more fully in Chapter 7 when considering multi-modal arrays of different species of particle, such as oxides and carbo-nitrides, which have very different sizes.

Despite these problems, the concept has been applied to grain refinement by aluminium nitride and niobium carbo-nitride,[6] and the outcome is as shown in Fig. 6.4. The critical particle size decreases progressively with increasing temperature, due to the decrease in volume fraction of aluminium nitride according to the solubility product (Chapter 3). A smaller initial grain size (R_0) also decreases the critical particle size, as indicated by Equation (6.4). The increase in actual particle size with increasing time and temperature is also shown; in this case the particle sizes were obtained from rather crude experimental observations on a variety of steels, rather than by detailed studies of particle coarsening. The effects of alumimium content and prior fine grain size on the temperature domains both of stable fine grained structures and of grain growth are clearly shown. Also, by calculating the particle sizes at different times, the effect of exposure time on the 'grain coarsening temperature' can be seen.

An important ommission from Fig. 6.4 derives from the use of generalised experimental data for particle size. Although the change in volume fraction of particles is taken into account through the calculation of r_c, no allowance is shown for the effects of increased aluminium in solution when increasing the total aluminium content. A 0.04wt% Al, 0.01wt%N steel is hyperstoichiometric; the aluminium dissolved in the austenite matrix will remain significant, even when all, or almost all, of the nitrogen is precipitated as aluminium nitride. As indicated by Equation (5.17), an increase in dissolved aluminium content would have the effect of increasing the particle coarsening rate, thus reducing the differential between the coarsening temperatures of high and low aluminium steels. A similar effect could be produced by changing the nitrogen content of the steel. Increasing the

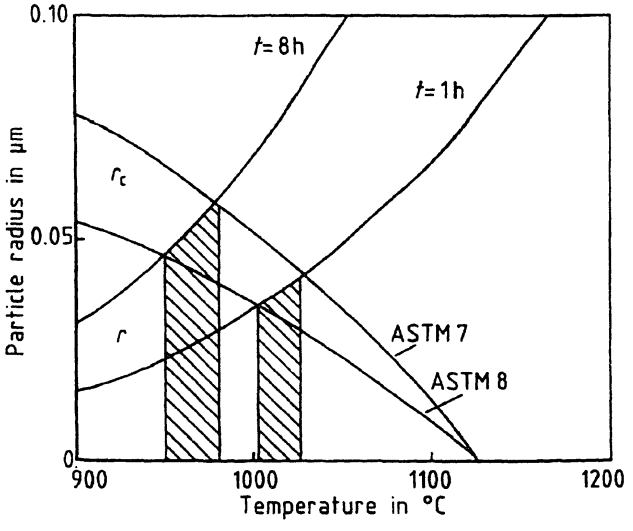


Fig. 6.4 The effect of austenitising temperature on the critical particle size for grain growth and on the observed particle size of a grain refined steel. The critical particle size decreases with increasing temperature due to particle dissolution. The observed particle size increases with increasing temperature due to diffusion and solubility effects [see Equation (5.17)].

nitrogen content of the steel would reduce the dissolved aluminium content at any temperature below the solvus.

A further important factor which is not shown in Fig. 6.4 is the effect of prior particle size. The particles were assumed to be 'freshly precipitated'. In fact, the particles cannot undergo Ostwald ripening during the precipitation stage since, by definition, the Ostwald ripening process only relates to a coarsening process where the diffusion flux is provided by compositional gradients arising from the particle size effect (Gibbs–Thomson equation), and would not operate in the super-saturated matrices that obtain during the precipitation process itself. Thus Equation (5.17)

$$r^3 - r_0^3 = 8\sigma SD\Omega t/9RT$$

must have an r_0 value, the effect of which may be negligible if r_0 is small with respect to the particle size, r, at the end of the exposure time.

An important consequence of this effect is seen in steels with microalloy (or aluminium) contents well in excess of that required to give an appropriate volume fraction of second phase particles at the normalising temperature. In such heavily loaded steels, a significant proportion of the carbo-nitride may remain undissolved at high temperatures, e.g. during soaking prior to hot rolling, before the application of the normalising treatment. If some part of the carbo-nitride is undissolved at these high temperatures, which can be of the order of 1250–1320°C for low carbon steels, then Ostwald ripening of the undissolved fraction will occur rapidly at these high temperatures, due to the high level of solute and the exponential increase in the diffusion coefficient. The presence of these large particles may have one or more of the following effects

(a) Increasing an element such as aluminium to levels far in excess of stoichiometry can reduce the nitrogen available for the subsequent formation of fine aluminium nitride particles, as shown in Fig. 6.5. It has been observed that very high aluminium additions can reduce the grain coarsening temperatures compared with those of the normal grain controlled steels.[7] It should be noted that increases in aluminium content up to the stoichiometric ratio would not have this disadvantageous effect.

(b) The presence of coarse undissolved carbo-nitrides may provide ready nucleation sites for further precipitation during cooling, thereby further reducing the number of fine particles.

(c) The presence of very coarse particles may influence the Ostwald ripening process by providing preferred (but very widely spaced) 'growth' particles. There is as yet no direct evidence of this phenomenon.

Despite the shortcomings of the particle coarsening treatment, the calculated grain coarsening temperature (based on $r = r_c$) showed good agreement with those observed experimentally (Fig. 6.6), except in the case of high niobium steels where the coarsening of undissolved particles at the hot-roll soaking temperature had a significant effect on the number of fine particles that could be formed during subsequent treatment.

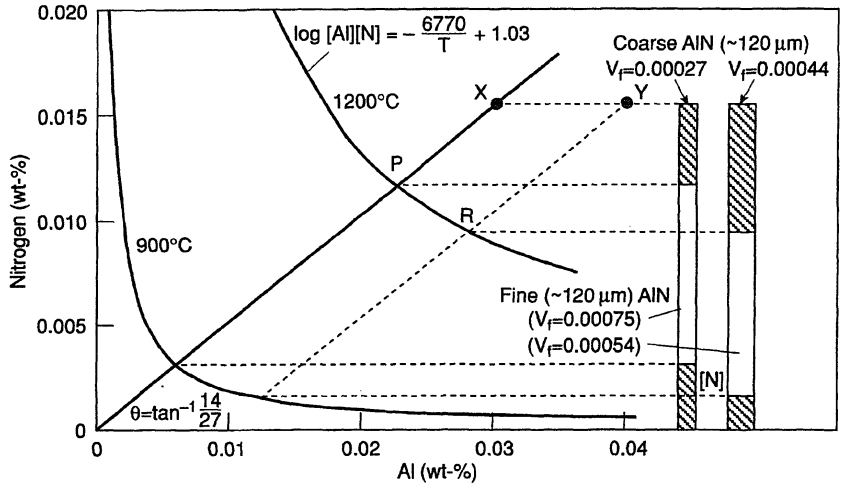


Fig. 6.5 The effect of pre-existing coarse nitrides caused by excessive solute addition on the fraction of fine particles that are available for grain refinement.

It is interesting, now having much of the data required for evaluation of the Wagner equation, to consider the effects of different solutes on the coarsening rates. The basic information for these calculations for vanadium and titanium nitrides is shown in Table 6.1 and is derived from the solubility data (Table 3.13) and the diffusion date (Table 5.2) and the molar volumes (Table 5.3). It should be noted that the solute concentration, S, in the Wagner equation must be expressed as the atom fraction in order to give correspondence with the molar volumes of the nitride phases. The approximate solution was used, and is quite adequate at low solute concentrations.

$$S = [M]A_{Fe}/100A_M \tag{6.6}$$

Table 6.1 Data for the calculation of particle coarsening rates in the austenite temperature range

	Vanadium	Titanium
Relative atomic mass, A_m	$V=51$	Ti=48
Molar volume Ω (m^3)	10.52×10^{-6}	11.44×10^{-6}
Solute-S (atom fraction)		
at 900°C	5.4×10^{-4}	0.47×10^{-4}
at 1000°C	12.6×10^{-4}	0.51×10^{-6}
at 1100°C	15.9×10^{-4}	0.89×10^{-6}
Diffusion coefficient-D ($m^2 s^{-1}$)		
at 900°C	4.30×10^{-17}	9.75×10^{-17}
at 1000°C	3.61×10^{-16}	7.38×10^{-16}
at 1100°C	2.22×10^{-15}	4.16×10^{-15}
Surface energy $-\sigma$ (Jm^{-2})	0.8†	0.8†

*; V Steel with 0.15wt%V; 0.015wt%N.
Ti Steel with 0.01wt%Ti; 0.005wt%N.
† Assumed value.

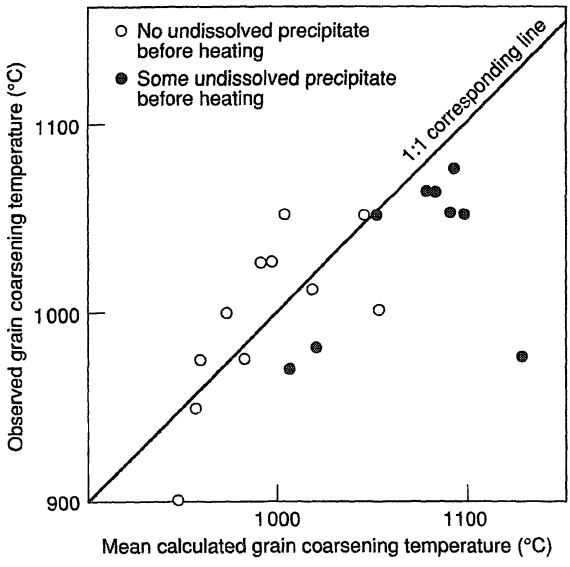


Fig. 6.6 Comparison of predicted and observed grain coarsening temperatures in aluminium and niobium grain refined steels. The predicted grain coarsening temperatures were obtained from the particle coarsening data shown in Fig. 6.4.

where S is the atom fraction of the dissolved microalloy, $[M]$ is the wt% of dissolved microalloy, A_{Fe} is the relative atomic mass of iron and A_M is the relative atomic mass of the microalloy.

The calculated particle radii obtained after different exposure times at 900°C and 1100°C are shown in Table 6.2. Two starting sizes (r_0) have been considered, i.e. 2 nm and 10 nm, which are not untypical of interphase particles and particles previously formed in austenite respectively. Increasing the temperature increases the rate of coarsening, in part due to the increase in solute concentration, S, but mainly due to the change in the diffusion coefficient, D, as indicated in Table 6.1. These effects far outweigh the specific inclusion of temperature, T, in the denominator of the Wagner equation (5.17). The effect of prior particle size is interesting. With a prior particle size of $r_0 = 2$ nm, the particle size increases significantly, particularly at 1100°C. With a prior particle size of $r_0 = 10$ nm, although the particle sizes at any given time and temperature are still larger than those starting at a smaller size, the difference in their radii decreases with increased coarsening exposures. The effect of prior size is due to the vastly increased diffusion flux required to achieve a unit increase in the radius when particles are large.

A very important feature of Table 6.2 is the difference in coarsening rates between vanadium nitride and titanium nitride. Vanadium nitride shows a much more rapid rate of coarsening than is shown by titanium nitride. This is illustrated in Fig. 6.7 for coarsening at 1100°C. The more rapid rate of coarsening of the vanadium nitride is evident at both prior particle sizes, but the slow rate of

Table 6.2 Particle coarsening in titanium-treated and vanadium-treated steels at 900°C and 1100°C calculated from Equation (5.17) using the data of Table 6.1

Temperature (°C)	Time (h)	Vanadium		Titanium	
		r^3 (nm^3)	r (nm)	r^3 (nm^3)	r (nm)
		(a) $r_0 = 2$ nm			
900	1/2	40	3.42	8.07	2.006
	1	72	4.16	8.14	2.012
	4	264	6.42	8.55	2.045
1100	1/2	2,090	12.79	12.75	2.336
	1	4,171	16.10	17.50	2.596
	4	16,662	25.54	46.00	3.583
		(b) $r_0 = 10$ nm			
900	1/2	1,032	10.11	1000.07	10.00023
	1	1,064	10.21	1000.14	10.00046
	4	1,256	10.79	1000.55	10.00183
1100	1/2	3,082	14.55	1004.75	10.016
	1	5,163	17.28	1009.50	10.032
	4	17,654	26.04	1038.00	10.125

coarsening of titanium nitride is particularly notable when the prior particle radius is 10 nm; austenitising for 4 h at 1100°C only increases the particle size from 10.0 nm to about 10.1 nm. The origin of this difference in the coarsening characteristics can clearly be found in Table 6.1, where the diffusion coefficient, D, and the molar volumes, Ω, would contribute to a more rapid coarsening rate for titanium nitride. The major factor controlling the relative coarsening rates of these two nitrides is to be found in the solute concentration, S, where the soluble titanium is approximately one thousand times less in the titanium steel than is the soluble vanadium content in the vanadium steel (expressed in atom fractions).

This difference in the coarsening rate of different species has been observed in practice and will be discussed more fully in Chapter 7, when considering the practical applications. For the purpose of normalised steels, it is sufficient to note that the solute concentration dependence of the coarsening rate implies that not only will the volume fraction of undissolved particles be dependent upon alloy composition, but also the coarsening rate of the particles will depend on the alloy composition through the variations in S, imposed by the stoichiometric ratio for a given alloy system, e.g. Fe–V–N, Fe–Al–N, etc. This effect does not appear to have been exploited systematically and certainly does not feature in the data shown in Fig. 6.4, as explained earlier. The only excuse that can be offered by the author, as co-initiator of Fig. 6.4, is that the range of variation of S, occurring in commercial steels, is limited to a factor of say 3–4 within a given alloy system, and as the cube of the particle radius increases linearly with time, then the particle radius will only vary by a factor of $3^{1/3}$–$4^{1/3}$ i.e. 1.4–1.6 from that shown in Fig. 6.4.

A significant assumption in the present application of the Wagner equation to the grain growth inhibition process concerns the interfacial energy between

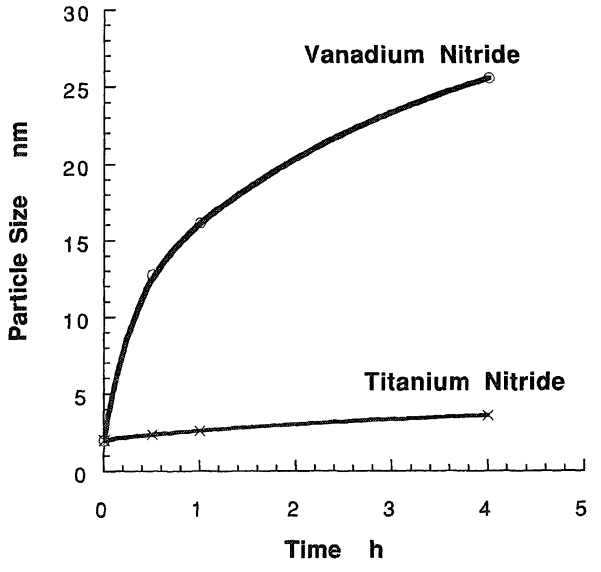


Fig. 6.7 Comparison of the calculated particle coarsening rates of vanadium and titanium nitrides at 1100°C.

particle and matrix. These have been assumed to have the same value for different carbides and nitrides. Any precise prediction of particle coarsening rates would of course require these values for comparison with observed coarsening rates, but again, variations in the surface energy, by say a factor of 2, would only affect the predicted particle radius by a factor of $2^{1/3}$ or 1.26. As the prediction of grain coarsening is dependent on the volume fraction and particle radius, then such approximations as are made by the metallurgist, as an applied scientist, may not be too serious.

The main conclusions to be drawn from this section, then, are that the requirement for austenite grain growth inhibition during normalising are reasonably well defined in terms of the volume fraction of particles and the particle size and stability. The principles of selection of steel chemistry to control these factors is also clear, and have been applied in the manufacture of normalised steels. Specific applications will be considered in Chapter 7.

6.2.3 Cooling from the Normalisation Temperature

The cooling stage of the thermal cycle during normalising is customarily, though not exclusively, effected by withdrawing the stock from the furnace, and allowing it to cool in air. The importance of this stage of the process concerns the transformation of the austenite structure to the ferritic state. As the mechanical properties of the steel are integrally linked to the microstructure that is developed during cooling, then the transformation of the austenite is of direct concern. Control of the austenite structure, described in the previous section, is only

important in that it affects the final ferritic structure, and therefore the properties of the steel.

Considerable understanding of the nature of transformations and transformation products[5] has been gained through the use of isothermal transformation diagrams as indicated in Fig. 6.8.[8] The C-curve of the austenite–ferrite and pearlite transformation is well understood as a nucleation and growth process occurring at temperatures below the A_{r3} and A_{r1} temperatures with the shortest transformation times occurring at about 600°C. The separate nucleation and growth of the bainitic transformation at lower temperatures has also been shown quite clearly to have a similar C-curve with the most rapid transformation occurring at a temperature that is dependent upon the steel composition. The intervention of the athermal martensitic transformation at temperatures below M_s, with no further martensitic transformation occurring on holding at temperatures between M_s and M_f, is also well documented for low alloy steels. Such diagrams, although useful in providing an understanding of transformation, do not provide the information required for transformation under conditions of continuous cooling.

Continuous cooling transformation diagrams, expressed in conventional form, i.e. with temperature as the ordinate and time as the abscissa, are difficult to use unless the natural cooling curves of various sections are superimposed. A more

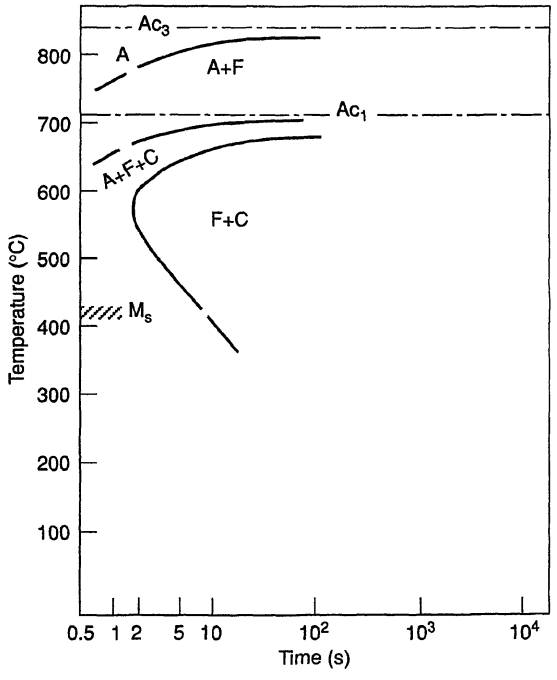


Fig. 6.8 Isothermal transformation curve of a low carbon steel. The most rapid transformation occurs at a temperature of about 600°C, above which the rate is reduced by a reduction in driving force, and below which it is reduced by diffusional constraints. After reference 8.

convenient form of the continuous cooling transformation diagram is shown in Fig. 6.9,[9] where the cooling rate prior to transformation at, say, 800°C for a low carbon steel is used as the abscissa. Temperature is shown on the ordinate in the usual way. Because the various sections, cooled in air, conform with a natural cooling rate (as defined above), the start, progress and finish of the austenite transformation can be obtained from a single vertical line at the appropriate cooling rate. Further, the abscissa can be calibrated in terms of bar diameter for the appropriate cooling medium (still air, oil or water), as these give natural cooling rates pertinent to the cooling rates obtaining during the determination of the transformation diagram. For this consideration of normalising treatments, only the air-cooled equivalent bar diameter is relevant in Fig. 6.9. The equivalent bar diameters of non-round sections can be obtained from BS5046: 1974, but a reasonable approximation for plate and sheet materials is that the equivalent bar diameter is twice the plate thickness. Thus a 20 mm plate would approximate 40 mm diameter bar as far as natural (air) cooling is concerned. A more detailed consideration of the definition of cooling rates is given in Reference 9.

The continuous cooling diagram shown in Fig. 6.9 is that of a 0.15%C–1.4%Mn–0.08%Nb steel having a prior austenite grain size of ASTM8. The major features of this diagram are

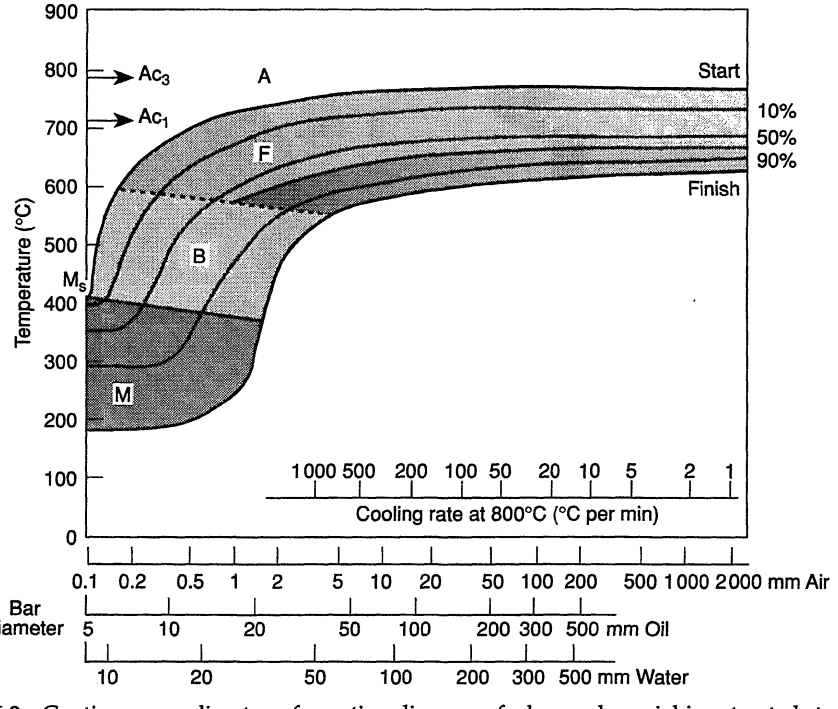


Fig. 6.9 Continuous cooling transformation diagram of a low carbon niobium treated steel. The manganese content was 1.4wt%, and the austenite grain size was A.S.T.M. 8 prior to transformation. After Atkins.[9]

(i) For cooling rates slower than that of a 5mm dia. bar (air cooled) the transformation product is wholly ferrite and pearlite.
(ii) Within this range of cooling rates, the 50% transformation temperature is depressed from 700°C at slow cooling rates (of the order of 1°C/minute) down to 630°C at a rate equivalent to that of a 5 mm dia. air cooled bar (about 700°C/minute).
(iii) At faster cooling rates between equivalent air cooled bar diameters of 5 mm and 2 mm, the transformation of austenite commences as polygonal ferrite but is completed by the formation of bainite.
(iv) At faster cooling rates than that of a 2 mm equivalent air cooled bar diameter, the polygonal ferrite product is progressively suppressed, and results in enhancement of the bainitic and martensitic transformation products.

For commercial low carbon and microalloyed steels, the transformation product at cooling rates less than 700°C/second would be of ferrite and pearlite, the proportions of each depending mainly on the carbon content. Increasing the carbon content would increase the proportion of pearlite as would be expected from the equilibrium diagram, Fig. 6.2, but increasing the cooling rate and/or the alloying elements, e.g. manganese, would cause a secondary increase in pearlite content. More importantly, however, the decrease in the ferrite transformation temperature at the faster cooling rate, within this range, results in an enhanced nucleation rate, and consequently produces a finer ferrite grain size for a given austenite grain size. Generally, the refinement of ferrite grain size due to transformation effects is much less than that due to the prior austenite grain size. Ferrite nucleates on the austenite grain boundaries, and a finer austenite grain size automatically enhances ferrite nucleation, and must inevitably produce finer ferrite grain sizes when the growing ferrite grains collide.

A second effect of the depression of the austenite–ferrite transformation temperature is that any dissolved microalloy carbo-nitride will form finer particles, as described in Chapter 5. Thus, strengthening by interphase precipitation would be expected to increase due to the particle refinement obtained at lower transformation temperatures, provided that the interphase precipitation is not suppressed completely by excessive cooling rates.

The refinement of the microstructure by control of the transformation temperature might be supposed to depend upon the section size of the stock, as indeed it is for a given composition of steel. However, the continuous cooling transformation diagram is dependent upon the steel chemistry and upon the austenite grain size. Increasing the alloy content of the austenite, or increasing the austenite grain size, causes a general displacement of the ferrite/pearlite transformation curves to slower cooling rates. Thus the depression of the transformation temperature effect in producing a fine structure can be made to occur in larger sections (i.e. at slower cooling rates) by adding alloying elements such as manganese, chromium, etc., or by coarsening the austenite grain size, although the latter procedure is self defeating in that the coarsening of the

austenite grain size would have a more pronounced direct effect of coarsening the ferrite grain size.

Tailoring the basic steel chemistry to provide maximum microstructural refinement in larger section sizes is a well established practice, but due care has to be taken to avoid the formation of bainite in a substantially polygonal ferrite matrix; bainite can have serious consequences with regard to toughness and sensitivity to hydrogen cracking. The addition of suitable quantities of alloys to maximise the microstructural refinement may of course have additional advantages in contributing to solid solution strengthening, as described in Chapter 2.

The attainment of a significant degree of interphase precipitate strengthening in normalised products requires that a significant proportion of the microalloy carbo-nitride is dissolved at the normalising temperature, defined as A_{c3} + 30°C. At such low temperatures in the austenite temperature range, it is clear that the only carbo-nitride that exhibits a sufficient solubility is vanadium carbo-nitride, as was shown in Chapter 3. Vanadium strengthening is in fact used extensively in normalised steels, but specific developments will be considered in more detail in Chapter 7.

One further consideration that must be given in any discussion of normalised steels relates to methods by which the cooling rate might be modified for a given section size, by the application of accelerated cooling. Various cooling systems are used to increase the cooling rate in the final stage of the normalising heat treatment. These range from fan coolers, which can give modest or even strong air flow around the stock and give a modest increase in cooling rate, to water mist sprays , or sprinkler systems, the latter being applied particularly for thicker plates. The application of accelerated cooling systems can impart the enhanced properties of a smaller section stock without the need for additional alloying elements. Care must be taken to avoid differential transformation due to the increased differences in cooling rate between surface and centre of the stock when cooling is accelerated in this way.

6.2.4 The Role of Microalloys in Normalising

From the foregoing discussion of the normalising treatment it is clear that the selection of a microalloying addition will depend upon the objectives of the treatment, i.e. whether the sole aim is to provide a grain refined steel, or whether a higher strength steel is required in the normalised condition.

For grain refinement alone, aluminium additions are common, although grain refinement by niobium carbo-nitride can offer an alternative. Titanium carbo-nitride, although showing limited solubility and dramatically reduced particle coarsening rates, is not used for this purpose in normalised products. An aluminium addition would be mandatory in order to deoxidise the steel to a level that would preclude the formation of titanium oxides during steelmaking, certainly for low carbon steels. Aluminium additions alone are sufficient to produce austenite grain refinement in normalised steels.

For higher strength normalised steels, vanadium additions are commonly used because of the high solubility of vanadium carbo-nitride. Both niobium and

titanium carbo-nitrides have such low solubilities that the required level of dissolved micro-alloy for subsequent interphase precipitation cannot be attained at normalising temperatures (see Chapter 3). In the case of vanadium, sufficient vanadium carbo-nitride can remain undissolved to control the austenite grain size, usually by enhancing the nitrogen content of the steel. More will be said of the design of vanadium-treated normalised steels in Chapter 7.

6.3 AS-ROLLED PRODUCTS

The normalising process, although providing improved consistency of product, when compared with *uncontrolled* hot-rolled product, has an attendant cost. The cost of normalising comprises the handling and storage of stock, depreciation of the capital plant, i.e. the normalising furnace, and the cost of consumables – mainly fuel. Such costs could be eliminated completely by controlling the rolling process to give a consistent product. Further, by suitably adjusting the hot-rolling process variables, products with properties that are equal to, or better than, those of normalised products could also be produced in the as-rolled condition. Studies of the rolling practices and the properties attainable were being explored extensively in the mid-1960s. Not untypical of these studies was the work on 'Controlled Rolling' carried out at the British Steel Research Association,[10,11] but this subject was also being developed, both in the laboratory and on a commercial scale, in Japan, U.S.A., Europe and Australia.

The controlled rolling processes are applicable to plain carbon steels as well as to micro-alloyed steels, and produce microstructural refinement, thus resulting in significant increases in yield strength of a wide range of steels through the Hall–Petch strengthening effect. The initial steps taken to control the rolling process essentially introduced a delay during the rolling process, so that a significant proportion of the hot-deformation would take place at lower temperatures, and would reduce the opportunity for inter-stand and post rolling austenite grain growth.

The hot-rolling process is simple in its engineering concept, in that shape changes from ingots to slabs, blooms or billets, or from these semi-finished products to plate, strip, sections and bars, can be achieved with relatively low power demands due to the low strength of steel at temperatures usually in the range from 1300°C, down to about 850°C. Even under these conditions, the power requirements of the hot-rolling mill and even the strength of the mill rolls and mill housings themselves are such that single deformations are restricted to 15% maximum, and are considerably less than this (perhaps only 5%) when the rolling stock is large. The strength of the stock is restricted during the hot-rolling process by the metallurgical changes that are implied by the term 'hot-rolling', i.e. the stock will undergo recovery and recrystallisation at least once, or perhaps several times, during the hot-rolling operation. The deformation per pass can also be limited, at least in the early stages, by consideration of hot ductility, this usually improving through the rolling process due to consolidation of casting defects and progressive refinement of the (austenite) structure. In the later stages of rolling, the

deformation sequence may be influenced by the need to control both shape and dimensions.

The net result of all these factors is that the hot-rolling operation is a multi-stage operation, and the overall deformation in converting ingots to semi-finished product, or semi-finished stock to the final shape, may require of the order of 10–20 separate deformations. It is this multiplicity of deformations (or passes), with the attendant changes between passes, that has required considerable advances in the understanding of the physical metallurgy of hot deformation.

The purpose of this section is to describe the changes in austenite structure occurring in the hot working schedule, and their effects on the subsequent transformation and transformation products, paying particular attention to the effects of microalloying elements on such changes.

6.3.1 Heating and Soaking for Hot Deformation

The initial stage of any hot working process is usually the reheating stage. The stock material is reheated to the soaking temperature, either from room temperature (known as cold charging) or from some intermediate temperature (known as hot charging). These two conditions can both be considered as indirect charging, and may be contrasted with a recent development known as direct charging, where the hot ingot or other stock is allowed to equilibrate at the soaking temperature with little or no additional heat being supplied. The energy savings associated with this latter practice are obvious.

In virtually all cases, the austenite grain size is coarse, usually of the order of 0.3–1.0 mm for indirectly charged stock, and even coarser in some cases for directly charged stock, where the as-cast structure may be retained or even enlarged. The size of the grains in directly charged stock will be dependent upon the casting conditions and the size of the cast product. Continuously cast billet stock (less than 150 mm square) would naturally be expected to have a finer prior structure than a large ingot of the order of 0.5–1 m^2 section. Irrespective of the stock, the as-soaked grain size would be gross prior to hot working.

In general, microalloying additions are substantially dissolved at the soaking temperature, although there have been instances where deliberate additions have been made in an attempt to restrict the austenite grain size prior to hot working, as for example with aluminium additions made to a steel containing a deliberately increased nitrogen content,[12] (the IN Steels), and with titanium additions to give the extremely stable titanium nitride particles.[13] However, at the higher soaking temperatures commonly used for low carbon steels (e.g. 1300°C), even these nitrides will undergo either substantial dissolution, or, in the case of titanium nitride particles, substantial particle coarsening (see Section 6.2.2). Thus, the starting point for hot deformation processes is a coarse grained austenite with virtually complete dissolution of the microalloy carbo-nitrides.

6.3.2 The Hot Deformation Process

In all hot deformation processes, including multi-pass hot rolling, the actual deformation applied is never instantaneous, but occurs over a period of time,

however short. Considerable understanding of the events that are likely to occur during the period of hot deformation have mainly been obtained from hot torsion testing, which allows substantial stable plastic deformation, unlike the hot tension test which rapidly develops a plastic instability with loss of control of the strain rate and plastic strain distribution. Other studies have been carried out using plain strain compression testing, and the results obtained do not necessarily show good agreement, even when the strains are compared on the same (equivalent) strain basis, due to the strain variations that occur naturally within torsion test specimens.

Typical stress–strain curves for deformation in torsion are shown in Fig. 6.10, and exhibit one of two generalised forms. With high temperatures, low strain rates and finer initial austenite grain sizes, the stress strain curve shows an initial peak stress, after which the stress falls to a minimum level, and subsequently the stress appears to oscillate sinusoidally, but with a slight decrease in amplitude as the total applied shear strain increases, Fig. 6.10(a). This phenomenon has been associated with progressive grain coarsening during torsional straining, and has been suggested to result from a lengthening of the recrystallisation nucleation time.[14] Under other conditions, i.e. low temperatures, high strain rates, and coarser initial grain sizes, only one stress peak is seen, Fig. 6.10(b), followed by an approximately constant stress, i.e. a steady state stress level, that is dependent upon the temperature and strain rate for a given steel, and which may vary from one steel to another depending upon the hot strength of the steel. Factors which retard recrystallisation, such as fine precipitation and solutes, tend to favour single-peak behaviour.

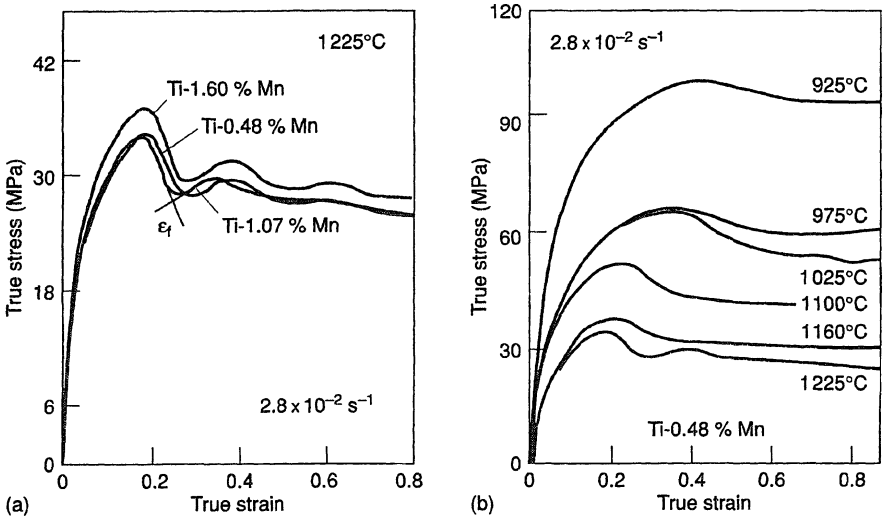


Fig. 6.10 Typical stress–strain relationships observed during hot torsion testing. (a) Multiple oscillations are observed when using high temperatures, low strain rates and fine initial grain sizes. (b) Single peak behaviour followed by a steady-state stress is observed at low temperatures, high strain rates, and with coarse initial grain sizes. After Chandra *et al.*[38]

In the torsion test, the initial increase in stress reflects the work hardening of the austenite. At some critical strain, εc, usually just prior to the peak strain, εp, (see Fig. 6.10(b)) recrystallisation commences,[15] and is responsible for the ensuing softening process. The recrystallisation strain is considered to extend from the critical strain ε_c to the strain, ε_s, at the onset of the steady state stress i.e.

$$\varepsilon_x = \varepsilon_s - \varepsilon_c \tag{6.7}$$

The critical strain, ε_c, has been evaluated in many experimental studies, and is often regarded to be similar in magnitude to ε_p, the peak strain, although there is considerable disagreement in the definition of 'similarity'. ε_c has variously been reported as $0.67\varepsilon_p$[16]–$0.86\varepsilon_p$,[17] and in view of the difficulty in unambiguously defining ε_c, it is commonly assumed that $\varepsilon_c \approx \varepsilon_p$. The complexity of the deformation process can be appreciated by considering that the early recrystallised material formed at a strain near ε_p will already be substantially deformed prior to the steady state being attained, i.e. near ε_s.

In the steady state condition, the steady state stress, σ_s, is maintained by a dynamic balance between the hardening process and the softening processes, i.e. dynamic recovery, and dynamic recrystallisation. The dependence of σ_s on the temperature and strain rate, $\dot{\varepsilon}$, is expressed in terms of the Zener–Holloman parameter, Z, which is the temperature compensated strain rate.

$$Z = \dot{\varepsilon} \exp(Q/RT) \tag{6.8}$$

where Q is an activation energy for the deformation process, and is typically of the order of 213 KJ mol^{-1}.[18]

The same steady state stress is obtained for any combination of temperature and strain rate that gives a single value of the Zener–Holloman parameter. The steady state flow stress is related to values of the Zener–Holloman parameter by

$$Z = A \exp \beta\sigma_s$$

$$\text{or} \qquad \sigma_s = \beta^{-1} \ln(Z/A) \tag{6.9}$$

where β and A are constants for a given material.

The more important feature to be derived from torsion testing, however, concerns the strain for the onset of dynamic recrystallisation, i.e. $\varepsilon_c \approx \varepsilon_p$. As shown by Sellars,[15] ε_p is dependent not only on the Zener–Hollomon parameter, but also on the austenite grain size prior to deformation. Even when the effects of temperature compensated strain rate and grain size are taken into account, there are still significant variations in the strain to initiate dynamic recrystallisation, arising from differences in steel chemistry. Thus

$$\varepsilon_p = \kappa d_0^{1/2} Z^{0.15} \tag{6.10}$$

where κ is of the order of 5×10^{-4} but may vary about this value by a factor of 2 or 3, or even more if precipitation processes are involved during the straining operation, and d_0 is the 'grain size' expressed in μm.

Values of $Z \geq 10^{11}$ are relevant to the majority of rolling operations, and correspond to a strain rate of $\dot{\varepsilon} \geq 2\,s^{-1}$ at a temperature of 1250°C, so that over the

range of temperatures and strain rates involved in hot rolling, the strain for the onset of dynamic recrystallisation ($\varepsilon_c \approx \varepsilon_p$) is generally in excess of 0.15 (14% reduction in thickness), and increases to 0.4 (33% reduction in thickness) under plain strain conditions, as Z increases to 10^{14} or more, when the grain size is 50 μm, i.e. $d_0^{1/2} = 7.1\ \mu m^{1/2}$ (n.b. It is assumed that the grain size is expressed as a grain diameter calculated from either mean linear intercept or the mean areal intercept on the basis of a spherical grain).

In hot rolling, initial deformation may take place at 1250°C, and initial deformations in excess of 15% are not common. Thus dynamic recrystallisation is unlikely to occur in the initial pass. As the temperature falls the temperature compensated strain rate would increase, even if the same strain rate was maintained, and the strain required to induce recrystallisation would also increase as outlined above. Thus, for individual hot rolling passes, dynamic recrystallisation would not be expected. If, however, the deformation is accumulated from one roll pass to another, i.e. there is no static recrystallisation between passes, then dynamic recrystallisation could occur in second or third passes of the rolling schedule. If the stock undergoes complete static recrystallisation between each pass, then dynamic recrystallisation would be unlikely to occur as strain accumulation will not occur. This is particularly true of the initial high temperature passes, because static recrystallisation is extremely rapid at temperatures of, say, 1200°C.

The hot deformation process during commercial rolling operations is of course far more complex than would appear from the previous discussion, due to variable strain rates during each rolling pass, temperature gradients caused by radiation to the air and conduction cooling (roll chill), and adiabatic heating due to the deformation.

As the stock enters the roll bite, the strain rate rises rapidly to a maximum value, and as the stock passes between the rolls, the strain rate decreases to zero as the stock leaves the pass. This variation in strain rate does not appear to affect the progress or kinetics of subsequent static recrystallisation compared with the same strain imposed at a constant strain rate.[19]

The effects of general radiation cooling produces a temperature gradient within the stock, which is further enhanced by the roll chill. The roll chill effect is local to the near surface zones and radidly recovers by thermal diffusion from the centre when the stock leaves the rolling pass. When the roll chill perturbation at the surface has recovered, the effect is reflected as a step loss of temperature.[20] Also, some 90% of the energy used in effecting the deformation is converted to heat, the remaining 10% being stored as increased grain boundary area per unit volume of stock, or as dislocations which provide the driving force for the recrystallisation process. The heat of deformation is easily estimated by assuming that the mean stress throughout deformation can be approximated by the steady state stress, σ_s, as defined by Equations (6.8) and (6.9). The energy, H, per unit volume for deformation is obtained from

$$H = \int \sigma \, d\varepsilon = \sigma_s \varepsilon \tag{6.11}$$

where ε is the true strain achieved. Given that 90% or more of this energy is converted to heat, the temperature rise can be reasonably estimated. More detailed information of the apportionment to stored energy and thermal energy has been published by Richardson *et al.*[21]

A further problem that can arise concerns the distribution of strain. In all of the preceding discussion, there is an implicit assumption that the strain is uniformly distributed. In many hot working processes this is strictly untrue, due in part to frictional constraints, and it is clear that local variations in strain, strain rate and temperature will require finite element models to accommodate such local variations. The importance of the inhomogeneities is that they cause corresponding local variations in microstructure.

6.3.3 Static Recrystallisation

Given that dynamic recrystallisation is an unlikely event in a single pass of a multipass plate rolling operation, then the prediction of static recrystallisation during the inter-pass periods becomes extremely important. If the stock material recrystallises completely, there is no inherited strain, and dynamic recrystallisation in the subsequent pass remains unlikely. If there is no recrystallisation between passes, then the strain is accumulated, and dynamic recrystallisation becomes a strong possibility.

The occurrence of static recrystallisation between passes is therefore an important aspect of hot working, particularly for plain carbon steels, where static recrystallisation rates are rapid. Also, the recrystallisation process (or its absence) is directly responsible for the evolution of microstructure during hot rolling, and constitutive laws which describe the microstructural changes are available, enabling a reasonable prediction of the microstructural changes to be made.

Following the single pass deformation, the process of recrystallisation commences with the nucleation and growth of recrystallised austenite grains. The fraction recrystallised, f, at any moment in time in the interpass interval is obtained using the Avrami equation

$$f = 1 - \exp(-c(t/t_x)^k) \tag{6.12}$$

where t is the time from leaving the rolls, t_x is the time to achieve a given fraction recrystallised and c and k are constants.

The constant c is defined from the condition where $t/t_x = 1$, when

$$c = -\ln(1 - f_x) \tag{6.13}$$

where f_x is the fraction recrystallised at t_x.

The constant k is almost universally found to have a value $k = 2$.[15] Substituting these values in the Avrami equation (6.12) gives

$$f = 1 - \exp(-0.693(t/t_{50})^2) \tag{6.14}$$

where t_{50} is the time to 50% recrystallisation (i.e. $f_x = 0.5$).

This equation describes the form of the recrystallisation curve, but not the kinetics of the process, the latter being controlled by t_{50}. For example, when $f=0.95$ (95% recrystallised) then $t=2.08t_{50}$, and when $f=0.05$ (5% recrystallised) then $t=0.27t_{50}$. The progress of recrystallisation is thus defined in terms of t_{50}, but t_{50} itself is not defined. Many studies have been carried out to define the factors controlling the rate of static recrystallisation, in order to define t_x, and thus define the whole of the recrystallisation process in terms of absolute time, rather than relative time.

The factors which control the rate of static recrystallisation are

(i) *Strain* (ε): the stored energy of deformation, in the form of increased grain boundary area, subgrain boundaries, dislocation cell structures, and forest dislocations provide the driving force for recrystallisation, and increasing the strain increases the stored energy and consequently the driving force, thus increasing the rate of recrystallisation.

(ii) *Temperature* (T): the nucleation and growth stages of static recrystallisation are thermally activated processes, and increasing the temperature increases the rate of recrystallisation through the usual Arrhenius relationship, i.e. an exponential effect with an activation energy appropriate to recrystallisation.

(iii) *Temperature compensated strain rate* (Z): the stored energy of deformation arises directly from the strain, but the rate of generation of the defects responsible for the stored energy results from a balance between the 'work hardening' process and the relaxation processes (annealing out of dislocations) during the deformation period, thus giving rise to the concept of the Zener–Hollomon parameter, i.e. the temperature compensated strain rate. Higher strain rates give a higher stored energy at a given plastic strain, and thus accelerate the recrystallisation process. The strain rate effect on recrystallisation has invariably been included in the form of the Zener–Hollomon parameter, due to the above effects.

(iv) *Prior grain size* (d_0): the nucleation of recrystallised grains is frequently, though not exclusively, associated with prior grain boundaries. Thus a refinement of the prior grain size will increase the nucleation rate and accelerate recrystallisation.

These factors have been incorporated into a general equation, where the factors which enhance the rate of recrystallisation result in a decrease in t_x in Equation (6.12) and therefore t_{50} in Equation (6.14). Although there are relatively minor disagreements on the precise values of the exponents, the time to 50% recrystallisation can be expressed as

$$t_{50} = BZ^m\varepsilon^{-4}d_0^2\exp(Q_{rex}/RT) \tag{6.15}$$

There is some doubt concerning the effect of the temperature compensated strain rate, Z. Sellars and Whiteman[18] suggested that the exponent m had a value of $-3/8$ coupled with an activation energy for recrystallisation of $Q_{rex}=480$ KJ mol^{-1}. Although there are differences in the absolute predictions of this equation and a

later version[15], the differences are relatively small when compared with the spread of experimental results on carbon–manganese steels. The main problem that arises in the prediction of recrystallisation times is that Equation (6.15) contains the physical metallurgy features of the hot rolling process but the only steel characteristic included is the austenite grain size. Solute effects on both recrystallisation and grain growth are well known, and within the collected data presented by Sellars[15] there is some evidence that low manganese steels would give lower values of B than would be obtained with higher manganese steels or with low alloy steels containing chromium or other solutes.

The prediction of recrystallisation times can therefore be made on the basis of the Sellars equation

$$t_{50} = B\varepsilon^{-4} d_0^2 \exp(300\,000/RT) \tag{6.16}$$

where t_{50} is the time to 50% recrystallisation (s), ε is the equivalent strain, d_0 is the prior austenite grain size (μm) and B is a composition dependent constant.

The value of B quoted by Sellars is $B = 2.5 \times 10^{-19}$ s μm^{-2}, which would appear to be reasonable for carbon–manganese steels containing 0.8–1.2% Mn. Some of the variability in the t_{50} values collated by Sellars was suggested to derive from differences in strain conditions and methods of assessing the extent of recrystallisation.

As pointed out earlier, static recrystallisation occurs with applied strains less than ε_c, which precludes the onset of dynamic recrystallisation. However, at applied strains near ε_c, a condition has been defined where recrystallisation nuclei are activated just prior to the cessation of deformation. Under these conditions, the activated nuclei start to grow immediately and cause marked deviations from the usual form of the Avrami equation, the value of k being reduced to $k = 1$, and giving a more extended recrystallisation curve with respect to time. This process has been termed 'meta-dynamic' recrystallisation by Djaic and Jonas.[22] The effect of meta-dynamic recrystallisation at these relatively high strains ($\approx \varepsilon_c$, and above) is that t_{50} becomes independent of strain. Appropriate equations for these conditions can be found elsewhere.[15]

On completion of static recrystallisation, the structure consists entirely of newly recrystallised austenite grains. In order to characterise the recrystallised austenite structure more fully, some estimate of the recrystallised austenite grain size is required. This relationship has also been studied extensively, in both austenitic stainless and transformable carbon–manganese steels, and it has been shown that the rerystallised grain size, d_{rex} (μm), is predominantly a function of the prior grain size and the applied strain.

$$d_{rex} = C d_0^{2/3} \varepsilon^{-1} \tag{6.17}$$

where d_0 is the grain size prior to deformation (μm), ε is the equivalent true strain and C is a constant.

The reported values of C for carbon–manganese steels show some variation in the range 0.35 to 0.83 ($\mu m^{1/3}$), and a mean value of $C = 0.5$ would not be unreasonable.

Following the establishment of a recrystallised structure having a grain size, defined by d_{rex}, at some time interval within the interpass period, then, in the absence of any second phase pinning particles, grain growth will occur, and has indeed been observed to do so by progressively increasing the isothermal hold time after deformation and then quenching. As before, the basic form of the relationship for grain growth can be expressed as

$$d^n - d_{rex}^n = kt \tag{6.18}$$

where d is the grain size at time t (s), n is the grain growth time exponent and k is a temperature dependent constant defined by

$$k = k_0 \exp(-Q_{GG}/RT) \tag{6.19}$$

where $k_0 = 3.87 \times 10^{32}\ \mu m^{10}\ s^{-1}$ $Q_{GG} = 400\ KJ\,mol^{-1}$.

The dimension of k_0 is expressed as $\mu m^{10} s^{-1}$ and this derives directly from the value of the grain growth exponent in Equation (6.18), when $n = 10$. High values of n are commonly found experimentally, and values of up to 12 have been quoted. It is unlikely that such high indices have any fundamental meaning, and merely give an empirical expression of the changes in average grain size. As indicated in Chapter 4, grain growth is a discontinuous process, and the continuous equation may necessarily be empirical in nature. As with the recrystallisation process, solute elements are known to change grain boundary mobility, and the effects on grain growth are well documented.[23,24] Newly formed grain boundaries are relatively free from solutes,and may show a much higher grain boundary mobility than is shown by solute-saturated grain boundaries. A change in the rate-controlling mechanism during grain growth, from rapid growth in the absence of a solute drag effect, to slow growth in the presence of solutes swept up during the growth process, could lead to the apparent high grain growth indices such as were obtained by Sellars. Alternatively, very slow growth at large grain sizes could be induced by a particulate distribution that was only capable of inhibiting grain growth at large grain sizes (e.g. a distribution of non-metallic inclusions). The exact nature of the mechanism that gives rise to such high values of n for Equation (6.18) has not yet been clarified.

Nevertheless, Equations (6.14)–(6.19) are basic constitutive equations upon which the evolution of microstructure is based during the hot working of plain carbon steels in the absence of dynamic recrystallisation. These equations describe the extent of recrystallisation, the recrystallised grain size and the subsequent grain growth occurring with each pass, and have been shown to give a satisfactory description of the final austenitic microstructure at the end of multi-pass hot rolling operations.[18] A typical calculation of the austenite grain sizes at various stages in the sequence of passes used for plate rolling is illustrated in Fig. 6.11, together with the temperature profile, taken from Reference 18. Constant deformations of 15% reduction in thickness per pass were used in the calculations, which were carried out for plates of various thicknesses. Fig. 6.11 shows that, for a plain carbon steel,

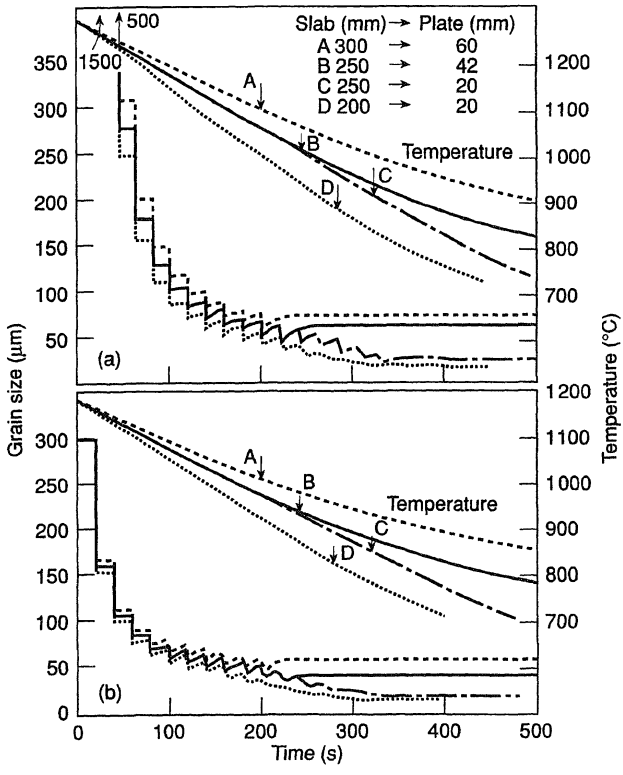


Fig. 6.11 The evolution of the austenite grain size in a plain carbon steel during a multi-pass hot rolling schedule. The temperature profile is also included, and the deformation per pass was maintained at a constant 15% reduction in area. (a) 1300°C; (b) 1180°C. After Sellars and Whiteman.[38]

(i) Progressive refinement of the austenite grains is predicted with the 15% reduction per pass rolling schedule

(ii) The effects of plate (and stock) thickness is complex, in that the cooling rates of the stock vary with thickness, thus changing the temperature at which the deformations are carried out, and also limiting the total deformation that can be applied. This generally increases with decreasing plate thickness, due to the limited variation in slab size that can be accommodated in a given hot rolling mill.

(iii) Lowering the soaking temperature promotes a finer grained austenite by reducing the initial austenite grain size and also the deformation temperatures throughout the rolling schedule.

The schedules shown in Fig. 6.11 are 'normal' in the sense that delays have not been introduced to allow cooling prior to further deformations, i.e. the materials have not been deliberately controlled rolled. Such delays, usually made on a specially designed delay table, have commonly been introduced between the roughing mill and finishing mill of many modern hot mills. The effects of delays

have been considered by Sellars,[15] and have been shown to produce a refinement of the final austenite grain structure. This type of controlled rolling, essentially considered by Kozasu *et al.*[25] to be a high temperature thermomechanical treatment (HTTMT), has been used extensively in industrial practice, and has proved effective in attaining refined structures with their attendant improvements in both strength and toughness.

6.3.4 The Effects of Microalloying Additions on the Evolution of Microstructure During Hot Rolling

The addition of microalloying additions to steel can have several effects on the microstructural changes that occur during the hot rolling process, and particularly during controlled rolling schedules. The extent to which these effects are invoked is dependent upon the particular microalloying element used and their concentrations. There are three major effects of these additions:

(i) Additions which result in undissolved carbo-nitrides at the soaking temperature will influence the starting grain size prior to the commencement of hot working.
(ii) There is considerable evidence that small amounts of dissolved vanadium, titanium, and particularly niobium, may retard the recrystallisation process, presumably by a solute drag mechanism on the recrystallised grain boundary.[26]
(iii) Strain-induced precipitation of the microalloy carbo-nitrides can result in the inhibition of recrystallisation by a pinning action of the particles on the sub-grain boundaries.

The dissolution and effects of undissolved fractions of carbo-nitrides on the initial austenite grain size follow the same principles as were described in the earlier section of this chapter for normalised steels, but because of the much higher temperatures used for soaking prior to hot working, e.g. 1150–1350°C, the additions required for most elements will be substantially higher. The exception of course is titanium, for which the extremely restricted solubility of titanium nitride allows the possibility of restricting the austenite grain growth with quite modest levels of addition.

The effects of microalloying on recrystallisation are typified by the results of Jonas and Weiss[27] shown in Fig. 6.12. The recrystallisation start and finish times for a plain carbon (C) and a niobium steel (Nb) are shown in Fig. 6.12(a). The plain carbon steel shows progressively longer recrystallisation times as the deformation temperature is lowered as would be expected from the constitutive equations already given in Section 6.3.3. The niobium steel however is slightly slower to recrystallise at 1000°C, and the retarding influence increases dramatically as the temperature is reduced to 900°C. At 850°C the recrystallisation process is less retarded by niobium than at 900°C, but, at lower temperatures, the retarding effect of niobium increases again. Jonas and Weiss suggest that these effects can be considered in terms of a solute effect of niobium, and a strain induced precipitation effect. Figure 6.12(b) shows the proposed effect of the dissolved

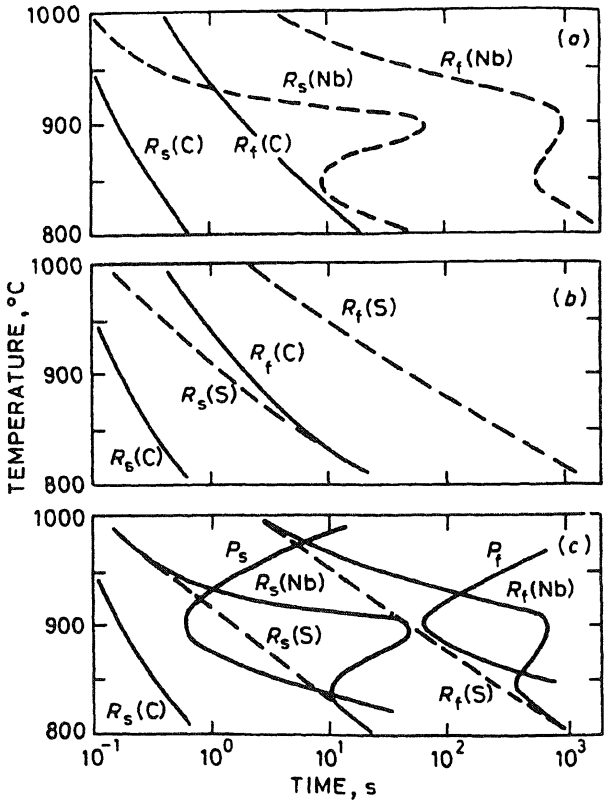


Fig. 6.12 (a) A comparison of the start of recrystallisation, R_s, and the finish of recrystallisation, R_f, of a plain carbon steel (C) and a niobium steel (Nb). (b) The suggested effect of dissolved niobium (solute effect) is indicated by the curves $R_s(S)$ and $R_f(S)$. (c) The additional effect of strain-induced precipitation is coincident with high rates of precipitation indicated by the precipitation start, P_s, and finish, P_f, curves. After Jonas and Weiss.[27]

niobium, i.e. a retarding influence which increases progressively as the temperature is lowered, as would be expected from a binding energy between solute and sub-grain boundaries. Superimposed on this effect, however, is the effect of strain induced precipitation as shown in Fig. 6.12(c). The enhanced retarding influence of niobium at 900°C coincides with the maximum rate of strain induced precipitation. At temperatures above 900°C precipitation is slowed by the reduced supersaturation, whilst at temperatures below 900°C precipitation is slowed by diffusional limitations.

This interpretation is not undisputed,[28] as the methods for assessment of the precipitation process, e.g. the presence of acid insoluble carbo-nitrides, changes in dispersion strengthening after air cooling etc., may not be definitive. However, a significant feature of the strain induced niobium carbo-nitride, clearly shown by electron microscopical examination, is that the carbo-nitride particles decorate the

sub-grain boundaries.[29] In a manner analagous to the inhibition of grain growth, fine particles will pin sub-grain boundaries[30] and retard the onset of recrystallisation, i.e. the growth of any favoured sub-grain. The inhibition of recrystallisation can be treated mathematically by the Zener pinning action, so that if the fine particles are randomly precipitated, then Equation (4.73) (see Chapter 4) can be invoked,

$$R_0 = (1 - 4/3Z)r/f \tag{4.73}$$

where R_0 is the *sub-grain* size, r is the (spherical) particle radius, Z is the size advantage of the growing sub-grain and f is the volume fraction of particles.

If, as indicated above, the particles are precipitated exclusively on sub-grain boundaries, then Equation (4.78) (see Chapter 4) can be invoked,

$$R_0 = (3 - 4/Z)^{1/2} r/f^{1/2} \tag{4.78}$$

The size of sub-grains is dependent upon the hot deformation conditions, but is commonly in the sub-micron range.[29,31] R_0 is now at least an order of magnitude less than that of a fine grained austenite, and would require the presence of extremely small particles if the particles were randomly distributed. The critical particle size would be reduced by at least an order of magnitude, or at least would require an order of magnitude increase in the volume fraction of particles for particles of a given size, due to the reduction in R_0. The increased efficiency of pinning particles selectively precipitated on grain boundaries, rather than randomly precipitated, has been considered previously,[32] and can be expressed either as the ratio of the critical particle sizes required to pin a given grain size, or the ratio of grain sizes that can be pinned by random and grain boundary precipitated particles, for a given volume fraction and particle size, according to Equations (4.73) and (4.78). A comparison of the grain or sub-grain sizes that can be stabilised according to these equations is shown in Table 6.3. The sizes that can

Table 6.3 Sub-grain stabilisation by second phase particles when the particles are either randomly distributed or form exclusively on sub-grain boundaries. The greater boundary pinning efficiency of the grain boundary precipitate is clearly seen in the much finer sub-grain structure that can be stabilised with a given small volume fraction of particles

Volume fraction of precipitate f Particle radius r μm	**0.0001 (0.01%)**	**0.0002 (0.02%)**	**0.0005 (0.05%)**	**0.0010 (0.10%)**
	Random distribution			
0.01 (10nm)	33.3	16.7	6.7	3.3
0.005 (5nm)	16.7	8.3	3.3	1.7
0.002 (2nm)	6.7	3.3	1.3	0.7
0.001 (1nm)	3.3	1.7	0.7	0.3
	Grain boundary distribution			
0.01 (10nm)	1.0	0.70	0.44	0.31
0.005 (5nm)	0.5	0.35	0.22	0.16
0.002 (2nm)	0.2	0.14	0.09	0.06
0.001 (1nm)	0.1	0.07	0.04	0.03

be stabilised are dependent upon the heterogeneity factor, Z, i.e. the size advantage of a particular grain or sub-grain. A value of $Z=2$ has been chosen for the comparison. It can be seen from Table 6.3 that the stabilised grain sizes for both equations decrease as the volume fraction increases and as the particle size is reduced. The ratio of the minimum grain sizes stabilised by the random and the grain boundary distributions varies with the volume fraction of particles, from 33 : 1 at a volume fraction of 0.0001 (0.01%) down to 11 : 1 at a volume fraction of 0.001 (0.10%), but is independent of the particle size. The significant feature of Table 6.3, however, is that a large volume fraction (0.1% by volume) of very fine 1nm, particles is required to stabilise a sub-micron sub-grain size when the particles are randomly distributed, but only a small volume fraction of 0.0001 (0.01%) of particles will successfully inhibit sub-grain growth when the particles are exclusively precipitated on the sub-grain boundaries, even where the particles are somewhat larger.

The experimental observations made on microalloyed niobium steels are thus self consistent in that deformation accelerates the niobium carbo-nitride precipitation process by providing sites for the easy nucleation of these particles on the sub-grain boundaries, when the solid solution is supersaturated. The particles so precipitated are automatically in a position to exert effective inhibition of sub-grain boundary migration, and thus pin the sub-grain structure, thereby inhibiting recrystallisation.

Protracted holding in the lower part of the austenite temperature range will cause further precipitation and particle growth as illustrated by the results of Le Bon and Saint-Martin.[33] The kinetics of the precipitation process are clearly influenced by the extent of deformation,[33,34] and the precipitation process occurs at progressively shorter times as the deformation is increased. However, even with a single deformation as high as 67% reduction, the time for precipitation is still finite, and can take up to one minute at 900°C. In a normal rolling process with smaller individual deformations the precipitation times could take several minutes, or even several tens of minutes.[34] It is clear that for commercial rolling passes the amount of precipitate available for the inhibition of recrystallisation may be considerably less than that which could be produced by complete precipitation, and the sub-grain precipitation is an appropriate mechanism to consider for the inhibition of recrystallisation. An important corollary to the times required for precipitation is that a not inconsiderable amount of the dissolved niobium will be available for precipitation during subsequent rolling passes.

If complete precipitation is achieved during the hot rolling operation, then Ostwald ripening may occur, ultimately giving larger and fewer particles, and the ripening could be somewhat faster if several particles are precipitated on a common sub-grain boundary, due to the accelerated diffusion that occurs along boundaries. Any strain induced precipitation in the austenite will naturally reduce the amount of niobium that is available for subsequent interphase precipitation during transformation after rolling. In fact, Amin *et al.*[35] have used the residual interphase precipitation strengthening as a measure of the extent of precipitation in the austenite, in order to investigate the effects of niobium and interstitial concentrations on the precipitation kinetics of the strain induced niobium

carbo-nitride. There is considerable evidence that the precipitation kinetics are influenced by these compositional variables,[34,35] as would be expected from the effects of supersaturation on precipitation behaviour. Unfortunately there is no analytical relationship, as yet, that can be applied between the compositional variables and their effects on the precipitation kinetics, and therefore on the recrystallisation behaviour.

The constitutive equations for the evolution of microstructure given for carbon–mangangese steels are dramatically changed when a microalloying element such as niobium is added to the steel. The effects of niobium on the constitutive equations have been reviewed by Sellars,[15] who suggested that there are three main domains in the hot working of niobium steels:

(i) At temperatures of 1000°C and above, the niobium steel behaves very much like the carbon steel with respect to the dependency of t_{50} on strain, temperature and prior grain size, but with the exception that the recrystallisation is slower ($t50$ is larger, due to the solid solution effect of niobium).

(ii) At temperatures between 1000°C and 890°C, the temperature dependence of t_{50} (the time to 50% recrystallisation) was considerably larger than in the plain carbon steels, the recrystallisation being much slower at lower temperatures. This stage corresponds with the interaction between strain induced precipitation and recrystallisation, down to the maximum rate in the precipitation C-curve, as indicated in Fig. 6.12.

(iii) At temperatures below 890°C, the temperature dependence of t_{50} is less than that of the plain carbon steel, being a compromise between the effect of lower temperatures slowing the recrystallisation process, and the effect of lower temperatures giving less strain-induced precipitation.

These effects are illustrated in Fig. 6.13, taken from the work of Sellars, where it can be seen that the temperature ranges of the three stages, and the degree of retardation of recrystallisation, appear to be dependent upon the niobium concentration in the steel. Such effects would undoubtedly affect the predictive capability of any model involving constitutive equations based on the above three domains, but, for steels containing 0.03–0.04wt%Nb, Sellars recommends the following equations for static recrystallisation.

$T > 1004°C$,

$$t_{50} = 2.52 \times 10^{-19} d_0^2 \varepsilon^{-4} \exp(325\,000/RT) \tag{6.20}$$

$1004°C > T > 890°C$

$$t_{50} = 5.94 \times 10^{-38} d_0^2 \varepsilon^{-4} \exp(780\,000/RT) \tag{6.21}$$

$T < 890°C$

$$t_{50} = 9.24 \times 10^{-9} d - 0^2 \varepsilon^{-4} \exp(130\,000/RT) \tag{6.22}$$

where t_{50} is the time to 50% recrystallisation (s), d_0 is the austenite grain diameter (μm), ε is the true strain applied, R is the gas constant (8.3143 $Jmol^{-1}K^{-1}$), and T is the absolute temperature (K).

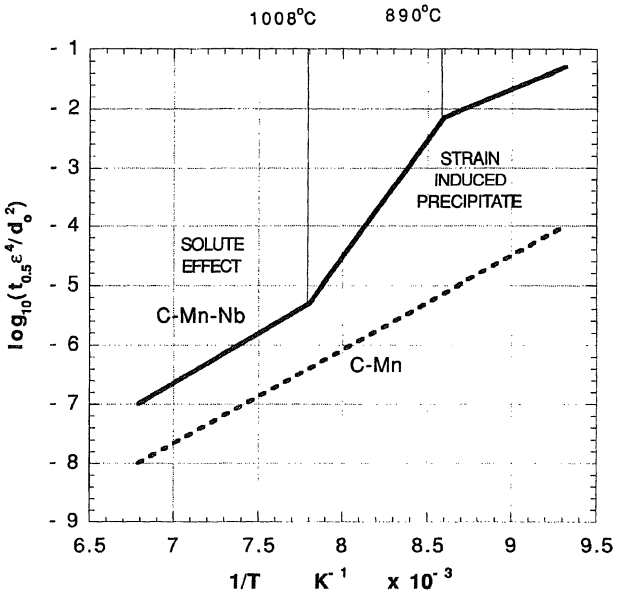


Fig. 6.13 The effect of a niobium addition on the constitutive equations for the recrystallisation of deformed austenite. Three regimes of recrystallisation are shown corresponding with (a) retardation by dissolved niobium, (b) retardation by strain induced precipitation and (c) reduced rates of strain induced precipitation. After Sellars.[15]

The constants have dimensions of $s \cdot \mu m^{-2}$ and the apparent activation energies are expressed in $Jmol^{-1}$.

The recrystallised grain size, d_{rex}, developed in niobium steels follows a similar relationship to that observed for carbon steels and can be expressed[15] as

$T > 950°C$,

$$d_{rex} = 0.9\, d_0^{0.67}\, \varepsilon^{-0.67} \tag{6.23}$$

Subsequent grain growth appears to follow a similar growth law to that given in Equation (6.18), but the proportionality constant, k, becomes much smaller, so that grain growth is virtually negligible in niobium-treated steels. In the presence of sufficient strain induced precipitation, grain growth could be inhibited, and would further justify the neglect of grain growth, certainly at temperatures below about 950°C. Sellars has in fact suggested that austenite grain growth can be neglected in niobium steels at temperatures below 1200°C under practical rolling conditions. The limitations of the growth equations and the need for further clarification was discussed thoroughly by Sellars. A comparison of the predicted evolution of the austenite grain structure of carbon-manganese and niobium microalloyed steels is shown in Fig. 6.14. All passes involved a 15% reduction in thickness in reducing the 200 mm slab to 20 mm plate. Such computed grain structure evolutions show reasonable agreement with both experimental and commercial rolling operations,

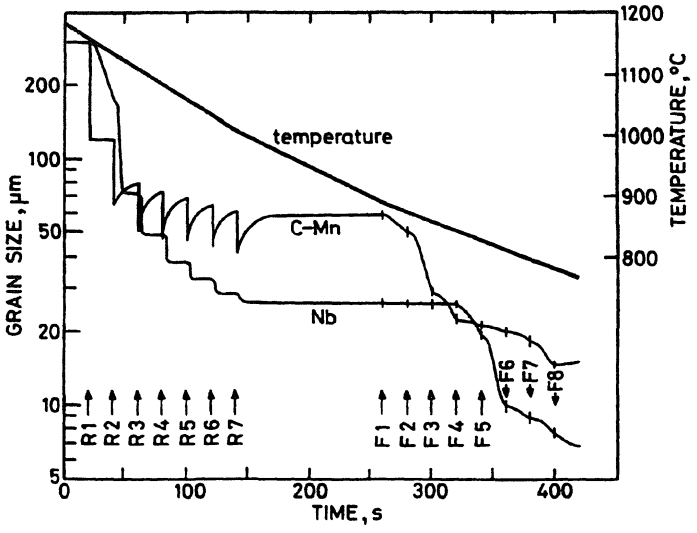


Fig. 6.14 A comparison of the evolution of the austenite grain structures during hot rolling schedules for carbon-manganese and niobium steels. After Sellars.[15]

and successfully simulate the effects of controlled rolling operations in carbon–manganese steels.

An important feature of the severe retardation of recrystallisation by niobium at deformation temperatures below 1000°C is the complex mixture of deformed and recrystallised grains that can exist. The retardation is such that the stock material can enter subsequent rolling passes in the unrecrystallised or partially recrystallised state. Under these conditions the unrecrystallised portions of the structure undergo further deformation, which increases the accumulated deformation and increases the driving force for recrystallisation. A common feature of low temperature rolled niobium steels is the persistence of extremely elongated austenite grains. These grains have a volume that is characteristic of relatively large grains, but the accumulated deformation gives a significant reduction in the thickness of the grain, i.e. in the direction normal to the rolling plane for plate and strip materials, or normal to the rolling direction for bars of various regular cross-sectional shapes, e.g. rounds and squares.

The effective size of the elongated austenite grains is related to its thickness, and the refinement of these grains is mechanical in nature, rather than a result of recrystallisation. For example, if a 200 mm thick slab with an austenite grain size of 200 μm could be rolled to 20 mm thick plate without any recrystallisation taking place, the austenite grain thickness (normal to the rolling plane) would on average be reduced to 20 μm which is similar to that obtained through recrystallisation refinement. Obviously such grains, which when deformed undergo plane strain conditions, would show length to thickness ratios of 100:1, are not expected in rolling schedules starting at temperatures of 1250°C or thereabouts, but significant grain thinning and grain elongation does occur as a result of the accumulated

deformation that is applied at low temperatures, e.g. below 1000°C. This distinctive feature of low temperature controlled rolled niobium steels has led to the adoption of the terms 'recrystallisation controlled rolling' and 'deformation controlled rolling', which distinguish the grain refinement attained by successive recrystallisation from that attained in microalloyed steels deformed below the 'recrystallisation temperature' where effective grain refinement relies upon effective thinning of the austenite grains (and also upon the internal dislocations arrays as will be discussed later). The concept of a recrystallisation temperature for a given steel is rather arbitrary, although effective, in that recrystallisation is 'slow' at temperatures below the recrystallisation temperature, and 'fast' at temperatures above it. Effectively the recrystallisation temperature distinguishes a temperature below which recrystallisation becomes sufficiently sluggish to be almost negligible in commercial rolling practices. The effects of various microalloy additions and concentrations on the recrystallisation temperature are shown in Fig. 6.15.[36] Niobium additions cause a more marked increase in the recrystallisation temperature than are observed with other microalloys.

Under conditions of 'deformation controlled rolling', the evolution of the austenite microstructure has to be considered in terms other than that implied by the simple constitutive equations for the recrystallised grain size and grain growth process, even though these remain as elements in the evaluation of the final structure. A simplified procedure for the evaluation of the austenite structure at temperatures near or below the 'recrystallisation temperature' is illustrated in Table 6.4.

Consider a part rolled slab which has a completely recrystallised grain structure, and an austenite grain diameter of 50 μm prior to entering the first pass in the vicinity of the recrystallisation temperature. With a true strain of $\varepsilon = 0.2$, i.e. $\ln t_0/t = 0.2$, where t_0 is the thickness before the pass and t the thickness after the pass, then the grains would be squashed to a thickness of 40.9 μm. In the time interval

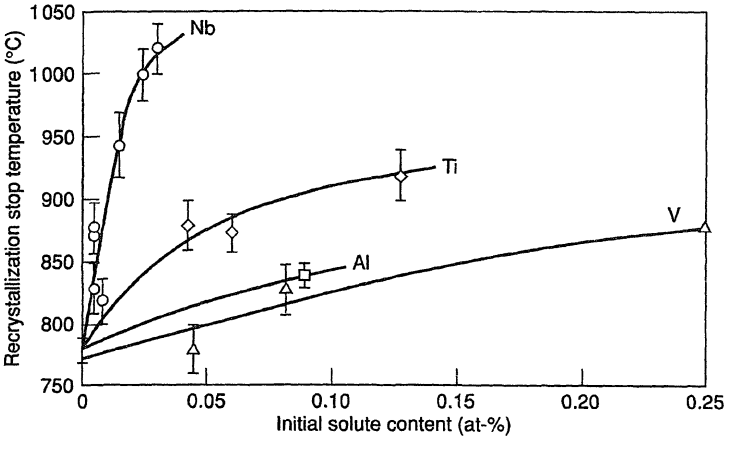


Fig. 6.15 The effects of microalloying additions on the recrystallisation temperature of austenite in a low carbon 1.4wt%Mn steel. After Cuddy.[36]

Table 6.4 Evolution of the austenite grain structure with partial recrystallisation

Before 1st pass	Recrystallised austenite grains ($d_\gamma = 50\,\mu m$)			
After 1st pass ($\varepsilon = 0.2$)	Deformed austenite grains $t_\gamma = 40.9\,\mu m$			
Before 2nd pass	(X_1) Recrystallised austenite ($d_\gamma = 35.7\,\mu m$)		($1 - X_1$) Deformed (20%) austenite ($t_\gamma = 40.9\,\mu m$)	
After 2nd pass ($\varepsilon = 0.2$)	Deformed austenite ($t_\gamma = 29.3\,\mu m$)		Double deformed austenite ($t_\gamma = 33.3\,\mu m$)	
Before 3rd pass	(X_1X_2) Recrystallised austenite ($d_\gamma = 28.5$)	$X_1(1 - X_2)$ Deformed austenite ($t_\gamma = 29.3$)	$(1 - X_1)X_3$ Recrystallised austenite ($d_\gamma = 22.5$)	$(1 - X_1)(1 - X_3)$ Deformed austenite ($t_\gamma = 33.5$)

between the first and second pass, recrystallisation may commence, but from the recrystallisation kinetics, may not be completed. Thus, there are two types of austenite entering the second pass. The volume fraction X_1 of recrystallised austenite will have a grain size dictated by the prior grain size (50 μm) and the strain ($\varepsilon = 0.2$), which, according to Equation (6.23), is $d_\gamma = 35.7\,\mu m$. The remaining fraction of the austenite $(1 - X_1)$ entering the second pass would comprise the squashed (40.0 μm thick) grains carrying a residual deformation of $\varepsilon = 0.2$.

Immediately after the second pass there will be two types of deformed austenite, one carrying a residual deformation from the second pass, and the other carrying the residual deformation from both passes, the grain thicknesses being as shown in Table 6.4. In the interval between the second and third passes, some recrystallisation may occur, presumably more so in those grains carrying the double deformation. The two proportions of recrystallised grains are shown as X_1X_2 for the singly deformed austenite, and $(1 - X_1)X_3$ for the doubly deformed austenite, and their recrystallised grain sizes are shown as 28.5 μm and 22.5 μm respectively, these being derived from Equation (6.23) with $d_0 = 35.7$ and 50 μm and the deformations being 0.2 and 0.4 respectively. The fractions of singly deformed austenite and doubly deformed austenite are shown as X_1 $(1 - X_2)$ and $(1 - X_1)(1 - X_3)$ respectively.

The values of the thickness of the deformed austenite grain, t_{γ_r}, are shown to facilitate the evaluation of the average effective grain size at any stage. For example, immediately before the third pass, the average austenite grain size would be evaluated as

$$d_{av} = 28.5X_1X_2 + 29.3X_1(1 - X_2) + 22.5(1 - X_1)X_3 + 33.5(1 - X_1)(1 - X_3)$$

The number of possible conditions of the austenite grains is given by $2^{(n-1)}$ where n is the number of the pass about to be entered. On entering the first pass, there is $2^0 = 1$ condition, i.e. an austenite grain structure with a grain size of 50 μm; on entering the second pass there are $2^1 = 2$ conditions, i.e. that recrystallised between the first and second passes, and that which remains unrecrystallised. As shown in Table 6.4, prior to the third pass there are $2^2 = 4$ possible conditions of the austenite, as described above. With 8–10 passes in the finishing train of many modern plate and strip mills, the number of possible austenite conditions would

be large, but it should be emphasised that not all possible conditions may be able to appear or persist, depending upon the temperature changes taking place. At lower temperatures, i.e. well below the recrystallisation temperature, then recrystallisation may be completely inhibited. Also, if stock enters the finishing train at temperatures well above the recrystallisation temperature then complete recrystallisation may eliminate the deformed austenites.

Such approaches to the evolution of the austenite structure are empirical in their application, even though they are based on the constitutive Equations (6.12)–(6.23). Some of the constitutive equations themselves contain an element of empiricism, but in general are based on sound metallurgical principles concerning recrystallisation and grain growth. The empiricism in the application really concerns the process by which recrystallisation takes place. The first recrystallised grains are observed to be grain boundary nucleated, and deformed grains are often encircled by smaller recrystallised grains which grow into the interior of the deformed grain. Other recrystallised grains may form on shear bands which are transgranular in nature, and thus allow recrystallised grains to appear within the deformed grains. The mathematically minded reader will realise that, although the recrystallised fractions given in Table 6.4 may be substantially correct, the assignment of a deformed grain thickness, t_{γ}, to the unrecrystallised fraction may be considerably in error if fractions of each deformed grain are recrystallised, rather than a fraction of those grains that are deformed being recrystallised. Nevertheless, the procedure given in Table 6.4 gives reasonable, if not precise, predictions of the final austenite grain structure, and has been used in the development of rolling schedules for a variety of steels.

Thus far, the discussion of the hot rolling and controlled rolling processes for microalloyed steels has centred on niobium steels. To some extent, niobium is an ideal microalloying element to consider for such processes in that it can exhibit most of the effects that microalloying additions may have. In particular

(i) The niobium carbo-nitrides can be substantially dissolved at commonly used soaking temperatures prior to hot rolling.
(ii) Of the microalloying elements dissolved, niobium has by far the largest effect in retarding recrystallisation.
(iii) Strain inducement of niobium carbo-nitride occurs at temperatures between about 1000°C and 800°C which represent a commonly used temperature range for the completion of the hot rolling process.

From this standpoint, it is useful to compare the effects of other microalloying additions, i.e. titanium and vanadium, with those of niobium in order to understand their effects, and particularly the effects of different concentrations of these elements.

The effects of titanium are strongly dependent upon the amount of titanium added. An addition of 0.04wt%Ti (to compare with the addition of 0.04wt%Nb) has little effect on the hot working characteristics of the steel, and the response to hot rolling is very similar to that of a plain carbon steel. The main reason for this behaviour is to be found in the extremely limited solubility of titanium nitride. Such a level of titanium results in the precipitation of the nitrogen-rich titanium

carbo-nitride from the liquid state. The appearance of the orange cuboids of titanium (carbo-) nitride in the optical microstructure is a familiar feature of these steels. These nitrides are some 5–10 μm in edge length and are ineffective in restricting grain growth except at the largest austenite grain sizes. (Lower titanium levels have been added to promote solid state precipitation of much finer titanium nitrides but these will be considered in detail in Chapter 7.) The extremely stable titanium nitride effectively rules out any substantial dissolution at the soaking temperature, thus precluding any solid solution effect of titanium on recrystallisation and also precluding any significant strain inducement of titanium carbo-nitride. This is in accord with the results of Irvine *et al.*,[37] who did not detect any difference between the recrystallisation kinetics of plain carbon steels and those of a 0.04wt%Ti steel containing 0.007wt%N.

The use of substantially larger titanium additions, however, can have different effects. With limited nitrogen contents (up to about 0.01wt% in electric arc steels, but with considerably less in steels produced by the BOS steelmaking process), the amount of titanium that is required to form titanium nitride is also limited, due to stoichiometry, and titanium additions in excess of these amounts then provide the ability to develop the more soluble carbide. Strictly speaking, the high temperature titanium carbo-nitride is substantially titanium nitride (see Table 3.18(b)), and the low temperature carbo-nitride would contain significantly more carbon under equilibrium conditions, particularly when the titanium level increases towards the stoichiometric ratio required for both carbon and nitrogen. However, the kinetics of diffusion and precipitation are relatively slow at low temperatures in the austenite range, and usually result in coarse (widely spaced) particles of nitrogen-rich titanium carbo-nitride from the high temperature soak, and fine carbon-rich titanium carbo-nitride particles precipitated at low temperatures as a result of strain inducement. As shown by Chandra *et al.*,[38] the overall effect of a high titanium addition of about 0.1wt%Ti on the recrystallisation of low carbon steels is to reproduce the effects seen in niobium steels, i.e. there is a retardation of recrystallisation due to the dissolved titanium, with a further effect of strain induced precipitation over the temperature range 1000–850°C peaking at 900°C . (It should be noted that these observations were based on relatively slow strain rate dynamic tests and relate to the dynamic recrystallisation process.)

The effects of vanadium reflect the high solubility of the carbo-nitride and especially the carbide. Vanadium in solution appears to have only a slight effect in retarding recrystallisation. Irvine *et al.*[37] failed to observe any significant effect of vanadium on recrystallisation, whilst Everett *et al.*,[39] using mill stand loading as a measure of interstand softening, found that vanadium steels showed retarded softening (0.1%V–0.014%N steels) though the extent of retardation was much less than that observed for niobium grade steels. It should be pointed out that much of the work on the thermomechanical treatment of vanadium steels has been confined to steels with boosted nitrogen contents. Because of the high solubility of vanadium carbide and the moderate solubility of vanadium nitride (see Chapter 3, Table 3.18(a)), steels with low nitrogen contents, e.g. 0.005wt%, would show little tendency to form stable carbo-nitrides even at temperatures as low as 900°C.

One feature common to all of the microalloyed steels was that, at temperatures

below about 1100°C, irrespective of the rate of recrystallisation, there was no significant grain growth after recrystallisation had been completed.

Much of the work on the effects of these microalloying elements on recrystallisation have been confined to single pass deformations and isothermal recrystallisation, and their effects in multi-pass complex commercial rolling operations are only understood in semi-quantitative terms. Certainly, the modelling of rolling operations for vanadium and titanium steels lags behind that being applied for niobium steels. In part, this may well be due to the smaller effects of vanadium and titanium on the recrystallisation kinetics. One area that has been studied in the case of vanadium steels concerns recrystallisation controlled rolling. The inhibition of grain growth at temperatures below 1100°C means that progressive grain refinement can be attained even at the temperatures encountered in the finishing stands of modern high speed bar mills (1000–1050°C), provided that the nitrogen contents of the vanadium steels are suitably enhanced to allow strain induced precipitation of vanadium nitride.

6.3.5 Controlled Rolling in the Austenite–Ferrite Range

The evolution of the austenite structure has so far been considered in two stages. In stage 1 of the rolling process, substantial recrystallisation occurs to give a recrystallised austenite grain structure. In stage 2 rolling, which occurs at lower temperatures, there is little recrystallisation and there is a mechanical refinement of the structure which gives rise to grain thinning. The use of controlled rolling in industry has covered both of these regions, the selection depending upon the form of the product, mill power, and steel chemistries. In high speed bar mills, the adiabatic heating, arising from deformation, can overcome the natural cooling of the bar stock to give a rise in temperature of the stock as it passes through the finishing train, so that finishing temperatures below about 1000°C migh be difficult to achieve without incurring serious losses in production rate. The rolling of thin plate, on the other hand can often involve low finishing temperatures, where, with niobium grade steels, it is inevitable that the deformed austenite structure will be developed.

The progressive development of controlled rolling practices, and the attainment of lower and lower finishing temperatures, to attain progressively finer austenite structures, ultimately led to the use of finishing temperatures in the two phase region where austenite and ferrite were present during the deformation process. This was referred to by Tanaka *et al.*[40] as the stage 3 rolling. There are a number of features of note which occur in stage 3 rolling.

(i) Deformation in this condition causes deformation of both the austenite and the ferrite grains.
(ii) Recovery and recrystallisation occurs in the ferrite to form a fine grained ferrite with a sub-grain structure, provided that an adequate deformation is given at these low temperatures – typically at or below 750°C.

(iii) Deformation and recrystallisation of the ferrite produces a preferred orientation of the ferrite grains during plate rolling to give a (100) texture in the rolling plane.

(iv) A deformed austenite will transform to ferrite at a higher temperature than a non-deformed austenite, i.e. the A_{r3} temperature is increased. This does not imply a change in the thermodynamic equilibrium temperature, but rather a reduction in the undercooling required to cause nucleation and growth of the ferrite at a given cooling rate. Tanaka *et al.* observed increases in the ferrite start temperature of about 40°C with deformations of about 30% or more in stage 2.

(v) Any further ferrite induced by straining the austenite during the stage 3 rolling operation will be undeformed ferrite. Only the ferrite existing prior to the deformation will be available for subgrain formation, recrystallisation, and texture development.

The importance of the stage 3 deformation is that the substructure in the ferrite causes a marked increase in strength, and the development of the (100) ferrite texture has marked effects on the toughness of plate materials rolled in this way. These aspects will be considered further in Chapter 7.

6.3.6 Transformation of Austenite to Ferrite in Hot-Rolled and Controlled-Rolled Products

The preceding sections have dealt with the evolution of the austenite grain structure during the hot rolling operation and have briefly considered the formation of ferrite in relation to the deformation process in stage 3 rolling. However, the objective of all of these thermo-mechanical treatments is to control the final ferrite–carbide structure and hence the mechanical properties of the product. It is necessary therefore to consider the relationships between the final state of the austenite and the ferrite–carbide structure that is developed by transformation during cooling, when the hot working operation is completed.

(a) Recrystallised Austenite Grains

The transformation of austenite to polygonal ferrite (and other transformation products) has received attention over a considerable period of time. The austenite–ferrite transformation occurs by a thermally activated nucleation and growth process. Studies of the kinetics of the austenite transformation under isothermal transformation conditions have shown that the nucleation rate of ferrite and also the growth rate initially increase with increasing undercooling below the equilibrium temperature, i.e. with reducing temperature, but at even lower temperatures the nucleation rates decreased as did the growth rates.[41] Also shown in this work was the variation of nucleation and growth rates with time (and coincidentially with the degree of transformation). The nucleation rate generally decreased with time (and transformation) at low levels of undercooling, and increased with time (and transformation) at high levels of undercooling. Growth rates appeared to be sensibly constant with time at a given temperature.

The transfer of these observations to continuous cooling conditions can only be made in a qualitative sense. Under slow cooling conditions, when extensive transformation can occur with relatively little undercooling, the nucleation rate will be low, as the driving force (chemical free energy change) is low when the undercooling is small. Roberts *et al.*[42] suggested that only a few favoured nucleation sites would be activated under these conditions, e.g. grain corners and edges. With faster cooling rates, the retention of austenite to lower temperatures will increase the driving force which would additionally activate less favourable nucleation sites, e.g. grain faces, thus promoting, after transformation, a finer ferrite grain size. The effect of increasing the cooling rate also gives less time for ferrite growth, and in the limit, would give incomplete ferrite transformation. These aspects have been considered by Pandi *et al.*[43] and Militzer *et al.*,[44] in calculating the effects of austenite grain size and cooling rate on the transformation start temperature and the progress of transformation of a low carbon–niobium grade steel. The effective grain refinement achieved by transformation from austenite to ferrite was expressed by

$$M = f_\alpha (d_\gamma / d_\alpha)^3 \tag{6.24}$$

where M is the average number of ferrite grains produced per austenite grain, f_α is the volume fraction of ferrite in the final microstructure, d_γ is the austenite grain diameter and d_α is the ferrite grain diameter.

M varies quite modestly for changes in cooling rate when the austenite grain size is fine (18 μm), increasing from $M = 2$ at a cooling rate of 1°C s^{-1} to $M = 20$ at a cooling rate of 80°C s^{-1}, i.e. d_γ / d_α changes from 1.4 to 2.9 over this range of cooling rate when the ferrite constitutes 80% of the final structure. An increase in the austenite grain size also causes a change in M, such that this steel, with an austenite grain size of 46 μm, cooled at 1°C s^{-1}, gave $M = 35$ (i.e. $d_\gamma / d_\alpha = 3.5$). At an even coarser austenite grain size (d_γ = 96 μm), it was found that $M = 210$. It is clear that a multiplicity of nucleation sites must be involved. With 210 ferrite grains per austenite grain, there would on an average 14-faced austenite grain (7 faces per grain) be some 30 ferrite grains. Intra-granular nucleation on non-metallic inclusions might alleviate this situation but would still leave a larger number of grains to be nucleated at interfaces. Extensive grain boundary nucleation is commonly observed, but would leave a substantial fraction of the grain interior to transform at lower temperatures, e.g. in the bainite region. This work was carried out using a niobium steel and consequently there was no evidence of ferrite grain growth after transformation due to the inhibiting effect of niobium carbo-nitride.

From the above observations, the effect of increasing the cooling rate is to increase the nucleation frequency of ferrite, and Militzer *et al.*[44] have shown that this is due to the increased level of undercooling which enhances the nucleation rate. The results of Militzer et al also showed that an increase in the austenite grain size would also increase the degree of undercooling at any given cooling rate, which would enhance the nucleation rate. What is less obvious from this approach is the effect of austenite grain size on the final ferrite grain size, due to the conflicting effects of larger austenite grains giving fewer nucleation sites per unit

volume and at the same time enhancing the undercooling with its consequent enhancement of nucleation rate.

Any successful application of this approach would require a complete understanding of the effects of cooling rate and prior austenite grain size on M_s and also an understanding of the effects of steel composition on the austenite–ferrite transformation characteristics.

Because of these difficulties, Militzer *et al.*[44] applied the more empirical approach of Suehiro *et al.*,[45] with slight modifications to take account of the ferrite fraction, and suggested that

$$d_\alpha = 1.2(F\exp(B_0 d_\gamma^n - E/T_s))^{1/3} \tag{6.25}$$

where d_α is the ferrite grain diameter (μm), F is the volume fraction of ferrite after complete transformation, d_γ is the austenite grain diameter (μm), T_s is the transformation start temperature (K) and B_0, n and E are constants.

The value of E was found to be 51 000 K^{-1} but the values of B_0 and n were composition dependent, with $B_0 = 52.3$ and $n = 0.0286$ for a 0.17%C Al-treated steel, and $B_0 = 52$ and $n = 0.0171$ for a 0.04%C Al-treated steel. The transformation start temperature was evaluated from a site saturation model developed to explain the effects of cooling rate and prior austenite grain size but which unfortunately still requires the input of experimental data to provide the T_s temperature. This requirement and the composition dependencies of B_0 and n in Equation (6.24), preclude the general use of this approach at present as a predictive model, but the data generated by Militzer *et al.* does serve to illustrate the complexity of the factors controlling the ferrite grain size. Figure 6.16 shows the effect of cooling rate

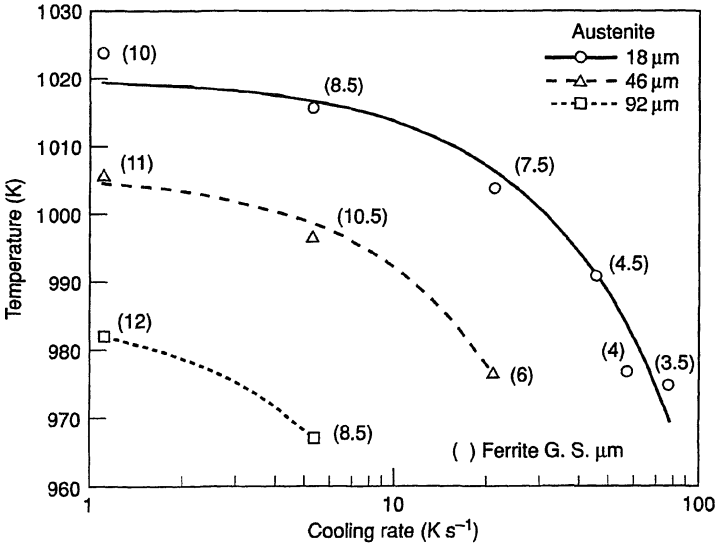


Fig. 6.16 The effects of prior austenite grain size and cooling rate on the ferrite grain size of a low carbon aluminium grain-refined steel. After Militzer *et al.*[43]

and prior austenite grain size on the transformed ferrite grain size of a 0.17%C–0.74%Mn–0.04%Al–0.0047%N steel. The transformation start temperature (defined by Militzer *et al.* as 5% ferrite formation) is depressed as the cooling rate is increased. This corresponds directly to the continuous cooling transformation curve shown in Fig. 6.9, apart from the fact that Militzer *et al.* used a linear cooling programme for transformation rather than the natural bar cooling rates employed for the determination of Fig. 6.9. Increasing the cooling rate thus depresses the transformation temperature, which in turn increases the degree of undercooling and thus enhances the ferrite nucleation rate. Because the ferrite nucleation rate is enhanced, the transformed ferrite grain size is much finer. This feature can be seen at all prior austenite grain sizes. There is, however, an upper limit to the cooling rate that can be applied and yet still give a substantially polygonal ferrite–pearlite structure. At cooling rates above this limit, polygonal ferrite transformation is suppressed and is replaced by acicular ferrites or bainite, with an attendant loss in toughness. The limiting cooling rate is reduced as the prior austenite grain size is increased, which in turn limits the fineness of the ferrite grain size that can be achieved. This is in accord with the known effect of the prior austenite grain size on hardenability. The hardenability of a steel increases with increasing prior austenite grain size. The effect of austenite grain size and its interaction with cooling rate is interesting. At slow cooling rates, increasing the austenite grain size enhances the undercooling which tends to balance the loss of easy nucleation sites normally associated with coarse austenite grains. At fast cooling rates, a fine austenite grain size promotes fine ferrite grains whilst a coarse austenite grain size promotes an acicular structure. As a result of these effects, reducing the austenite grain size has little effect on the ferrite grain size at a given cooling rate (as low as $1\,K\,s^{-1}$), but reducing the austenite grain size at a given degree of undercooling (same transformation temperature) produces a dramatic refinement of the ferrite grain size. It should be pointed out that at cooling rates that are much slower than the slowest rate used by Militzer *et al.* the undercooling associated with a coarse austenite grain structure would be much reduced and the ferrite grain size would increase dramatically. The effect of the prior austenite grain size on the transformed ferrite grain size is thus highly dependent upon the cooling rate for a given steel, and due consideration must also be given to the critical cooling rate for non-polygonal transformation products at the more rapid cooling rates.

The effect of steel composition on the transformation kinetics has obvious importance in relation to both the ferrite nucleation and growth, and the limiting cooling rate for polygonal structure development, and is particularly significant in relation to the development of a fine grain size in, for example, plate material of a given thickness. The transformation curves indicated in Fig. 6.16 are sensitive to steel chemistry, and increasing the manganese content for example reduces the transformation temperature at a given cooling rate, and will reduce the critical cooling rate above which acicular structures are formed, thereby displacing the curves in Fig. 6.16 to slower cooling rates. The fact that virtually all elements will influence the transformation characteristics gives rise to complex solute interaction effects, but does not alter the basic principles. Also, the work of Militzer *et al.* was based on low temperature reheated samples, so that the effects of dissolved

microalloys and their effects on the ferrite transformation kinetics and products were not assessed. Such effects are expected to be similar in nature to those of other alloying elements, although the magnitude of their effects are uncertain.

There are other more empirical approaches which have been used to describe the effects of cooling rate and the prior austenite grain size on the ferrite grain size, and can be used for restricted steel composition and processing ranges.[46–49] For example, Anelli[47] suggested the following equation for low carbon steels

$$d_\alpha = A d_\gamma^{0.4}(1 - \exp(B d_\gamma)(60 C_R)^{-0.14} \tag{6.26}$$

where d_α is the ferrite grain size (μm), d_γ is the prior austenite grain size (μm), A is a composition dependent constant, B is a constant ($=0.075$) and C_R is the cooling rate $\mathrm{K\,s^{-1}}$.

Hodgson and Gibbs[48] expanded the equation of Sellars and Beynon[50] to include compositional factors for carbon and manganese to give

$$d_\alpha = (A + BC_e) + (A_1 + B_1 C_e) C_R^{-0.5} + A_2(1 - \exp B_2 d_\gamma) \tag{6.27}$$

where C_e is the carbon equivalent ($=\mathrm{wt\%C} + \mathrm{wt\%Mn}/6$)

$$\begin{aligned} A &= -0.4 \\ B &= 6.37 \\ A_1 &= 24.2 \\ B_1 &= -59.0 \\ A_2 &= 22.0 \\ B_2 &= 0.015 \end{aligned}$$

This equation was developed for steels with a carbon equivalent, C_e, less than 0.35. The constants were different for steels with $C_e > 0.35$, in that there was no interaction between steel composition and cooling rate, i.e. $B_1 = 0$, with corresponding adjustments to the other constants.

(b) Retained Deformation in Unrecrystallised Austenite

The effects of retained deformation in non-recrystallised austenite (i.e. austenite in microalloyed steels deformed at low temperatures) has been recognised for some considerable time. Early observations of these effects were made by Kozasu *et al.*,[25] who noted that deformed austenite grains were particularly effective in nucleating ferrite during transformation. Not only was the austenite grain boundary area per unit volume increased by deformation, but ferrite was also nucleated on deformation bands within the austenite grains. Measurements of the grain boundary area per unit volume Λ_g, and of the area of deformation bands per unit volume, Λ_b were carried out according to the methods described by Underwood[51]

$$\Lambda_g = 0.43 N_p + 1.57 N_n \tag{6.28}$$

where N_p is the number of grain boundary intercepts per unit length measured parallel with the rolling direction and N_n is the number of grain boundary intercepts per unit length measured normal to the rolling plane.

N_p and N_n are clearly different when the grains are elongated, but in a recrystallised structure $N_p = N_n$, and therefore

$$\Lambda_g = 2N^n = 2N_p \tag{6.29}$$

For the deformation bands

$$\Lambda_b = N_L / \sin\theta \tag{6.30}$$

where N_L is the number of deformation bands intersected per unit length of intercept normal to the rolling plane and θ is the angle between the deformation band and the normal to the rolling plane

Kozasu *et al.*[25] evaluated these quantities metallographically as shown in Fig. 6.17. The grain boundary surface area increased progressively with increasing deformation below the recrystallisation temperature as would be expected. At small deformations, there was little evidence of deformation bands, but with deformations in excess of 30%, the deformation band density increased

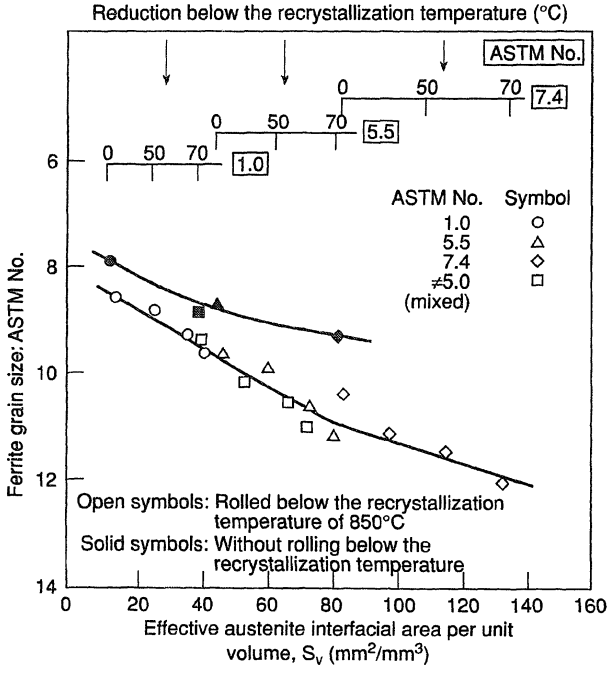


Fig. 6.17 The effect of effective austenite interfacial area on the transformed ferrite grain size. The effective austenite interfacial area includes not only austenite grain boundaries, but also the area of deformation bands formed at high levels of retained deformation structure. After Kozasu *et al.*[25]

dramatically up to about 25 mm^{-1} with a total reduction of 63% below the recrystallisation temperature. Interestingly, the deformation band density was independent of temperature (at temperatures below the recrystallisation temperature), strain rate and prior austenite grain size, within the ranges investigated, and appeared to be solely dependent upon the extent of deformation below the recrystallisation temperature.

Using the concept of an effective grain boundary area for ferrite nucleation in the deformed austenite, obtained by summing the grain boundary and deformation band areas, Kozasu *et al.*[25] showed that the ferrite grain size was generally finer in the deformed austenite than in recrystallised austenite with the same effective grain boundary area. Whilst this may, in part, be due to difficulties in assessing the deformed austenite structure from the inevitably transformed microstructure, Roberts *et al.*[42] have suggested that the grain boundaries of deformed austenite become corrugated, and that the bulges in these corrugated boundaries constitute favoured heterogeneous nucleation sizes. Such corrugations might also be present in the deformation bands if these form at an early stage of the sub-recrystallisation deformation, so that both types of nucleation site are enhanced with respect to their nucleation potency. Certainly, this explanation is supported by the increase in the temperature for the start of the austenite–ferrite transformation, noted by both Kozasu *et al.* and Roberts *et al.*

The nature of ferrite grain refinement, when the ferrite formed from deformed austenite, clearly involves more than the increase in grain boundary area, and the effects of deformation bands and boundary corrugation have been demonstrated clearly when substantial deformation is applied below the recrystallisation temperature. As part of their modelling work, Sellars and Beynon[50] took account of the retained strain in the austenite by the use of a multiplying factor, m, defined as

$$m = 1 - 0.45\varepsilon_r^{1/2} \tag{6.31}$$

where ε_r is the strain applied below the recrystallisation temperature, i.e. the retained strain.

The ferrite grain size produced by deformed austenite is then obtained from that predicted by Equation (6.27) (i.e. for undeformed austenite), multiplied by m. Hodgson and Gibbs[48] offered an equation in which the effect of retained strain was integrated, rather than appearing as a subsequent multiplying factor. The empirical nature of these equations, although allowing some appreciation of the magnitude of the changes and the effects of the independent variables, may restrict their use to relatively narrow composition ranges. The complexity of the austenite–ferrite transformation with regard to the grain size changes has already been emphasised, and it is clear that further clarification is still required.

When austenite is deformed at temperatures where partial recrystallisation may occur, subsequent deformation may not be uniform. Kozasu *et al.*[25] drew attention to the preferred deformation of the softer recrystallised grains, leaving the harder unrecrystallised grains with much less accumulated deformation. Strain partitioning would thus cause less accumulated deformation of the unrecrystallised

structure and therefore a tendency to develop fewer deformation bands. The persistence of these unrecrystallised grains gives a local coarse ferrite grain structure that would only be homogenised by adequate deformation below the recrystallisation temperature, thereby reducing the thickness of the unrecrystallised grains and introducing deformation bands.

6.4 SUMMARY

The effects of thermo-mechanical treatments on microstructure have been described; although the text is largely concerned with simple thermal treatments and with hot rolling, the physical metallurgy principles are applicable to any hot deformation process such as forging. In a simple thermal cycle such as normalising, grain refinement is an important feature of the normalised structure, and the use of microalloys (or aluminium), with the limited solubility of their interstitial compounds, plays an important role. Should higher strengths than are attainable by grain refinement alone be required, in steels in the normalised condition, then the use of vanadium, with the associated higher solubility of its carbo-nitrides, is necessary to provide interphase precipitation.

Thermo-mechanical treatments, involving the hot deformation of steels, are important in dictating the evolution of the microstructure during multi-pass deformation sequences. The evolution of microstructure is considered in three stages. The first stage, at temperatures above 1000°C, relates to the breakdown of the coarse 'as soaked' austenite grain structure by sequential deformation and recrystallisation. The second stage, at temperatures of 950°C down to the start of the austenite–ferrite transformation, relates to further austenite grain refinement in the case of plain carbon manganese steels, and to the development and retention of deformed austenite grain structures in the case of microalloyed steels, particularly when using niobium as the microalloy. The third stage of rolling relates to deformation after the start of the austenite–ferrite transformation. Deformation of the ferrite occurs with a consequent marked increase in the strength of the product due to the retention of cold working effects in the ferrite, i.e. the existence of sub-structures in the ferrite grains.

The effects of microalloys on the austenite recrystallisation and grain growth processes arise from two effects, i.e. the effects of solutes and the effects of strain-induced precipitation of the microalloy carbo-nitrides. Niobium is particularly potent in this respect.

The transformation of austenite to ferrite can produce an additional grain refining effect, which is dependent upon the cooling rate for a given austenite structure. Refinement of the prior austenite grain size is important in providing additional ferrite grain nucleation sites (grain boundary corners, edges or faces), whilst increasing the retained strain in deformed austenite grains is important in providing additional ferrite nucleation on deformation bands within the austenite grains. All of these effects interact with the basic steel chemistry, in a rather

complex manner, to control the final ferrite grain size. The application of these principles for specific cases are considered in Chapter 7.

REFERENCES

1. H. W. PAXTON: *Transformation and Hardenability in Steels*, Climax Molybdenum Co., Ann Arbor, Michigan, 1967, p.3.
2. J. E. BURKE and D. TURNBULL: *Prog. in Met. Phys.*, 1952, **3**, p.220.
3. M. HILLERT: *Acta Met.*, 1965, **13**, p.227.
4. H. HU and B. B. RATH: *Met. Trans.*, 1970, **1**, p.3181.
5. E. C. BAIN: *Functions of Alloying Elements in Steel*, American Society for Metals, 1939.
6. T. GLADMAN and F. B. PICKERING: *J. Iron and Steel Inst.*, 1967, **205**, p.653.
7. T. GLADMAN: *Developments in Carbon Steels*, Iron and Steel Inst., Special Report No.81. London 1963, p.68.
8. Atlas of Isothermal Transformation Diagrams, United States Steel Corp., Pittsburgh, PA, 1963.
9. M. ATKINS: *Atlas of Continuous Cooling Transformation Diagrams for Engineering Steels*, British Steel Corp.
10. R. PHILLIPS and J. A. CHAPMAN: *J. Iron and Steel Inst.*, 1966, **204**, p.615.
11. J. J. IRANI, D. BURTON, J. D. JONES and A. B. ROTHWELL: *Strong, Tough Structural Steels*, Iron and Steel Inst., Publication No.104, London, 1967, p.110.
12. H. NAKAMURA: *Behaviour of Aluminium Nitride and its Effect on the Mechanical Properties of Steels*, I.H.I., Tokyo, 1966.
13. T. J. GEORGE and J. J. IRANI: *J. Australian Inst. of Metals*, 1968, **13**, p.94.
14. T. SAKAI, M. G. AKBEN and J. J. JONAS: *Thermomechanical Processing of Microalloyed Austenite*, Eds. A. J. DeArdo, G. A. Ratz and P. J. Wray, Met. Soc. A.I.M.E. Pittsburgh, PA, 1981, p.237.
15. C. M. SELLARS: *Hot Working and Forming Processes*, Eds. C.M. Sellars and G. J. Davies, Book 264, The Metals Society, London, 1980, p.3.
16. A. LEBON, J. ROFES-VERNIS and C. ROSSARD: *Metal Science*, 1975, **9**, p.36.
17. C. ROSSARD: *Microstructure and the Design of Alloys*, Vol. 2, Inst. Metals, London, 1974, p.175.
18. C. M. SELLARS and J. A. WHITEMAN: *Metals Science*, 1979, **13**, p.187.
19. J. P. SAH and C. M. SELLARS: *Hot Working and Forming Processes*, Eds. C. M. Sellars and G. J. Davies, Book 264, The Metals Society, London, 1980, p.62.
20. C. M. SELLARS: *Materials Science and Technology*, 1985, **1**, p.325.
21. G. J. RICHARDSON, D. N. HAWKINS and C. M. SELLARS: *Worked Examples in Metalworking*, Inst. of Metals, London, 1985.
22. R. A. P. DJAIC and J. J. JONAS: *Met. Trans*, 1973, **4**, p.261.
23. K. T. AUST and J. W. RUTTER: *Trans. Met. Soc. A.I.M.E.*, 1959, **215**, pp.119 and 820.
24. K. LUCKE and H. P. STUWE: *Recovery and Recrystallisation of Metals*, Ed. L. Himmal. Interscience, New York, 1963, p.171.
25. I. KOZASU, C. OUCHI, I. SAMPEI and T. OKITA: *Microalloying '75*, Union Carbide, New York, 1977, p.120.
26. J. W. MARTIN and R. D. DOHERTY: *Stability of Microstructure in Metallic Systems*: Cambridge University Press, Cambridge, 1976, p.134.
27. J. J. JONAS and I. WEISS: *Met. Sci.*, 1979, **13**, p.238.
28. C. M. SELLARS: *Recrystallisation and Grain Growth in Multi-Phase Materials*, Eds. N. Hansen, A. R. Jones and T. Leffers, RISO Conference, Roskilde, (Denmark), 1980, p.291.
29. A. J. DEARDO, J. M. GRAY and L. MEYER. *Niobium*, Ed. H. Stuart, *Trans.*, Met. Soc. A.I.M.E., New York, 1984, p.685.
30. F. B. PICKERING, I. D. MCIVOR and T. GLADMAN: *J. Iron and Steel Inst.*, 1971, **209**, p.380.

31. E. L. BROWN and A. J. DEARDO: *Hot Working and Forming Processes*, Eds. C. M. Sellars and G. J. Davies, Book 264, The Metals Society, London, 1980, p.21.
32. T. GLADMAN: *Scripta Met. et Materialia*, 1992, **27**, p.1569.
33. A. B. LEBON and L. J. DE SAINT-MARTIN: *Microalloying '75*, Ed. M. Korchynsky, Union Carbide Corp., New York, 1977, p.90.
34. T. M. HOOGENDORN and N. H. SPANRAFT: ibid., p.75.
35. R. K. AMIN, G. BUTTERWORTH and F. B. PICKERING: *Hot Working and Forming Processes*, Eds. C. M. Sellars and G. J. Davies, Book 264, The Metals Society, London, 1980, p.27.
36. L. J. CUDDY: *Thermomechanical Processing of Microalloyed Austenite*, Eds. A. J. DeArdo, G. A. Ratz and P. J. Wray AIME, Warrendale, PA, p.129.
37. K. J. IRVINE, T. GLADMAN, J. ORR and F. B. PICKERING: *J. Iron and Steel Inst.*, 1970, **208**, p.717.
38. T. CHANDRA, M. G. AKBEN and J. J. JONAS: *Proc. 6th Int. Conf. on Strength of Metals and Alloys*, Ed. R. C. Gifkins, Pergamon Press, Oxford, 1982, Vol. 1, p.449.
39. J. R. EVERETT, A. GITTINS, G. GLOVER and M. TOYAMA: *Hot Working and Forming Processes*, Ed. C. M. Sellars and G. J. Davies, Book 264, The Metals Society, London 1980, p.16.
40. T. TANAKA, N. TABATA, T. HATOMURA and C. SHIGA: *Microalloying '75*, Ed. M. Korchynsky, Union Carbide, New York, 1977, p.107.
41. D. J. SWINDEN and J. H. WOODHEAD: *J. Iron and Steel Inst.*, 1971, **209**, p.883.
42. W. ROBERTS, H. LIDEFELT and A. SANDBERG: *Hot Working and Forming Processes*, Eds. C. M. Sellars and G. J. Davies, Book 264, The Metals Society, London, 1980, p.38.
43. R. PANDI, M. MILITZER, E. B. HAWBOLT and T. R. MEADOWCROFT: *H.S.L.A. Steel '95*, Eds. G. Liu, H. Stuart, H. Zhang and C. Li. Chinese Society for Metals, Beijing, 1995, p.265.
44. M. MILITZER, E. B. HAWBOLT and T. R. MEADOWCROFT: ibid., p.271.
45. M. SUEHIRO *et al.*: *Trans I.S.I.J.*, 1987, **27**, p.439.
46. I. TAMURA: ibid., 1987, **27**, p.763.
47. E. ANELLI: *I.S.I.J. International 1992*, **32**, p.440.
48. P. D. HODGSON and R. K. GIBBS: ibid., 1992, **32**, p.1329.
49. P CHOCQUET *et al.*: *Mathematical Modelling of Hot Rolling of Steels*, Ed. S. Yue, Canadian Inst. Metals, Hamilton, Ontario, 1990. p.34.
50. C. M. SELLARS and J. BEYNON: *High Strength Low Alloy Steels '85*, Eds. D. Dunne and T. Chandra, South Coast Printers, 1985, p.142.
51. E. E. UNDERWOOD: *Quantitative Microscopy*, Eds. R. T. DeHoff and F. N. Rhines, McGraw-Hill, New York, 1968, p.77.

CHAPTER 7

Properties and Applications

7.1 INTRODUCTION

The basic information on the solubilities of the microalloy carbo-nitrides, the ability of these carbo-nitrides to confer grain refinement and precipitation/dispersion strengthening and the appropriate structure–property relationships have been described in the previous chapters. The application of the basic principles to the development of specific products is considered in the present chapter. The advantages and disadvantages of specific microalloying elements have to be considered in relation to the process routes for various product types, and the attainable properties are often dependent upon the limitations of the process routes that may be imposed by such considerations as mill power, section size, cooling facilities and heat treatment facilities (mainly for annealing or normalising). All of these must be considered in relation to the manufacture of particular products, and the most appropriate microalloy can then be selected.

Such considerations may change with time, as new plant and new processes are introduced. Attention was drawn to the changes in casting practice in Chapter 1. One of the advantages of niobium and vanadium in ingot casting was that these additions could be made to rimming or semi-skilled steels because of their low affinity for oxygen. Aluminium and titanium additions could only be made to a heavily deoxidised steel with the attendant loss of product yield when material containing shrinkage cavities was discarded (up to 20% of the ingot weight). The development and expansion of continuous casting meant that all steels are well deoxidised to avoid CO gas evolution in the concast product . The advantages claimed for niobium and vanadium in balanced and semi-killed steels are now lost, because virtually all steels are concast with an attendant rise in the product yield of these well deoxidised melts. The adoption of continuous annealing lines in strip production has significantly altered the thermal cycles that can be applied to both hot and cold rolled strip material. Whereas cooling rates and dwell times used to be constrained by the thermal mass of a coil, perhaps weighing several tonnes, continuous annealing furnaces provide an extended range of heating and cooling rates, particularly with the addition of accelerated cooling at the end of the continuous annealing cycle, to that attainable by heat flow through the strip thickness.

A further factor that must be considered is that many products require the optimisation of more than one particular property. High strength notch ductile steels are required having high strengths coupled with high levels of toughness.

Maximising the yield strength of a material could be meaningless if toughness considerations proved to be limiting for the stress response of a product, i.e. where brittle fracture could occur at lower stresses than would be required to cause macroscopic plastic failure. Selected strengthening mechanisms that are least harmful, or even beneficial, to toughness can be selected. Also, high strength formable steels may require that the steel compositions are independently manipulated to give high strength by grain refinement and dispersion strengthening and to give high levels of bendability by controlling the non-metallic inclusion population.

In the development of products and their subsequent bulk manufacture, some consideration must be given to National or International Standards. When design engineers require a certain combination of properties, there needs to be some assurance of the level of properties that can be attained. National and International Standards are available for many products and steel types, and show the minimum property levels or composition ranges that have to be guaranteed by any supplier to a particular standard and grade. However, there may be many steels available that are produced for specific purposes, and which are produced by a particular company under a 'brand name'. Different companies offer similar property ranges in materials with different brand names, which makes the selection of materials particularly difficult. Nevertheless, reference will be made to National and International Standards where appropriate.

7.2 CHARACTERISTICS OF THE MICROALLOYING ELEMENTS

Microalloying elements have some characteristic effects in steel that are common to all of them. Other effects are specific to a particular element. These have been described in some detail in previous chapters but are summarised briefly in this section.

(a) Vanadium

The solubility of vanadium carbide is extensive, even at low temperatures in the austenite range, whilst that of vanadium nitride, which is somewhat lower, would allow only partial dissolution at low temperatures in this range, e.g. 900°C. In order to guarantee a fine grained structure in the normalised condition, the nitrogen content of vanadium steels (0.15wt%V maximum) is usually increased to levels above 0.01wt%N. The higher solubilities of the vanadium compounds (and their solid solutions) ensures that there is adequate dissolution to give interphase precipitation provided that the austenite–ferrite transformation conditions are suitable. This particular characteristic of vanadium has found application not only as vanadium steels, but also as a supplement to interphase precipitation strengthening in both niobium and titanium steels.

(b) Niobium

Niobium has a solubility product that allows substantial dissolution of niobium carbo-nitrides only at elevated temperatures. At low temperatures in the austenite

range the carbo-nitride shows such restricted solubility that dispersion strengthening is not generally observed. The undissolved carbo-nitride at these temperatures acts as an effective grain refiner. The marked change in carbo-nitride dissolution between high and low temperatures (1300°C and 900°C) in the austenite temperature range allows substantial strain induced precipitation at temperatures below about 1000°C, and produces what is arguably the most obvious distinctive effect of niobium, i.e. the marked retardation of recrystallisation at these temperatures. Although similar effects can be observed in titanium and vanadium steels, these are generally not so marked.

(c) Titanium

The extremely low solubility of titanium nitride is such that the addition of even modest microalloying addition levels can induce precipitation of a nitrogen rich (almost exclusively nitride) titanium carbo-nitride in the liquid steel. An extremely stable fine nitride distribution can be attained by restricted titanium additions which avoid extensive precipitation in the liquid state. Titanium levels in excess of that required to combine stoichiometrically with the nitrogen result in combination with the carbon, the solubility of which is similar to niobium carbide, thus allowing effects similar to those of niobium; these effects, however, are only observed when the titanium content greatly exceeds that required to combine with the nitrogen. The high level of stability of titanium nitride produces a significant reduction in the sensitivity to strain ageing. More will be said on this aspect in a later section of this chapter, but non-ageing steels are achieved by fixing the nitrogen as titanium nitride, and this effect can be produced in hot rolled products if a high titanium content is used.

Finally, of the microalloying elements commonly used in steel, titanium is unique in being able to form a sulphide or carbo-sulphide. Although titanium, in common with many other sulphide-forming elements, is capable of producing solid solution hardening of the manganese sulphide inclusions normally existing in steel,[1] thus reducing the plastic deformation of the sulphides during hot working, there is competition between manganese and titanium for the sulphur. At low titanium levels (or high manganese levels), manganese sulphide is formed with titanium in solid solution. At high titanium levels, the more stable titanium sulphide is formed and this is present as hard non-deformable particles under hot working conditions, thus changing the sulphides from elongated ovoids to spheres with attendant changes in ductility (see Chapter 2). A broad rule of thumb guide to the minimum titanium level necessary to provide sulphide shape control (i.e. the formation of TiS rather than MnS) is given by

$$\text{wt\%Ti} > \text{Mn}/10 + 4(\text{wt\%N}) + (\text{wt\%S})$$

i.e. after allowing for the titanium present as TiN and TiS, the residual titanium content (wt%) must be higher than 10% of the manganese content (wt%). For example, in a 1%Mn–0.01%N–0.01%S steel, the titanium level must be greater than $(0.1 + 0.04 + 0.01) = 0.15$wt%Ti.

(d) Aluminium

This is commonly used as a deoxidant (aluminium deoxidised steel) but this does not necessarily leave any significant residual aluminium in the steel. With an aluminium treated steel, not only is the steel heavily deoxidised with aluminium but there is a residual aluminium content of about 0.02wt%Al or more. Under these circumstances, aluminium nitride is stable at low temperatures in the austenite range, but will dissolve progressively as the temperature is increased. The extent of dissolution at high temperatures in the austenite range (e.g. 1350°C) is dependent upon the levels of aluminium and nitrogen of course, but the solubility product for aluminium nitride is low, the only common microalloy nitride having a lower solubility product being titanium nitride. Aluminium nitride has the distinction of forming a separate nitride, which has a hexagonal crystal structure, rather than forming any substantial solid solution with the face centred cubic microalloy carbo-nitrides. It should be noted that aluminium carbide is not stable in steel.

These features of aluminium and microalloy additions are applied according to the circumstances of the thermal and thermo-mechanical cycles that constitute the process route to a variety of product shapes, and product property requirements.

7.3 LOW CARBON STRUCTURAL STEELS

Low carbon steel plate was one of the first products to have property enhancements by the use of microalloy additions. This rapidly spread to strip products, and later to sections and bars.

7.3.1 Hot-Rolled Plate Products

Plate production had traditionally followed a process route starting with an ingot, converting this to a slab by hot rolling, and, in a quite separate rolling treatment, converting the slab to plate. With the introduction of continuous casting, the cast product is already in slab form, and plates are produced by either indirect rolling (cooled and reheated before rolling), or more recently, by direct rolling, which involves transfer of the hot concast slab directly to the rolling mill, with an attendant conservation of energy.

Irrespective of the early stages of manufacture, the thermal cycle for the hot rolling of plate is as shown in Fig. 7.1, and involves the following:

(i) A soaking stage to achieve a homogeneous temperature distribution, the temperature being commonly in the range 1200°C–1320°C. Higher carbon steels are frequently soaked at the lower temperatures to avoid decarburisation, when the mildly oxidising furnace atmosphere reacts with carbon at the surface of the slab.

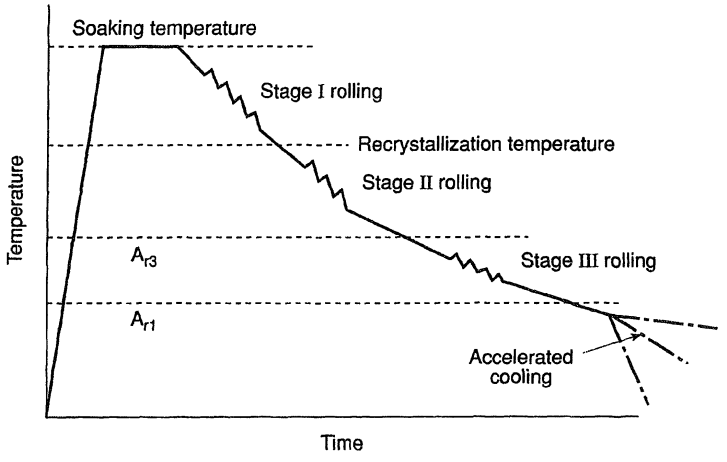


Fig. 7.1 Thermal cycle for the hot rolling of plate. Variations in the soaking temperature, time, deformation schedule and final cooling rate, contribute to the evolution of the microstructure and the properties attained.

(ii) Deformation in several rolling passes, each pass being restricted to less than a 30% reduction in thickness, particularly in the early stages of the rolling process. These pass deformations are applied at progressively lower temperatures due to natural cooling of the hot stock material.

(iii) A temperature profile during plate rolling, which is also influenced by adiabatic heating from the deformation process itself and by conduction between stock and the cold roll surfaces.

Natural cooling of a slab in air would be expected to give a progressive decrease in cooling rate, due to the reduction in the temperature differential between the stock and its environment, but the thinning of the stock that occurs at each deformation pass, due to the reduced diffusion distance, accelerates the cooling, to give an overall cooling rate during deformation which may approximate linear cooling. After the deformation process, the plate may be cooled naturally, or may be subjected to accelerated cooling, e.g. by water jets or mist sprays, in order to depress the allotropic transformation temperature.

These aspects need to be considered in realistic models as shown in Chapter 6, where constitutive equations for the accompanying changes in the structure of the austenite were described, together with those for the allotropic change from austenite to ferrite.

Controlled rolling in plate materials that are to be used in the as-rolled condition may involve either the use of a lower soaking temperature so that each deformation is effected at a lower temperature, or the introduction of a delay period in the rolling schedule, so that the finishing sequence of passes (i.e. post delay period) is effected at lower temperatures. An adequate deformation must be applied in the finishing sequence to ensure a fine (or a heavily deformed) austenite grain structure.

From a physical metallurgy standpoint, the soaking temperature is important in controlling the initial austenite grain size, and also the extent of dissolution of microalloy carbo-nitrides. The controlled rolling of plates commonly involves the use of niobium with its attendant large effect on austenite recrystallisation. The solubility product of the niobium carbo-nitride is such that it is often completely dissolved at the soaking temperature, although unusually high niobium levels and nitrogen contents, coupled with low soaking temperatures (see Chapter 3) may result in incomplete dissolution. Strain inducement of the niobium carbo-nitride will undoubtedly occur during controlled rolling, resulting in a loss of interphase strengthening. This may be compensated by additional interphase precipitation strengthing using vanadium, if the high strength levels must be maintained.

Some indication of these effects are shown in Fig. 7.2 for a niobium steel, and Fig. 7.3 for a niobium-vanadium steel.[2] The niobium steel (0.1wt%C–0.6%Mn–0.08wt%Nb–0.4%Si) in the normalised condition showed an extension of the Hall–Petch relationship to finer ferrite grain sizes than are attainable in a plain carbon steel of the same chemical composition, indicating that the higher yield strengths are solely a result of the ferrite grain refinement caused by control of the austenite

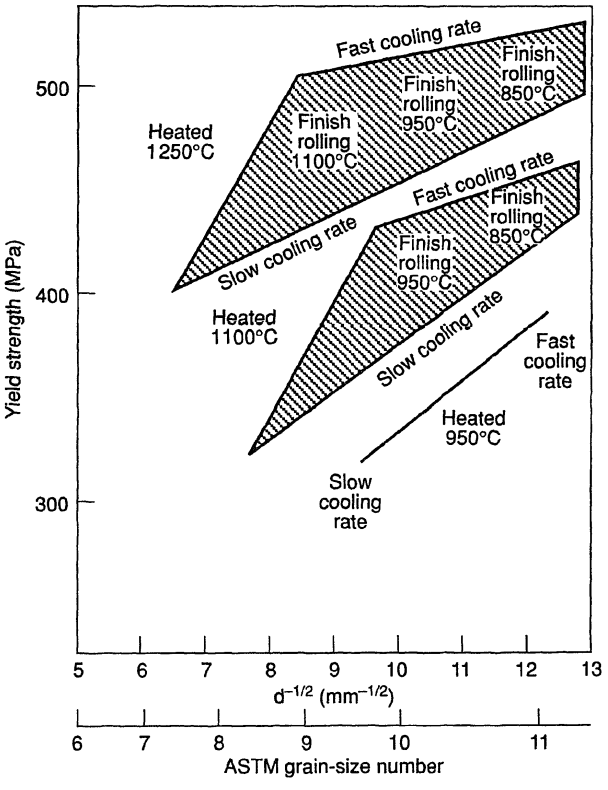


Fig. 7.2 The effects of thermomechanical process variables on the yield strength of a 0.1wt%C–0.4wt%Si–0.6wt%Mn–0.08wt%Nb steel. After Irvine *et al.*[2]

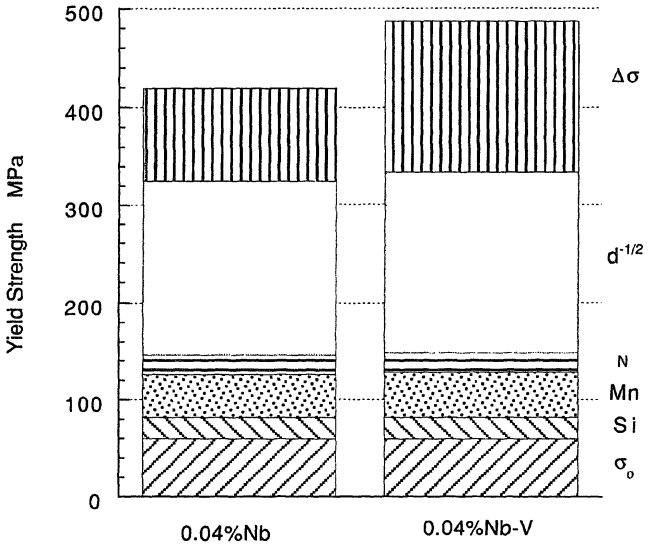


Fig. 7.3 Comparison of the yield strengths and strengthening conributions of hot-rolled 0.1wt%C–0.2wt%Si–1.4wt%Mn steel containing either 0.04wt%Nb or 0.04wt%Nb–0.07wt%V.

grain size at the normalising (950°C) temperature. Heating to progressively higher soaking temperatures increased the yield strength quite dramatically due to the dissolution of the carbo-nitride and this resulted in significant interphase precipitation strengthening for a given ferrite grain size. Both the ferrite grain size strengthening and the interphase strengthening were enhanced by increasing the cooling rate as would be expected from the reduction in transformation temperature that accompanies faster cooling rates. Decreasing the finish rolling temperature enhances the ferrite grain refinement, due to the finer austenite structures produced. However, due to strain inducement of the niobium carbo-nitrides in the austenite, the extent of interphase precipitation strengthening is reduced as the rolling temperature is decreased, giving rise to only slight changes in yield strength due to the balance between added grain refinement and reduced interphase precipitation strengthening. This effect can produce a consistency of strength in the product, despite fluctuations in the rolling conditions, but the impact properties may require serious consideration. The embrittlement vectors for precipitation strengthening and grain refinement are very different being $+0.3°C\ MPa^{-1}$ and $-0.7°C\ MPa^{-1}$ respectively (see Chapter 2). If the coarser (ferrite) grain size obtained by increasing the finishing temperature results in a loss of strength of the order of 50 MPa, and this is replaced by enhanced interphase precipitation strengthening, then the ductile/cleavage impact transition temperature would be raised by $(50 \times -0.7) = 35°C$ due to grain coarsening, and by a further $50 \times 0.3 = 15°C$ due to precipitation strengthening. Thus, despite a virtual

constancy of yield strength, variations in finishing temperature could result in a serious raising of the impact transition temperature by up to 50°C.

The contributions to the yield strength of a 0.1wt%C–1.4wt%Mn–0.2wt%Si–0.04wt%Nb–0.07wt%V–0.008wt%N steel are compared in Fig. 7.3 with those of a niobium steel having the same base composition, but without the vanadium, both being in the controlled rolled condition.[2] The steels were soaked at 1200°C and hot rolled with a finishing temperature of 900°C. The Nb–V steel has a significantly higher yield strength (of about 490 MPa) than that of the Nb steel (at about 420 MPa). Both had structures comprising some 92% of polygonal ferrite and 8% of pearlite. Early work on structure–property relationships have shown that the yield strength of these low carbon steels is virtually unaffected by small proportions of pearlite, and is governed by the state of the ferrite.[3] From Chapter 2, the Peierls stress, σ_o, and the solid solution strengthening contributions of silicon, manganese and nitrogen (see Tables 2.1 and 2.3) are shown in Fig. 7.3. In the case of nitrogen, it is unlikely that all of the nitrogen is in solid solution, due to the precipitation of the carbo-nitrides of niobium or niobium–vanadium. In the absence of any indication of the extent of carbo-nitride precipitation, either in the austenite due to strain inducement, or in the ferrite to produce interphase precipitation strengthening, it has been assumed that 50% of the nitrogen in the steel is precipitated in the form of microalloy carbo-nitride; complete solution or full precipitation would only change the nitrogen solid solution strengthening contribution by ±20 MPa from this assumed position. The grain size contribution to the yield strength, expressed in the Hall–Petch relationship, was obtained from the measured mean linear intercepts, and the appropriate k_y value (see Table 2.2). The grain size contribution was similar for both the niobium and niobium–vanadium steels.

Summing the Peierls's stress, solid solution strengthening, and grain size contributions would produce a yield strength of about 330 MPa. The differences between this level and the measured yield strengths of the two steels is a measure of the Ashby–Orowan dispersion strengthening contribution, $\Delta\sigma$, shown in Equations (2.59) and (2.60) and in graphical form in Fig. 2.18, and were 94 and 153 MPa for the niobium and niobium–vanadium steels respectively. In order to compare the observed dispersion strengthening with the Ashby–Orowan expression (based on volume fractions of fine particles and particle size), the approximate weight %Nb as fine particles needs to be converted to a volume fraction. This can be achieved using the relative atomic masses and lattice parameter measurements from Chapter 3.

For example, the relative atomic masses of vanadium and carbon are 51 and 12 respectively. The lattice parameter, a, given for VC[(4)] is 0.4152nm and there are 4 molecules of VC per unit cell in a f.c.c. structure. The density of vanadium carbide, ρ_{vc}, is therefore given by

$$\rho_{vc} = 4(51 + 12)/A(0.4152 \times 10^{-7})^3 (\mathrm{Mg\,m^{-3}}) \tag{7.1}$$

where A is Avogadro's number $= 6.023 \times 10^{23}$

$$\rho_{vc} = 5.85\,\mathrm{Mg\,m^{-3}} \tag{7.2}$$

When the proportion of second phase is small, the wt%VC can be converted to volume % by

$$\text{vol\%VC} = \text{wt\%VC} \times \rho_{Fe}/\rho_{vc} \tag{7.3}$$

and when the vanadium is present as vanadium carbide

$$\text{wt\%VC} = \text{wt\%V} \times (51 + 12)/51 \tag{7.4}$$

Given that the density of a α-iron is 7.9 MG m^{-3}, then from Equations (7.3) and (7.4)

$$\text{vol\%VC} = \text{wt\%V} \times (51 + 12)\rho_{Fe}/51\rho_{v} \tag{7.5}$$

or

$$\text{vol\%VC} = 1.664(\text{wt\%V}) \tag{7.6}$$

The volume fraction is obviously one hundredth of this. The lattice parameters, densities and multiplying factors for other microalloy carbides and nitrides are shown in Table 7.1. The densities of the nitrides are higher than those of the carbides, and the densities of both the carbides and nitrides increase as the relative atomic mass of the microalloy increases. One problem arising from the multi-stage precipitation processes (i.e. undissolved particles after soaking, strain-induced particles in the austenite and interphase precipitation) is that the composition of the carbo-nitrides cannot be predicted (they are a result of dynamics rather than equilibrium) and a more general approximation may have to be made for a particular carbo-nitride, as shown in Table 7.1. The situation becomes even worse when the microalloying elements are combined, and involves an even broader approximation, because the differences between the different microalloy carbo-nitrides are much larger than the differences between the carbide and nitride phases for each individual microalloy. Nevertheless, such approximations will not give rise to large errors as can be seen by reference to Fig. 2.18; the difference in multiplying factor for the most dense (NbN) and least dense (TiC) particles is less than a factor of two, and, due to the $f^{1/2}$ dependency in the Ashby–Orowan equation (2.59), the error in $f^{1/2}$ is less than a factor of 1.4 for a given particle size. Corresponding changes in particle size from 3 to 4 nm or from 10 to 14 nm would be required to balance the maximum error in the conversion factor. The use of an

Table 7.1 Conversion of the wt% microalloy metal to the volume % of microalloy carbide, nitride, or carbo-nitride (based on room temperature lattice parameters)

Compound	Lattice parameter '*a*', nm	Relative atomic mass	Density (Mg m^{-3})	Multiplying factor *m**	Multiplying factor *m*†
TiN	0.4233	Ti=48 N=14	5.43	1.87	1.93
TiC	0.4314	Ti=48 C=12	4.96	1.99	
VN	0.4118	V=51 N=14	6.18	1.63	1.64
VC	0.4152	V=51 C=12	5.85	1.66	
NbN	0.4387	Nb=93 N=14	8.42	1.08	1.10
NbC	0.4462	Nb=93 C=12	7.85	1.13	

* Vol% MX = *m*(wt%M) where M = Ti, V, or Nb, and X = C or N.
† Vol% M(C,N) ≈ *m*′(wt%M).

appropriate average for any given complex carbo-nitride would halve the above errors. Such errors have been considered here because of the information that would be required for a specific solution. This information would include a measurement of the lattice parameter of the (complex) carbo-nitride, and a knowledge of the chemical composition of the precipitated particles. Such complete information is rare, and, where available, has indicated that different carbo-nitride particles in a given steel may have different chemical compositions (and therefore different lattice parameters) The differences in chemical composition are commonly related to the stage at which the precipitation has taken place, e.g. titanium nitride formed in the liquid phase, nitrogen rich carbo-nitrides undissolved at elevated temperatures in the austenite range, and relatively carbon rich particles formed either at low temperatures in the austenite temperature range or during interphase precipitation. Such differences in chemical composition will also occur with respect to the metallic content of complex carbo-nitrides. It should be remembered that the Gibbs–Thomson equation for carbo-nitrides involves a change in the solubility product with particle size, and this in turn requires a change in the chemical composition of the carbo-nitride with particle size.

The errors in the expected volume fraction thus arise from two main sources:

(i) uncertainties concerning the extent of strain induced precipitation in the austenite during commercial hot rolling schedules;
(ii) uncertainties concerning the mass to volume concentration conversions.

It is assumed that due allowance will be made for incomplete dissolution of the carbo-nitride at the soaking temperature should this occur.

Despite these errors, the $\Delta\sigma$ values are depicted in Fig. 7.4 as column heights; the right-hand side of the column indicates full interphase precipitation of the dissolved Nb (C,N) or (Nb,V)(C,N) with multiplying factors $m' = 1.10$ and $m' = 1.46$ respectively, whilst the left-hand side of the column allows for an arbitrary 50% of strain-induced precipitation in the austenite which is assumed *not* to play any role in dispersion strengthening. The particle sizes that would be expected to give the observed $\Delta\sigma$ values are in the range of 3–6 nm and show agreement with sizes observed for interphase precipitated particles in continuously cooled niobium steels, or even in isothermally transformed vanadium steels when the transformation temperature is 750°C or lower (see Table 5.1).

Figure 7.4 suggests (rather than proves) that the observed values of the dispersion strengthening contribution are in accord with those expected from the volume fractions of interphase precipitation for the Nb and NbV steels according to the Ashby–Orowan predictions. The final values of the dispersion strengthening contributions, however, may well depend on the hot rolling schedules applied. For plates undergoing extensive deformation in the strain inducement temperature range, it is possible to obtain negligibly small values of $\Delta\sigma$. This effect may be offset to a certain degree by the attainment of finer austenite grain sizes, with a consequent refinement of the ferrite grain size, and an added grain size contribution to the yield strength in accord with the Hall–Petch relationship.

Further, the effects of plate thickness and steel composition can influence the transformation temperature, the effect of plate thickness being imposed through

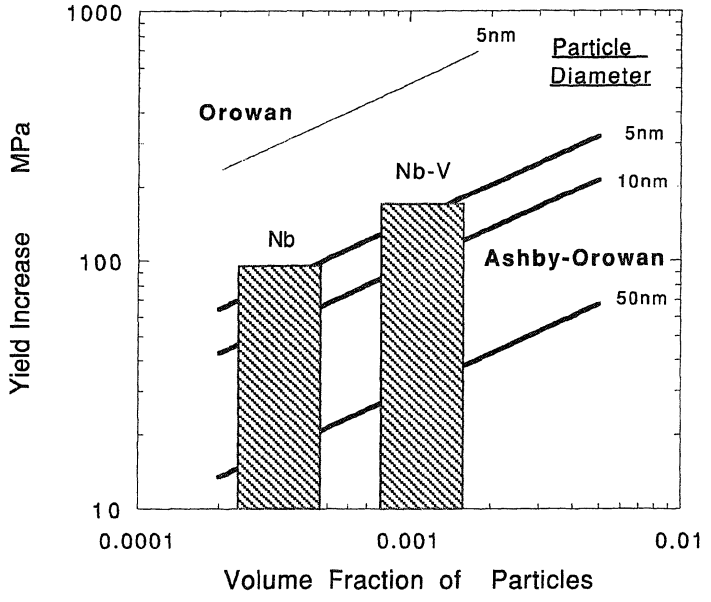


Fig. 7.4 Comparison of the experimentally observed $\Delta\sigma$ values with the dispersion strengthening predicted by the Ashby–Orowan relationship. The column width represents possible losses in interphase precipitation due to the strain induced precipitation of carbo-nitride in the hot rolling process.

the cooling rate operating during natural cooling. Thick plates, with their slow natural cooling rates, and 'lean' alloy compositions (low carbon, manganese, etc. contents), are conducive to high transformation temperatures (see Chapter 6) and this results in coarser ferrite grain sizes and coarser, more widely spread, interphase precipitated particles, both of which result in lower yield strengths. Thinner plates, with their faster natural cooling rates, and 'rich' alloy compositions, are conducive to low transformation temperatures, thus promoting finer ferrite grain sizes and finer interphase precipitated particles, provided that the alloy content does not cause ferrite inhibition with the consequent formation of bainite or martensite at the operative cooling rate.

An important development concerning the effects of cooling rate was the introduction of *accelerated cooling* practices. Thick plates can be made to cool more rapidly by the application of water sprays as mentioned previously. The effects of the increased cooling rate can provide a finer ferrite and a finer distribution of inter-phase precipitated carbo-nitrides in thicker plates. This process has natural limitations inasmuch as the acceleration of cooling in large sections inevitably leads to marked temperature differentials between the surface and centre of the plate. In the limit, the surface zones may be quenched to a bainitic (or martensitic) structure in order that the central zone should give an optimum fine structure. With some intermediate cooling regime, the surface zones may develop the optimum structure, whilst the central zone has coarser grains and precipitates.

These problems increase as the plate thickness increases. Nevertheless, the use of accelerated cooling extends the range of plate thicknesses that can achieve optimum microstructural refinement, and provides an alternative to increasing the alloy content in order to attain the same optimum transformation temperature. The application of accelerated cooling thus reduces the carbon or alloy content required to attain the required microstructure and hence the required properties, and this has an important effect in reducing the carbon equivalent and consequently improving the weldability.

The control of transformation temperature, as described above, is important to the development of properties. This concept is well illustrated in attaining the higher levels of strength in plate materials, where minor additions of copper, nickel, chromium and molybdenum are made to a microalloyed low carbon 1.5wt%Mn steel to offer yield strengths of up to 520 MPa in plates up to 20 mm thickness. Some indication of the effects of alloy composition[4] can be seen in Fig. 7.5. The combinations of strength and toughness (as measured by the 50% crystallinity impact transition temperature using Charpy-V notch specimens) that can be attained by the controlled rolling of experimental silicon-killed carbon-manganese and carbon-manganese niobium steels are illustrated. Increasing the controlled rolling deformation and decreasing the finish rolling temperature down to 750–800°C produces an improvement in grain refinement for each steel type

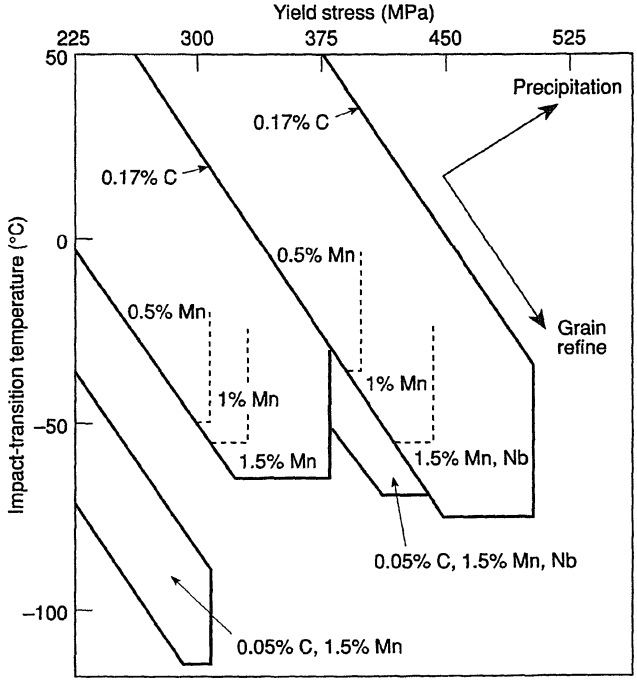


Fig. 7.5 Strength–toughness combinations obtained in carbon-manganese and and niobium microalloyed steels after controlled rolling. The resultants for grain refinement, dispersion strengthening, and composition changes are also shown. After Irvine *et al.*[4]

with a consequent change in the combination of strength and toughness according to the grain refinement vector (Chapter 2). For a given controlled rolling schedule and post rolling cooling rate, higher manganese levels result in a greater degree of refinement of the ferrite grain size, and thus increase the attainable strengths and toughness levels.

In addition to the manganese effect, Fig. 7.5 also shows the effects of carbon content and of niobium carbo-nitride interphase strengthening. An understanding of the property changes is best achieved by considering the direct and indirect effects of compositional changes. In the case of manganese, described above, there is a direct effect of manganese in imparting solid solution strengthening to the extent of 31MPa per 1wt%Mn, without any significant direct effect on the impact transition temperature. The indirect effect of manganese (as far as the present discussion is concerned we will neglect the possibility of bainite formation) is in refining the ferrite grain size for a given rolling schedule. There is no direct vector for the effect of manganese on grain size that would be valid for all rolling conditions and other combinations of steel chemistry, and so the indirect effect of manganese has been assessed from measured changes in the grain size, caused by adding manganese, i.e. $\Delta d_{Mn}^{-1/2}$. The change in grain size due to the manganese additions has effects on both the yield strength and the transition temperature according to the grain refinement vector, the extent of which is dictated by the magnitude of $\Delta d_{Mn}^{-1/2}$. The resultant effect of manganese is obtained from the sum of the solid solution effect and the grain refining effect. For example, in the 0.17wt%CNb steels, over the range 0.5–1.5wt%Mn, $\Delta d_{Mn}^{-1/2}$ is approximately $2\,mm^{-1/2}$ per 1wt%Mn. The changes in yield strength and the accompanying changes in transition temperature arising from the vectors for solid solution and grain refinement strengthening are shown in Table 7.2(a).

The resultant change on increasing the manganese content of the 0.17wt%Nb steels from 0.5–1.5wt%, is to increase the yield strength by 66 MPa and to decrease the transition temperature by some 23°C, as indicated by the results marked in Fig. 7.5. Similarly, a resultant can be obtained for the addition of niobium to 0.17%C–1.5% Mn steels in these controlled rolled steels. Adding niobium changes the ferrite grain size (mean linear intercept) from 5 μm in the carbon-manganese steel to 4 μm in the niobium steel. These correspond to $d^{-1/2}$ values of $14\,mm^{-1/2}$ and $16^{-1/2}$ respectively, i.e. $\Delta d_{Nb}^{-1/2}$ is again $2\,mm^{-1/2}$. The niobium also gives interphase strengthening, which can be obtained from the difference in yield strengths, ΔY, after allowance has been made for the grain size contributions. For example, the observed effect of adding niobium was to increase the yield strength by 93 MPa. The vector contributions and the resultant are shown in Table 7.2(b). This resultant is reflected in Fig. 7.5 where the general agreement with observed impact transition temperatures is clearly seen. The vectors given in Table 7.2(b) show that the beneficial grain refining effect of niobium more than offsets the adverse dispersion strengthening effect of niobium.

The effect of increasing the carbon content of the 1.5wt% Mn–Nb steels is of interest in that the direct effect of adding carbon is to increase the pearlite fraction of the microstructure, and, in accord with Equations (2.60) and (2.63), should produce a direct increase in the impact transition temperature with no direct

Table 7.2. Vectors and resultants for hot rolled plate steels showing the changes in yield strength and fracture appearance transition temperature arising from direct and indirect effects

(a) Increasing the manganese content of a 0.17%C – Nb steel from 0.5–1.5%

Factor	ΔY	Vector	ΔITT°C
ΔY (solid solution)	31 MPa	0	0
ΔY (grain refinement)	$2 \times 17.4 = 35$ MPa	−0.66	−23
Resultant	66 MPa	–	−23

(b) Adding 0.04% Nb to a 0.1%C – 1.5% Mn steel

Factor	ΔY	Vector	ΔITT°C
ΔY (grain refinement)	$2 \times 17.4 = 35$ MPa	−0.66	−23
ΔY (dispersion)	$(92 - 35 =)$ 57 MPa	+0.26	+15
Resultant	92 MPa	–	−8

(c) Increasing the carbon content from 0.05–0.15% in a 1.5% Mn–Nb steel

Factor	ΔY	Vector	ΔITT°C
ΔITT (pearlite)	–	–	$12 \times 2.2 = +26$
ΔY (grain refinement)	$(3 \times 17.4) = 52$ MPa	−0.66	−34
ΔY (dispersion)	$(62 - 52) = 10$ MPa	+0.26	+3
Resultant	62 MPa	–	−5

increase in strength. However, the indirect effects of carbon are important here. With a difference in yield strength of 62 MPa between the 0.05wt%C and 0.17wt%C steels, the direct and indirect effects of increasing the carbon are as shown in Table 7.2(c). It should be noted that the value of $\Delta d_c^{-1/2}$ was $3\,\text{mm}^{-1/2}$ and the change in pearlite content was $\Delta\text{Pe} = 12\%$ (i.e. from 8% pearlite in the 0.05%C steel to 20% pearlite in the 0.17%C steel). The resultant shows good agreement with the observed change in transition temperature, Fig. 7.5, and despite the adverse direct effect of carbon, the resultant effect is beneficial due to the dominance of the grain refining effect.

It should be pointed out that the resultants for changes in carbon content etc. are closely linked to the effects of these compositional changes on the microstructural variables, and these effects can vary considerably according to the circumstances under which such changes are made. A classical example of such variations can be seen from Fig. 7.5, where the effect of a niobium addition on the resultant is very different in the 0.05wt%C–1.5wt%Mn steels compared with that in the 0.17wt%C–1.5wt%Mn steels. In the low carbon steels the toughness is adversely affected, whereas in the higher carbon steels, the toughness is improved by the niobium addition.

There are obviously many other indirect effects that may have to be considered such as incomplete dissolution of the niobium carbo-nitride, the extent of strain inducement in the austenite, and the effects of rolling temperature and/or alloy content on the proportion of pearlite, but, within the scope of the work described in Fig. 7.5, these indirect effects appear to be of secondary importance.

The properties of commercially controlled-rolled 0.15wt%C–1.5wt%Mn–Nb steels are shown in Fig. 7.6. The yield strength and impact properties show generally good agreement with those obtained experimentally (Fig. 7.5). The effect of plate thickness on the attainable properties is very noticeable. With 13 mm thick plates, yield strengths of up to 460 MPa can be attained, coupled with an impact transition temperature (10 mm V-Notch Charpy impact test) below −50°C. With 38 mm thick plate, yield strengths of up to 390 Mpa were attained in conjunction with an impact transition temperature of −10°C. The change in strength and toughness properties with section size follow closely the grain refinement vector, and clearly indicate the difficulties associated with the controlled rolling of thick plates.

There are several reasons why thicker plates give rise to coarser ferrite grains.

(i) There is usually a smaller overall deformation in transforming slab to thick plate, compared with transforming the same slab to thin plate. This may limit the degree of austenite grain refinement that can be achieved.

(ii) In the absence of any reduction in slab soaking temperature or any hold period prior to the finishing stage of controlled rolling, the rolling will be completed at higher temperatures, thus permitting a larger austenite grain size to develop.

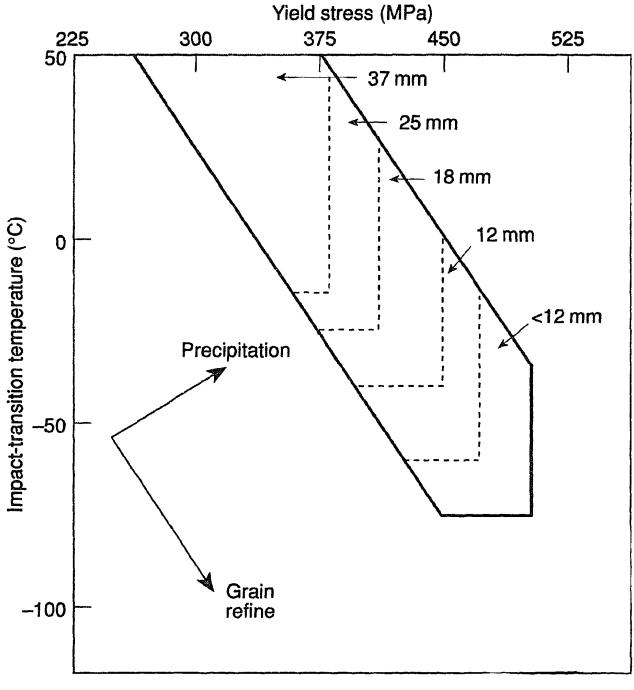


Fig. 7.6 Commercially controlled rolled C–Mn–Nb plate, showing the typical effect of plate thickness. After Irvine *et al.*[4]

(iii) Whilst the finishing temperature for thick plate could be reduced by the use of lower soaking temperatures, the amount of deformation per pass with thick plate may be severely limited by the mill load capacity. Also, lower soaking temperatures may result in incomplete dissolution of niobium carbo-nitride.

(iv) Interrupted rolling to allow cooling of the stock prior to the finishing passes gives rise to the same mill load capacity limitations as would be experienced by low soaking temperatures, because substantial deformation has to be applied after the interruption to avoid the persistence of mixed austenite grain sizes and the consequent development of mixed ferrite grain sizes.

(v) The slower cooling rate of thicker plates would undoubtedly contribute to a coarser ferrite grain size for a given austenite grain size. As indicated previously, accelerated cooling would be helpful in this respect and would provide a ferrite grain size more in keeping with the thinner plates. However, if the thicker plates have a coarser austenite structure, accelerated cooling to give the same overall cooling rate as that found for thin plates might result in suppression of the ferrite and the development of brittle acicular structures, due to the enhanced hardenability of steels with coarser austenite grain sizes.

There is little doubt that better property combinations will always be more readily attainable in thinner plates than in thicker plates as indicated by Fig. 7.6. This problem is addressed in the following section.

The use of aluminium in controlled rolled plate products offers little by way of improving the product properties, because aluminium nitride, at common aluminium levels, is substantially dissolved at slab soaking temperatures, and is extremely slow to precipitate in austenite.[5] Consequently the properties of controlled rolled aluminium treated steels are commonly similar to those of the same steel without aluminium. Aluminium has little effect on the recrystallisation of austenite as shown earlier. With higher aluminium contents and higher nitrogen levels (0.010–0.015wt%N) it is possible to retain some aluminium nitride at the elevated temperatures that are used for slab soaking, and thereby attain a certain restriction of austenite grain growth (the I–N process). This practice has, however, been superceded by the use of more stable particles, notably titanium nitride.

The use of titanium as a microalloying addition in controlled rolled plate products is generally restricted to its role as a grain refining additive. Although substantial additions of titanium are capable of giving high levels of interphase strengthening, and will also cause a retardation of the recrystallisation of austenite, the extreme stability of titanium nitride causes the formation of titanium nitride cuboids in the melt (see Chapter 3). The size of these cuboids is of the order of 2–10 μm. The presence of hard second phase particles of this size has deleterious effects on the impact toughness, and can raise the impact transition temperature by some 60–90°C. Stress intensification at these hard particles causes the particle to crack, and the stress intensification at the crack tip, in turn, causes the crack to propagate in the matrix. A more detailed account of carbide cracking and

consequent crack propagation is given by Smith[6] and Knott.[7] A similar effect has been observed for the large filamental cementite particles developed in slowly cooled low carbon steels (Fig. 7.7), where carbide particles cause an increase in the impact transition temperature that is dependent on carbide thickness. Carbides less than 1 μm thick appear to have little effect on the impact transition temperature. The impact transition temperature is rapidly raised as the carbide thickness is increased from 1 μm to 1.5 μm. With carbide thicknesses above 5 μm the impact transition temperature increases only slightly with increasing carbide thickness. The shift in impact transition temperature is substantial, being of the order of +60°C when 5 μm carbides are present. In the case of titanium treated steels, the beneficial effects of the removal of nitrogen from solution [see Equation (2.63)] by titanium is more than offset by the formation of gross titanium nitride cuboids in the melt, which would occur at all but the lowest titanium addition levels.

Vanadium additions are frequently made for the higher strength controlled rolled plate steels but usually in combination with niobium. Advantage is taken of the ability of niobium to inhibit recrystallisation of the austenite, in order to attain the required ferrite grain size, and the strength is then enhanced by augmentation of the volume fraction of interphase niobium/vanadium carbo-nitride precipita-

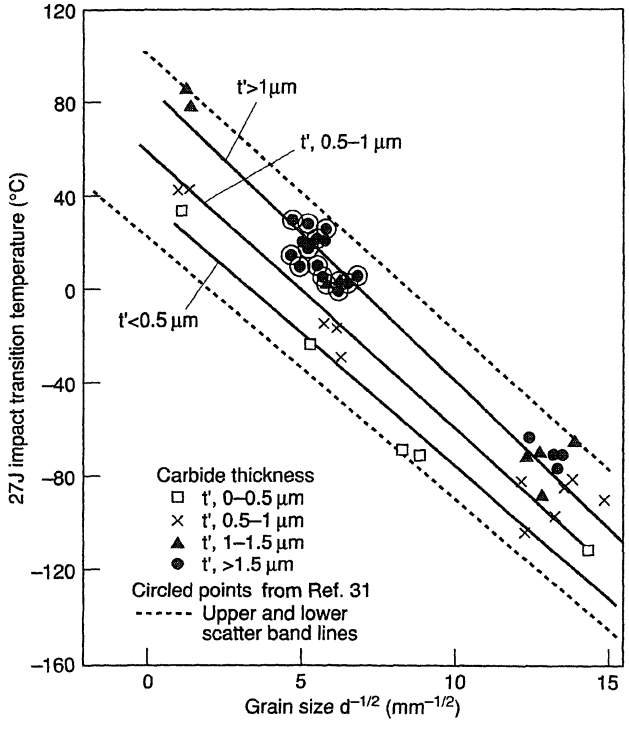


Fig. 7.7 The effect of filamental carbide thickness on the Charpy V-notch impact transition temperature (27J criterion). After Mintz *et al.*[105]

tion. The effect of vanadium on recrystallisation is weak, due to the relatively high mobility of the vanadium atom, which reduces the solute drag, and the high solubility of vanadium carbo-nitride (compared with niobium carbo-nitride), which restricts the temperature range over which strain induced precipitation can affect the recrystallisation process.

Pickering[8] has drawn attention to the differences in ranking of the microalloying elements in their solute drag effects and their strain-induced precipitation effects, as indicated by Cuddy[9] and Yamamoto *et al.*[10] The solute effect increases in the order Mn, Al, V, Nb and Ti, whereas the strain induced precipitation effect increases in the order V, Al, Ti and Nb. The generally small effects of aluminium and vanadium are generally agreed, whilst the effect of titanium as described above, is highly dependent upon the titanium and nitrogen levels. Niobium shows consistent and substantial effects in retarding the recrystallisation of austenite, as was shown in Fig. 6.15. A further important feature of this diagram is that the elevation of the recrystallisation stop temperature increases progressively with niobium contents up to at least 0.08wt%, indicating the usefulness of high niobium additions when very low temperature rolling needs to be avoided, e.g. in moderately thick plates.

7.3.2 Normalised Plate

The difficulties associated with the controlled rolling of thick plate, i.e. excessive mill loading when thick stock requires substantial deformation at low temperatures in the austenite range, or the excessive dwell times to achieve low finishing temperatures when the stock thickness is substantial, were described in the previous section.

An alternative approach to the development of high strength and toughness in thick plate is to use a simple normalising treatment. The thermal cycle, shown in Fig. 6.1, involves heating to a temperature some 30°C above the A_{c3} temperature and soaking at this temperature. This permits the development of a fully austenitic structure having a fine grain size that is characteristic of the normalising temperature and steel chemistry. Subsequent cooling from the normalising temperature is normally carried out in still air, but recent developments allow acceleration of the cooling rate by air turbulence or by mild water sprays. As in the case of hot-rolled plates, accelerated cooling gives a finer ferrite grain size for a given austenite grain size, an effect which could be attained more expensively by increasing the alloy content. Care must be taken to limit the cooling rate or alloy addition to avoid suppression of polygonal ferrite, with the consequent formation of bainite or martensite that would be detrimental to toughness.

In the normalising process, the ferrite grain refinement is directly related to the austenite grain refinement, which, at normalising temperatures, is attained by the use of finely precipitated nitrides or carbo-nitrides to inhibit austenite grain growth by the Zener drag effect. The normalising temperatures for low carbon steels are in the region of 860°C–930°C, and the solubilities of aluminium nitride and titanium or niobium carbo-nitrides are such that there will be little solution of such particles at these temperatures. Nitrogen enhancement in a vanadium steel

may also ensure that the nitrogen-rich vanadium carbo-nitride would also result in effective austenite grain refinement. Vanadium carbide, on the other hand, has a high level of solubility even at these low temperatures (see Chapter 3), and will not cause grain refinement. It is important to acknowledge that the grain refining additions merely inhibit the growth of austenite grains that are formed during the heating cycle of the normalising treatment, and do not directly influence the size of the grains that are formed on transformation. The austenite grain size is a result of the reaustenitisation reaction, when the new austenite grains nucleate at ferrite-carbide interfaces or on ferrite grain boundaries. In much the same way as the ferrite grain size is dependent upon the nucleation sites in austenite, and the cooling rate, so the austenite grain size is dependent on the nucleation sites in the ferrite-carbide aggregate and heating rate. The austenite grain size that is developed may be influenced by the prior ferrite-carbide structure, but is generally much larger than that which could be stabilised by fine nitride or carbo-nitride particles as described in Chapter 6.

The grain size in reaustenitised low carbon steel, subjected to commercial heating rates, is typically in the range 10–20 μm (mean linear intercept) or ASTM grain size No. 10–8, although in thick plates with coarse initial structures and slow heating rates they can be coarser.

The level of microalloy addition required to guarantee the inhibition of austenite grain growth is dependent upon the austenite grain size, the particle size of the carbo-nitrides and the coarsening rate of these particles in relation to the time at the austenitising temperature. The relationship between the austenite grain size, R_0, the volume fraction of particles, f, and the particle size, r, for the onset of grain growth can be expressed, from Equation (4.73) as

$$f = r(1 - 4/3Z)/R_0 \tag{7.7}$$

The addition of grain refining particles of microalloy carbo-nitrides or of aluminium nitride restricts austenite grain growth, according to the *undissolved* fraction of particles, f. Assume that the austenite grain size is equivalent to ASTM 8, i.e. having a mean linear intercept of 20 μm (Table 4.3), an equivalent diameter of $20 \times 1.61 = 32\,\mu$m (Table 4.5), or an equivalent radius of 16 μm. This gives a reasonable estimate of $R_0 = 16\,\mu$m. With a heterogeneity value of $Z = 2$ and a particle size of $r = 16$ nm (see Fig. 6.4), then the volume fraction of particles required to inhibit grain growth for a period of 1 h is given, from Equation (7.7), as

$$\begin{aligned} f &= 0.016(1 - 4/6)/16 \\ &= 0.00033 \text{ (i.e. 0.033 vol\%)} \end{aligned} \tag{7.8}$$

The weight percentage of the microalloying element or aluminium that needs to be present as the carbo-nitride or nitride to give this volume fraction can be obtained from the conversion factors in Table 7.1. For example, if aluminium nitride particles are used the wt%Al that needs to be present as nitride is $0.033/3.65 = 0.009$wt%Al. The total aluminium required in the steel must include the aluminium in solution in the austenite that is in equilibrium with the aluminium nitride, and this would obviously be dependent upon the nitrogen content, since,

from Equation (3.5), the solubility product, k_s, evaluated at 900°C from Table 3.1, is given by

$$k_s = [Al][N] = 1.8 \times 10^{-5} \tag{7.9}$$

where $[Al]$ is the dissolved aluminium content (wt%) and $[N]$ is the dissolved nitrogen content (wt%).

The solubility of aluminium nitride at 900°C is shown in Fig. 7.8, together with the locus of aluminium and nitrogen contents that correspond with both the required volume fraction of aluminium nitride, from Equation (7.8), and the solubility from Equation (7.9). The method of displacement of the 'fixed volume fraction' relationship from the solubility curve is also shown. The equation for the 'fixed volume fraction' line is given in this case by

$$(Al_T - 0.009)(N_T - 0.009 \times 14/27) = k_s \tag{7.10}$$

where Al_T is the total aluminium content of the steel (wt%) and N_T is the total nitrogen content of the steel.

(N.b. It is assumed here that all the aluminium and all the nitrogen will be present either in solution or as aluminium nitride; if, for example, some aluminium is present as alumina or some other stable oxide, then this must be discounted from the total aluminium. Usually, the alumina content in the steel is very low due to alumina flotation after deoxidation but before solidification, and may be neglected. In some circumstances, however, it may prove necessary to make this correction.)

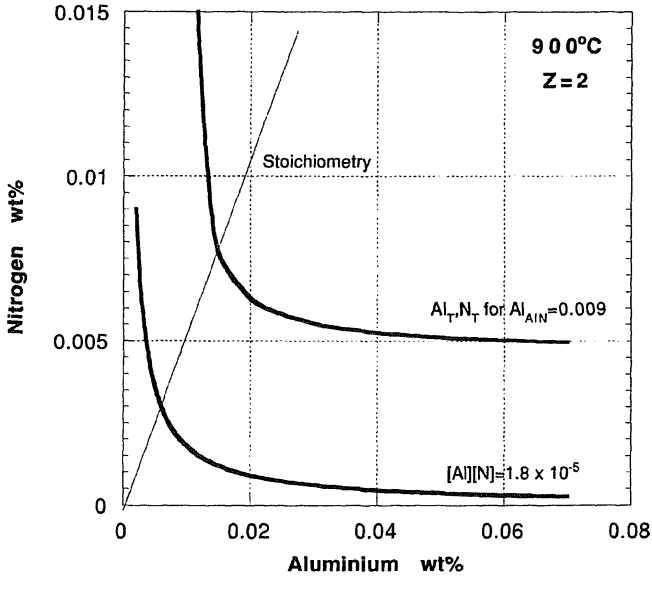


Fig. 7.8 The aluminium and nitrogen contents of steels that will produce sufficient aluminium nitride at 900°C to inhibit grain growth in austenite with a grain size of ASTM 8.

The range of aluminium and nitrogen contents that will give the necessary aluminium nitride for the conditions specified can be obtained from Fig. 7.8. For an electric arc steel, with a typical nitrogen content of 0.008wt%N, the aluminium content (excluding that present as alumina) would be, from Equation (7.10),

$$Al_T = (1.8 \times 10^{-5}/(0.008 - 0.009 \times 14/27) + 0.009$$
$$= 0.0144\text{wt\%}$$

With lower nitrogen contents, e.g. 0.005wt%, which is not untypical of B.O.S. manufacture, the aluminium required would be 0.063wt%. This emphasises the importance of the nitrogen level, and with 0.004wt%N, or less, as can be obtained in many secondary steelmaking processes, it would be impossible to produce the necessary aluminium nitride level. The remedy for this problem is either to make a deliberate nitrogen addition, or to use a carbide forming microalloy, e.g. NbC.

Commercially, it is common to make a somewhat higher aluminium addition due to variations in aluminium recovery during the steelmaking operation. The aluminium loss is related to the oxygen level at the time that the aluminium is added. Aluminium levels in the range 0.02 to 0.03wt% are commonly used (provided that there is a sufficiency of nitrogen). Care must be taken to avoid excessive aluminium additions due to the formation of large aluminium nitride particles at the slab soaking temperature if the aluminium and nitrogen levels exceed that permitted by the solubility product at the soaking temperature, as discussed in Chapter 6.

The effect of aluminium in solution on the particle coarsening rates does not appear to have been studied systematically. According to the Wagner equation, some effect of aluminium in solution would be expected, but the aluminium contents in commercial steels are commonly in excess of that required for the stoichiometric combination with nitrogen to form aluminium nitride. Also the rate of change of particle radius, depending as it does on the cube root of the aluminium in solution, should not suffer a very marked change with variations in the solute content over the range that is commonly used in commercial steels.

In the case of vanadium steels, the same procedure can be followed to establish the vanadium (and nitrogen) contents that are required to give the grain refining capability specified by Equations (7.7) and (7.8), i.e. a grain size of ASTM 8 after up to 1 h at the normalising temperature of 900°C (assuming $Z = 2$), and requiring a volume fraction of particles ($r = 16$ nm) of 0.00033. The conversion factor for wt%V to vol% VN is substantially lower than that for aluminium to aluminium nitride, thus requiring a larger vanadium addition. Also, the solubility of vanadium nitride is an order of magnitude higher than that of aluminium nitride which means that, for a given nitrogen content, the dissolved vanadium requirement (wt%) will be about ten times that of the aluminium. With a conversion factor of 1.63 for wt%V to the volume fraction of vanadium nitride particles, the vanadium required to give 0.033 vol%VN is 0.033/1.63, i.e. 0.02wt%V. The solubility product for vanadium nitride in austenite at 900°C (Table 3.17) is given as

$$k_s = [V][N] = 1.6 \times 10^{-4} \tag{7.11}$$

The required vanadium and nitrogen contents are then given by

$$(V_T - 0.02)(N_T - 0.02 \times 14/51) = 1.6 \times 10^{-4} \quad (7.12)$$

For a total nitrogen content of 0.008wt%N the total vanadium content that would give 0.033vol%VN, derived from Equation (7.12), is 0.084wt%V. Increasing the nitrogen content to 0.015wt% by a deliberate nitrogen addition would reduce the required total vanadium content to 0.04wt%. These vanadium levels are obviously much higher than those given for aluminium, reflecting the factors described above.

Strictly speaking, the solubility calculation should be carried out for vanadium carbo-nitride rather than vanadium nitride, as described in Chapter 3, but in view of the high solubility of vanadium carbide and the consequent small fraction of carbon in the carbo-nitride, the assumption of vanadium nitride is sufficiently reasonable to show the principles involved.

The higher solubility of vanadium nitride compared with aluminium nitride in austenite allows a further development of strength. For example, in the steel with 0.008wt%N, the vanadium addition required to maintain the fine austenite grain size was 0.084wt%V, of which 0.02wt%V was present as growth inhibiting particles, and 0.064wt%V was in solution in the austenite. Under these conditions, air cooling from the normalising temperature will encourage interphase precipitation of vanadium carbo-nitride during the austenite–ferrite transformation, thus contributing dispersion strengthening in addition to ferrite grain refinement. Further, the increased solubility of vanadium carbo-nitride at elevated temperatures, e.g. the soaking temperature, means that substantially more vanadium can be added without the problem of having large undissolved particles at the soaking temperature prior to hot rolling, thus enabling not only more fine carbo-nitride to be produced at the normalising temperature, but significantly more interphase precipitated carbo-nitrides during air cooling from the normalising temperature. Commercial steels with 0.10–0.15wt%V are manufactured with the express aim of developing high levels of interphase precipitation strengthening. In addition to the large vanadium additions, steels with aluminium for grain refinement and vanadium for interphase strengthening have been developed, and are produced commercially with the direct objective of attaining yield strength levels of 460MPa in thicker plates in the normalised conditions.

The yield strength build-up of a normalised high strength C–Mn–Al–V plate steel is shown in Fig. 7.9 and closely resembles that of the hot-rolled Nb–V steel shown in Fig. 7.3. A feature of normalised steels containing a hyperstoichiometric aluminium content is the marked improvement that can be attained in impact transition temperature. This has been attributed to the reduced 'free' nitrogen content[2] arising from the low solubility of aluminium nitride at the normalising temperature, and can lower the impact transition temperature of a steel (other factors being equal) by as much as 50°C.

The importance of manganese content in controlling the transformation temperature, and therefore the ferrite grain refinement and dispersion strength-

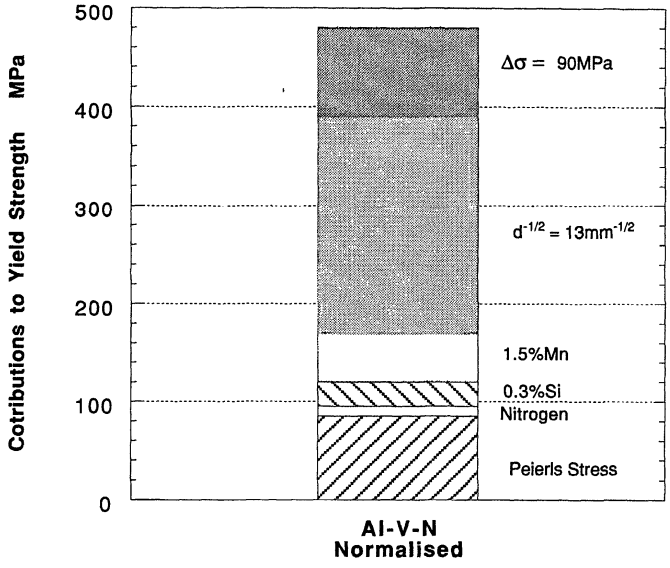


Fig. 7.9 Yield strength build up of a normalised C–Mn–Al–V steel plate.

ening effects, is illustrated in Fig. 7.10. Increasing the manganese content from 0.5–1.5% would be expected to increase the yield strength directly (as a solid solution effect) by some 32 MPa. The actual increase is about 120 MPa arising from the indirect effects of manganese in reducing the ferrite grain size and enhancing the interphase precipitation strengthening contributions. In round terms, the changes in strength resulting from the increase in manganese content from 0.5–1.5wt% are 30 Mpa from extra solid solution strengthening, 60 Mpa from extra ferrite grain refinement and 20 Mpa from extra interphase precipitation strengthening.

A further interesting feature of vanadium strengthening concerns the relative efficiencies of vanadium carbide and vanadium nitride in their contribution to inter-phase precipitation strengthening. It should not be inferred that the similar dispersions of vanadium carbide and vanadium nitride would give different strengthening effects, but rather that the characteristics of the dispersion, i.e. the particle size and volume fraction of interphase precipitate, will be different in an Fe–V–C (low nitrogen) alloy compared with that developed in an Fe–V–N alloy (with or without carbon). Balliger and Honeycombe[12] have shown that the inter-sheet spacing of the interphase precipitate in Fe–V–C alloys was slightly larger that that in Fe–V–N alloys for a given (isothermal) transformation temperature (Fig. 7.11), and that vanadium carbide particles suffer more rapid coarsening (Ostwald ripening) than do vanadium nitride particles when aged at an elevated temperature in the ferrite range (Fig. 7.12). These observations may reflect the differing solubilities of the carbide and nitride phases in ferrite. Vanadium carbide shows appreciable solubility in ferrite at elevated temperatures, which may reduce the driving force for precipitation and enhance the Ostwald ripening process, when compared with vanadium nitride. Unfortunately, there are no data for the

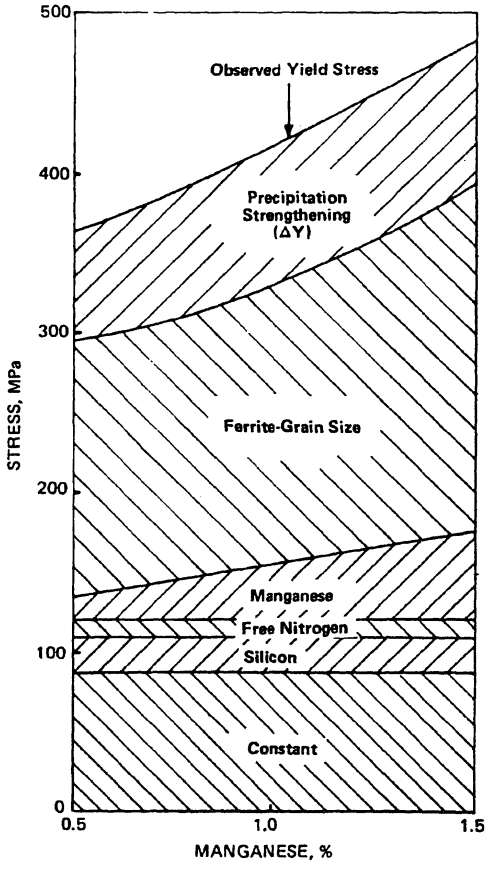


Fig. 7.10 The effect of increasing the manganese content of a C–Mn–V steel on the contributions to the yield strength. Note the larger contributions from grain size and dispersion strengthening as well as the extra solid solution strengthening.

solubility of vanadium nitride in ferrite, and one can only infer that it will be less soluble than vanadium carbide from the observed solubilities in austenite.

The implications of these differences between the carbide and nitride phases are that low nitrogen steels will tend to give a smaller precipitation strengthening effect than that of a high nitrogen steel for a given vanadium content and cooling rate, as indicated in Fig. 7.13, for a 0.09wt%V steel. The dispersion strengthening contribution to the yield strength varies from 100–150 MPa in the low nitrogen steel depending on the cooling rate, whilst, over the same range of cooling rates, the dispersion strengthening varies from 180–260 MPa. The volume fraction of vanadium carbo-nitride in a 0.09wt%V steel would be 0.09×1.64 (see Table 7.1) $= 0.0015$, assuming that full precipitation had occurred. From Equation (2.59), the particle sizes that would correspond with the magnitude of the observed dispersion strengthening is in the range 10–6 nm for the low nitrogen steel, and 5–

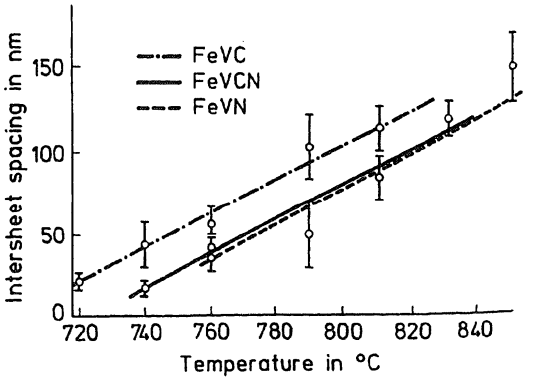


Fig. 7.11 Inter-sheet spacings in isothermally transformed Fe–V–C and Fe–C–N alloys. After Balliger and Honeycombe.[12]

2 nm for the high nitrogen steel. This difference in particle sizes might be reduced if precipitation was less than complete in the low nitrogen steel; this would reduce the particle size somewhat, but bearing in mind the root dependency of the precipitation strengthening on the volume fraction, the reduction in particle size would not be proportional to the reduction in volume fraction.

The difference in the behaviour of low nitrogen and high nitrogen vanadium steels is well documented, and the results shown in Fig. 7.13 are fairly typical of this phenomenon. However, in normalised steels, enhanced nitrogen contents in steels with any substantial vanadium addition would merely serve to increase the undissolved vanadium nitride at the austenitising temperature, thereby conferring increased grain coarsening resistance, but would not enhance the precipitation

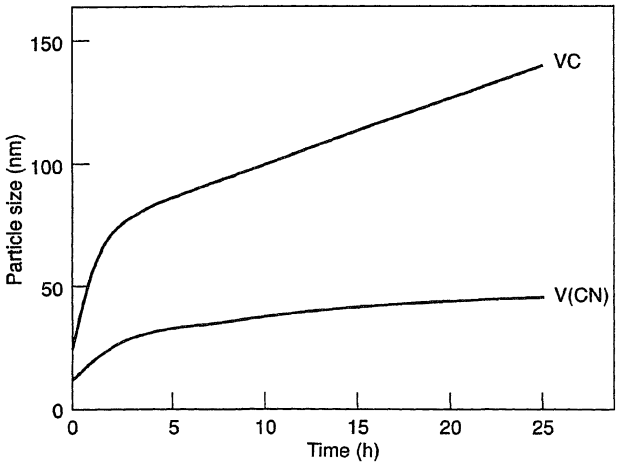


Fig. 7.12 The effects of sub-critical annealing on particle coarsening in Fe–V–C and Fe–V–N alloys. After Balliger and Honeycombe.[12]

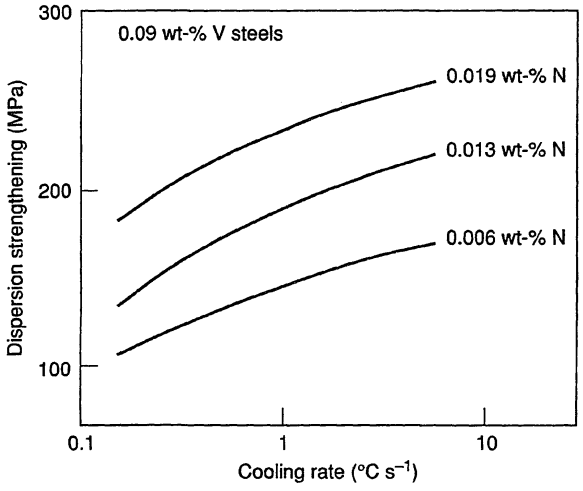


Fig. 7.13 The effect of nitrogen content on the interphase precipitation contribution to the yield strength of continuous cooled 0.09wt%V steels. After Pickering.[8]

strengthening contribution, which would be more characteristic of vanadium carbide precipitation. This is particularly true of the aluminium–vanadium steels where aluminium nitride formation at the normalising temperature results in a low nitrogen vanadium carbo-nitride interphase precipitate. Typical precipitation contributions in normalised vanadium and vanadium–aluminium steels are of the order of 100–150 MPa. The precipitation strengthening contribution from what is substantially a vanadium carbide in normalised steels is, however, still subject to variation in cooling rate and alloying element content (manganese, etc.) through their effects on the austenite–ferrite transformation temperature, and offers useful strength increases in these normalised steels, as indicated in Fig. 7.9.

A general overview of the strength and toughness (as represented by the impact transition temperature) of normalised carbon-manganese and microalloyed steels is portrayed in Fig. 7.14. The addition of niobium to carbon-manganese steels causes grain growth inhibition at the normalising temperature, with a consequent refinement of the ferrite grain size after continuous cooling transformation. The solubility of niobium carbo-nitride is insufficient to give any significant precipitation strengthening in the normalised condition. However, the grain refining action enables higher strengths and lower transition temperatures to be attained. Additions of aluminium and nitrogen also allow this same effect to be obtained, but, additionally, the low solubility of aluminium nitride confers improved impact toughness, as indicated by Equation (2.63), at a given strength level. The addition of vanadium allows dispersion strengthening in the normalised condition, together with grain refinement, thus allowing higher strengths to be attained. The C–Mn–Al–V–N steels give even better combinations of strength and toughness, due to the combinations of dispersion strengthening, grain refinement and low 'free' nitrogen contents.

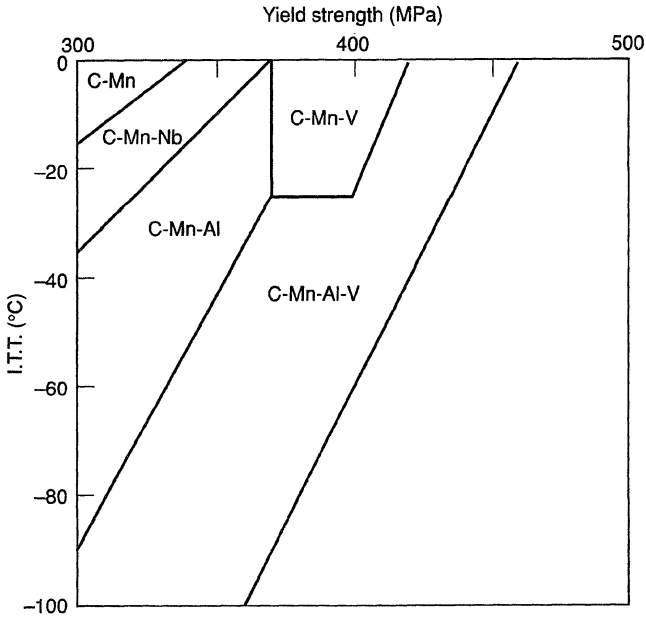


Fig. 7.14 Yield strength and toughness combinations in carbon-manganese and microalloyed steels in the normalised condition.

7.3.3 Acicular Structures and Sub-grain Structures

The development of large diameter gas transmission pipelines, particularly in North America and Russia in the 1970s, provided a number of challanges to the steel manufacturer. The increased pipe diameter requires a thicker walled pipe to contain a given pressure, or requires a higher strength steel. A major disadvantage of a thicker walled pipe is the increased fabrication cost associated with handling and welding thicker plates, and, consequently, considerable attention was given to the development of higher strength steels. For many of the lower strength specifications, usually based on the American Petroleum Institute Specification API-5L (1988), microalloyed steels could be used. The X65 Grade, i.e. having a minimum yield strength of 65 000 pounds per square inch (450 MPa), was commonly manufactured as a carbon–manganese steel with microalloy additions. The specification allows the use of niobium, vanadium, or titanium, and the steel could be supplied in the as-rolled or normalised condition.

Strength levels that would meet the X70 Grade (480 MPa) can still be attained with a microalloyed steel, provided that the control of transformation temperature is optimised by appropriate additions of manganese, nickel and chromium (nickel and chromium levels are commonly restricted to the higher residual levels in order to contain the steelmaking costs). However, there are alternative methods of attaining and exceeding this higher strength level.

Two principal methods of extending the strength range whilst maintaining low costs and good weldability are

(i) Controlled rolling to include Stage 3 deformation, i.e. continue the rolling operation after ferrite transformation has started. This procedure causes deformation of the ferrite and results in dislocation arrays in the ferrite, i.e. sub-grains with an attendant increase in strength. Texture development can also occur if extensive deformation takes place at such low temperatures.

(ii) Alloying with an element such as molybdenum to suppress the formation of polygonal ferrite and promote the development of an acicular structure of either bainite or a mixed acicular/polygonal ferrite. The unit cell size of the acicular structure (the plate width) is commonly of the order of 1 μm.

(a) Deformation Induced Sub-Structures

Steels subjected to third stage deformation, i.e. in the temperature range below about 700°C, have a microstructure consisting of mixtures of recrystallised ferrite undeformed ferrite, and deformed ferrite grains, the proportions of each depending upon the extent of deformations, the deformation temperature and the composition of the steel. In steels given a substantial deformation at temperatures of 600–650°C, all ferrite grains may contain substructure, usually in the form of well recovered dislocation cell structures or sub-grains, each sub-grain being separated by a low angle sub-grain boundary. The sub-grain structure causes a significant increase in the yield strength,[14,15] as shown in Fig. 7.15.

Rolling schedules that are completed in the second stage region produce properties that are commensurate with the solid solution, ferrite grain size and dispersion strengthening contributions. Rolling schedules that are completed in the third stage region show a further increase in yield strength due to the

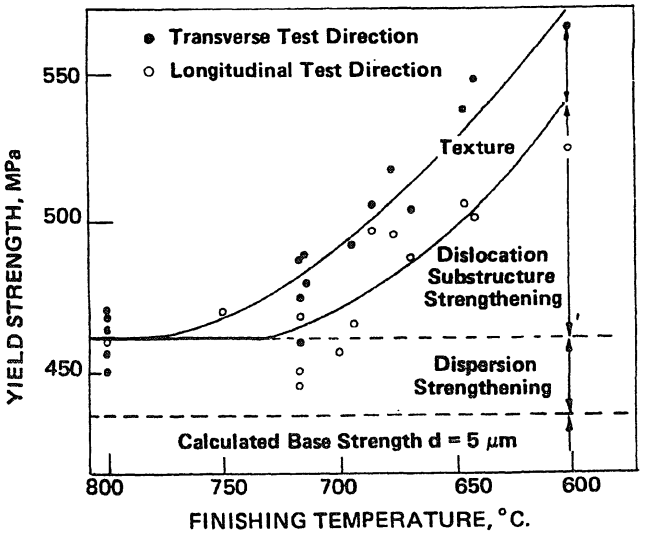


Fig. 7.15 Extensive rolling following the commencement of the austenite to ferrite transformation results in marked increases in strength due to sub-grain formation. After Bramfitt and Marder.[15]

substructural (dislocation) strengthening. The quantitative assessment of the sub-grain strengthening is complex. The various strengthening mechanisms discussed previously have been considered as additive in nature, which is not unreasonable, considering the different mechanisms involved. Solid solution strengthening produces a drag effect on dislocations, precipitation (or dispersion) strengthening causes dislocations to bulge between obstacles – to an extent dictated by either looping or cross slip, whilst grain refinement provides an obstacle for which dislocations need to be generated in adjacent grains by stress intensification. A well defined sub-grain structure undoubtedly provides additional strength, but there is considerable doubt as to whether this contribution is additive. Interpretations of yield strength, σ_y, based on the additivity of sub-grain strengthening, in the form

$$\sigma_y = K + k_d d_s^{-1/2} \tag{7.13}$$

where K is the yield strength of the structure without sub-grain boundaries and d_s is the sub-grain size (mli), have shown that the magnitude of k_d, the sub-grain strengthening coefficient, is much lower than that of k_y, the grain size strengthening coefficient in the Hall–Petch equation. Kosik *et al.*[16] have considered the sub-structure effect as a cold working effect, and, following Langford and Cohen[17] have incorporated the cell size as

$$\sigma_y = K + k_d' d_s^{-1} \tag{7.14}$$

A relatively simple treatment, however, has been recommended,[18] in which the effective grain size, d_E, of the sub-structured ferrite is defined by

$$d_E^{-1} = d^{-1} + d_s^{-1} \tag{7.15}$$

where d^{-1} is the number of high angle boundaries per unit length, d_s^{-1} is the number of low angle boundaries per unit length and d_E^{-1} is the total number of boundaries per unit length.

The effective grain size, d_E, determined in this way, is then substituted directly into the Hall–Petch equation instead of the high angle boundary grain size, d. The normal Hall–Petch equation with the usual value of k_y (See Chapter 2) will then give an adequate prediction of the yield strength in well recovered sub-structures. Bramfitt and Marder[15] also considered structures with mixtures of normal and sub-structured ferrite, and assigned the contributions from each according to their respective volume fractions, so that a structure with 50% of sub-structured grains would have a yield strength half way between those of structures without sub-structured ferrite and those with a fully sub-structured ferrite.

Although the substitution of d_E for d (both being mean linear intercepts) in the Hall–Petch equation gives reasonable predictions of the yield strength, the effect of sub-structure on the impact properties is less straightforward. The low angle boundary does not constitute an obstacle to the propagation of a cleavage crack. The misorientation of the ferrite lattice across the boundary is at most a few degrees, and the cleavage fracture appears to propagate across such boundaries with ease. The beneficial effect of grain refinement on the impact transition

temperature is not reflected in the effect of sub-grain boundaries. It has been shown that the strengthening effect of sub-structures is accompanied by a raising of the impact transition temperature. The effects of grain size and sub-grain size on the impact transition temperature appear to reflect the depression of the impact transition temperature to an extent that is dependent on the product of the grain size strengthening and the grain refinement vector, and a raising of the transition temperature that is dependent on the product of the extra strengthening from the sub-structure and an embrittlement type vector, the latter having a value of approximately +0.26°C per MPa and is very similar to that for dispersion strengthening. Thus the impact transition temperature would be obtained from two terms, i.e.

(i) Grain size contribution $-0.66\ k_y d^{-1/2}$.
(ii) Sub-structure effect $+0.26\ (k_y d_E^{-1/2} - k_y d^{-1/2})$.

In this way, the solid solution and grain refinement contributions to the yield strength can be assigned their conventional vectors for impact transition temperature prediction, but any further increase in strength, whether from precipitation or sub-grain structure, can be assigned the +0.26°C MPa^{-1} vector.

Such predictions of the impact transition temperature, however, may be wildly in error, due to the appearance of a quite different phenomenon – that of separations. A disadvantage of the third stage deformation structure is the development of laminar separations during impact testing. The common geometry for impact testing of samples from plates is that the Charpy notch represents a notch in the plate edge, normal to the rolling plane. The triaxial stresses developed at the notch root may allow the propagation of a substantially ductile fracture, but laminar (cleavage) separations occur in the rolling plane. The development of these laminar (cleavage) separations, during the deformation and fracture of the Charpy specimen gives rise to effects that are similar to those described by Embury *et al.*[13] for mild steel laminates arranged in the crack divider mode (Fig. 7.16). The impact transition temperature is lowered due to the relaxation of the triaxiality, but the energy absorption when the ductile face of the Charpy fracture shows laminar separations is also dramatically reduced. Tanaka *et al.*[14] showed the severe reduction in the ductile shelf energy that accompanies the development of laminar separations, and further demonstrated that the impact transition temperature and the ductile shelf energy decreased as the number of laminar separations increased (Fig. 7.17). This phenomenon is important in the case of steels for linepipe applications, where a high energy absorption is needed to cause crack arrest should a (longitudinal) ductile crack be initiated from some defect.

(b) Bainite Structures

Early forays into the development of high strength steels, prior to the introduction of microalloy additions, had been directed towards 'low' carbon bainitic structures.[19,20] 'Low' carbon contents at that time were associated with levels of 0.12–0.15wt%C. Although useful increases in strength could easily be attained, with yield (0.2% proof) strengths in the range 350–750 MPa, the impact transition temperatures were generally near ambient or above. In order to attain the bainitic

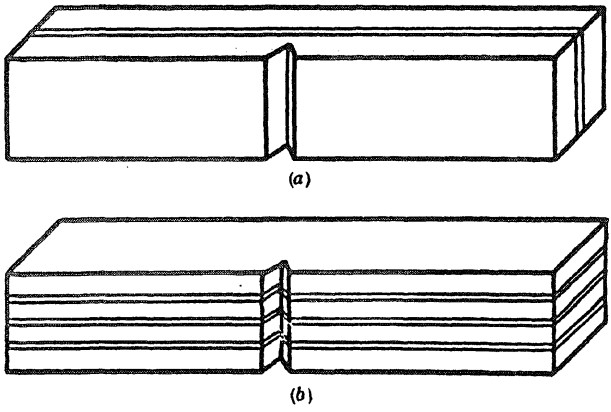


Fig. 7.16 A mild steel laminate with lamina arranged in the crack arrester (a) and crack divider (b) mode. Delamination relaxes the triaxiality of the stress system at the notch root. After Embury *et al.*[13]

structures during air cooling treatments, these steels contained molybdenum, and advantage was taken of the marked effect of boron in suppressing the transformation of austenite to polygonal ferrite.

The bainitic microstructure is developed by the sympathetic nucleation of laths or plates of bainite within each austenite grain, and forms by a diffusion controlled shear process. The sympathetic nucleation process leads to the formation of 'packets' of laths, each lath being separated, within the packet, by a low angle boundary.[21] Several such packets may be formed within an austenite grain, depending upon the active variant of the orientation relationship between the austenite and the bainitic ferrite, thereby providing a high angle boundary between the packets of bainitic ferrite. The basic structure of bainite thus consists of high angle boundaries between packets of bainitic laths, and low angle boundaries between the laths in each bainitic packet.

As in the case of stage 3 controlled rolled structures, the intercept length between any boundary is important for the yield strength, whist the intercept length between high angle boundaries is important for the impact transition temperature. The lath thicknesses are generally of the order of 0.5–2.0 μm. which causes significant strengthening when considered in the context of the Hall–Petch equation. The lath packet sizes tend to be somewhat smaller than the prior austenite grain size, but, in general, are directly proportional to the austenite grain size.

The strength of bainite is also augmented by other factors, which include the solid solution strengthening effects of elements such as manganese, silicon and molybdenum, but is particularly sensitive to the temperature at which the austenite–bainite transformation occurs. At the higher transformation temperatures, upper bainite appears with iron carbide being formed (due to the carbon enrichment) between successive upper bainite plates. There is some uncertainty

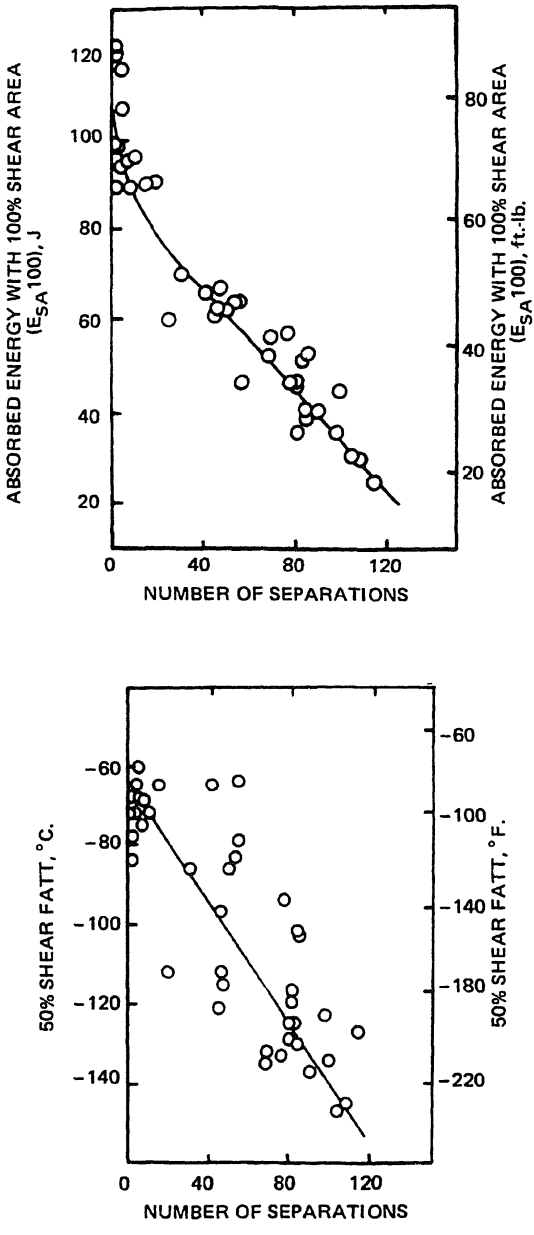


Fig. 7.17 The effect of laminar separations in the notch root of the Charpy impact test specimen (a) on the energy absorption to fracture and (b) on the impact transition temperature. After Tanaka *et al.*[14]

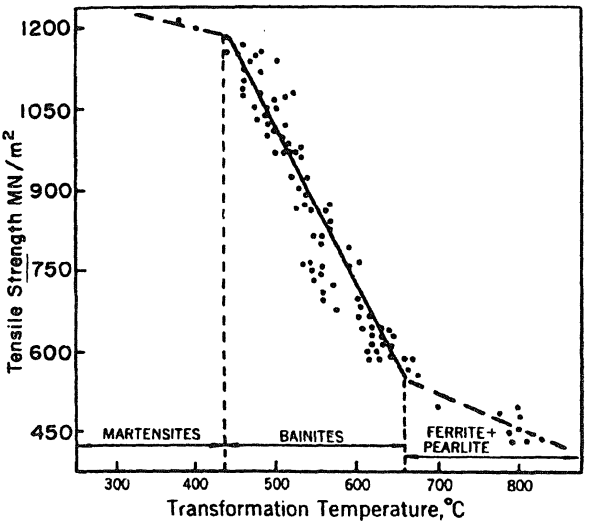


Fig. 7.18 The effects of transformation temperature on the yield and tensile strengths of 0.5wt%Mo–B low carbon bainitic steels. After Irvine and Pickering.[20]

concerning their contribution to the yield strength, as they are exclusively associated with the sub-grain boundaries (the interlath boundaries). At the lower transformation temperatures, lower bainite appears. The supersaturation of the first bainite formed is considerably higher than that of upper bainitic plates, and cementite is precipitated within the bainitic plates. The intra-lath carbides would be expected to contribute significantly to the yield strength particularly as they are much smaller than the inter-lath cementite observed in upper bainite. The size of the intra-lath carbides decreases and their numbers increase as the transformation temperature is lowered.

The diffusion controlled shear transformation that is a feature of the bainite transformation also results in a relatively high dislocation density in the bainite. The dislocation density generally increases as the transformation temperature is reduced, partly due to the increased volume change that accompanies a decrease in the transformation temperature, and partly due to annealing effects that are more pronounced at the higher transformation temperatures.

Thus, the factors contributing to the strength of bainite include:

(a) Grain size (or sub-grain size i.e. lath size).
(b) Carbide distribution and size.
(c) Dislocation density.

There is also the possibility that a supersaturation of carbon may persist in the bainitic structure, in association with the dislocations. Internal friction studies have shown small Koster peaks (due to the association of carbon and dislocations) in

bainitic steels, the magnitude of which increased with decreasing transformation temperature.

Unfortunately, a decrease in transformation temperature tends to increase the strengthening contribution of all of these factors simultaneously. The bainitic lath thickness and the carbide size decrease with decreasing transformation temperature, whilst the dislocation density and carbon supersaturation increase with decreasing transformation temperature. Pickering,[21] in studies of continuously cooled (normalised) 0.5%Mo–B steels, illustrated the effects of transformation temperature on the tensile and yield strengths, Fig. 7.18, and whilst some attempt has been made to rationalise the effects of bainite lath thickness and carbide dispersion, the ommission of dislocation density and dissolved carbon or other solutes makes this interpretation somewhat speculative (Fig. 7.19).

The impact toughness of these 0.12–0.15wt%C–0.5wt%Mo–B steels, as mentioned earlier, were generally near or above ambient temperature. The reasons for the relatively high impact transition temperatures obviously reflect the substructural and carbide dispersion strengthening, coupled with the presence of large second phase particles, such as the cementite in upper bainitic structures. Also, in order to provide 'active' boron, the nitrogen has to be fixed by a more stable nitride former; commonly, a 0.04wt%Ti addition is made to combine with the nitrogen, thereby preventing the formation of boron nitride and the attendant loss of the boron hardenability effect. The use of titanium at this level produces

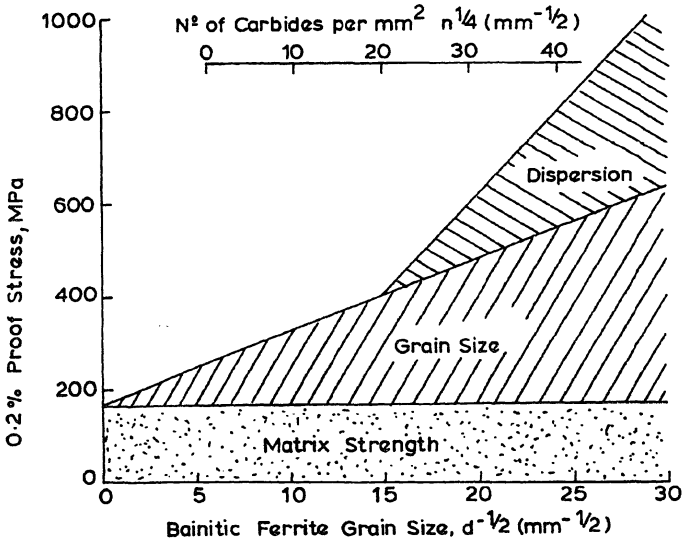


Fig. 7.19 Possible contributions of lath size and carbide dispersion to the yield strength of bainitic steels. Upper bainitic structures show greater lath thicknesses, and the fewer and coarser carbides are associated with the lath boundaries, thus contributing nothing to the yield strength.

coarse titanium nitride cuboids that in turn may be detrimental to the impact properties. The beneficial effects of austenite grain refinement is restricted in steels with coarse titanium nitrides, unless a carbide-based grain refiner is used. The operative variable, i.e. the bainitic packet size, is slightly less than the prior austenite grain size, but, as shown by Ohtani *et al.*,[22] is directly proportional to it, and constitutes the unit cleavage fracture path.

Interest in the bainitic steels waned for a period, mainly because of the advent of the high strength microalloyed steels with their excellent combinations of strength and toughness. Habraken and Economopoulos[23] noted that the impact properties of very low carbon bainitic steels could be dramatically improved by controlled rolling (stage 2 rolling process). The requirement for increasingly higher yield strength in line pipe (*X*70 and *X*80 grades with yield strengths of 480 and 550 MPa respectively) encouraged this development, and commercial acicular ferrite steels subsequently were developed. Smith *et al.*[24] described the development of a Mn–Mo–Nb steel containing 0.04–0.06wt%C, 1.6–1.9wt%Mn, 0.25wt%Mo and 0.05–0.09wt%Nb, developing high strength and toughness in the as-rolled condition. The carbon content is restricted to about 0.06wt%C (max) in order to maintain good toughness. The microstructures showed mixtures mainly of acicular ferrite with some very fine polygonal ferrite grains. Smith *et al.* avoided using the term 'bainite', because of the substantially cementite-free structures that were developed. The carbon enrichment between ferrite plates in these low carbon higher alloy steels resulted in the formation of the M–A constituent – an intimate mixture of austenite and martensite distributed as small regions throughout the structure. These structures were developed by conventional controlled rolling (i.e. finish rolled at low temperatures but above the A_3 temperature) to give a fine effective austenite grain size which in turn limited the packet size. The role of niobium in these steels is firstly to control the austenite structure during the controlled rolling operation, and, secondly, to contribute to the strength of the pipe, by precipitation, particularly after an ageing (or stress relieving) heat treatment.

The general level of strengh and toughness attained in these acicular ferrite steels, i.e. 550 MPa yield strength and an impact transition temperature (standard 10 mm Charpy V-Notch test) of -20 to -40°C, can be seen to extend to the range of yield strengths attainable by conventional controlled rolling with little sacrifice of toughness (cf. Fig. 7.5), as would be expected from the sub-structure embrittlement vector discussed in relation to third stage controlled rolled plates.

The acicular ferrite steels commonly show continuous yielding behaviour due to the retention of internal stresses associated with intermediate and low temperature transformation products, and the 0.2% proof stress is then used to describe the (generic) yield strength. This has some significance in relation to pipes manufactured by the U–O–E process route, where flat plates are cold formed into the pipe shape. The cold bending gives rise to a reduction in yield strength, due to the Bauschinger effect, when microalloyed ferrite-pearlite steels are used. The acicular ferrite steels, however, show a progessive increase in strength through the U-ing, O-ing, and cold expanding processes of pipe manufacture, as shown by Civallero *et al.*[25]

7.4 LOW CARBON STEEL HOT-ROLLED STRIP

Hot rolling mills for strip steels usually start with 100–200 mm thick slabs, which are either narrow (of the order of 0.5 m in width) or wide (up to about 2 m in width), which are rolled to strip with thicknesses in the range 2–8 mm. The slab is reheated and then hot rolled in much the same way as in plate rolling from a metallurgical standpoint, but the rapid final delivery of the extremely lengthy hot rolled strip is accommodated by a coiler, which effectively rolls the strip into a cylindrical mass. Thus the strip (especially the thinner gauges) cools rapidly from leaving the final rolling pass until it is coiled, and then cools very slowly as a cylindrical mass. If the coil is wrapped at too high a temperature, then consecutive laps tend to weld together and the coil cannot be unwrapped. In order to avoid this problem either the run-out between the hot mill and the coiler must be lengthened, or some method of accelerating the cooling has to be introduced. Accelerated cooling systems have featured in all continuous hot strip mills for some 30–40 years, and, whatever the reason for their introduction, these systems have proved to be a most important tool in the control of microstructure.

A typical mill lay-out[26] is shown in Fig. 7.20, and includes the reheating furnaces, a roughing train, finishing train, cooling system and down-coilers. Metallurgically, the soaking temperature controls the dissolution of microalloying elements and the initial austenite grain size, whilst the hot rolling process controls the evolution of the austenite grain structure, grain size, and strain inducement of microalloy carbo-nitrides in austenite. In a continuous hot mill, control of the individual pass deformations has to conform with the mill design capabilities. After each successive deformation, the velocity of the stock material increases as the thickness of the stock is reduced and the length increases. The increase in stock velocity has to be matched by increased roll speed, and the differential in the roll speeds between successive passes is limited by the individual stand motors. Nevertheless, rolling speeds and deformations in modern mills, coupled with conventional soaking practices (important in controlling the mill load), generally produce a fine grained austenite. The extent of strain-induced precipitation in such

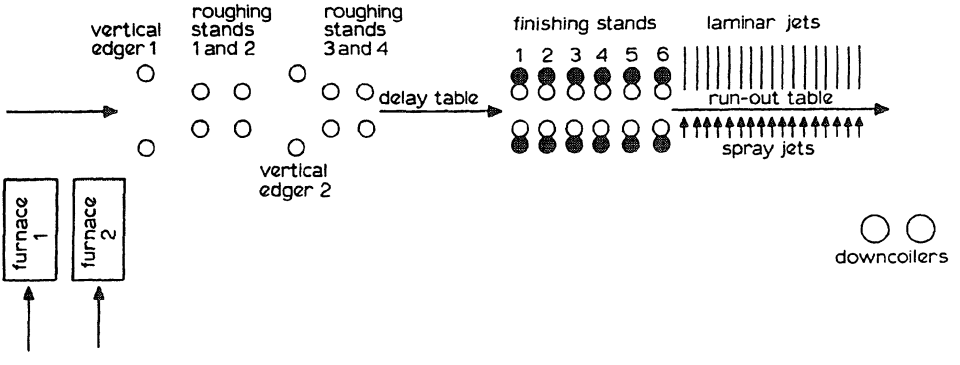


Fig. 7.20 Schematic layout of a hot strip mill. After Kilworth and Wannell.[26]

mills is limited, due to the high rolling speeds and consequently the limited time available for precipitation.

The accelerated cooling helps to maintain the austenite structure developed at the final deformation pass by severely restricting the time in the austenite temperature range, and also controls the equilibrated temperature in the coil. The importance of the accelerated cooling and coiling operation, in metallurgical terms, is that the austenite transformation temperature can be controlled to occur in the coil. As indicated above, cooling of the coil is relatively slow, the mass of the coil being of the order of 1 tonne to 10 tonnes, and the austenite decomposition approaches isothermal transformation conditions. Thus the ferrite grain size and the interphase precipitation particle size can be controlled by changing the coiling temperature for any given steel composition, provided that the alloy composition is sufficient to prevent transformation of the austenite during the cooling stage prior to coiling.

An overview of the metallurgical implications of hot strip rolling is presented in graphical form in Fig. 7.21 for a titanium carbo-nitride dispersion strengthened microalloyed steel.[18] Because of the high titanium level, it can be assumed that the nitrogen is fully precipitated as titanium nitride at the soaking temperature, and that the sulphur in the steel is in the form of titanium sulphide. Some support for these assumptions is given by the facts that

(i) these steels do not exhibit strain ageing, irrespective of processing conditions
(ii) the sulphide inclusions have a modified shape, appearing as spherical rather than elongated inclusions.

Thus, the initial metallurgical framework is set by the steel composition (carbon and 'free' titanium contents), the solubility of titanium carbide and the slab soaking temperature, as shown in Fig. 7.21 at A. The solubility limits and stoichiometry are linearised and have slopes of -1 and $+1$ respectively by using logarithmic co-ordinates. Steel compositions can be selected to maximise the titanium carbide dissolution at a given carbon content, bearing in mind the slab soaking temperature. With a carbon content of about 0.08wt%C, a near stoichiometric 'free' titanium content of 0.32wt%Ti could be considered for a soaking temperature of 1300°C, but at a lower soaking temperature of 1200°C this level would result in considerable quantities of expensive but ineffective undissolved titanium carbide. A free titanium level of 0.15wt%Ti would be more appropriate to the slab soaking temperature of 1200°C at this carbon level. The shaded area in block A of Fig. 7.21 indicates potential steel chemistries. The principles of selection as indicated above are

(i) The free titanium content, i.e. titanium not combined with nitrogen, should be sub-stoichiometric with respect to the carbon content.
(ii) The titanium carbide should be completely dissolved at the slab soaking temperature.

This simple approach may be slightly in error, bearing in mind the thermodynamics of carbo-nitride solubility outlined in Chapter 3, but within the

time scales of commercial treatments there is no guarantee that thermodynamic equilibrium of the carbon in the carbo-nitride would be attained, particularly with the larger nitrogen rich particles formed in the melt in these high titanium steels. The simple approach is therefore recommended.

The extent of titanium carbo-nitride precipitation is thus set by the steel

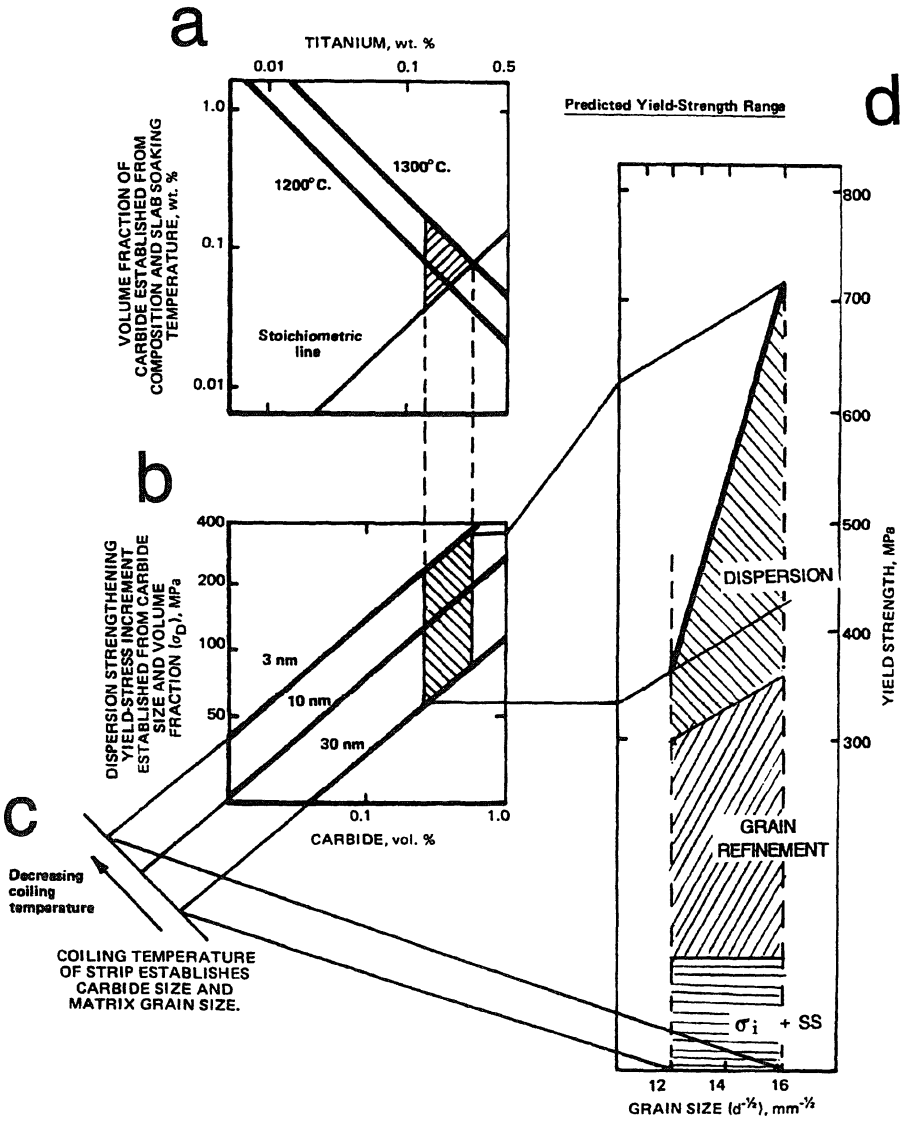


Fig. 7.21 Schematic representation of the effects of compositional and processing variables on the yield strength of a microalloyed steel after hot rolling and coiling. The coiling temperature influences both the interphase precipitate size and the ferrite grain size.

chemistry and the soaking temperature. This can be translated into interphase precipitation strengthening, through the Ashby–Orowan relationship [Equation (2.59)], as shown by block B in Fig. 7.21. The Ashby–Orowan relationship is portrayed graphically in block B, again using logarithmic co-ordinates, and the scale of the (log) volume fraction of precipitate is set at the same value as the log (wt%Ti) in block A, but displaced sideways to give a direct conversion through the proportionality constant for wt%Ti to vol% titanium carbide from Table 7.1, a displacement of log 1.99. The wt%Ti in solution can then be translated directly to f in the Ashby–Orowan relationship by a vertical line from block A to block B. The interphase precipitate particle size is controlled by the coiling temperature, and this is portrayed in nomographic style by the coiling temperature scale marked C in Fig. 7.21. In this way the earlier variables and the coiling temperature are used to define the interphase precipitate strengthening contribution to yield strength through the Ashby–Orowan relationship.

The coiling temperature also controls the ferrite grain size developed from the fine grained austenite, as indicated by the nomographic link from C to the abscissa of block D in Fig. 7.21. The contributions to yield strength can then be built in block D, using the $d^{-1/2}$ abscissa and transposing the logarithmically expressed precipitate strengthening from block B to the linear scale of block D to give the yield strength predictions.

The coiling temperature scale is omitted in Fig. 7.21 as this may vary depending upon the hot mill configuration and the austenite structure after rolling. For example, in the Brinsworth Narrow Hot Strip Mill, when rolling high-strength titanium grades of steel, the coiling temperature scale would range from 750°C at the coarser particles and coarser grain size shown, to 550°C for the finer particles and finer grain sizes. Figure 7.21 may not show the full academic rigour required for universal application, but serves to illustrate the principles involved in the development of high strength steel products, and gives an excellent basis for quality control when producing a family of steels of differing strength levels.

Strain-induced precipitation of titanium carbide in the austenite would obviously detract from the contribution of interphase precipitation of carbide to the yield strength and would lead to a loss of strength. However, the loss of dispersion strengthening in relative terms is less than the loss of interphase precipitate fraction, due to the $f^{1/2}$ function in the Ashby–Orowan equation. For example, a 20% loss of titanium carbide by strain inducement would only lead to a 10% loss of the dispersion strengthening contribution. Such losses can reasonably be neglected in hot-rolled strip products, but much higher loss in plate rolling might have significant consequences for the dispersion strengthening of plate.

The principles of alloy design, described above, equally can be applied in the case of vanadium microalloyed steels and niobium microalloyed steels. The solubility and stoichiometric ratios required in block A of Fig. 7.21 would need to be replaced by those for the appropriate carbide/nitride/carbo-nitride, which might raise serious problems as it would no longer be possible to discount the niobium or vanadium nitrides as insoluble. However, at the levels of carbon, nitrogen, vanadium and niobium commonly used in hot-rolled low carbon strip steels, all of the niobium and particularly vanadium carbo-nitrides would dissolve

at 1200°C, and, provided that the microalloy content was sub-stoichiometric, could be translated directly into the appropriate volume fraction of interphase precipitated particles.

The use of the high titanium addition has advantages in providing a wide range of strengths from a given steel composition as indicated in Fig. 7.21. This feature offers advantages in limiting the slab stocks required for different strength steels. The high titanium level also provides an automatic inclusion shape control effect as described earlier. However, there is a disadvantage to the wide range of strengths that can be attained, in that a very tight control of the hot rolling process is essential to the attainment of the desired properties. In the early developments of high strength strip steels, the attainment of a minimum guaranteed strength level was regarded as adequate without regard to the extent to which the actual yield strength exceeded the specified minimum yield strength. For example, steels produced to a specification requiring a *minimum* yield strength of 400 MPa could have a yield strength of 420 MPa or 600 MPa. Many of the applications of hot rolled strip involve some cold forming operation, e.g. cold pressing of wheel centres, or the transverse bending of strip to form a lorry chassis member (*note* – a transverse bend is defined as a fold around the longitudinal axis of the strip). An excessive yield strength not only increases the forming load, but also increases the elastic springback when the forming load is released. Variable yield strengths (above the specified minimum level) give rise to variable springback and variations in the shape of the pressed component. This has led to the introduction of customer specifications involving not only the minimum yield strength, but also a maximum range of yield strengths, of the order of 50 Mpa, which would result in a specified yield strength range of 400–450 MPa in the example cited. Very tight mill control is required in the case of the high titanium steels, particularly when producing to the lower strength ranges, e.g. up to 460 MPa.

This sensitivity to process control can be reduced in steels with a lower latent hardening capability, as illustrated for a 0.12wt%V–0.02wt%N microalloyed steel[27] in Fig. 7.22. The effects of decreasing the coiling temperature on the precipitated particle size and ultimately on the suppression of precipitation are indicated. The maximum yield strength attainable is about 620 MPa and the range of coiling temperatures that would give yield strengths between 570 and 620 MPa is of the order 500°C–670°C. For lower strength steels, a lower latent hardening potency would confer the same broad range of coiling temperatures that would give the restricted yield strength range.

Attention has been drawn to the applications of these microalloyed strip steels, which often require some degree of cold formability. In hot-rolled strip, the relevant measures of cold formability relate to the maximum uniform elongation, which gives an indication of the forming strain that can be applied prior to the onset of plastic instability, and the reduction of area, which gives a measure of the fracture resistance of the steel when subjected to deformation processes that do not involve plastic instability e.g. bending.

Uniform elongation is controlled by the Considere criterion as outlined in Chapter 2. Microalloying additions increase the yield (and flow) strengths of steel without changing the work hardening rate, and consequently the uniform

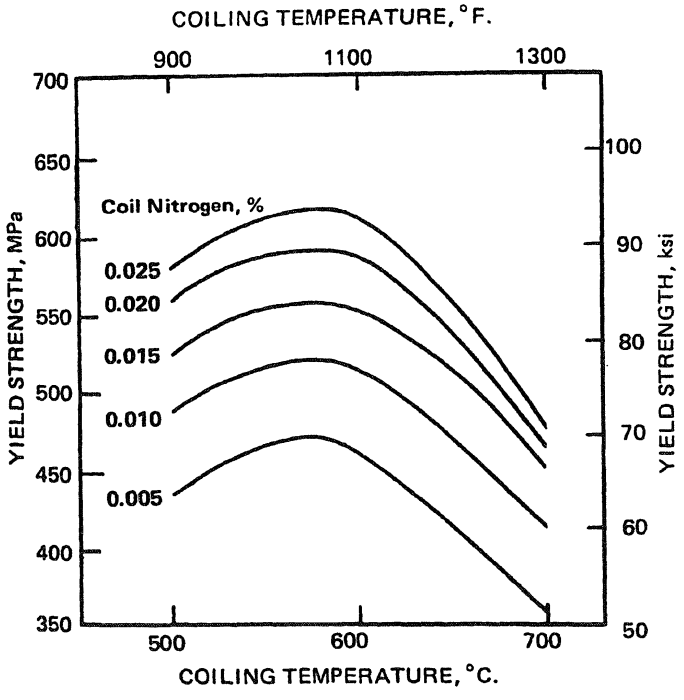


Fig. 7.22 The effect of coiling temperature on the yield strength of a 0.12wt%V – 0.02wt%N steel, showing the wide range of coiling temperatures that give yield strengths in the range of 570–620 MPa. After Grozier.[27]

elongation is reduced roughly in proportion to the increase in yield strength. It can therefore be expected that the microalloyed steels will show a lower formability than do lower strength carbon manganese steels. This is generally true, and due consideration has to be given to the level of formability of such steels. This feature will be considered in greater detail in Section 7.6.4 when considering dual phase steels.

The problem of ductile fracture control is not limited to strip steels, and is considered in the following section.

7.5 INCLUSIONS AND DUCTILE FRACTURE

The theoretical aspects of ductile fracture were considered in Chapter 2, and can be summarised briefly as follows:

(i) As steels are strained at low temperatures, voids are nucleated by either second phase particle cracking or by decohesion of the interface between the second phase and the matrix.

(ii) These voids grow, on further straining, at a rate that is dictated by the geometry of the voids, particularly the acuity of the void edge, i.e. the frontal radius of curvature.
(iii) At some critical strain, coalescence of the voids occurs and rapidly causes catastrophic failure.

Cementite has significant effects on the fracture strain of medium and high carbon steel. The cementite particles, however, are reasonably strongly bonded to the ferrite matrix, and failure is commonly initiated by carbide shear cracking. In low carbon steels, however, the stresses required to cause carbide shear cracking require considerable plastic deformation of the ferrite matrix, and fracture can often precede carbide cracking due to the presence of non-metallic inclusions in the steel. These inclusions include both sulphides and oxides, and commonly initiate failure by interface decohesion. There have been many studies of inclusions and their effects on high strain properties (i.e. those associated with ductile fracture),[28–30] and these are of direct relevance to many of the applications of both plate and strip products.

Attention has already been directed to the avoidance of brittle (cleavage) fractures in plate products by grain refinement, but grain refinement is not a prime factor in ductile fracture resistance. Energy absorption and crack arresting characteristics in line-pipe are associated with inclusion effects and these must be controlled. In the welding of structural steels, thermal stresses in restrained weldments can cause low ductility (ductile) fractures to give lamellar tearing, which is an inclusion controlled phenomenon. As mentioned in the previous section on strip, the transverse bend properties are controlled by inclusions, and tight radius bends make specific demands on the inclusion content and shape. Additionally, pressing operations involving hole expansion, in components manufactured from strip, require inclusion control in order to prevent cracking at the edge of the expanded hole. There are many other aspects of the ways in which inclusions affect the fracture characteristics of steel, such as hydrogen induced cracking in line-pipe, and fatigue cracking[30] in high strength steels, many of which are relevant to the application and performance of microalloyed steels.

Having described the sequence of events involved in the ductile fracture process, i.e. void nucleation, void growth and void coalescence, and considering the theoretical developments in ductile fracture theory, the main features of any inclusion distribution that control ductility are the inclusion shape (particularly the frontal radius of curvature) and the volume fraction of inclusions.[31] Void initiation is virtually spontaneous in the case of non-metallic inclusions, the voids being initiated by interface decohesion in the earliest stages of plastic deformation. The initial shape of the void is essentially that of the inclusion on which the void is formed. The void growth rate, although dependent on the inclusion shape, is also dependent upon the stress and strain state involved in the deformation process itself,[32] as pointed out in Chapter 2, so that the void volume is less in the case of wire drawing (because of the biaxial compression and uniaxial tension) than in the case of simple uniaxial tension, which in turn would be less than that observed in biaxial tension. Nevertheless, the effects of inclusion shape and content on the true

strain to fracture in the tensile test (or % reduction of area) is qualitatively the same as their effects on the Charpy ductile shelf energy, or on the strain to fracture in transverse bends (as measured by the ratio of bend radius to plate or strip thickness).

The two main inclusion factors, content and shape, have led to two different approaches to improving ductile fracture resistance:

(i) Inclusion shape control.
(ii) Reducing inclusion contents.

These approaches have been pursued vigorously and will be considered in terms of the developments concerning sulphides, and then the developments concerning oxides, these broad categories of inclusions constituting virtually all of the non-metallic inclusions encountered in steel.

7.5.1 Sulphide Shape Control

The sulphide that naturally occurs in steels is manganese sulphide; the manganese added to steel forms manganese sulphide and prevents the formation of the less stable low melting point iron sulphides that render steels incapable of hot deformation. Manganese sulphide is plastic at hot rolling temperatures and suffers hot deformation in much the same way as the austenite matrix, being deformed by dislocation mechanisms and having a characteristic strength. The hot strength of manganese sulphide is very similar to that of low carbon austenite, and the plastic deformation of the manganese sulphides is very similar to that of the steel matrix. Relative plasticities, v, in the range 0.8–1.4 are commonly observed[33] for MnS inclusions, the actual value being dependent on the deformation temperature, the extent of deformation, the inclusion chemistry and the inclusion size. The relative plasticity is defined[34] as the ratio of true strain in the inclusion to the true strain in the matrix,

$$v = \ln(b/b_0)/\ln(l/l_0) \tag{7.16}$$

The experimental method of assessing inclusion plasticity usually involves the measurement of the ratio of inclusion length, b, to inclusion thickness, a, on a longitudinal section normal to the rolling plane. The relative plasticity determined in this way can be obtained from either

$$v = 2\log\lambda/3\log h \tag{7.17}$$

or

$$v = \log\lambda/2\log h \tag{7.18}$$

where $\lambda = b/a$, $h = l/l_0 = A_0/A$, l = final stock length, l_0 = initial stock length, A = final stock area and A_0 = initial stock area

Equation (7.17) relates to a square bloom reduced to a square product (i.e. equal transverse compressive strains normal to the rolling plane and in the rolling plane), whilst Equation (7.18) relates to plane strain deformation, i.e. slab rolled to

plate or strip product with no change in width during the rolling reduction, and where the length strain is equal and opposite to the thickness strain.

Some of the variation in the plasticity of manganese sulphide inclusions is dependent on inclusion chemistry. Type I MnS inclusions,[35] which contain appreciable iron and oxygen contents, have lower relative plasticity values than Type II MnS (virtually pure MnS). The effects of such impurities (including iron) have been shown[28,36] to harden manganese sulphide. This is attributed to solid solution strengthening, but as shown, by Banks and Gladman,[33] may involve other strengthening mechanisms such as precipitation hardening and the stabilisation of recovered substructures within the sulphide. These observations clearly show that the addition of elements which harden the sulphides would give lower relative plasticity, and would either prevent the manganese sulphide from becoming elongated, or would reduce the degree of elongation of the manganese sulphide during the rot rolling process. Such effects are of particular interest in controlled rolled steels, as the relative plasticity of manganese sulphide tends to increase with decreasing deformation temperature. Such additions need to have some solubility in the manganese sulphide, and should induce a significant hardening effect on the manganese sulphide. The effect of an alloying element of this type on the hardness of MnS is illustrated in Fig. 7.23. The strengthening effect of calcium in MnS is also potent, and is active over a wide temperature range.[8] It has a similar effect to that observed with titanium. A feature of these and other elements is that high levels of addition will result in the formation of an alternative sulphide, and this is the case for titanium, calcium and the rare earths (cerium, lanthanum, neodymium and praesodymium). The increased stability of the rare earth sulphides is reflected in their melting points[37] as follows

Compound	Melting point (°C)
MnS	1530
LaS_2	1970
La_2S_3	2100
CeS	2100
Ce_2S_3	2150
Ce_3S_4	2050
NdS	2140
Nd_2S_3	2200

With higher melting points, by some 500°C, the rare earth sulphides should be harder at any given temperature.

The sulphide shape controlling additions, therefore, act by hardening the manganese sulphide, or by replacing the manganese sulphide with a harder sulphide. Both calcium and titanium (and also zirconium) can act in both ways, depending on the level of addition, whilst the rare earths act by replacing manganese sulphide. Low levels of rare earth additions merely replace a fraction of the manganese sulphide. The effects of titanium, calcium and rare earth additions, on inclusion plasticity,[33] are shown in Figs. 7.24 and 7.25. The titanium levels portrayed in Fig. 7.24(a) are generally lower than those required to cause full substitution of manganese sulphide by titanium sulphide. The relative plasticity

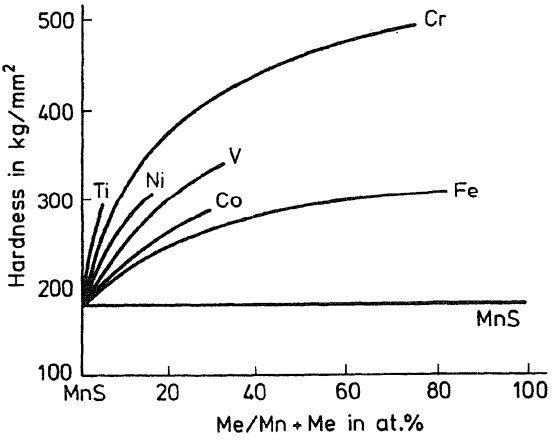


Fig. 7.23 The effects of substitutional solutes in the manganese sulphide on the hardness of the sulphide. After Keissling and Lange.[28]

changes due to titanium are consequently small in the higher sulphur steel, but are significant in the case of the lower sulphur steels. This may also reflect the effects of sulphide size (Fig. 7.26). Lower sulphur steels usually give smaller inclusions for a given cooling/solidification rate, and these in turn have lower plasticity. A similar effect is seen in calcium treated steels (Fig. 7.24(b)) where the calcium level is shown as a Ca : S wt% ratio. Again the effect of inclusion size may be operative, as indicated in Fig. 7.26. For a given inclusion size, the relative plasticity decreases in the order

Type II MnS, – Type I MnS, – MnS with Ti, – MnS with Ca

The effect of rare earth additions (rare earth additions are commonly made in the form of Misch Metal which contains some 40–50%Ce, 40%La, and the remainder is neodymium and praesodymium) is shown in Fig. 7.25. Despite the fact that rare earth additions cause the formation of large (10–20 μm) rare earth sulphides and oxy-sulphides, these highly refractory materials are virtually non-deformable at the temperatures used for the hot working of steel, and, with a sufficient addition of rare earths, result in a relative plasticity of $v = 0$.

The consequences of the change in relative plasticity are directly related to the inclusion shape changes. For example, in plate rolling, plastic inclusions may be regarded as flattened discs with their major axes lying in the rolling plane and the minor axis being normal to the rolling plane. If a through thickness tensile test is performed on the plate, the disc diameter is normal to the tensile axis, and the value of r in Equation (2.88), i.e. the ratio of the disc thickness to disc diameter will be small. The effect of changing this ratio, by modifying the relative plasticity of the inclusion, is illustrated, using Equation (2.88), in Fig. 7.27 for steels with 0.01wt%S and 0.02wt%S. Increasing the ratio of sulphide disc thickness to disc diameter up to 1, increases the strain to fracture from 1.7 and 1.2 up to 3.9 and 3.2 for the 0.01 and 0.02wt%S steels respectively. These changes correspond with

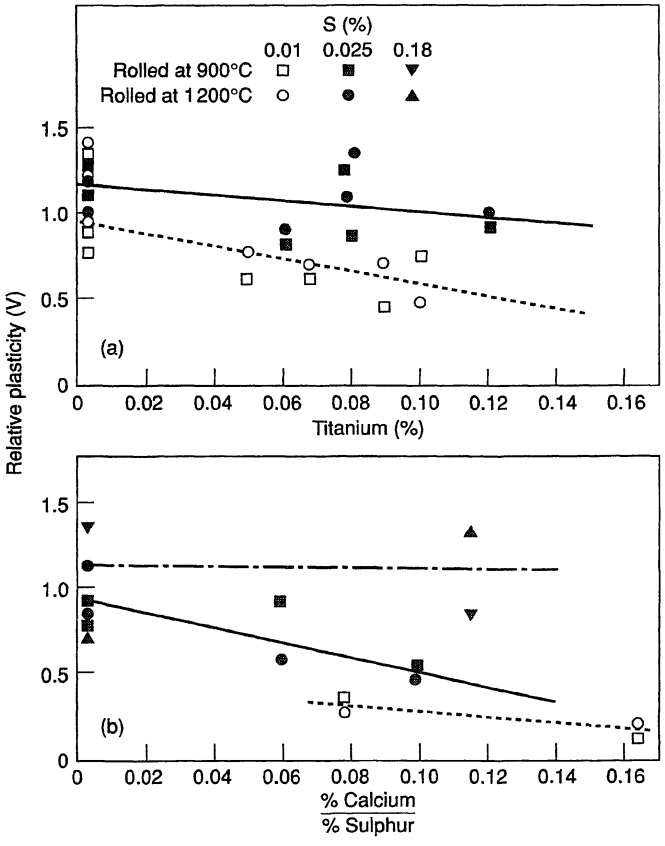


Fig. 7.24 The effects of (a) titanium and (b) calcium additions on the relative plasticity of the sulphide of low carbon steels. After Banks and Gladman.[33]

increases in the % R of A from 60% to above 95%. Although the theory of ductile fracture has several shortcomings, as discussed previously, the test results of Pircher and Klapdar[38] show a qualitatively similar change in the through thickness reduction of area values of commercially produced plates (Fig. 7.28).

The extension of the ratio of b/a to values greater than unity reflects the effects of elongated inclusions when the tensile axis is parallel with the inclusion elongation. The magnitude of the change in the strain to fracture with a given change in b/a is less than that observed at b/a values less than unity, so that, although the longitudinal ductility would be reduced by inclusion shape control, the ductility would only be reduced to the value of 75–80% R of A. With perfect shape control, then the inclusion shape should be isotropic, as should the fracture strain, with values of 75–80% R of A irrespective of the test direction. A significant feature of Fig. 7.27 relates to the thickness/diameter ratio of the plate-like inclusions. Given that the relative plasticity of manganese sulphide inclusions is approximately $v = 1$, then the magnitude of the hot rolling reduction would be important in fixing the

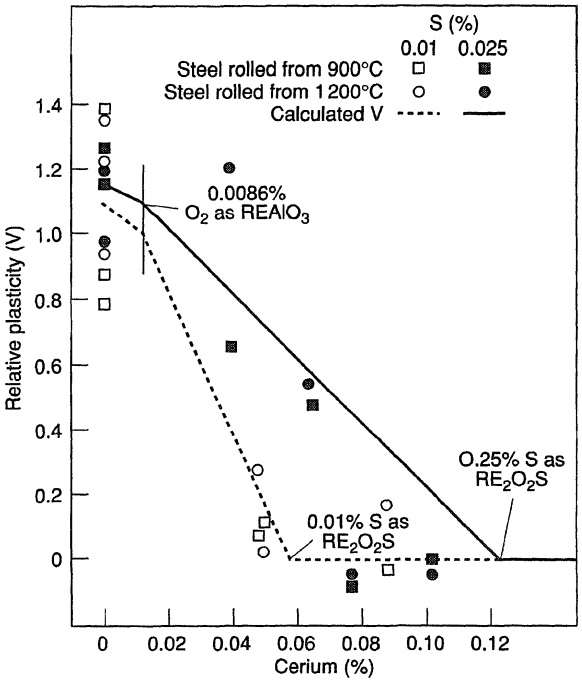


Fig. 7.25 The effects of rare earth additions on the mean relative plasticity of sulphides in low carbon steels. After Banks and Gladman.[33]

inclusion shape in the absence of any shape control additive, and steels undergoing greater hot reduction will have poorer through thickness ductility. The advantages for plates produced from concast slab over those produced from large ingots are thus obvious. In the case of steels with effective shape control, there will be no difference in the ductility irrespective of the hot rolling reduction.

The true strain to fracture and % R of A scales shown in Fig. 7.27 if augmented with an absorbed energy (J) scale would serve to indicate the approximate energy absorption in the fully ductile Charpy V-Notch impact test. High fracture strains are commensurate with high ductile shelf energies.

The effect of inclusion shape control on the longitudinal bend ductility of a 0.15wt%C – 0.4wt%Mn – 0.03wt%Nb steel is shown in Fig. 7.29. This steel has a sulphur level of about 0.015wt%, and in the unmodified condition could undergo a 180° bend around a former which has a radius of 1.5x the strip thickness without cracking. Inclusion modification by rare earth treatment improves the longitudinal bendability (i.e. the transverse ductility), so that the strip can be folded flat without any sign of longitudinal cracks developing on the outer tensile edge of the bend. The ratio of the rare earth to sulphur content (each expressed in wt%) that is required to give complete shape control must be greater than 4 : 1, which is slightly in excess of the stoichiometric ratio of (Ce, La) S. It should be noted that the rare earth elements are extremely strong oxide formers, and, in the absence of very low

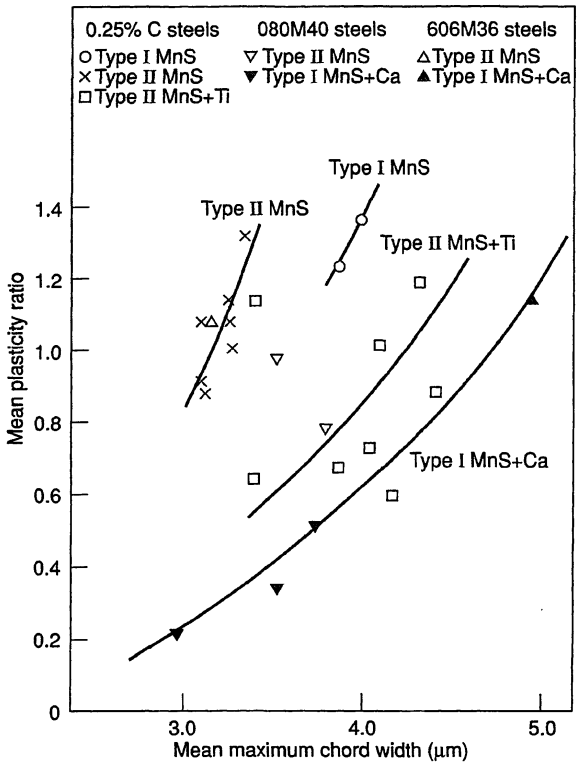


Fig. 7.26 The effects of inclusion size on the relative plasticity of manganese sulphide inclusions. The effects of solutes in the manganese sulphide are also shown. After Banks and Gladman.[33]

initial oxygen contents, show the formation of very stable oxy-sulphides, usually of the form $(R.E)_2O_2S$, or even oxides $(R.E.)_2O_3$,[39] which may reduce their effectiveness in controlling the shape of the sulphides.

The affinity of the sulphide shape controlling agent for oxygen is not confined to the rare earths. Titanium, zirconium and calcium also show very stable oxides, and control of the oxygen prior to their addition, coupled with prevention of reoxidation during steelmaking, is an essential feature of sulphide shape control.

7.5.2 Desulphurisation

As outlined above, sulphide shape control is achieved by additives which either harden the manganese sulphide or replace the manganese sulphide with a much harder sulphide. In either case, the addition of the sulphide shape controlling agent involves a direct cost, and as the required amounts of these agents increase with increasing sulphur content, so does the cost of sulphide shape control. Attempts to reduce the cost of these agents by reducing the sulphur content of the steel rapidly led to an alternative approach to improved ductility.

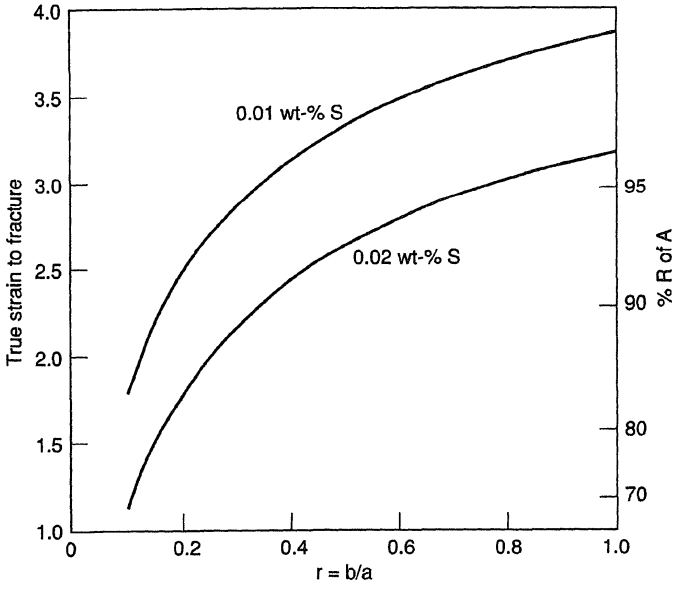


Fig. 7.27 Theoretical predictions of the effects of inclusion shape control on the true strain to fracture in steels with 0.01wt%S and 0.02wt%S.

As indicated in Fig. 7.28, decreasing the sulphur content even in the absence of shape control can produce a significant improvement in the short transverse reduction of area. This, coupled with the cost of shape control in higher sulphur steels, led to the development of desulphurisation treatments capable of reducing the sulphur level to less than 0.001 wt%S. Desulphurisation of steel is best achieved in a highly reducing environment (with respect to oxygen) for, as pointed out above, oxygen and sulphur compete for the sulpho-philic elements. The formation of the sulphide then needs to be augmented with a sulphide collecting medium, such as a low oxygen potential basic slag, thereby freeing the steel of the sulphides. Accounts of desulphurisation have been published[30,39] and the modern practice of desulphurisation can be summarised as follows:

(i) Substantial sulphur removal is effected in molten iron, when low oxygen conditions prevail, by the mixing of sulphide-forming compounds such as soda ash, magnesium-coke or lime rich slag, with the molten iron.
(ii) The low sulphur iron is converted to steel, for example in the basic oxygen steelmaking (BOS) plant, and after deoxidation, lime or calcium bearing alloys are injected into the melt to produce CaS, which is then retained in a highly basic low oxygen slag, efficient mixing of the metal and slag being promoted by the inert carrier gas used in the injection process.

The final removal of sulphur by the calcium-rich alloys or compounds also confer a sulphide shape-controlling action either due to the calcium sulphide

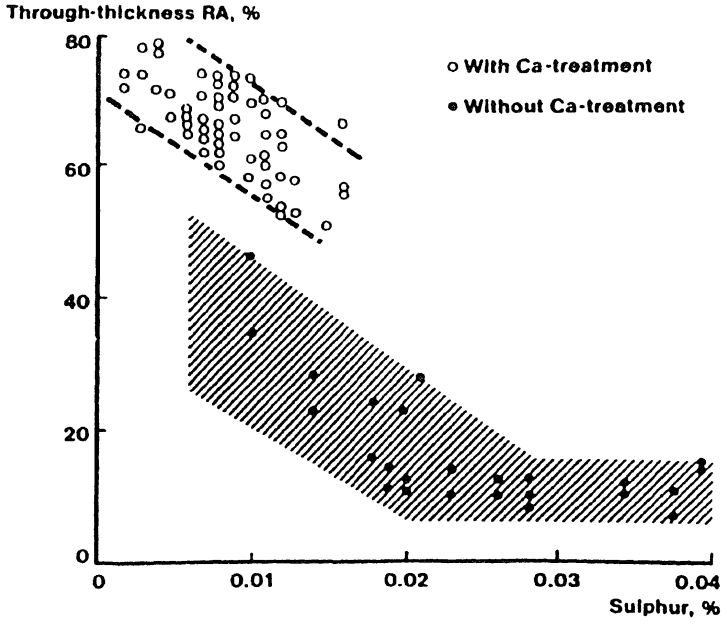


Fig. 7.28 The effects of sulphide content and shape control (by calcium treatment) on the through-thickness ductility of commercially produced plate. After Pirchner and Klapdar.[38]

retention or due to the retention of sufficient calcium to give a hardened manganese sulphide.

It is interesting to note that at these low levels of sulphur the solubility of manganese sulphide at slab soaking temperatures of 1250°C, even with up to 1wt%Mn, is becoming relatively substantial. As shown by Hale and Nutting,[40] the solubility product, k_s, of MnS can be expressed as

$$k_s = [Mn][S]f_s^{Mn} \tag{7.19}$$

where $[Mn]$ is the dissolved manganese content (wt%), $[S]$ is the dissolved sulphur content (wt%) and f_s^{Mn} expresses the effect of manganese on the activity coefficient of sulphur in austenite.

The solubility product and the activity coefficient of sulphur increase with increasing temperature as given by

$$\log k_s = 2.929 - 9020/T \tag{7.20}$$

$$\log f_s^{Mn} = [0.097 - 215/T][Mn] \tag{7.21}$$

where T is the temperature (K)

The solubility is shown in Fig. 7.30. At 1250°C, the solubility of sulphur in a 1%Mn steel is of the order of 0.001wt% (10 ppm), so that, for very low sulphur

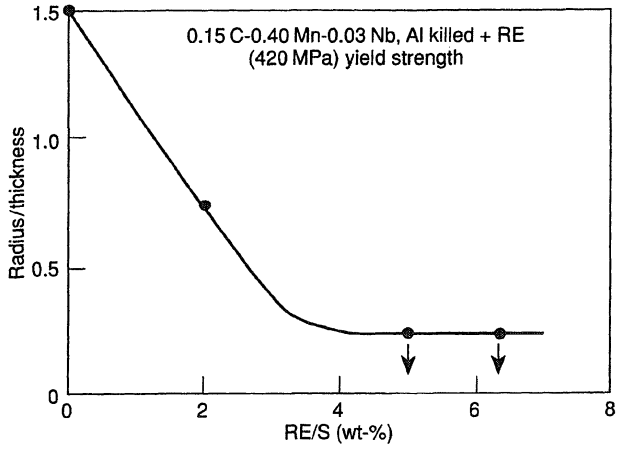


Fig. 7.29 The effect of inclusion shape control on the longitudinal bend ductility of hot rolled strip. The bend ductility is assessed from the minimum bend radius that can be sustained without causing cracking and is expressed as the ratio of the bend radius to the strip thickness. After Wilson *et al.*[39]

steels, a substantial proportion of the MnS would be dissolved, and would therefore not be available for elongation during rolling.

7.5.3 Deoxidation

Deoxidants are added to steel to remove oxygen from solution in the liquid metal. Failure to reduce the dissolved oxygen could result in a vigorous carbon–oxygen reaction during cooling and solidification, causing the evolution of carbon monoxide gas and a porous steel after solidification. Deoxidation with aluminium, silicon or manganese (or a combination of these elements) results in a deoxidised steel, but one in which the solid deoxidation product may still be present, i.e. the steel is not necessarily oxide free. The oxides are generally less dense than steel by a factor of $\times 2$, and thus tend to float from the liquid steel. However, due to convection currents in the liquid metal, such flotation may not guarantee oxide removal. Assistance can be given by inert gas bubbling, where the bubbles may carry the solid oxides to the liquid metal surface where they become absorbed into the slag. Clean steels have been produced, using aluminium to form alumina particles, which are then encouraged to float out, and may be absorbed into the slag or onto the ladle walls. Thus, deoxidation costs are introduced, the cost increasing with the oxygen level that has to be removed from solution.

The relevant efficiencies of the various deoxidants[41] are shown in Fig. 7.31. The low oxygen contents attainable with aluminium deoxidation are clearly shown to prevent titanium losses, and would restrict the oxygen available for combination with the slightly more stable oxide formers such as calcium and rare earths. In fact the oxygen level of the liquid metal can be lowered even further than is shown for aluminium alone, due to the synergistic effects of common deoxidants.[30] A

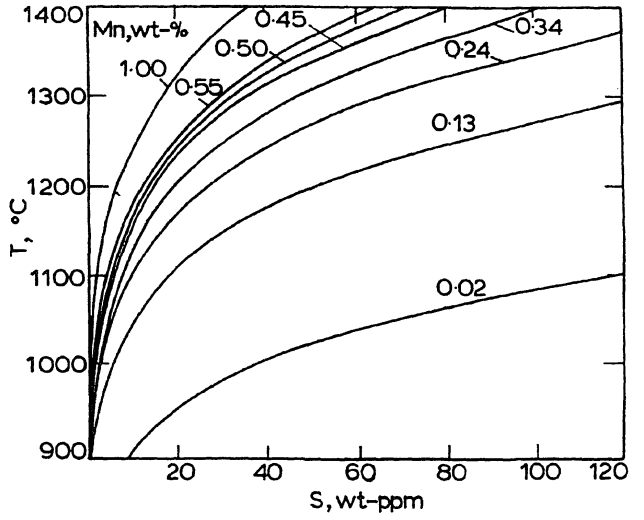


Fig. 7.30 The solubility of manganese sulphide in austenite. Extensive dissolution of the manganese sulphides can occur in low sulphur steels at the temperatures used for soaking prior to hot rolling (1200°C and above). After Hale and Nutting.[40]

significant feature of Fig. 7.31, however, relates to the effects of carbon as a deoxidant when the partial pressure of CO is reduced. Vacuum treatment, with the accompanying reduction in the partial pressure of CO, enables low oxygen levels to be attained, and as the deoxidation product is gaseous (CO) it is not retained in the steel. This can either eliminate the need for deoxidants which give solid deoxidation products at moderate carbon levels, or can reduce dramatically the amount of, for example, aluminium that needs to be added to give effective deoxidation in very low carbon steels. This in turn reduces the initial fraction of oxidic inclusions, and, as these are equally susceptible to flotation and absorption, results in cleaner steels.

In the course of the development of cleaner steels, the indigenous oxides formed during deoxidation were not the only oxides to have been considered. Exogenous oxides have also been reduced, and careful attention has been given to the quality of refractory materials used in ladles, nozzles and hollow-ware, thus restricting the opportunities for metal/refractory interactions.[30]

The use of secondary steelmaking processes has been instrumental in the development of high quality steels, allowing vacuum treatments, sulphur control, and sulphide shape control, and improving the recovery of alloy additions. Whilst this was, in the past, regarded as an expensive additional treatment for only the most demanding grades of steel, secondary steelmaking is now regarded as the main method of steel refinement, with B.O.S. and electric arc furnaces being relegated to the status of primary melting units. The cost of secondary steelmaking has, to a large extent, been balanced by removing time consuming refining from the B.O.S. and E.A.F. (electric arc furnace) processes, thus effectively improving the plant productivity.

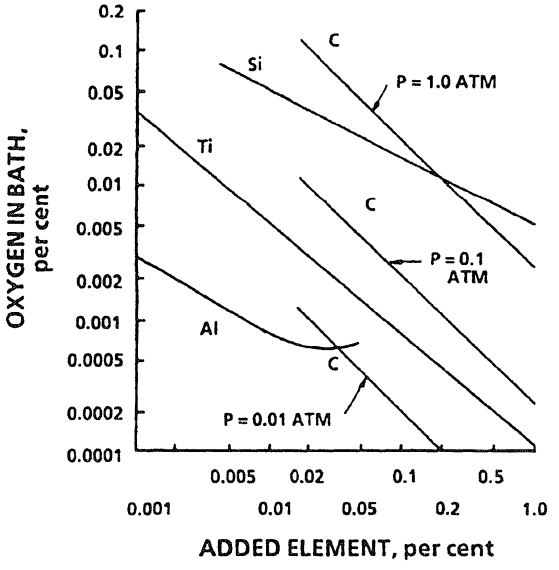


Fig. 7.31 The deoxidation potential of common deoxidants and carbon. The effect of reducing the CO partial pressure on the deoxidising capability of carbon is also shown.

7.5.4 The Role of Carbides

Carbides may also contribute to void initiation either by particle cracking or by interface decohesion. A comparison of isolated spheroidal carbides in ferrite with pearlite carbide in ferrite–pearlite structure[31] has shown that pearlitic carbides are more deleterious to ductility than are spheroidal carbides for a given volume fraction of carbide. The major difference between carbides and inclusions lies in the inherent strength of the carbide and the strength of the bond between carbide and matrix, which lead to significant void nucleation strains. When the inclusion content of low carbon steel is high and the inclusion shape is adverse, then void nucleation, growth and coalescence can occur prior to any significant void formation at carbides (Fig. 2.30). As the inclusion content is reduced or the inclusion shape is improved, so the fracture strain increases, and, eventually, the carbide phase will become involved in the ductile fracture process. In the limit, when inclusions have been eliminated, the ductility will be characteristic of the carbide content. In higher carbon steels, the effects of carbides may dominate the ductile fracture process, and although it is still possible that the stress intensification that occurs near inclusions may accelerate local carbide cracking, essentially, the level of fracture ductility will be governed by the carbide.

The significance of the interaction between inclusions and carbides is that the level of ductility in low carbon steels may become 'carbide limited' at low inclusion contents, and the fracture strains may be lower than those predicted

solely on the basis of inclusions (see Figs 7.27 and 7.28). Reducing the carbon level during steel making leads to an increase in the oxygen content of the metal. If the steel is then deoxidised with silicon or aluminum, the oxides will subsequently exert an influence on the ductile fracture process, giving rise to an optimum carbon level, as shown in Fig. 7.32. Vacuum treatments, which allow further formation of gaseous CO as the deoxidation product, result in higher ductilities and a lower optimum carbon level. It should be pointed out that the formation of solid deoxidation products do not necessarily have the adverse effects shown in Fig. 7.32 if the deoxidation product is allowed to float out of the molten steel after deoxidation. Nevertheless, the existence of high oxygen levels always offers the *potential* for high oxide contents, and vacuum treatments will reduce the initial oxygen content at any given carbon level.

The effects of carbides on the Charpy ductile shelf energy, shown by Burns and Pickering[42] in Fig. 2.22, and summarised in Fig. 7.33, were observed at carbon levels above the optimum for air melted steels. The highest ductile fracture strains and shelf energies would be obtained by limiting both the inclusion content and the carbide fraction. In low carbon steels the major harmful effects are those connected with inclusions. In high carbon steels the fracture strain will inevitably reflect the effects of carbide cracking. As shown in the previous sections, dramatic improvements in fracture strain and ductile shelf energy are attained by desulphurisation, inclusion shape control, and the removal of oxides either by flotation or by vacuum treatment.

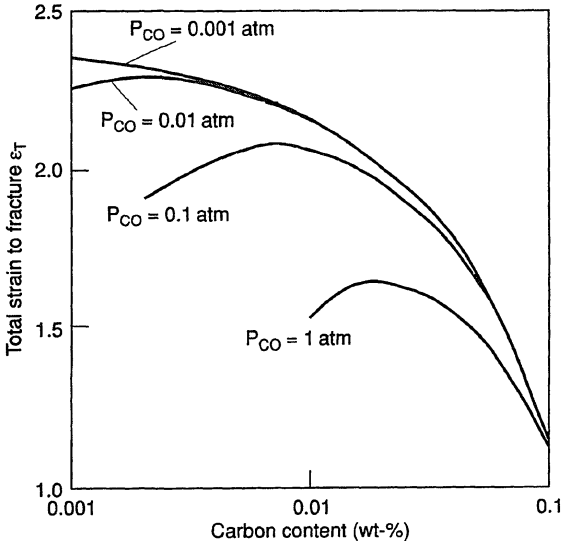


Fig. 7.32 The effects of carbides and non-metallic inclusions on the strain to fracture in tensile testing.

7.6 LOW CARBON COLD ROLLED AND ANNEALED STRIP

Many applications for steel require thin sheet or strip with thicknesses in the range 0.3–2 mm. Such material cannot be produced by hot rolling due to scaling (oxidation) rates, chilling effects, and dimensional control. A modern hot mill is capable of producing well dimensioned strip in thicknesses down to a minimum of 2 mm. Many of the applications for the thin strip, such as motor car body panels and containers (cans), as well as cold pressed parts for a variety of machinery, require that the steel has a high level of formability. Attention has already been drawn to forming limitations arising from plastic instability, and from fracture, in Chapter 2. The factors controlling fracture have been discussed in the previous section (7.5). The factors controlling plastic instability in simple tension are indicated by the Considere Criterion, and relate to the control of flow stress and work-hardening rate. Most of the strengthening factors discussed previously in relation to the yield strength have similar effects on the flow stress, although the magnitude of these effects might differ. Grain refinement, precipitation strengthening and solid solution strengthening all increase the flow stress, and although all of these factors increase the work hardening rate, the effect on work hardening is generally less that that on the flow stress, thus resulting in a generalised view that these strengthening mechanisms will reduce the maximum uniform strain. A direct consequence of this generalisation is that the highest level of uniform strain is obtained with low strength steels. Further, although the pearlite content of the steel does not directly affect the yield strength, it reduces the Luders' extension and consequently increases the flow stress, again to a greater extent than it increases the work hardening rate, thereby reducing the maximum uniform strain. Consequently, low carbon low strength steels have been developed extensively for applications requiring the highest levels of formability.

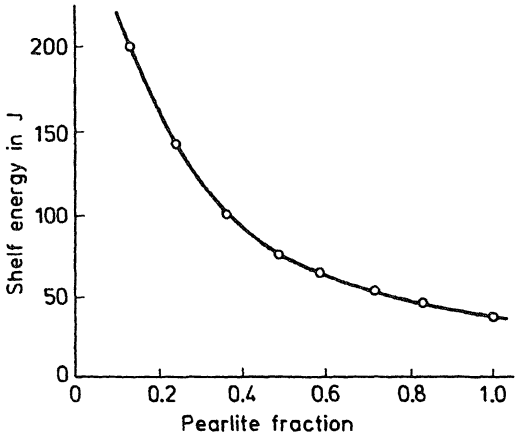


Fig. 7.33 The effects of carbon content on the impact properties of carbon steels. The ductile shelf energy is reduced dramatically by increasing the (pearlitic) carbide content of the steel due to the reduction in ductile fracture strain. After Burns and Pickering.[42]

The deformation of this sheet or strip, however, introduces other factors into the consideration of formability, and the manufacture of such materials by cold rolling and annealing also introduces the possibility of using crystallographic textures to enhance the resistance to local plastic instability. In recent years, the introduction of continuous annealing has required considerable process development work in order to maintain, and even improve upon, the levels of strength and formability of cold rolled and annealed sheet and strip.

7.6.1 Formability

As outlined above, a high level of uniform strain is attained by low levels of strength. In sheet pressing operations, the strain state developed can be very different from those involved in tensile testing, and the assessment of formability of these materials may be based on factors other than the n values in the Ludwig–Hollomon equation (see Chapter 2). Consideration has to be given to crystallographic orientation in the cold rolled and annealed thin sheet or strip. A very important consequence of the development of crystallographic texture is the operation of selected slip planes during cold deformation. This gives rise to plastic anistropy, in which for a given principal strain, the accommodating orthogonal strains can be varied depending upon the type of texture. An excellent account of the role of texture in controlling the plastic anistropy has been given by Abe.[43]

The development of strong (111) textures after cold rolling and annealing, and the attendant improvement in plastic anisotropy, is associated with the recovery and re-crystallisation processes involved in the annealing treatment, and also with the metallurgical state of the strip prior to cold rolling. The presence of finely distributed particles prior to cold rolling interferes with the recovery and recrystallisation processes, and reduces the selective development of (111) textures, thereby reducing the plastic anistropy. The microalloy interphase precipitates behave in this way, and, as might be expected, severely retard recrystallisation. The fine particles act as pinning particles for the subgrain structures, and it has been shown that the fine particles that are capable of significantly increasing the yield strength will also effectively inhibit recrystallisation.[44] Annealing treatments that will allow particle coarsening and recrystallisation also give rise to a severe loss of dispersion strengthening.

Thus, conventional interphase strengthening by microalloy additions has several adverse effects on the formability of low carbon steel strip:

(i) Dispersion strengthening raises the flow stress and yield strength and reduces the maximum uniform strain, i.e. the strain to the onset of plastic instability, thus reducing the stretch formability.
(ii) Fine dispersed precipitates retard the recrystallisation of cold rolled strip
(iii) Dispersion strengthening reduces the development of preferred crystallographic orientations and thereby reduces the plastic anisotropy that is conducive to good deep drawability.

The development of high strength formable strip has consequently been along other lines, as for example by using the solid solution strengthening effects of

silicon and phosphorus, which are just as viable in cold rolled and annealed strip as they are in hot rolled products. Although these elements raise the yield and flow strengths, this effect is counterbalanced to some extent by their relatively large effects on the work hardening rate. The effects of various solutes on the flow stress, σ, at a true strain of $\varepsilon = 0.2$, and on the work hardening rate ($d\sigma d\varepsilon$) at the same true strain, are shown in Table 7.3. Although all of the solutes shown have greater effects on the flow stress than on the work hardening rate, the differential between the two effects is less in the case of silicon and phosphorus than for the other solutes (manganese and nitrogen). Thus, for a given increase in flow stress, the loss of uniform strain (or stretch formability) is least for those elements which produce the larger increase in work hardening rate, i.e. silicon and phosphorus.

The use of microalloying additions as grain refining agents, although having little effect on maximum uniform strain,[31] effectively inhibits grain growth during annealing, and thereby prevents the development of favoured crystallographic textures.

Microalloy additions however, have found applications in two of the more recent developments of cold rolled and annealed thin strip. These are the interstitial free steels and dual phase steels.

7.6.2 Interstitial Free Steels

The presence of interstitial elements has profound effects on the properties of steel. It is the mere presence of the interstitial atoms, carbon and nitrogen, that results in the discontinuous yield behaviour of steel. The solubility of carbon in ferrite that is in equilibrium with cemenite is given by

$$\log[C] = -2710/T + 1.07 \tag{7.22}$$

where [C] is the dissolved carbon content (wt%) and T is the absolute temperature, K.

The maximum solubility of carbon in ferrite at the eutectoid temperature is approximately 0.02wt%C, and this decreases to extremely low values of the order of 10^{-8}wt%C at room temperature. There is a strong bond between carbon (or nitrogen) atoms and the dislocation core (0.5eV or 0.8×10^{-19}J), and Honeycombe[45] has pointed out that the dislocation core should be saturated with carbon atoms (1 carbon atom per atom row of the dislocation core) at all temperatures below about 700K. With a dislocation density of some $10^8\,cm^{-2}$, which is fairly typical of a well annealed ferrite, the carbon content required to saturate all of the dislocations is

Table 7.3 Effects of solutes on flow stress and work hardening rate at a true strain of $\varepsilon = 0.2$

Solute	Increase in flow stress at $\varepsilon = 0.2$ MPa/wt%	Increase in W.H.R. at $\varepsilon = 0.2$ MPa/wt%
Mn	68	23
Si	148	115
P	862	554
N	4004	1509

only of the order of 2×10^{-7}wt%C. Given the binding energy, U, of 0.5eV(0.8×10^{-19}J), the matrix carbon fraction, C_0, that is in equilibrium with the carbon fraction, C, in the dislocation core sites, when the core is saturated, i.e. $C = 1$, can be obtained from

$$\ln(C/C_0) = U/kT \tag{7.23}$$

where k is Boltzmann's constant $= 1.38 \times 10^{-23}$JK^{-1} and T is the temperature (K).

Dislocation core saturation at ambient temperatures requires a matrix carbon content of 10^{-8}wt% which is approximately that given above for the solubility of unstressed cementite in ferrite. Thus, even if the interstitial carbon content attains the true equilibrium value at room temperature, discontinuous yielding would be observed. Hudd[46] has pointed out that the attainment of equilibrium levels of carbon in ferrite is difficult, and that even in well annealed steels the dissolved carbon contents are a few orders of magnitude higher than the equilibrium level, thus ensuring saturated dislocation cores and discontinuous yielding. A major difficulty in this area of study is the absence of techniques capable of measuring these extremely low levels of interstitials.

Although not explicitly stated in the literature, the ferrite–cementite equilibrium should operate with the true interstitial carbon in the b.c.c. ferrite lattice as the carbon concentration variable; the carbon concentration on the dislocations and the carbon concentration on grain boundaries should also relate to the true interstitial carbon content of the b.c.c. ferrite. These effects lead to some variation in the 'dissolved' carbon content in equilibrium with cementite. If the carbon present as atmospheres and on grain boundaries is included in the 'dissolved' carbon content, then it would increase with increasing dislocation density and refinement of the grain size.

These observations for the behaviour of carbon in ferrite also apply to nitrogen in ferrite, the main difference being that the solubility of the stable iron nitride (Fe_4N) is considerably higher than that of cementite, Fe_3C. This increased solubility, coupled with the generally lower nitrogen contents of commercial steels (usually in the range 0.003–0.012wt%N), can often result in a dominant proportion of nitrogen remaining in solution in the ferrite, with dislocation core saturation and discontinuous yielding as natural consequences.

As pointed out in Chapter 2, the incidence of discontinuous yielding produces Luders bands, and in lightly deformed areas of pressings the Luders bands and the Luders fronts cause unsightly markings that are not hidden by subsequent coating and painting processes. The traditional method of overcoming the discontinuous yield phenomenon and the formation of 'stretcher–strain' markings in pressings is to subject the final strip to a 'pinch–pass'. This involves a cold rolling reduction of about 2% strain, prior to cold forming. This procedure introduces new unlocked dislocations into each of the grains in the structure, and results in continuous yielding behaviour. In the presence of a significant interstitial content, the interstitial carbon and nitrogen atoms are attracted by the elastic strains surrounding the dislocations, and ultimately arrive at the dislocation core. The theoretical mechanisms and kinetics of this process are well established,[47] and

observations of the times required for the discontinuous yield point to return is in accord with the flow of interstitial atoms to the dislocation core.

The return of the yield point due to the segregation of carbon and nitrogen atoms to the dislocation cores is known as *strain ageing*. In the presence of an abundance of interstitial atoms, the return of the yield point is followed by an increase in the yield strength and an increase in the tensile strength of the material, and this is defined by the term *strain age-hardening*. Strain age-hardening is accompanied by an increase in the impact transition temperature of the steel and this is termed *strain age embrittlement*.[48] The interstitial levels associated with strain age-hardening and strain age embrittlement are far in excess of that required to give saturated atmospheres, and it has been suggested that carbide precipitation occurs on the dislocations, adding to the dislocation locking and providing significant obstacles for mobile dislocations, i.e. provides an element of dispersion strengthening.

The kinetics of strain ageing are highly dependent upon the interstitial content, and the return of the yield point is accelerated as the interstitial content increases, ranging from months at low interstitial contents (2×10^{-4} wt%) down to a few hours at high interstitial contents (10^{-2} wt%). This variation in the kinetics of strain ageing results in the concept of a 'shelf life' for annealed and pinch passed strip. If the interstitial content is low, as for example where the nitrogen is fixed as a stable alloy nitride, e.g. TiN or AlN, and the interstitial carbon content is low due to the annealing cycle, then the pinch-passed strip can be held in stock for a few months before pressing without the risk of strain ageing and the attendant formation of stretcher strain markings on the pressing.

It is clear from the foregoing discussion that an alloying addition which forms very stable carbides and nitrides and which would virtually eliminate interstitial carbon and nitrogen in the ferrite, would also eliminate the discontinuous yield phenomenon. Whilst low-ageing steels have been produced for many decades by using aluminium, titanium or boron, to form a stable nitride, the extension of this idea to form a stable carbide is relatively recent. One of the features of these modern 'interstitial free' steels is their extremely low carbon and nitrogen contents. The amount of carbide/nitride former that needs to be added has to exceed the stoichiometric ratio required to form the carbide and nitride. When the carbon and nitrogen content of the steel is limited, then smaller alloying additions are required. The carbon and nitrogen contents of modern interstitial free steel are each limited to about 0.003wt%. It is clear that such low carbon and nitrogen steels require the sophisticated steel refinement methods involving a vacuum treatment during secondary steelmaking, but it is equally clear that the amounts of titanium and niobium that are required to stabilise the carbide and nitride phases are correspondingly small. The development of these interstitial free steels emphasises a new and important role for microalloys in low carbon strip steels, i.e. the 'gettering' or stabilising effect in eliminating interstitial carbon and nitrogen. The gettering effect of titanium and niobium have been used in austenitic stainless steels since the mid-1930s, but their application to plain carbon steels in this way is relatively new.

Whilst it is tempting to assess the low interstitial contents of microalloyed steels

on the basis of their solubility products in ferrite, and to compare this with the solubility of cementite (Fig. 7.34), there is no clear indication of the final solute contents after slowly (or rapidly) cooling from the annealing temperature. In the case of microalloy carbides or carbo-nitrides, the mobility of the substitutional solute becomes extremely low at temperatures below about 400–500°C, so that the maximum solute may be somewhere between that predicted by the annealing temperature and that at 400°C. The carbon content of the ferrite may then be dictated by the solubility of cementite.

The composition of the modern interstitial free steels is tailored to give an essentially pure iron,[48] with a minimum solute content. As pointed out by Hudd,[46] high levels of the preferred (111) orientation, and therefore plastic anisotropy, are observed when titanium and niobium levels are near or just in excess of that required for the stoichiometric combination with carbon and nitrogen to form the carbo-nitride. Excesses of interstitials result in low values of the mean plastic anisotropy ratio. These effects are similar to those previously observed for manganese and sulphur in aluminium-killed batch annealed steels, where the maximum values of preferred orientation and plastic anistropy were associated with near stoichiometric compositions, thereby avoiding excesses of manganese or sulphur in the form of solutes; the precipitation of MnS in these steels leaves a pure iron matrix at least as far as manganese and sulphur are concerned. Stoichiometric additions of aluminium in these same steels, with respect to oxygen and nitrogen,

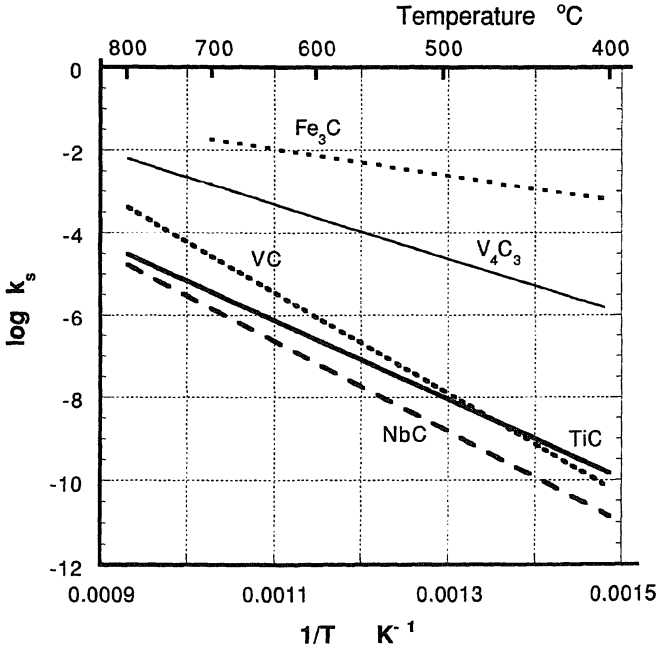


Fig. 7.34 The solubilities of microalloy carbides in ferrite compared with the solubility of cementite (Fe_3C).

also keep aluminium and nitrogen solute levels low and are conducive to high levels of plastic anisotropy. The minimisation of solutes in modern continuously annealed interstitial free steels is also augmented by a minimisation of the fraction of second phase particles by control of the overall impurity levels in the steel. A typical commercial composition for an interstitial free steel is as follows:[49]

Element	Wt%
C	0.003
N	0.003
Si	0.01–0.60
Mn	0.10–0.20
S	0.005
P	0.070
Ti	0.010
Nb	0.020
B	0.003
Al	0.03

The very low interstitial levels (C and N) require low stoichiometric levels of titanium and niobium. These steels are obviously re-phosphorised to increase the strength level, and may be re-siliconised to further increase the strength. The manganese content is limited, and a natural consequence of this is that titanium sulphide is formed in preferrence to manganese sulphide. In recent studies,[49,50] the titanium sulphide has been found to transform, at least partially, to titanium carbo-sulphide, $Ti_4C_2S_2$, at temperatures below about 1200°C. In fact, extremely complex precipitates comprising TiN, TiS, $Ti_4C_2S_2$, and (Ti,Nb)(C,N) composite particles have been observed in the hot rolled steel.

Yoshinaga *et al.*[51] have studied the solubilities of TiS and the carbo-sulphide, $Ti_4C_2S_2$, in austenite, and have suggested the following equations

$$\log[Ti][S] = -3,252/T - 2.01 \tag{7.24}$$

$$\log[Ti][C]^{1/2}[S]^{1/2} = -5,208/T - 0.78 \tag{7.25}$$

Whilst these equations are commensurate with a change in the equilibrium phase at some temperature in the austenite range, it is clear that these temperatures will be highly dependent upon the composition of the steel, bearing in mind the role of nitrogen in controlling the level of available titanium, and the roles of titanium and niobium contents in controlling the free carbon.

It is clear that these interactions are highly complex, and the complexity is heightened by the extremely low levels of both interstitial and microalloy solutes. Whilst the partitioning of elements such as carbon between interstitial, dislocation and grain boundary sites can generally be ignored in the majority of steels, the low solubilities of microalloy compounds in ferrite, and the low levels of carbon and nitrogen in these 'interstitial free' steels, could make such considerations important, and still offers an interesting area for original research.

The partitioning of carbon (and/or nitrogen) atoms to dislocations and grain boundaries has two important effects in 'interstitial free' steels, concerned with *bake hardening* and *low temperature embrittlement.*

Bake hardening relates to the accelerated strain ageing[52] that occurs in cold worked parts that, after painting, are cured at a temperature in the range 140–200°C. This phenomenon is capable of increasing the strength of the cold formed component, thereby improving the dent resistance of the part (this is of particular relevance in car body applications). In truly interstitial free steels there is no bake hardening phenomenon, as there are no interstitial carbon or nitrogen atoms available in the ferrite to form the atmospheres that would lock the dislocations. The bake hardening treatment does not affect the continuous yielding behaviour observed in interstitial free steels. If, however, the annealing temperature of the cold worked interstitial free steels is increased and results in a slight dissolution of the carbo-nitride, then the interstitial atoms form atmospheres on baking, and give a useful increase in strength. The level of interstitial however must be controlled to prevent natural ageing of the annealed strip prior to cold forming the part. Excessive interstitial levels will result in the rapid formation of atmospheres on the dislocations in the annealed strip, which will then give discontinuous yielding and the possibility of stretcher strain markings. Takechi[49] has suggested that a dissolved carbon or nitrogen level of about 5 ppm is low enough to avoid natural ageing of the annealed strip in any reasonable period of time, whilst still being capable of raising the yield strength (0.2% Proof stress) by about 40 MPa on bake hardening. Although much higher bake hardening responses can be obtained by annealing to give higher levels of dissolved carbon or nitrogen, these are accompanied by rapid natural ageing and large Luders' extensions, and must therefore be avoided. It is interesting to observe that Takechi recommends a dissolved carbon level of 5 ppm rather than an interstitial level of 5 ppm. Finally, the magnitude of the bake hardening effect is increased by decreasing the ferrite grain size (Fig. 7.35). This is in accord with the view that the magnitude of k_y in the Hall–Petch equation has a much higher value when the dislocations are locked by saturated atmospheres than is observed in the presence of 'free' dislocations, i.e. dislocations without interstitial atmospheres.

Low temperature embrittlement has been observed in interstitial free steels and is associated with brittle intergranular fracture following cold working operations. This has been attributed to the lack of carbon or nitrogen atoms in grain boundary sites due to the extremely low interstitial levels. This allows other horophile impurities (n.b. a horophile impurity is one which shows a marked tendency to occupy grain boundary sites rather than the normal substutitional or insterstitial lattice sites) such as phosphorus to partition between substitutional and grain boundary sites, thereby giving an intergranular embrittlement which is far greater than the solid solution embrittling effect of phosphorus. Tither *et al.*[53] have suggested that niobium is also horophile in nature, and that niobium atoms are selectively partitioned to grain boundary sites in preference to phosphorus atoms. In this way, Ti–Nb interstitial free steels, with an excess of niobium atoms, exhibit a freedom from low temperature intergranular embrittlement that is not observed in near stoichiometric Ti interstitial free steels. This implies that phosphorus atoms will lower the grain boundary cohesive forces, but niobium will not.

The property requirements of interstitial steels are thus complex in that they fulfil a role requiring the highest levels of formability and freedom from natural

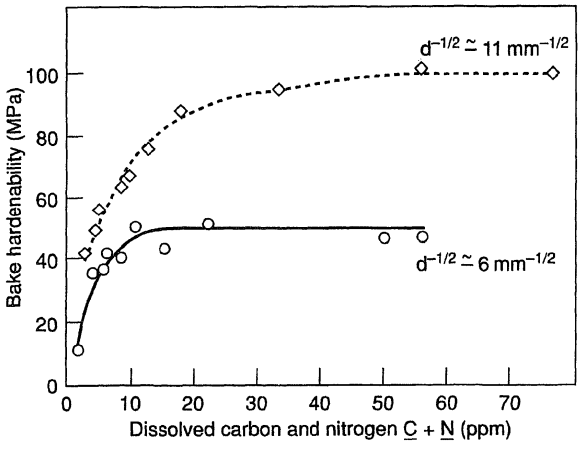


Fig. 7.35 The effect of ferrite grain size on the bake hardening response of interstitial freee steels. After Takechi.[49]

strain ageing coupled with an adequate level of strength in the final component. Desirable properties of these interstitial free steels are

Plastic Anistropy, r_m	> 2.0
% Elongation, El	> 50.0%
Luders' extension	< 0.4%
Ageing index, AI	0–40 MPa
Yield strength	200–250 MPa
Tensile strength	350–450 MPa

These steels have been developed to take advantage of the modern continuous annealing lines that are a feature of modern strip production. The extra deep drawing quality of low carbon steel aluminium-killed (AK) strip, obtained by using high finish rolling temperatures, low hot band coiling temperatures and slow heating rates in the batch annealing process, would not develop high levels of plastic anistropy at the high heating rates involved in continuous annealing.[46,54] Thus the introduction of the continuous annealing process required the development of the interstitial free steels with their virtual insensitivity to the heating rate in the annealing process.

7.6.3 Dual Phase Steels

In the search for high strength steels of improved formability, workers at the Ford Motor Company[55–58] were examining a range of high strength steels. Their interest was stimulated by the need for weight savings in automobiles whilst maintaining or improving the safety aspects. The properties of particular interest were fatigue resistance for improved component life, crushing resistance for energy absorption in vehicle damage (both of which were equated with tensile strength), and a high level of uniform elongation in order to confer high levels of formability together with reasonable levels of residual ductility in the cold formed

component. In addition to the conventional microalloyed steels, cold rolled and recovery annealed steels, and dual phase steels were examined. In recovery annealed steels, the major strengthening mechanism derives from the retained cold deformation, present as a well defined subgrain structure. The dual phase steels have a microstructure comprising a polygonal ferrite matrix together with dispersed islands of high carbon martensite. Initially, the development work was carried out on hot band gauges (3–5 mm thick strip), the microstructure being developed by heating to an intercritical temperature (i.e. between A_{r1} and A_{r3}), followed by quenching. Such a simple heat treatment is obviously applicable to a wide range of product types, but is particularly suited to the continuous annealing of thin strip (cold rolled gauges below 2 mm in thickness) where quenching facilities can be introduced immediately following the hot zone.

The fraction of high carbon austenite that is formed is obviously related to the intercritical temperature, as shown in Fig. 7.36. Simple lever rule calculations show that the proportion of austenite increases, and the carbon content of the austenite decreases, as the temperature is increased in this range. In plain carbon steels, the amount of austenite will be dependent on the intercritical temperature and the carbon content of the steel, whilst the carbon content of the austenite will depend only on the intercritical temperature. The introduction of alloying elements such as manganese or chromium will change the proportion of austenite and the carbon content of the austenite at any given annealing temperature. The proportion of martensite in the microstructure after cooling from the intercritical temperature is dependent upon the proportion of austenite, the cooling rate from the intercritical temperature, and the steel composition. At slow cooling rates and low alloy contents the austenite will decompose to give high temperature transformation products such as ferrite and pearlite. As the cooling rate or alloy content is increased, the transformation characteristics of the austenite change, and at some critical cooling rate/alloy content, the high temperature decomposition of austenite will be inhibited, and the austenite decomposition product will be entirely martensitic. The use of low carbon steels (0.10–0.15wt%) will usually allow

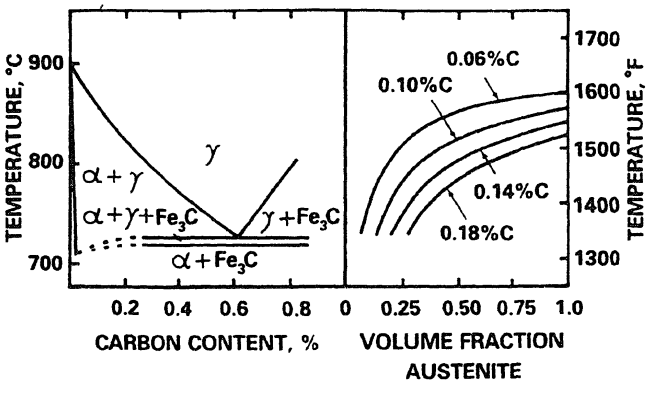


Fig. 7.36 The effects of carbon content and intercritical annealing temperature on the martensite content of dual phase steels. After Repas.[106]

some ferrite formation at all but the highest cooling rates and the sensitivity of the fraction of martensite to variations in intercritical annealing temperature is thereby reduced. Inter-critical annealing just above the A_1 temperature gives a high carbon austenite that does not allow ferrite formation. Intercritical annealing at higher temperatures gives more austenite of a lower carbon content so that some ferrite is formed during the cooling transformation and reduces the austenite content to a lower level with an associated higher carbon content.

The essential findings of Rashid and Davies and their co-workers are summarised in Fig. 7.37.[59] Increases in tensile strength attained by increased martensite in dual phase steels, increases in retained cold work in recovery annealed steels and conventional grain refinement and dispersion strengthening in microalloyed steels, all lead to a reduction in elongation as measured in the tensile test. However, the loss of ductility with increasing tensile strength is much less in the case of dual phase steels than in microalloyed steels, and these in turn show a higher ductility level at a given tensile strength than is shown by the recovery annealed steels. The attractive combination of a high tensile strength coupled with a high elongation led to studies of the mechanism by which dual phase steels are able to maintain reasonably high levels of elongation, and to alternative methods for the production of the dual phase microstructure.

As discussed in Chapter 2, the onset of plastic instability in the tensile test is controlled by the Considere Criterion, and indicates that necking will commence when the true flow stress, σ_t, exceeds the work hardening rate, $d\sigma/d\varepsilon$.[60] Strictly, this defines the limit of uniform tensile elongation, but, obviously, the localised strain in the neck of the tensile specimen after maximum load will contribute to the overall elongation measured over the original gauge length. The latter contribution is related to the reduction in area[61] and to a different (though possibly related) set

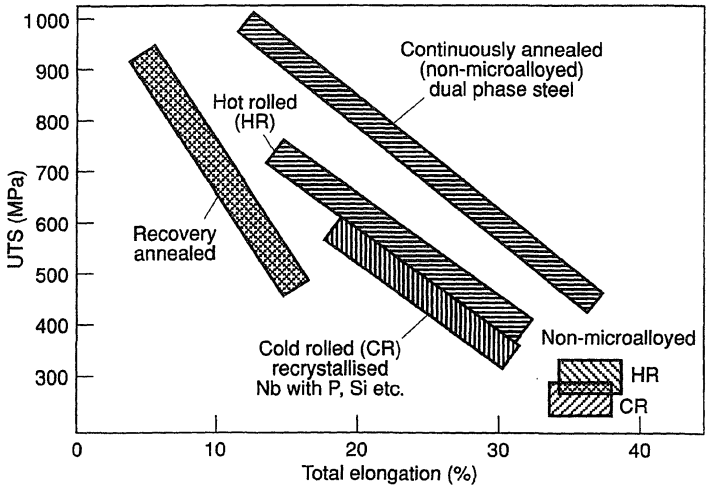


Fig. 7.37 The effect of increased strength on the tensile elongation of dual phase, microalloyed, and recovery annealed steels. The dual phase steels show the highest residual tensile elongation at any given tensile strength. After DeArdo *et al.*[107]

of variables. In the plain carbon and microalloyed steels, the flow stress can be changed, but the work hardening rate is little affected, giving a reduction in elongation with increasing strength.

Although the grain size and precipitation strengthening mechanisms may cause slight increases in work hardening rate, these effects are generally very small. Morrison[62] showed that although the n and k values of the Ludwik–Hollomon equation

$$\sigma = k\varepsilon^n$$

varied quite strongly with grain size, the observed levels of work hardening, $d\sigma/d\varepsilon$, showed little effect.

In recovery annealed steels the strengthening mechanism is predominantly due to the dislocation density introduced during the cold working operation prior to the recovery anneal. The effect of increased cold working, as evidenced directly from the true stress–true strain curve, is to reduce the subsequent work hardening rate dramatically, thus giving the lowest levels of elongation in Fig. 7.37. The dual phase steels clearly give higher elongations at a given tensile strength than are attained in either the conventional microalloyed steels, with ferrite–pearlite structures, or the recovery annealed steels.

The discontinuous yielding phenomenon is irrelevant to the major plastic instability, due to the wide differences between the Luders' strain and the strain to maximum load in virtually all commercial steels. A major feature of dual phase steels is that they exhibit continuous yielding behaviour, possibly because of the high level of internal stress developed when some 10–15% of austenite transforms at low temperatures to martensite in the matrix of ferrite. Certainly a significant dislocation array is formed in the ferrite around the martensite islands (Fig. 7.38), indicating residual stress levels of the order of the yield strength of the ferrite.

Detailed observations of the strain distribution between the ferrite and martensite phases were made by Balliger and Gladman[63] who showed that the martensite islands in the ferrite–martensite aggregate remained undeformed until the specimen strain greatly exceeded the instability strain (Fig. 7.39 (b) and (c)). The ferrite becomes severely deformed and exhibits severe flow patterns around the martensite islands (Fig. 7.40). This behaviour is unlike that seen in ferrite–pearlite steels, where the pearlite regions suffer the same plastic strain as that applied to the specimen as a whole (Fig. 7.39 (a)).

Theoretically, the deformation of dual phase steels can be represented by the strength and work hardening model of Ashby,[64, 65] which describes the change in flow stress due to the presence of hard undeformable second phase particles in a ductile matrix. Ashby envisaged a plastic shell forming around the particles and expanding outwards as straining proceeds. The main prediction of the Ashby theory is that true stress, σ, can be related to true strain, ε, by

$$\sigma = \sigma_0 + kG(bf_m\varepsilon/0.41d_m)^{1/2} \tag{7.26}$$

where σ_0 is a constant for a given material, k is a constant ($\approx$1), G is the shear

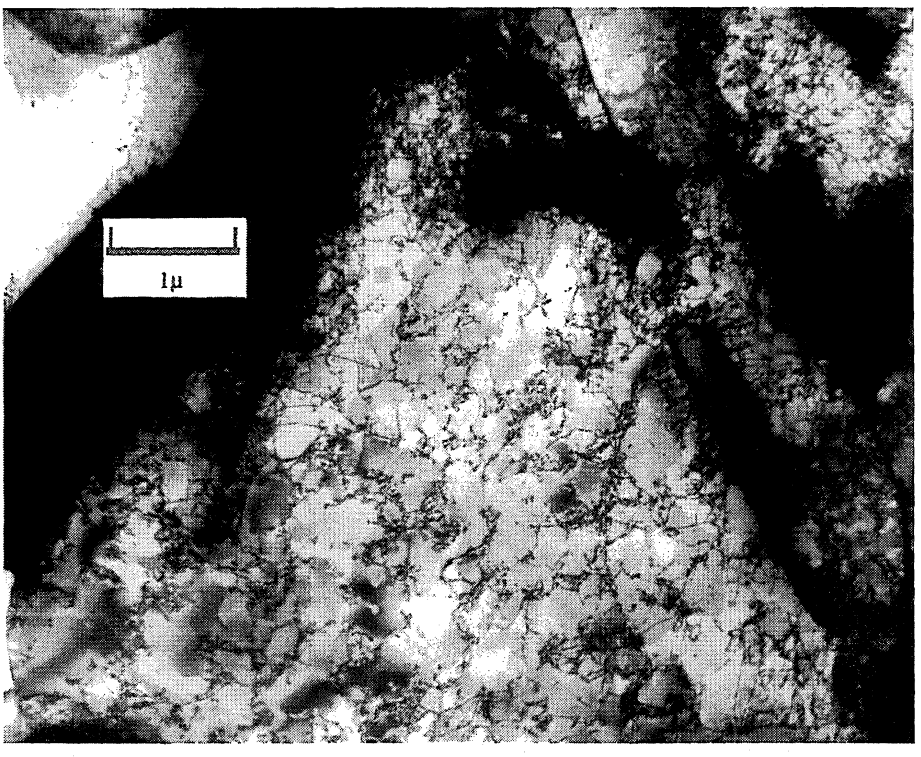


Fig. 7.38 The formation of martensite in a matrix of ferrite causes a high local dislocation density, high residual stresses, and continuous yielding. Transmission electron micrograph. After Balliger and Gladman.[63]

modulus of the matrix (82 400 MPa), b is the Burger's vector of the matrix dislocations (0.247×10^{-6} mm), f_m is the volume fraction of martensite and d_m is the average martensite island diameter, mm.

The work hardening rate may simply be obtained by differentiation of Equation (7.26) to give

$$d\sigma/d\varepsilon = 0.78kG(b/\varepsilon)^{1/2}(f_m/d_m)^{1/2} \tag{7.27}$$

The work hardening rate is seen to be proportional to the square root of the volume fraction of martensite, and inversely proportional to the square root of the mean diameter of the martensite islands. Although the experimentally observed work hardening rates showed a good correlation with the function $(f_m/d_m)^{1/2}$ (Fig. 7.41), the proportionality constant between work hardening rate and $(f_m/d_m)^{1/2}$ was significantly less than that expressed in Equation (7.27) by a factor of almost two, and, unlike the theoretical expression, showed a significant intercept. Subsequently, Lanzillotto and Pickering[66] invoked the extended theory of work hardening due to Brown and Stobbs,[67] which took account of the long range internal stresses that develop and which are directly related to the volume fraction

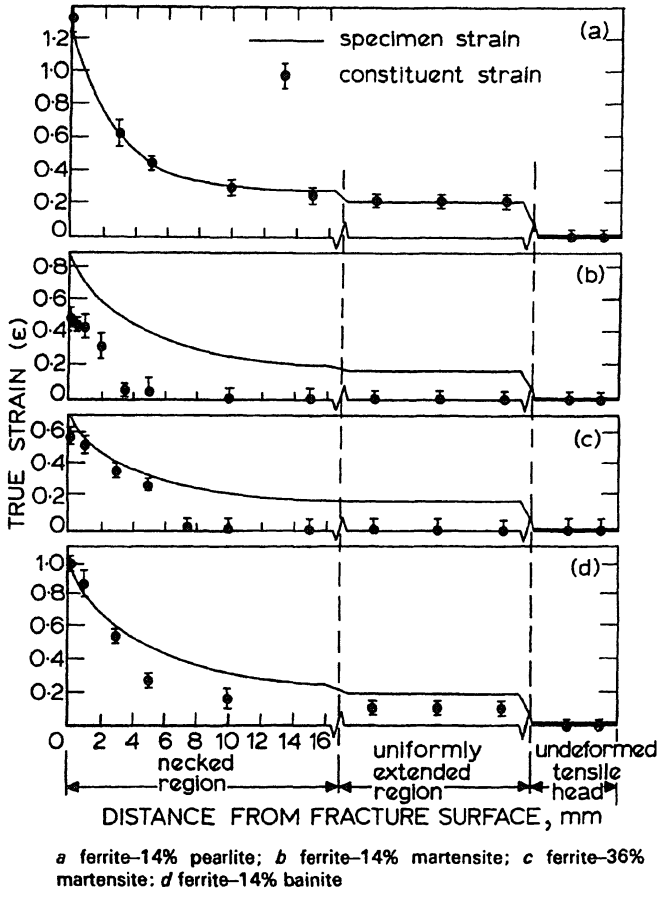


Fig. 7.39 Distribution of strain between the microstructural constituents in (a) a ferrite–pearlite steel with 14% pearlite; (b) a dual phase steel with 14% martensite; and (c) a dual phase steel with 36% martensite. After Balliger and Gladman.[63]

of martensite. The corresponding equations developed by Lanzillotto and Pickering were

$$\sigma = \sigma_0 + 63.9\varepsilon^{1/2}(f_m/d_m)^{1/2} + 36.8\varepsilon^{1/2}(f_m^2/d_m)^{1/2} \tag{7.28}$$

$$d\sigma/d\varepsilon = 63.9/2\varepsilon^{1/2}(f_m/d_m)^{1/2} + 36.8/2\varepsilon^{1/2}(f_m^2/d_m)^{1/2} \tag{7.29}$$

These equations showed excellent agreement with the observed work hardening rates at martensite levels of $f_m = 0.2$ and 0.3 (Fig. 7.42), but the overall results suggested that the work hardening rate has a significant value at $f_m = 0$, as would be expected from a steel with a ferrite or ferrite–pearlite structure but which is not predicted by Equations (7.27) and (7.29). Nevertheless, both approaches show quite clearly that the work hardening rate is increased by

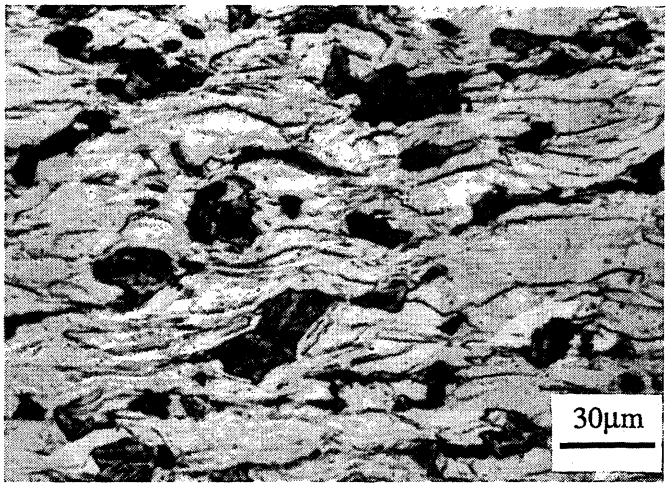


Fig. 7.40 A cold worked dual phase steel showing the severe flow patterns in the ferrite caused by the presence of the hard martensite islands. Optical micrograph (× 400). After Balliger and Gladman.[63]

(i) increasing the volume fraction of martensite; and
(ii) decreasing the martensite island size.

The significant increases in work hardening rate resulting from the hard non-deforming martensite islands produces an improved elongation in the tensile test as illustrated in Fig. 7.43. Similar increases in the flow stress produced without a corresponding increase in work hardening rate would give uniform elongations shown by the path A–D–E, compared with the path A–B–C for the dual phase steel. It is also interesting to note that refinement of the martensite island size at a given martensite content not only increases the work hardening rate but also increases the uniform elongation at a given tensile strength (Fig. 7.44).

Control of the martensite fraction is obtained through the carbon content of the steel, the intercritical annealing temperature and the cooling rate, as explained previously. Control of the martensite island size is dependent upon the coarseness of the prior structure. On heating into the intercritical temperature range, re-austenitisation starts at the prior pearlite regions, and, when the heating rate is high, at the ferrite grain boundaries, although on heating to intercritical temperatures it is the carbide distribution that dominates in controlling the austenite island size and the ensuing martensite island size. Very fine pearlite regions in the ferrite–pearlite structure, prior to intercritical annealing, result in very fine austenite particles at the intercritical temperature, and therefore fine martensite island sizes in the final dual phase steel strip. It is in the control of the prior hot band structure that microalloys are important to the properties of dual phase steels. All of the technical expertise in producing grain refined hot rolled strip is directly relevant to the production of dual phase steels. Controlled rolling processes that produce fine grained austenite will also produce a fine ferrite grain

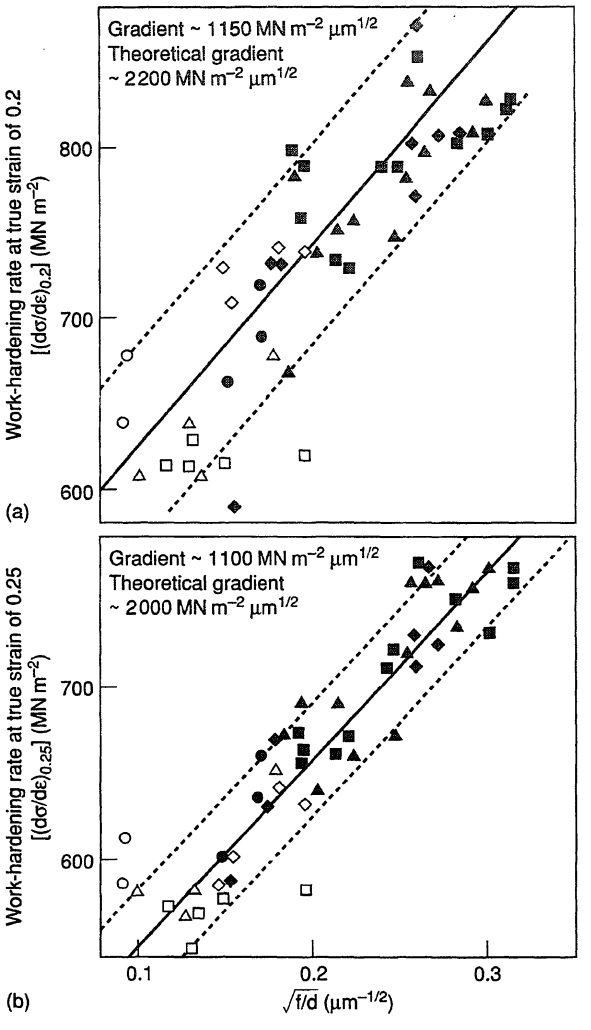


Fig. 7.41 The effects of martensite fraction and martensite island size on the work hardening rate. The work hardening rate is proportional to the function $(f_m d_m)^{1/2}$ as indicated by Equation (7.27). After Balliger and Gladman.[63]

size and a fine pearlite distribution. Microalloy additions that encourage a fine ferrite–pearlite structure will also be conducive to the production of a small martensite island size. Commercial dual phase steels include a grain refining additive in order to control the prior structure, and are processed, at the hot rolling stage, to develop the fine structure.

The fraction of martensite is dominant in controlling the tensile strength, and the refinement of the martensite island size mainly contributes to improved ductility. The general levels of tensile strength and ductility attained are shown in Fig. 7.45, which also indicates the advantages to be attained from treatments aimed at

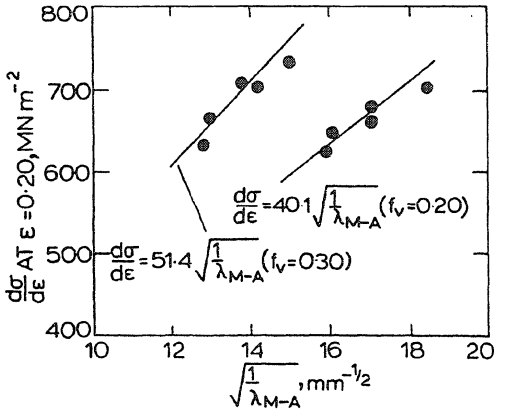


Fig. 7.42 The effects of martensite fraction and martensite island size on the work hardening rate (after Lanzillotto and Pickering[66]) using Equation (7.29).

producing a fine prior structure. These latter treatments produce high levels of elongation at a given tensile strength level. A further benefit of the martensite island refinement is the associated increase in the fracture strain. Refinement of the martensite island size results in a higher void nucleation strain, the major voids being formed in these steels by cracking of the martensite islands, as shown by Balliger.[68]

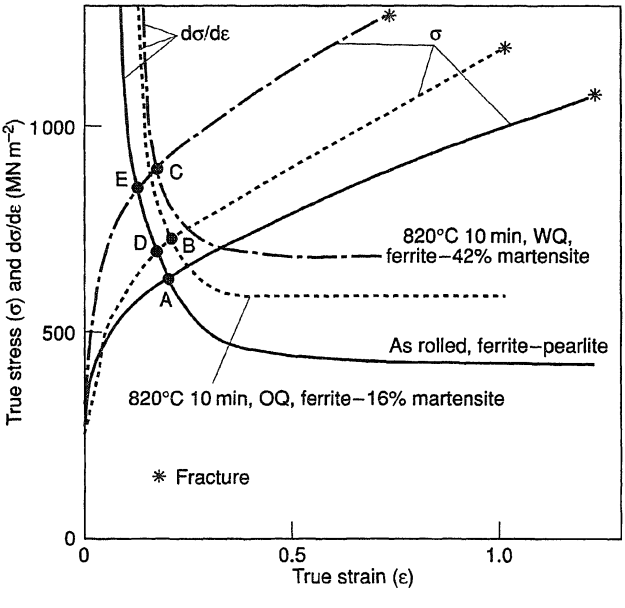


Fig. 7.43 The effects of work hardening rate on the maximum uniform elongation during tensile straining. After Balliger and Gladman.[63]

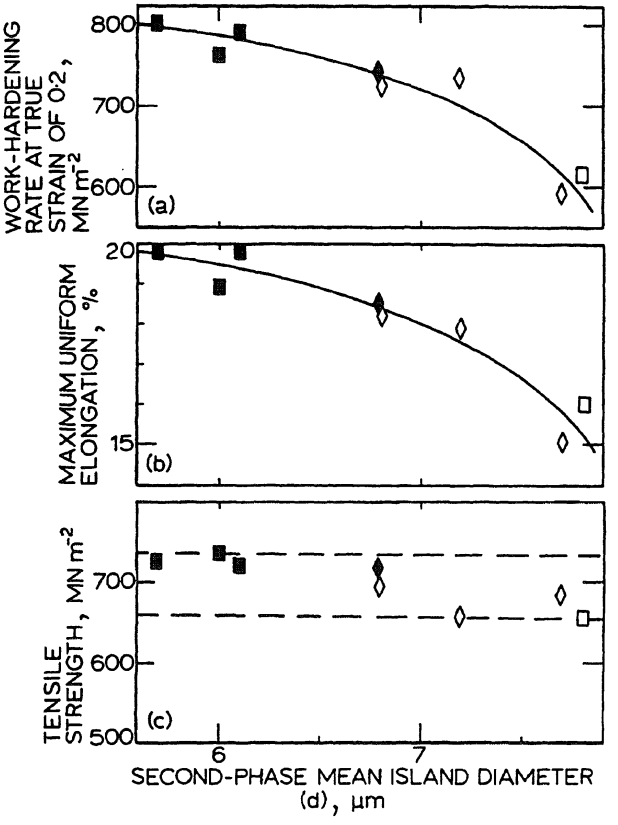


Fig. 7.44 The effects of refining the martensite island size on the tensile elongation at a given tensile strength. After Balliger and Gladman.[63]

An important feature of dual phase steel is the alloy content, which must be adequate to prevent transformation of the intercritical austenite to pearlite. A continuous annealing furnace with a fast quenching facility would obviously require little in the way of alloying, but in the absence of fast quenching, additions of silicon and manganese are made in order to ensure that the austenite will transform to martensite. Additions of 1wt% Si or more are commonly made (to take advantage of the solid solution effects of this element), and manganese levels of 1.5wt% Mn or more are made in these low carbon steels (approximately 0.1% C). These additions inhibit the formation of pearlite during cooling in the intercritical annealing treatment. The relationship between the critical cooling rate, R_c (°C s^{-1}), for martensite formation and the chemical composition of the steel is given by Abe[43] as

$$\log R_c = 5.36 - 2.36(\text{wt\%Mn}) - 1.06(\text{wt\%Si}) - 2.71(\text{wt\%Cr}) - 4.72(\text{wt\%P}) \quad (7.30)$$

The relative effects of the solute elements commonly found in the intercritically

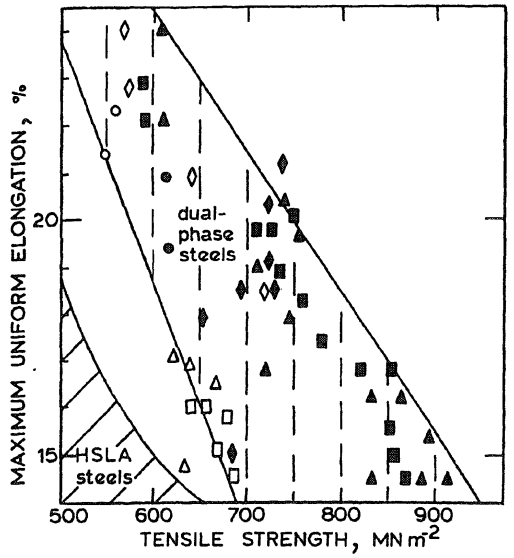


Fig. 7.45 The properties of dual phase steels. The benefits of a fine martensite island size to the tensile elongation are reflected over the whole range of martensite fractions. (Filled symbols show finer structures.) After Balliger and Gladman.[63]

annealed steels on the critical cooling rate are clearly shown. The dual phase structure will develop at any cooling rate equal to, or greater than, R_c.

The effects of alloying on the decomposition of high carbon austenite, present as the minor phase in low carbon steels, led to an alternative process route for dual phase steel in the hot-rolled condition.[69,70] The addition of 0.6wt% Cr and 0.4wt% Mo to a 0.06wt%C–1.3wt%Mn–1wt%Si steel so retarded the pearlite transformation that, at the slow cooling rates of hot band, coiled at moderate temperatures, a predominantly ferrite microstructure was developed containing an appropriate proportion of martensite islands. These dual phase steels showed exactly the same combinations of tensile strength and elongation as those produced by the intercritical annealing route, but appear to have found little application, possibly because of the alloying costs.

The dual phase steels have been described here as ferrite–martensite aggregates, but the decomposition of the isolated austenite regions may result in a mixed martensite/austenite (M/A) structure after cooling. The retained austenite in these regions is however likely to be highly unstable, so that the application of even a small amount of cold deformation will result in the strain induced transformation of austenite to martensite, and at the point of plastic instability the MA regions are substantially martensitic. In more highly alloyed steels, the austenite may be retained in more substantial amounts, and it is claimed[49] that the strain of transformation and the resultant hardening by martensite during cold forming will add substantially to the total elongation of these steels.

The dual phase steels have been developed to extend the range of strength levels in formable cold rolled and annealed strip to cover the tensile strength range 800–

1000 MPa, and although their level of formability will not allow the complex deep pressing operations that are permitted by interstitial free steels, they have an important place in the development of lightweight high energy absorbing automobile steels. Bumper reinforcement and door impact beams are particular applications for these high strength strip materials.

7.7 MEDIUM AND HIGH CARBON STEELS

The successful application of microalloying additions to low carbon steels was eventually extended to medium and high carbon steels. The solubility limits of niobium carbide described in Chapter 3 quite obviously favour the application of niobium to low carbon steels. High carbon levels restrict the dissolution of niobium carbide in austenite. The same is true of titanium, though not of vanadium. Further, the strength levels attainable in high carbon steels, in either the quenched and tempered condition or the normalised condition, was thought to be adequate. Also, the higher carbon steels were not, in most applications, subjected to joining by welding. An interesting and apparently unrelated development, however, was to change the approach to higher carbon steels. Crankshafts in the internal combustion engine had traditionally been manufactured from medium carbon quenched and tempered low alloy steels having high levels of tensile strength (1000 MPa), fatigue resistance, and toughness. Evolutionary changes in engine design had resulted in a considerable shortening of the piston movement and therefore 'throw' of the crankshaft. Materials of lower toughness could therefore be considered as cheaper alternatives to the quenched and tempered medium carbon low alloy steels. Austempered ductile iron (ADI) crankshafts could be cast and heat treated, thereby eliminating the cost of intermediate forging stock fabrication and forging of the crankshaft. The search for a cheaper route for the manufacture of a steel crankshaft then began, and attention was directed to a medium carbon microalloyed steel which would develop the required strength level (about 1000 MPa) upon air cooling from the forging heat, thereby eliminating the cost of heat treatment, and eliminating the cost of reclaiming components distorted during quenching and tempering.

Other cost reduction activities were also taking place in high carbon wire, such as the elimination of costly lead-patenting treatments by the introduction of air-patenting. Both treatments produce a fine pearlitic struture, but the lead-patenting treatment produced finer structures and higher strength levels. The development of higher strength air-patented steels then ensued in order to provide the same high strength level as was obtained by lead patenting, but at a reduced cost.

These forces led to the development of a range of improved microalloyed steels which are now finding applications in a wide range of components. An account of the microstructure–property relationships of medium and high carbon ferrite–pearlite steels is given in this section, together with the application of the metallurgical principles to the product development.

7.7.1 Microstructure – Property Relationships in Higher Carbon Steels

As mentioned in Chapter 2, the predominant feature responsible for the strength of pearlite is the interlamellar spacing in the eutectoid structure. Gensamer *et al.*[71] showed the significant increase in strength attainable from the refinement of the interlamellar spacing, and suggested a negative linear relationship between the yield strength and the logarithm of the interlamellar spacing. Other workers have used either a simple inverse relationship between strength and spacing, or, more commonly, the reciprocal root relationship

$$\sigma_y = \sigma_0 + k_s s^{-1/2} \tag{7.31}$$

where s is the interlamellar spacing of the pearlite.

The functional relationship between the yield strength and the interlamellar spacing in a pearlitic microstructure, shown by Equation (7.31), is the same as that between yield strength and ferrite grain size in a ferritic microstructure. The strengthening coefficient, k_s, would not necessarily be expected to have the same value as k_y in the Hall–Petch equation, as s is the minimum ferrite path in the pearlite structure and is smaller than the average slip path in the interlamellar ferrite, whereas, depending upon the definition of d in the Hall–Petch equation, the d value is either equal to (for the mean linear intercept) or greater than (for the spatial grain diameter) the mean slip path length in the ferrite grain.

As in the case of the low carbon steels, the value of σ_0 in Equation (7.31) can be expanded to include solid solution terms and other terms can be added, as for example a precipitation strengthening term. However, such an equation would be relevant only to a fully pearlitic steel, whilst many of the commercial medium and high carbon steels have a ferrite–pearlite structure in which pearlite is the dominant phase. A simple law of mixtures would not seem appropriate in view of the negligible contribution of pearlite to the strength of low carbon steels with up to 25% by volume of pearlite.

Regression analysis on a wide range of medium to high carbon steels[72] has shown that the yield strength, σ_y, tensile strength, σ_T, and impact transition temperature, I, can be related to the compositional and microstructural variables by equations of the form

$$\sigma_y = f^n \sigma_\alpha + (1 - f^n)\sigma_p$$

where σ_y is the yield strength of the aggregate (MPa), f is the fraction of ferrite, σ_α is the yield strength of the ferrite (MPa), σ_p is the yield strength of the pearlite (MPa) and n is an index describing the non-linear contributions of the pearlite and ferrite.

In the case of yield strength and of tensile strength, the index was $n = 1/3$, indicating that the ferrite fraction contributes more to the yield and tensile strength than would be expected on a pro-rata basis. The impact transition temperature, on

the other hand, showed an index of $n = 1$, indicating a simple law of mixtures. The equations derived in this work were as follows:

$$\sigma_y = f^{1/3}[35 + 58.5(\%Mn) + 17.4d^{1/2}] + (1 - f^{1/3})[178 + 3.85s^{-1/2}] + 63.1(\%Si) + 425(\%Nf)^{1/2} \quad (7.32)$$

where σ_y is the yield strength (MPa), d is the mean linear intercept ferrite grain size (mm), s is the interlamellar spacing (mm) and f is the volume fraction of ferrite. The manganese, silicon and free nitrogen ($\%N_f$) contents are expressed as wt%.

The contributions of the ferrite and pearlite fractions are illustrated in Fig. 7.46, which is based not only on the variation in yield strength arising from the changes in the pearlite fraction, but also on changes in the grain size of the ferrite and interlamellar spacing of the pearlite as the pearlite fraction is increased. The latter changes are not obvious due to the changing contributions of the ferrite and the pearlite.

The tensile strength, σ_T, of the same steels was described by

$$\sigma_T = f^{1/3}[246 + 1142(\%N_f)^{1/2} + 18.2d^{-1/2}] + (1 - f^{1/3})[719 + 3.56s^{-1/2}] + 97(\%Si) \quad (7.33)$$

again indicating the roles of grain size in the ferrite and interlamellar spacing in the pearlite.

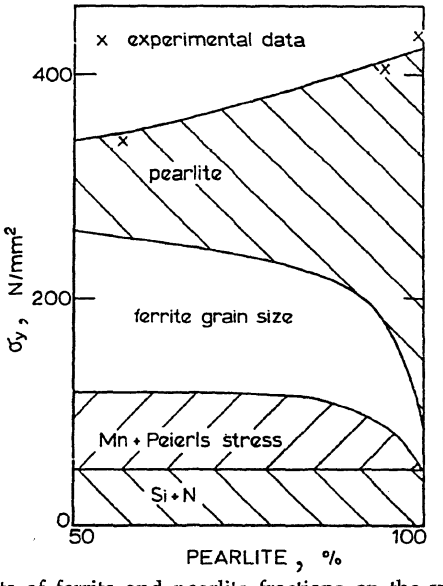


Fig. 7.46 The effects of ferrite and pearlite fractions on the yield strength of a ferrite–pearlite aggregate. The relationship shown also includes the progressive refinement of the ferrite grain size and the interlamellar spacing with increasing carbon (and therefore pearlite) content. After Gladman *et al.*[72]

The impact transition temperature, I, showed quite complex effects of the pearlite variables as indicated by

$$I = f[-46 - 11.5d^{-1/2}] + (1-f)[-335 + 5.6s^{-1/2} - 13.3p^{-1/2} + 3.48 \times 10^6 t] + 49(\%\text{Si}) + 762(\%N_f)^{1/2} \quad (7.34)$$

where I is the Charpy V-notch 50% F.A.T.T. (°C), p is the pearlite colony size (mm)and t is the carbide lamella thickness (mm).

The impact transition temperature in the higher carbon ferrite–pearlite steels can be changed by manipulation of either the ferrite or the pearlite variables, the pearlite colony size in pearlite steels having a similar effect to that of the grain size in fully ferritic steels. The combined effects of interlamellar spacing and carbide thickness indicate an optimum interlamellar spacing. Decreasing the interlamellar spacing reduces the carbide thickness, and as the impact transition temperature decreases linearly with decreasing carbide thickness, but increases as $s^{-1/2}$, then an optimum transition temperature can be obtained (Fig. 7.47), for a given carbon content in the pearlite. More dilute pearlites, obtained by alloying or by more rapid cooling, offer a means of further improving the impact transition temperature by decreasing the carbide plate thickness at a given interlamellar spacing.[72] Thus, a dilute pearlite should be capable of providing good combinations of strength and toughness. There has been little systematic exploitation of this aspect of medium and high carbon steels.

Equations (7.32)–(7.34) illustrate some of the factors that are involved in controlling the mechanical properties of medium carbon steels, and although many of the factors show good agreement with qualitative expectations, these is no universal agreement on the exact form of the structure property relationships.[73–79] Whilst Embury and Fisher,[73] Hyzak and Bernstein[74] and Karlson and Linden[75] have also used the $s^{-1/2}$ relationship for strength properties, other workers such as Dollar and Gorczyca[76] have used s^{-1} as the relevant parameter for strength assessment. Other models are available, and Kouwenhoven,[79] for example, has applied a simple law of mixtures to interpret the property changes of ferrite pearlite steels.

An important feature of such models, however, is that they provide a useful base for further developments. Changes in properties attained by changing the cooling rate for example, should be encompassed by the microstructural changes incorporated in Equations (7.32)–(7.34). Increasing the cooling rate will refine the ferrite grain size of medium carbon steels, increase the pearlite fraction and refine the interlamellar spacing of the pearlite, thus increasing the strength. Increasing the manganese content of continuously cooled steels would have similar effects due to the lowering of the transformation temperature. (Note – the effect of manganese is to increase the interlamellar spacing of pearlite under isothermal transformation conditions,[80,81] due to the reduced pearlite nodule growth rate at any given temperature.) However, if a novel strengthening addition is made, then the model, as expressed by the above equations, is useful as a base level from which to judge the significance and magnitude of any property changes. The addition of microalloys, for example, to medium and high carbon steels may

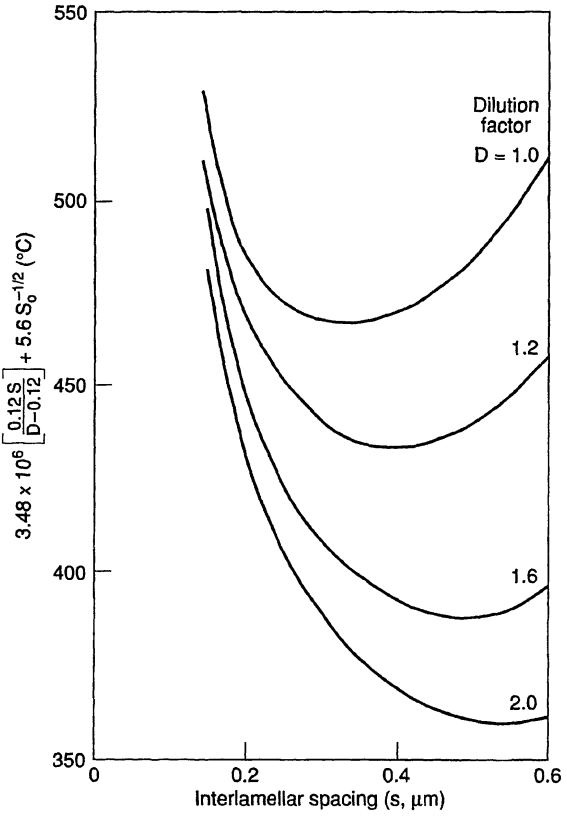


Fig. 7.47 The effects of pearlite spacing and dilution on the impact transition temperature of a fully pearlitic structure. Note the occurrence of an optimum pearlite spacing. After Gladman *et al.*[72]

modify the microstructural features involved in Equations (7.32)–(7.34), but also offers the possibility of introducing dispersion strengthening, which would be revealed as a significant deviation from the predicted values. In the work cited above,[72] separate additions of aluminium, niobium, titanium and vanadium were made to a number of high carbon steels in the normalised, air cooled from 1100°C, and controlled rolled conditions. The major observations for these steels reflected both direct and indirect effects of the microalloying additions, such as occur in the low carbon microalloyed steels. Grain refinement and nitrogen fixing effects were observed for the titanium, aluminium and niobium steels together with the consequences of the effects of austenite grain refinement on the transformation characteristics, i.e. changes in the ferrite grain size and the interlamellar spacing of the pearlite. In the case of the vanadium steels, the observed yield and tensile strengths were significantly higher than those predicted from the microstructural features and incorporated in Equations (7.32) and (7.33). Such deviations show that vanadium, in addition to any nitrogen fixing, grain refinement or pearlite refining actions, also introduces an additional strengthening mechanism. The yield and

tensile strengths of the vanadium steels, particularly those austenitised at high temperatures, showed deviations of more than 100 MPa, i.e. of the same order as those produced in low carbon steels by interphase strengthening (see Fig. 7.4).

The development of high strength microalloyed medium and high carbon forging steels as a lower cost alternative to hardened and tempered low alloy steels gained impetus in the late 1970s.

7.7.2 Microalloying of Medium and High Carbon Steels

The effects of microalloying in medium and high carbon steels is complex, bearing in mind the significant contribution of the pearlite fraction and pearlite spacing to the yield strength of the ferrite–pearlite aggregate, and also the possible contribution of an interphase precipitation strengthening effect. Nevertheless, the same metallurgical principles that proved so effective in providing an understanding of the low carbon microalloyed steels can also be applied to high carbon steels. Consider first the solubility of the microalloy carbides at temperatures that are relevant to the forging of medium carbon steels or the hot rolling of high carbon steels (such as rail steels), i.e. temperatures of the order of 1150–1200°C. The solubility products at 1200°C (from Table 3.17) are as shown in Table 7.4. The limited solubility of titanium and niobium in high carbon austenite compared with that of vanadium is clearly shown. It must be emphasised that the solubilities shown in Table 7.4 are those associated with the high carbon content and do not indicate the microalloy levels that would need to be added to steels containing nitrogen for which the solubility products of the carbo-nitrides are considerably lower. The microalloy solubilities indicated in Table 7.4 represent the maximum dissolved levels that can be in equilibrium with a high carbon austenite in which the dissolved carbon levels are 0.4wt% or 0.8wt%. The levels of titanium and niobium that would be dissolved at 1200°C, although limited, would still be capable of producing some degree of dispersion strengthening according to the Ashby–Orowan equation as illustrated in Fig. 7.4. However, this presupposes that strain induced precipitation in the austenite during hot working could be avoided, which is unlikely given the high supersaturation levels at lower temperatures in the hot working range. The observed strengthening levels are likely to be much lower than those predicted from the above microalloy solubilities. For example, in the case of a niobium steel with 0.8wt%C in solution, the maximum dispersion strengthening would be of the order of 50 MPa and this could be seriously reduced by strain induced precipitation during hot working. Such reduced levels may be undetectable within practical property variances.

Table 7.4 Solubility of microalloy carbides in high carbon austenite at 1200°C

Carbide	k_s at 1200°C	Dissolved microalloy at 0.4wt%C	Dissolved microalloy at 0.8wt%C
Vanadium	1.9	>1.0wt%	>1.0wt%
Titanium	1.7×10^{-2}	0.042	0.021
Niobium	1.1×10^{-2}	0.027	0.015

Vanadium, on the other hand, shows such a high level of solubility that, within the range of carbon and vanadium levels found in microalloyed vanadium steels, the solubility limit imposes no restriction on the level of dissolved vanadium that can exist in equilibrium with high dissolved carbon levels in the austenite at 1200°C, and, consequently, does not limit the dispersion strengthening that can be attained from vanadium carbide (or carbo-nitride) precipitation. The significant levels of dispersion strengthening in vanadium microalloyed medium carbon steels noted earlier[72] have been exploited in the development of medium carbon forging steels for a wide range of applications, such as connecting rods, steering linkages and stub axles,[82] all requiring an adequate level of strength and fatigue resistance. The strength levels attained in medium carbon steels, microalloyed with vanadium, are suited to these applications, and provide cost savings by developing the properties in the as-forged condition, rather than by a subsequent (and costly) heat treatment. In the development of these steels, and their subsequent examination, it has been shown that the added strengthening mechanism involved in these vanadium steels is associated with vanadium carbo-nitride precipitation in both the pro-eutectoid ferrite and in the ferrite lamellae of the pearlite structure; the latter precipitation is shown in Fig. 5.5.

In a detailed study of the strength of eutectoid steels containing vanadium, Ridley *et al.*[78] showed that the increase in yield strength (or 0.1% proof stress) produced by the addition of vanadium could be attributed to two features. Firstly, adding vanadium reduced the interlamellar spacing of the pearlite. This effect is undoubtedly due to a reduction in the temperature of transformation of austenite to pearlite. Secondly, at any given interlamellar spacing of pearlite, the proof stress increased with increasing vanadium content, as shown in Fig. 7.48, and was accompanied by the precipitation of fine vanadium carbo-nitrides in the pearlitic ferrite.

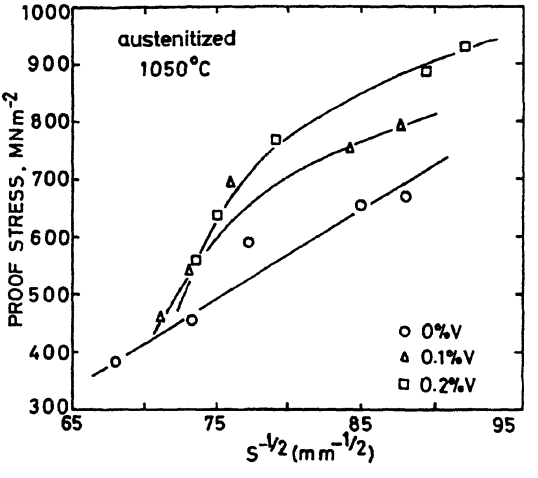


Fig. 7.48 The effect of vanadium additions on the proof strength of pearlitic steels. The strength of the vanadium steel is higher than that of the plain carbon steel at any given interlamellar spacing. After Ridley *et al.*[78]

Electron microscopical examination by Ridley *et al.* showed a variety of precipitate distributions. In rapidly cooled samples (5–10 Ks^{-1}), there was no evidence of precipitation. In the more slowly cooled samples (0.04-1 Ks^{-1}), precipitates were observed, some of which exhibited the rows characteristic of interphase precipitation. There was clear evidence of a precipitate free zone adjacent to the cementite lamellae which was suggested to arise from vanadium partitioning to the cementite. The observed increases in yield strength due to vanadium at the finer interlamellar spacings have been attributed by Von Den Steiner *et al.*[83] to the formation of fine pre-precipitation clusters of vanadium and interstitial atoms.

The complexity of vanadium carbo-nitride precipitation in high carbon steels has been well documented by Fourlaris *et al.*,[84] who studied the isothermal transformation of vanadium alloyed high carbon steels. Pro-eutectoid ferrite showed both interphase precipitation and precipitate-free zones, whilst the pearlitic ferrite showed interphase and/or fibrous carbides in some areas together with precipitate-free zones, and a complete freedom from vanadium carbo-nitride in other regions (Fig. 5.6). It is possible that the precise morphology of the vanadium carbo-nitride at any point of a given microstructure would be dependent upon the individual ferrite or pearlite grain transformation rates (which are strongly influenced by temperature), the supersaturation of vanadium and interstitials, and the proximity of cementite particles or lamellae. Woodhead and Quarrel[85] have shown that the equilibrium microstructure at 700°C in a steel containing 0.2wt%V is in fact ferrite and cementite, and that the vanadium atoms partition to the cementite.

The complexities of vanadium strengthening in high carbon steels are reduced if consideration is limited to microalloyed steels (usually with less than 0.15wt%V) and to the cooling rates pertinent to large forgings or rail steels. Under these conditions, high austenitising temperatures will result in complete dissolution of vanadium carbo-nitrides, and the cooling rates will be such as to allow interphase precipitation and an increment in yield strength that is broadly in accord with the Ashby–Orowan equation. The sensitivity of the yield strength to cooling rate is generally more pronounced than in low carbon steels because a reduction in cooling rate not only increases the particle size of the interphase precipitates, but also allows partitioning of vanadium into the lamellar cementite phase, thereby reducing the volume fraction of interphase precipitates. In addition to these effects of cooling rate on the interphase precipitation strengthening, there is a direct effect of cooling rate on the interlamellar spacing itself which is so important to the strength of pearlitic microstructures.

The limitations on the dissolved levels of niobium or titanium in high carbon austenite do not imply that they do not have significant effects on steel properties. The extent of dispersion strengthening may be limited, but the other effects of these elements, such as the marked inhibition of recrystallisation of austenite by niobium during the hot working process, can still operate. The inhibition of grain growth of the austenite during the hot working process will also be viable. The undissolved fraction of niobium and titanium carbo-nitride may also restrict grain growth at the soaking temperature. These effects are more likely to improve

toughness by refining the pearlite colony size, but could be used to maintain toughness in steels strengthened by interlamellar spacing refinement, for example, in steels with small alloying additions of chromium or molybdenum.

The effects of nitrogen contents and carbo-nitride solubilities are important in defining the total microalloy addition that is required to attain a given level of dissolved microalloy. The effect of increasing the carbon level of the steel also has the effect of increasing the carbon fraction of the carbo-nitride, as indicated in Table 3.16 for niobium carbo-nitride, and in Table 3.18(a) for vanadium carbo-nitride. Thus the amount of microalloy that needs to be added to attain the desired level of dissolved microalloy must include not only that which is required for the nitrogen in the carbo-nitride but also that which is required for the carbon in the carbo-nitride. This aspect of microalloying in high carbon steels has not yet been fully exploited.

An important aspect of microalloyed medium and high carbon steels in the form of rails and forgings is that high soaking temperatures are used prior to hot working. This naturally leads to the development of a coarse grained structure, which, on tranformation, would result in a coarse pearlite colony size. The coarse pearlite colony size would in turn lead to poor toughness, as shown in Equation (7.34). As described in Chapter 6, the hot working process is capable of refining the austenite grain size, initially by recrystallisation, and in the later stages, if the deformation temperature falls below the recrystallisation temperature, by grain elongation or flattening. In the manufacture of irregular forgings, such as stub axles and steering links, the extent of deformation, and the deformation temperature, can vary significantly within the component. Those parts of the forging which undergo significant deformation can undergo significant grain refinement, but this will certainly depend on the deformation temperature. Other parts of the forging may suffer little deformation, and may retain the original coarse austenite grain size with an attendant loss of toughness. A similar argument can be made for irregular rolled sections such as rails, where control of the rail head structure can be difficult due to differential cooling of the head, web and flange. Thus, the control that can be applied to the hot rolling of plate, strip and bar products, where the deformation and deformation temperatures are ostensibly uniform, cannot be applied to irregular sections and forgings. In such cases, one approach to the improvement of toughness has been to use a potent grain refining agent that is capable of maintaining a fine austenite grain size even at the soaking temperature prior to the application of deformation. The broad principles of grain refinement have been outlined in Chapters 4 and 6, but the specific application to grain growth inhibition by particle drag at temperatures up to 1300°C is worthy of further consideration, and involves the use of one of the most stable of microalloy nitrides, i.e. titanium nitride. The use of titanium nitride in this way is not restricted to forgings, but can be applied across the whole spectrum of hot worked steels, provided that the soaking temperatures are not excessive. This practice has been classified under the generic title of 'titanium nitride technology' and was initially introduced for plate rolling.[86] The application of titanium nitride technology to grain growth inhibition at elevated temperatures in the austenite range is described in the following section.

7.7.3 Titanium Nitride Technology

A general overview of the effects of microalloying additions on the grain coarsening temperature of austenite is shown in Fig. 7.49. In aluminium, vanadium and titanium steels, these are largely controlled by the microalloying level and the *nitrogen* content, due to the pronounced stability of the nitrides compared with their respective carbides. The differential between the solubilities of the carbide and nitride is somewhat reduced in the case of niobium and, as indicated in Section 7.7.2, niobium carbide can be stable at quite high temperatures (1200°C) with modest niobium additions to high carbon steels. However, the extremely low solubility of titanium nitride in austenite ($k_s = 1.9 \times 10^{-6}$ at 1300°C) has resulted in the development and extensive application of 'titanium nitride technology'.

The solubility curves of titanium nitride in austenite and in liquid, derived from data presented in Chapter 3, are shown in Fig. 7.50. In high carbon steel (say, 0.8wt%C) the solidus and the liquidus temperatures are approximately 1380°C and 1470°C respectively. The data of Matsuda and Okamura[87] were used to describe the solubility of titanium nitride in austenite, and although the solubility obtained from their data is considerably in excess of that shown by the data of Narita,[88] both show the very limited solubility of titanium nitride in steel. Figure 7.50 illustrates the very low levels of titanium that are needed to cause titanium nitride formation at near solidus and liquidus temperatures, even when the higher solubility data is selected. The solubility of titanium nitride in liquid steel at the liquidus temperature is based on the data of Narita.

From Fig. 7.50, the steel compositions (in terms of titanium and nitrogen) that will allow precipitation of titanium nitride in the liquid state (above the

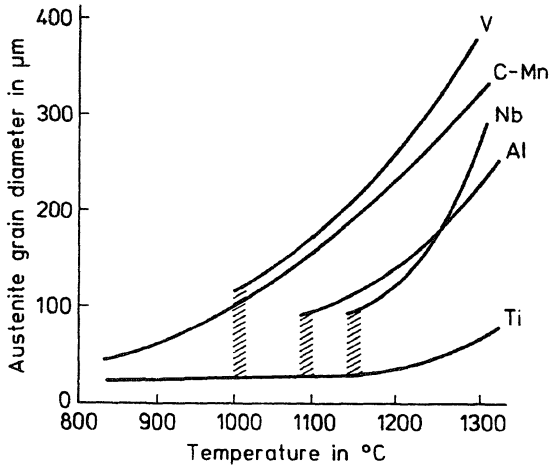


Fig. 7.49 The general effects of microalloy additions on the grain coarsening temperature of austenite. Specific grain coarsening temperatures are dependent upon the microalloy content, nitrogen content, and the effects of prior thermal or thermomechanical cycles on the precipitated particle size. After Speich *et al.*[108]

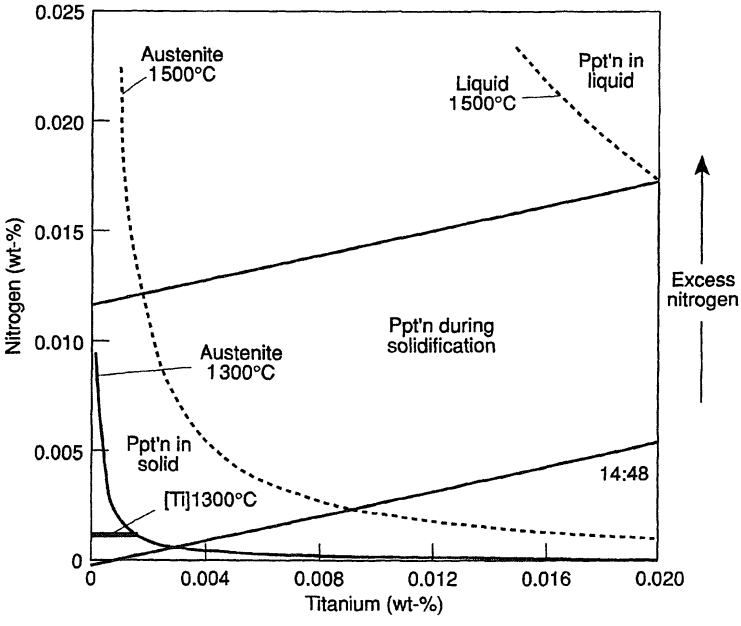


Fig. 7.50 Solubility diagram for titanium nitride, showing the effects of titanium and nitrogen contents on precipitation in the liquid state. The effect of excess nitrogen in the dissolved titanium content in the austenite is also indicated. This has direct relevance to the kinetics of Ostwald Ripening.

liquidus temperature) are clearly shown. For example, with a nitrogen content of 0.005wt%N, extrapolation of the liquid solubility curve suggests that any titanium level above 0.068wt%Ti will result in the precipitation of titanium nitride in the liquid at 1500°C. At this same nitrogen level, some precipitation of titanium nitride from the liquid steel would be expected in steels with more than 0.005wt%Ti at temperatures between the liquidus and solidus even in the *absence* of alloy partitioning between the liquid and the (solid) austenite. However, during solidification some alloy partitioning can be expected as discussed by Gladman[89] and by Adrian,[90] and enrichment of the liquid in titanium and nitrogen will occur, thus promoting precipitation at higher temperatures in this range than would be anticipated from a simple consideration of the solubility of titanium nitride in liquid steel. In fact, some precipitation of titanium nitride from the liquid can be expected at all titanium levels which exceed the solubility of titanium nitride in austenite at the solidus temperature, the amount decreasing as the titanium content in the steel is reduced to approach the limit of solubility in austenite at the solidus temperature. A fuller consideration of alloy partitioning has been given by Adrian. At titanium levels near the solubility limit of titanium nitride in austenite at the solidus temperature, it might reasonably be expected that the bulk of the titanium nitride precipitation would occur in the *solid* state. For example with the

0.005wt%N steel selected above, titanium levels less than 0.005wt%Ti should result in the bulk of precipitation occurring in the solid state.

The significance of the liquid and solid state precipitation is in the particle size of the titanium nitride. Particle size (edge lengths) of titanium nitride cuboids precipitated in the liquid can be up to about 5 μm, whilst those formed from the liquid during the solidification process can be reduced to some 0.5–1 μm. Solid state precipitation is much finer, giving particles of the order of 10–20 nm, although their size is highly dependent on the high temperature exposure of the solid steel, due to the nucleation conditions and the Ostwald ripening phenomenon.

As described in Chapter 4, large particles are far less potent for grain growth inhibition, and the formation of the large titanium nitride particles should be avoided. On the other hand, the very small volume fractions of solid state precipitated particles limit the high temperature exposure that can be applied before Ostwald ripening causes the particle size to become critical and grain growth commences. Grain coarsening under these conditions occurs by secondary recrystallisation (abnormal grain growth), and loss of grain refinement in this way can give coarser grain sizes than would be obtained in the absence of pinning particles.[91] The introduction of continuous casting, together with the more rapid cooling implicit in this process, provides some advantage over conventional ingot routes with respect to the titanium nitride particle size. The magnitude of this effect is not clear, although Sage and Cochrane[92] have shown a marked dependence of titanium nitride particle size on the post solidification cooling rate in the fusion zone of welds (Fig. 7.51).

Having obtained a fine distribution of particles, the efficiency of grain refining particles in preventing grain growth is increased if the particle coarsening rate at

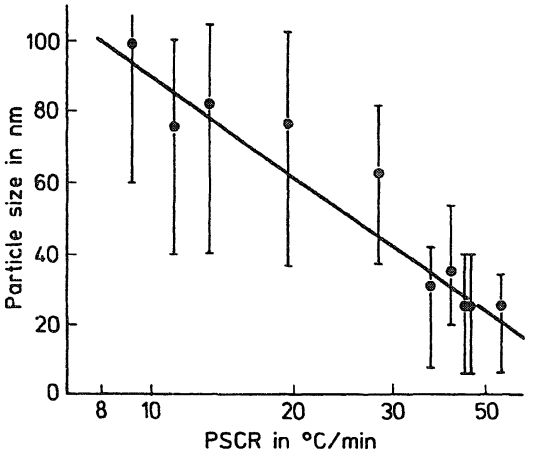


Fig. 7.51 Effect of post-solidification cooling rate (PSCR) on the titanium nitride particle size in the fusion zone of weldments. After Sage and Cochrane.[92]

elevated temperatures can be reduced. The advantage of titanium nitride in steels is in part attributed to the very low solubility, which then controls the solute content of the rate limiting specie, and reduces the diffusion flux. This is reflected in the Wagner equation discussed previously [Equation (5.17)]:

$$r^3 - r_0^3 = 8\sigma SD\Omega t/9RT \tag{7.35}$$

where S is the concentration of the rate limiting specie. In the case of titanium nitride particles the relevant solutes are titanium [*Ti*] and nitrogen [*N*], for which the diffusion coefficient of titanium is many orders of magnitude lower than that of nitrogen, and results in titanium being the rate-limiting solute. The slow rate of coarsening of titanium nitride has already been discussed in Chapter 5, but an important feature of titanium nitride technology is the selection of a steel composition that will minimise the dissolved titanium, S, in Equation (7.35). Reference to Fig. 7.50 shows that the soluble titanium at a given temperature can be limited by the excess nitrogen in the steel, i.e. selecting a steel composition that has a nitrogen content in excess of that required for stoichiometric combination with the titanium. Thus, the titanium in solution at a temperature of, say, 1200°C can be reduced by increasing the nitrogen content above the stoichiometric ratio. There is obviously a limit to the extent to which the nitrogen can be increased, due to the formation of coarse titanium nitride particles in the liquid as the product of the total titanium and nitrogen contents is increased.

In commercial steels, the titanium and nitrogen levels are of the order of 0.01wt%Ti–0.005wt%N, and these levels are capable of giving grain coarsening temperatures in the range 1250–1300°C, thus proving viable for the restriction of grain growth in medium carbon forging steels and high carbon rails soaked at temperatures in the range 1150–1250°C. The excess nitrogen is useful in vanadium steels where it will enhance the interphase precipitation of the vanadium carbo-nitride.

A significant feature of these steels arises from the small volume fraction of particles. Very often, these steels will exhibit an austenitic grain size of about ASTM 5–6, which, although not coarse, is not as fine as the austenitic grain sizes of normalised grain refined steels when larger fractions of particles, coarsening more slowly at these lower temperatures, will stabilise austenite grain sizes of ASTM 7–9 or finer.

Titanium nitride technology is applied to steels containing other microalloying additives as well as titanium, as for example in the vanadium steels cited above. The complexity of Ti–Nb or Ti–V steels in terms of the solubility have already been described in Chapter 3. The complexities in Ostwald ripening where compositional changes may accompany particle coarsening have also been mentioned. Whilst an acceleration of particle coarsening on adding niobium to a titanium refined steel has been reported, and many instances of reduced grain coarsening temperatures have been seen, there is no ready explanation for this effect. Further, there is limited experimental evidence that some Ti–Nb steels may not show the accelerated coarsening and reduced grain coarsening temperatures, and this is clearly an area for further investigation.

7.8 WELDABILITY OF MICROALLOYED STEELS

In the opening chapter of this book, attention was drawn to the introduction of high volume modern welding techniques, and the suitability of the low carbon microalloyed high strength structural steels to the fusion welding processes. It would be inappropriate to omit any further reference to welding, even though the primary understanding of the welding process was developed on plain carbon and aluminium grain refined steels.

The development of high strength microalloyed steels has involved two major strengthening mechanisms, i.e. ferrite grain refinement and dispersion strengthening by fine microalloy carbo-nitrides. These mechanisms have enabled the higher strength levels to be achieved without the need for the elevated carbon contents that were used previously, i.e. in the range 0.15–0.25wt%C. Many of the modern structural steels have lower carbon levels in the range 0.06–0.12wt%C despite their higher strengths. In this brief account of the significance of microalloyed steels, the basic principles of welding will be considered, together with the effects of steel composition and welding variables. Also brief mention is made of some areas of current steel research interest.

7.8.1 The Welding Process

There are many welding processes available, but for structural steels the most commonly used are the submerged arc welding process (SAW) and the manual metal arc (MMA) welding process. In both of these processes, the energy is supplied by an electric arc, struck between a filler metal electrode and the work-piece, resulting in a molten pool of metal formed from the electrode and the edges of the work-piece. The electrodes move along the joint locus, melting more of the (continuously fed) electrode and the edges of the parts to be joined, whilst leaving behind a molten pool to solidify and cool at a rate that is determined by the heat reservoir of the molten pool and the heat sink afforded by the parts being welded. The physics of the heat flow have been expressed in the Rosenthal heat flow equation.[93] The arc is considered as a moving point heat source from which energy is used in forming the molten pool, and in heating the surrounding metal, as the heat is conducted away from the molten pool. If the point source is moving at a constant velocity, a steady state temperature distribution is established around the point source. The resulting effect is that of a plate moving through a short temperature cycle, the peak temperature of any part of the weldment being dependent upon its distance from the point heat source (Fig. 7.52). The heating rate is dependent upon the heat input and point source velocity, and the cooling rate is also a function of the heat input and the mass of cold plate available as a heat sink. These short thermal cycles can, of course, dramatically change the microstructure not only in the fusion zone, where solidification and the allotropic transformations occur, but also in the heat affected zone (HAZ), where the peak temperature may reach the solidus at points near the fusion line, and a very coarse austenite grain size may develop. At slightly more remote positions, lower peak temperatures may simulate a rapid normalising treatment, producing a fine grained austenite.

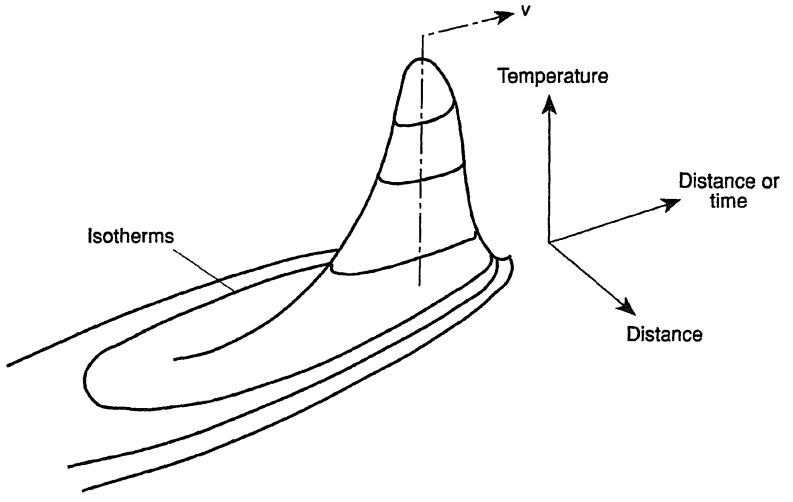


Fig. 7.52 The steady state temperature distribution around a moving point heat source. After Easterling.[94]

At even more remote points, the peak temperatures may simulate a sub-critical anneal, with some spheroidisation of the pearlitic regions.

The relatively rapid cooling rates of weldments from the fully austenitised regions of the HAZ, and particularly from the coarse grained austenite near to the fusion line, will, of course, affect the transformation products that are formed during cooling to ambient temperature. The tendency to form martensite or bainite rather than polygonal ferrite will be enhanced by the rapid cooling, but the transformation product will also be influenced by the steel composition. Higher carbon and alloy contents will favour martensite/bainite structures, whilst low carbon and low alloy contents will favour ferrite–pearlite structures.

The effects of composition and cooling rate on the transformation characteristics under these thermal cycles have been modelled by Easterling[94] and more recently by Bhadeshia[95] with considerable success.

There are two important features of these transformation characteristics

(i) The formation of brittle constituents coupled with the thermal stresses developed by the cooling of a restrained weldment can lead to cold cracking or re-heat cracking.

(ii) In the absence of cracking, the mechanical properties of the HAZ are a function of the HAZ microstructure, and the presence of hard or brittle phases can affect the toughness of the weldment and its ability to withstand exposure to hydrogen.

These effects also relate to the fusion zone of the weld, for although the carbon content is usually much lower than the plate material, alloy and carbon can be picked up by the mutual fusion of feed-wire and parent plate, in what is essentially an 'as-cast' structure. This, of course, is an over simplification of the

microstructural changes, as in many large section multi-pass welds, the coarse grained austenite region of the HAZ of one weld run may well become the sub-critically annealed region of the HAZ of a subsequent weld run. In multi-pass welds, the microstructural features at any point will reflect the number and sequence of thermal cycles experienced at that point as a result of multi-pass welding operations.

7.8.2 Practical Welding

The thermal cycles and transformation characteristics in a weldment depend on a variety of factors, covering both the welding variables (steel dimensions, weld geometry, heat input) and steel composition. Cotton[96] has presented a nomogram indicating the combinations of variables that are required to produce satisfactory crack free welds for offshore structures. A modification of this nomogram is shown in Fig. 7.53, and relates

(i) the thermal severity factor (expressed in mms. of plate thickness involved in the joint – see Fig. 7.53);

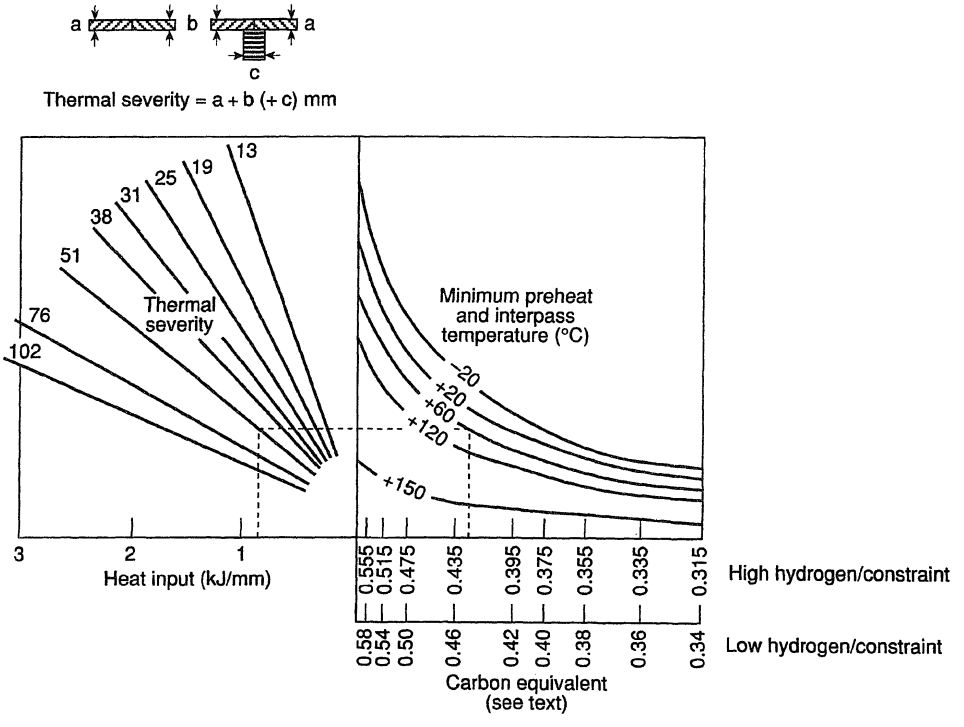


Fig. 7.53 The effect of welding variables on the maximum permitted carbon equivalent. Pre-heating is expensive and steels with lower carbon equivalents that eliminate the need for pre-heat offer considerable savings in the cost of fabrication. After Cotton.[96]

(ii) the heat input of the weld (expressed in $kJ\,mm^{-1}$);
(iii) The weld preheat required (°C)

to the carbon equivalent of the steel. The thermal severity factor reflects the heat sink, and reflects the area of cold metal through which the heat is abstracted from the weld. The greater the area, the more rapid will be the cooling rate in the fusion zone and the HAZ. The increase in cooling rate caused by the increased thermal severity requires a lower carbon equivalent in the steel. The cooling rate can be reduced either by increasing the heat input (kJ/mm) per run, which effectively gives a larger mass of hot metal, or by increasing the pre-heat or inter-pass temperature, both of which reduce the thermal gradient across the HAZ, and increase the carbon equivalent that can be used without failure.

For a given weld geometry, having a thermal severity equivalent to 50 mm summed thicknesses (2×25 mm plates in a butt weld, or 3×17 mm plates in a T-junction), welded with a heat input of 1 kJ/mm, a pre-heat of 60°C would be required for a steel with a carbon equivalent of 0.45. Reducing the carbon equivalent to 0.40 would eliminate the need for any pre-heating, thereby reducing the cost of fabrication. It should be noted that there are different carbon equivalent scales shown in Fig. 7.55, depending on the degree of restraint imposed on the weld and/or the hydrogen content of the electrodes. Highly restrained welds or higher hydrogen electrodes require steels with lower carbon equivalents.

There are many different formulae for the carbon equivalent of a steel. Basically, the carbon equivalent represents the effects of carbon and other alloys on the hardenability of the steel, the effects of the alloying elements being scaled according to their relative effects on the critical cooling rate. As indicated in Fig. 7.53, the carbon equivalent (C.E.) recommended by the International Institute of Welding is given by

$$\text{C.E.} = \text{C} + \text{Mn}/6 + (\text{Cr} + \text{Mo} + \text{V})/5 + (\text{Ni} + \text{Cu})/15 \qquad (7.36)$$

This equation covers a wide range of steels, but the Ito and Bessyo[97] equivalent is sometimes preferred for modern low carbon steels:

$$\text{C.E.} = \text{C} + \text{Si}/30 + (\text{Mn} + \text{Cu} + \text{Cr})/20 + \text{Ni}/60 + \text{Mo}/15 + \text{V}/10 + 5\text{B} \qquad (7.37)$$

The main point, however, is that modern microalloyed steels, with their lower carbon contents (decreased by about 0.1wt% or more compared with the pre-1960 steels), have higher strengths *and* improved weldability. The significance of a reduction in the carbon equivalent by 0.1 is readily appreciated from Figure 7.55. Low carbon equivalents in modern high strength weldable steels permit significant cost savings in fabrication and are also capable of improving the properties of the weld fusion zone and the HAZ.

7.8.3 Metallurgical Developments in Welds

As described in Section 7.8.2, a major advantage of microalloyed steels is associated with the reduction in carbon content that offers a greater freedom from costly welding procedures. The microalloyed steels offer further advantages in that

the microalloying elements may confer improved properties on the weldment. Attention has already been directed to the elimination of lamellar tearing by reducing the sulphide and oxide levels, and applying inclusion shape control procedures. The application of these low sulphur steels has not been without penalty, however, as the reduction in sulphides renders the steels more susceptible to hydrogen cracking. Manganese sulphide inclusions offer a sink for hydrogen in the steel and reduce the risk of hydrogen cracking. A reduction in the level of sulphur meant that there were fewer sinks and therefore an increased risk of underbead cracking due to hydrogen. Lower hydrogen contents are now a requirement in these low sulphur steels in order to avoid this problem and take full advantage of the freedom from lamellar tearing.

There are two other principal effects of microalloys in weld microstructures that are currently under development. These are

(i) Grain size control in the coarse grained HAZ near the fusion line.
(ii) Microalloy control of the microstructural transformations in the HAZ (and fusion zone).

The benefits of titanium nitride technology in medium and high carbon steels were discussed in Section 7.7. This same technology has relevance to the high temperature H.A.Z. in controlling the grain size and/or the extent of the coarse grained region. The effect of titanium nitride on the austenite grain size at

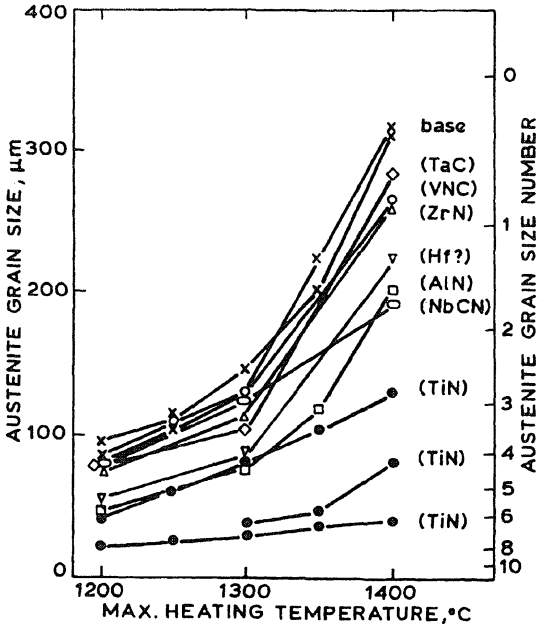


Fig. 7.54 Austenite grain size control in the HAZ near the fusion line. Titanium additions offer finer austenite grain sizes, and also restrict the width of coarse-grained heat affected zone. After Kanazawa.[98]

temperatures up to 1400°C[98] are shown in Fig. 7.54. It is clear that titanium-containing steels have finer austenite grain sizes than steels with other additives, but the grain sizes attained at 1400°C are not exactly 'fine'. Details of the changes in carbo-nitride particles and their sizes have been considered by Suzuki *et al.*[99] in relation to short term welding cycles. Particle dissolution, particle re-precipitation of near equilibrium compositions and Ostwald ripening were observed in steels containing titanium or titanium and niobium. The idea of controlling the austenite grain size was to refine the microstructure developed after transformation. At the cooling rates pertinent to weldments, the microstructures of the HAZ are complex, but may contain acicular transformation products such as Widmanstatten ferrite, ferrite side plates developed from grain boundary polygonal ferrite, acicular ferrite and bainite. Refinement of the austenite grain size would therefore reduce the mean cleavage crack path – as discussed for bainitic steels – and improve the toughness. Improvements in toughness were in fact attained, but as pointed out by Dolby,[100] the reason for the improvement in toughness was a refinement of the cleavage crack path length, *not* by austenite grain refinement, but by the formation of the acicular (basketwork) ferrite morphology rather than the bainitic (parallel



Fig. 7.55 Acicular ferrite (white) nucleated on 1 μm globular particles of manganese titanate – $MnO \cdot TiO_2$.

plate) ferrite morphology. Dolby suggested that the acicular ferrite was nucleated on the titanium nitride particles and that this effect was far more effective in refining the crack path than is the austenite grain size.

This effect of introducing nucleants into the steel to induce the acicular ferrite structure has been extended by controlling the oxide type. 'Titanium oxide' steels have been produced[101] which are aluminium free. In the absence of aluminium,

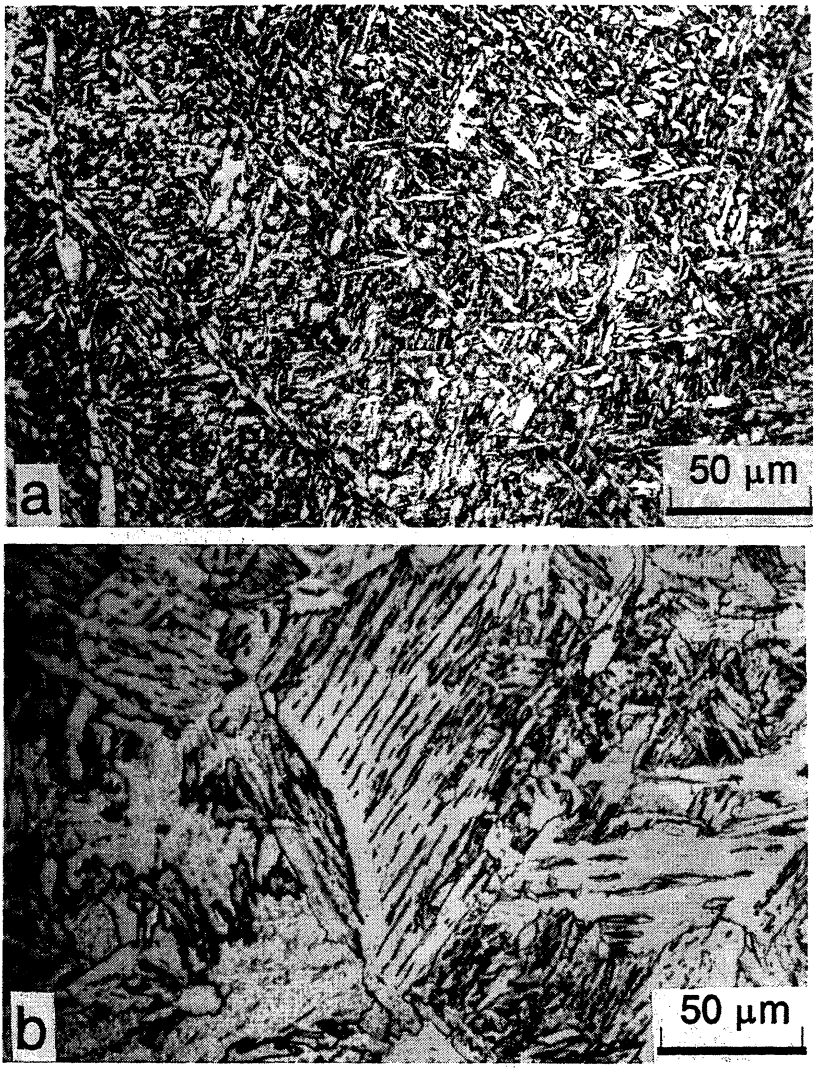


Fig. 7.56 A comparison of (a) the acicular ferrite morphology with (b) the bainitic ferrite morphology. The 'lath packet size' concept is clearly seen in the case of the bainitic ferrite, and clearly contrasts with the basket weave structure of the acicular ferrite.

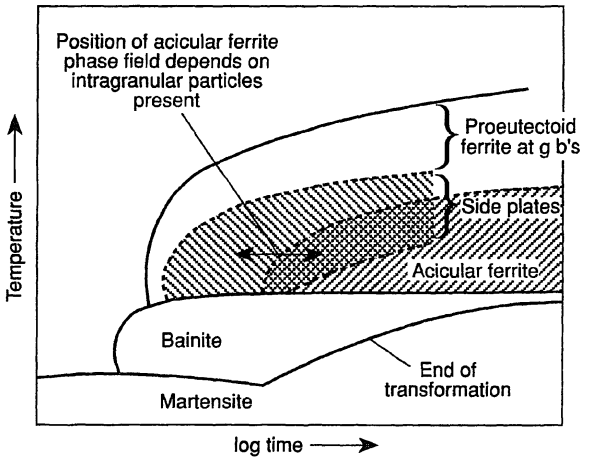


Fig. 7.57 Schematic continuous cooling diagram showing the conditions for the formation of the acicular ferrite structure. These are virtually indistinguishable from the conditions that would produce a bainitic ferrite structure in other low carbon steels. After Dolby.[100]

titanium is the most stable oxide former, and a titanium oxide Ti_2O_3 or $MnO.TiO_2$[102] is formed. These oxides, present in the form of sub-micron particles, act as very potent acicular ferrite nuclei (Fig. 7.55) and improve the toughness of the HAZ. The use of high titanium electrodes to promote titanium oxides and nitrides in the fusion zone of welds is well established.

The difference between acicular ferrite and the bainitic ferrite morphology is shown in Fig. 7.56. Although schematic diagrams are available (Fig. 7.57) which indicate the temperature range of formation of acicular ferrite and the associated cooling rates, the mechanism for acicular ferrite formation requires further clarification. With regard to the effects of microalloying additions, titanium oxides and nitrides have been shown to induce the acicular ferrite structure by a seeding effect. Recent observations[103,104] have shown that the addition of vanadium as a microalloy causes an extensive acicular ferrite formation (Fig. 7.56) although there is no clear understanding of the reason why vanadium additions (and not niobium) should have such effects.

REFERENCES

1. R. Kiessling and N. Lange: *Non-Metallic Inclusions in Steel*, The Metals Society, London, 1978.
2. K. J. Irvine, F. B. Pickering and T. Gladman: *J. Iron and Steel Inst.*, 1967, **205**, p.161.
3. F. B. Pickering and T. Gladman: *Metallurgical Developments in Carbon Steels*, Iron and Steel Inst., Special Report No. 81, 1963, p.10.
4. K. J. Irvine, T. Gladman, J. Orr and F. B. Pickering: *J. Iron and Steel Inst.*, 1970, **208**, p.717.
5. F. G. Wilson and T. Gladman: *Aluminium Nitride in Steel*, International Materials Reviews, 1988, **33**, p.221.

6. E. SMITH: *Effect of Second Phase Particles on the Mechanical Properties of Steels*, Iron and Steel Institute, London, 1971, p.37.
7. J. F. KNOTT: ibid., p.44.
8. F. B. PICKERING: *Materials Science and Technology*, Eds. R. W. Cahn, P. Haasen, E. J. Kramer, VCH, Weinheim, 1992, Vol. 7, p.41.
9. L. J. CUDDY: *Thermomechanical Processing of Microalloyed Steels*, Eds. A. J. DeArdo, G. A. Ratz and P. J. Wray, AIME, Warrendale, PA, 1982, p.129.
10. S. YAMAMOTO, C. OUCHI, and T. OSUKA: ibid, p.613.
11. T. GLADMAN and F. B. PICKERING: *J. Iron and Steel Inst.*, 1967, **205**, p.653.
12. N. K. BALLIGER and R. W. K. HONEYCOMBE: *Met. Science*, 1980, **14**, p.121.
13. J. D. EMBURY, N. J. PETCH, A. E. WRAITH and E. S. WRIGHT: *Trans Met. Soc. AIME*, 1967, **239**, p.114.
14. T. TANAKA, N. TABATA, T. WATOMURA and C. SHIGA: *Microalloying '75*, Ed. M. Korchynsky, Union Carbide, New York, 1977, p.107.
15. R. L. BRAMFITT and A. R. MARDER: *Processing and Properties of Low Carbon Steel*, AIME, 1967, p.191.
16. O. KOSIK, D. J. ABSON and J. J. JONAS: *J. Iron and Steel Inst.*, 1971, **209**, p.624.
17. J. LANGFORD and M. COHEN: *Trans. A.S.M.*, 1969, **62**, p.623.
18. T. GLADMAN, D. DULIEU and I. D. MCIVOR: *Microalloying '75*, Ed. M. Korchynsky, Union Carbide, New York, 1977, p.32.
19. W. E. BARDGETT and L. REEVE: *J. Iron and Steel Inst.*, 1949, **163**, p.277.
20. K. J. IRVINE and F. B. PICKERING: *J. Iron and Steel Inst.*, 1960, **194**, p.133.
21. F. B. PICKERING: *Transformation and Hardenability in Steels*, Climax Molybdenum, Ann Arbor, 1967, p.109.
22. H. OHTANI, F. TERASAKI and T. KUNITAKE: *Trans. Iron and Steel Inst. Japan*, 1972, **12**, p.118.
23. L. J. HABRAKEN and M. ECONOMOPOULOS: *Transformation and Hardenability in Steels*, Climax Molybdenum, Ann Arbor, 1967, p.69.
24. Y. E. SMITH, A. P. COLDREN and R. L. CRYDERMAN: *Toward Improved Ductibility and Toughness*, Climax Molybdenum, Kyoto, 1967, p.119.
25. M. A. CIVALLERO, C. PARRINI and N. PIZZIMENTI: *Microalloying '75*, Ed. M. Korchynsky, Union Carbide, New York, 1977, p.451.
26. S. R. KILWORTH and P. H. WANNELL: *Hot Working and Forming Processes*, Eds. C. M. Sellars and G. J. Davies, The Metals Society London, 1980, p.113.
27. J. D. GROZIER: *Microalloying '75*, Ed. M. Korchynsky, Union Carbide, New York, 1977, p.241.
28. R. KIESSLING and N. LANGE: *Non-Metallic Inclusions in Steel*, The Metals Society, London, 1978.
29. I. KOZASU and J. TANAKA: *Sulphide Inclusions in Steel*, Eds. J. J. deBarbadillo and E. Snape, A.S.M. Metals Park, OH, 1975, p.286.
30. A. NICHOLSON and T. GLADMAN: *Ironmaking and Steelmaking*, 1986, **13**, p.53.
31. T. GLADMAN, B. HOLMES and I. D. MCIVOR: *The Effects of Second Phase Particles on the Mechanical Properties of Steel*, Iron and Steel Inst., London, 1971, p.68.
32. P. F. THOMASON: *Ductile Fracture of Metals*, Pergamon Press, Oxford, 1990.
33. T. M. BANKS and T. GLADMAN: *Metals Technology*, 1979, **6**, p.81.
34. T. MALKIEWICZ and S. RUDNIK: *J. Iron and Steel Inst.*, 1963, **201**, p.33.
35. C. E. SIMS and F. B. DAHLE: *Trans. Amer. Foundry Soc.*, 1938, **46**, p.65.
36. C. H. LEUNG and L. H. VAN VLACK: *Met. Trans.*, 1981, **12A**, p.987.
37. K. A. GSCHNEIDER: *Sulphide Inclusions in Steel*, Eds. J. J. deBarbadillo and E. Snape, A.S.M. Metals Park, Ohio, 1975, p.159.
38. H. PIRCHER and W. KLAPDAR: *Microalloying 75*, Ed. M. Korchynsky, Union Carbide, New York, 1977, p.232.

39. W. G. WILSON, D. A. R. KAY, and A. VAHED: *Desulphurisation of Steel and Shape Control*, Iron and Steel Society of AIME, Warrendale, PA, 1980, p.132, also W. G. WILSON and A. MCLEAN, ibid, p.1.
40. G. E. HALE and J. NUTTING: *International Met. Reviews*, 1984, **29**, p.273.
41. E. T. TURKDOGAN, S. IGNATOWICE and J. PEARSON: *J. Iron and Steel Inst.*, 1955, p.349.
42. K. W. BURNS and F. B. PICKERING: *J. Iron and Steel Inst.*, 1964, **202**, p.889.
43. M. ABE: *Materials Science and Technology*, Eds. R. W. Cahn, P. Haasen and E. J. Kramer, V.C.H., Weinheim, 1992, Vol. 7, p.285.
44. T. GLADMAN: *Mat. Sci. and Technol.*, 1990, **6**, p.1131.
45. R. W. K. HONEYCOMBE: *Steels - Microstructure and Properties*, Edward Arnold, London, 1981.
46. R. C. HUDD: *Metals and Materials*, Feb. 1987, p.71.
47. A. H. COTTRELL and B. A. BILBY: *Proc. Phys. Soc.*, 1949, **62A**, p.49.
48. W. B. HUTCHINSON and K. USHIODA: *Scand. J. Met.*, 1984, **13**, p.269.
49. H. TAKECHI: *HSLA Steels '95*, Eds. G. Liu, H. Stuart, W. Zhang and C. Li, Chinese Science Tech. Press, 1995, p.72.
50. G. TITHER and H. STUART: ibid., p.22.
51. N. YOSHINAGA, K. USHIODA, S. AKAMATSU and O. AKISUE: *CAMP*, Iron and Steel Inst. Japan, 1993, **6**, p.1709.
52. J. D. BAIRD: *Iron and Steel 1963*, May, p.186; June, p.326; July, p.368; Aug. p.400; Sept, p.450.
53. G. TITHER, C. I. GARCIA, M. HUA and A. J. DEARDO: *Physical Metallurgy of I.F. Steels*, Iron and Steel Inst. Japan, 1994, p.293.
54. R. H. GOODENOW: *Trans A.S.M.*, 1966, **59**, p.804.
55. M. S. RASHID: *S.A.E. Preprint*, No. 760206, 1976.
56. R. G. DAVIES: *Met. Trans. A.I.M.E.*, 1978, **9A**, p.41.
57. R. G. DAVIES: ibid., p.451
58. R. G. DAVIES: ibid., p.671.
59. R. G. DAVIES and C. L. MAGEE: *Dual Phase and Cold Pressing Vanadium Steels in the Automobile Industry*, Vanitec, Ed. A. M. Sage, 1978, p.25.
60. E. W. HART: *Acta Met.*, 1967, **15**, p.351.
61. A. MELANDER: *Scand. J. Metallurgy*, 1980, **9**, p.51.
62. W. B. MORRISON: *Trans. A.S.M.*, 1966, **59**, p.824.
63. N. K. BALLIGER and T. GLADMAN: *Metal Science*, 1981, **15**, p.95.
64. M. F. ASHBY: *Z. Metallkund*, 1964, **55**, p.5.
65. M. F. ASHBY: *Phil. Mag.*, 1966, **14**, p.1157.
66. C. A. N. LANZILLOTTO and F. B. PICKERING: *Metal Science*, 1982, **16**, p.371.
67. L. M. BROWN and W. M. STOBBS: *Phil. Mag.*, 1971, **23**, p.1201.
68. N. K. BALLIGER: *Advances in the Physical Metallurgy and Applications of Steels*, Book 284, The Metals Society London, 1982, p.75.
69. A. P. COLDREN and G. TITHER: *J. Metals*, 1978, p.6.
70. G. TITHER, A. P. COLDREN and J. W. MORROW: *Proc. 20th Mechanical Working Conference*, AIME, Chicago, 1978, p.72.
71. M. GENSAMER, E. B. PEARSALL, W. S. PELLINI and J. R. LOW JNR: *Trans A.S.M.*, 1942, **30**, p.983.
72. T. GLADMAN, I. D. MCIVOR and F. B. PICKERING: *J. Iron and Steel Inst.*, 1972, **210**, p.916.
73. J. M. EMBURY and R. M. FISHER: *Acta Met.*, 1966, **14**, p.147.
74. J. M. HYZAK and I. M. BERNSTEIN: *Met. Trans.*, 1976, **74A**, p.1217.
75. B. KARLSON and G. LINDEN: *Mat. Sci. Eng.*, 1975, 17, p.153.
76. M. DOLLAR and M. GORCZYCA: *Met. Sci.*, 1983, **17**, p.349.
77. A. R. MARDER and B. L. BRAMFITT: *Met. Trans.*, 1976, **7A**, p.365.
78. N. RIDLEY, M. T. LEWIS and W. B. MORRISON: *Advances in Physical Metallurgy and Applications of Steels*, Book 284, Metals Society, London, 1982, p.199.
79. H. J. KOUWENHOVEN: *Trans. A.S.M.*, 1969, **62**, p.437.

80. I. D. McIvor: *Chemical Metallurgy of Iron and Steel*, University of Sheffield, 1971, p.272.
81. G. E. Pellissier, M. F. Hawkes, W. A. Johnson and R. F. Mehl: *Trans. A.S.M.*, 1942, **30**, p.1049.
82. D. J. Naylor: *Ironmaking and Steelmaking*, 1989, **16**, p.246.
83. A. Von Den Steiner, S. Engineer, E. Horn and G. Preis: *Stahl und Eisen*, 1975, **95**, p.209.
84. G. Fourlaris, A. J. Baker and G. D. Papadimitriou: *Acta Met. et Mat.*, 1995, **43**, p.3733.
85. J. H. Woodhead and A. G. Quarrell: *J. Iron and Steel Inst.*, 1965, **203**, p.605.
86. T. George and J. J. Irani: *J. Australian Inst. Metals*, 1968, **13**, p.94.
87. S. Matsuda and N. Okumura: *Trans. Iron and Steel Inst. Japan*, 1978, **18**, p.198.
88. K. Narita: *Trans. Iron and Steel Inst. Japan*, 1975, **15**, p.145.
89. T. Gladman: *H.S.L.A. Steels - Processing, Properties, and Applications*, Eds. G. Tither and S. Zhang, T.M.S. Warrendale, PA, 1992, p.3.
90. H. Adrian: *Microalloying '95*, Pittsburgh, June, 1995, p.285
91. T. Gladman: *Materials Science Forum*, 1992, **94–96**, p.113.
92. A. M. Sage and R.C. Cochrane: *Development of a Weldable Normalised V-Ti Structural Steel*, Vanadium International Technical Committee, London, 1988.
93. D. Rosenthal: *Trans. ASME*, 1946, **68**, p.849.
94. K. E. Easterling: *Introduction to the Physical Metallurgy of Welding*, Butterworths, London, 1983.
95. H. K. D. H. Bhadeshia: *Recent Trends in Welding Science and Technology*, A.S.M. Int., Metals Park, OH, 1990, p.189.
96. H. Cotton: *The Contribution of Physical Metallurgy to Engineering Practice*, The Royal Society, London, 1976.
97. Y. Ito and K. Bessyo: *Weldability Formula of High Strength Steels*, IIW Document No. IX - 576–78, 1968.
98. S. Kanazawa: *Trans. Iron and Steel Inst. Japan*, 1976, **16**, p.486.
99. S. Suzuki, G. C. Weatherly and D. C. Houghton: *Acta Met.*, 1987, **35**, p.341.
100. R. E. Dolby: *Advances in the Physical Metallurgy and Applications of Steels*, Book 284, The Metals Society, London, 1982, p.111.
101. Y. Terada, R. Chijiiwa, H. Takehiro, T. Kikuma and K. Funato: *HSLA Steels, Processing, Properties, and Applications*, Eds. G. Tither and S. Zhang, T.M.S., Warrendale, PA, 1992, p.519.
102. T. Gladman and D. J. Senogles (to be published).
103. M. Zhang and D. V. Edmonds: *H.S.L.A. Steels '95*, Eds. G. Liu, H. Stuart, H. Zhang and C. Li, Chinese Sci. Tech Press, 1995, p.133.
104. P. Mitchell, P. H. M. Hart and W. B. Morrison: *Microalloying '95*, I.S.S., Pittsburgh, June, 1995, p.149.
105. B. Mintz, W. B. Morrison and R. C. Cochrane: *Advances in the Physical Metallurgy and Applications of Steels*, The Metals Society, London, 1982, p.222.
106. P. Repas: *Dual Phase and Cold Pressing Vanadium Steels in the Automobile Industry*, Vanitec, London, 1978, p.13.
107. A. J. DeArdo, J. M. Gray and L. Meyer: *Niobium*, Ed. H. Stuart, Met. Soc. AIME, Warrendale, PA, 1984, p.685.
108. G. R. Speich, L. J. Cuddy, C. R. Gordon and A. J. DeArdo: *Phase Transformations in Ferrous Alloys*, Eds. A. R. Marder and J. I. Goldstein, AIME, Warrendale, PA, 1984, p.341.

Index

abnormal grain growth 217
accelerated cooling 6, 273, 298
acicular ferrite 354
air patenting 336
American Petroleum Institute (API) specifications 289
anelasticity 29
annealed strip 317
API (American Petroleum Institute) specifications 289
Ashby-Orowan relationship 51, 53, 300
austempered ductile iron 336
austenite transformation 226, 227, 252
Avrami equation 235

bainite 226, 292, 354
bake hardening 324
Bauschinger effect 297
bendability 309, 313
British Standard specifications 2

carbide cracking 68, 76, 278, 315
carbon equivalent 352
cleavage fracture 61
coiling temperature 298
cold formability 302, 318
cold working 56
comparator chart 149
connecting rods 342
Considere criterion 302, 317
continuous annealing 13
continuous casting 11
continuous cooling transformation 227
continuous hot strip mill 298
continuous yielding 30, 67, 328
controlled rolling
coring in carbonitrides 131
cost benefits 1-4, 12, 13, 310, 336
crank shafts 336

decohesion 70
deformation bands 256
diffusion data 206
deoxidation 13, 313
deoxidation potential 315
desulphurisation 6, 308, 310
discontinuous yielding 20, 320
dislocation atmospheres 31
dislocations 23
dispersion strengthening 48
dual phase steel 325
ductile - brittle transition 59
ductile fracture 69
ductile shelf energy 59, 292, 316

embrittlement vectors 63, 65, 274, 276
equivalent bar diameters 227
Euler's law 140

Feret diameter 153
ferrite side plates 354
filamental carbides 68
forgings 7, 336, 342
fracture strain 76
free nitrogen 62, 284, 338
friction stress 46

Gibbs-Thomson equation 202, 205
grain boundary precipitates 180, 183
grain coarsening temperature 218, 220, 345
grain growth 216, 164, 238
  curvature 167
  energy change 170
  inhibition 176
  topological 167
grain refinement 39, 176
grain shapes 146
grain size control 137
grain size measurement 148
grain topology 137

Griffith's equation 57

Hall-Petch relationship 40, 45
H-beams 7
heat affected zone 353
heat of deformation 234
Heyn intercept 150
Hillert-Staffanson equations 128
hot rolled plates 266
hot working 230

impact transition temperature 59
inclusions 5, 303
inclusions shape control 5, 305
ingot casting 2, 7
intercritical annealing 326
intergranular embrittlement 324
interlamellar spacing 337
internal friction 29, 35
interpass temperature 351
interphase precipitation 189
interstitial atoms 29
interstitial free steels 8, 319
iron - iron carbide equilibrium 215
isothermal transformation 226

killed steels 2

lamellar tearing 5, 304
laminar separations 292
Larsen-Miller parameter 198
lattice parameters 108, 207
lead patenting 336
low temperature embrittlement 324
Luders bands 20, 320
Ludwik equation 21
Ludwik-Hollomon equation 22

M-A constituent 297
manganese titanate 356
martensite 227, 326
maximum uniform strain 22, 302, 327
mean areal intercept 155, 158
mean linear intercept 150, 152, 159, 161
medium and high carbon steels 336
microalloyed steels
  development of 2
  discovery of 1
molar volumes 207
mutually exclusive compounds 103

normalised plate 280
normalising 213

orientation relationships 189, 191
Orowan equation 50, 53
Orowan-Irwin equation 58
Ostwald ripening 201, 243, 348
oxides 12, 314, 316, 355, 356

particle coarsening 287
particle spacing 52, 193, 287
patenting 336
pearlite colony size 338
pearlite dilution 340
Peierls-Nabarro forces 26
Peierls stress 28
pinch-passing 320
pipelines 6, 304
planimetric measurement 151
plastic anisotropy 318
plastic instability 22, 327
polygonal ferrite 228, 354
precipitation in austenite 186
precipitation hardening 199
precipitation kinetics 132
preheat temperature 351

random second phase 178, 180
rare earths 10, 306
reaustenitisation 215
recrystallisation
  dynamic 232
  kinetics 237, 241
  meta-dynamic 237
  static 234, 235, 245
  temperature 247
recrystallisation controlled rolling 251
refractory materials 314
relative plasticity 305

Schlegel diagram 139
secondary recrystallisation 217
secondary steel making 13, 314
semi-killed steel 2
shear stress 27
slip 26
Snoek peaks 34
solid solution strengthening 28
solubility
  of aluminium nitride 87
  of carbon in ferrite 319
  of carbo-nitrides 108
  of complex carbo-nitrides 123

of manganese sulphide 312
of niobium carbide 97, 322
of niobium nitride 91
of titanium carbide 99, 322
of titanium carbo-sulphide 323
of titanium nitride 92
of titanium sulphide 323
of vanadium carbide 95, 322
of vanadium nitride 89
solubility product 82
solute strengthening coefficients 36
springback 302
steelmaking 11
steering linkages 342
stoichiometric ratio 84
strain 20
strain age embrittlement 321
strain age hardening 321
strain ageing 321
strain induced precipitation 187
stress 20
stress state 75, 304
stretcher-strain markings 320
structure-property relationships 19
stub axles 342
sub-grain precipitation 242
sub-grain strengthening 290
sulphides 77, 199, 305, 312

Taylor factor 26
tensile strength 1, 327
thermal severity 351
Thomson-Freundlich equation 202, 205
titanium nitride technology 7, 345
titanium oxide 355
toughness 57
transport vehicles 9
triaxiality 292

U-O-E pipes 297

vacuum carbon deoxidation 13, 316
void coalescence 73
void growth 69

weldability 352
weld heat imput 351
welding 3, 349
Widmanstätten ferrite 354
work hardening 21, 233, 319, 328

yield strength 19

Zener equation 178
Zener-Hollomon parameter 233, 236
Zener pinning 176